fluctuations along the crystal in the presence of a 400-mT HMF—was also obtained by Iino et al. [77] in a 200-mm CZ silicon growth configuration.

Analyzing the carbon and boron distribution in the LEC growth of GaAs, Terashima et al. [78] obtained a decrease of their concentration when an HMF field was applied. This decrease was correlated with a decrease in the amplitude of temperature fluctuations. The axial distribution of carbon was found to be much more uniform in the presence of an HMF of approximately 130 mT, which suggests an increase in the carbon segregation coefficient toward unity.

In one of the first theoretical studies on the influence of HMF on the distribution of the solute in a crystal, Kobayashi [32] demonstrated that the forced convection due to the rotating crystal is not affected by the magnetic field and that the effective distribution coefficient will approach, with an increase of the HMF, the value given by the BPS theory obtained from the value of the equilibrium distribution coefficient as a result of the suppression of thermal convection. In contrast, a VMF suppresses the forced convection and generates an effective distribution coefficient close to unity with an increase of the VMF intensity.

The influence of the HMF on oxygen distribution was analyzed by Ravishankar et al. [35] and Iino et al. [77]. It was demonstrated that the oxygen concentration decreases with an increase of the HMF strength to 150 mT and remains almost unchanged for higher values. This behavior can be a consequence of the melt flow, which prevents the oxygen-rich melt in the crucible bottom from reaching the S–L interface, as well as of the Marangoni convection, which is not damped as in the case of VMF and increases the evaporation loss of SiO.

Numerical models can give a more complex view of the oxygen distribution under an HMF. Kakimoto and Ozoe [71] have shown the limit of the BPS theory due to the intrinsic inhomogeneity of oxygen distribution in the melt under HMF. The main reason is the oxygen evaporation—it generates an inhomogeneous distribution of oxygen on the surface in contrast with boron and phosphorus, which are distributed almost homogeneously at the top of the melt and at the S–L interface. Collet et al. [75] developed a complex numerical model to analyze the inhomogeneities generated by the real for of the HMF.

23.3.2.2 Bridgman Methods and Vertical Gradient Freeze

Utech and Flemings [19] found that, similar to VMF, an HMF oriented along the crucible axis also dampens the temperature fluctuations in the melt and eliminates the dopant striations in HB growth of tellurium-doped indium antimonide crystals.

By applying an HMF in the VB growth of indium antimonide, Kim [79] showed that the random temperature fluctuations in the melt turn into periodic oscillations for an HMF intensity between 92 and 142 mT and are completely suppressed for an HMF above 170 mT. In the last case, a striation-free crystal growth was achieved.

Sen et al. [80] used an HMF in a VB configuration for the growth of indium–gallium antimonide. They show that an HMF of 400 mT produced a strong decrease in the

density of grain boundaries and of twin boundaries; they correlated these effects with the reduction of temperature fluctuations. In the VB growth of HgCdTe under an HMF in the range of 200–500 mT, Su et al. [81] showed an abrupt decrease in the mole fraction of CdTe when the magnetic field was applied.

Lan et al. [50] developed a three-dimensional numerical model to study the influence of an HMF on the flow and segregation in a VB setup for gallium-doped germanium. They demonstrated that the damping by HMF is more effective than by VMF and that the axial segregation can be pushed to the diffusion-controlled limit much more easily in the case of HMF. On the other hand, the radial solute segregation is large and highly asymmetric due to the nonuniform local dopant mixing caused by the melt flow. In a further study, Lan and Yeh [82] proposed an ampoule rotation together with the application of an HMF in order to improve the dopant nonuniformity. Today, HMF is rarely used in Bridgman or VGF configurations and is less investigated in comparison with a VMF.

23.3.2.3 Floating Zone

Kimura et al. [83] were the first to study the effects of an HMF on the FZ melting of gallium-doped silicon. They found that an HMF of 180 mT causes a significant reduction in fluid motion and the striation pattern is rendered more regular and orderly. In another study, Robertson and O'Connor [84] showed that a higher HMF of 550 mT has a strong effect on the growth interface shape, the Ga distribution, and the crystal morphology. The striation etch pattern reveals a reduction in the concavity of the growth interface when the HMF is present and the crystal is rotated. For nonrotating crystals, the HMF breaks the symmetry and the cross-section of the crystal has an elliptical form, with the major axis aligned along the magnetic field direction. Oscillations in dopant concentrations have been observed and the effective segregation coefficient of the gallium was found to increase in the presence of the HMF as a consequence of the increase of the diffusion boundary layer thickness.

Similar effects were seen in FZ growth of GaAs (6-mm diameter) [63] with the striations suppressed under an HMF of 60 mT. In a microgravity GaAs FZ experiment, Herrmann and Müller [85] employed an HMF configuration to damp the thermocapillary convection. Although the HMF used was nonuniform due to the equipment constraints, a significant reduction of the amplitude of the concentration fluctuations was found.

23.3.3 Cusp-Shaped Magnetic Field

VMF and HMF have both favorable and unfavorable effects on the melt convection in different crystal growth methods. Although VMF and HMF significantly damp the melt flow, they have also undesirable effects: VMF degrades the uniformity of the radial dopant distribution and HMF breaks the geometrical symmetry of the melt flow. A CMF, which is generated by a pair of Helmholtz coils operated in opposed current mode

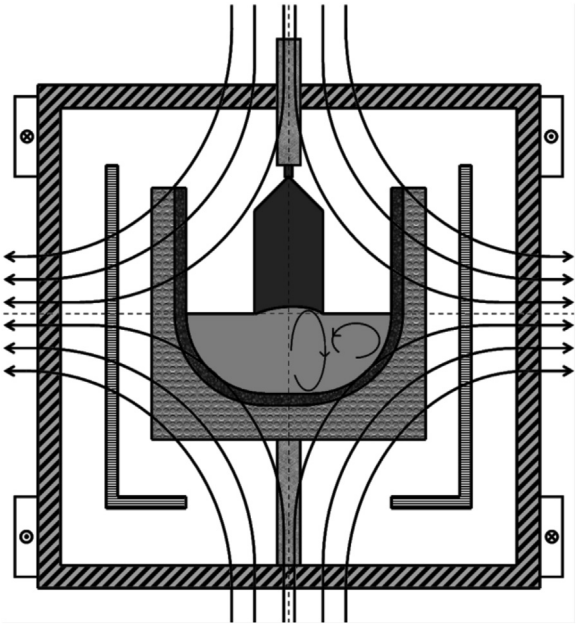

FIGURE 23.6 Schematic representation of a cusp magnetic field configuration.

(Figure 23.6), was designed to damp undesirable flows while minimizing the damping of desirable flows. Such a field configuration uses the advantage of an HMF to preserve a radial flow in the S–L interface plane while using the advantage of a VMF to dampen the turbulent convection in a large fraction of the melt. It is axially symmetric and perpendicular to the whole melt–crucible interface and it decreases the boundary layer at the crucible wall. In fact, there is a zone under the crystal free of magnetic field, while the crucible walls are exposed to large field strengths. In comparison to the VMF and HMF, which have just one control parameter (the field strength), the CMF can be operated with two control parameters—the strength and the relative position of the CMF center to the S–L interface.

The maximal intensity of the CMF used in applications is in the range of tens of mT, in comparison to the intensities of VMF and HMF, which are in the range of hundreds of mT. The CMF is used mainly in CZ applications. There are also some reports on applications in the FZ technique.

23.3.3.1 Czochralski Method

The first application of a CMF in a CZ configuration was reported independently by Hirata and Hoshikawa [86] and Series [87]. They showed the potential of the CMF to realize localized control of thermal convection at the melt–crucible interface, independent of that at the free melt surface. The S–L interface was located in the symmetry plane between the two coils and was maintained in this position by continuously moving the

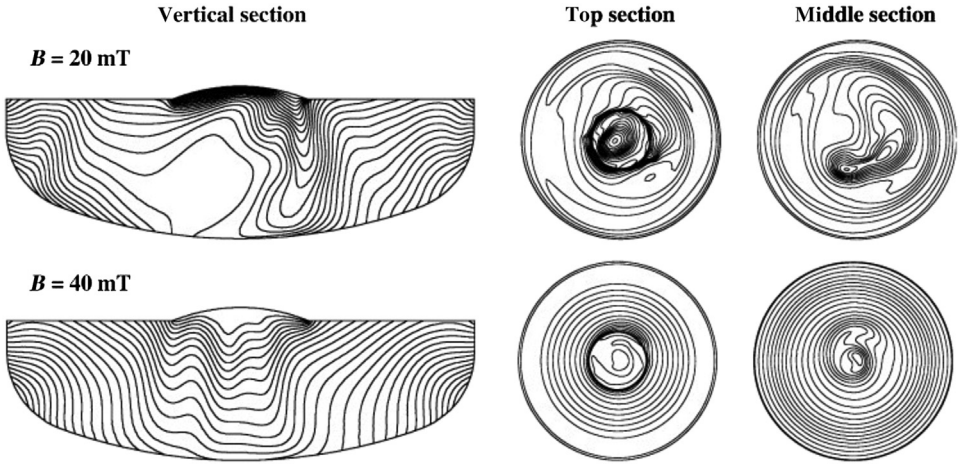

FIGURE 23.7 Isotherms in a vertical section and two horizontal sections placed at the free surface of the melt (top section) and at half height of the melt (middle section), for two magnetic field intensities. Isotherms step is 1.5 K. *From Ref. [91], with permission from Elsevier.*

crucible upwards to compensate for the decrease of the melt height by the crystal growth. The main effects of the CMF on the melt flow are summarized in this section.

Temperature field and fluctuations. The mechanism by which the CMF configuration affects the melt flow was investigated both by numerical modeling and experimental investigations [27,88–93]. All of these contributions showed that the stabilizing effect on the flow and temperature field near the crucible wall (where the applied field is the highest) is stronger than under the crystal. This effect can be clearly seen in Figure 23.7, where the calculated temperature field for two intensities of the magnetic field at a fixed time in a vertical section and two horizontal sections are presented. The stabilizing effect is stronger with the increase of the magnetic field. Experimental measurements and numerical simulations performed by Hirata and Hoshikawa [89] for the CZ growth of silicon crystals showed that, in a crucible with a 15 cm diameter, the amplitude of the temperature fluctuations under the crystal decreases significantly when a CMF field is applied (from 2.8 K with no magnetic field to 0.5 K). Performing measurements and numerical simulations in a larger crucible with a diameter of 36 cm, Vizman et al. [91] found that under the crystal remains a higher amplitude of temperature fluctuations, of about 10 K, when a CMF is applied. This can be because the zone under the crystal is less influenced by the magnetic field. The same effect was found numerically by Savolainen et al. [92] in a 50 cm diameter crucible. Liu et al. [93] carried out a numerical comparison between HMF and CMF and found that, due to the different damping mechanisms, a CMF provides a stronger suppression effect of thermal instabilities than an HMF, for the same magnetic field intensity.

Watanabe et al. [94] investigated the temperature fluctuations under the crystal in a small crucible (7 cm in diameter) for different positions of the CMF center relative to the

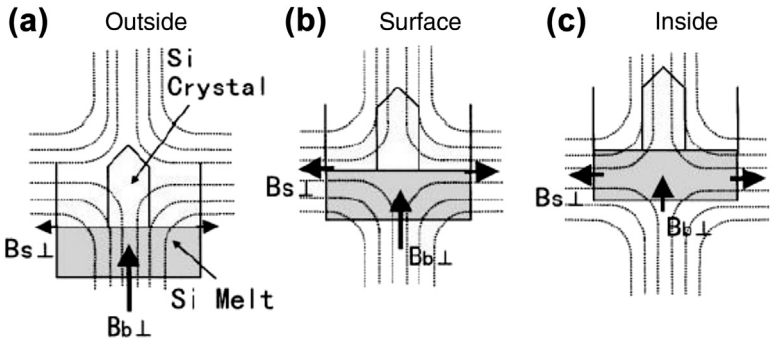

FIGURE 23.8 The CMF configurations: (a) the center of the CMF positioned 20 mm above the melt-free surface (outside), (b) the center of the CMF positioned at the melt-free surface (surface), and (c) the center of the CMF positioned 20 mm below the melt-free surface. *From Ref. [94], with permission from Elsevier.*

S–L interface (outside, surface, and inside; see Figure 23.8). They found a significant amplitude of temperature fluctuations below the crystal for the outside and surface CMFs, but almost no fluctuations for the inside CMFs configuration. Contrary to this result, in a much larger crucible of 50 cm diameter, Savolainen et al. [92] showed by numerical modeling that there is no significant difference between surface and inside CMF configurations.

Dopant distribution. Because CMF has a minimum influence on the melt convection near the S–L interface, Series [87] demonstrated experimentally that the axial phosphorus and carbon incorporation in the crystals was similar to the nonmagnetic crystals. The radial uniformity of the dopants was much higher in comparison with VMF crystals.

Hirata and Hoshikawa [86] found that the nonrotational dopant striations were reduced by the CMF and rotational striations were not detected, probably due to the axially symmetric damping of the melt convection. This is superior to the conventional HMF or VMF, in which nonrotational striations are reduced but rotational striations are often increased.

Oxygen incorporation is another area where CMF plays a beneficial role. Hirata and Hoshikawa [95] analyzed the oxygen distribution in the silicon crystals grown by the CZ method under a CMF and found the following characteristics:

- The axial homogeneity of oxygen concentration is improved by the CMF in comparison with no magnetic CZ, similar to that obtained in the HMF case.
- The radial homogeneity improved also in comparison to the case with no magnetic field, as an effect of the damping of the thermal convection and the centripetal flow at the free surface.
- Oxygen concentration decreases steadily with the increase of the CMF strength due to the damping of the convection adjacent to the melt–crucible interface, whereas those adjacent to the free surface do not change as much. Thus, the crucible dissolution (which is the oxygen source) decreases relative to the rate of oxygen evaporation at the melt free surface.

- The oxygen concentration in the crystal can be controlled by the field strength at constant, high crystal, and crucible rotation rates. This is very different from the HMF or VMF cases, which require changing the crucible or crystal rotation rates for oxygen concentration control.

Sim et al. [96] demonstrated that the growth of large single silicon crystals of 200 mm in diameter with extremely low oxygen concentration and with a radial gradient less than 2% is possible with the CZ method under CMF. The influence of the relative position of the CMF center to the S–L interface on the oxygen distribution was investigated by Watanabe et al. [94]. They found that the growth striations, which were related to the fluctuations of the oxygen concentration, were clearly visible for the outside and surface CMF configurations but were not observed for the inside configuration (Figure 23.9). Numerical models have also been developed to understand the oxygen transport in CZ silicon growth under a CMF [90,97].

23.3.3.2 Floating Zone

No experimental data are available in the literature for the application of a CMF in FZ growth. Based on numerical modeling, Morthland and Walker [98] suggested that a CMF can influence the radial distribution of dopants, creating large field strength near the S–L interface and a small angle between the local field vector and the normal at each point on the free surface.

Lan [58] showed that, because the coils are quite far from the sample, extremely large currents are required to generate a sufficient field strength in the melt, comparable with a VMF. Unexpectedly, the weak flow in the core region affects the dopant redistribution and results in an even larger radial segregation in comparison with VMF or CZ growth. In a further study, Lan and Liang [99] investigated a superposition of CMF, a rotation of the

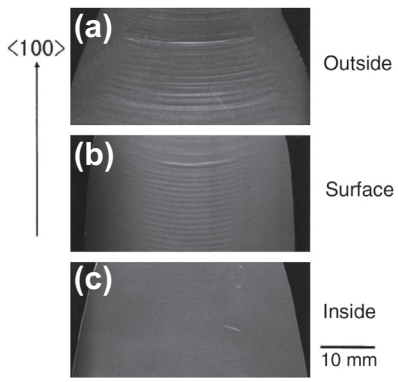

FIGURE 23.9 Growth striations in the grown crystals taken by the X-ray topograph method: (a) for the outside CMF configuration, (b) for the surface CMF configuration, and (c) for the inside CMF configuration. *From Ref. [94], with permission from Elsevier.*

feed rod, and a counterrotation of the crystal. They found that the mixing in the core region seems to be better and, as a result, the dopant uniformity is improved.

23.4 Effects of Nonsteady Magnetic Fields

The interest in the application of nonsteady magnetic fields in crystal growth of single crystals has increased in recent decades, mainly because of their potential to influence heat and mass transfer through the well-defined flow generated by relatively low nonsteady induction forces. A simplified analysis performed by Rudolph and Kakimoto [11] estimated that the required magnetic induction necessary to counteract a buoyancy force density of $150/\mathrm{Nm}^3$ is $B \approx \sqrt{150/\sigma\pi f L} = 1.4\,\mathrm{mT}$ for the frequency $f = 50\,\mathrm{Hz}$ and characteristic length $L = 0.4\,\mathrm{m}$. This value is almost one order of magnitude lower than in the case of steady magnetic fields (see Section 23.2). From a technological point of view, this means smaller size and lower costs for the magnets. The main types of nonsteady magnetic fields used in crystal growth are alternating magnetic field (AMF), rotating magnetic field (RMF), and traveling magnetic field (TMF). Sometimes, nonsteady magnetic fields are used in combination with steady magnetic fields.

An RMF was first used by Pfann and Dorsi [100] in the zone melting process. Mullin and Hulme [101] were the first to use an AMF in a zone-refining process; they obtained an enhanced purification rate due to the force melt mixing.

23.4.1 Rotating Magnetic Field

An RMF is basically generated by a three-phase asynchronous electrical engine (sketched in Figure 23.10) and induces currents in a conducting melt. The wires of the winding forming three coils are integrated into slots of the iron sheet package. Connecting these coils to a three-phase power supply yields a rotating transversal magnetic field in the horizontal plane (Figure 23.10).

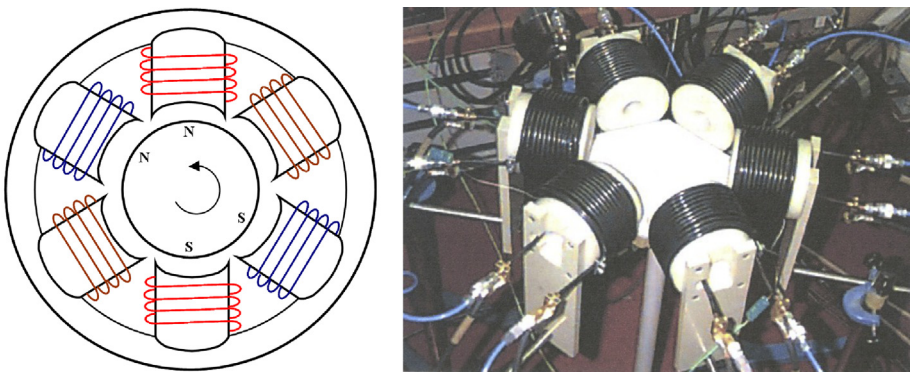

FIGURE 23.10 Sketch of the stator of an asynchronous electric engine. *Photo from the thesis of P. Dold.*

Applied to a melt, an RMF induces an azimuthal electromagnetic force, which generates mainly an azimuthal flow. A secondary meridional flow also arises due to the imbalance of the centrifugal force and the radial pressure gradient in the boundary layer in the vicinity of the horizontal container walls. This imbalance is known as Ekman pumping [102], and the rate of this secondary flow is about one order of magnitude smaller than the primary, azimuthal flow [12].

In a survey on RMF applications in the process of bulk single crystal growth, Gelfgat [103] distinguished four flow regimes that sequentially occur in the melt under an RMF:

- Small values of an RMF induce a laminar flow regime with a structural symmetry of the azimuthal and meridional flows.
- A further increase in the field induction generates a stationary nonlinear flow regime.
- If the RMF induction is higher than a critical value, an oscillating flow regime occurs in the melt. It is strongly nonlinear and nonstationary.
- A further increase of the RMF induction generates a quasi-stationary stable flow regime in the melt.

Complex stability analysis of the interaction between the natural convection and RMF were carried out by Friedrich et al. [104], Kaiser and Benz [105], and Grants and Gerbeth [106].

Many model experiments have been developed over time in order to get a fundamental understanding of the effect of an RMF on the melt flow and to evaluate the numerical models. In these experiments, different low Prandl number fluids were used: mercury [102,107], gallium [108–110], or InGaSn [111]. Dold and Benz [109] and Friedrich et al. [104] investigated the stable and the unstable Benard configuration and showed that RMF can be used to significantly dampen the temperature fluctuations caused by time-dependent, buoyancy-driven forces. A more complete review on these experiments and on other RMF applications can be found in Ref. [12]. The effect of an RMF on the growth process was studied in bulk crystal growth methods, such as VB, HB, VGF, CZ, and FZ, as discussed in the following sections.

23.4.1.1 Czochralski Method

The first application of an RMF in a CZ configuration was reported by Shaskow and Shushlebina [112]. They showed that the convective temperature fluctuations in the melt were reduced and the dopant inhomogeneities decreased when an RMF was applied. Later, just a few real growth experiments were reported in literature. Hoshikawa et al. [113] have grown a 100 mm diameter boron-doped silicon crystal with a CZ puller, where the graphite heaters were connected to a three-phase current source. Their results show that a low-oxygen-content silicon crystal can be obtained when the rotation of the crucible, the seed crystal, and the melt rotation imposed by RMF are in the same direction. Zhou and Huang [114] and Spitzer [115] numerically investigated a similar configuration and qualitatively obtained the same effect. Kakimoto [116] demonstrated

that the secondary flow in a meridional plane enhances heat and impurity transfer from the crucible wall to the S–L interface.

Another growth experiment was performed by Brückner and Schwerdtfeger [117]. They developed a modified Czochralski technique to pull single crystals without mechanical rotation of the crystal and of the crucible by bringing forth the controlled convection in the melt solely by RMF. Crystals of copper, germanium, and silicon were grown successfully with this technique.

Grants and Gerbeth [118] experimentally studied the phenomenon of temperature field stabilization by an RMF in a simplified physical low-temperature model of a medium-size Czochralski facility, with a 140 mm diameter crucible filled with gallium melt. The stabilization occurs as the result of a flow transition from a large-scale buoyancy driven to a small-scale magnetically driven turbulence. The amplitude of temperature fluctuations at the side wall was suppressed by a factor of five immediately after the flow transition and decreased further as the strength of the RMF increased. The fluctuation damping was even more pronounced in the core of the flow, where a factor of 50 may be reached. They also found that the stabilizing effect disappears in a high-frequency RMF. Based on these results and using a scale-up evaluation, Grants and Gerbeth [118] estimated that an RMF with an amplitude of 0.95 mT at 50 Hz frequency is sufficient for a significant suppression of the temperature fluctuations in an LEC GaAs crucible with a diameter of 300 mm.

23.4.1.2 Bridgman Methods and Vertical Gradient Freeze

RMF was successfully applied for the first time in gallium-doped germanium crystal growth experiments by Dold and Benz [119] in the VB technique and by Friedrich et al. [120] in the VGF technique. Both groups reported a change in the S–L interface curvature, from concave to a slight W-shape when an RMF is applied, due to the secondary convective motion. The axial macrosegregation did not seem to be influenced by the RMF because of a totally mixed regime. Friedrich et al. [120] also observed an increase of the radial dopant homogeneity. This behavior can be understood as an effect of the increased flow velocity in the vicinity of the interface, which led to a better mixing of the melt. Applying an RMF of 2 mT/50 Hz, Dold and Benz [119] found that the dopant striations due to the buoyancy convection are strongly reduced.

Si-doped GaAs crystal of 50 mm in diameter under an RMF were grown by Pätzold et al. [121]. Under the forced flow, a significant reduction of the bending of the concave interface was obtained and a W-shaped interface was observed at an aspect ratio of approximately 1.5. Lyubimova et al. [122] performed numerical modeling for VB-grown GaAs and also showed that higher magnetic field intensity results in the S–L interface shape change from concave to W-shaped.

RMF influence on the VB growth of gallium-doped germanium crystals was investigated by Volz et al. [123]. The RMF also has a marked effect on the interface shape in this case, changing it from concave to nearly flat as the RMF strength is increased. It was also shown that time-dependent flow instabilities occur when the critical magnetic Taylor

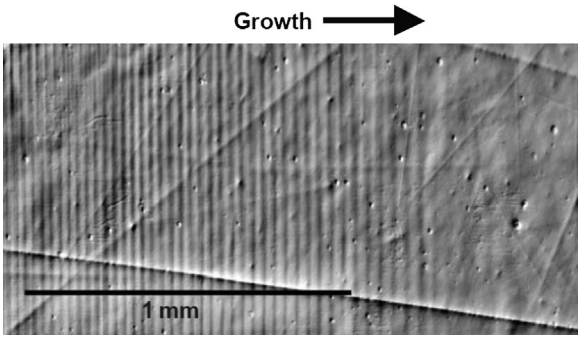

FIGURE 23.11 Transition from unstable to stable flow in VB growth of Ga-doped Ge for a critical Taylor number of 6×10^4. *From Ref. [123], with permission from Elsevier.*

number is exceeded; this can be observed by noting the appearance of striations in the grown crystals (Figure 23.11). In a similar experiment, Bellmann et al. [124] found that the accumulation of the Ga solute near the center of the melt during growth under natural buoyancy is reduced by the electromagnetically induced flow.

Using numerical simulations to study the VGF growth of 2-in InP crystals, Schwesig et al. [125] suggested that an RMF offers no possibility to minimize the strong concave curvature of the interface very close to the crucible wall. By means of numerical modeling, Wang et al. [126] found that, in VGF submerged heater growth, RMF seems to be not as efficient as a combination of an axial magnetic field and an electrical current. Bellmann et al. [127] performed a global numerical study of Ga segregation in the VGF growth of Ga-doped Ge under the influence of an RMF. Galindo et al. [128] built a low-temperature flow experiment using a GaInSn alloy and a numerical model to study the complex fluctuation flow patterns in a combined VGF-type buoyancy and RMF flow.

23.4.1.3 Floating Zone and Traveling Heater Method

Because of the high velocity in the melt of approximately 15 cm/s [105], a higher intensity of the RMF is needed in the FZ process to counteract the Marangoni convection compared to the buoyancy convection in VB/VGF. Using an RMF field of $B = 7.5$ mT/50 Hz, Dold et al. [129] obtained an FZ silicon crystal of 14 mm in diameter with substantially reduced dopant inhomogeneities. Their main results were as follows:

- The intensity of the dopant nonuniformities is strongly reduced by the RMF.
- The fluctuations of the dopant concentration are reduced under the influence of the RMF.
- Axial macrosegregation decreased upon application of the magnetic field.
- A symmetrization of the S–L interface shape was observed in the RMF growth and the interface curvature is slightly flatter.

The effect of the intensity reduction of the dopant striations, which are caused by time-dependent Marangoni convection with increasing RMF, was also observed by Fischer et al. [110] in FZ-GaAs. Higher diameter equipment, relevant for industrial Si-FZ,

have not been experimentally investigated in literature. Raming et al. [130] numerically investigated an Si-FZ configuration of 100 mm diameter and suggest that an RMF can lead to just a slightly improved (more homogeneous) macroscopic radial resistivity profile, whereas microscopic axial resistivity oscillations will increase. Liu et al. [131] have applied RMF in the FZ growth of oxide crystals ($Bi_{12}SiO_{20}$) and reported that an applied RMF of 25 mT/50 Hz is efficient enough to control the oxide melt flow during the growth process, and the quality of as-grown BSO single crystals is obviously improved. This effect was explained as being generated by the Lorentz force, which is created by an interaction between the magnetic field and electric current in the melt due to the ionic electrical conductivity of the oxide melt.

A linear stability analysis for the thermocapillary convection in the floating zone process with an RMF was performed by Walker et al. [132]. Other numerical investigations of the melt flow in the FZ were performed by Ma et al. [133] and Yao et al. [134].

Beneficial effects of RMF were also observed in the traveling heater method growth of CdTe and (Hg, Cd)Te crystals by Salk et al. [135] and Senchenkov et al. [136], who performed RMF experiments in an ampoule designed for the PHOTON 7 mission, both in gravity and microgravity conditions. It was observed that RMF generates a stable steady flow in the Te-zone, improving the radial and axial distribution of the Te inclusions.

23.4.2 Alternating Magnetic Field

From a technical point of view, an AMF can be achieved more simply than an RMF or a TMF, by only a single coil. Only a few reports can be found in the literature on the application of AMF in crystal growth processes, much less and not as systematic as in the case of RMF or TMF.

The first low-temperature model experiment relevant for a CZ configuration was developed by Wetzel et al. [137]. They used eutectic InGaSn as a model melt in a 20-in standard CZ crucible. The equipment was supplied with two types of AMF inductors: a bottom AMF and a side AMF (see Figure 23.12). A numerical approach was validated against the experimental results and used in the flow analysis. It was found that the AMF generated by the side inductor causes a two-vortex structure in the outer melt region, but it leaves the inner region underneath the crystal almost unaffected. Because of the increased mixing, a lowered temperature and a widening of the isotherms in the outer region toward the crucible wall were observed. In the case of the AMF generated by the bottom inductor, a flow cell was observed in the outer region near the crucible wall, which was rotating opposite to the original buoyancy-driven convection. As in the case with an AMF side inductor, there was a significant decrease in the temperatures in the outer melt region. The same behavior was obtained numerically by Virbulis et al. [27] in a real silicon CZ puller for a 200 mm crystal and 24-in crucible.

Mercier and Nishizawa [138] numerically studied the influence of the AMF on the solution growth of SiC from silicon melts. Due to a higher temperature difference in the

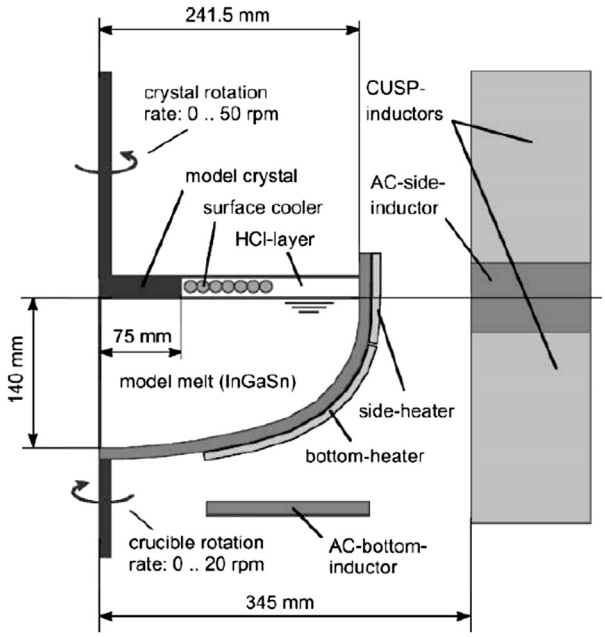

FIGURE 23.12 Laboratory CZ setup: main parts and dimensions. *From Ref. [137], with permission from Elsevier.*

melt, the buoyancy force density is almost seven times higher than in a classical CZ. Therefore, even a higher Lorentz force generated by an AMF cannot totally control the melt convection. However, at high Lorentz force density, a bottom inductor, located below the melt, was seen to generate a more efficient pattern for the enhancement of the carbon transport from the dissolution area to the crystal growth front in comparison to a side inductor.

For an FZ configuration, Raming et al. [130] demonstrated by numerical modeling that an additional low-frequency AMF can lead to a more forced convection in the molten zone, therefore resulting in better mixing of the dopant concentration field. This leads to a more homogeneous macroscopic radial resistivity profile, whereas axial microscopic resistivity oscillations may increase too.

A more systematic study was carried out to investigate the influence of an AMF on the VB growth of (Ga, In)Sb by numerical modeling [139,140] and growth experiments [141]. From transient numerical analysis, it was found that the axial and radial segregation can be maintained at lower values during the whole growth process if the magnetic field intensity is progressively increased during the solidification. In this case, the interface deflection was also maintained at reasonably constant values. In the growth experiment [141], a polycrystalline, crack-free, and nondestabilized (Ga,In)Sb ingot was obtained under a 2 mT AMF. The results indicated that the S–L interface deflection decreases with the increase of AMF and that the radial segregation was almost constant along the ingot, which confirm efficient mixing of the melt near the S–L interface. In a later study, Mitric

and Duffar [142] proposed a theoretical model to estimate the optimal parameters of the AMF to overcome the solutal effect. Based on the analytical estimations, a magnetic field of 3 mT and 5000 Hz has been found to be optimal for efficient mixing. Although the AMF seems to be very efficient for effective mixing (as it is also in metallurgy), more growth experiments are necessary to prove if AMF is favorable for crystal growth.

23.4.3 Traveling Magnetic Field

Lately, melt flow control by means of TMF has been one of the most active research directions in the optimization of crystal growth processes from melt. The TMF coil system consists of a number of coils, which are arranged vertically one over the other (Figure 23.13). The coil system is fed by an electrical current characterized by amplitude, frequency, and phase shift. The resulting magnetic field travels either upward or downward. The magnetic induction B can be described as a wave model with wavelength $\lambda = 2\pi/k = nh$ (with k being the wave number, n being the number of coils, and h being the distance between coils). A conventional TMF arrangement consists of three coils in a delta connection. More variability can be achieved when the coils are coupled in a star connection. In this case, each coil can be supplied separately, and frequency and phase shift can be varied over a wide range [14].

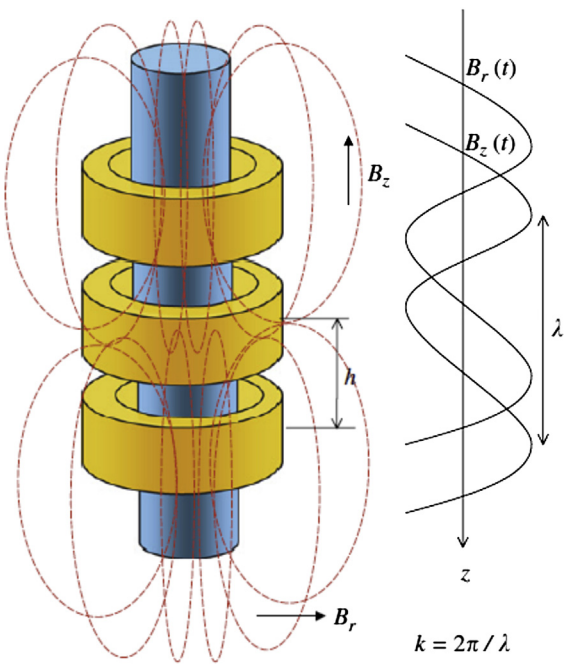

FIGURE 23.13 The principle of a traveling magnetic field using three axially parallel coils. Bz and Br are the axial and radial magnetic field components, respectively. $\lambda = 2\pi/k = nh$ is the magnetic wavelength, where n is the number of coils, h is the distance between coils; and k is the wave number. *From Ref. [14], with permission from Elsevier.*

The advantage of a TMF is the creation of a Lorentz force, which acts as a body force in the direction of gravity and directly induces a meridional flow. The generated Lorentz force can be adjusted not only to counteract the buoyancy force but also to create conditions similar to varying levels of gravity. Because of the melt aspect ratio variation (due to the solidification), the critical magnetic Taylor number, indicating the transition from stationary to time-dependent flows, also varies. Normally, the critical magnetic Taylor number increases with a decrease in the aspect ratio.

The first theoretical and experimental studies on TMF were reported by Gelfgat et al. [143] and Ramachandran et al. [144]. Complex stability analysis of the thermally stratified melt flow under TMF has been carried out by Grants and Gerbeth [15], Gelfgat [145], and Grants et al. [146].

The design of magnet configuration is one of the most important issues to make the control of melt flow by magnetic fields attractive for industrial applications. Usually, the magnets are positioned outside the growth chamber; therefore, they should produce a much higher induction force than the one actually needed for convection control. A significant economical effect can be achieved when the magnetic field generator is placed close to the melt. A promising idea for industrial applications is to couple the generation of heat and the magnetic field in a so-called internal heater-magnet module. Such a configuration was first used by Hoshikawa et al. [113] to produce an RMF in a CZ silicon growth experiment.

A novel special configuration of a heater-magnet module based on a hole-cylindrical body with an upwards-winding slit for the generation of TMF was proposed by Rudolph [14] and Klein et al. [147] (Figure 23.14). This idea was successfully implemented in different types of industrial-scale crystal growth configurations: LEC growth of 3-in GaAs crystals [148], VGF growth of 4-in Ge crystals [149], and G5 multicrystalline Si crystallizer of 640 kg Si-ingots [150].

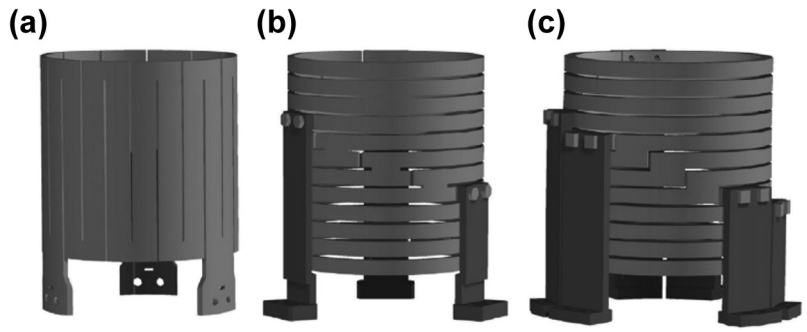

FIGURE 23.14 Layouts of three graphite heaters for LEC growth of semiconductor compounds without (a) and with TMF (b and c). The nearly identical dimensions facilitate the replacement in one and the same puller vessel. (a) Conventional "picket fence" (meander) heater fed by three-phase current in delta connection. (b and c) Magnet-heater modules with staircase-shaped current path, subdivided in three sections for TMF generation by feeding with three-phase current of given phase shift in delta (b) and star connection (c). *From Ref. [14], with permission from Elsevier.*

In the following sections, details of the use and the effect of TMF are discussed for the different crystal growth methods from melt.

23.4.3.1 Czochralski Method

The first attempt to use a TMF in a CZ method was made by Wetzel [151] in 2001. Since then, the influence of a TMF on CZ growth was studied mainly through numerical modeling and model experiments. One of the few reports on experimental results in the CZ growth of large silicon crystals was made by Tomzig et al. [152]. They showed that a nearly ideal uniform oxygen distribution along the grown crystals can be obtained, even better than under RMF and AMF conditions (see Figure 23.15).

Temperature fluctuations in a CZ-like configuration were studied both numerically and experimentally by Krauze et al. [76] in a model experiment in which an InGaSn eutectic with a 10.5 °C melting point was used. It was demonstrated that the corresponding electromagnetic force distributions do not depend on the velocity distributions in the melt and cause an intense and well-defined melt flow. Temperature fluctuations in the outer crucible region and radial temperature difference in the melt decrease with an increase of magnetic field intensity. This effect is stronger for TMF-down in comparison with TMF-up. In a later paper, Krauze et al. [153] presented and validated an improved numerical model based on an LES turbulence model.

More complex numerical models were used to study the influence of a TMF generated by a magnet-heater module. Klein et al. [147] performed numerical simulations in an LEC configuration with a 4-kg GaAs melt. They showed that TMF generated by a magnet-heater module significantly reduces the temperature oscillations with low

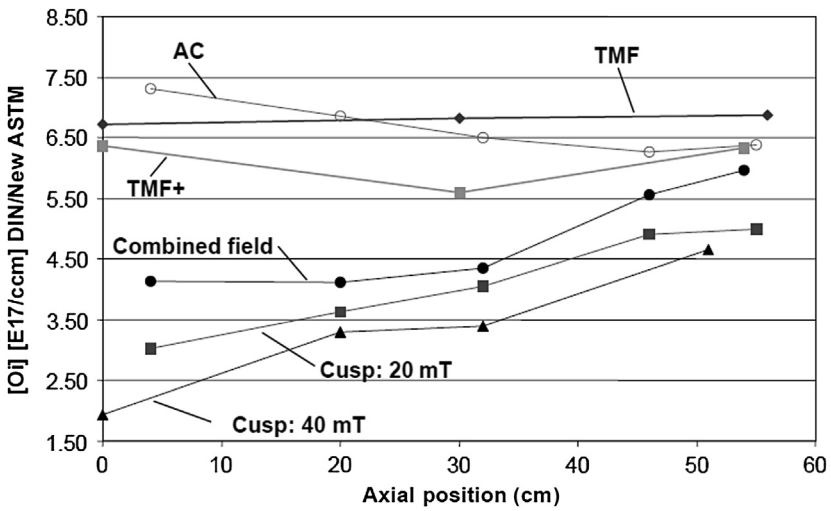

FIGURE 23.15 Axial oxygen concentration of 300-mm crystals grown with different magnetic fields: (a) AC: 6 mT, (b) TMF: 5 mT, (c) TMF+: 5 mT, (d) Combined field: cusp 20 mT/AC 6 mT, (e) Cusp 20 mT, (f) Cusp 40 mT. *From Ref. [152], with permission of Elsevier.*

frequency, contrary to a configuration with an external coil, where only a small positive effect could be shown [154]. The asymmetry effects induced by the magnet-heater design were investigated by Kasjanow et al. [155]. It was concluded that, for an LEC setup, these effects can be effectively graduated by crucible and crystal rotations. The first semi-insulating GaAs crystal grown by the LEC method using a TMF generated in a magnet-heater module was reported by Rudolph et al. [148].

The following correlations between as-grown crystal qualities and TMF parameters have been observed:

- A slight reduction of the peripheral interface concavity at low field frequencies
- A damping of nonsteady convection perturbations by stabilizing the stream stationarity within the melt, especially when high field frequencies are applied
- A lowering of the dislocation density by radial temperature leveling with a decrease of thermal stress, especially at low field frequency
- Enhanced transport of oxygen and boron releasing from boric oxide layer by TMF-induced high-speed vortices toward growing crystal, which increases the O and B incorporation but reduces the As content

For photovoltaic applications, Rudolph et al. [156] proposed a new pulling technology in a CZ puller for the growth of silicon crystals with both quadratic cross-sections and relatively low as-grown oxygen content. A stable low radial temperature gradient in the melt, in the range of 1–2 K/cm, was obtained by applying a special double TMF mode generated in a graphite magnet-heater ensemble consisting of three side coils around the crucible and two consecutive spirals below the crucible bottom. As a result, a silicon single crystal with a near-quadratic cross-section of $91 \times 91\ \text{mm}^2$ and length up to 100 mm was obtained. Miller et al. [157] performed 3D simulations of the melt flow in the configuration described above; they showed that the TMF as used in the experiments causes a strong vortex with a heat transport from the crucible's bottom to the crystal. This heat transport stabilizes the low-temperature gradient along the free surface and the stable growth of the silicon crystal with {110} facets becomes possible.

23.4.3.2 Bridgman Methods and Vertical Gradient Freeze

Taking into account two criteria for the optimization of VGF growth process—a nearly flat S–L interface and a minimization of the von Mises stress—Schwesig et al. [125] demonstrated by numerical analysis that a downward-oriented TMF has a beneficial influence on the quality of a 2-in InP crystal in contrast to an upward-oriented TMF. In the case of TMF-down, the deflection of the S–L interface as well as the maximum flow velocity is decreasing at small values of magnetic induction (<5 mT). At higher values of magnetic induction, the maximum flow velocity is increasing again and a W-shaped interface is observed. Time-dependent flow occurs at about 8 mT for all investigated aspect ratios. The von Mises stress at the S–L interface decreases significantly with increasing magnetic induction. Similar results were obtained by Lyubimova et al. [122] for GaAs and Yesilyurt et al. [158] for Ge crystals grown by the VB method.

A model experiment close to the conditions used for VGF crystal growth was developed by Lantzsch et al. [159]. The melt flow was analyzed in dependence on a dimensionless shielding parameter, defined as $S = 2\pi\mu_0\sigma f R^2$ (with σ being electrical conductivity, f being frequency, and R being the radius). For $S > 10$, the flow velocity was shown to decrease significantly, whereas almost no influence was found for a smaller shielding parameter. A more detailed analysis of this flow sensitivity is presented in Galindo et al. [160] and Niemietz et al. [161].

By numerical modeling, Frank-Rotsch et al. [162] studied the influence of a TMF generated by a magnet-heater module on the interface shape in an industrial-size VGF growth of a 4-in Ge crystal. It was found that a favorable interface with a slightly convex part in the central region was obtained by applying a downward-directed TMF with a drastically reduced frequency of 20 Hz. The optimal parameters predicted by numerical simulation were used to optimize a real growth experiment. As a result, for the first time, 4-in Ge single crystals were grown using the VGF technique in a TMF generated in a heater-magnet module [149]. Striations were also minimized by effective damping of the convection-driven temperature fluctuations.

Dropka et al. [163] numerically demonstrated that, due to the larger skin depths of the materials with lower electrical conductivity, a much larger current amplitude or a much higher frequency are necessary to generate a Lorentz force of desired intensity and distribution. A rigorous numerical model developed by Yeckel and Derby [164] has shown that TMF is only slightly effective at controlling the interface shape in an industrial-scale VGF of cadmium zinc telluride growth. This is because buoyancy overwhelms the Lorentz force throughout the melt for typical currents and frequencies of existing TMF systems.

Based on numerical modeling, Dropka and Frank-Rotsch [165] proposed a novel electromagnetic stirring approach using pulse-downward TMF generated by a magnet-heater module for a complete suppression of the instability in temperature distribution caused by asymmetry in furnace design. A downward TMF in an accelerated VGF growth of 4-in GaAs was used to improve the interface deflection toward a convex morphology during the fast growth [166].

23.4.3.3 Directional Solidification

The quality of the silicon ingot obtained by the directional solidification (DS) method is strongly dependent on the growth parameters that control the melt flow and interface shape. An active control of the melt flow is possible using magnetic fields and TMF is a strong candidate. This gives the crystal grower additional process parameters, such as the inductor current and the direction of the TMF. A deep understanding of the influence of the growth and process parameters on the crystallization interface is crucial for the optimization of the ingot quality. To understand the basic features of the melt flow in a DS-like configuration under a TMF, Dadzis et al. [167] developed a low-temperature model experiment and 3D time-dependent flow simulations. They reported that in a $10 \times 10\ \text{cm}^2$ crucible with GaInSn isothermal melt, an applied TMF generates a typical

toroidal flow structure with some extension into the melt corners. It was also shown that the flow structure is sensitive to the TMF geometry, melt height, and melt axis shift. A horizontal vortex was found to dominate the central part of the melt for smaller melt heights. In a later study, Dadzis et al. [168] investigated the same configuration but imposed an axial temperature gradient. It was reported that transitions from the flow regime dominated by the Lorentz force (high velocity and melt mixing) to the regime where the Lorentz force is balanced by the buoyancy forces (low velocity and melt mixing) may occur; these may have a critical characteristic in which the flow velocity drops and the temperature difference increases rapidly.

Dropka et al. [169], using 3D modeling, studied the influence of the TMF generated by a magnet-heater module on the silicon melt flow in an industrial-size crucible of $70 \times 70 \times 20\ \text{cm}^3$. It was shown that different field configurations (TMF-up or TMF-down) have a significant influence on the flow structure, and they can both damp and enhance the mixing (Figure 23.16). In a later study, Dropka et al. [170] investigated the mixing efficiency of a double-frequency TMF, generated within a magnet-heater module around a rectangular container with molten silicon. The double-frequency electromagnetic stirring is performed with a summary TMF composed of two oppositely directed longitudinally traveling fields with different strengths, frequencies, and

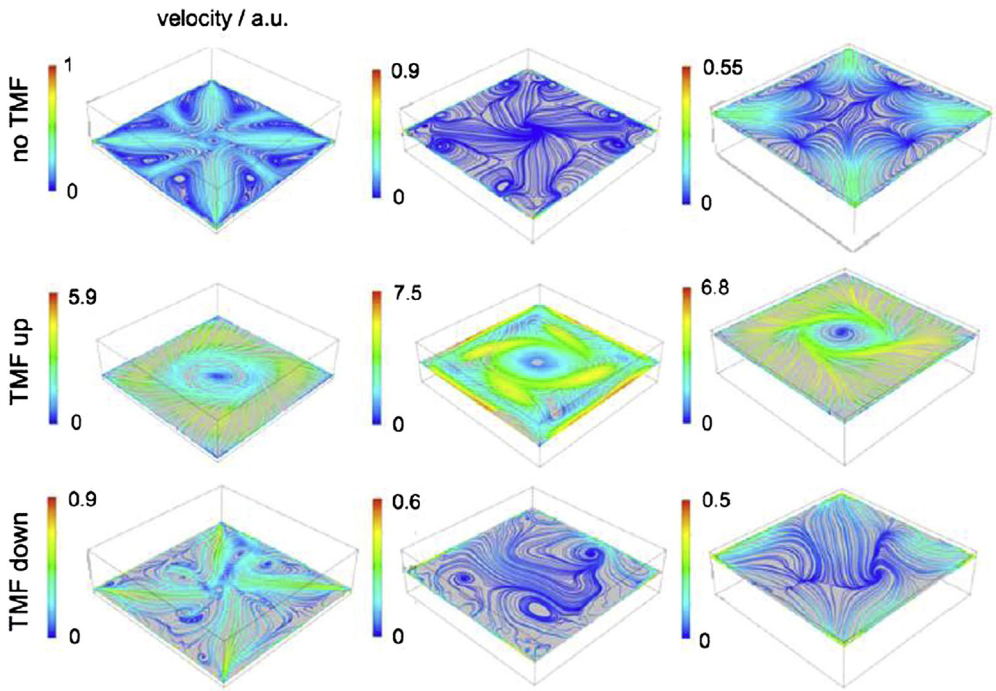

FIGURE 23.16 Velocity streamlines at different cross-sections in the melt: without TMF (*top*), TMF down (*middle*), and TMF up (*bottom*). Streamlines are the representation of the velocity field projected on the plane. *From Ref. [169], with permission from Elsevier.*

phase shifts. Such variations produce variable skin depths and horizontal velocity profiles. It was demonstrated numerically that, in comparison to the buoyancy-driven natural convection and single-frequency TMF, at double-frequency TMF mode the flow in the bulk volume is intensified without the generation of hazardous velocities in the peripheral region. This is beneficial for the melt mixing and general process purity. The same numerical model was used by Dropka et al. [171] to evaluate the efficiency of a novel electromagnetic stirring approach using a carousel magnetic field generated by a bottom magnet-heater module consisting of several spiral coils arranged horizontally around the vertical axis. It was found that, in comparison to the conventional sidewise electromagnetic stirring, the flow maximum is shifted from the peripheral region toward the melt bulk, increasing the stirring within the central region and thus decreasing the diffusion boundary thickness more effectively and uniformly.

Multicrystalline silicon ($22 \times 22 \times 13$ cm^3) grown under a TMF field generated by a magnet-heater module has been reported by Kießling et al. [172] (Figure 23.17(a)). It was demonstrated that TMFs can be used to influence the melt convection, reduce the thickness of the diffusion boundary layer, and adjust the shape and morphology of the S–L growth interface. The influence of the TMF orientation on the S–L interface shape was also analyzed. It was found that a TMF-up configuration generates a concave curvature of the S–L interface, whereas a TMF-down configuration generates a convex one

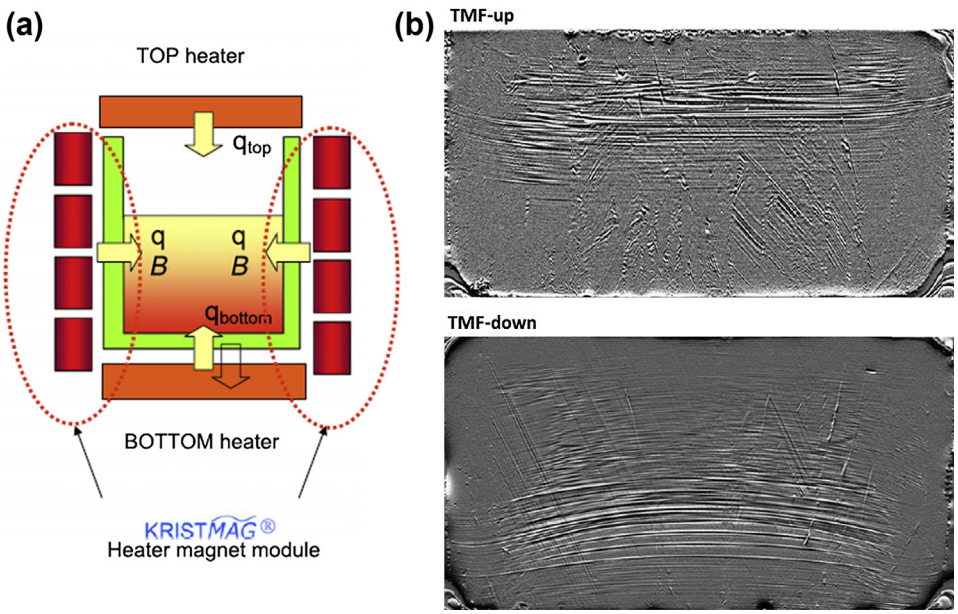

FIGURE 23.17 (a) Sketch of the DS growth arrangement for Si, showing top and bottom heaters and four coils of the side heater to produce TMFs. (b) Images of the S–L interface revealed from striation morphology analysis by lateral photo-voltage scanning on vertical cuts shows a concave curvature at the rim as a result of an applied TMF-up and a convex shape as a result of an applied TMF-down. *After Ref. [172], with permission from Elsevier.*

(Figure 23.17(b)). The same qualitative results were obtained in numerical simulations performed by Dadzis et al. [173] and Vizman et al. [174].

Kudla et al. [150] reported the successful growth of a G5 multicrystalline silicon (640 kg) in an industrial-scale crystallizer equipped with a magnet-heater module for the TMF generation. Effective melt mixing and precise control of the interface shape have been achieved using TMF, which resulted in a very homogeneous infrared (IR) transmission without second-phase inclusions in most of the solidified volume. Dislocation densities were relatively low and bunching was only rarely observed, resulting in overall high carrier lifetimes.

23.5 Combined Action of Various Types of Magnetic Fields and Electric Currents

Sometimes, more types of actions should be taken in the process of melt control to optimize the quality of the grown crystals, such as a reduction of temperature fluctuations combined with better mixing. A combination of a steady magnetic field (to damp the flow) and a nonsteady magnetic field (to impose a forced convection) could be imagined to fulfill such a task and to offer a larger variety of control parameters for the contactless optimization of heat and mass transfer.

The first application of the combined action of VMF and RMF was reported by Yamashita et al. [175] to lower the oxygen concentration in Czochralski silicon. In a theoretical study, Mößner and Gerbeth [176] analyzed the stability thresholds of RMF and buoyancy-driven flows, also by additionally superimposing a VMF. Because of the stabilizing effect of the VMF, the critical magnetic Taylor number (from where the flow became instable) was found to increase strongly when VMF is superimposed on the RMF. A similar combination between RMF and VMF was studied by means of numerical simulations by Yildiz and Dost [177] in the liquid-phase diffusion growth process of 12 mm SiGe single crystals. Under the effect of the combined magnetic fields (0.3 T VMF and 5 mT/10 Hz RMF), the growth process became diffusion dominant and the S–L interface was almost flat.

The stability analysis of a Rayleigh-Benard flow under the combined action of an RMF and CMF in a gallium melt was carried out by Grants et al. [178]. It was demonstrated that the CMF just sharpened the transition diagram in terms of the fluctuation amplitude, while the transition in terms of the structure change was not influenced too much by the CMF.

Galindo et al. [179] numerically investigated the influence of the combined action of an AMF field and VMF or CMF on the melt flow in a 4-in Si-CZ growth process. It was shown that the VMF and CMF damp the flow and, at the same time, the main action of the AMF was to generate a reversed flow direction at the melt free surface (from the crystal to the crucible) and to improve the oxygen distribution. A better overall damping effect was found for the CMF because it provided no preferred direction to the flow field.

Tomzig et al. [152] reported the successful growth of 300 mm silicon crystals by the CZ method under the combined action of AMF and CMF. They showed that the oxygen

content can be very effectively adjusted between the highest (in the case of AMF) and the lowest (in the case of CMF) oxygen level (Figure 23.15). The increase of the oxygen in the growing crystal in the case of AMF was explained due to the direct transport of the SiO from the hot wall to the S–L interface without SiO reduction due to evaporation. The experiments had additionally shown that the application of AMF reduces the crucible wall temperature, which is favorable for the silica crucible lifetime, with strong implications for cost reduction.

A special method for the melt control in CZ systems was proposed by Watanabe et al. [180]. The so-called electromagnetic Czochralski method (EMCZ) combines a VMF and a static electric current passing through the melt from the growing crystal to an electrode attached to the melt surface (Figure 23.18). Because the main path of the electrical current is directed in the radial direction, the electromagnetic force ($\vec{F} = \vec{I} \times \vec{B}$) is therefore generated in the azimuthal direction; consequently, the melt is rotated.

Silicon crystals with 30 mm diameters were grown using the EMCZ method by Watanabe et al. [181]. A low crystal rotation ($\sim$1 rpm) and no crucible rotation were considered. Melt rotation rates from 0 to more than 105 rpm were obtained with $I = 0$–8 A and $B = 0$–0.1 T. A continuous change in the oxygen concentration and the homogenization of the oxygen distribution along the radial direction were obtained due to the reduction of the diffusion layer, both at the melt–crucible interface and at the crystal–melt interface, by forced flow caused by the electromagnetic force. The influence of the electrode design (the number of electrodes and position) was numerically investigated by Kakimoto et al. [182] in the same configuration.

Watanabe et al. [181] reported the growth of a 200 mm silicon crystal by the EMCZ method. Two configurations were used—electric current + VMF and electric current + CMF—with the symmetry plane placed under the S–L interface (inside configuration). The crystals grown with CMF-EMCZ method have a higher oxygen concentration and a more homogeneous oxygen distribution than the crystals grown by VMF-EMCZ. This result means that, for large-diameter crystals, the melt rotation under VMF was not effectively mixing the oxygen in the melt and that the VMF was strong

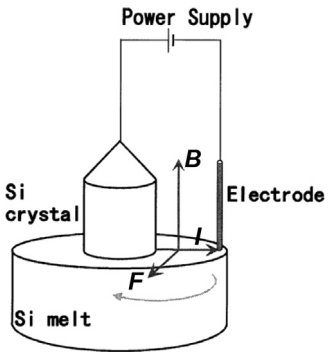

FIGURE 23.18 The principle of the EMCZ method. *From Ref. [180], with permission from Elsevier.*

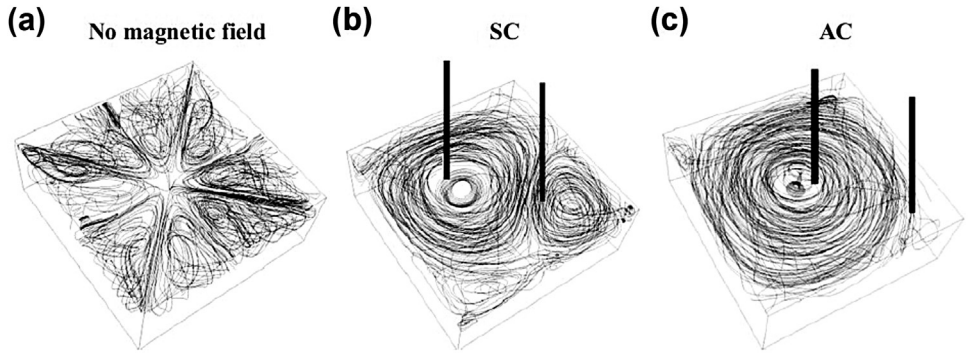

FIGURE 23.19 Particle tracking with no magnetic fields (a), for a symmetric configuration (b), and for an asymmetric configuration (c). $I = 10$ A; $B = 10$ mT. Particle tracking plots are shown in a zone 10 cm above the S–L interface. *From Ref. [185], with permission from Elsevier.*

enough to reduce the melt flow just below the S–L interface. On the contrary, CMF has a lower influence on the flow below the S–L interface and seems to be a better option for large-diameter crystals. Numerical simulations performed by Vizman et al. [183] showed that the S–L interface shape of 200-mm diameter Si crystals is greatly modified to a concave shape as a result of the temperature distribution at the interface by the controlled melt flow induced by electromagnetic force. The interface deflection was higher for the EMCZ configuration with CMF than with VMF. Point defect behavior in Si crystals grown by EMCZ method was investigated by Kim et al. [184]. The results indicate that in comparison to a simple CMF-CZ configuration, in the case of a CMF-EMCZ configuration the increased heat transfer due to electromagnetic force makes the interface concave and the pulling speed at which OSF (oxygen-induced stacking fault) is formed in the crystal increases.

Based on numerical modeling, Vizman and Tanasie [185] proposed a combination of electric current and VMF for melt stirring in a directional solidification method of multicrystalline silicon. They have shown that an electric current (2–10 A) that passed through two electrodes placed at the melt surface and a VMF of 10 mT can efficiently stir a melt with a size of $68 \times 68 \times 68\ \text{cm}^3$. Melt flow configuration was found to depend strongly on the position of the electrodes on the melt surface; thus, it changes from a two-vortex type for a symmetrical configuration (with the electrodes placed symmetric from the central point) to a one-vortex type for the asymmetric configuration (with one electrode placed at the center point; see Figure 23.19).

23.6 Conclusions and Outlook

The discussions presented in this chapter have shown that magnetic fields offer the crystal grower a large variety of control possibilities for contactless optimization of heat and mass transfer processes from growth equipments. There is already a huge research

Table 23.1 Summary of the Effects of Magnetic Field Applications in Crystal Growth Processes

Type of Magnetic Field	Beneficial Effects	Detrimental Effects
VMF	**1.** Damp thermal convection **2.** Eliminate temperature fluctuations **3.** Increase effective segregation coefficient **4.** Eliminate growth-striae (dopant bands) in the crystal **5.** Increase axial uniformity of oxygen (CZ-Si) **6.** Increase radial uniformity of dopants (VB)	**1.** Local instabilities can occur in the melt **2.** Increase temperature difference in the melt (CZ-Si) **3.** Increase the level of oxygen and deteriorate its radial uniformity (CZ-Si) **4.** Deteriorate radial uniformity of dopants (FZ)
HMF	**1.** Damp vertical flow **2.** Eliminate temperature fluctuations **3.** Eliminate growth-striae (dopant bands) in the crystal **4.** Decrease the level of oxygen (CZ-Si)	**1.** Destroy the axial symmetry of the melt flow **2.** Deteriorate the symmetry of dopant distribution (VB) **3.** Elliptical form of the crystal in FZ with no crystal rotation
CMF	**1.** Damp thermal convection **2.** Eliminate temperature fluctuations **3.** Smaller magnetic field intensity (in comparison with VMF and HMF) **4.** Reduce nonrotational dopant striations (CZ) **5.** Increase axial and radial uniformity of oxygen (CZ-Si) **6.** Decrease the level of oxygen (CZ-Si)	**1.** Higher amplitude of temperature fluctuations near the S–L interface possible
RMF	**1.** Generate stable steady azimuthal flow **2.** Eliminate temperature fluctuations **3.** Decrease dopant inhomogeneities **4.** Reduce dopant striations to a high degree (VB)	**1.** Weak meridional mixing **2.** W-interface shape possible (VB)
TMF	**1.** Lorentz force in the direction of gravity **2.** Generate a meridional flow **3.** Eliminate temperature fluctuations **4.** Uniform oxygen distribution (CZ-Si) **5.** Lowering the dislocation density (LEC-GaAs) **6.** Coils placed close to the melt	**1.** Limited effect in the central region of large-scale melts due to the skin effect
AMF	**1.** Efficient mixing in the melt **2.** Lower axial and radial segregation (VB-(Ga,In)Sb)	**1.** No influence on the melt flow underneath the crystal for large CZ melt

base in this field, a large body of literature, and an important number of applications in crystal growth industry. A short summary of the beneficial and detrimental effects of the application of magnetic fields in crystal growth processes is presented in Table 23.1.

Because of their versatility and lower costs for the magnets, nonsteady magnetic fields have been intensively studied in recent years. With development of the experiments on laboratory scale and more realistic computer models, industrial crystal growth applications of magnetic fields will become more based on a detailed analysis rather than intuition. In the coming years, the research suggesting new magnetic field designs

or beneficial modifications to the existing configurations will likely be concretized in industrial applications. This success will depend on the degree of fulfillment of the industry's cardinal demands, such as increased process output, improved crystal quality, and reduced costs.

References

[1] von Ammon W, Gelfgat Yu, Gorbunov L, Muehlbauer A, Muižnieks A, Makarov Y, et al. Application of magnetic fields in industrial growth of silicon single crystals. In: Proc. of the 15th Riga and 6th PAMIR conference on fundamental and applied MHD; 2005. p. 41.

[2] Ma Y, Watanabe K, Awaji S, Motokawa M. Appl Phys Lett 2000;77:3633.

[3] Mwaba MS, Gu J, Gorliz MR. J Cryst Growth 2007;303:381.

[4] Wang J, Zhang K, Peng Z, Chen Q. J Cryst Growth 2004;266:500.

[5] Sazaki G, Yoshida E, Komatsu H, Nakada T, Miyashita S, Watanabe K. J Cryst Growth 1997;173:231–4.

[6] Ataka M, Katoh E, Wakayama NI. J Cryst Growth 1997;173:592–6.

[7] Moreno A, Quiroz-Garcia B, Yokaichiya F, Stojanoff V, Rudolph P. Cryst Res Technol 2007;42:231.

[8] Series RW, Hurle DTJ, North-Holland. Use of a magnetic field in melt growth. In: Hurle DTJ, editor. Handbook of crystal growth, vol. 2a. Elsevier; 1994. p. 259.

[9] Kakimoto K. In: Scheel HJ, Fukuda T, editors. Crystal growth technology. Wiley; 2003. p. 139.

[10] Ozoe H, Szmyd J, Tagawa T. In: Molokov Sergeĭ, Moreau R, Moffat HK, editors. Magnetohydrodynamics: historical evolution and trends. Springer; 2007. p. 375.

[11] Rudolph P, Kakimoto K. MRS Bull 2009;34:251.

[12] Dold P, Benz KW. Prog Cryst Growth Charact Mater 1999;38:39.

[13] Bliss D. In: Dhanaraj G, Byrappa K, Prasad V, Dudley M, editors. Springer handbook of crystal growth. Springer; 2010. p. 205.

[14] Rudolph P. J Cryst Growth 2008;310:1298.

[15] Grants I, Gerbeth G. J Cryst Growth 2004;269:630.

[16] Muižnieks A, Krauze A, Nacke B. J Cryst Growth 2007;303:211.

[17] Miyazawa Y. Prog Cryst Growth Charact Mater 1999;38:261.

[18] Pfann WG, Hagelbarger DW. J Appl Phys 1956;27:12.

[19] Utech HP, Flemings MC. J Appl Phys 1966;37:2021.

[20] Chedzey HA, Hurle DTJ. Nature 1966;210:933.

[21] Müller G. J Cryst Growth 1993;128:26.

[22] Ristocelli JR, Lumley JL. J Cryst Growth 1992;116:447.

[23] Gräbner O, Mühe A, Müller G, Tomzig E, Virbulis J, von Ammon W. Mater Sci Eng B 2000;73:130.

[24] Vizman D, Gräbner O, Müller G. J Cryst Growth 2001;233:687.

[25] Voronkov VV. J Cryst Growth 1982;59:625.

[26] Vizman D, Friedrich J, Müller G. J Cryst Growth 2001;230:73.

[27] Virbulis J, Wetzel Th, Muižnieks A, Hanna B, Dornberger E, Tomzig E, et al. J Cryst Growth 2001;230:92.

[28] Kim KM, Smetana P. J Appl Phys 1985;58:2731.
[29] Terashima K, Katsumata T, Orito F, Fukuda T. Jpn J Appl Phys 1984;23:L302.
[30] Burton JA, Prim RC, Slitcher WP. J Chem Phys 1953;21:1987.
[31] Hurle DTJ, Series RW. J Cryst Growth 1985;73:1.
[32] Kobayashi S. J Cryst Growth 1986;75:301.
[33] Riley N. J Cryst Growth 1987;85:417.
[34] Series RW, Hurle DTJ, Barraclough KG. J Appl Math 1985;35:195.
[35] Ravishankar PS, Braggins TT, Thomas RN. J Cryst Growth 1990;104:617.
[36] Series RW. J Cryst Growth 1989;97:85.
[37] Kobayashi N. J Cryst Growth 1991;108:240.
[38] Salnick ZA. J Cryst Growth 1992;121:775.
[39] Kakimoto K, Yi K, Eguchi M. J Cryst Growth 1996;163:238.
[40] Hofmann D, Mosel F, Müler G. In: Grossman G, Lebedo L, editors. Proc. Of the 5th conf. on semi-insulating III-V materials, Malmo (1988). Bristol (UK): Hilger; 1988. p. 429.
[41] Ozawa S, Kimura T, Kobayashi J, Fukuda T. Appl Phys Lett 1987;50:329.
[42] Hurle DTJ, Jakeman E, Johnson CP. J Fluid Mech 1974;64:565.
[43] Kuhl R, Wilke H. In: Vol. 41 of Congress of the International Astronautical Federation. Dresden (GDR): IAF; 1990. 90–398.
[44] Kim DH, Adornato PM, Brown RA. J Cryst Growth 1988;89:339.
[45] Matthiesen DH, Wargo MJ, Motakef S, Karlsonn DJ, Nakos JS, Witt AF. J Cryst Growth 1987;85:557.
[46] Park YJ, Min SK, Hahn SH, Yoon JK. J Cryst Growth 1995;154:10.
[47] Becla P, Han J-C, Motakef S. J Cryst Growth 1992;121:394.
[48] Yao M, Chait A, Fripp AL, Debnam WJ. J Cryst Growth 1997;173:467.
[49] Ma N, Walker JS. J Cryst Growth 2000;208:757.
[50] Lan CW, Lee IF, Yeh BC. J Cryst Growth 2003;254:503.
[51] Baumgartl J, Müller G. J Cryst Growth 1996;169:582.
[52] Duffar Th, Nabot J Ph, Barat C, Favier JJ, Cambon G. Microgravity Sci Technol 1993;6:74.
[53] Mühlbauer A, Muižnieks A, Virbulis J, Lüdge A, Riemann H. J Cryst Growth 1995;151:66.
[54] Rudevics A, Muižnieks A, Riemann H, Luedge A, Ratnieks G, von Ammon W. J Cryst Growth 2005; 275:e561.
[55] Dold P, Cröll A, Benz KW. J Cryst Growth 1998;183:545.
[56] De Leon N, Guldberg J, Salling J. J Cryst Growth 1981;55:406.
[57] Robertson Jr GD, O'Connor D. J Cryst Growth 1986;76:111.
[58] Lan CW. J Cryst Growth 1996;169:269.
[59] Kaiser Th, Benz KW. J Cryst Growth 1998;183:564.
[60] Cröll A, Szofran FR, Dold P, Benz KW, Lehoczky SL. J Cryst Growth 1998;183:554.
[61] Cröll A, Benz KW. Prog Cryst Growth Charact Mater 1999;38:7.
[62] Lie KH, Walker JS, Riahi DN. J Cryst Growth 1991;109:167.
[63] Herrmann FM, Baumgartl J, Feulner T, Müller G. In: Proc. VIIIth Europ. symp. on materials and fluid sciences in microgravity. Brussels: ESA SP–333; 1992. p. 57.

[64] Witt AF, Herman CJ, Gatos HC. J Mater Sci 1970;5:822.

[65] Hoshi K, Suzuki T, Okubo Y, Isawa N. In: Extended Abstracts Electrochem. Soc., vol. 80-1. Pennington (NJ): Electrochemical Society; 1980. p. 811.

[66] Hoshi K, Isawa N, Suzuki T. OYOBUTURI (in Japanese) 1984;53:38.

[67] Terashima K, Fukuda T. J Cryst Growth 1983;63:423.

[68] Mihelčić M, Wingerath K. J Cryst Growth 1987;82:318.

[69] Oshima M, Taniguchi N, Kobayashi T. J Cryst Growth 1994;137:48.

[70] Ozoe H, Iwamoto M. J Cryst Growth 1994;142:236.

[71] Kakimoto K, Ozoe H. J Cryst Growth 2000;212:429.

[72] Ivanov NG, Korsakov AB, Smirnov EM, Khodosevitch KV, Kalaev VV, Makarov Yu N, et al. J Cryst Growth 2003;250:183.

[73] Liu L, Kakimoto K. J Cryst Growth 2005;275:e1521.

[74] Kalaev VV. J Cryst Growth 2007;303:203.

[75] Collet Y, Magotte O, Van den Bogaert N, Rolinsky R, Loix F, Jacot M, et al. J Cryst Growth 2012; 360:18.

[76] Krauze A, Muižnieks A, Mühlbauer A, Wetzel Th, von Ammon W. J Cryst Growth 2004;262:157.

[77] Iino E, Takano K, Kimura M, Yamagishi H. Mater Sci Eng B 1996;36:142.

[78] Terashima K, Nishio J, Okada A, Washizuka S, Watanabe M. J Cryst Growth 1986;79:463.

[79] Kim KM. J Electrochem Soc 1982;129:427.

[80] Sen S, Lefever RA, Wilcox WR. J Cryst Growth 1978;43:526.

[81] Su C-H, Lehoczky SL, Szofran FR. J Cryst Growth 1991;109:385.

[82] Lan CW, Yeh BC. J Cryst Growth 2004;266:200.

[83] Kimura H, Harvey MF, O'Connor DJ, Robertson GD, Valley GC. J Cryst Growth 1983;62:523.

[84] Robertson Jr GD, O'Connor DJ. J Cryst Growth 1986;76:100.

[85] Herrmann FM, Müller G. J Cryst Growth 1995;156:350.

[86] Hirata H, Hoshikawa K. J Cryst Growth 1989;96:747.

[87] Series RW. J Cryst Growth 1989;97:92.

[88] Hicks TW, Organ AE, Riley N. J Cryst Growth 1989;94:213.

[89] Hirata H, Hoshikawa K. J Cryst Growth 1992;125:181.

[90] Kakimoto K, Eguchi M, Ozoe H. J Cryst Growth 1997;180:442.

[91] Vizman D, Gräbner O, Müller G. J Cryst Growth 2002;236:545.

[92] Savolainen V, Heikonen J, Ruokolainen J, Anttila O, Laakso M, Paloheimo J. J Cryst Growth 2002; 243:243.

[93] Liu X, Liu L, Li Z, Wang Y. J Cryst Growth 2012;360:38.

[94] Watanabe M, Eguchi M, Hibiya T. J Cryst Growth 1998;193:402.

[95] Hirata H, Hoshikawa K. J Cryst Growth 1989;98:777.

[96] Sim B-C, Lee I-K, Kim K-H, Lee H-W. J Cryst Growth 2005;275:455.

[97] Won YC, Kakimoto K, Ozoe H. J Cryst Growth 2001;233:622.

[98] Morthland TE, Walker JS. J Cryst Growth 1996;158:471.

[99] Lan CW, Liang MC. J Cryst Growth 1997;180:381.

[100] Pfann WG, Dorsi D. Rev Sci Instrum 1957;28:720.
[101] Mullin JB, Hulme KF. J Electron Control 1958;4:170.
[102] Davidson PA, Boyson F. Appl Sci Res 1987;44:241.
[103] Gelfgat Yu M. J Cryst Growth 1999;198–199:165.
[104] Friedrich J, Lee YS, Fischer B, Kupfer C, Vizman D, Müller G. Phys Fluids 1999;11:853.
[105] Kaiser Th, Benz KW. Phys Fluids 1998;10:1104.
[106] Grants I, Gerbeth G. J Fluid Mech 2002;463:229.
[107] Robinson T, Larsson K. J Fluid Mech 1973;60:641.
[108] Volz MP, Mazuruk K. Exp Fluids 1996;20:454.
[109] Dold P, Benz KW. Cryst Res Technol 1995;30:1135.
[110] Fischer B, Friedrich J, Weimann H, Müller G. J Cryst Growth 1999;198–199:170.
[111] Barz RU, Gerbeth G, Wunderwald U, Buhrig E, Gelfgat Yu M. J Cryst Growth 1997;180:410.
[112] Shaskow YM, Shushlebina NY. Fiz Khim Obrab Mater 1972;1:34.
[113] Hoshikawa K, Kohda H, Hirata H, Nakanishi H. Jpn J Appl Phys 1980;19:L33.
[114] Zhou X, Huang H. J Cryst Growth 2012;340:166.
[115] Spitzer K-H. Prog Cryst Growth Charact Mater 1999;38:59.
[116] Kakimoto K. J Cryst Growth 2002;237–239:1785.
[117] Brückner F-U, Schwerdtfeger K. J Cryst Growth 1994;139:351.
[118] Grants I, Gerbeth G. J Cryst Growth 2007;308:290.
[119] Dold P, Benz KW. Cryst Res Technol 1997;32:51.
[120] Friedrich J, Kupfer C, Fischer B, Müller G. In: Fluid mechanics and its applications. The Netherlands: Kluwer; 1998.
[121] Pätzold O, Grants I, Wunderwald U, Jenkner K, Cröll A, Gerbeth G. J Cryst Growth 2002; 245:237.
[122] Lyubimova TP, Croell A, Dold P, Khlybov OA, Fayzrakhmanova IS. J Cryst Growth 2004;266:404.
[123] Volz MP, Walker JS, Schweizer M, Cobb SD, Szofran FR. J Cryst Growth 2005;282:305.
[124] Bellmann MP, Pätzold O, Gärtner G, Möller HJ, Stelter M. J Cryst Growth 2009;311:1471.
[125] Schwesig P, Hainke M, Friedrich J, Müller G. J Cryst Growth 2004;266:224.
[126] Wang X, Ma N, Bliss DF, Iseler GW, Becla P. J Cryst Growth 2006;287:270.
[127] Bellmann MP, Pätzold O, Wunderwald U, Stelter M, Möller HJ. J Cryst Growth 2007;303:250.
[128] Galindo V, Niemietz K, Pätzold O, Gerbeth G. J Cryst Growth 2012;360:30.
[129] Dold P, Cröll A, Lichtensteiger M, Kaiser Th, Benz KW. J Cryst Growth 2001;231:95.
[130] Raming G, Muižnieks A, Mühlbauer A. J Cryst Growth 2001;230:108.
[131] Liu Y, Ai F, Pan XH, Zhang Y, Zhou YF, Feng CD. J Cryst Growth 2010;312:1622.
[132] Walker JS, Martin Witkowski L, Houchens BC. J Cryst Growth 2003;252:413.
[133] Ma N, Walker JS, Lüdge A, Riemann H. J Cryst Growth 2001;230:118.
[134] Yao L, Zeng Z, Li X, Chen J, Zhang Y, Mizuseki H, et al. J Cryst Growth 2011;316:177.
[135] Salk M, Fiederle M, Benz KW, Senchenkov AS, Egorov AV, Matioukhin DG. J Cryst Growth 1994; 138:161.
[136] Senchenkov AS, Barmin IV, Tomson AS, Krapukhin VV. J Cryst Growth 1999;197:552.

[137] Wetzel Th, Muižnieks A, Mühlbauer A, Gelfgat Y, Gorbunov L, Virbulis J, et al. J Cryst Growth 2001; 230:81.

[138] Mercier F, Nishizawa S. J Cryst Growth 2011;318:385.

[139] Stelian C, Delannoy Y, Fautrelle Y, Duffar Th. J Cryst Growth 2004;266:207.

[140] Stelian C, Delannoy Y, Fautrelle Y, Duffar Th. J Cryst Growth 2005;275:e1571.

[141] Mitric A, Duffar Th, Diaz-Guerra C, Corregidor V, Alves LC, Garniera C, et al. J Cryst Growth 2006; 287:224.

[142] Mitric A, Duffar Th. J Cryst Growth 2008;310:1511.

[143] Gelfgat Y, Krümins Yu, Abricka M. Magnetohydrodyn 1999;35:1.

[144] Ramachandran N, Mazuruk K, Volz MP. J Jpn Soc Microgravity Appl 2000;17:98.

[145] Gelfgat A Yu. J Cryst Growth 2005;279:276.

[146] Grants I, Klyukin A, Gerbeth G. J Cryst Growth 2009;311:4255.

[147] Klein O, Lechner Ch, Druet P-É, Philip P, Sprekels J, Frank-Rotsch Ch, et al. J Cryst Growth 2008; 310:1523.

[148] Rudolph P, Czupalla M, Lux B. J Cryst Growth 2009;311:4543.

[149] Frank-Rotsch Ch, Rudolph P. J Cryst Growth 2009;311:2294.

[150] Kudla Ch, Blumenau AT, Büllesfeld F, Dropka N, Frank-Rotsch Ch, Kießling F, et al. J Cryst Growth 2013;365:54.

[151] Wetzel Th. Fortschritt-Berichte. VDI Reihe 9, No. 328. Dusseldorf: VDI Verlag; 2001.

[152] Tomzig E, Virbulis J, Ammon WV, Gelfgat Y, Gorbunov L. Mater Sci Semicond Process 2003;5: 347.

[153] Krauze A, Jēkabsons N, Muižnieks A, Sabanskis A, Lācis U. J Cryst Growth 2010;312:3225.

[154] Lechner Ch, Klein O, Druet P-E. J Cryst Growth 2007;303:161.

[155] Kasjanow H, Nacke B, Eichler St, Jockel D, Frank-Rotsch Ch, Lange P, et al. J Cryst Growth 2008; 310:1540.

[156] Rudolph P, Czupalla M, Lux B, Kirscht F, Frank-Rotsch Ch, Miller W, et al. J Cryst Growth 2011;318: 249.

[157] Miller W, Frank-Rotsch Ch, Rudolph P. J Cryst Growth 2011;318:244.

[158] Yesilyurt S, Motakef S, Grugel R, Mazuruk K. J Cryst Growth 2004;263:80.

[159] Lantzsch R, Galindo V, Grants I, Zhang C, Pätzold O, Gerbeth G, et al. J Cryst Growth 2007;305:249.

[160] Galindo V, Grants I, Lantzsch R, Pätzold O, Gerbeth G. J Cryst Growth 2007;303:258.

[161] Niemietz K, Galindo V, Pätzold O, Gerbeth G, Stelter M. J Cryst Growth 2011;318:150.

[162] Frank-Rotsch Ch, Jockel D, Ziem M, Rudolph P. J Cryst Growth 2008;310:1505.

[163] Dropka N, Frank-Rotsch Ch, Miller W, Rudolph P. J Cryst Growth 2012;338:208.

[164] Yeckel A, Derby JJ. J Cryst Growth 2013;364:133.

[165] Dropka N, Frank-Rotsch Ch. J Cryst Growth 2014;386:146.

[166] Dropka N, Frank-Rotsch Ch. J Cryst Growth 2013;367:1.

[167] Dadzis K, Ehrig J, Niemietz K, Pätzold O, Wunderwald U, Friedrich J. J Cryst Growth 2011;333:7.

[168] Dadzis K, Niemietz K, Pätzold O, Wunderwald U, Friedrich J. J Cryst Growth 2013;372:145.

[169] Dropka N, Miller W, Menzel R, Rehse U. J Cryst Growth 2010;312:1407.

[170] Dropka N, Miller W, Rehse U, Rudolph P, Büllesfeld F, Sahr U, et al. J Cryst Growth 2011;318:275.

[171] Dropka N, Frank-Rotsch Ch, Rudolph P. J Cryst Growth 2013;365:64.

[172] Kießling F-M, Büllesfeld F, Dropka N, Frank-Rotsch Ch, Müller M, Rudolph P. J Cryst Growth 2012; 360:81.

[173] Dadzis K, Vizman D, Friedrich J. J Cryst Growth 2013;367:77.

[174] Vizman D, Dadzis K, Friedrich J. J Cryst Growth 2013;381:169.

[175] Yamashita K, Kobayashi S, Aoki T, Kawata Y, Shiraiwa T. Semiconductor fabrication: technology and metrology. American Society for Testing Materials; 1989. 7.

[176] Mößner R, Gerbeth G. J Cryst Growth 1999;197:341.

[177] Yildiz E, Dost S. J Cryst Growth 2007;303:279.

[178] Grants I, Pedchenko A, Gerbeth G. Phys Fluids 2006;18. Art. No 124104.

[179] Galindo V, Gerbeth G, von Ammon W, Tomzig E, Virbulis J. Energy Convers Manage 2002;43:309.

[180] Watanabe M, Eguchi M, Hibiya T. Mater Sci Semicond Process 1999;38:L10.

[181] Watanabe M, Eguchi M, Wang W, Hibiya T, Kuragaki S. J Cryst Growth 2002;237–239:1657.

[182] Kakimoto K, Tashiro A, Shinozaki T, Ishii H, Hashimoto Y. J Cryst Growth 2002;243:55.

[183] Vizman D, Watanabe M, Friedrich J, Müller G. J Cryst Growth 2007;303:221.

[184] Kim K-H, Sim B-C, Choi I-S, Lee H-W. J Cryst Growth 2007;299:206.

[185] Vizman D, Tanasie C. J Cryst Growth 2013;372:1.

24

Oscillatory-Driven Fluid Flow Control during Crystal Growth from the Melt

Peter Capper[1], Evgeny Zharikov[2]

[1]SELEX ES, SOUTHAMPTON, UK; [2]D. MENDELEYEV UNIVERSITY OF CHEMICAL TECHNOLOGY OF RUSSIA, MOSCOW, RUSSIA

CHAPTER OUTLINE

24.1 Introduction **952**
24.2 Constant-Speed Rotation in Melts **953**
24.3 Accelerated Crucible Rotation Technique **955**
24.3.1 Introduction and Theory 955
24.3.2 CMT Growth 959
24.3.3 High-*x* CMT Material 960
24.3.4 ACRT in the Growth of CdTe/$Cd_{1-x}Zn_xTe$ 964
24.3.5 ACRT in Group-IV Growth 967
24.3.6 ACRT in Other Material Systems 968
24.4 Axial Vibration Control **968**
24.4.1 Physical Nature of the Phenomenon 969
24.4.2 Effects of AVC on Crystal Growth from the Melt 971
24.4.3 Application of AVC in Crystal Growth Methods 973
24.4.4 Crystal Materials Grown by the AVC Technique 980
24.5 Other Types of Oscillatory Techniques **981**
24.5.1 Ultrasonic Vibration 981
24.5.2 Coupled Vibrational Stirring 982
24.6 Conclusions and Outlook **983**
References **988**

Handbook of Crystal Growth. http://dx.doi.org/10.1016/B978-0-444-63303-3.00024-9
Copyright © 2015 Elsevier B.V. All rights reserved.

24.1 Introduction

Despite the progress made in recent decades in the various epitaxial growth techniques, bulk crystals are still used actively in numerous electronic and photonic applications, as well as passively as epitaxial substrates, for example [1–3]. In these bulk growth activities, although the basic growth mechanisms have been explained, there is still a growing need to improve the size and quality of crystals while reducing production costs. Rudolph and Kakimoto [4] have outlined various means of controlling the uniformity and stability of crystal growth from the melt by complementing internal parameters (e.g., temperature field, pressure, growth velocity) by external influences (e.g., mechanical, electrical, and mechanical fields). Stirring during crystal growth can often be essential to enhance solute transport through the growth fluid, to homogenize the solute concentration in the fluid and solid, and to reduce the thickness of the solute diffusion boundary layer (in order to prevent constitutional supercooling and hence the morphological instability of the crystal). Why are the properties of the crystal not markedly affected by the periodic disturbances applied to growth fluids? The answer lies in a comparison of the time scales involved. Movement of solute species in melt growth is normally on the order of hundreds of centimeters per second. With growth rates in the region of 10^{-2} cm/s and induced fluctuations in the region of centimeters per second, solute movement dominates. In addition, if the characteristic ratio of D/δ^2 (with D being the diffusion coefficient and δ the boundary layer thickness) is less than the frequency of any hydrodynamic changes and their related temperature oscillations, then mass diffusivity cannot follow the thermal changes.

Consideration of fluctuation effects in directional crystallization showed [5] that, after a single disturbance at the growth interface, the steady-state composition is reached within a time:

$$t \approx 2\delta^2/D,$$

where δ is the boundary layer thickness and D is the diffusion coefficient. Taking typical values of $\delta = 10^{-4}$ m and $D = 10^{-8}$ m^2/s, we obtain a time on the order of 1 s. This means that the solutal transient of the growing interface is quite slow, and the interface acts as a "low-pass filter" [6] preventing the influence of growth rate perturbations or temperature oscillations with certain frequencies. The frequency limit from the above estimation is approximately 1 Hz. The same value can also be obtained from the analysis presented in Ref. [7]. According to estimates in [8], the critical value could be approximately 10 Hz. Below this limit (a few hertz), any fluctuations are dangerous. On the contrary, higher-frequency perturbations, including those typical for AVC values, should be damped.

Table 24.1 shows a summary of both steady and unsteady force fields that have been applied to crystal growth systems over the years. Although other areas will be covered in various chapters throughout this handbook, this chapter focuses on nonsteady mechanical means of affecting crystal growth, including the accelerated crucible rotation technique (ACRT) and various forms of vibration. After a short section covering other

Table 24.1 External Parameters that Influence Melt Flow Dynamics

Force Field	Mechanical (*g*)	Thermal (T)	Electrical (*E*)	Magnetic (*B*)
Steady	RCC, μg, multi-g	TFR	DC	SMF
Nonsteady	ACRT, AVC, CVS, USV	TFR	AC	RMF, TMF, AMF

Note: RCC, rotation of crucible and/or crystal; μ*g*, microgravity; multi-g = centrifugation, TFR, thermal field rotation; *E*, electric field; *B*, magnetic induction; DC, direct current; AC, accelerated current; ACRT, accelerated crucible technique; AVC, axial vibrational control; CVS, coupled vibrational stirring; USV, ultrasonic vibration; SMF, steady magnetic field; RMF, rotating magnetic field; TMF, traveling magnetic field; AMF, alternating (pulsed) magnetic field.
Adapted from Rudolph and Kakimoto [4].

mechanical means of melt mixing, the subsequent three main sections will discuss the topics of ACRT, axial vibrational control (AVC), and other vibration techniques.

Oscillatory techniques offer the means to control melt transport conditions in nonelectroconductive melts that cannot be controlled using magnetic fields (see Chapter 23 in Volume IIB). That is, they have an effect on any fluid and open up possibilities to govern the crystal growth of not only semiconductors but also dielectrics, salts, etc.

24.2 Constant-Speed Rotation in Melts

A study of the relative importance of the rotation rate and thermal stability was conducted by Rossby [9]. By plotting the Rayleigh number ($\mathrm{Ra} = g\alpha\Delta T h^3(\nu\kappa)^{-1}$, where g is the gravitational constant, α is the volume expansion coefficient, ΔT is the temperature difference, h is the melt height, ν is the melt viscosity, and $\kappa = \lambda C_\mathrm{p}^{-1}\rho^{-1}$, where λ is the heat conductivity and C_p is the heat capacity) against the Taylor number ($\mathrm{Ta} = 4\omega^2 h^4(\nu)^{-2}$, where ω is the rotation rate). Two regions can be identified on such a plot characterized by stable laminar and irregular turbulent flow, respectively. Typical values are $\mathrm{Ra} = 10^5$ at $\mathrm{Ta} = 10^7$ and $\mathrm{Ra} = 10^6$ at $\mathrm{Ta} = 10^9$. These criteria set practical limits on the rotation rates and melt depths of certain important growth systems, particularly as scale-up is considered.

Constant-speed rotation of either the crystal or crucible, or both, have been used for many years in all of the major bulk crystal growth techniques, such as Czochralski, Bridgman, vertical gradient freeze, and high- and low-temperature solution techniques [1,4]. Crystal characteristics that are influenced by constant-speed rotation include uniformity in both the radial and axial directions, segregation of matrix elements (in ternary compounds), striations (growth-induced inhomogeneities parallel to the growth interface), and secondary phases, to name only a few. Striations have several underlying causes, such as temperature fluctuations due to convective oscillations or nonsymmetry, hydrodynamic variations, and surface macrosteps (see the review by Scheel [10]). In each material system, a particular cause of striations is often found; for example, in Czochralski-grown silicon, striations are linked to the crystal rotation rate (see Chapter 2 in Volume IIA). Various means have been attempted to reduce striations, such as growth

under microgravity conditions [11] or centrifugation [12]. Eidelman et al. [13], used forced convection, via counterrotating crystals and crucibles, in small melt volumes in Czochralski growth to produce 700 mm/550 kg halide scintillator crystals. Scheel [10] described more than six types of melt flow below a Czochralski crystal that need to be considered or overcome to control melt mixing. Double crucibles can alleviate some of these problems, albeit with some practical difficulties. Scheel proposed an alternative of a solid ring located coaxial with and below the crystal to separate the flows from the melt fraction inside the ring and produce a quasi-stationary region below the crystal. Ostrogorsky and Muller [14] suggested a submerged heater in vertical Bridgman, where a thin melt and stabilizing the temperature gradient should minimize striations. By applying rotation to the baffle in this technique, Dutta and Ostrogorsky [15] were able to improve compositional homogeneity and reduce chemical stresses in grown $In_{1-x}Ga_xSb$ crystals.

Study of the rotation of the crystal or a special rotating stirrer in crystallization from melt has attracted renewed attention regarding the large volumes of metal alloy and semiconductor melts, such as silicon melt. Electromagnetic control of melt flow can have a limited effect on heat and mass transfer in the central area of large-scale Si ingots grown from the melt due to skin-depth issues [16,17]. Numerical studies of directional solidification of multicrystalline silicon with use of a rotating stirrer in the melt have been performed by Dumitrica et al. [18]. They demonstrated the promise of mechanical stirring to control the melt convection in directional solidification of large-scale silicon ingots; in particular, a strong increase of both melt convection and solid–liquid interface deflection was found.

Thermal field rotation is a new method of governing heat and mass transfer in a liquid phase, as proposed by Kokh and coworkers [19–22]. They organized a traveling heat wave propagating along the crucible wall by alternate switching of the vertical heating elements located around the crucible. As a result, the rotation of a nonuniform and cyclically changing heat field appeared on the crucible wall, producing the contactless generation of azimuthal flows in the melt. The outside impact decreased the role of the centrifugal force in melt motion, smoothed away the convection instability, and eliminated completely the melt disturbance as a result of the absence of mechanical rotation of the crystal/crucible. The authors found that changing the heating from an axisymmetric to a nonsymmetric, nonstationary configuration resulted in an increase in the convective flow and thus led to an increase of the melt uniformity because the convective cell occupies almost the entire melt domain. Curie's symmetry principle must play a significant role in crystal growth technology assisted with heat field rotation. Thus, by setting up a certain symmetry of the external thermal field in accordance with Curie's principle, one may expect the attainment of possible symmetrization of the convective flows in the system. The governing heat and mass transfer by rotation of the heat field was successfully realized by the authors in Czochralski, Bridgman, top-seeded solution growth, Kyropoulos, and some other growth techniques.

24.3 Accelerated Crucible Rotation Technique

24.3.1 Introduction and Theory

ACRT has been used extensively in the past to help melt homogenization in high-temperature solution growth of garnets and to improve crystal size by reducing the boundary layer thickness, as well as to prevent unwanted second-phase material from forming. In this section, we present a further example of the use of ACRT—that of cadmium mercury telluride (CMT, $Cd_xHg_{1-x}Te$), which is still the pre-eminent infrared material, despite the difficulties associated with its production and subsequent processing. By varying the x value, the material can be made to cover all of the important infrared (IR) ranges of interest (i.e., 1–3, 3–5, and 8–14 μm). Bridgman growth takes place in simple two-zone furnaces, with the pure elements contained in thick-walled, high-purity silica ampoules. The thick ampoule walls are needed to contain the high (up to ~70 atm) mercury vapor pressures within the ampoules. It was found to be necessary to purify both the mercury and the tellurium on site before use to obtain the required electrical properties. There is marked segregation of the matrix elements in standard Bridgman growth that is both a disadvantage and an advantage [23]. Its disadvantage is that the yield of material in terms of composition for the most commonly required regions is low. The advantage is that all regions of interest can be produced in the same crystal, to some extent. A further advantage is that segregation of impurities also occurs, which leads to low background donor levels in Bridgman material. The other main disadvantages of the standard Bridgman technique are that the material is nonuniform in composition in the radial direction and the growth direction, resulting in low yields, and there are numerous grain and subgrain boundaries.

Limits on controlling melt mixing in the Bridgman process necessitated a means of stirring melts contained in sealed, pressurized ampoules. The ACRT of Scheel [24] was used because it had been seen to increase the size of crystals, eliminate unwanted phases, and increase stable growth rates in high-temperature solution growth of a range of crystals. The first reported use of ACRT in CMT Bridgman growth was given by Capper and Gosney [25]. These effects were developed and discussed in more detail in later papers (see Refs [26–28] for reviews) and are outlined here.

The following three processes are fast by comparison with buoyancy-driven convection and occur on acceleration/deceleration:

1. Transient Couette flow, which occurs on rapid deceleration (spin-down), particularly in tall containers. Liquid adjacent to the container walls decelerates faster than liquid in the bulk and centrifugal forces drive the inner portions of liquid toward the wall. Horizontal vortices form in counterrotating pairs. This only occurs beyond a critical rotation rate, given by a value of 270 for the dimensionless Reynolds number:

$$\mathrm{Re} = R^2 \Delta\Omega_c \sigma / \eta \tag{24.1}$$

where $\Delta\Omega_c$ is the step change in rotation rate (rpm), such that $\Delta\Omega_c \times 2\pi/60$ rad/s; R is the container radius (cm); σ is the fluid density (g/cm^3); and η is the dynamic viscosity of fluid (g/cm/s).

2. Spiral shearing flow, which occurs on both spin-down and spin-up, and is again caused by fluid at the walls changing its velocity faster than liquid in the bulk. It is characterized by the thickness, d, of a layer close to the wall where the rotation rate is half its initial value, and by τ_1, the time taken by the central part of the fluid to reduce to this level:

$$d = R(E\Omega_o t)^{0.5} \approx (\eta t/\sigma)^{0.5} \tag{24.2}$$

$$\tau_1 = 0.1(E\Omega_o)^{-1} \approx 0.1\sigma R^2/\eta \tag{24.3}$$

where t is the time after the container stops rotating (s), Ω_o is the maximum rotation rate (rpm), and E is the Ekman number ($\eta/\Omega_o R^2\sigma$). Spin-up/spin-down times should be $<\tau_1$ to maximize stirring.

The number of spiral arms is given by:

$$N = \Omega_o \sigma R^2/16\pi\eta \tag{24.4}$$

with separation,

$$\Delta r = 4\pi\eta/\sigma\Omega_o r \tag{24.5}$$

where r is the radius of the point in question. Δr should be kept at 0.01–0.1 cm to ensure diffusion can act as the mixing process.

3. Ekman flow, which occurs above a solid boundary placed perpendicular to the axis of rotation. During spin-up, fluid adjacent to the boundary is forced to the side walls and returns diffusely and more slowly through the bulk, with the reverse occurring on spin-down.

The Ekman layer thickness is given by:

$$d_E = (\eta/\Omega_o\sigma)^{0.5} \tag{24.6}$$

with a maximum radial fluid velocity of:

$$V = \Omega_o R \tag{24.7}$$

and a maximum vertical fluid velocity of:

$$W = (\eta\Omega_o/\sigma)^{0.5} \tag{24.8}$$

The flow decreases within a time:

$$\tau_E = R(\sigma/\eta\Omega_o)^{0.5} \tag{24.9}$$

Figure 24.1 shows the ACRT rotation sequence used and Figure 24.2 depicts the various flows as seen in water simulation trials using a flat-based ampoule to simulate a crystal–melt interface [26]. All three predicted flow patterns were seen and showed qualitative agreement with the parameters given in Eqns (24.2)–(24.9). The most vigorous stirring arose due to Ekman flow for distances of $\sim R$ to $2R$ from the container base (Ekman volume), particularly when a flat-based container was used.

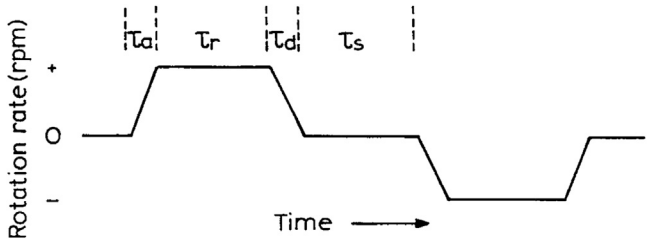

FIGURE 24.1 ACRT rotation sequence. *Reprinted from Capper et al. [26], copyright (1988) reproduced with permission from the Minerals, Metals and Materials Society.*

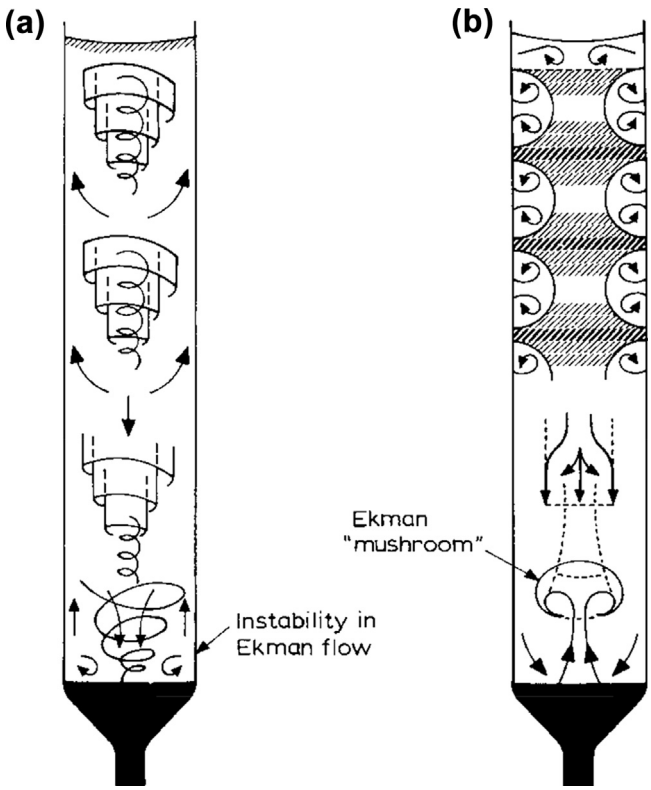

FIGURE 24.2 Flows in a flat-based container during (a) spin-up and (b) spin-down. *Reprinted from Capper et al. [26], copyright (1988) reproduced with permission from The Minerals, Metals and Materials Society.*

Brice et al. [28] summarized the models developed for flows induced by ACRT by identifying three distinct flow regimes as the acceleration/deceleration rate increases. For small accelerations, axially symmetric fluid flows increase the symmetry of heat and mass flows. Moderate accelerations produce axial and radial fluid flows at the base of the column (R to $2R$) that stir the fluid in this region only. Large accelerations give rise to unstable asymmetric flows. The system is characterized by the Reynolds number. Table 24.2 lists the critical Reynolds numbers and the corresponding rotation rates for

Table 24.2 Critical Reynolds number (Re_c) and Corresponding Critical Rotation Rates for ACRT in 13-, 20-, 50-, and 75-mm Diameter Ampoules

Event	Re_c	Critical rotation rates (rpm)			
		13 mm	20 mm	50 mm	75 mm
Ekman flow starts	15	≥2	~1	0.1	0.05
Ekman flow fully developed	70	10	4	0.6	0.25
Couette flow unstable	270	38	16	2.4	1.1
Ekman flow unstable	500	69	30	4.5	2.1

$\nu = \eta/\sigma = 0.006$, kinematic viscosity in cm^2/s.
Adapted from Capper et al. [29,30] with permission from Elsevier.

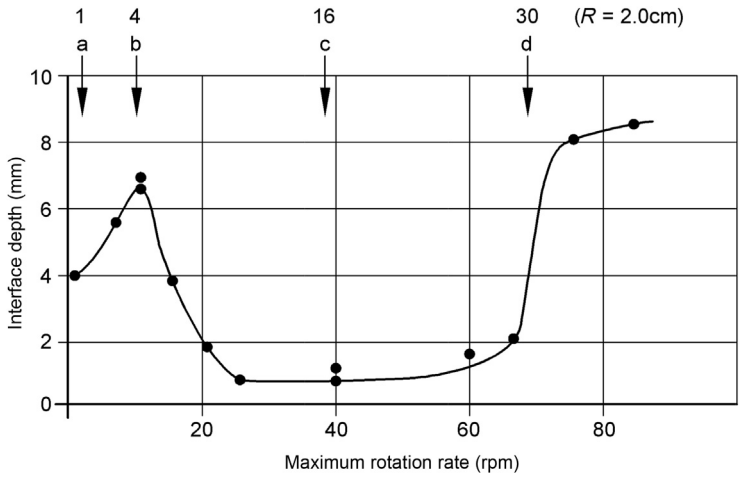

FIGURE 24.3 Interface depths in quenched crystals versus maximum ACRT rotation rates for 13-mm diameter crystals, with rotation values for 20-mm crystals superimposed at the top. *Adapted from Capper et al. [30], copyright (1988) reproduced with permission from Elsevier Science.*

the values of R (0.65 cm) and η/σ (0.006 cm^2/s) typical of CMT melts. These values of Re_c are superimposed onto the interface depth (from crystal quenching studies) versus the rotation plot of Figure 24.3 [30], together with other diameters typical of later CMT growth (20, 50, and 75 mm) and CdTe growth (50 and 75 mm). For points (a) and (b), Ekman flow is delayed because the ampoule base is not perpendicular to the rotation axis in the conical-based ampoules used for growth. Once Ekman flow is fully established, the interface depth decreases to a minimum. Couette instabilities are predicted to occur at point (c) and were seen in the simulations, although they do not affect the interface depth because they only occur in the upper regions of the liquid not near to the solid–liquid interface. As the Reynolds number increases further, Ekman flow will become unstable at point (d), and the interface depth consequently increases. Too

Table 24.3 ACRT Parameters

Parameter	Figure/Equation	Aim
1. Acceleration/deceleration time, τ_a, τ_d	Figure 24.1	τ_a, $\tau_d << \tau_E$ (to maximise use of Ekman flow)
2. Ekman time, τ_E	Equation (24.9)	$\tau_E >> \tau_a$, τ_d
3. Ekman layer thickness, d_E	Equation (24.6)	$d_E < 0.05$ cm
4. Vertical/horizontal fluid velocities, W, V	Equations (24.7) and (24.8)	$V\tau_E$, $W\tau_E > R$ (to pass Ekman volume through Ekman layer)
5. Separation of spiral arms, Δr	Equation (24.5)	$\Delta r < 0.1$–0.001 cm (to enable homogenization via diffusion)
6. Run/stop times, τ_a, τ_d	Figure 24.1	τ_a, $\tau_d << \tau_E$ (to maximize use of Ekman flow)
7. Reynolds number, Re	Equation (24.1)	Re < 500 (for stable Ekman flow)

Reprinted from Capper et al. [23], with permission from Elsevier.

much melt mixing can be introduced by certain ACRT conditions, which leads to deterioration in crystal properties.

Table 24.3 details the various ACRT parameters and the desired magnitudes of these to ensure a high level of controlled melt mixing. Bidirectional rotation is employed and rapid acceleration/deceleration (in 1–2 s) is easily achieved at any rotation rate. The Ekman layer thickness d_E, from earlier flux growth, should be <0.05 cm, which necessitates rotation rates >20 rpm. Horizontal and vertical flow velocities, V and W, are $>> R/\tau_E$ for all rotation rates, ensuring that the Ekman volume passes through the Ekman layer at each ACRT cycle. Rotation rates of >20 rpm will ensure that Δr is within the preferred range of 0.1–0.01 cm to homogenize the fluid body by diffusion. Both run (at maximum rate) and stop times, τ_r and τ_s, can be set to values close to the Ekman time, τ_E, to ensure mixing occurs for as long as possible and that decaying Ekman flow is minimized.

24.3.2 CMT Growth

The major effect of ACRT is to stir the melt during growth and produce flatter solid–-liquid interfaces. In turn, the radial and axial compositional uniformity of the material are improved, normally by a factor of at least ten-fold, and the grain and subgrain densities are reduced somewhat. The increase in uniformity enables larger-diameter material to be produced (up from 13 to 50 mm in our case). Assessment of the material includes wavelength mapping of both radially cut slices and axially cut planks; the latter gives useful information on the shape and change in the solid–liquid interface as growth proceeds. Images taken with an IR camera and a blackbody source revealed features in slices, such as cracks, inclusions of second phase, and swirl patterns; the origin of the latter is as yet unknown. We are currently routinely growing 20-mm diameter, 200-mm long crystals of $\sim$0.5 kg weight with good uniformity of composition and good electrical properties for first-generation photoconductive IR detector programs that require low carrier concentration n-type material. Compositions produced range from x of $\sim$0.93 ($\sim$0.91 μm) through to $x = 0.0$ (i.e., HgTe)—the latter in the tail ends of the crystals.

Application of ACRT opened up a large number of possible parameter combinations [23,29,31–34]. Quenching studies of crystals grown under a wide variety of conditions showed interface depths of ≈ 1 mm for $x = 0.12$ and 0.19 start crystals, unlike the values of 1 and 4 mm, respectively, seen in equivalent standard Bridgman crystals. Increasing the maximum rotation rate produced the interface depths shown in Figure 24.3. The preferred region in which to operate is clearly $25 < \Omega_o < 60$ rpm for a 13-mm diameter crystal. As growth rate increased, interface depth changed much less than in Bridgman growth, suggesting that faster stable growth rates are possible with ACRT. From the simulation studies, it was apparent that a small stagnant region occurred in the tip of a conical-based ampoule. Quenching studies in flat-based ampoules revealed not only a flat interface but also that the slow-grown material, produced prior to quenching, was single crystal. These studies demonstrated the power of Ekman stirring and the importance of initiating the growth of a single crystal grain.

In the early days of ACRT development, various rotation sequences and start compositions were investigated using 13-mm diameter crystals and x uniformity and crystal structure determined [23]. After comparing results, $x = 0.19$ was chosen as the preferred start composition. For these crystals grown with short run and stop times (8 and 1 s), there was a region (several centimeters long) of $x = 0.21$ material with axial and radial x uniformity of ± 0.002. A similar Bridgman crystal would produce <0.8 cm of similar x material with considerably larger radial x variations; that is, ACRT gives a five- to ten-fold increase in potentially usable material. See Figure 24.4 for a schematic of the Bridgman grower used [35].

24.3.3 High-x CMT Material

This section focuses on the work undertaken to produce near-IR material, for which higher starting x values are used. The assessment of the near-IR material has included wavelength mapping of radially cut slices and images taken with an IR camera to reveal features in slices, cracks, and inclusions of second-phase and swirl patterns; the origin of the latter is unknown. This work is being undertaken to improve our basic understanding of the properties of CMT in the near-IR region and to investigate the suitability of the material for use in various IR optical applications.

Figure 24.5(a) shows the pseudobinary phase diagram of the HgTe-CdTe system (Yu and Brebrick [36]). This demonstrates the fundamental problem in the near-equilibrium growth of CMT by melt growth methods, i.e., the wide separation between the liquidus and the solidus. However, this is actually a benefit when we are trying to produce higher x material. Because the starting x is increased, the first-to-freeze material also increases in x, although not at quite the same rate due to the relative curvatures of the liquidus and solidus. The initial goal was to produce material of $x \sim 0.7$, corresponding to ~ 1.3- to 1.4-μm cut-off wavelength. Figure 24.5(a) shows that this necessitates using starting x values of 0.33–0.35. Figure 24.5(b) shows the pressure–temperature phase diagram for various x values [36]. The region above the P^o_{Hg} line is essentially Hg vapor, with solid of

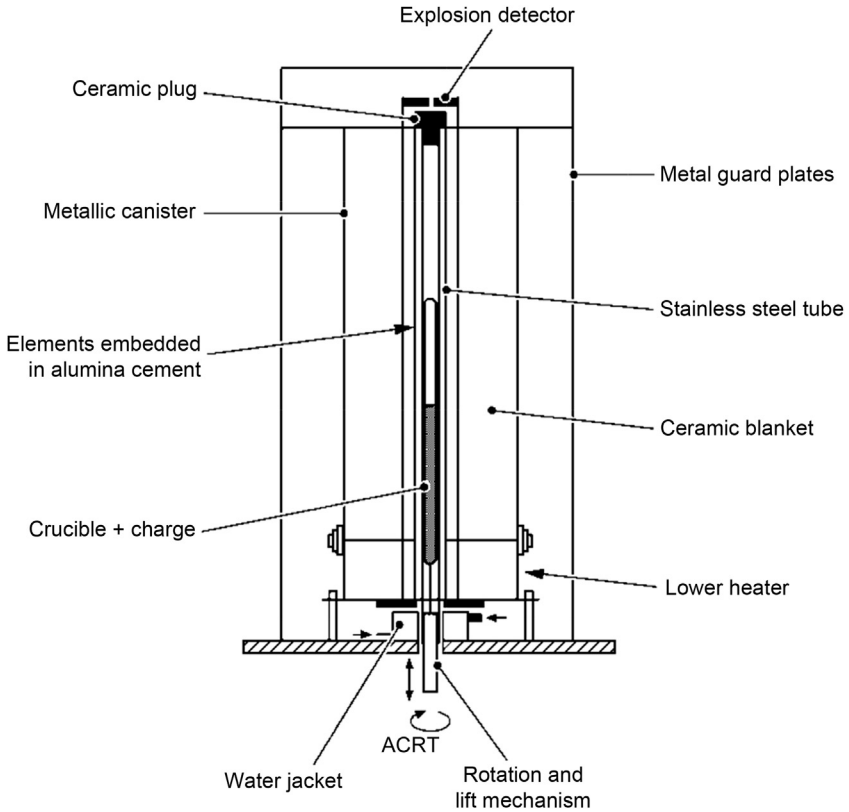

FIGURE 24.4 Bridgman/ACRT growth apparatus. *Reprinted from Capper et al. [35], copyright (1979) reproduced with permission from Elsevier Science.*

the indicated x values existing in the loops on the lower right and liquid to the left of the loops. This amply demonstrates how the maximum growth temperature and hence the Hg vapor pressure increases as x increases.

The loading procedure for these high-x crystals was as for the earlier crystals. We have had to develop the seal-off procedure to reduce the possibility of explosions due to the high pressures. This entailed ensuring that the wall thickness remained at the 7-mm value of the ampoule body and ensuring that there were no re-entrant angles in the seal-off area. By making the internal surface of the seal-off smooth, we have greatly reduced the occurrence of explosions and have successfully grown at temperatures >950 °C—approximately 130 °C above "standard" growth temperatures used before in this system.

Start compositions of $x = 0.19$–0.8 have been used and the melts were homogenized by melting/rocking as for standard charges. The growth process remained essentially unchanged for these high-x crystals [32,37]. Slices were cut (at >1-mm thickness) from the resulting crystals using a diamond peripheral-wheel cutting machine and then

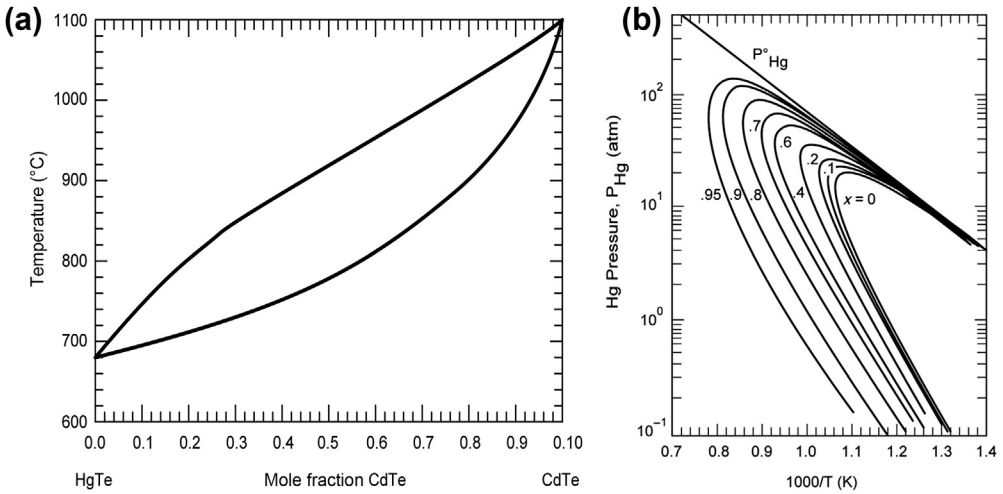

FIGURE 24.5 (a) Pseudobinary phase diagram for HgTe-CdTe system (L = liquid, S = solid). (b) Pressure–temperature diagram for CMT. *Reprinted from Yu and Brebrick [36], copyright (1994) reproduced with permission from IEE.*

polished and assessed for x uniformity with infrared transmission (IRT) measurements, as well as the mid-IR camera system.

Figure 24.1 shows the ACRT sequence that was also used for these high-x crystals. Standard bidirectional rotation is still employed with rapid acceleration/deceleration (in 1–2 s). From considerations of the simple model (Table 24.2), it was seen that maximum rotation rates for these 20-mm diameter crystals should be between 4 and 30 rpm. Also for these crystals, short run and stop times (8 and 1 s, respectively) were used as for standard crystals. To maximize the Ekman stirring—that is, to increase the vertical and horizontal flow velocities (to values of $> R/\tau_E$)—we chose to use 25 rpm as the maximum rate. This rotation rate also ensures that the spiral separation is $\sim$0.03 cm at its maximum value, which ensures full mixing by diffusion between the spiral arms (see Eqn (24.5)).

Another assessment tool that is used for these high-x crystals is that of IR imaging. By placing a blackbody on one side of the slice (polished on both sides to $\sim$1 mm thickness) and a midwave camera system (CEDIP) on the other, images can be taken that reveal IR-absorbing defects. (This camera system uses an OSPREY detector manufactured at Selex ES from liquid phase epitaxial [LPE] material). This is a rapid, noncontact assessment method that can be used for all slices with cut-off wavelengths less than that of the camera system's detector.

Highly uniform, extremely high-x value material has been produced using these techniques. Figure 24.6 shows the uniformity map and IR transmission image of the shortest-wavelength 20-mm slice grown to date.

A second aim of this work was to scale-up growth using ACRT to maintain x uniformity. Several 40-, 50-, and 70-mm diameter crystals have been grown. Figure 24.7

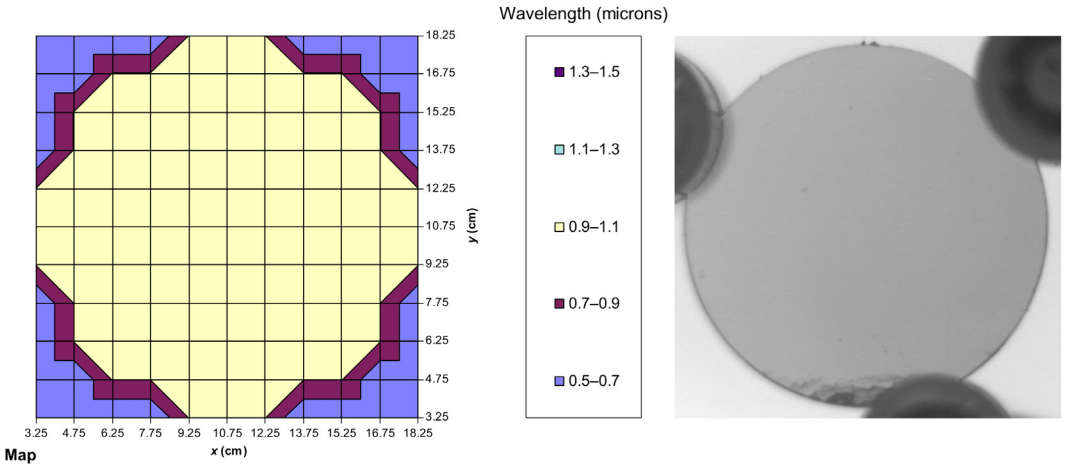

FIGURE 24.6 Radial distribution of wavelength (in μm at room temperature—0.91 μm ≡ x ~0.93) in 20-mm diameter slice. *Courtesy of Selex ES.*

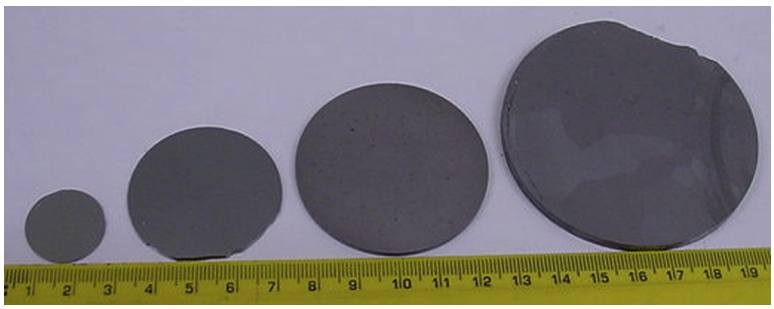

FIGURE 24.7 Comparison of 20-, 40-, 50- and 70-mm CMT slices. *Courtesy of Selex ES.*

shows slices from 20-, 40-, 50-, and 70-mm diameter crystals. The 70-mm crystal is the largest diameter CMT crystal grown anywhere, to this author's knowledge. In tandem with increasing diameter, the weight of crystals was also increased to maintain the number of usable slices. The largest weight currently used for 50-mm diameter crystals is ~2 kg. The highest x value seen in these 50-mm crystals (from a 30% start) is ~1.5 μm (x ~0.67). Figure 24.8 shows the wavelength uniformity of this slice, together with the IR image of the adjacent slice, where a central area (~36 × 36 mm in size) can be seen to be clear of defects or grain boundaries. Figure 24.8 also shows the overall size of this 50-mm diameter crystal.

In the preferred case of short cycle times, outlined above, Gray et al. [38], have confirmed the observations in our quenched crystals that no striations should be present.

Liu et al. [39], have modeled the ACRT process in small-diameter CMT with a rotation sequence very similar to that described above. They showed that the optimum conditions

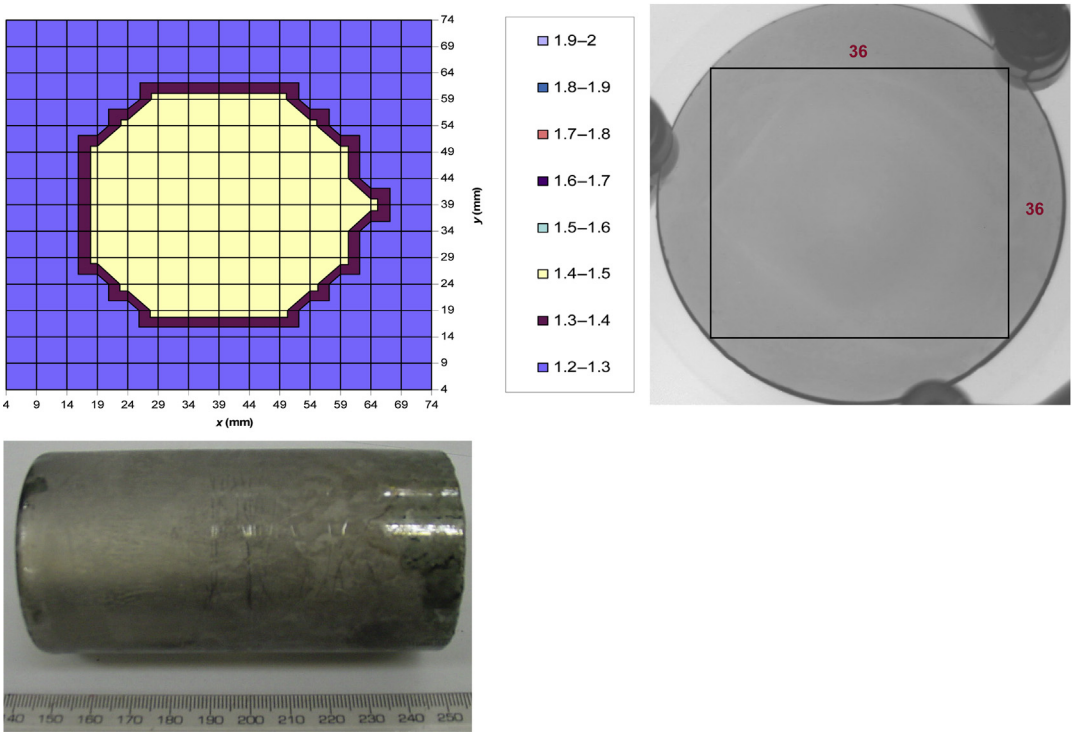

FIGURE 24.8 Radial distribution of wavelength (in μm at room temperature) in 50-mm diameter high-*x* slice from 30% start. *Courtesy of Selex ES.*

for flows, temperature, solute distribution, and interface depth were ~45 rpm with a total time of ~36 s, which are very close to the values of 40 rpm and ~33 s mentioned above. Jie [40] also modeled this system and found that the interface position shifted by up to 80 mm during growth with an axial temperature gradient of 10 K/cm, which has implications for the compositional control. Increasing growth rate caused this shift to occur more rapidly, but by the same overall extent, when no ACRT was used; however, with ACRT, this interface shift occurred independently of the growth rate and eventually reached ~100 mm in the last-to-freeze region. Thus, there was a need to vary the lowering rate during the growth process to keep the actual growth rate constant.

Bloedner and Gille [41] used ACRT in traveling heater method (THM) growth of 16-mm diameter CMT using various sequences. They were able to achieve marked improvement in growth rate, with no increase in second-phase precipitates or evidence of striations (more details on ACRT THM are given in Chapter 12 of Volume IIA).

24.3.4 ACRT in the Growth of CdTe/$Cd_{1-x}Zn_xTe$

The first use of ACRT in the growth of CdTe was by Wald and Bell [42]. The growth of larger-diameter, 50-mm material with ACRT was described by Capper et al. [43]. This

size was chosen to produce suitable grain sizes for 20×30 mm liquid-phase epitaxy substrate production for the subsequent growth of CMT layers. It was anticipated from earlier work on ACRT growth of CMT [23] that larger grain sizes would be produced. On studying the parameter values in Table 24.3 for the larger-diameter case (i.e., 50-mm), two distinct ACRT combinations of parameters were recognized: the combinations that maximize flows (items 1–6 in Table 24.3) and the combination that maintains stable Ekman flow (item 7 in Table 24.3). With $R = 25$ mm, combinations of 40 rpm with 15 s run/stop times and 4 rpm with 50 s run/stop times corresponded to the two regimes. Experimentally, it was found that crystals grown under the first regime consisted of many grains, yielding no usable substrates. This strongly suggested that stable Ekman flow was required to produce large grains. To confirm whether rotation rates <5 rpm were absolutely necessary, a crystal was grown with 10 rpm and 12 run/stop times. A weighing error caused this crystal to produce polycrystalline growth, but an interesting feature was seen on the top of the crystal, where the segregated liquid cadmium was quenched during ACRT stirring. Figure 24.9 shows what appear to be spirals on the acid-etched top surface. The spiral separation was ~ 0.1 cm near the periphery, increasing to ~ 0.5 cm near the center, as predicted from Eqn (24.5), and the number of spiral arms was in qualitative agreement with Eqn (24.4). This provided the first direct evidence that such ACRT flows exist in these high-temperature melts. When crystals were grown using 4 rpm with 50 s run/stop times, a single grain was seen to run the entire length of the 7-cm crystal, albeit with some edge grains, too. This suggests that ACRT did indeed increase the overall grain structure (see Figure 24.10).

Figure 24.10 shows the result of using a necked ampoule base in ACRT growth. It was concluded by comparison with other crystals that the constriction reduces the number of grains propagating through to the full-diameter region. At this point, Ekman flow dominates and, if stable, should minimize the nucleation of secondary grains.

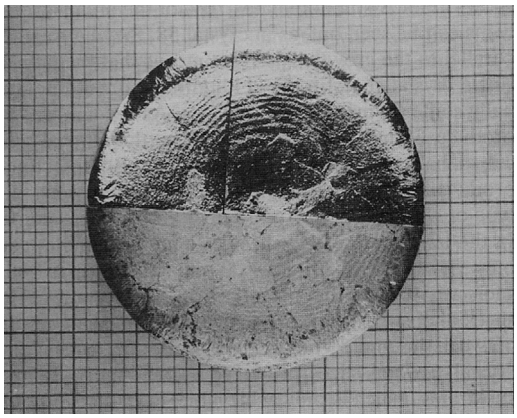

FIGURE 24.9 "Sprials" caused by ACRT on frozen Cd on top of CdTe crystal. *Reprinted from Capper et al. [43], copyright (1993) reproduced with permission from Elsevier.*

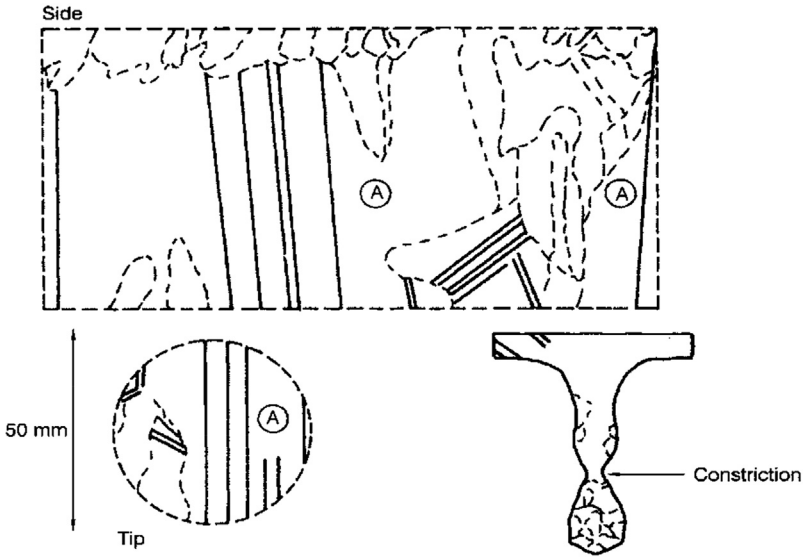

FIGURE 24.10 Grain map of CdTe crystal using ACRT and a constriction in the first-to-freeze region. *Reprinted from Capper et al. [43], copyright (1993) reproduced with permission from Elsevier.*

Figure 24.10 shows that this is successful because grain A is present over ~75% of the area. The cut in the central section shows that grain A occupies ~75% of the crystal volume. Several twins propagate through the length of the crystal, but these lie roughly parallel to the growth axis. This results in the largest single crystal (111) slices being potentially ~65 × 50 mm in size. As the aim of the work was generally to produce 30 × 20 mm slices; this crystal was cut in half to maximize the potential number of substrates. Obviously both sections could, and indeed did, produce 30 × 20 mm slices. Several slices from this crystal produced two 30 × 20 mm substrates. This is only achievable in 50-mm diameter crystals if the (111) twins lie nearly parallel to the growth axis. Sliding-boat Te-rich LPE growth (see Chapter 10 in Ref. [3]) requires regular, rectangular, or square, substrates, so having the (111) direction parallel to the growth axis is an obvious advantage.

Application of ACRT was also found to reduce the level of second-phase Te precipitates, strain (as measured by X-ray diffraction curve widths), and etch pit densities in CdTe (these were also equivalent to the then-current literature values). Chemical analysis of the Zn distribution in CdTe/$Cd_{1-x}Zn_xTe$ (CZT) crystals showed that ACRT moved the segregation coefficient much closer to unity, meaning that more of the ACRT crystal had a Zn level for lattice matching to the CMT to be grown on it (see Figure 24.11). The near maximum transmission value, at 750/cm, showed that the impurity levels in these ACRT crystals was also extremely low due to the enhanced segregation caused by ACRT melt mixing. Finally, substrates from some of these ACRT crystals were used to produce LPE layers of CMT with acceptable properties for use in IR detector manufacturing.

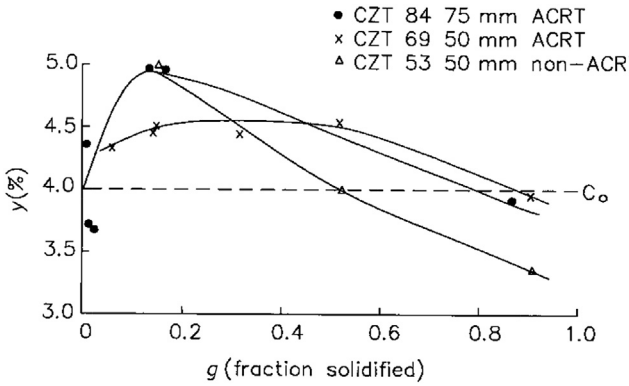

FIGURE 24.11 Segregation of Zn in non-ACRT and ACRT crystals of CdZnTe. *Reprinted from Capper et al. [23], copyright (1994) reproduced with permission from Elsevier.*

Wang et al. [44] studied the effects of ACRT on impurity behavior in vertical Bridgman-grown CZT. Segregation coefficients of several impurities were determined; however, because the one ACRT crystal was more heavily doped, no meaningful comparisons with non-ACRT crystals could be made. Wang et al. [45], studied the effects of ACRT and seeding in 60-mm diameter CZT crystals. They found that seeding clearly improved crystallinity and dislocation densities compared with ACRT growth but that ACRT improved the Zn distribution; that is, it reduced the segregation coefficient closer to unity and produced a similar improvement in impurity (In) behavior, mirroring that seen by Capper et al. [43]. However, this study [45] only compared one seeded crystal with one ACRT crystal, grown under otherwise identical conditions.

Jie et al. [46] used ACRT in their growth of 5-mm diameter $Hg_{1-x}Mn_xTe$ and modeled the Mn distribution. The segregation coefficient was found to vary with axial position.

24.3.5 ACRT in Group-IV Growth

There have been several reports of the extension of ACRT to the growth of group-IV elements and compounds. Bairava Ganesh et al. [47,48] used ACRT to induce striations in mc-Si used for photovoltaics to determine the growth rate during unidirectional solidification. A growth rate of ∼0.4 mm/min was found in 50-mm sized samples. It was noted that the carbon concentration was more homogeneously distributed with ACRT and there was also a reduction in the number of impurity precipitates. Belleman et al. [49] used transient simulation of mc-Si with ACRT over a 10-h growth time. For 12.5-cm diameter, 10-cm high crystals, a rotation rate of ∼1 rpm and an Ekman time of 600 s were used. It was found that ACRT increased the radial segregation of impurities, which perhaps is not too surprising at such low rotation rates and for such large samples.

ACRT becomes even important for crucible-free floating zone (FZ) growth of oxygen-free large-diameter (200 mm) silicon crystals [50,51]. To overcome the difficulty of growth front break out in the radial direction, especially at large diameters, the growing crystal is periodically rotated through a sequence of rotation angles. The direction of

rotation is changed, after each rotation, by a rotation angle belonging to the sequence. As a result, the diameter constancy is controlled markedly.

Kusunoki et al. [52] used ACRT in their Si-Ti solvent growth of SiC for use as substrates for the LPE growth of SiC layers. ACRT allowed growth rates to be increased up to 200 μm/h, enabling growth of 5-mm thick substrates. This is another example of ACRT as an "enabling" technique to produce something normal melt growth cannot readily produce to further progress production of a key material, in this case SiC. The resultant LPE layers had high quality, low impurity levels, and good electrical properties.

Seki et al. [53] employed ACRT in their top-seeded solution growth of SiC for high-power electronics applications. In 12-mm diameter crystals, a 30-rpm rotation rate was used to produce the desired 3C polytype for higher electron mobilities, at the expense of the undesirable 6H polytype.

24.3.6 ACRT in Other Material Systems

Several other materials systems have seen benefits from the addition of ACRT to the growth process. Distanov et al. [54] used unidirectional ACRT, with maximum rotation rates between 20 and 60 rpm, to grow good-quality Ag_3AsS_3. These crystals were used in nonlinear optics applications.

Lui et al. [55] found that ACRT suppressed constitutional supercooling in the growth of succinonitrile in acetone at room temperature, and hence morphological instabilities. Near the interface, the forced convection from ACRT was seen to be dominant. This same group [56] used both simulations and visualization techniques to look at the effects of various ACRT sequences. They found that the trapezoidal sequence is best because it maintains a controlled amount of melt mixing throughout the ACRT cycle, in agreement with the conclusions outlined in Section 24.3.2.

Uda et al. [57] used ACRT to grow 50-mm diameter crystals of langasite ($La_3Ga_5SiO_{14}$) for piezoelectric applications. Employing rotation rates of 0–25 rpm reduced the occurrence of undesirable secondary phases of lanthanum gallate and gallium oxide.

Kim et al. [58] and Dutta [59] used ACRT to increase melt stirring in their growth of antimony-based quaternary compounds because it is easily adapted for larger sizes and for sealed crucibles. They also noted that ACRT can be used in shallow melts where baffles/stirrers are not easily incorporated. To reduce constitutional supercooling, they needed to reduce the growth, but this proved to be uneconomical; hence, ACRT was used to increase the growth rate, by a factor of three in this case. In their (Ga,In)Sb ternary system, ACRT was also found to reduce crystal cracking.

24.4 Axial Vibration Control

The vibrational technique AVC applies axial low-frequency (tens of hertz) and small-amplitude (tens to hundreds of micrometers) vibration to the growth system [60,61]. The technique of applying vibration is realized either by vibration of the growing crystal

or by oscillation of a special submerged inert body/baffle, which is located near the crystal–melt interface and oscillates, inducing vibrational convection flows. Applying the vibration to the growth container/ampoule was experimentally and theoretically investigated for the Bridgman technique [62,63] and for the vertical zone-melting process [64,65].

The first studies of the influence of axial low-frequency vibrations on crystal growth from the melt appeared in the 1950s and 1960s [66–70]. Since that time, a number of papers on this subject have been published. The positive effects were found to occur to a different extent for a wide region of intensity/amplitude and frequency of vibration. The influence of vibrations on crystal growth in the ultrasonic (from tens of kHz to several MHz), acoustic (usually tens to hundreds of Hz), and even subsonic ranges (from 0.5 to 5 Hz) has been investigated. The displacement amplitudes are usually confined to several micrometers for ultrasound [71] and reach 10–25 mm in experiments on the influence of infrasound [72,73]. A detailed list of published papers can be found in reviews [74,75]. Data on the favorable influence of vibrations on various crystal properties have been obtained. However, those pioneering studies of vibrations were nonsystematic and casual: one author published usually no more than one or two papers. This situation is understandable and explicable because the mechanisms were unknown and really efficient use of axial vibration in crystal growth was very difficult to perform.

24.4.1 Physical Nature of the Phenomenon

The application of axial low-frequency vibration to the submerged body produces stable symmetric vibrational flows in the bulk liquid. This was shown by the primary numerical modeling of this phenomenon carried out by Avdonin et al. [76] and Zharikov et al. [77], both in 1989. The body with a dihedral rectangular edge executed linear harmonic vibrations in a stationary infinite liquid. The solution reveals the existence of a stationary average flow characterized by two areas of circulation, with opposite direction of motion flowing from the vibrating body edge (Figure 24.12). The average flow induced by oscillations of a solid body immersed in a liquid arises due to nonlinear effects. The physical nature of this phenomenon lies in the formation of a nonstationary boundary layer near the body surface and its periodic break-off, which causes the stationary movement in the liquid.

According to numerical simulation of vibration in the Czochralski process performed by Lyubimov et al. [79], the average AVC flow represented by two toroidal vortices of comparable intensity and specific directions could transform along with an increase of the vibration frequency into regular Schlichting flow when an external vortex occupies most of the flow area. The critical frequency for flow transition from AVC-type to Schlichting flow depends on the radius of curvature of the vibrating body edge: the smaller the radius, the larger the critical frequency. Lyubimov et al. [79] demonstrated this correlation by the corresponding diagram for some fixed value of vibration amplitude. A numerical study [80] has shown that, in the case of a vibrating disk located under

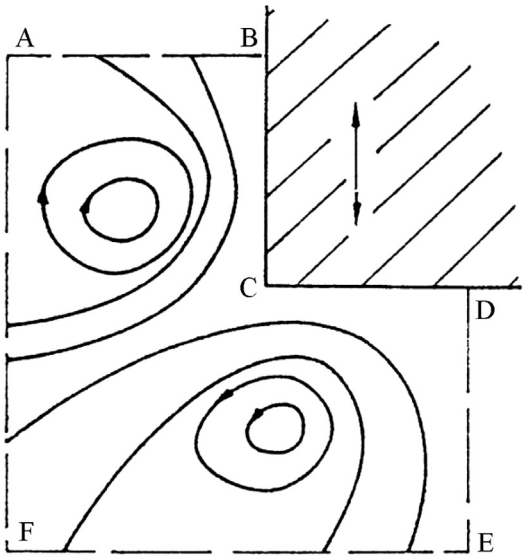

FIGURE 24.12 Fluid motion under vibration of a dihedral rectangular edge. *Adapted from Zharikov et al. [78].*

a solid–liquid interface (see below), the vibrational efficiency is determined not only by the sharpness of the oscillating disk edge but also by the ratio of an edge radius to a cylindrical disk thickness. Another mechanism leading to similar transformation of the flow pattern is given by Zharikov [81]. This is connected with the penetration depth of the solid–liquid interface regarding the position of the free surface of the liquid.

For a comparison of the various vibration regimes, the nondimensional vibrational Reynolds number is used:

$$\mathrm{Re_v} = \frac{2\pi f A R}{\nu} \tag{24.10}$$

An alternative is its variation, the pulsating Reynolds number:

$$\mathrm{Re_p} = \frac{2\pi f A^2}{\nu} \tag{24.11}$$

Another parameter characterizing the vibration regimes is vibrational acceleration, which is useful for analysis of parametric dependences and comparison of experimental data related to the same material within a series of experiments:

$$I_a = (2\pi f)^2 A \left[\mathrm{m/s^2}\right] \tag{24.12}$$

In Eqns (24.10)–(24.12), f is the vibration frequency, A is the vibrational amplitude, ν is the kinematic viscosity, and R is the vibrating body radius.

Bulk fluid flows of vibrational convection initiated by oscillations with low-frequency and small-scale amplitude is a specific type of stationary flow in the fluid. It differs from known fluid flow, which is evident from a comparison with acoustic flows [82] and Schlichting flow [83]. The phenomenon of vibrational convection cannot be explained by

the theory of acoustic flow because the characteristic dimension of the vortices in such currents is similar to or greater than the wavelength of the sound [82]. In contrast, the typical wavelengths for the vibrations under study are about 10 m, whereas the characteristic dimensions of the circulation, as a rule, are three orders of magnitude less. Steady-state convective flow generated by vibrations is established at lower amplitudes than the Schlichting flow. The appearance of small-scale vortices near the edge of the vibrating body is a significant difference from ordinary flows within the boundary layer.

The influence of low-frequency and small-amplitude axial vibration on crystal growth from a liquid phase is not confined to formation of bulk flows shown in Figure 24.12. Various new effects of vibration were discovered during the subsequent studies [74,75,80,81], as discussed in the following sections. Although the effects were observed in the case of particular vibration-assisted growth configurations, there are reasons to believe that these effects have a common character.

24.4.2 Effects of AVC on Crystal Growth from the Melt

Axial vibrational control allows one to efficiently govern the heat and mass transfer as well as the growth kinetics during crystallization from the melt. The introduction of axial vibration with frequency of tens to hundreds of hertz and amplitude up to hundreds of micrometers into a liquid phase provides the growth of high-quality crystals with high growth rates, under the control of stoichiometry and dopant distribution. AVC can noticeably alter both the composition and dopant segregation/distribution in the crystal. Such behavior was shown for both the Czochralski and Bridgman methods. AVC provides leveling of both dopant concentration and stoichiometry along and across the crystal [84–87]. The AVC-assisted Bridgman method under controlled pressure technique allowed the growth of CdTe and PbTe crystals with the required nonstoichiometry, which was constant along the crystal length [86,88,89].

The numerical modeling performed by Fedyushkin et al. [90,91], Fedyushkin and Bourago [92], and Avetisov et al. [93] has shown that vibrations can reduce the thickness of boundary layers at solid–liquid interfaces [90,91], which is of critical importance when growing single crystals. Using vibrational agitation of the melt, one can change the value of the temperature gradient at the interface—that is, one can change the kinetics and rate of crystal growth. The boundary layer thickness depends on the amplitude, the frequency, and the Prandtl (Pr) number of the melt. The melts with large Pr numbers, such as oxides and salts, are controlled by low-frequency vibration very efficiently. The influence on melts with small Prandtl numbers will be essential with an increase of the amplitude and the frequency of vibration (with increase of the vibrational Reynolds number Re_v).

A change of the hydrodynamic situation and temperature conditions near the interface provides the possibility to control the shape of crystallization front. Simulations demonstrated that the shape of the crystal–melt interface is strongly dependent on vibrational parameters [93]. Experimentally, the flattening of the solid–liquid interface

was obtained for growth of $NaNO_3$ crystals by both AVC-assisted Czochralski [74,80,94] and Bridgman [86] methods.

In a series of papers, Avetisov et al. [80,86,88,94–96] demonstrated that the Bridgman and Czochralski configurations significantly improved structural perfection of crystals (decrease of dislocation density, crystal mosaicity, and point-defect concentration) grown under AVC conditions compared to nonvibrational crystals. This is connected mostly with changes at the solid–liquid interface and nearby arising due to the vibrational influence. There are the changes of boundary layers thickness and temperature gradients values, as well as changes of the melt structure near the interface such as destruction of clusters, initiation of reconstructive processes, etc.

Crystal growth under axial vibration results in a substantial increase of the maximum allowable growth rate. It was shown [86] that the growth rate of $NaNO_3$ crystals grown by the Bridgman method under vibration of a submerged baffle with frequency 50 Hz and amplitude 0.2 mm could be increased from 2 mm/h to 10 mm/h without loss of crystal quality. Along with increasing of the vibration amplitude at fixed frequency (50 Hz), the dislocation density in $NaNO_3$ crystals grown by the AVC-assisted Bridgman technique decreased down to unit values (Figure 24.13(b)).

The AVC-grown crystals by the Czochralski method were characterized as dislocation free at pulling rates less than 10 mm/h and vibrational frequency higher than 10 Hz (Figure 24.13(a)). The reason for the significant decrease of dislocation density and substantial enhancement of growth rate along with maintenance of crystal quality could be attributed to a reduction of the diffusion layer thickness at the crystallization front and an increase in the diffusion rate, as well as to the influence of the vibrational force on heat and mass transfer at the interface and the influence on precrystallization phenomena, which stimulate the destruction of clusters in the liquid at the boundary layer. It should be noted that the latter behavior is more pronounced for strongly associated

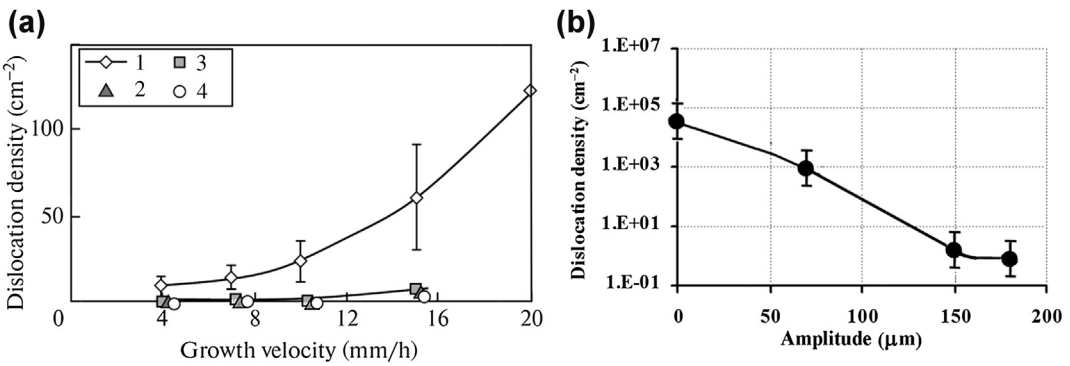

FIGURE 24.13 Dislocation density in $NaNO_3$ single crystals grown under vibration (a) by Czochralski method (type II) versus growth rate with amplitude 1 mm and different frequencies (1) 0; (2) 10 Hz; (3) 17 Hz; (4) 25 Hz. *(Adapted from Avetissov et al. [95].)* (b) by the Bridgman method versus amplitude at oscillation frequency 50 Hz *(Adapted from Avetissov et al. [86].)*.

melts of compounds with high ionicity, such as fluorides, oxides, silicates, and some A^2B^6 semiconductors.

Reducing of the diffusion layer together with destruction of clusters at the interface result in an increase of the diffusion speed of melt species and their easier incorporation into a growing crystal. This leads to enhancement of the growth rate and building of a more perfect crystal. An additional contribution to the decrease of the dislocation density could give the energy of vibration itself, which plays a role of external force stimulating the motion of dislocations and their further annihilation.

Improvements of the structural perfection of crystals grown under the AVC impact was confirmed for $NaNO_3$ by studies of the Raman spectra and measurements of X-ray rocking curves [80,95]. In the case of $Bi_{12}SiO_{20}$ crystals grown under low-frequency vibration by Zhang et al. [97], the extension of the short-wavelength spectral absorption edge and corresponding narrowing of X-ray rocking curves in a certain range of vibration amplitudes that appear also as evidence of improvement of crystal perfection was demonstrated.

There are many documentary pieces of evidence about melt clusterization, polymerization processes in the melts, and precrystallization phenomena (see, e.g., Refs [98–101]). Actually, the energy of motion of an oscillating body, together with induced heat and mass flows through their impact on boundary layers and bulk melts, could lead to structural reconstruction of melt, especially close to the crystallization front [78].

Direct measurements of the heat of crystallization of $NaNO_3$ and CdTe melts subjected to agitation by low-frequency vibration using the oscillating baffle submerged in the melt (AVC-assisted Bridgman configuration) demonstrated [96] up to a 30% increase compared to the melt without agitation. This can be explained as a real influence of low-frequency vibration on the microstructure of the melt. The calculation made by the authors of this paper led them to the conclusion that low-frequency vibration of the solid baffle can partially destroy the existing clusters in the melt, which is especially the case for the associated melts, such as oxide, silicate, and borate melts.

24.4.3 Application of AVC in Crystal Growth Methods

AVC can easily be adapted to many methods of crystal growth from a fluid medium (melt or solution). Application of AVC to different techniques of crystal growth from the melt was presented elsewhere [81,102]. By now, it is realized with regard to Czochralski, top-seeded solution growth, vertical Bridgman (VGF), zone melting, and floating zone methods, which will be discussed in more detail. The most comprehensive work has been done for AVC-assisted Czochralski (AVC-Cz) and Bridgman (AVC-Br) techniques. Accordingly, the majority of this section discusses these two important melt growth methods assisted with controlled vibrational influence.

Of particular interest is the use of controlled low-frequency vibration for crystal growth experiments in space. For acceleration magnitudes of 10^{-4} g and less, flows generated by controlled vibration can be used to suppress undesirable convective effects

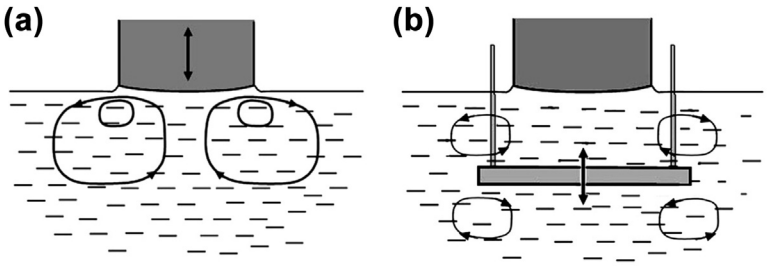

FIGURE 24.14 Vibrational flows in AVC-assisted Czochralski method. AVC-Cz type I: vibration of crystal (a). AVC-Cz type II: vibration of submerged baffle (b). *Adapted from Zharikov [102].*

caused by "g-jitter." The convective heat flow component caused by the controlled vibration can be of the same order of magnitude or larger than the conductive heat-transfer mode. The first experimental confirmation of AVC promise to control the fluid flows in space and create the new efficient technologies of crystal growth in microgravity was done on the Mir space station by Zharikov et al. [103].

AVC-assisted Czochralski I method. In the Czochralski configuration (type I), the crystal itself plays the role of a vibrating body, which is contacting the surface of melt and produces intensive vibrational flows in the bulk melt (Figure 24.14(a)). The advantage of this kind of vibrational impact, in comparison to other flow initiation strategies, is that it exerts a great influence on transport processes in immediate proximity to the solid–liquid interface. In Figure 24.15, the size of vibrational vortices and flow velocity for AVC-Cz (type I) are plotted versus the vibration amplitude. It is seen that the size of the vortex linearly depends on the vibration amplitude (Figure 24.15(a)). The average linear flow velocity in the vortex strongly increases along with the amplitude of vibration and also increases with the viscosity of the liquid (Figure 24.15(a)).

Experimental studies of interaction between vibrational and thermal convections in the Czochralski configuration showed that vibration could efficiently compete with the natural convection flows because the direction of melt motion in vibrational vortices is opposite to that of thermal convection. Along with an increase of the vibrational Reynolds number, the vortices of vibrational convection suppress the thermal convective flows and spread to the crucible wall, occupying more and more space until the whole volume of the crucible becomes occupied only by vibrational flow [61].

AVC flows allow efficient suppression of the temperature oscillations at the interface arising due to irregular thermogravitational convection flow [104]. As was shown by Avetisov et al. [80], the application of low-frequency vibration to the submerged disk in the Czochralski configuration type II (see Figure 24.14(b)) produces a decrease in the thermoconvectional fluctuations of temperature near the solid–liquid interface from 8 K for conventional Cz to 0.2 K.

The suppression of the thermal convective flows leads to smoothing of compositional fluctuations in doped crystals [84,90,91]. Experiments on AVC-assisted high-temperature Czochralski growth of yttrium-scandium-gallium garnet doped by erbium and

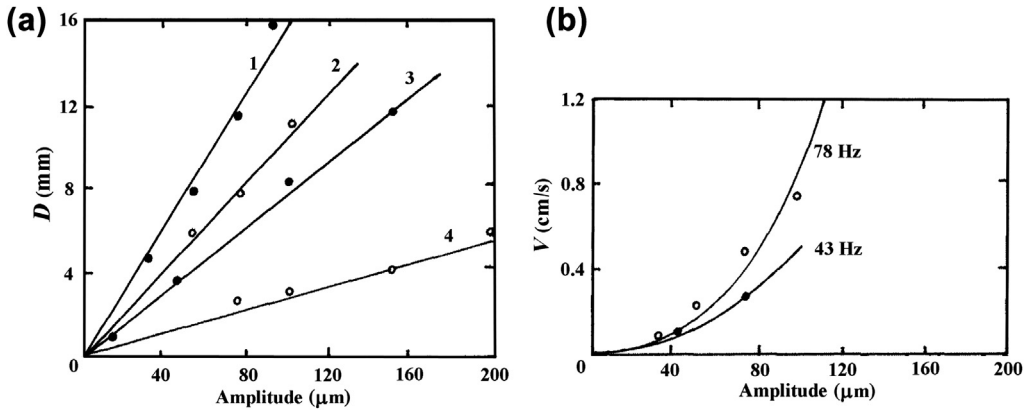

FIGURE 24.15 The size of vibrational vortices (a) and flow velocity (b) for AVC-Cz (type I) upon the vibration amplitude. *Adapted from Zharikov et al. [61].*

chromium ions Er,Cr:YSGG (melting point 1910 °C) showed [84] noticeable weakening of striations.

The simultaneous interplay of the vibration, thermal convection, and rotation for the Czochralski configuration was investigated by numerical calculations [92] for the case of opposite rotations of the crystal and the crucible. It was shown that interaction of these three factors leads to the appearance of flows with a complex structure consisting of two domains. For the particular parameters of calculations ($A = 100$ μm, $f = 50$ Hz, Gr = 214,610, Pr = 5.43), it was found that the flow structure in the external domain is caused by the thermal convection; in the internal domain, the flow pattern is formed by both the vibration and rotation. Conflict between the vibration and the rotation takes place. The preliminary results of these calculations suggest that this conflict could lead to homogeneity alterations of the temperature field. Further parametric investigation of this triple interaction is necessary to get a proper view of the complex phenomenon.

Intensive axial low-frequency vibration applied to a vibrating body in the Czochralski configuration produces not only bulk flow but also complex surface flow (Figure 24.16). It is polyharmonic motion that includes two different but closely related flows [106]. The first of these is a standing surface wave that expands from the vibrating crystal to the crucible wall. The other type of flow superimposed on this wave appears as large vortices, similar to cells—the dimension of which is several times greater than the length of the surface wave. In Figure 24.16(a), one can see only surface vertical cells; however, along with an increase of vibrational Reynolds number Re_v in addition to them, the standing surface wave appears (Figure 24.16(b)). The wavelength of the standing wave, the number of vibrational vortices, and the velocity of the liquid motion in them are controlled by the vibration parameters (see Figure 24.16(c)). For instance, in the case presented in Figure 24.16(b), the number of surface vortices is eight and the velocity of surface flow $V = 2.2$ cm/s.

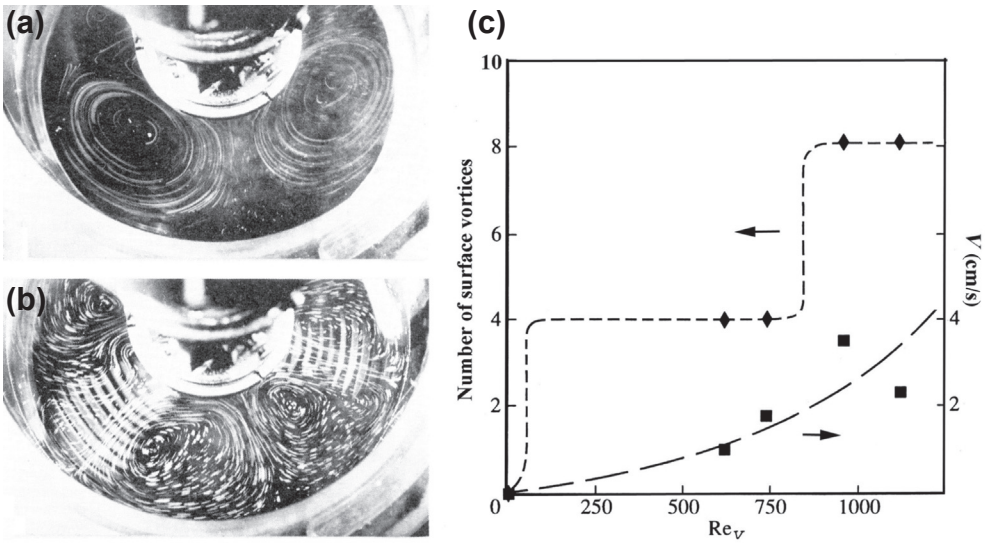

FIGURE 24.16 Surface flows in Czochralski configuration under vibration of crystal (AVC-Cz type I). *Left:* (a) and (b) change of flow pattern as a function of vibrational Reynolds number. *Right:* (c) number of surface vortices (rhombohedra) and flow velocity depending on vibrational Reynolds number. *From Verezub et al. [105].*

The surface vortices could be involved in a slow motion around the crucible axis in a ring gap between the vibrating crystal and the crucible wall. An additional effect produces the crucible rotation, which creates a shearing perturbation. This leads to a reduction of a number of surface vortices by their association into pairs [105].

The numerical calculations of interaction between the low-frequency vibration ($A = 100$ μm, $f = 50$ Hz) and the Marangoni convection (Mn = 500) showed [92] that the vibration allows one to weaken the influence of the thermocapillary Marangoni convection in Czochralski crystal growth. The vibration makes the temperature distribution at the free surface more homogeneous, reducing the thermal gradients along the melt surface. The growth of crystals in low-temperature gradients is preferable because it results in a better quality; in addition, it was already successfully demonstrated, for instance, in the case of sapphire growth by Kyropoulos and HEM (Heat Exchanger Method) or, in the case of BGO crystals, grown by a low-thermal gradient Czochralski technique (for a review, see Ref. [102]). On the other hand, if it is necessary to increase the radial gradients in the system for some reason, it can be done by well-known regular technological measures, holding the neutralization of the surface-tension-driven flow by forced surface vibrational flow.

The action of thermocapillary convection on crystal growth processes is generally considered to be undesirable. It significantly affects the crystal growth for the free-surface fluids, especially in reduced-gravity environments. However, even under normal gravity, the thermocapillary effect can be very important in the overall transport pattern. It is more pronounced for high Prandtl fluids, such as oxide melts; however, the

results indicate (e.g., Ref. [107]) that also in low-Pr melts, the thermocapillary impact is important and may significantly affect the quality of the crystal by influencing the turbulent transport of heat and mass near the growing crystal. Thermocapillary convection is shown [108] to have an influence on various solidification parameters, such as the shape of the solid–liquid interface and the solute segregation. It was demonstrated for both Czochralski and float zone processes that thermocapillary convection becomes unstable (oscillatory) at high enough Marangoni numbers, which gives rise to temperature oscillation in the melt [109,110], thus generating impurity striations in growing crystal. Therefore, it is necessary to take into consideration a contribution of Marangoni tension in directional solidification processes [111]. A review of various numerical and experimental studies of the surface-tension-driven flow in crystal growth melts can be found in Refs [112,113].

The action of thermocapillary convection on crystal growth and the transition to unsteady behavior is hard to control [114]. In particular, the observations of Azami et al. [115] indicate that the surface flow, and its instability pattern, of the CZ melt cannot be fully suppressed by a magnetic field. Hence, the phenomenon of the complex surface flow formation due to axial low-frequency vibration gives a unique opportunity to control/compensate for undesirable surface flows caused by both thermocapillary and thermoconcentration Marangoni convections [106].

AVC-assisted Czochralski-II method. Another scheme of AVC introduction in the Czochralski configuration has been proposed [95]. According to this scheme, the forced flows in the melt are generated by axial oscillations of a disk submerged under the crystal (see Figure 24.14). The vibrational flows are directed from the disc toward the crystal and the bottom of crucible. In the area between the disc and crystal, the direction of forced vibroconvective flows is opposite to the direction of thermoconvection flows and facilitates melt mixing in the entire volume of the crucible.

The experiments carried out according to the new version of AVC-assisted Czochralski were performed by growth of $NaNO_3$ crystals and $NaNO_3$-$LiNO_3$ solid solutions, as well as by physical modeling using water–glycerin mixtures with viscosities from 1 to 100 cP [80,87,93–95,116]. It was found that this new scheme allows stable symmetrical vibrational bulk flows to be obtained within the entire range of viscosities.

The vibrating disk is fabricated from the same inert material as the crucible. For instance, in physical modeling experiments with water–glycerin solutions, the quartz glass was used for both disk and crucible fabrication. The same material was used during the growth of nitrate crystals of different compositions. For growth of larger $NaNO_3$ and $NaNO_3$-$LiNO_3$ crystals from 1000-cm^3 crucibles, the disk was fabricated from alumina, which made it possible to prepare more sophisticated baffle configurations [116].

AVC-assisted Bridgman method. The insertion of a submerged body, which is located in the melt near the solid–liquid interface and subjected to low-frequency vibration, induces macroscopic vibrational convection flows, as in the Czochralski case

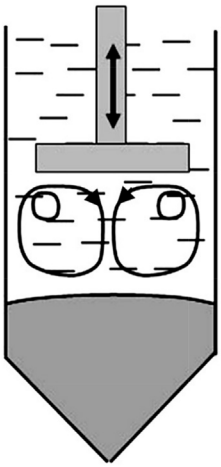

FIGURE 24.17 Vibrational flows in AVC-assisted Bridgman/VGF method. *Adapted from Zharikov [102].*

(Figure 24.17). For growth of PbTe [85] and CdTe [89] by the Bridgman technique from evacuated closed ampoules, the specific unit for the excitation of low-frequency vibration was constructed [88]. It contains a system of external permanent magnets, providing a free suspension of the internal permanent magnet as well as the electromagnet, which provided vibrations of the latter magnet with a specified frequency and amplitude. In this case, both the reactor and baffle were made from graphite.

Flow from the vibrating baffle down to a crystal causes efficient stirring in the melt, produces a displacement of the crystal–melt interface, and changes its shape. Manipulation of the amplitude–frequency input can be used to obtain a practically flat crystal–melt interface.

Numerical simulation of CdTe growth by the axial vibration control technique in the Bridgman configuration [89] showed that switching on the disk oscillation causes an increase in the temperature gradient between the disk and the crystal–melt interface. The flow velocity also increases by one order of magnitude compared to the non-vibrating regime.

Physical modeling on water–glycerin mixtures showed [117] that an increase of the vibrational intensity (Re_v) as well as the diameter of the vibrating disk resulted in more intensive vibrational flow. The change in diameter of the vibrating baffle considerably altered the flow pattern in the melt [118]. The normalized difference between the cross-sectional area of the ampoule and the cross-sectional area of the vibrator is used as a geometrical parameter:

$$S_k = \frac{D^2}{d^2} - 1 \tag{24.13}$$

where D is the internal diameter of the ampoule and d is the diameter of the vibrating body.

The application of vibrating disks of different shapes in the AVC-assisted Bridgman method have been investigated by physical modeling of transparent model liquids [117] and by numerical simulation [89]. In the case of vibration of the whole ampoule in the Bridgman method, the mechanism of the resultant vibrational convection differs from vibration of a body with sharp edges in a fluid. The closed-ampoule translational vibration under isothermal conditions does not result in any flow. The liquid in this case behaves as a rigid body. The vibrations of an ampoule with a free liquid surface can produce rather intensive flows, but usually they are limited by the surface and cannot exert much influence directly on the crystallization front.

In the presence of an axial temperature gradient when the fluid density is nonuniform, fluid motion known as thermovibrational convection may ensue. However, the magnitude of this motion strongly depends on the orientation of the vibrational direction with respect to the local density gradients. Fedoseyev and Alexander [119] showed that the inclined oriented direction of vibration in relation to the ampoule axis enhances the intensity of convection flows. It was shown that axial vibration of the ampoule is the least efficient and the maximum observed effect corresponds to an angle of 90°.

Several papers discuss low-frequency vibration axially applied to the ampoule in vertical Bridgman growth [62,97,120,121]. No notable effect of vibration on microstructure, compositional profile, interface shape, etc. was found by Caram et al. [121] or Yuan et al. [62] for such a configuration of experiment. Feigelson and Borshchevsky [120], who grew CdTe crystals, and Zhang et al. [97], who studied the growth of $Bi_{12}SiO_{20}$, have shown that low-frequency axial vibration applied to the growth ampoule could produce a perceptible effect. These papers demonstrated the improvement of crystal perfection by a decrease in dislocation density [120] and by control of X-ray rocking curves and short-wavelength spectral absorption edge of the grown crystals [97].

AVC-assisted floating zone method. The controlled vibration induces a flow that streams away from the vibrating end wall along the zone surface, returning through the bulk [122]. Because this flow has a direction opposite to the adjacent thermocapillary flow in the floating zone, it can compensate for this undesirable convection. As a result, the vibration end of the solid–liquid interface becomes flatter, indicating the presence of more uniform axial temperature gradients and flat isotherms near the interface.

Several authors have investigated the use of axial vibration in the floating zone method by experimental studies and by numerical simulation [79,122–125]. It was found that vibration produced a notable influence on the heat transport and on the interface curvature. Grugel et al. [123] and Shen et al. [122] observed a flattening of the interface accompanied by a reduction of radial temperature gradients, as well as a change in the eutectic microstructure of $NaNO_3$-$Ba(NO_3)_2$ upon application of the vibration.

AVC-assisted zone melting method. Oscillations in this method were applied to the ampoule (container) in both the vertical [64] and horizontal [126] versions. The mechanisms of initiation and development of vibrational flow in this method are more complicated than in the case of ampoule vibration in the Bridgman method or in the case

of the AVC-assisted floating zone method due to the larger number of boundaries where the density is changing, which may create the complicated interplay of the forced flows. In the horizontal version, an additional contribution makes the free surface of liquid.

Experiments on the growth of $NaNO_3$ crystals by a horizontal zone melting process [126] showed that vibration considerably suppresses the temperature oscillations in the melt and allows the shape of the solid–liquid interface to be governed and made flatter. Strutynska [64] found that vibration significantly affected the hydrodynamics, heat and mass transfer, the distribution of impurities, and kinetics of growth of the investigated Bi_2Te_3-based thermoelectric materials. Owing to the vibration effect on the melt, the distribution of impurities becomes more uniform, and the radial and axial homogeneities of materials are increased. According to measurements, the material homogeneity with regard to Seebeck coefficient improved by a factor of 2—and in respect to electric conductivity, by a factor of 3.

The effects of axial vibration on the heat flow, the growth rate, and the interface shapes have been studied numerically for vertical zone melting [65]. It was found that the low-frequency axial vibration can be effective for the control of melt flows and the growth interface. Nevertheless, to prevent crystal growth from periodic remelting, the author recommends frequencies higher than 10 Hz.

24.4.4 Crystal Materials Grown by the AVC Technique

Up to now the AVC-assisted crystal growth by Czochralski method has been realized for $NaNO_3$, $NaNO_3$–$LiNO_3$ solid-solutions [61,95], and some complex oxides with garnet structure (particularly Er,Cr:$Y_3Sc_2Ga_3O_{12}$), as discussed above. Pankrath et al. [127] reported the successful growth of $K(Ta_{1-x}Nb_x)O_3$ solid solutions with composition $0.30 < x < 1$, by applying the AVC technique with a vibration frequency of 50 Hz and an amplitude of 0.5 mm to the Czochralski configuration using the top-seed-solution growth method. These vibration parameters were considered optimal, allowing the striation-free $K(Ta_{1-x}Nb_x)O_3$ samples to be obtained.

AVC-assisted crystal growth by the Bridgman method has been realized for both low melting point and high melting point dielectric and semiconductor materials [86,88,97,128,129]. In particular, the AVC-Br technique was adapted for growth of $NaNO_3$, AgBr, AgBrCl, $Bi_{12}SiO_{20}$, PbTe, and CdTe crystals and the corresponding equipment for crystal growth was fabricated, including an AVC-assisted computer-controlled transparent furnace for growth of low melting point compounds [128] and a high-temperature sealed furnace for crystallization of decomposing materials [88].

Crystal growth of Bi_2Te_3-Bi_2Se_3 and Bi_2Te_3-Sb_2Te_3 solid solutions by an AVC-assisted vertical zone melting technique has been reported [64]. It was shown that vibration of the ampoule during the growth contributes to leveling of the crystallization front and mixing of melt components. Owing to the vibration effect on the melt, the distribution of impurities became more uniform, and the radial and axial homogeneities of materials were increased.

24.5 Other Types of Oscillatory Techniques

24.5.1 Ultrasonic Vibration

Imaging of convection in a Czochralski configuration under ultrasound waves was studied in model liquids using the crystallizing naphthalene–camphor eutectics [130], water–glycerol mixture [131] and distilled water [132]. In one study [133], water–glycerol mixture and acetone were using as model liquids. Ultrasound was introduced into the model liquid from a piezotransducer through a waveguide from the top [130] or to the crucible bottom [132–134]. When the melt agitation was organized from the top, the initiated acoustic flows were directed downwards from the vibrating surface. With bottom insertion of ultrasound, an upward flow formed in the liquid from the center of the crucible bottom toward the crystal model has been found. Hayakawa et al. [134] introduced ultrasonic vibrations (USV) of 10 kHz and 60 W. The velocity of flows caused by ultrasonic vibration was very high compared with that of both the forced and thermal convections due to rotation and buoyancy, respectively. According to Ref. [134], because the ultrasonic vibrations have a thermal effect, they can reduce the region of a supercooled melt. As a result, the shift and reduction of the facet region occurs under the ultrasonic vibrations.

Kozhemyakin and coworkers [132,133] used the higher-energy ultrasound with frequencies in the MHz range with an ultrasound intensity up to 0.3 W/cm^2, which was smaller than the cavitation threshold. They found that instead of the fluid flow, the standing wave forms after a few seconds in the central part of the bulk liquid by the diameter of waveguide between the crucible bottom and the solid–liquid interface. The distances between the standing wave antinodes were around 1 mm, which corresponded to half the wavelength of the ultrasound. They prevented the motion of convective flows in the region of standing waves. At the same time, in the periphery of the liquid, stable rotating vortices exist that stir the peripheral area of liquid. As a result, nonuniform heat and mass transfer conditions form in the melt.

In the regime of an ultrasonic standing wave, the heat sources are localized in an area of maximal shift and they are periodically distributed along the axis of the ultrasound resonator. The crystal growth rate will be modulated, which leads to the formation of striations in the crystal with a space period equal to half the wavelength of the ultrasound. According to Ref. [135], the striations in the central part of $Ga_{0.03}In_{0.97}Sb$ single crystals vanish when ultrasound at a frequency in the MHz range is applied.

A number of studies were concerned with the influence of ultrasound on the distribution of doping impurities in the crystal growth of compound semiconductors, dielectrics, and on the crystallization of various metallic alloys [131,136–139]. A reduction of the diffusion layer thickness, enhancement of the temperature gradient at the interface, and intensification of the zone refinement purification was found by Abramov et al. [140] when ultrasound (frequency 19.7 kHz, power up to 60 W) was applied to naphthalene growth by zone melting.

Numerical calculation of the influence of ultrasonics on the VGF process applied centrally from the topside of the crucible [141] demonstrated that using an ultrasonic frequency of 581 kHz produces Schlichting flow inside the hydrodynamic boundary layer, which helps to remove the harmful diffusion boundary layer, for instance, as the authors underlined, during directional solidification of silicon ingots for photovoltaics. The use of USV in the VGF growth of germanium crystals in addition to a double-frequency traveling magnetic field [142] showed the increase of the melt mixing within the diffusion boundary layer by intense Schlichting curling. As a result, the morphological interface stability can be enhanced and the axial carrier distribution approached the theoretical curve of complete melt mixing.

A novel approach to application of ultrasound to the Czochralski growth system has been proposed by Kozhemyakin [143]. In addition to ultrasonic waves introduced in parallel to the pulling axis from the crucible bottom, ultrasound with another frequency was entered into the melt perpendicular to the growth direction under the solid–liquid interface from the sidewall of the crucible. The author emphasizes that all previous experiments with axially directed ultrasonic waves were unsuccessful in getting striation-free single crystals. On the contrary, with the introduction of ultrasound in two orthogonal directions at frequencies differing by factor of 2 (0.71 MHz parallel and 1.44 MHz perpendicular to the pulling axis), the striations in grown InSb crystals with a convex solid–liquid interface were totally eliminated.

A few papers have been published on the influence of ultrasound on bubble entrapment by the growing crystals and their optical quality [142,144]. Vyshnevskiy et al. [139] investigated the bubble formation in sapphire and Ti:sapphire crystals grown by Czochralski in an ultrasonic field. It was found that the effect of ultrasound on the bubble entrapment from the melt by the growing crystal depends on the ultrasonic frequency. The reduction of the rate of bubble entrapment by the growing crystal by a factor of 2–2.5 was achieved by using ultrasound with frequency 350–400 kHz.

24.5.2 Coupled Vibrational Stirring

Liu et al. [145] developed a method for rapidly stirring liquids called coupled vibrational stirring (CVS), which appeared to be useful in crystal growth applications; in particular, it could be applied to the vertical Bridgman growth. CVS involves the application of orthogonally coupled low-frequency vibrations to the growth ampoule in the x–y plane and produces strong flows emanating from the free fluid surface. Because CVS flows are generated at the free surface of the liquid and propagate downward, a velocity gradient develops, with the fastest flows near the surface. Both the velocity profile and the depth of flows are highly dependent on fluid viscosity, vibrational frequency, and crucible diameter [146].

The CVS technique was applied to several real crystal growth systems. In the transparent $CsCdCl_3$ Bridgman melt system [145], the solid–liquid interface position was found to be a function of the vibrational frequency. Liu et al. [147] showed that

CVS-induced flows improved the initial grain selection and chemical homogeneity of Bridgman-grown CdTe crystals, but with some degradation in crystalline quality. DeMattei and Feigelson [148] examined the effects of CVS on temperature profiles during the growth of $PbBr_2$. The application of CVS flattened the temperature gradient in the melt; however, at the same time, the temperature gradient at the interface was dramatically increased as a result of CVS flows.

Feigelson and Zharikov [149] and Zawilski et al. [150] used three different systems to investigate the impact of CVS-generated flows in a Bridgman growth environment. In addition to water/glycerin solutions, which were used as a physical modeling system to study fluid flow, CVS was applied to two growth systems—namely, sodium nitrate ($NaNO_3$) and lead magnesium niobate–lead titanate (PMNT) with the general formula $(1-x)$ $PbMg_{l/3}Nb_{2/3}O_3$—$xPbTiO_3$. Zawilski et al. [150] showed that the crystal–melt interface position is a function of vibrational frequency and a continuous frequency ramp is necessary to reduce the growth rate fluctuations. CVS was found to be useful in manipulating the growth interface shape of $NaNO_3$ at high growth rates. A flatter interface curvature was obtained at high growth rates (>10 mm/h) in the presence of CVS flows. In the PMNT system, the use of a continuous vibrational frequency ramp during growth was shown to produce improved growth control.

24.6 Conclusions and Outlook

This chapter has described several nonsteady mechanical means of stirring melts to influence the growth of crystals of various types. The two main themes have been forced stirring by the accelerated crucible rotation technique and various forms of vibrational control, and the theoretical bases of these two types of stirring have been outlined, as summarized in Table 24.4. In the former case of stirring by ACRT, major improvements in compositional uniformity, compositional ranging, size of crystals produced, segregation of both matrix and impurity elements, grain size, and overall crystal quality are seen in the important II–VI compounds of cadmium mercury telluride and cadmium zinc telluride used in infrared detectors and optical components and in epitaxial substrates, respectively. More recently, ACRT has also been applied to a range of elemental (e.g., silicon) and compound materials (e.g., silicon carbide, Ag_3AsS_3, langasite ($La_3Ga_5SiO_{14}$), and Sb-based quaternaries), with improved properties seen in the majority of cases.

Another technique of mass-transfer control in crystal growth is axial vibrational control, which uses the introduction of low-frequency and small-amplitude axial vibration into liquid phase either by a submerged inert solid body or by the crystal itself. AVC produces a specific type of stationary flow in the fluid that results in a number of positive effects in crystal growth and affords improved crystal perfection. AVC-assisted melt crystal growth has now been realized in several growth techniques and for a number of oxides, salts, and semiconductors. AVC has not as yet been as broadly or industrially applied as ACRT. Nevertheless, the low-frequency axial vibration technique

Table 24.4 Crystals Grown by Oscillatory Techniques (Exemplary, Not Exhaustive)

Crystal	Growth Technique	Oscillatory Technique	Oscillation Parameters	Effect on Crystal Quality and Properties	References
CMT	Vertical Bridgman	ACRT	Various depending on crystal diameter	Improved radial and axial compositional uniformity, reduced number of grains, improved segregation of impurities	[33,34]
CMT	THM	ACRT	Various	Increased growth rates	[41]
CdTe	THM	ACRT	Various	Increased growth rates	[42]
CZT	Vertical Bridgman	ACRT	Various depending on crystal diameter	Reduction in number of grains, improved segregation of Zn, reduced Te precipitates, reduced strain and etch pit densities	[43]
CZT	Vertical Bridgman	ACRT	Added seeding	Reduction in number of grains, improved segregation of Zn, reduced etch pit densities	[44]
mc-Si	DS	ACRT	Induced striations for monitoring purposes	Improved segregation of C, reduced precipitates	[47,48]
mc-Si	DS	ACRT	Used 1 rpm and 600 s Ekman time	Improved radial distribution of impurities	[49]
Si	FZ	ACRT		Improved diameter control	[50,51]
SiC	Solvent growth	ACRT		Higher growth rates	[52]
SiC	Top-seeded solution growth	ACRT		Enabled polytype selection	[53]
Ag_2AsS_3		ACRT	20–60 rpm	Improved crystal quality	[54]
Succinonitrile		ACRT		Reduced constitutional supercooling and hence morphological instabilities	[55]
$La_3Ga_5SiO_{14}$		ACRT	0–25 rpm	Reduced unwanted phases	[57]
Sb-based quaternaries	Vertical Bridgman	ACRT	Various depending on crystal diameter	Improved growth rates and reduced crystal cracking	[58,59]
KCl NaCl LiF	Czochralski	AVC-Cz I	$f = 2$–20 Hz	• Faceting of lateral surface of crystals in accordance with crystallography direction (roughly square or rectangular shape)	[66]

$CsCdCl_3$	Vertical Bridgman	CVS	$f = 0.8$–5 Hz	• Interface position shifting downward with increased frequency • Small influence on interface shape	[145]
AgClBr AgBrI doped by Tl AgClBrI doped by Tl	Vertical Bridgman	AVC-Br	$f = 15$–100 Hz $A \leq 1.5$ mm	• Control of interface shape • Improved crystal quality	[151]
$PbBr_2$ doped by Ag	Vertical Bridgman, VGF	CVS	$f = 7.1$ Hz	• Increase of growth rate	[148]
$NaNO_3$	Czochralski	AVC-Cz I AVC-Cz II	$f = 10$–200 Hz $A = 0.01$–1.0 mm	• Control of interface shape • Reduction of dopant striation • Improved structural uniformity	[77,94]
	Vertical Bridgman	AVC-Br	$f = 10$–100 Hz $A = 75$ μm–1.2 mm	• Strong reduction in dislocation density • Flattening the interface shape control the impurity distribution	[152]
	Vertical Bridgman	CVS	$f = 5.5$–6.3 Hz	• Interface position change with increased frequency	[146]
$NaNO_3$—18 wt% $Ba(NO_3)_2$ Eutectics	Floating zone	Vibration of one of the supporting end-walls	$f = 1.0$–1.5 kHz $A = 10$–20 μm	• Elimination of radial temperature gradients • Suppression of thermocapillary convection • Flattening interface • Improved structural uniformity	[122]
Ge	Czochralski	AVC-Cz I	$f = 2$–20 Hz	• Faceting of lateral surface of crystals in accordance with crystallography direction (roughly square or rectangular shape)	[66]
	Vertical Bridgman	Container vibration	$f = 0.5$–200 Hz $A \leq 5 \times 10^{-1} g_o$	• No effect registered	[153]
	VGF	USV applied axially from the top	f (in the kHz-MHz range)	• Enhanced morphological interface stability • Improved axial carrier distribution	[142]
Si doped by Sb (2×10^{18}/cm^3)	Floating zone under microgravity (Maxus-4 flight)	Vibration of one of the supporting end-walls	$f = 3.95$ kHz $A = 1.1$ μm	• Reduction of dopant striation • Interface flattening	[154]

Continued

Table 24.4 Crystals Grown by Oscillatory Techniques (Exemplary, Not Exhaustive)—cont'd

Crystal	Growth Technique	Oscillatory Technique	Oscillation Parameters	Effect on Crystal Quality and Properties	References
GaAs	Vertical Bridgman	Container vibration	$f = 100$ Hz	• Improved crystallinity	[155]
	Czochralski (LEC)	USV applied axially from the crucible bottom	$f = 150$ kHz	• Reduced striation • Improved As distribution	[138]
InSb: Te	Czochralski	AVC-Cz I	$f = 50$ Hz	• Improved crystallinity	[70]
	Czochralski	USV applied axially from the crucible bottom	$f = 10$ kHz P = 150 W	• Improved dopant distribution • Elimination of facet regions	[156]
	Czochralski	USV applied axially from the crucible bottom	$f = 0.15$–10 MHz	• Reduced striations	[138]
	Czochralski	USV applied in two orthogonal directions: parallel and perpendicular to pulling axis	$f_1 = 0.71$ MHz (parallel to pulling axis from crucible bottom) $f_2 = 1.25$; 1.44 and 2.0 MHz (perpendicular to pulling axis from crucible sidewall)	• Striation-free crystals (with 1.44 MHz US perpendicular to pulling axis)	[143]
InSb–GaSb	Czochralski	AVC-Cz I	$f = 100$ Hz $A = 0.1$–0.14 mm	• Improved homogeneity • Enhanced by several times growth rate	[68]
	Czochralski	USV applied axially from the crucible bottom	$f = 10$ kHz P = 150 W	• Improved crystallinity (increased with increase USV output power)	[157]
	Czochralski	USV applied axially from the crucible bottom	$f = 0.69$–1.44 MHz	• Significant decrease of striation • Increase of carrier mobility more than 40%	[158]
	Vertical Bridgman	Container vibration	$f = 20$ Hz $A = 0.5$ mm	• Small change of interface shape • No radial composition variation observed	[62]
CdTe	Vertical zone melting	Container vibration	$f = 0.3$–3.5 Hz $A = 2$–5 mm	• Reduced number of grains • Growth of large single crystals	[157]

	Vertical Bridgman	Container vibration	$f < 1000$ Hz A < 0.1 mm	• Reduced dislocation density	[120]
	Vertical Bridgman	CVS	$f = 5.5$ Hz E $= 3.2$ mm $T_m = 8$ s	• Improved grain structure • More uniform free carrier	[147]
	Vertical Bridgman	AVC-Br	$f \leq 150$ Hz $A = 0.02$–1.0 mm	• Maintenance of constant nonstoichiometry along the crystal	[89]
Bi-Sb (5 at%)	Czochralski	USV applied axially from the crucible bottom	$f = 0.15$–10 MHz	• Reduced striations	[138]
Bi_2Te_3–Bi_2Se_3 Bi_2Te_3–Sb_2Se_3	Zone melting	Container vibration	$f = 50$–100 Hz $A = 100$–150 μm	• Improved radial and axial homogeneity	[64]
Al_2O_3 Al_2O_3 doped by Ti^{3+} (0.07 wt%)	Czochralski	USV applied axially from the crucible bottom	$f = 100$–400 kHz P $= (2$–$5) \times 10^4$ Pa I $= (0.5$–$2.0) \times 10^{-2}$ W/cm^2	• Reducing the pores density in crystal by factor 2–2.5 due to bubbles rejection from growth interface	[139]
$(1-x)$ $PbMg_{1/3}Nb_{2/3}$—x $PbTiO_3$ (PMNT)	Vertical Bridgman	CVS	$f = 6.3$ Hz Gradually decreased	• No improvement of crystal quality	[150]
$K(Ta_{1-x}Nb_x)O_3$) $0.30 \leq x \leq 1$	TSGG	AVC-Cz I	$f = 50$ Hz $A = 0.3$ mm	• Striation-free crystals	[127]
$Y_3Sc_2Ga_3O_{12}$:Er,Cr	Czochralski	AVC-Cz I	$f = 50$ Hz $A = 17$–35 μm	• Controlled alteration of interface shape • 2-fold reduced striation	[84]
$B_{12}SiO_{20}$	Vertical Bridgman	Container vibration	$f = 50$ Hz $A = 50$–100 μm	• 2-fold decrease in dislocation density • 10% increase of optical transmission	[159]

Notes: A is amplitude of vibration, ACRT is accelerated crucible rotation technique, AVC is axial vibrational control technique, Br is Bridgman technique, Cz is Czochralski technique, CVS is coupled vibrational stirring technique, DS is directed solidification, E is axial eccentricity, f is frequency of vibration, FZ is floating zone method, I is intensity of ultrasound, LEC is liquid encapsulated Czochralski technique, LF is low frequency, mc is multicrystalline, P is acoustic pressure, T_m is total mixing time, THM is traveling heater method, TSGG is top-seeded solution growth technique, USV is ultrasonic vibration, VGF is vertical gradient freeze technique.

and the AVC-assisted melt growth are challenging new ways to grow high-quality crystals.

Two additional oscillatory techniques were described in this chapter more briefly: coupled vibrational stirring and ultrasonic action on melt crystal growth. CVS was applied to the vertical Bridgman growth of several different compounds and found to be useful in producing efficient stirring of fluids, as well as manipulating the temperature gradients in the melt and growth interface shape. The application of ultrasonic vibrations to crystallization processes demonstrates a large variety of different effects, and this has been studied for many years. New findings on the ultrasonic influence of melt crystal growth promise the efficiency of its application to improve the crystal perfection, especially by elimination of growth striations.

References

[1] Capper P, editor. Bulk crystal growth of electronic, optical and optoelectronic materials. Chichester: Wiley; 2005.

[2] Scheel HJ, Capper P, editors. Crystal growth technology. Weinheim: Wiley-VCH; 2008.

[3] Capper P, Rudolph P, editors. Crystal growth technology. Weinheim: Wiley-VCH; 2010.

[4] Rudolph P, Kakimoto K. Mater Res Soc Bull 2009;34:1.

[5] Rosenberger F. Fundamentals of crystal growth I. macroscopic equilibrium and transport concepts. New York: Springer Verlag, Berlin, Heidelberg; 1979.

[6] Hurle DTJ, Rudolph P. J Cryst Growth 2004;264:550.

[7] Haddad FZ, Garandet JP, Henry D, Ben Hadid H. J Cryst Growth 1999;204:213.

[8] Hurle DTJ, Jakeman EJ. Cryst Growth 1969;5:227.

[9] Rossby C-G. J Fluid Mech 1969;36(2):309.

[10] Scheel HJ. J Cryst Growth 2006;287:214.

[11] Duffar T. In: Capper P, editor. Bulk crystal growth of electronic, optical and optoelectronic materials. Chichester: Wiley; 2005 [chapter 17].

[12] Regel LL, Wilcox WR. Processing by centrifugation. Germany: Springer, Heidelberg; 2001.

[13] Eidelman LG, Goriletsky VI, Nemenov VA, Protsenko VG, Radkevich AV. Cryst Res Technol 1985;20:167.

[14] Ostrogorsky AG, Muller G. J Cryst Growth 1994;137:64.

[15] Dutta PS, Ostrogorsky AG. J Cryst Growth 1998;194:1.

[16] Dropka N, Miller W, Rehse U, Rudolph P, Büllesfeld F, Sahr U, et al. J Cryst Growth 2011;318:275.

[17] Cramer A, Eckert S, Galindo V, Gerbeth G, Willers B, Witke W. J Mater Sci 2004;39(24):7285.

[18] Dumitrica S, Vizman D, Garandet J-P, Popescu A. J Cryst Growth 2012;360:76.

[19] Kokh AE, Kononova NG. Solid State Electron 2000;44:819.

[20] Kokh AE, Kononova NG, Bekker TB, Vlezko VA, Mokrushnikov PV, Popov VN. Crystallogr Rep 2005;50:160 [translated from Kristallografiya 50 (2005) 169].

[21] Kokh AE, Vlezko V, Kokh K, Kononova N, Villeval Ph, Lupinski D. J Cryst Growth 2012;360:158.

[22] Kokh KA, Popov VN, Kokh AE, Krasin BA, Nepomnyaschikh AI. J Cryst Growth 2007;303:253.

[23] Capper P. Prog Cryst Growth Charact 1994;28:1.

[24] Scheel HJ. J Cryst Growth 1972;13/14:560.

[25] Capper P, Gosney JJG. UK Patent 8 115 911 May, 1981.

[26] Capper P, Gosney JJG, Jones CL, Pearce EJ. J Electron Mater 1986;15:361.

[27] Capper P, Gosney JJG, Jones CL, Kenworthy I. J Electron Mater 1986;15:371.

[28] Brice JC, Capper P, Jones CL, Gosney JJG. Prog Cryst Growth Charact 1986;13:197.

[29] Capper P. Prog Cryst Growth Charact 1989;19:259.

[30] Capper P, Brice JC, Jones CL, Coates WG, Gosney JJG, Ard CK, Kenworthy I. J Cryst Growth 1988; 89:171.

[31] Capper P, Coates WGC, Jones CL, Gosney JJG, Kenworthy I, Ard CK. J Cryst Growth 1990;102:858.

[32] Capper P, Maxey CD, Butler C, Grist M, Price J. J Cryst Growth 2005;275:259.

[33] Capper P. In: Kasap S, Capper P, editors. Handbook of electronic and optoelectronic materials. Springer, Heidelberg; 2006. p. 303.

[34] Coates WGC, Capper P, Jones CL, Gosney JJG, Ard CK, Kenworthy I, Clark A. J Cryst Growth 1989; 94:959.

[35] Capper P, Harris JE, Nicholson D, Cole D. J Cryst Growth 1979;46:575.

[36] Yu T-C, Brebrick RF. Properties of narrow gap cadmium-based compounds. In: Capper P, editor. EMIS datareview series No. 10. London: IEE; 1994. p. 55.

[37] Capper P, Maxey CD, Butler C, Grist M, Price J. J Mater Sci Mater Electron 2004;15:721.

[38] Gray RT, Larrousse MF, Wilcox WR. J Cryst Growth 1988;92:530.

[39] Liu X, Jie W, Zhou Y. J Cryst Growth 2000;209:751.

[40] Jie W. J Cryst Growth 2000;219:379.

[41] Bloedner RU, Gille P. J Cryst Growth 1993;130:181.

[42] Wald FV, Bell RO. J Cryst Growth 1975;30:29.

[43] Capper P, Harris JE, O'Keefe E, Jones CL, Ard CK, Mackett P, et al. Mater Sci Eng 1993;B16:29.

[44] Wang T, Jie W, Zhang J, Yang G, Zeng D, Xu Y, et al. J Cryst Growth 2007;304:313.

[45] Wang T, Jie W, Xu Y, Zha G-q, Fu L. Trans Nonferrous Met Soc China 2009;19:s622.

[46] Jie W, Li Y, Liu X. J Cryst Growth 1999;205:510.

[47] Bairava Ganesh R, Matsuo H, Kangawa Y, Arafune K, Ohshita Y, Yamaguchi M, et al. Cryst Growth Des 2008;8:2525.

[48] Bairava Ganesh R, Matsuo H, Kawamura T, Kangawa Y, Arafune K, Ohshita Y, et al. J Cryst Growth 2008;310:2697.

[49] Belleman MP, Meese EA, Arnberg L. J Cryst Growth 2011;318:239.

[50] Altmannshofer L, Grundner M Virbulis J. Patent DE 10137856, 2001.

[51] Altmannshofer L, Grundner M Virbulis J. Patent US 6,840,998, 2002.

[52] Kusunoki K, Kamei K, Yashiro N, Hattori R. Mater Sci Forum 2009;615–617:137.

[53] Seki K, Kogawa S, Ujihara T, Chaudouet P, Chaussende D, Takeda Y. J Cryst Growth 2011;335:94.

[54] Distanov VE, Nenashev BG, Kirdyashkin AG, Serboulenko MG. J Cryst Growth 2002;235:457.

[55] Lui YC, Roux B, Lan CW. Int J Heat Mass Transfer 2007;50:5031.

[56] Lui YC, Roux B, Lan CW. J Cryst Growth 2007;304:236.

[57] Uda S, Wang S-Q, Kimura H, Huang X. In: Scheel HJ, Capper P, editors. Crystal growth technology. Weinheim: Wiley-VCH; 2008 [chapter 15].

[58] Kim HJ, Chandola A, Bhat R, Dutta PS. J Cryst Growth 2006;289:450.

[59] Dutta P. In: Scheel HJ, Capper P, editors. Crystal growth technology. Weinheim: Wiley-VCH; 2008 [chapter 12].

[60] Zharikov EV, Prihod'ko LV, Storozhev NR. The phenomenon of formation of steady-state fluid flow under solid body vibration. Preprint No. 18 General Phys Inst Acad Sci USSR Moscow 1989:1 [in Russian].

[61] Zharikov EV, Prihod'ko LV, Storozhev NR. J Cryst Growth 1990;99:910.

[62] Yuan W, Banan M, Regel LL, Wilcox WR. J Cryst Growth 1995;151:235.

[63] Uspenskii V, Favier JJ. Int J Heat Mass Transfer 1994;37:691.

[64] Strutynska LT. J Thermoelectr 2012;4:53.

[65] Lan CW. Int J Heat Mass Transfer 2000;43:1987.

[66] Izergin AP, Pavlenko YuS, Stroitelev SA. Izv Vyssh Uchebn Zaved Fiz 1959;(1):107.

[67] Langenecker B, Frandsen WH. Philos Mag 1962;7:2079.

[68] Nikitina GV, Romanenko VN, Tuchkevich VS. In: Crystallization and phase transitions. Minsk: Izd. Acad. Sci. USSR; 1962. pp. 379–85 [in Russian].

[69] Kirgintsev AN, Avvakumov EG. Sov Phys Crystallogr 1965;10:449.

[70] Witt AF, Gatos HC. J Electrochem Soc 1967;114(4):413.

[71] Agranat BA, Dubrovin MN, Khavskii NN. Akusticheskij Zhurnal 1976;22:141 [in Russian].

[72] Petrov TG. Method of growing single crystals. USSR Pat. No. 136,057, 1960, [in Russian].

[73] Ship V, Vanichek V. In: Shubnikov AV, Sheftal NN, editors. Growth of crystals. New York: Consultants Bureau; 1962. p. 191.

[74] Zharikov EV, Prikhod'ko LV, Storozhev NR. Vibrational convection during the growth of crystals. In: Givargizov EI, Grinberg SA, editors. Growth of crystals, vol. 19. New York: Consultants Bureau; 1993. p. 71.

[75] Myal'dun AZ, Prostomolotov AI, Tolochko NK, Verezub NA, Zharikov EV. Vibrational control of Czochralski crystal growth. In: Givargizov EI, Melnikova AM, editors. Growth of crystals, vol. 21. New York: Kluwer Academic Publishers; 2002. p. 181.

[76] Avdonin NA, Kalis Kh E, Zharikov EV, Storozhev NR. Appl Prob Math Phys Latv St Inst Riga 1989:4.

[77] Zharikov EV, Prikhod'ko LV, Storozhev NR. Cryst Res Technol 1989;24(8):761.

[78] Zharikov EV, Zavartsev YuD, Laptev VV, Samoilova SN. Cryst Res Technol 1989;24(8):751.

[79] Lyubimov DV, Lyubimova TP, Meradji S, Roux B. J Cryst Growth 1997;180:648.

[80] Avetissov ICh, Sukhanova EA, Orlova GYu, Belogorokhov IA, Zharikov EV. J Cryst Growth 2012;360:167.

[81] Zharikov EV. Advanced technologies of crystal growth from melt using vibrational influence. In: Capper P, Rudolph P, editors. Crystal growth technology. Semiconductors and dielectrics. Weinheim: Wiley-VCH Verlag; 2010. p. 41.

[82] Nyborg WL. Acoustic streaming. In: Mason WP, editor. Physical acoustics, IIB. New York: Academic Press; 1965.

[83] Schlichting G. Boundary-layer theory. 7th ed. New York: McGraw-Hill; 1979.

[84] Verezub NA, Zharikov EV, Kalitin SP, Lavrishchev SV, Myaldun AZ, Papin Yu M, et al. Crystallography 1996;41(6):1056.

[85] Fedyushkin AI, Bourago NG, Polezhaev VI, Zharikov EV. Proc. 2nd Pan Pacific Basin workshop on microgravity sciences. USA: Pasadena; 2001. paper CG-1065.

[86] Avetissov ICh, Zinovjev AYu, Romanenkov MV, Romanenkova LV, Zharikov EV. New achievements in materials science. In: Proc. II France–Russia seminar, Moscow; November 10–12, 2005. p. 48. Moscow.

[87] Avetissov ICh, Sadovskii AP, Sukhanova EA, Zharikov EV. J Cryst Growth 2011;318:979.

[88] Avetissov ICh, Mel'kov A Yu, Zinov'ev A Yu, Zharikov EV. Crystallogr Rep 2005;50(1):S124.

[89] Avetissov ICh, Sukhanova EA, Khomyakov AV, Zinovjev AYu, Kostikov VA, Zharikov EV. J Cryst Growth 2011;318:528.

[90] Fedyushkin AI, Bourago NG, Polezhaev VI, Zharikov EV. Proc. VII Russian symp. mechanics of microgravity. Moscow: IPM RAS; 2001 [in Russian], p. 365.

[91] Fedyushkin AI, Bourago N, Polezhaev V, Zharikov E. J Cryst Growth 2005;275:e1557.

[92] Fedyushkin AI, Bourago NG. Proc. 2nd Pan Pacific Basin workshop on microgravity sciences. USA: Pasadena; 2001. paper CG-1072.

[93] Avetissov ICh, Sukhanova EA, Sadovskii AP, Kostikov VA, Zharikov EV. J Cryst Growth 2010;312: 1429.

[94] Avetissov ICh, Sadovskii AP, Sukhanova EA, Zharikov EV, Belogorokhov AI, Levonovich BN. J Cryst Growth 2010;312:1104.

[95] Avetissov ICh, Zharikov EV, Zinovjev A Yu, Sadovskii AP. Dokl Phys 2009;54:410.

[96] Avetissov ICh, Sadovskii A, Belov S, Khomyakov A, Rekunov K, Kostikov V, et al. CrystEngComm 2013;15:2213.

[97] Zhang Y, Liu Y, Jiang W, Pan XH, Jin WQ, Ai F, et al. Cryst Res Technol 2009:248.

[98] Ubbelhode AR. Melting and crystal structure. Oxford: Clarendon Press; 1965.

[99] Rudolph P, Koh HJ, Schäfer N, Fukuda T. J Cryst Growth 1996;166:578.

[100] Chelikowsky JR, Derby J, V Godlevsky V, Jain M, Raty JY. J Phys Condens Matter 2001;13:R817.

[101] Ginkin V, Kartavykh A, Zabudko M. J Cryst Growth 2004;270(3–4):329.

[102] Zharikov EV. J Cryst Growth 2012;360:146.

[103] Zharikov EV, Avetisov ICh, Lazarenko TA, Chigrai AA, Levtov VL, Novikov VA, et al. Experimental study of vibrational convection in a fluid on orbital complex "Mir". In: Proc. VII Rus. symp. "Mechanics of weightlessness. Outputs and prospects of fundamental studies of gravitationally sensitive systems", Moscow; 2001. p. 137 [in Russian].

[104] Verezub NA, Zharikov EV, Myaldun AZ, Prostomolotov AI. Crystallogr Rep 1996;41:335.

[105] Verezub NA, Zharikov EV, Myaldun AZ, Prostomolotov AI, Tolochko NK. Crystallogr Rep 1996;41: 151.

[106] Verezub NA, Zharikov EV, Myaldun AZ, Prostomolotov AI. Dokl Acad Sci 1996;350:474.

[107] Kumar V, Biswas G, Brenner G, Durst F. Int J Heat Mass Transfer 2003;46:1641.

[108] Sampath R, Zabaras N. J Comput Phys 2001;168:384.

[109] Schwabe D, Scharmann A. J Cryst Growth 1981;52:435.

[110] Hong Y, Jin W-Q, Pan X-H. Chin Phys Lett 2004;21:1986.

[111] Li Z, Liu L, Nan X, Kakimoto K. J Cryst Growth 2012;346:40.

[112] Schwabe D. Surface-tension-driven flow in crystal growth melts. In: Freyhardt HC, editor. Crystals: growth, properties and applications, vol. 11. Berlin: Springer-Verlag; 1988. p. 75.

[113] Kuhlmann HC. Thermocapillary convection in models of crystal growth. New York: Springer-Verlag; 1999. p. 172.

[114] Mueller G, Ostrogorsky A. Convection in melt growth. In: Hurle DTJ, editor. Handbook of crystal growth, bulk crystal growth, vol. 2b. North-Holland, Amsterdam; 1993. p. 711 [chapter 13].

[115] Azami T, Nakamura S, Eguchi M, Hibiya T. J Cryst Growth 2001;233:99.

[116] Avetissov ICh, Sadovskii AP, Belov SN, Khan CK, Mozhevitina EN, Sukhanova EK, et al. J Cryst Growth 2014. http://dx.doi.org/10.1016/j.jcrysgro.2013.12.060i.

[117] Bushmakin OA, Verezub NA, Zharikov EV, Myal'dun AZ, Prostomolotov AI. Fluid Dyn 1997;32(N3):366.

[118] Zharikov EV, Myaldun AZ, Prostomolotov AI, Skorenko AV, Verezub NA. In: Gershuni GZ, Alexander I, editors. Vibrational effects in fluid dynamics. Perm State Univ; 2000. p. 1.

[119] Fedoseyev AI, Alexander JID. J Cryst Growth 2000;211:34.

[120] Feigelson RS Borshchevsky A. Method of growing single crystal cadmium telluride. US Patent 4,465,545, August 14, 1984.

[121] Caram R, Banan M, Wilcox WR. J Cryst Growth 1991;114:249.

[122] Shen XF, Anilkumar AV, Grugel RN, Wang TG. J Cryst Growth 1996;165:438.

[123] Grugel RN, Shen XF, Anilkumar AV, Wang TG. J Cryst Growth 1994;142:209.

[124] Dold P, Benz KW, Croell A, Roux B, Lyubimov D, Lyubimova T, et al. Acta Astronaut 2001;48:639.

[125] Lyubimova TP, Scuridin RV, Croell A, Dold P. Cryst Res Technol 2003;38:635.

[126] Verezub NA, Myaldun AZ, Prostomolotov AI, Milvidskii MG. Heat and mass transfer processes and growth of single crystals and thin-film structures. In: Proc II Russian symp. Obninsk; September 22–24, 1997. p. 110.

[127] Pankrath R, Doeppner K, Kuper C, Hesse H. XI-th Int Conf Cryst Growth 1995:131. The Hague, The Netherlands, Abstracts.

[128] Avetissov ICh, Zharikov EV, Zinov'ev A Yu, Mel'kov A Yu. Instrum Exp Tech 2004;47:554.

[129] Korsakov AS, Zhukova LV, Zharikov EV, Vrublevsky DS, Korsakov VS. Tsvetnye Met 2010;1:69 [in Russian].

[130] Abramov OV, Astashkin YuS, Stepanov VS. Akusticheskij Zhurnal 1979;25(2):180 [in Russian].

[131] Hayakawa Y, Kumagawa M. Cryst Res Technol 1983;20(1):3.

[132] Kozhemyakin GN. J Cryst Growth 2003;257:237.

[133] Kozhemyakin GN, Nemets LV. Crystallogr Rep 2009;54(4):707.

[134] Hayakawa Y, Sone Y, Ishino F, Kumagawa M. Jpn J Appl Phys 1983;22:206.

[135] Zolkina LV, Kozhemyakin GN. Funct Mater 2005;12(4):714.

[136] Abramov OV. Ultrasonics 1987;25:73.

[137] Jia S, Nastac L. Chem Mater Eng 2013;1:69.

[138] Kozhemyakin GN. Crystallogr Rep 2004;49(2):318.

[139] Vyshnevskiy SD, Kryvonosov EV, Lytvynov LA. Inorg Mater 2009;45(9):1009.

[140] Abramov OV, Teumin II, Filonenko VA, Eskin GI. Akusticheskij Zhurnal 1967;13(2):161 [in Russian].

[141] Ubbenjans B, Frank-Rotsch Ch, Virbulis J, Nacke B, Rudolph P. Cryst Res Technol 2012;47(3):279.

[142] Frank-Rotsch Ch, Juda U, Ubbenjans B, Rudolph P. J Cryst Growth 2012;352:16.

[143] Kozhemyakin GN. J Cryst Growth 2012;360:35.

[144] Kumagawa M, Tsuruta T, Nishida N, Ohtsuki J, Takahashi K, Adachi S, et al. Cryst Res Technol 1994;29(8):1037.

[145] Liu W-S, Wolf JF, Elwell DF, Feigelson RS. J Cryst Growth 1987;82:589.

[146] Zawilski KT, Custodio MCC, DeMattei RC, Feigelson RS. J Cryst Growth 2003;258:211.

[147] Liu YC, Shiau J-J, Feigelson RS, Route RK. J Cryst Growth 1990;102:807.

[148] DeMattei RC, Feigelson RS. J Cryst Growth 1993;128:1062.

[149] Feigelson RS, Zharikov EV. Investigation of crystal growth of dielectric materials by the Bridgman technique using vibrational control. Final Technical Report for NASA contract # NAG 8-1457-06; 2002.

[150] Zawilski KT, Custodio MCC, DeMattei RC, Feigelson RS. J Cryst Growth 2005;282:236.

[151] Korsakov A, Zhukova L, Korsakova E, Zharikov E. J Cryst Growth 2014;386:94.

[152] Barmin IV, Senchenkov AS, Avetisov ICh, Zharikov EV. J Cryst Growth 2005;275(1–2):e1487.

[153] Strelov VI, Zakharov BG, Sidorov VS, Ananyev PA. J Cryst Growth 2002;241:74.

[154] Croell A, Dold P, Kerat U, Lyubimova T. Proc. 16th ESA symp., ESA SP-530, St. Gallen, Switzerland; June 2–5, 2003. p. 123.

[155] Borshchevskii AS, Tretjakov DN. Kristall Tech 1968;34:69.

[156] Kumagawa M, Oka H, Quang N, Hayakawa Y. Jpn J Appl Phys 1980;19:753.

[157] Woodbury HH, Lewandowski RS. J Cryst Growth 1971;10:6.

[158] Kozhemyakin GN, Zolkina LV, Rom MA. Crystallogr Rep 2008;53:1236.

[159] Zhang Y, Liu Y, Jiang W, Pan XH, Jin WQ, Ai F. J Cryst Growth 2008;310:5432.

25 Segregation and Component Distribution

Aleks G. Ostrogorsky[1,*], Martin E. Glicksman[2]

[1]MECHANICAL & AEROSPACE ENGINEERING DEPARTMENT, ILLINOIS INSTITUTE OF TECHNOLOGY, CHICAGO, IL, USA; [2]MECHANICAL & AEROSPACE ENGINEERING DEPARTMENT, FLORIDA INSTITUTE OF TECHNOLOGY, MELBOURNE, FL, USA
*RESEARCH ON SEGREGATION WAS PARTIALLY SUPPORTED BY NASA.

CHAPTER OUTLINE

25.1 Introduction 997
25.2 Segregation Coefficients 998
25.2.1 Segregation under Local Equilibrium 998
25.2.2 Nonequilibrium and the Fourier Number 999
25.2.3 Nonequilibrium in the melt 999
25.2.4 Effective Segregation Coefficient, k_{eff} 1000
25.3 Limit Theories: "Perfect Mixing" and "No-Mixing" 1001
25.3.1 Perfect Mixing 1001
25.3.2 "No-Mixing," Diffusion-Controlled Segregation 1003
25.3.2.1 Initial Transient 1003
25.3.2.2 Steady State Segregation 1004
25.3.2.3 Final Transient 1004
25.4 Convective Heat and Mass Transfer 1005
25.4.1 Flow Patterns in Crystal Growth 1005
25.4.1.1 One-Dimensional Perpendicular Convection 1005
25.4.1.2 Two- and Three-Dimensional Flow Patterns 1006
25.4.1.3 Perpendicular Convection 1006
25.4.1.4 Lateral Convection 1006
25.4.2 Convection Flux, j 1006
25.4.2.1 Fick's First Law 1007
25.4.2.2 Film Thickness Formulation 1008
25.4.2.3 Mass Transfer Convection Coefficient 1009
25.4.3 Phenomenological Approach and Correlations for Nusselt Numbers 1009
25.4.4 Classification of Melt Convection 1010
25.4.4.1 Forced Convection 1011

Handbook of Crystal Growth. http://dx.doi.org/10.1016/B978-0-444-63303-3.00025-0
Copyright © 2015 Elsevier B.V. All rights reserved.

25.4.4.2 Natural Convection 1011
25.4.4.3 Convection Driven by Freezing 1011
25.4.4.4 Thermocapillary Convection 1012
25.4.4.5 Mixed Convection 1012
25.5 Segregation Theories Based on Solute Layer Thickness 1012
25.5.1 BPS Theory 1012
25.5.2 Wilson–Garandet's Model: Forced Convection Alone 1014
25.5.3 Models Considering Natural Convection and/or Lateral Melt Convection 1015
25.6 Segregation Model with Nusselt Numbers and Mixed Convection 1016
25.6.1 Combined Mass Transfer Coefficient 1016
25.6.2 Phenomenological Approach to Determine the Combined Mass Transfer Coefficient 1017
25.6.3 Effective Segregation Coefficient, k_{eff}, as Function of Combined Nusselt Number 1018
25.7 Correlations for Nusselt Numbers 1018
25.7.1 Correlations for Disk-Driven Forced Convection 1018
25.7.1.1 Exact Similarity Solution for Laminar Flow and Sc $\rightarrow \infty$ 1018
25.7.1.2 Empirical Correlations, Laminar Flow 1019
25.7.1.3 Empirical Correlations, Turbulent Flows 1020
25.7.2 Empirical Correlations for Natural Convection 1021
25.7.2.1 Vertical Walls 1021
25.7.2.2 Horizontal Disks 1022
25.7.2.3 Rayleigh–Bénard Convection 1023
25.8 Directional Solidification: Segregation without Forced Convection 1023
25.8.1 Segregation Under Vanishing Natural Convection ($Gr \rightarrow 0$) 1024
25.8.1.1 Diffusion Coefficients Extracted under Minimum Convection 1027
25.8.2 Bottom-seeded VB Growth 1028
25.9 CZ Process: Segregation Controlled by Mixed Convection 1029
25.9.1 Segregation under Steady Forced (Negligible Natural) Convection 1029
25.9.1.1 Diffusion Coefficients of Impurities in Germanium 1029
25.9.2 CZ Process with Mixed Convection $Re^2 \approx Gr$ 1031
25.9.2.1 Diffusion Coefficients of Impurities in Silicon 1031
25.9.2.2 CZ Growth of Large Crystals at Low Rotation Rates 1032
25.10 Zone Melting 1034
25.10.1 Introduction 1034
25.10.2 Single-Pass ZM, "Perfect" Mixing 1037
25.10.3 Effective Segregation Coefficient in Zone Purification 1038
25.10.4 Single-Pass ZM, "Partial" Mixing 1038
25.10.5 Multipass ZM 1039

25.11 Lateral Segregation 1039
25.11.1 Curved Solid–Liquid Interface 1039
25.11.2 Convection 1040
25.11.3 Nonequilibrium Segregation 1043
25.11.4 Local Nusselt Numbers 1044
25.12 Microsegregation 1044
25.12.1 Doping Striations 1045
25.13 Summary 1045
References 1046

25.1 Introduction

Fluid flow during crystal growth generally enhances mass transfer by transporting melt with high solute concentration near the solid–liquid interface and replacing it with fluid having a lower bulk-melt concentration. Segregation and component distribution—two critical aspects for achieving successful crystal growth—are consequently controlled by melt convection.

Melt flows are governed by a well-known set of nonlinear partial differential equations, the Navier–Stokes equations, which are rarely solvable by analytic techniques. As a result, classic chemical segregation theories usually consider only limiting cases of zero melt velocity (diffusive mixing) or "infinite" melt velocity (perfect mixing). Sixty years ago, the seminal Burton, Prim, and Slichter (BPS) theory was developed to consider how finite levels of melt convection accompanying crystal growth affect segregation [1,2]. The influence of convection was captured through an "effective" segregation coefficient, k_{eff}, which was modeled by postulating a supposed "stagnant solute layer" at the crystal–melt interface of thickness δ. The "stagnant" layer thickness, δ, was estimated in BPS theory using an analytical solution of the governing hydrodynamic equations developed by Cochran and Levich [3–5], describing forced laminar convection near a rotating disk.

All effective segregation coefficient models for crystal growth, until recently, were based on a solute boundary layer thickness, δ, developed in laminar flow, thus ignoring the complicating, but important, effects of turbulence and unavoidable buoyancy-induced (natural) convection. The Cochran–Levich solution remains as the only equation for estimating δ in wide use today by crystal growers.

The effective segregation coefficient, k_{eff}, is controlled by the rate of solute transfer from the interface, i.e., by the solute flux, j, transported from the advancing crystal–melt interface. Convection fluxes in general (viz., heat and mass transfer rates) are usually calculated in engineering by appealing to empirical correlations developed from laboratory experiments, rather than from fundamental theoretical estimates. The use of empirical correlations is a widely accepted practice in many engineering applications

and has become necessary for most industrial crystal growth applications, as melt flows in bulk crystal growth are often turbulent. This statement remains especially true for low Prandtl number fluids, such as the semiconductor and metallic melts.

In this chapter we focus on reviewing the recently proposed combined convection (CC) model, which relates the effective segregation coefficient ($k_{eff,CC}$) to the solute convection flux. The solute flux is calculated using a phenomenological approach, a method that takes advantage of empirical correlations established for laminar or turbulent flows, combining, as needed, both natural (buoyancy-induced) and forced (extrinsically driven) convection to represent solute segregation under realistic crystal growth conditions. This phenomenological approach is well justified, considering the overall complexity and diversity of melt flows during crystal growth.

More specifically, the chapter focuses on solute segregation encountered in several industrially important crystal growth processes based on three fundamentally different configurations: Czochralski (CZ), directional solidification (DS), and zone melting (ZM). We emphasize the benefits of forced convection relative to natural convection, which is unavoidable, unsteady, and difficult to control.

25.2 Segregation Coefficients

In monocomponent (unary) systems, and in congruently melting multicomponent systems, redistribution of components, segregation leading to local changes in composition, does not occur during freezing. Segregation, or component redistribution, otherwise always occurs in noncongruent systems. Of particular interest to crystal growers is the segregation of impurities and dopants[1] occurring in melt-grown semiconductor crystals, which include directional solidification/crystal growth, and purification achieved by zone refining.

25.2.1 Segregation under Local Equilibrium

Phase diagrams provide the equilibrium concentrations established locally at the interface in the solid and liquid phases. Their ratio is used to define the equilibrium segregation coefficient, k_0, conventionally defined as,

$$k_0 = \frac{C_s(x=0)}{C_L(x=0)} = \frac{C_s}{C_0}, \tag{25.1}$$

where x is the distance away from the interface. C_S and C_0 are the solute concentrations in the solid and in the liquid phase measured, respectively, at the crystal–melt interface, i.e., $x = 0$. The liquidus and solidus lines on the binary phase diagram remain straight for ideal and dilute solutions, and, if straight, yield a value for k_0 that is independent of concentration and temperature. Otherwise, k_0 is defined as the changing ratio of C_S to C_0 across any solid–liquid tie line.

[1]Intentionally added impurity atoms to control electronic properties.

The equilibrium segregation coefficient, k_0, is a fundamental thermodynamic property of a binary solid–liquid system and not a function of the crystal growth process parameters or hydrodynamic melt properties; k_0 appears in a great number of mathematical macrosegregation expressions involving redistribution of the solute during crystal growth [6]. Two cases of chemical segregation are encountered, depending on the binary system: (1) $k_0 < 1$, where solutes are rejected at the interface into the melt phase, and (2) $k_0 > 1$, where solutes are preferentially absorbed into the crystalline phase. The former is more common than the latter, but both situations occur. For brevity of the mathematical presentations in this chapter, and without loss of generality, we shall proceed by discussing segregation for the more common case of $k_0 < 1$.

25.2.2 Nonequilibrium and the Fourier Number

Full thermodynamic equilibrium during crystal growth is seldom, if ever, attained within the developing solid. The reason that achieving full equilibrium throughout the solid phase during crystal growth is so difficult in practice is that atomic diffusion in the solid is too slow a process to allow extensive homogenization within a growing crystal. The time needed for homogenization by atomic diffusion in the solid sets a time scale that can be calculated using the dimensionless Fourier number, defined as

$$Fo = \frac{Dt}{L^2},$$

where L (cm) is a characteristic length, and t (s) is time. In the case of mass transfer, $D(\mathrm{cm}^2/\mathrm{s})$ is the diffusion coefficient, or chemical diffusivity. In the case of heat transfer, $Fo = \alpha t/L^2$, where thermal diffusivity $\alpha(\mathrm{cm}^2/\mathrm{s})$ replaces chemical diffusivity, D. The Fourier number is the dimensionless "characteristic" time for the occurrence of a diffusion transient over the length scale, L. Thus, the time needed to achieve homogenization by diffusion is, $t \gg L^2/D$.

Typical values of diffusion coefficients of dopants and impurities in crystalline silicon close to its melting point, T_m, are circa $D = 10^{-10}\ \mathrm{cm}^2/\mathrm{s}$. Thus, for a 1-cm-long Si crystal, near 1400 °C, $t \gg 10^{10}$ s, or about 10^5 days! Even short-range microscopic fluctuations in the dopant concentration will remain "frozen" in the solid (where $L \approx 1\ \mu\mathrm{m} = 10^{-4}$ cm) often due to crystal rotation during growth and unsteady or turbulent melt convection. At room temperature, near 300 K, dopant diffusivities in Si drop to circa $10^{-50}\ \mathrm{cm}^2/\mathrm{s}$, a value so small that for practical purposes is effectively zero. It is assumed in this chapter, moreover, that diffusion does not occur within the solid over the typical time scales considered here for crystal growth, and that whatever segregation does occur during crystal growth remains unaltered in the product phase. Clearly, long-term annealing at elevated temperature of a crystalline solid can reduce its as-grown segregation level.

25.2.3 Nonequilibrium in the melt

Melt equilibrium at or near a crystal–melt interface is disturbed by segregation. Solute additions and impurities are usually rejected during crystal growth at the crystal–melt

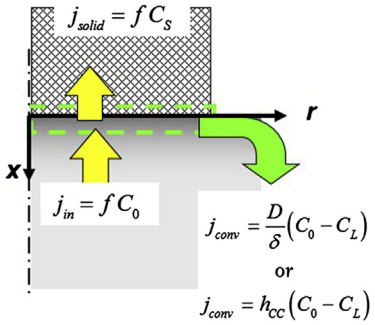

FIGURE 25.1 Lateral convection caries solute way from the interface. Convective flux j_{conv} is calculated using the film thickness or combined convection (CC) coefficient formulation.

interface, or, less frequently, preferentially absorbed into the growing solid. As a result, a concentration or solute boundary layer having some thickness, δ, develops ahead of the interface. The concentration of impurities, $C_L(x)$, within this boundary layer changes from its initial equilibrium value, $C_L(0) = C_0$ at the interface, to a lower, or higher, value $C_L(\delta) = C_L$ in the bulk melt, depending, of course, on the value of k_0 relative to unity.

Figure 25.1 shows the solute fluxes acting at a growing crystal–melt interface. During steady state solidification at some specified freezing rate, f (cm/s), all solute rejected at the moving interface must be transported away by lateral melt convection. The mass transfer, specified by a convective mass transfer coefficient, h, relates the convective flux, j_{conv}, to the local concentration difference from the equilibrium value, C_0. The mass transfer coefficient, h, for CZ crystal growth, accounts for the net influences of "combined" convection, which include: (1) forced convection, (2) natural convection, and (3) perpendicular convection.

The actual thickness of the solute layer, δ, that develops is controlled by the state of melt convection. Without the presence of any convection, for a typical crystal growth rate of $f = 0.3$–3 cm/h, and assuming $D = 10^{-4}\text{cm}^2/\text{s}$, a purely diffusive boundary layer develops, where the thickness $\delta = D/f \approx 0.1 - 1$ cm. In the presence of melt convection, however, δ is reduced to $\delta < 0.1$ mm.

25.2.4 Effective Segregation Coefficient, k_{eff}

In the presence of melt convection, one may still relate the solid to the liquid solute concentrations by an "effective" segregation coefficient, defined as,

$$k_{eff} = \frac{C_s}{C_L} = \frac{C_s(x = 0)}{C_L(x > \delta)}. \tag{25.2}$$

Thus, C_L represents the melt concentration just beyond the outer limit of the solute boundary layer, $C_L(x > \delta)$. Sufficiently vigorous convection reduces the layer thickness, δ, and, in principle, as the convection intensity becomes "infinitely" strong, a limit is approached as $\delta \to 0$, namely, $k_{eff} \to k_0$.

The governing mathematical statement for conservation of solute atoms in a convecting melt is the convection–diffusion equation,

$$\frac{\partial C}{\partial t} + \vec{v} \cdot \vec{\nabla} C = D\nabla^2 C. \tag{25.3}$$

This general equation couples mass transfer to melt flow, via the fluid velocity vector, $\vec{v}$. Melt flow itself, however, is governed by a set of hydrodynamic, nonlinear, partial differential equations, called the Navier–Stokes equations (N–S). Only a few analytical "similarity"[2] solutions to the N–S equations exist [7]. The following list of important similarity solutions, and their sources, provides useful insights into interfacial convection, which lead to all the basic forms of axial and radial segregation that will be considered later in this chapter. These include:

1. Laminar flow and convection near a rotating disk, by von Karman/Cochran [3,5] and Levich [4].[3]
2. Laminar forced flow and convection along flat plates (Blasius and Polhausen [8,9]), (see Section 25.11.2).
3. Laminar natural convection along a vertical plate (Polhausen and Ostrach solution [9,10]).

For any other configuration (excepting laminar, one-dimensional flows in pipes and ducts), one must rely on empirical correlations rather than on exact analytical solutions to the N–S.

25.3 Limit Theories: "Perfect Mixing" and "No-Mixing"

Figure 25.2 depicts the concentration of solute after normal freezing (i.e., plane-front directional solidification) for a system with $k_0 < 1$, taken to two important limiting cases: (1) "perfect mixing" in the melt, and (2) "no mixing" (diffusion only). It is assumed further that the solute distribution depends only on the axial distance from the interface, x. Lateral segregation is temporarily ignored but included in remarks in Section 25.11.

25.3.1 Perfect Mixing

G. Gulliver (1921) [11] and E. Scheil (1942) [12] independently solved the mass conservation problem of interfacial segregation under local equilibrium. Both investigators

[2]In fluid mechanics, a similarity solution is a mathematical solution of the velocity profile within a boundary layer that is self-similar, i.e., appearing to be identical, save for a uniform size-scale factor, or magnification. Such self-similar solutions allow a temporary reduction in the number of independent variables.

[3]The similarity solution for laminar ow near a rotating disk was obtained by von Karman in 1921 [5] and Cochran in 1934 [3]. Levich [4] in turn solved for the concentration field in a fluid driven by a rotating disk, which he coupled to the hydrodynamic velocity field. It provides the foundation of BPS theory and several subsequent models for the effective distribution coeffcient, k_{eff}. (See, for example, Section 25.5.)

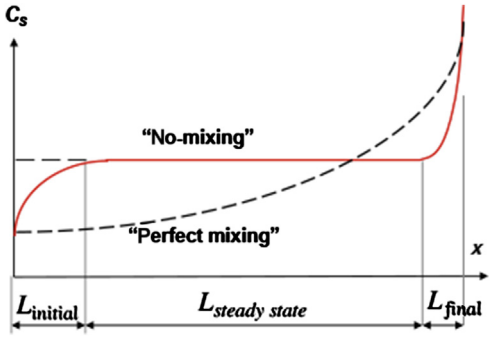

FIGURE 25.2 Limiting profiles of axial component distribution: dashed line is "perfect mixing." Full line is "no mixing." All actual segregation profiles controlled by convection fall between the limiting profiles.

assumed, (1) perfect mixing in the liquid phase to maintain a homogeneous melt, and (2) no subsequent diffusion in the solid phase. The Gulliver–Scheil solution gives a one-dimensional segregation curve containing only one system-based parameter, the equilibrium segregation coefficient, k_0, which is available for many binary systems in either tabular form and/or in graphical form on the equilibrium phase diagrams, or computed using thermochemical data. The Gulliver–Scheil segregation distribution for perfect mixing in the melt, as a function of the fraction of the molten charge solidified, f_S, is given by

$$\frac{C_S}{C_L^i} = k_0 (1 - f_S)^{(k_0 - 1)}, \tag{25.4}$$

where C_L^i is initial dopant concentration in the melt. Independent of the geometry, the fraction solidified, f_S, may be expressed as the volumetric ratio

$$f_S = \frac{V_S}{V_S + V_L}.$$

For the case of parallelepipeds with a charge of length L, $f_S = x/L$, where x indicates the length solidified. Melt equilibrium due to perfect mixing becomes realistically approximated when crystals are grown at a slow rate from well-stirred melts, e.g., the situation closely met in CZ growth of large-diameter crystals. The actual concentration profiles achieved in the solid will depend on details of the melt convection and the freezing rate. If the growth rate of a crystal is not extremely slow, one must employ an effective segregation coefficient, where k_{eff} becomes a fitting parameter in the Gulliver–Scheil equation, namely,

$$\frac{C_S}{C_L^i} = k_{eff} (1 - f_S)^{(k_{eff} - 1)}. \tag{25.5}$$

The effective segregation coefficient can be measured by conducting a normal freezing experiment and applying Eqn (25.5) to the segregation data. Simple mold geometries should be used to facilitate measuring the fraction solidified. Note that the measured k_{eff}

includes the complicated influences of melt convection, interface stability, and freezing speed. Solute concentration, C_S, relative to the initial concentration, C_L^i, is measured for several values of the fraction solidified, f_S. Equation (25.5) can be written as [13],

$$\log_{10}\left(\frac{C_S}{C_L^i}\right) = \log_{10} k_{eff} + (k_{eff} - 1)\log_{10}\left[1 - f_S\right], \tag{25.6}$$

and plotted log–log. Both the ordinate intercepts of the lines and their slopes provide independent estimates for k_{eff}.

25.3.2 "No-Mixing," Diffusion-Controlled Segregation

A suction flow normal to the interface is unavoidable when growing any material from the melt. Suction flow is a one-dimensional, perpendicular melt motion[4] driven by freezing. This generally weak flow is caused by the crystallization growth rate, f, and the small mass density difference between the growing crystal and its melt. The perpendicular flow velocity at the interface is

$$V_{perp.} = f\left(\frac{\rho_S}{\rho_L}\right), \tag{25.7}$$

where f is the crystal growth rate and ρ_S and ρ_L are, respectively, the mass densities of the solid and liquid phases. Solute is transported by the suction flow toward the interface, where segregation occurs. As a result, a solute boundary layer develops having some thickness δ.

The key assumptions used are: (1) uniform initial dopant concentration in the melt C_L^i; (2) constant growth rate, f; and (3) during the initial transient, the remaining melt length, L, is larger than δ. The crystal grown under diffusion-controlled segregation will develop three distinct regions: (1) initial transient, (2) steady state segregation, and (3) final transient, see Figure 25.2.

25.3.2.1 Initial Transient

During the initial transient, a crystal's concentration increases until $C_S = C_L^i = k_0 C_0$. Tiller et al. [14] derived an approximate solution for the initial transient region by assuming that the concentration profile at the interface is described by the following differential equation,

$$D\frac{d^2C}{dx^2} + f\frac{dC}{dx} = 0 \tag{25.8}$$

The same differential equation is employed in the BPS segregation model published later the same year. Solution of Eqn (25.8) yields a solute concentration profile in the stagnant liquid near the interface, of the following exponential form,

[4]In fluid mechanics, the flow perpendicular to a porous interface is known as "uniform suction flow." Its effect is to stabilize the boundary layers by reducing their thickness. (See Schlichting [7].)

$$\frac{C_S(x)}{C_L^i} = k_0 + (1 - k_0)\left[1 - e^{-k_0 \frac{xf}{D}}\right] \tag{25.9}$$

Tiller's Eqn (25.9), results in about 30% error for profiles measured in Te-doped InSb ($k_0 = 0.5$) and in 78% Zn-doped InSb ($k_0 = 2.9$) [15]. It is hard to justify using Eqn (25.9) in view of the exact solution, published later by Smith et al. (1955 [16]), who found

$$\frac{C_S(\chi, k_0)}{C_L^i} = \underbrace{\frac{1}{2}\left(1 + erf\sqrt{\chi}\right)}_{F_1(\chi)} + \underbrace{\left(k_0 - \frac{1}{2}\right) e^{-4k_0(1-k_0)\chi} erfc\left[(2k_0 - 1)\sqrt{\chi}\right]}_{F_2(k_0,\chi)} \tag{25.10}$$

with

$$\chi \equiv \frac{xf}{4D},$$

where x is the axial distance from the starting seed. For:

1. $k_0 \approx 0.5$, $F_2(k_0,\chi) = 0$, the transient portion ends at $C_S/C_L^i = 0.99$, or $L_{initial} \approx 11(D/f)$.
2. $0.5 < k_0 < \infty$, $F_2(k_0,\chi) < 0$, the transient portion of the crystal decreases.
3. $k_0 > 0.5$, $F_2(k_0,\chi) > 0$, the transient portion of the crystal lengthens.

An ideal, uniform, axial, and radial composition can be achieved in practice only for crystal growth under steady state diffusion-controlled segregation. Binary systems with $0.5 < k_0 < \infty$, and grown at higher growth rates, are especially amenable to diffusion-controlled growth, because the initial transient remains relatively short, producing a usefully long homogeneous section of the crystal.

For example, in 2002 during the SUBSA investigation aboard the International Space Station (ISS), four Te-doped InSb crystals ($k_0 = 0.5$) [17] and three Zn-doped InSb crystals ($k_0 = 2.9$) [18] were grown under microgravity conditions. The growth rate was $f = 0.5$ (cm/hr). The initial transient length was $L_{\text{transient}} = 0.93$ cm and 0.7 cm, respectively, for Te and Zn, with the time scale of the initial transients of $\tau_{trans} \approx 1\ h$. The diffusion coefficients were determined to be: for Te, $D = 1.0 \times 10^{-4}$ cm^2/s and for Zn, $D = 1.2 \times 10^{-4}$ cm^2/s. When identical crystal growth was carried out terrestrially, by contrast, natural convection precluded significant diffusion-limited solute buildup at the interface, so that the initial transients lasted only several seconds, and their length became negligible [19].

25.3.2.2 Steady State Segregation

Steady state segregation, where a homogeneous composition is obtained, initiates when $x > L_{trans}$, so that $k_{eff} = 1$. The concentration of solute incorporated into the crystal exactly equals the initial melt concentration, $C_S = C_L^i$, thus allowing a time-invariant solute balance and achieving steady state growth.

25.3.2.3 Final Transient

Final transient segregation begins when the solute boundary layer traveling ahead of the advancing interface approaches the end of the melt. Thus, one finds that

the final transient is brief, the affected length of crystal is relatively short, and is approximately equal to the thickness of the steady state solute boundary layer. Thus,

$$L_{final} \approx D/f.$$

Usually batch crystal growth processes are terminated for other reasons before the final transient occurs.

25.4 Convective Heat and Mass Transfer

Melt convection during crystal growth is complicated by the fact that it combines advection—the macroscopic transport of solute coupled to fluid motion—with diffusion, the microscopic random motions of individual atoms or molecules. Convection phenomena are further classified "natural" or "forced," "laminar" or "turbulent." Natural convection is driven by body forces, such as gravity interacting with density gradients within the melt, and is usually unavoidable under terrestrial crystal growth conditions. In forced convection, fluid is driven by an external source, e.g., crystal rotation, moving magnetic fields, or crucible rotation.

Bulk fluid flow enhances mass transfer by carrying the fluid near the interface, which has a higher solute concentration, C_0, and replacing it with fresh fluid having a lower concentration $C_L \ll C_0$. Convection, as explained earlier, can drastically reduce the time and distance over which the initial transient occurs during crystal growth. In the presence of vigorous melt convection, such transients, even for small k_0 values, might last only a few seconds [19]. Quasi-steady state crystal growth occurs when the solute flux rejected at the interface, $j_{rej.} = f(C_0 - C_S)$, is transported away by convective melt motion and its mass flux, j_{conv}.

25.4.1 Flow Patterns in Crystal Growth

25.4.1.1 One-Dimensional Perpendicular Convection

Perpendicular convection, driven by the growth rate, f, is the only one-dimensional advective process always occurring during melt growth. It is, of course, unavoidable, but weak, and has a low associated velocity, usually $\leq$30 μm/s. This weak suction flow, under terrestrial crystal growth conditions, is normally overwhelmed by natural convection, which achieves much higher velocities, typically about 10 mm/s.

Numerical simulations have convincingly demonstrated that some level of natural convection will always be present, even at gravity levels as small as $10^{-5}g_0$, where $g_0 = 9.81$ (m/s^2) is the average gravitational acceleration on earth (see Section 25.8.1). Numerous melt growth experiments conducted in various orbiting laboratories support this finding. Thus, a one-dimensional flow model is realistic *only under controlled microgravity conditions*, where the buoyancy-driven fluid flow velocity components, $\{u,v,w\}$, are negligible compared to f.

25.4.1.2 Two- and Three-Dimensional Flow Patterns

The steady state continuity equations for incompressible fluid flow are

$$\frac{\partial u}{\partial x}+\frac{\partial v}{\partial y}=0 \quad \text{(rectangular coordinates)} \tag{25.11}$$

$$\frac{\partial u}{\partial r}+\frac{u}{r}+\frac{\partial w}{\partial z}=0 \quad \text{(cylindrical coordinates)} \tag{25.12}$$

These equations state that one-dimensional flows are possible if, and only if, components u and v are either constant or zero. One-dimensional flows are observed only in pipes or ducts, where $u=\text{const.}$ and $v=0$. Convection occurring in a melt can never result in a one-dimensional flow.

Typical flow patterns occurring near a growing crystal growth interface are depicted in Figure 25.3. Crystal growth configurations for (1) CZ, (2) vertical Bridgman (VB), and (3) horizontal Bridgman (HB) are shown. Note especially that perpendicular flows carry rejected impurities toward the interface, whereas lateral flows transport solute along the interface and eventually back into the bulk melt.

25.4.1.3 Perpendicular Convection

In the z-direction, the flow velocity is $v_z=f+w$. As $z\rightarrow 0$, the term f dominates, because the velocity component $w\rightarrow 0$. Outside of the solute layer, $w\gg f$.

25.4.1.4 Lateral Convection

Melts typically flow tangentially along the solid–liquid interface and thus transport away latent heat and rejected solute laterally, as indicated schematically in Figures 25.1 and 25.3 [20]. The melt velocity component along the crystal–melt interface in either the x- or r-direction is u.

The intrinsic importance of lateral flow on component redistribution is emphasized in segregation models for k_{eff} developed by Yen and Tiller [21] and by Mueller and Ostrogorsky [20,22]. The key issue stressed in both of these models is that all solute that is not absorbed into the interface would be transported laterally, not axially. Again, it is stressed that solutes cannot "escape" axially, by simply diffusing back into the bulk melt. This situation becomes evident from the limiting case of "no-mixing," where component $w=0$ (see Eqn (25.10)), and since the solute cannot escape, one finds that $k_{eff}=1$.

25.4.2 Convection Flux, j

A key goal of convection mass transfer theory is to determine the magnitude of the convection flux, j (cm/s). Despite the complexities and nonlinearity of convection, the associated mass flux, j, is observed to be proportional to its driving force, which is proportional to the solute concentration difference. Convection mass fluxes can be calculated using three approaches: (1) Fick's first law, (2) static layer thickness, or (3) convection coefficients.

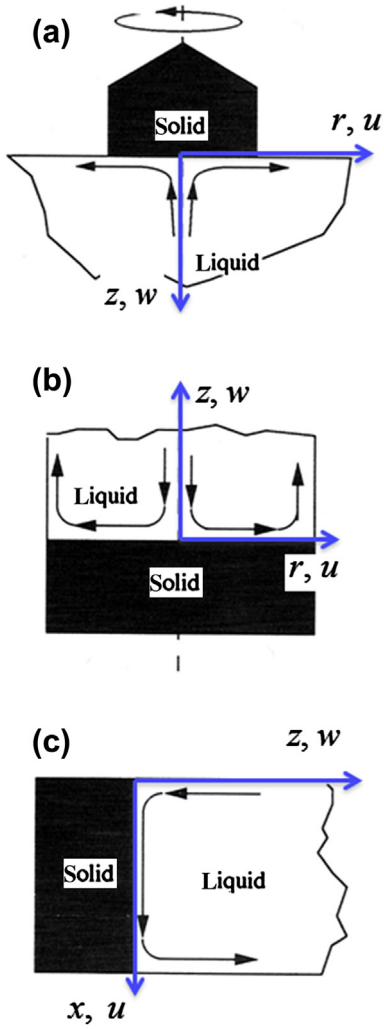

FIGURE 25.3 Schematic of flow patterns near the growth interface. (a), (b) axisymmetric flows, and (c) nonaxisymmetric flows.

25.4.2.1 Fick's First Law

At the crystal–melt interface, the hydrodynamic no-slip condition[5] requires zero tangential fluid velocity. Thus, at $x = 0$, transport occurs solely by diffusion, so in one dimension the mass flux is

$$j \equiv -D \left. \frac{dC_L}{dx} \right|_{x=0} \tag{25.13}$$

[5]Fluid "sticks" to the solid.

25.4.2.2 Film Thickness Formulation

If one assumes that diffusion occurs through a fictitious "film" or stagnant layer, the mass flux may be written as,

$$j \approx D\left(\frac{C_0 - C_L}{\delta_{static}}\right). \tag{25.14}$$

Equation (25.14) is an approximation of Fick's first law, where the gradient, $dC_L/dx|_{x=0}$, is replaced by the ratio of concentration difference to layer thickness, δ_{static}. A fictitious layer with thickness δ_{static} lacks a physically realistic foundation, so that the main limitation of Eqn (25.14) is that the nonexistent distance, δ_{static}, which does not, in principle, exist, also cannot be calculated. A film-thickness-based formulation becomes meaningful, and useful, provided that the concentration gradient, $dC_L/dx|_{x=0}$, is known, or estimated, from the appropriate analytical solution of a hydrodynamic boundary layer equation. Then, such a gradient-defined layer thickness may be set equal to the concentration difference divided by the concentration gradient in the following manner,

$$\delta_{grad} \equiv \frac{\Delta C}{dC_L/dx|_{x=0}} = D\left(\frac{\Delta C}{j}\right). \tag{25.15}$$

As is shown in Figure 25.4, such a gradient-defined layer thickness, δ^{grad}, may be obtained by extending a tangent at $x = 0$ (dashed line) to the actual concentration profile normal to the interface [19]. One finds that $\Delta C/\delta^{grad} = dC_L/dx|_{x=0}$. Equation (25.15) was, in fact, employed by Levich to calculate δ^{grad}, which provided the foundational fluid mechanical aspect of the BPS model. See Eqn (25.25).

For convection driven by a rotating infinite disk, the actual thicknesses of the velocity and solute boundary layers are, respectively [3,4],

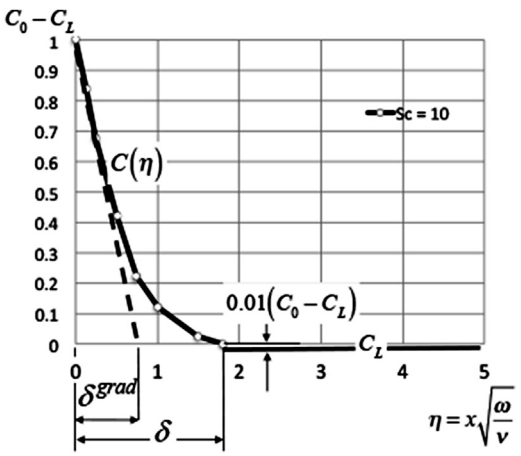

FIGURE 25.4 Actual and gradient thickness of solute boundary layer. η is dimensionless distance from the interface [7,8]. Note that $\delta \approx 2.5\delta^{grad}$.

$$\delta_\nu \approx 4\left(\frac{\nu}{\omega}\right)^{1/2},$$

and

$$\delta = \delta_\nu Sc^{-1/3} \approx 4D^{1/3}\nu^{1/6}\omega^{-1/2}. \tag{25.16}$$

25.4.2.3 Mass Transfer Convection Coefficient

Newton's law of cooling [8,9] defines the convective heat transfer coefficient, h^{HT}, based on the ratio of the heat flux, q, to the temperature difference, $T_0 - T_L$, namely,

$$h^{HT} = \frac{q}{T_0 - T_L}$$

where T_0 and T_L are, respectively, the temperature at the interface, $x = 0$, and within the bulk liquid. By analogy,[6] a comparable mass transfer coefficient can be similarly defined as,

$$h = \frac{j}{C_0 - C_L}, \tag{25.17}$$

where j is mass flux. Combining Fick's first law Eqn (25.13) with Eqn (25.17) defines the corresponding mass transfer coefficient as

$$h \equiv \frac{j}{C_0 - C_L} = \frac{-D\frac{dC}{dx}\big|_{x=0}}{C_0 - C_L}. \tag{25.18}$$

An exact value for h is readily obtained if the concentration gradient, $\frac{dC}{dx}\big|_{x=0}$, is obtained from the appropriate analytical fluid flow solution.

25.4.3 Phenomenological Approach and Correlations for Nusselt Numbers

As noted earlier, Navier–Stokes equations are usually not solvable excepting the cases of laminar flow along flat plates or rotating disks. Furthermore, the accuracy of such simplified solutions applied to crystal growth problems is often limited by the very assumptions that made the analytical solutions possible. For example, the Cochran–Levich solution, valid when the Schmidt number $Sc \to \infty$, still admits a 17% error when $Sc = 10$ (see Section 25.7.1.2). Therefore, in engineering practice one must adopt phenomenological approaches and rely instead on empirical rate/flux relationships that are based on laboratory experiments. The phenomenological mass transfer coefficient, h, is then determined by measuring the flux j. See again Eqn (25.18).

In order to reduce the number of independent variables, such phenomenological correlations are always given in dimensionless form. The dimensionless heat and mass

[6]This analogy is based on the observation that a temperature gradient is the driving potential for heat transfer, whereas the concentration gradient in a mixture is the driving potential for mass transfer.

transfer coefficients are called Nusselt numbers [8,9],[7] and these quantities can be calculated from the corresponding ratios of the thermal and diffusive fluxes under both hydrodynamic and static conditions,

$$Nu^{HT} \equiv \frac{h^{HT}L}{k} = \frac{h^{HT}\Delta T}{\frac{k}{L}\Delta T} = \frac{q_{convection}}{q_{diffusion}},$$

and

$$Nu \equiv \frac{hL}{D} = \frac{h\Delta C}{\frac{D}{L}\Delta C} = \frac{j_{convection}}{j_{diffusion}}, \tag{25.19}$$

where k is the thermal conductivity, and L is the characteristic length of the interface. Thus, the common physical interpretation of a Nusselt number, Nu, in heat and mass transfer is that it scales the ratio of a convective flux, $j_{convection}$, to the corresponding diffusive flux, $j_{diffusion}$, which is the flux expected under identical conditions in the same fluid held, hypothetically, stagnant.

The main advantage of using a convective-coefficient (i.e., Nusselt number) formulation relative to using the solute layer thickness is that numerous empirical correlations exist for Nusselt numbers that were developed for various flow configurations, including, especially, turbulent natural convection in liquid metals.

25.4.4 Classification of Melt Convection

Convection, as mentioned earlier, can be natural or forced, depending on how the flow is driven. It is well established [8,9] that the ratio of the Grashof number, Gr, to the Reynolds number squared, Re^2, captures the relative strengths of buoyancy-to-inertial forces acting on an element of fluid,

$$\frac{Gr}{Re^2} \sim \left(\frac{Buoyancy}{Inertia}\right).$$

where,

$$\mathrm{Re} = \frac{VR}{\nu} = \frac{\omega R^2}{\nu},$$

and R is the crystal radius and ω is its rotation rate. Buoyancy can arise from gradients in either temperature, due to thermal expansion, or from gradients in composition, due to mass density changes with composition. The latter effect is usually more significant than the former whenever a solute is present of significantly different atomic weight from the solvent,

$$Gr = \frac{g\Delta\rho/\rho L^3}{\nu^2} = \frac{g\beta\Delta T L^3}{\nu^2} + \frac{g\beta_C\Delta T L^3}{\nu^2}.$$

Here, $g = 9.81$ (m/s^2) is the average terrestrial gravitational acceleration, β and β_C are the corresponding temperature and concentration expansion coefficients of the melt, and ν (cm^2/s) is the kinematic viscosity of the melt.

[7]The corresponding dimensionless mass transfer coeffcient is also called the Sherwood number, Sh.

Three distinguished limits may be considered for natural convection during crystal growth:

1. $Gr/Re^2 < 0.1$, natural convection is negligible.
2. $0.1 < Gr/Re^2 < 10$, neither is negligible.
3. $Gr/Re^2 > 10$, forced convection is negligible.

Natural convection for melt growth processes conducted terrestrially may only be ignored in small-diameter CZ melts, crystallizing at high rotational rates.[8]

25.4.4.1 Forced Convection

Fluid flow, when driven by some external source, allows the Reynolds number of the flow, *Re*, to be calculated. Using forced convection it becomes easier to maintain a crystal growth process at a steady rate, and, moreover, employing forced flow also allows enhanced heat and/or mass transfer to occur, to achieve faster crystal growth rates. Techniques that have proven successful for achieving forced-flow crystal growth from the melt include: crystal rotation, or crucible rotation; accelerated crucible rotation technique (ACRT) [23]; application of external magnetic fields with conducting melts [24]; and insertion of oscillating baffles [25]. The Nusselt number, for forced convection mass transfer, may be expressed as,

$$Nu = \frac{h_{FC}L}{D} = F(Re^n, Sc^m). \tag{25.20}$$

where $n = 1/2$ for laminar flow and $n = 0.8$ for turbulent flow; m = 1/3.

25.4.4.2 Natural Convection

Natural convection is driven by buoyancy forces due to mass density differences $\Delta\rho$, caused by temperature differences, ΔT, and or concentration differences, ΔC. The Nusselt number, for natural convection mass transfer, may be expressed as,

$$Nu_{NC} = \frac{h_{NC}L}{D} = F\left(Gr^n, Sc^m, \mathrm{Pr}^k\right), \tag{25.21}$$

where $n = 1/4$ for laminar flow, and $n = 1/3$ for turbulent flow; $m = 1/3$.

25.4.4.3 Convection Driven by Freezing

Perpendicular or suction flows, due to crystallization, may also be classified as "forced convection," since the interface velocity, *f*, is known. Such perpendicular flows on earth can reduce the solute layer thickness and, as a result, increase the concentration gradient at the interface; whereas in space experiments, where natural convection tends to be weak, perpendicular flows control segregation. The Péclet number, expressible as the product of the Reynolds and Schmidt numbers, is dimensionless interface velocity,

[8]Burton et al. [1,2] conducted experiments at 57, 144, 575, and 1440 rpm. Hence, natural convection was negligible.

$$Pe_f = \frac{fL}{D} = Re_f \cdot Sc \tag{25.22}$$

25.4.4.4 Thermocapillary Convection

Thermocapillary (Marangoni) convection is driven by surface tension gradients. Thermocapillary convection is unavoidable when free melt surfaces are present during crystal growth. On earth, with the presence of strong buoyancy forces, thermocapillary convection is usually less important then either forced or natural convection. The chief exception occurs where thermocapillary convection can actually dominate the flow state in microgravity crystal growth and in floating zone crystal growth. Its specific influences on solute segregation will not be elaborated any further.

25.4.4.5 Mixed Convection

Mixed convection is the term describing various combinations of forced and natural convection [8,9]. See Section 25.6.2.

25.5 Segregation Theories Based on Solute Layer Thickness

Next we consider several theories of solute segregation, where the effective segregation coefficient is a function of the solute boundary layer thickness, i.e., $k_{eff} = F(\delta)$. The following definitions are used in modern crystal growth literature, see Figure 25.4:

1. Physical film thickness.
2. Gradient of tangential film thickness, δ_{grad}, defined by Eqn (25.15). The profile $C_L(x)$ is linear.
3. Fictitious stagnant film thickness, δ_{exp}. See BPS theory below.

25.5.1 BPS Theory

A seminal paper concerning solute segregation during melt crystal growth by BPS appeared in 1953 [1,2]. This theory was the first attempt to introduce melt convection as a factor influencing solute segregation during unidirectional crystal growth. BPS theory provides a one-dimensional solute segregation model, which consequently ignores any associated transport of solute in directions lateral to the crystal–melt interface. As pointed out earlier in this chapter, such an approach is physically incorrect, as melt convection is not realistically unidirectional and always moves some of the fluid laterally along the crystal–melt interface. By restricting convection to one-dimensional steady state incompressible flow, Eqn (25.3) reduces to

$$D\frac{d^2C}{dz^2} - V_z\frac{dC}{dz} = 0. \tag{25.23}$$

Here velocity $V_z = w + f$, is just the sum of the normal fluid velocity, w,[9] and the interface speed, f. Next, BPS assumes that within the "stagnant layer," δ, the normal flow velocity merely matches the interface speed, f. Equation (25.23), subject to that assumption, becomes identical to Tiller's expression, Eqn (25.8), the solution to which yields an exponential concentration profile in the melt adjacent to the advancing interface,

$$\frac{C_L(x) - C_S}{C_0 - C_S} = e^{-\frac{f}{D}x}. \tag{25.24}$$

BPS then truncates the full exponential solute concentration profile by introducing a fictitious stagnant layer thickness, $x = \delta$, claiming further that $C_L(\delta) = C_L$, a condition introduced into Eqn (25.24), which provides the outer matching condition for the concentration field where the stagnant boundary layer ends and the outer perfectly mixed melt begins. Next, introducing $k_0 = C_S/C_0$, BPS obtains its "effective segregation coefficient,"

$$k_{eff} = \frac{C_S}{C_L} = \frac{k_0}{k_0 + (1 - k_0)e^{-\Delta}}, \tag{25.25}$$

expressed by a dimensionless exponent $\Delta = -f\delta_{\exp}/D$. The term δ_{exp} is the thickness of the exponentially decaying solute profile, which supposedly develops within the putative "stagnant film" given by Eqn (25.24). Now the quantity δ_{exp} may be determined from Levich's similarity solution to the hydrodynamic equations governing convection, namely,

$$\delta_{FC}^{grad} = 1.61\, D^{1/3}\nu^{1/6}\omega^{-1/2} \tag{25.26}$$

The subscript *FC* in Eqn (25.26) denotes that the layer thickness, δ_{FC}^{grad}, is actually controlled by forced convection alone. The superscript *grad* in Eqn (25.26) reminds the reader that the solute layer thickness, δ_{FC}^{grad}, is not based on the physical solute concentration profile δ, given by Eqn (25.16), but rather on the linear profile illustrated in Figure 25.4.

Why does replacing the exponential profile thickness, δ_{exp}, with one determined from the linear solute layer thickness estimate, δ_{FC}^{grad}, work so well? The answer to this question is that Eqn (25.25) is actually applicable only to CZ crystal growth, and specifically where the dimensionless exponent is small, i.e., where $\Delta \ll 1$,[10] so that a one-term expansion remains accurate, and

$$e^{-\Delta} \approx 1 - \Delta$$

Therefore, one obtains

$$k_{eff} = \frac{k_0}{k_0 + (1 - k_0)e^{-\Delta}} \approx \frac{k_0}{1 - (1 - k_0)\Delta} \tag{25.27}$$

[9] According to Cochran, $w = 0.51w^{3/2}\nu^{-1/2}x^2$ valid for $x < \sqrt{\nu/w}$.
[10] δ_{grad} will be small because of the intense forced convection.

The above connection was first noted by Lynne Wilson, who remarked, "We feel that the right answer has been obtained for the wrong reason" [26]. It is interesting to note that in the classic 1965 book, in the section "Partial Stirring," J.C. Brice derived the relation,

$$k_{eff} = \frac{k_0}{1 - (1 - k_0) f \frac{\delta^{grad}}{D}},$$

and proceeds to present the BPS model, see p. 81 in [27]. In conclusion, Eqn (25.26) is a similarity solution for the solute segregation in CZ crystal growth, the validity for which is limited by the following five assumptions used in its derivation:

1. Melt flow is characterized as laminar, symmetric, and rotating;
2. The disk (growing crystal face) is infinitely large and impermeable, so δ is not a function of f;
3. The Schmidt number for the melt is large, $Sc \to \infty$; See Section 25.7.1.
4. Buoyancy forces are negligible compared to forces applied by the crystal face;
5. Solute transfer is one-dimensional.

In conclusion, Eqn (25.26) is applicable only to laminar melt flows occurring in small-diameter CZ melts where $Re^2 \gg Gr$.

The physical basis for, and the mathematical consistency of, BPS segregation theory has been challenged since 1970. BPS predictions for the segregation, in fact, could neither be validated nor refuted, because the diffusion coefficients for solutes D—key melt parameter—were not known precisely enough (see Section 25.9).

25.5.2 Wilson–Garandet's Model: Forced Convection Alone

Wilson (1978) [26] and Garandet et al. (1993) [30] recognized the shortcomings of stagnant layer segregation models. Their model also considers forced convection acting alone but eliminates the questionable assumption of a stagnant solute layer. Lateral melt convection along the crystal–melt interface is again ignored, so melt flow again is assumed to be one-dimensional. The Wilson–Garandet formula for the effective segregation coefficient is the *linearized* BPS estimate, Eqn (25.27),

$$k_{eff} = \frac{k_0}{1 - (1 - k_0)\Delta}. \tag{25.28}$$

But dimensionless solute layer thickness, Δ, is instead defined by the following definite integral,

$$\Delta = \frac{f\delta}{D} = \int_0^\infty \exp\left(-z - Bz^3\right) dz, \tag{25.29}$$

where the constant in the integrand of Eqn (25.29) is defined as, $B = 0.17 f^{-3} \omega^{3/2} \nu^{-1/2} D^2$. The integration variable, z, designates the perpendicular distance from the interface [1,3,4]. This model is exact, but again its validity remains limited in scope by the five

assumptions concerning the similarity solution (listed in Section 25.5.1, BPS theory). Hence the Wilson–Garandet formula provides a solid estimate for k_{eff}, providing that the CZ crystal is rotating rapidly [31], so natural convection may be ignored.

25.5.3 Models Considering Natural Convection and/or Lateral Melt Convection

Camel and Favier (1984) [32], chose an order-of-magnitude analysis to extract scaling laws that delineate longitudinal solute segregation in HB crystal growth. In contrast to the BPS and Wilson–Garandet forced-convection models, Favier and Camel analyzed the influences of natural convection on solute segregation. Natural convection, as discussed earlier in this Chapter, ensures lateral melt flow along an advancing crystal–melt interface.

Yen and Tiller [21] also pointed out that in BPS's one-dimensional analysis of only an axial normal flow component was considered. Neither buoyancy-driven natural convection nor lateral convection was considered, although in many instances it may be the dominant flow mode. Yen and Tiller instead incorporated the important effects of lateral melt convection into their solute redistribution analysis by introducing an "effective" solute source/sink term in the solute transport equation, as

$$D\frac{d^2C}{dz^2} - V_z\frac{dC}{dz} - \dot{q} = 0. \tag{25.30}$$

Ostrogorsky and Mueller [20,22] derived a correlation for the effective segregation coefficient using integral boundary layer analysis, Figure 25.5. Their segregation model for k_{eff} becomes a function of the actual/physical thickness of the solute layer, δ, given by Eqn (25.16). Natural convection was considered using scaling arguments. This

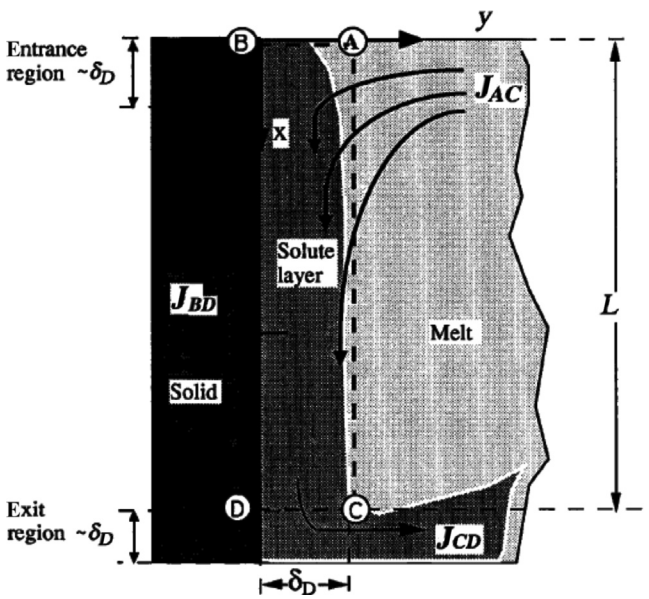

FIGURE 25.5 Schematic of lateral convection, from Ostrogorsky and Mueller [20].

segregation model provides a criterion for the maximum convective velocity that allows diffusion-controlled segregation. Interestingly, this criterion suggests that diffusion-controlled segregation of a binary system with a low value for the equilibrium segregation coefficient ($k_0 \ll 0.1$) might, in fact, not be possible even in an ideal microgravity environment.

In conclusion, the solute segregation models developed by Camel and Favier (1984) [32], Yen and Tiller [21], and Ostrogorsky and Mueller [20] include the important melt flow feature of lateral melt convection. Without the presence of some lateral melt convection, solute transport away from the crystal–melt interface would cease, and k_{eff} would become equal to unity.

25.6 Segregation Model with Nusselt Numbers and Mixed Convection

The application of forced melt convection during bulk crystal growth proves to be advantageous from several standpoints. Initially, forced convection was incorporated only in CZ, using crystal rotation, and similarly in float zone (FZ) processing. As the advantages of forced melt convection and the disadvantages of natural melt convection became clearer, novel adaptations involving forced melt flow were implemented for Bridgman/Vertical Gradient Freeze (VGF) crystal growth. These innovations included the use of traveling magnetic fields [24] (see Vol. IIb, Chapter 23), forced mechanical vibrations, and rotating/oscillating immersed baffles [25] (see Vol. IIb, Chapter 24). The melt convection during crystal growth resulting from the application of these techniques usually produces a mix of natural and forced convection, and perpendicular suction flow. Such complex flow states will be referred to as "combined convection."

25.6.1 Combined Mass Transfer Coefficient

Mass conservation at steady state in the presence of combined melt convection requires that the solute flux rejected at the crystal–melt interface, j_{rej}, is transported away into the bulk melt by a combined convective flux, j_{CC} [33]. See again Figure 25.1. Expressions for the rejected mass flux and the combined convective flux are, respectively,

$$j_{rej.} = f\left(C_0 - C_S\right),$$

and

$$j_{CC} = h_{CC}\left(C_0 - C_L\right),$$

where h_{CC} is the "combined" mass transfer coefficient. Referring again to Figure 25.1, solute mass conservation requires their balance, specifically,

$$f(C_0 - C_S) = h_{CC}(C_0 - C_L).$$

Rearranging the above mass balance, and substituting the equilibrium segregation coefficient, k_0, yields the relationship for the effective segregation coefficient for combined melt convection, $k_{eff,CC}$, as [33],

$$k_{eff,CC} = \frac{C_S}{C_L} = \frac{k_0}{1-(1-k_0)\frac{f}{h_{CC}}}. \tag{25.31}$$

Equation (25.31) is a statement of mass conservation, and, as such, is exact, recognizing, of course, that practical applications of Eqn (25.31) require a suitable correlation linking the crystal growth rate, f, with the combined mass transfer coefficient, h_{CC}.

25.6.2 Phenomenological Approach to Determine the Combined Mass Transfer Coefficient

In order to take advantage of existing empirical correlations for the mass transfer coefficient for forced and natural melt convection, h_{CC} is modeled as follows.

1. *"Mixed" convection:* Based on extensive heat transfer data, it is common practice to correlate combined or mixed natural and forced convection by the following formula,

$$h_{mix} = \left(h_{FC}^m \pm h_{NC}^m\right)^{1/m}. \tag{25.32}$$

The value of the exponent, m, varies between 3 and 4, depending on the flow configuration. The value $m = 3$ correlates data obtained from vertical surfaces. Values for m that fall between 3.5 and 4 are used to correlate flow data from horizontal surfaces [8,9]. The sign within Eqn (25.32) is selected as positive when forced and natural convection reinforced, i.e., act in the same direction, thereby enhancing the overall mixed flow state. The sign in Eqn (25.32) is selected as negative when forced and buoyant convection oppose each other, leading to a weakened mixed flow state. For processes where $Gr \gg Re^2$, e.g., Bridgman crystal growth, one allows $h_{mix} = h_{NC}$. For processes where $Re^2 \gg Gr$, one chooses $h_{mix} = h_{FC}$.

2. *Perpendicular flows can reinforce mixed convection:* Perpendicular (suction) flow $f(\rho_S/\rho_L)$ can reinforce mixed convection, and for situations where $f/h > 0.1$, it should not be ignored. As correlations for interfaces with suction flow are not currently available, it has been suggested to use an effective combined convection coefficient, h_{CC}, of the following form [33],

$$h_{CC} = h_{mix}\left[1+\left(\frac{f}{h_{mix}}\right)^n\right]^{1/n} = \left[h_{mix}^n + f^n\right]^{1/n}, \tag{25.33}$$

where n is an arbitrary exponent. This mathematical form is selected because Churchill and Usagi [34] established that such a correlation is remarkably successful in correlating rates of heat, mass, and momentum transfer. According to reference [35], $n = 1.4$.

Combining Eqns (25.32) and (25.33) gives the combined convection mass transfer coefficient as,

$$h_{CC} = \left[\left(h_{FC}^m \pm h_{NC}^m\right)^{n/m} + f^n\right]^{1/n} \tag{25.34}$$

Note, once again that typically, $h_{mix} \gg f$. Perpendicular convection becomes important primarily in reduced gravity situations, where $h_{mix} = h_{NC}$ is small.

25.6.3 Effective Segregation Coefficient, k_{eff}, as Function of Combined Nusselt Number

Empirical correlations for mass transport coefficients are conveniently given in terms of a CC Nusselt number, Nu_{CC}. Thus, one can rewrite Eqns (25.31) and (25.34) in terms of dimensionless parameters,

$$k_{eff,CC} = \frac{k_0}{1 - (1 - k_0)Pe_f/Nu_{CC}}, \tag{25.35}$$

and

$$Nu_{CC} = \left[Nu_{mix}^n + Pe_f^n\right]^{1/n} = \left[\left(Nu_{FC}^m \pm Nu_{NC}^m\right)^{n/m} + Pe_f^n\right]^{1/n}, \tag{25.36}$$

where $Pe_f = fL/D$, see Eqn (25.22). Nu_{NC} and Nu_{FC} are given by empirical correlations found for pure forced convection and pure natural convection. See below.

25.7 Correlations for Nusselt Numbers

Numerous established correlations are available for natural convection and convection driven by rotating disks. To our knowledge, there are no correlations relating Nusselt numbers to the magnetic Taylor number or to other parameters characterizing moving magnetic fields.

25.7.1 Correlations for Disk-Driven Forced Convection

Many correlations for laminar and turbulent flows are given in the 1963 monograph by L.A. Dorfman [36], and in the recent monograph *Convective Heat and Mass Transfer in Rotating Disk Systems* by Igor V. Shevchuk (2009) [28]. The key correlations for convection occurring in CZ melts are listed in [31].

25.7.1.1 Exact Similarity Solution for Laminar Flow and Sc $\rightarrow \infty$

Levich's similarity solution for the mass flux is expressed as

$$j = 0.62D^{2/3}\nu^{-1/6}\omega^{1/2}(C_0 - C_L). \tag{25.37}$$

Levich specified neither the mass transfer convection coefficient, h, nor the Nusselt number, Nu, both of which are obviously based on the mass flux,

$$h = 0.62D^{2/3}\nu^{-1/6}\omega^{1/2} = 0.62D\sqrt{\frac{\omega}{\nu}}Sc^{1/3}. \tag{25.38}$$

and,

$$Nu_{FC} = \frac{hR}{D} = 0.62Re^{1/2}Sc^{1/3}(Sc \to \infty). \tag{25.39}$$

25.7.1.2 Empirical Correlations, Laminar Flow

Doped semiconductor melts, Si and Ge, have Schmidt numbers in the range $10 \le Sc \le 100$ [31]. The Nusselt number correlations for this important range are:

$$Nu_{FC} = 0.485Re^{1/2}Sc^{0.373}\left(5 \le Sc \le 100\right), \tag{25.40}$$

as proposed by Ostrogorsky [31], and

$$Nu_{FC} = \frac{0.62045 \cdot Re^{1/2}Sc^{1/3}}{\left(1 + 0.298Sc^{-1/3} + 0.14514Sc^{-2/3}\right)}(2 \le Sc \le \infty), \tag{25.41}$$

as proposed by Newman [37]. In Figure 25.6, the above forced convection Nusselt number correlations, Nu_{FC}, are plotted as a function of the Schmidt number. The curve labeled "Exact," is the numerical solution of the governing equations. Levich's "exact" solution Eqn (25.39), which requires $Sc \to \infty$, shows a 7% error at $Sc = 100$ and a 17%

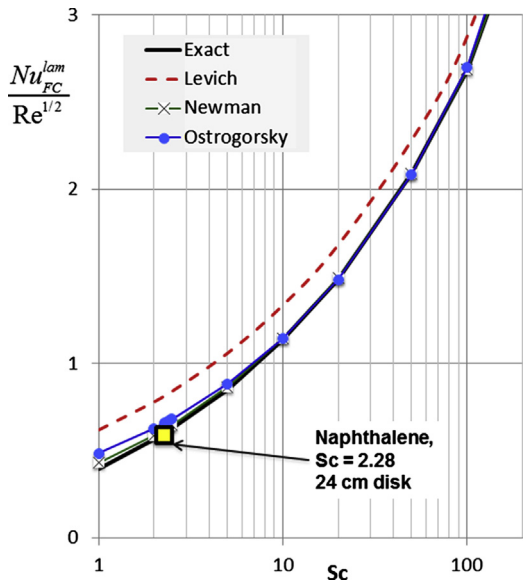

FIGURE 25.6 Exact numerical solution from [28], and correlations for Nusselt numbers, divided by $Re^{1/2}$, for laminar flow versus Schmidt numbers, *Sc. Data point is from Chen et al.; see [29].*

disparity at $Sc = 10$ [31]. The correlation Eqn (25.40), indicates less than 1% error, for $10 \leq Sc \leq 100$ and less than 4% error for $5 \leq Sc \leq 500$ [31]. The correlation, Eqn (25.41), even more impressively provides less than 4% error for the range $2 \leq Sc \leq \infty$ [31].

It is also encouraging to see near perfect agreement with the experimental data point, obtained using a 24-cm-diameter disk and evaporating naphthalene at a Schmidt number $Sc = 2.28$.

25.7.1.3 Empirical Correlations, Turbulent Flows

Melt convection in CZ crystal growth is turbulent from the combined action of strong centrifugal and buoyancy forces. Yet CZ melt flow should be laminar based on the Reynolds numbers alone, excepting growth of large CZ Si crystals at high rates of rotation. For flat disks, the lamellar–turbulent transition occurs at $Re \approx 8.8 \times 10^4$, with flow reaching a fully turbulent state at $Re \approx 3.2 \times 10^5$ [38]. By contrast, a 20-cm-diameter Si crystal rotating at 30 RPM has a Reynolds number of $Re \approx 100{,}000$.

Numerous correlations for turbulent flow driven by a rotating disk can be found in reference [28]. Here we present the two correlations by Dossenbach: (1) for fully turbulent flow, $Re > 300{,}000$,

$$\overline{Nu^{turb}} = 0.0108 Re^{0.87} Sc^{1/3}, \tag{25.42}$$

and (2) transition from laminar to turbulent flow, valid for $Re_{tr} < Re < 1.8 \times 10^6$ (see Figure 25.7) [28],

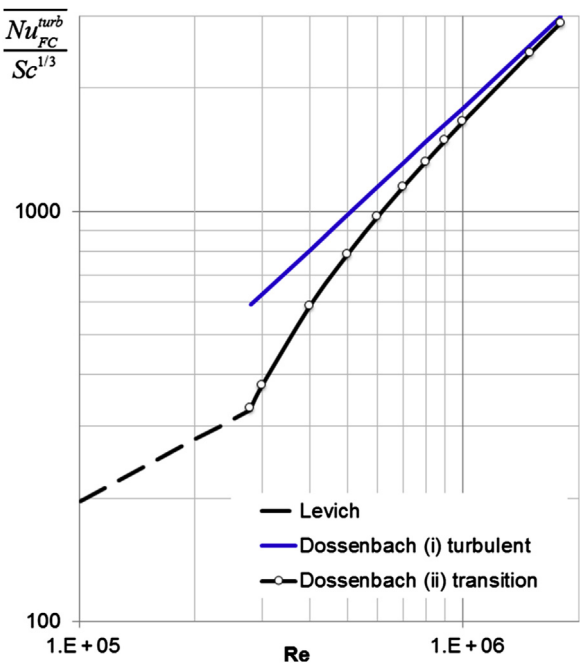

FIGURE 25.7 Average Nussel number divided by $Sc^{1/3}$ as a function of *Re*, for turbulent flow, from [31].

$$\overline{Nu^{tr}} = \frac{Sc^{1/3}}{Re^{0.5}}\left[0.62Re_{tr} + 0.0108\left(Re^{1.37} - Re_{tr}^{1.37}\right)\right]. \tag{25.43}$$

The transition occurs at $Re_{tr} = 278{,}000$.

25.7.2 Empirical Correlations for Natural Convection

The general form of a Nusselt number correlation for natural convection is given by Eqn (25.20). The majority of these correlations were developed using heat transfer data,[11] but by analogy also hold for mass transfer, provided that mass transfer does not alter the fluid velocity. When $Sc \gg Pr$, a heat transfer correlation may be transformed into a mass transfer correlation by using the following substitution [39,40]:

$$\text{For } Pr/Sc \to 0, Nu^{HT} \to Nu, \text{ and } Gr \cdot Pr \to Gr \cdot Sc \cdot Le^{1/3} \tag{25.44}$$

where $Le = Sc/Pr = \alpha/D$ is the Lewis number. For silicon melts, $Pr = 0.014$, and for silicon melts doped by B, P, or As, $Sc \approx 15$ [31]. Thus, for this semiconductor melt $Sc \gg Pr$ and $Le \approx 1070$.

Natural convection in large CZ melts is complex, as it depends on the solid–liquid interface diameter, d, the overall melt geometry, vertical and horizontal thermal gradients, etc. Here we consider well-established correlations developed for natural convection in liquid metals and applicable to semiconductor crystal growth.

25.7.2.1 Vertical Walls

A vertical solid–liquid interface, oriented parallel to gravity, is typical of the crystal growth configuration for both HB growth and horizontal zone refining. This configuration is also relevant to CZ crystal growth, because vertical heated crucible walls drive natural melt convection. Churchill and Chu's [39] empirical correlation was tested against experimental heat or mass transfer data. Their correlation may be expressed as,

$$Nu_L^{HT} = \frac{h^{HT}L}{\lambda} = \left\{0.825 + \frac{0.387(Gr_L Pr)^{1/6}}{\left[1 + (0.492/Pr)^{9/16}\right]^{8/27}}\right\}^2.$$

It is valid for any Prandtl number, Pr, and the range of Rayleigh numbers, $0.1 \le Ra_L \le 10^{12}$. L is the wall length, and $Ra_L = Gr_L Pr$. For the case of mass transfer, substitution of Eqn (25.44) gives the result,

$$Nu_L = \frac{hL}{D} = \left\{0.825 + \frac{0.387(Gr_L Sc)^{1/6} Le^{1/18}}{\left[1 + (0.492/\mathrm{Pr})^{9/16}\right]^{8/27}}\right\}^2. \tag{25.45}$$

where Le is Lewis number.

[11] Convection heat transfer experiments are more precise and easier to conduct than are convection mass transfer experiments.

Masliyah and Nguyen's [41] correlation was developed from mass transfer experiments, using the binary system 2-bromopyridine in water. The Nusselt number correlation they found is

$$N_L = \frac{hL}{D} = 0.258(Gr_L \cdot Sc)^{0.289}. \tag{25.46}$$

This correlation was tested for $2 \times 10^{12} \leq Gr_L Sc \leq 10^{13}$. For 2-bromopyridine in water, $Pr = 6.7$, $Sc = 2500$, and $Le = 373$. This system is roughly comparable to the Lewis number for doped silicon melt, $Le = Sc/Pr = 1070$. For comparison, Nusselt versus Grashof number correlations Eqns (25.45) and (25.46) based on a vertical wall are given in Figure 25.8, along with the Ostrach's similarity solution for laminar flow [10] and Sparrow and Greg's correlation, see [44].

25.7.2.2 Horizontal Disks

The solid–liquid interface can be modeled as a downward-facing cooled disk for both CZ and Kyropoulos crystal growth processes, which feature relatively large melt volumes and small crystals. McDonald and Connolly [43] carried out experiments with a cooled, horizontal, downward-facing circular plate ($d = 20$ cm) immersed in a tank of liquid sodium metal. Experiments were carried out over the Grashof number range $6 \times 10^8 \leq Gr \leq 5 \times 10^9$. Those investigators found the Nusselt number correlation for heat transfer as

$$Nu_d^{HT} = \frac{h^{HT} d}{\lambda} = 0.262\left[Gr_d \cdot Pr^2\right]^{0.35}.$$

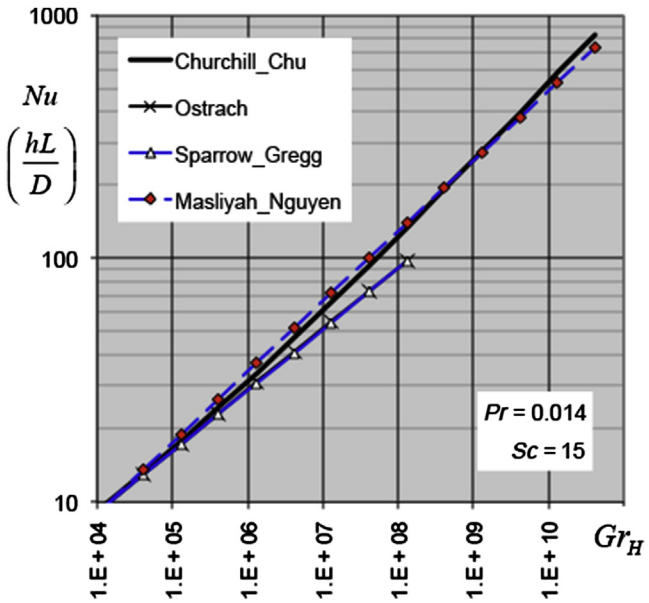

FIGURE 25.8 Comparison of mass transfer correlations for vertical walls. $Sc = 15$ is typical for impurities in silicon [44].

The Nusselt number correlation for the case of mass transfer was similarly found to be [44],

$$Nu_d = \frac{hd}{D} = 0.262[Gr_d \cdot Sc \cdot Pr]^{0.35} Le^{0.35/3}. \tag{25.47}$$

Reference [44] illustrates the excellent agreement between the above correlations with key correlations for heat and mass transfer.

25.7.2.3 Rayleigh–Bénard Convection

Rayleigh-Bénard convection between a cooled interface and the heated crucible bottom may be used for large-diameter Kyropoulos or CZ crystal growth. The Globe–Dropkin correlation [45] was tested for the parameter ranges $3 \times 10^5 \leq Gr \cdot Pr \leq 7 \times 10^9$ and $0.02 \leq Pr \leq 8750$, where for heat transfer,

$$Nu_L^{HT} = \frac{h^{HT} L}{\lambda} = 0.069(Gr_L \cdot Pr)^{1/3} Pr^{0.074},$$

and for mass transfer,

$$Nu_L = \frac{hL}{D} = 0.069(Gr_L \cdot Sc)^{1/3} Le^{1/9} Pr^{0.074}. \tag{25.48}$$

Reference [44] illustrates the good agreement between the above correlations and several other well-established correlations for liquid metals.

25.8 Directional Solidification: Segregation without Forced Convection

Natural convection is almost always unsteady in semiconductor melts. It is turbulent for $Gr > 10^9$. The level of unsteady convection depends both on the melt size and radial temperature gradients, as well as on the interfaces shape, etc.—all of which continually change during growth. Unsteady convection yields significant fluctuations in growth rate, leading to compositional inhomogeneities and misoriented nucleation and growth [24].

Radial inhomogeneity during directional crystal growth is high compared to CZ growth. Research on this topic focused initially on minimizing natural convection, by application of axial and transverse magnetic fields, insertion of baffles and other flow restrictors, etc. Numerical modeling conducted in the 1980s [46,47], however, eventually revealed that the highest lateral segregation usually occurs when the melt flow velocity is low. Lateral segregation during HB crystal growth reaches a maximum when the Grashof number $Gr_H \approx 10^3$ [46]. See also Section 25.11.2. Reduction of natural convection through the use static magnets or melt baffles helps to prevent turbulence but does not necessarily yield significant improvements of either crystalline and chemical perfection of the crystals so grown. This disappointing fact remains true even for directional solidification conducted in microgravity. Therefore, research conducted during the past decade focused mainly on introducing strong, controllable, forced convection rather than attempting to actually minimize levels of natural convection.

In conclusion, one finds that natural convection is an unavoidable phenomenon; moreover, it is virtually impossible to eliminate natural convection entirely, given that the flow direction and magnitude of its velocity are extremely difficult to control. As a result, both macroscopic and microscopic component redistributions are notably inferior (less well controlled) when compared to those obtained via the CZ growth process. In those instances where directional solidification is carried out without forced convection, the effective segregation coefficient simplifies because $Nu_{mix} = Nu_{NC}$. Thus,

$$k_{eff,NC} = \frac{k_0}{1 - (1 - k_0)Pe_f \Big/ \left[Nu_{NC}^{1.4} + Pe_f^{1.4}\right]^{1/1.4}}. \tag{25.49}$$

where $Pe_f = fL/D$, see Eqn (25.22). The correlation found for Nu_{NC} may be selected on the basis of the orientation of the crystal–melt interface; $k_{eff,NC}$, is expected to vary as the melt size changes. Thus, Eqn (25.49) provides only a first-order model of the segregation process.

It appears that future improvements of directional crystal growth will rely more heavily on schemes that use forced convection-dominated processes, where, $Re^2 > Gr$, rather than reduction of natural convection.

25.8.1 Segregation Under Vanishing Natural Convection ($Gr \to 0$)

DS experiments carried out in orbital laboratories during the 1970s and 1980s were focused on achieving diffusion-controlled solute segregation (see Section 25.3.2). In addition, magnetic fields reaching 3 T were applied in an effort to diminish natural convection [48].

Diffusion-controlled solute segregation occurs when the advective flux, $j_{advection}$, via bulk melt motion, becomes insignificant compared to the diffusion flux, so their ratio, $j_{advection}/j_{diffusion} \to 0$. As noted earlier, however, diffusion-controlled solute segregation acting alone should result in an ideal uniform axial and lateral segregation [49]. To reduce the distorting influence of natural convection, one must reduce the buoyancy forces. On orbiting platforms, the quasi-static gravitational acceleration is routinely reduced by factors of about 10^{-5} or less. The Grashof number is commensurately reduced, since $Gr \approx g\Delta TL^3$, as neither the melt's viscosity, ν, nor its thermal expansion coefficient, β, can be altered. Therefore, the goal of pioneering microgravity experiments conducted in near-Earth orbit[12] was to approach to as a high degree as possible the ideal diffusion-controlled segregation. At that early time for microgravity experiments, the "gap" between theory and experiments was attributed to "gravity-induced convection effects" [49,50]. It was expected that reducing the gravitational acceleration (and the Grashof number) by a factor of roughly 10^{-5} or less should also reduce buoyancy forces to the point that the convective mass flux would be negligible compared to the diffusion flux.

[12]As occurred during the Skylab [49] and Apollo-Soyuz missions.

To the contrary, it actually turned out that nearly every segregation experiment conducted in orbital (low-gravity) environments was disturbed by convection driven by buoyancy and/or surface tension (Marangoni) forces. Steady state segregation was achieved only during the Skylab mission by growing Te-doped InSb [49] and, again more recently, Te- and Zn-doped InSb [17,18]. Yet, the Ga-doped Ge crystal growth experiments, conducted during the Apollo–Soyuz mission [50], clearly revealed appreciable convective influences on the measured solute segregation. This unexpected result can be explained now by using the CC model given by Eqn (25.49).

In microgravity conditions, the most pervasive influence altering a diffusion-limited segregation pattern arises from accelerations acting parallel to the interface [22], as would be the terrestrial situation for the HB configuration. See Figure 25.9, where a horizontal temperature difference, ΔT, drives convection. The solid–liquid interface is the vertical cooled wall (see Section 25.7.2.1).

When applying the Nusselt number correlations to extremely low flow velocities, one should consider the following correction. All such correlations are developed for solid (impermeable) walls, where for "zero" flow velocity $j_{advection} = 0$ and $Nu = 1$,

$$Nu \equiv \frac{j_{convection}}{j_{diffusion}} = \frac{j_{advection} + j_{diffusion}}{j_{diffusion}} = 1 \tag{25.50}$$

During crystal growth, however, the crystal–melt interface acts as a porous boundary. Without the presence of some advection, solute cannot be transported by diffusing against the perpendicular flow velocity (i.e., $j_{diffusion} = 0$). Thus, one should use the so-called "excess" Nusselt number [31], namely, the amount by which the Nusselt number exceeds unity,

$$Nu^{excess} \equiv \frac{j_{advection}}{j_{diffusion}} = \frac{j_{convection} - j_{diffusion}}{j_{diffusion}} = Nu - 1 \tag{25.51}$$

Using the excess Nusselt number only becomes a significant correction in microgravity environments, since on Earth, typically $Nu^{excess} \approx Nu$.

Figure 25.10 shows $k_{eff,NC}$ calculated using Eqn (25.49), for Ga-doped Ge crystal growth experiments, conducted during the Apollo–Soyuz mission [50]. $Nu_{NC}^{excess} = Nu - 1$ was calculated using

1. Churchill and Chu's Eqn (25.45);
2. Ostrach's similarity solution [9,10];
3. Masliyah and Nguyen's Eqn (25.46).

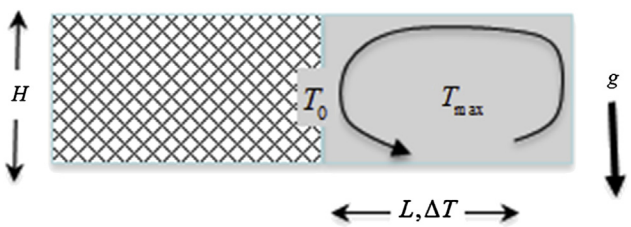

FIGURE 25.9 Schematic of horizontal Bridgman (HB) process: characteristic lengths and temperature differences.

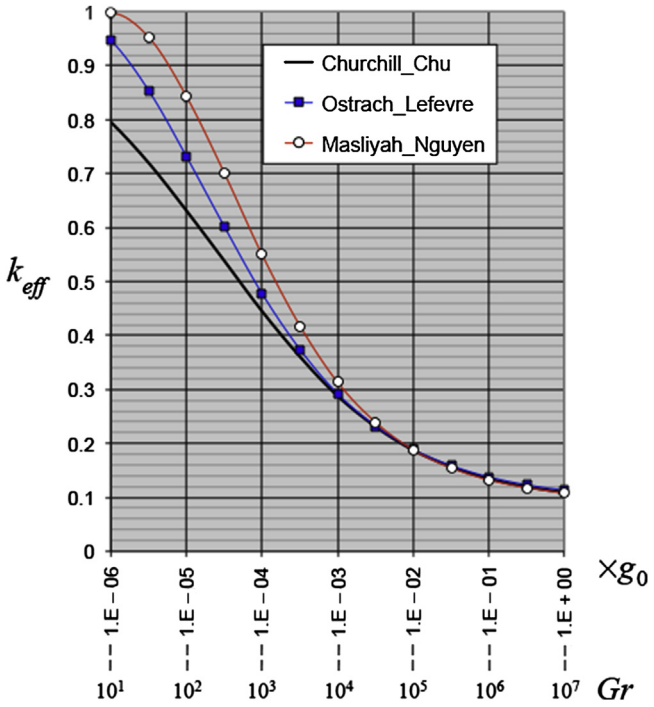

FIGURE 25.10 k_{eff} for $10^{-6}g_0 < g < g_0$ ($g_0 = 981$ cm/s^2) calculated using Eqn (25.49) for parameters used by Witt et al. [50]. Nu_{NC} was calculated using Eqn (25.45), Eqn (25.46), and Ostrach's similarity solution for laminar flow [8,9].

Overall, the agreement found among these correlations is solid for $Gr > 10^4$, see Figure 25.10. Churchill and Chu's correlation has been tested for $GrPr > 0.1$ (or $Gr > 10$ since $Pr \approx 0.01$). Therefore, it should be accurate down to $10^{-6}g_0$. Ostrach's similarity solution is valid only for laminar "boundary-layer" flow, or typically $Gr > 10^4$. For ground-based experiments, all three correlations give $k_{eff} \approx 0.11$, whereas Witt et al. reported $k_{eff} \approx 0.099$.

At $10^{-5}g_0$, Eqn (25.49), with Churchill and Chu's correlation, gives $k_{eff,NC} \approx 0.63$, whereas from the segregation profiles reported by Witt et al.[13] one calculates $k_{eff} \approx 0.6$ [50].

Figure 25.11 illustrates the effect of the crystal growth rate. The solute boundary layer is thinner at high growth rates and, therefore, is less sensitive to convection. For the case of Ga-doped Ge, grown at $10^{-6}g_0$, growth rate $f \approx 10$ (cm/hr) would yield $k_{eff} \approx 0.95$. By contrast, $f \approx 1$ (cm/hr) would yield $k_{eff} \approx 0.5$. Thus, diffusion-controlled segregation becomes infeasible at low growth rates, under conditions, for example, that are needed to grow semiconductor alloy crystals.

Figure 25.12 focuses on the significance of the equilibrium segregation coefficient k_0. It shows clearly that diffusion-controlled melt growth on orbital platforms becomes practical only with systems having moderate to high k_0-values ($0.5 \leq k_0 \leq \infty$). This fact

[13]The initial dopant concentration in the melt was $C_L^i = 1.78 \times 10^{19}$ cm^{-3}. Accordingly, the first to freeze section had a concentration $C_s(0) = k_0 C_L^i = 1.55 \times 10^{18}$ cm^{-3}. The highest concentration achieved in the solid was at 2 cm, where $C_s = 1.1 \times 10^{18}$ cm^{-3}.

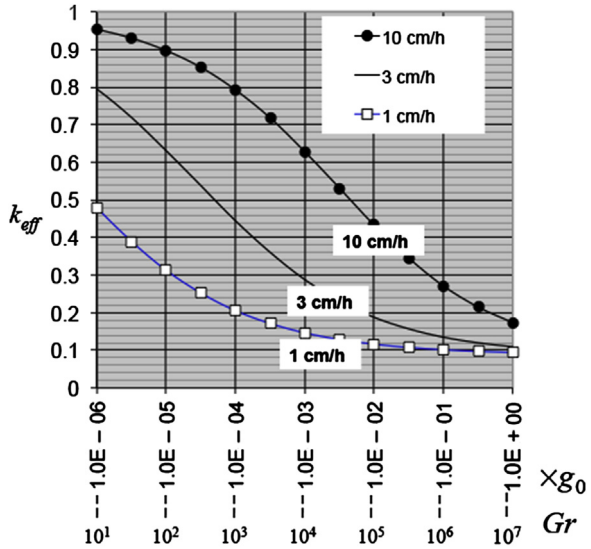

FIGURE 25.11 $k_{eff,NC}$ as a function of growth rate f (cm/h) and gravity level, calculated for parameters used by Witt et al. [50].

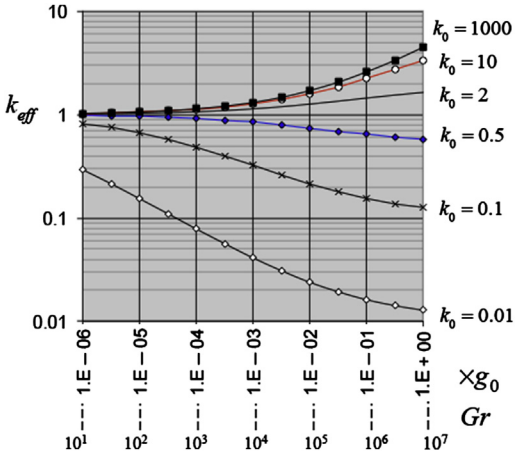

FIGURE 25.12 $k_{eff,NC}$ as a function of k_0 and gravity level, calculated for parameters used by Witt et al. [50].

was not recognized in the 1970s and 1980s, and futile attempts were made to grow Sn-doped InSb ($k_0 = 0.057$) [49] or Sb-doped Ge ($k_0 = 0.003$) [50–52]. In low gravity, systems with $k_0 = 10$ to 1000 yield nearly the same k_{eff}-values.

25.8.1.1 Diffusion Coefficients Extracted under Minimum Convection

Solute segregation developed under diffusion-controlled conditions provides a suitable setting for estimating the diffusion coefficients of dopants and impurities in

semiconductor melts. Yet published data based on this approach often reveal that minute levels of unpredictable, unsteady convection "boost" mass transfer, yielding inflated values of the "effective" diffusion coefficients. Examples of this convective interference are Ga-doped Ge, the reported values for which are $D = 1.7 \times 10^{-4}$ cm^2/s (microgravity experiments [50]), $D = 2.1 \times 10^{-4}$ cm^2/s (shear cell data, [53]), $D = 1.5 \times 10^{-4}$ cm^2/s (3 T axial magnetic field, [48]), and $D = 1.2 \times 10^{-4}$ cm^2/s (5 T axial magnetic field, [54]).

Dutta and Ostrogorsky [54] provide a table that lists some diffusion coefficients obtained under diffusion-controlled, or nearly diffusion-controlled, conditions. They reported $D = 0.8 \times 10^{-4}$ cm^2/s using a submerged heater/baffle—which acted as a flow restrictor—in a 20-zone Mellen furnace. The advantage of using a submerged baffle under terrestrial conditions, relative to the microgravity environment, is that buoyancy forces are steady and point in the direction that opposes convection.

It is interesting to note that the lowest value observed for the diffusion coefficient of Ga-doped Ge was obtained by analyzing CZ segregation data, as described in Section 25.9 below.

25.8.2 Bottom-seeded VB Growth

Crystal growth using bottom-seeded VB has the melt radially heated and, in cases where large-diameter crucibles are required, supplemental heat is added from above. The vertical temperature gradient is stabilizing. However, convection is driven by horizontal temperature gradients. The velocity field depends on the curvature of the interface, horizontal and vertical ΔTs, melt height, crucible material, and other melt parameters. Given the overall complexity of the melt flow, it is advantageous to study segregation and component distribution using three-dimensional numerical modeling techniques, which are capable of including the many interacting parameters that are involved. This is especially true when dealing with molten Si contained in large square crucibles for photovoltaic applications, where melt sizes can reach 1000 kg.

In VB, both crystalline and chemical perfection are often improved by imposing forced convection. This approach, using melt flow control, has been well established through the use of the accelerated crucible rotation technique (ACRT) [23]. Attempts were also made to apply "dominating" forced convection by introducing vibration (see Vol. IIB, Chapter 24) or an oscillating submerged baffle [25]. During the past decade, however, the application of moving magnetic fields (MF) has emerged as the best practice for imposing forced convection during directional solidification. Examples of such moving magnetic fields include traveling MF [24], rotating MF [55], alternating MF, etc. Each of these magnetic field flow-control methods has resulted in a significant improvement in lateral homogeneity, interface shape and symmetry, and crystalline perfection. For further details on the use of moving magnetic fields to stimulate forced convection, see Vol. IIB, Chapter 23, or the excellent review by Rudolph [24].

25.9 CZ Process: Segregation Controlled by Mixed Convection

In Section 25.8 we concluded that natural convection tends to be unsteady, difficult to account for, and thus generally undesirable during crystal growth. Forced convection, by contrast, typically used in CZ growth, is desirable. We proceed by focusing next on solute segregation controlled by forced convection.

25.9.1 Segregation under Steady Forced (Negligible Natural) Convection

The diffusion coefficients of most impurities in semiconductor melts are low, so that even a minute level of convection can alter the diffusion-mediated distribution of impurities in the melt. As noted in Section 25.8.1, weak buoyancy-driven flows have arisen and disturbed numerous microgravity experiments, inflating the apparent values of the diffusivity. This situation remains true even for those measurements conducted in fine capillaries and shear cells. Shear cell measurements, in fact, are usually conducted at a temperature well above the system's melting point,[14] whereas for the purposes of segregation modeling, one would like instead to know the value for the diffusion coefficient in the solute boundary layer at a temperature that is close to the melting point.

Applying a specific amount of laminar forced convection is a good alternative approach, compared to the more difficult and less reliable options of eliminating convection in microgravity. For example, in small CZ melts, the velocity field remains steady and easy to account for. Thus, one concludes that the most reliable approach used to determine the diffusion coefficient is from analysis of the segregation profiles obtained in small CZ systems, provided that melt viscosity is reasonably well known.

25.9.1.1 Diffusion Coefficients of Impurities in Germanium

In 1953, Burton et al. [1,2] reported CZ growth of germanium crystals at various growth rates f and rotation rates ω. To minimize the influence of natural convection, extremely high crystal rotation rates were used: 57, 144, 575, and 1440 RPM, corresponding to $Re^2/Gr = 16$, 110, 1600, and 11,000, respectively.

As the diffusion coefficients of Ga and Sb in molten Ge were not known at that time, Burton et al. [2] applied their segregation data to calculate the apparent diffusivities, rather than to verify the BPS model. Using incorrect viscosity, $\upsilon = 0.0025$ cm^2/s, Burton et al. reported that for gallium, $D_{Ga} = 0.75 \times 10^{-4}$ cm^2/s. Kodera [56] used $\upsilon = 0.0055$ cm^2/s, and got $D_{Ga} = 1.03 \times 10^{-4}$ cm^2/s.

[14]The data indicate that close to the melting point viscosity significantly increases. Based on the Stokes–Einstein equation, viscosity varies reciprocally with diffusivity.

Table 25.1 Recommended Values of Diffusion Coefficients in Molten Germanium

Dopant	k_0	D (cm^2/s)	Reference for Data	Reference for Calculation
B	17	2.7×10^{-4}	Bridges [58]	[33]
Ga	0.087	0.67×10^{-4}	Burton et al. [2]	Equation (25.52)
Sb	0.003	0.5×10^{-4}	Burton et al. [2]	Equation (25.52)

Table 25.1 contains the diffusion coefficients, recalculated using combined Eqns (25.35), (25.36), (25.40), (25.42), and (25.45) listed below as:

$$k_{eff,CC} = \frac{k_0}{1-(1-k_0)Pe_f \Big/ \left[\left(Nu_{FC}^{3.5} \pm Nu_{NC}^{3.5}\right)^{1.4/3.5} + Pe_f^{1.4}\right]^{1/1.4}} = k_{measured} \tag{25.52}$$

where $Pe_f = fR/D$ and

$$Nu_{FC} = 0.485\left(\frac{\omega R^2}{\nu}\right)\left(\frac{\nu}{D}\right)^{0.373} \textit{laminar flow} \tag{25.52.1}$$

$$\overline{Nu^{turb}} = 0.0108\left(\frac{\omega R^2}{\nu}\right)^{0.87}\left(\frac{\nu}{D}\right)^{1/3} \textit{turbulent flow} \tag{25.52.2}$$

$$Nu_{NC} = \left\{0.825 + \frac{0.387(Gr_L Sc)^{1/6} Le^{1/18}}{\left[1+(0.492/\mathrm{Pr})^{9/16}\right]^{8/27}}\right\}^2 \tag{25.52.3}$$

$k_{measured}$ is the experimentally determined value of $k_{eff,CC}$. Natural convection was ignored by setting $Nu_{NC} = 0$. For Ga-doped Ge, $k_0 = 0.087$ and $\nu = 0.00135$ cm^2/s. The crystal radius was $R = 1$ cm.

The diffusion coefficients given in Table 25.1 were calculated by iterating on D, to fit $k_{measured}$ for all growth rates, and rotation rates [31,33]. Assuming laminar flow, the diffusion coefficient $D = 0.67 \times 10^{-4}$ cm^2/s gave a solid fit to the data, at 57, 144, and 575 RPM. At 1440 RPM, the Reynolds number, $Re = 1.2 \times 10^5$, was sufficiently high to assume turbulent flow, see Section 25.7.1.3. Thus, for 1440 RPM, the correlation Eqn (25.52.2), gave a good fit to $k_{measured} \approx 0.09$[15] at $f = 70$ μm/s.

In conclusion, small CZ systems, subject to $Re_R^2 \gg Gr$, are suitable for measuring the diffusion coefficients of impurities because:

- Forced convection can be characterized more precisely than natural convection.
- k_{eff} depends only on f, R, ω, ν, k_0, and D. Typically, f, ω, and R are known. Thus, if k_0 and ν are known, D can be calculated from k_{eff}.
- The segregation data reflect realistic diffusion conditions in the solute layer at the interface, such as temperature, viscosity, and potential association, or clustering, in compound semiconductors.

[15] $k_{measured} \approx k_0 = 0087$ indicates nearly perfect mixing, caused by turbulent flow.

25.9.2 CZ Process with Mixed Convection $Re^2 \approx Gr$

Intense mixed convection, with $0.1 \leq Re_R^2/Gr \leq 10,$ is typical for the CZ process; k_{eff} is close to k_0, unless extremely high pulling rates are used. Laminar forced convection, driven by crystal rotation, yields no lateral segregation. However, natural convection, crucible rotation, and turbulence all disturb the laminar flow driven by the crystal and cause lateral and microsegregation.

25.9.2.1 Diffusion Coefficients of Impurities in Silicon

The widely used diffusion coefficients of impurities in molten silicon have all been obtained from CZ segregation data, published by Turkovskii (1962 [57]) and Kodera (1963 [56]). Both authors used the BPS model to extract diffusion coefficients, although, in contrast to Burton et al. [2], their experiments were performed at relatively modest rotation rates.

The crystal radius R was not reported by Turkovskii or Kodera. This was possible because the BPS model does not account for crystal/melt size. R is not included in Eqns (25.25) or (25.26). Infinite rotating crystal and melt are assumed.

Turkovskii grew Al-, P-, and As-doped silicon crystals at 10, 12, and 60 RPM [57]. The diffusion coefficients obtained at 10 or 12 RPM were consistently higher than the coefficients obtained at 60 RPM. For example, for Al-doped Si, $D_{Al}^{12RPM} = 3.26 \times 10^{-5}\text{cm}^2/\text{s}$, whereas $D_{Al}^{60RPM} = 1.31 \times 10^{-5}\text{cm}^2/\text{s}$.

Kodera [56] grew doped silicon crystals at 5 to 200 RPM. Unfortunately, erroneous kinematic viscosity, $\nu = 0.0106 \times 10^{-4}\ \text{cm}^2/\text{s}$, was used in the BPS model, whereas the established value is $\nu = 0.0035 \times 10^{-4}\ \text{cm}^2/\text{s}$. Furthermore, a single "RPM-averaged" diffusion coefficient was reported for each dopant. For example, for phosphorus doping, $D_P = (5.1 \pm 1.7) \times 10^{-4}\ \text{cm}^2/\text{s}$.

Kodera's data were revisited, by fitting the BPS model, for each RPM, without averaging [31]. Again, Kodera obtained diffusion coefficients at 5 and 10 RPM that were consistently higher than his values at higher rotation rates. For example, for phosphorus, at 5 RPM, $D_P^{5RPM} = 9.4 \times 10^{-4}\text{cm}^2/\text{s}$, and at 55 RPM, $D_P^{55RPM} = 3.9 \times 10^{-4}\text{cm}^2/\text{s}$. For details, see Figure 3 in reference [31].

In 1968, Shaskov and Gurevich used the capillary-reservoir method for diffusivity measurement and reported drastically different D values [42], see Table 25.2.

Assuming R = 1.5 cm, 12 RPM corresponds to $Re_R = 942$ and $Re_R^2/Gr \sim 0.2$. Thus, one must conclude that natural convection increased the apparent transport rate of impurities and elevated the apparent diffusivity. The data obtained at 5 to 12 RPM should not have been used in Eqn (25.26), where the velocity filed and the solute layer thickness δ are controlled by the crystal rotation rate ω. For $Gr \gg Re_R^2$, δ is controlled by the Grashof and Prandtl numbers (i.e., ΔT, L, β, g, etc.), and not by the Reynolds number (i.e., ω).

Equation (25.52) was applied to Turkovskii and Kodera's segregation data, see [31]. As shown in Figure 25.13, by using just a single value of D, one can fit the $k_{measured}$ at

Table 25.2 Values of Diffusion Coefficients in Molten Silicon Calculated Using Eqn (25.52)

Dopant	Tetrahedral Covalent Radius A	k_o	D (cm^2/s) Shaskov and Gurevich	D (cm^2/s) Eqn (25.52)	References for Data
B	0.88	0.8	3.3×10^{-4}	1.7×10^{-4}	[56]
P	1.1	0.3	2.7×10^{-4}	2.1×10^{-4}	[56,57]
As	1.18	0.35		2.2×10^{-4}	[56,57]
Ga	1.26	0.008	0.66×10^{-4}	1.3×10^{-4}	[56]
Al	1.26	0.002		0.13×10^{-4}	[57]
Sb	1.36	0.023	1.4×10^{-4}	0.7×10^{-4}	[56]
In	1.44	0.0004	0.17×10^{-4}		see [31]

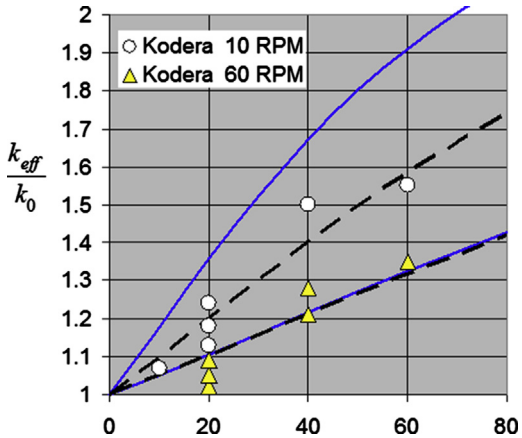

FIGURE 25.13 Symbols are data reproduced from Kodera, for P-doped Si. Dashed lines are Eqn (25.52) for "mixed" convection; one value of D (recorded in Table 25.2) fits data at 10 and 60 RPM. Full lines: natural convection is ignored ($Nu_{NC} = 0$). Full and dashed lines overlap for 60 RPM, where $Re^2 \gg Gr$.

10 RPM and 60 RPM, for $0 < f < 70$ μm/s. To illustrate the significance of natural convection at 10 RPM, these calculations were repeated assuming $Nu_{NC} = 0$ (full lines).

The calculated D values are listed in Table 25.2 along with the capillary-reservoir diffusivity measurements by Shaskov and Gurevich [42].

25.9.2.2 CZ Growth of Large Crystals at Low Rotation Rates

In the commercial production of large-diameter electronic grade Si crystals, the crystal rotation rate is typically less than 15 RPM, which corresponds to a Reynolds number of $Re_R = \omega R^2/\nu \approx 10^5$, assuming crystal diameter $d = 20$ cm.

Melt mass varies from 80 to 200 kg, with the corresponding Grashof numbers, $Gr \sim 10^{10}$, so that $Re_R^2 \sim Gr$. Natural convection is driven by (1) hot, vertical, crucible

walls and (2) the crystal–melt interface, which acts as a "cooled horizontal disk." Both oppose the forced flow driven by the rotating crystal. Furthermore, crucible rotation is also driving forced convection. The resulting "combined-convection" is so complex that numerical three-dimensional modeling provides the only reliable approach to optimize the distribution of impurities in the resulting crystal.

We proceed to reduce the number of parameters by ignoring crucible rotation. Without crucible rotation, we consider combined crystal- and buoyancy-driven convection.

Figure 25.14 illustrates the relative importance of forced and natural convection on k_{eff}. Melt height H was kept constant and equal to the crystal diameter, $d = H = 20$ cm. Natural convection was modeled as a "cooled horizontal disk" using Eqn (25.47) for Nu_{NC}. The cooler crystal–melt interface induces downward buoyancy forces, opposing forced convection, hence a minus sign is used in Eqn (25.52). The characteristic temperature difference is $\Delta T_{\max} = 5\ ^\circ$C. The corresponding Grashof number is $Gr = 5.8 \times 10^8$. Rotation rates of 1, 3, 5, 10, and 30 RPM yield corresponding Re_R^2/Gr parameters of 0.02, 0.19, 0.53, 2.1, and 19.

The Nusselt numbers for forced convection were then calculated using Eqn (25.40) for rotation rates of 1–15 RPM. For 30 RPM, Eqn (25.42) was applied to determine Nu_{FC}.

The dashed line in Figure 25.14 represents Eqn (25.52), plotted for 0 RPM. The full line at 1 RPM overlaps with this dashed line, as forced convection is negligible ($Re_R^2 \approx 0.02Gr$). For 1, 3, and 5 RPM, the flow direction is downward, because $Gr_d > Re_R^2$. At 5 RPM, convection is weakest, and k_{eff} is highest, because the centrifugal rotation forces are nearly balanced by buoyancy.

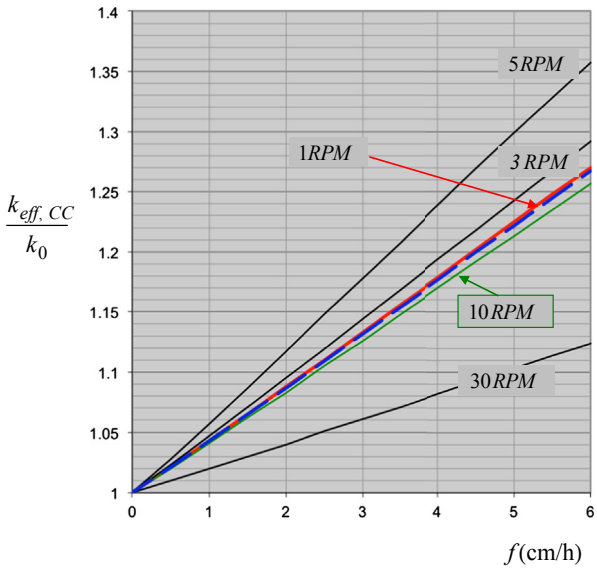

FIGURE 25.14 Segregation controlled by combined convection (CC), forced, natural, and perpendicular. k_{eff} was calculated using Eqn (25.52). Interface acts as horizontal cooled disk. Buoyancy forces act downward "opposing" forced convection, hence "−" sign is used in Eqn (25.52).

At 6 to 7 RPM, the flow changes direction and reverses for 10 and 30 RPM. This flow transition is known to cause abrupt interface shape changes in oxide CZ crystal growth, as the crystal radius and the Reynolds number both increase during the so-called "shouldering" stage early in the process [59]. Carruthers suggested that the transient flow state occurs when $Gr \approx Re^2$, a condition that occurs when buoyancy and rotational forces are equivalent [59].

25.10 Zone Melting

25.10.1 Introduction

The process of ZM for achieving single crystallinity was first reported by E. N. da C. Andrade and R. Roscoe in 1937, in their now-classic paper on single crystal plasticity [19]. In 1952, zone refining was applied for the first time by W.G. Pfann in the purification of germanium to allow the demonstration at Bell Laboratories of transistor switching [13]. A decade later, H.C. Theurer extended Pfann's method to silicon, using a clever adaptation called the "float-zone" (FZ) method, used for ultrapurification and single crystal growth.

Several books have been devoted to the fundamental theory and practice of zone refining, beginning with Pfann's classic monograph on this process and its variants [13], updated in the recent textbook/monograph *Principles of Solidification* by M.E. Glicksman [6], which presents the state of the art, including recent experiments and other contributions that consider the effective distribution coefficient, k_{eff}, as a function of the solute layer thickness, δ [60,61].

Only a relatively short zone of the total charge is melted at any given time in ZM. Typically, zone length, Z, is about 10% of the total ingot length, L, so that $Z \sim \frac{L}{10}$. See Figure 25.15. The purposes of zone refining processes are to: (1) maximize the crystal purity and the amount of material so purified, thus reducing recycle and waste, and (2) minimize the time required to perform the process. One must manage to have $k_{eff} \ll 1$ and also move the molten zones at a reasonably high rate, f.

Zone refining often requires multiple passes, or "stages," using, where possible, multiple molten zones through long charges. The total process may entail weeks to complete. In the interest of reducing process time, one is compelled to employ a relatively brisk zone translation rate, f, although it is well known that increasing the growth rate also elevates the value of k_{eff}. As k_{eff} approaches unity, an individual zone pass becomes less efficient and wastes time and material.

Figure 25.16, reproduced from Pfann [13], uses BPS segregation theory to illustrate the effect of the "normalized" growth rate, $f\delta/D$, on the value of δ. It is evident that two limits exist:

1. $k_{eff} \to k_0$, for $f\delta/D \to 0$, whereas
2. $k_{eff} \to 1$, for $f\delta/D > 5$.

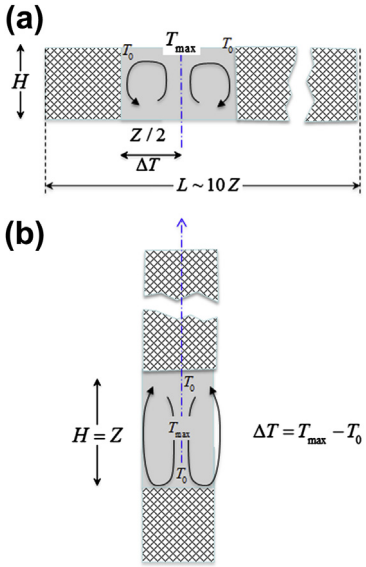

FIGURE 25.15 Characteristic lengths and temperature differences in (a) horizontal and (b) vertical zone melting (ZM).

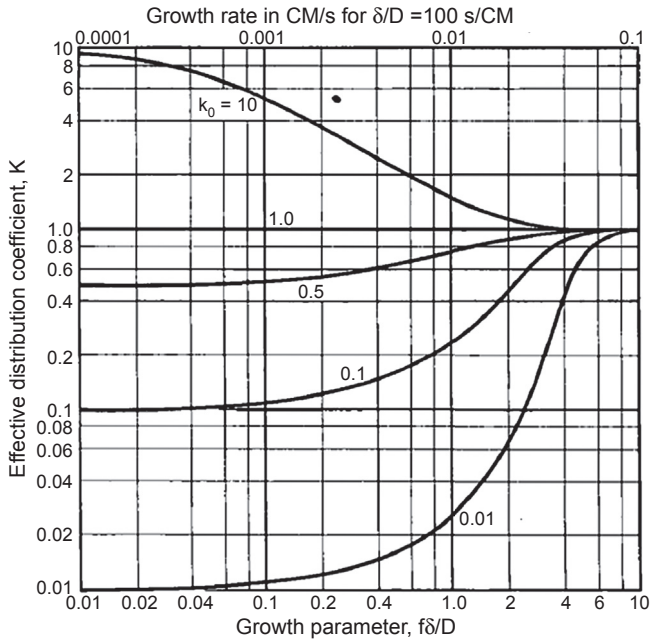

FIGURE 25.16 Dependence of k_{eff} on normalized growth rate $f\delta/D$ for several values of k_0. *From Pfann's book [13]. Note that top abscissa is* f *(cm/s) for* δ/D = *100 (s/cm).*

Thus, one observes that excessive growth rates lead to severely reduced macrosegregation and little net purification. Moreover, if the zone speed is set too high, constitutional supercooling will occur, leading to interface instability and microsegregation, which also results in the formation of undesirable microstructures such as cells and dendrites, where $k_{eff} \approx 1$, and impurities are simply retrapped locally among the last portions of the microstructure to freeze.

A serious drawback to using Figure 25.16 is that the solute boundary layer thickness, δ, is fictitious and, as a result, remains unknown. Crystal growers cannot determine the growth rate, f (cm/hr), needed to attain a desired value for the effective distribution coefficient, k_{eff} in the zone. One notes that the Cochran/Levich Eqn (25.26) is applicable to the case of *rotating* crystals, which may not be appropriate to zone purification. Furthermore, in Eqn (25.26), δ is not a function of growth rate, which is physically incorrect.

Figure 25.17 shows the dependence of k_{eff} on the zone speed, f (cm/hr). The curves were plotted using Eqn (25.49), where k_{eff} is a function of the Nusselt number, which is calculated using Eqn (25.45). Assuming that the value of the equilibrium segregation coefficient, k_0, is known, one may choose both an "appropriate" zone speed, f, and k_{eff}. Again, achieving efficient zone refining requires, (1) maintaining a small k_{eff}, which minimizes the number of passes to attain a desired level of purity, and (2) a relatively high f, to minimize the total transit time for a zone through the total charge. Additional details for implementing zone purification are provided below.

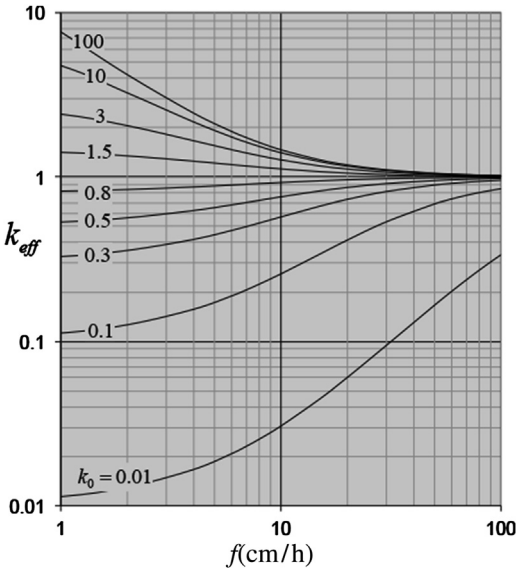

FIGURE 25.17 Dependence of k_{eff} on growth rate f (cm/h), calculated using Eqn (25.49) with Eqn (25.45). For horizontal zone melting (ZM), molten germanium properties ($Pr = 0.01$), $H = 2.5$ cm and $\Delta T = 20$ K $Gr \approx 10^7$

A brief review of macrosegregation theory for single-pass zone refining is given next. The zone speed and the number of passes (stages) are the two most important parameters that a crystal grower needs to determine before attempting zone purification.

25.10.2 Single-Pass ZM, "Perfect" Mixing

If the molten zone is assumed to remain under "perfect" mixing, where $k_{eff} = k_0$, then the concentration of impurities throughout the melt is uniform. This limiting condition can, in fact, be approached, provided that the zone speed is kept extremely low, e.g., $f \ll 1$ cm/hr. See Figure 25.16. This condition, although ideal, is of little practical interest in zone refining. Were such a slow zone speed established, the resulting axial concentration profile takes the exponential form [6,13]:

$$\frac{C_S(x)}{C_L^i} = 1 - (1 - k_0)e^{-k_0 \frac{x}{Z}}, \quad \text{for } 0 \le x \le (L - Z) \tag{25.53}$$

where C_L^i denotes the initial solute concentration in the charge, which is assumed to be uniform. It is advantageous that the zone be kept as short as practicable, however, to achieve both efficient, per pass, purification along with minimal charge loss. For the last zone length to freeze, the mass balance calculation shows that

$$\frac{C_S(x)}{C_L^i} = \left[1 - (1 - k_0)e^{-k_0 \frac{L-Z}{Z}}\right]\left(\frac{1 - x}{Z}\right)^{k_0 - 1} \quad \text{for } (L - Z) \le x \le L$$

As the melt volume is kept as small as possible, compared to that in ordinary directional freezing, one finds that the concentration of rejected impurities in the zone, $C_{zone}(x)$, builds up rapidly. Again, in the limit of perfect mixing, the concentration in the solid will be $C_S(x) = k_0 C_{zone}(x)$. Figure 25.18 shows for $k_0 = 0.1$ and $Z = L/10$, the variation of

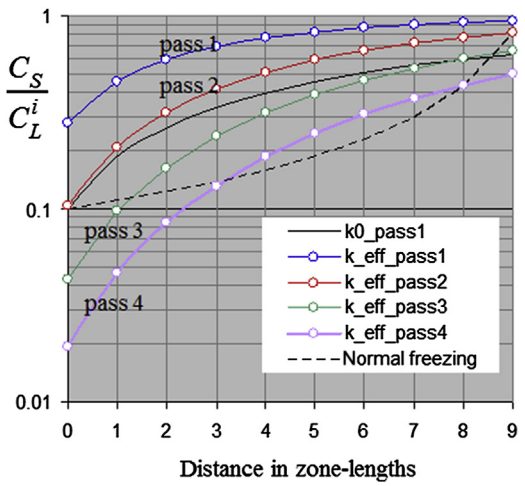

FIGURE 25.18 Relative impurity concentration versus distance, scaled in zone lengths, for multipass zone melting (ZM). Dashed line is normal freezing with $k_0 = 0.1$. Full line is one pass with k_0. Lines with circles are passes one to four with $k_{eff} = 0.28$.

relative impurity concentration, C_S/C_L^i, versus distance in zone lengths. The solid line is the profile expected after a single "slow" passage, as described by Eqn (25.53). The purification obtained from a single zone pass is actually inferior to that obtained from just Gulliver–Scheil segregation, Eqn (25.4) (dashed line). The benefits of zone refining only become evident after applying multiple passes.

25.10.3 Effective Segregation Coefficient in Zone Purification

The effective segregation coefficient is not a function of the fraction solidified because the zone length, Z, and the melt temperature do not change significantly during the process but rather rise slowly ($k_0 < 1$) with increasing purity. The Grashof number and the related Nusselt number characterizing flows in the zone also remain approximately constant throughout a pass, in contrast to what is expected in normal freezing. Figure 25.15 shows the characteristic length and ΔT for two common configurations: (1) horizontal boat, and (2) vertical ampoule.

In the absence of any forced convection, perhaps induced by induction heating or moving magnetic fields, k_{eff} can be calculated using Eqn (25.49). The correlation for Nu_{NC}, may be selected on the basis of the orientation of the crystal–melt interface. For example, in Figure 25.17, this was done using Eqn (25.45), assuming a horizontal boat configuration, a charge with germanium melt properties, a melt height $H = 2.5$ cm, a maximum superheat of $\Delta T = 20$ K, and a diffusivity, $D = 10^{-4}$ cm^2/s. The dimensionless parameters are: $Gr \approx 10^7$, $Pr = 0.01$, $Sc = 13$.

25.10.4 Single-Pass ZM, "Partial" Mixing

The zone speed chosen in practical zone refining is often high, typically exceeding several cm/hr (e.g., $f = 5$ cm/hr). Neglecting the brief initial transient near the beginning of the charge under convection-controlled segregation, one obtains a realistic $C_S(x)$ profile[16] by simply replacing k_0 with k_{eff} in Eqn (25.53),

$$\frac{C_S(x)}{C_L^i} = 1 - (1 - k_{eff})e^{-k_{eff}\frac{x}{Z}}, \quad \text{for } 0 \le x \le (L - Z). \tag{25.54}$$

To keep purification efficient, $1 - k_{eff}$ should stay large, and close to $1 - k_0$. As a rough estimate for k_{eff} one may use

$$1 - k_{eff} = 0.8(1 - k_0). \tag{25.55}$$

According to Figure 25.17, for $f = 1$ cm/hr, the effective segregation coefficient is $k_{eff} \approx k_0 = 0.1$. For $k_0 = 0.1$, Eqn (25.55) "suggests" $k_{eff} = 0.28$, which corresponds to zone speed of $f = 11$ cm/hr (the intersection of the horizontal $k_{eff} = 0.28$ line with the $k_0 = 0.1$ contour at a zone speed of $f = 11$ cm/hr). Thus, 11 passes with $k_{eff} = 0.28$ can be performed in the same time needed to run one pass with $k_{eff} \approx 0.1$ at a speed of 1 cm/h.

[16] In the literature, such profiles are labeled as "partial" mixing [19].

25.10.5 Multipass ZM

Obtaining a profile after the second pass and the subsequent passes becomes difficult, and one must resort to numerical methods, as the solute distribution in the charge is no longer uniform. A manageable expression for calculating multipass zone refining was presented by Milliken, based on a simplification of Lord's expression for the solute distribution [13], namely,

$$\frac{C_n(a)}{C_L^i} = 1 - (1 - k_{eff})[n - \Sigma(n)]e^{-k_{eff}a} \tag{25.56}$$

where the summation for n-passes in Eqn (25.56) is given by

$$\Sigma(n) = \sum_{s=1}^{n-1} (n-s)k_{eff}^{s-1} e^{-sk_{eff}} \frac{(s+a)^{s-2}}{s!}\{a(s-1) + (1 - k_{eff}a)(s+a)\}$$

Here a is the distance expressed in zone lengths, Z [13]. Equation (25.56) was used to plot zone passes one to four in Figure 25.18, using a value of $k_{eff} = 0.28$. It is evident from this calculation that three zone passes performed at a zone speed of $f \approx 11$ cm/h, with $k_{eff} = 0.28$, yield better multipass purification than does a single slower pass at $f \approx 1$ cm/h with a lower $k_{eff} = 0.1$. Furthermore, three passes at a zone speed of $f \approx 11$ cm/h can be performed in about 30% of the time needed for a single pass at 1 cm/h.

25.11 Lateral Segregation

Lateral segregation usually results in the nonuniform distribution of impurities in the y-direction,[17] perpendicular to the growth direction, x. This segregation has several causes including the fact that sections of a wafer cut perpendicular to the x-axis were actually grown at slightly different fractions solidified, f_S. Also, as convection causes some variation in the solute concentration in the melt, near-equilibrium segregation results in an uneven concentration in the solid. Finally, if nonequilibrium effects occur at the interface, say near a facet, the concentration at the interface would be controlled by interface kinetics.

25.11.1 Curved Solid–Liquid Interface

Solid–liquid interfaces are rarely ever macroscopically planar. As a result, a wafer cut perpendicular to the crystal axis contains regions grown at different times, i.e., at slightly different fraction solidified, f_S, so axial segregation, which invariably occurs in crystal growth processes, causes different concentrations in different areas across the wafer, which appear as lateral segregation.

Figure 25.19 illustrates the position of an advancing curved interface at different times. An impurity having $k_0 < 1$ will have a lower concentration at t_1 compared to t_2. The wafer cut along the horizontal plane A–A will have sections crystallized at different

[17]The radial, r-direction, is used for the cylindrical coordinate system.

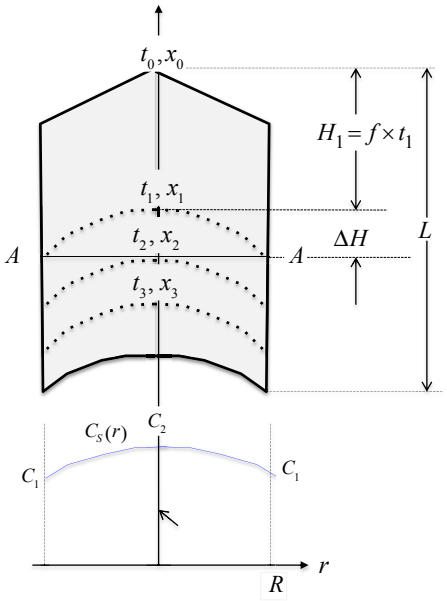

FIGURE 25.19 Lateral segregation caused by curved interface for normal freezing. Schematic and C_s, for an impurity distribution with $k_0 < 1$.

times, with different fractions solidified. Specifically, the periphery grew at t_1,f_{S1}, whereas the center grew at t_2,f_{S2}. Hence, based on Gulliver–Scheil Eqn (25.5), one expects a higher solute concentration at t_2,f_{S2}, as indicated in the U-shaped profile.

Axial segregation can be avoided in principle by attaining strict steady state, diffusion-controlled segregation, and/or by using melt replenishment. In this regard, the submerged heater method has been quite effective, as shown in Figure 25.20.

25.11.2 Convection

Lateral flows along the interface in the y-direction sweep and carry away the impurities rejected at the interface. The analytical solutions discussed below are essential for understanding lateral segregation caused by convection.

(a) Radial segregation in CZ-grown crystals

The von Karman/Cochran/Levich solution [3–5] for laminar flow and concentration field near an infinite rotating disk indicate that, ideally, the solute layer thickness δ and concentration at the liquid phase at interface C_0 should not change in the radial direction. Therefore, there should be no lateral segregation in CZ-grown crystals. Experimental evidence reveals to the contrary that lateral segregation does occur. The possible reasons for this include:

1. Buoyancy-induced natural convection opposes and alters CZ-forced convection.
2. Crucible rotation "disturbs" the Cochran–Levich flow.

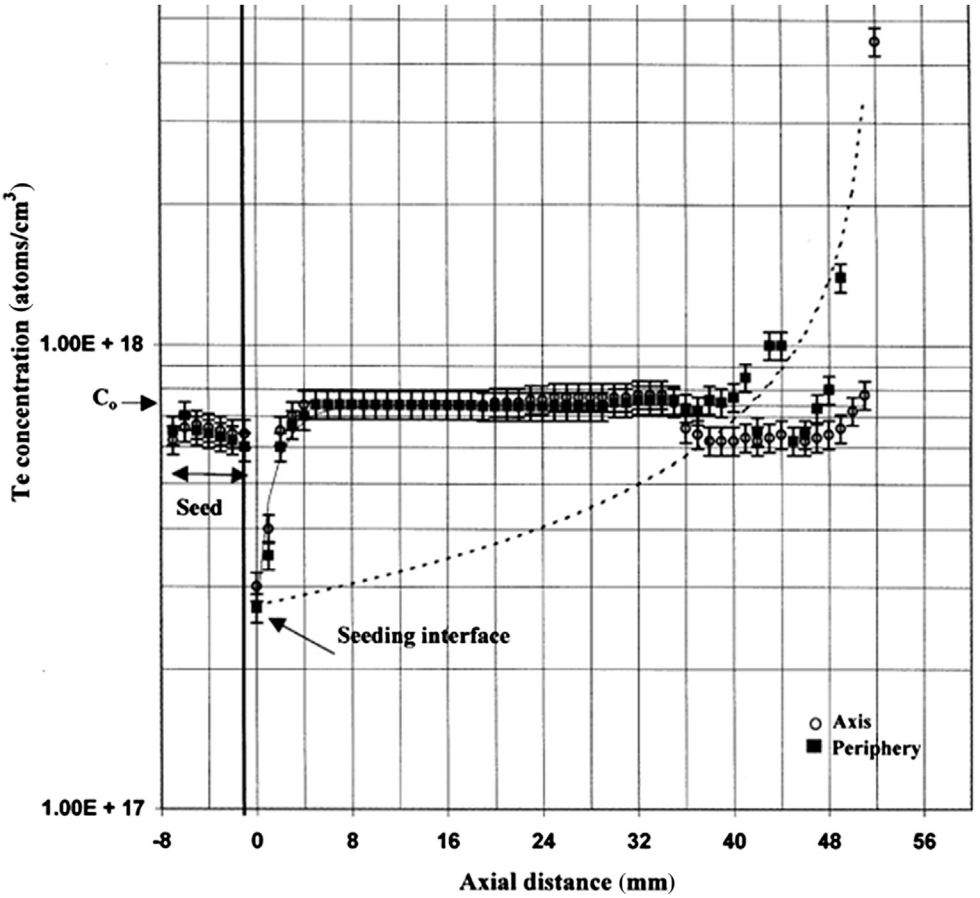

FIGURE 25.20 Te concentration in GaSb crystal, grown using the *SH* method, in multizone Mellen furnace. Open circles represent Te concentration along the axis; the filled squares are obtained along the edge of the crystal. Dashed line is the theoretically calculated profile for complete mixing using. From [62].

3. Crystal and melt are, of course, always finite in extent.
4. The velocity boundary layer thickness in turbulent flow is [63],

$$\delta_v(r) = 0.526\left(\frac{\nu}{\omega}\right)^{\frac{1}{5}} r^{\frac{3}{5}}. \tag{25.57}$$

Using Eqn (25.16), the solute layer thickness increases, leading to lateral segregation,

$$\delta(r) \sim r^{\frac{3}{5}} Sc^{-\frac{1}{3}}$$

(b) Convection along a flat plate and Bridgman growth

The similarity solutions developed by Blasius and Polhausen [9] illustrate how boundary layers and concentration profiles develop with flows directed along a

solid–liquid interface. Their solutions hold for laminar flow providing that the interface remains reasonably flat. For a constant bulk flow velocity, U, along the interface in the y-direction, the similarity solutions show that layer width is given by

$$\delta(y) = 5yRe_y^{-\frac{1}{2}}Sc^{-\frac{1}{3}} = 5D^{\frac{1}{3}}\nu^{\frac{1}{6}}\sqrt{\frac{y}{U}}, \tag{25.58}$$

where $Re_y \equiv Uy/\nu$. The gradient in layer thickness, $\delta(y)$, is therefore

$$\frac{d\delta}{dy} \sim \frac{1}{\sqrt{Uy}} \sim \frac{1}{\sqrt{Re_y}}. \tag{25.59}$$

By using Eqn (25.13), $\delta = \frac{D}{j}(C_0 - C_L)$, one obtains

$$\frac{dC_0}{dy} = \propto \frac{1}{\sqrt{Re_y}}. \tag{25.60}$$

Thus, dC_0/dy, is high at low Re. Equation (25.60) provides the theoretical underpinning for the observations that lateral segregation strengthens at low flow Re and Gr numbers.

The third fundamental similarity solution is given by Ostrach [9,10]. He found that in buoyancy-driven laminar flow along a vertical wall, the boundary layer thickness varies inversely with the fourth root of the Grashof number,

$$\delta(y) \sim \frac{y}{Gr^{1/4}} \tag{25.61}$$

$$\frac{\partial\delta}{\partial y} \propto \frac{1}{Gr_y^{1/4}} \tag{25.62}$$

Equations (25.60) and (25.61) are consistent as $Re_y \sim \sqrt{Gr_y}$. Thus, in natural convection, lateral segregation is weak at high Gr_y numbers,

$$\frac{dC_S}{dy} \propto \frac{1}{Gr_y^{1/4}} \tag{25.63}$$

Similarity solutions are applicable only to laminar boundary layer flow, where $10^3 \leq Gr_y \leq 10^9$. Below $Gr \approx 10^3$, lateral nonuniformity of the solute concentration is reduced by diffusion.

The pioneering modeling papers on segregation in Ga-doped Ge, by Polezhaiev [46] and Brown et al. [47,64], confirm that in HB growth ΔC_{max} occurs at $10^3 \leq Gr_H \leq 10^4$ [46], where the subscript H designates melt height. In the VB configuration, the maximum value for ΔC_{max} occurs for $Ra_L = Gr_L Pr \sim 10^8$ [64]. Adoranto and Brown's Grashof number, $Gr_L \sim 10^6$, appears to be much higher, because it is based on the melt height, L, and *not* on the interface size, d. The aspect ratio was $L/d \approx 6$, giving a Grashof number $Gr_d \sim 10^3$, which is a value in good agreement with the similarity solution. The value of $Gr_d \sim 10^3$ shown in Figure 25.10 corresponds to a low gravity level reduced to a value of about $10^{-4}g_0$.

Figure 25.21 shows the uniform radial segregation obtained by using an oscillating baffle in the VB configuration. Radial uniformity in this case remains exceptionally good because the melt is constantly homogenized by intense mixing.

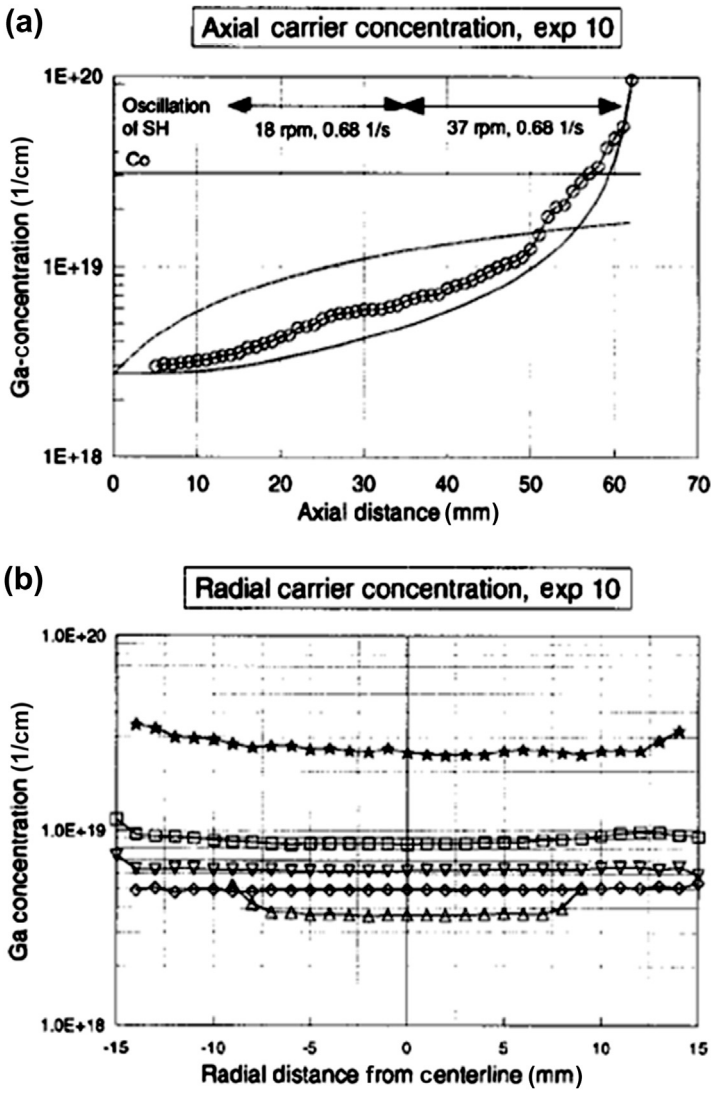

FIGURE 25.21 (a) Axial and (b) radial concentration of Ga in Ge crystal grown using the SH method, in multizone Mellen furnace. (b) Lines with symbols correspond to different axial locations, spaced by 10 mm. The line with stars in last-to-freeze portion ($x = 55$ mm) and SH if out from the melt [25].

25.11.3 Nonequilibrium Segregation

The linear, local equilibrium relation given by Eqn (25.1) would no longer apply when the concentration in the solid at the crystal–melt interface is controlled by (nonequilibrium) interface kinetics. Such nonequilibrium segregation occurs, more prevalently, at faceted interfaces, where stronger interfacial supercooling necessarily develops to allow higher lateral growth rates. In addition, the effective segregation coefficient can also depend on the crystallographic orientation of the interface. This

circumstance becomes evident when the solid–liquid interface is nonplanar, and the crystal grows on and off its facet orientations. For example, in the case of Te-doped InSb, the effective distribution coefficient that equals to the equilibrium one, $k_0 = 0.5$, along its atomically rough interface increases to 4.2 on the facet orientations [65]. The interested reader concerned with such nonequilibrium segregation is encouraged to review the detailed arguments by Rosenberger [19] and the chapter "Dendritic Growth" by Glicksman [6].

Incorporation of ionized (electronically active) impurities in semiconductors, according to reference [65], may also be influenced by the position of the Fermi level (see Vol. IIB, Chapter 27).

25.11.4 Local Nusselt Numbers

Convection is a two-dimensional process where diffusion occurs normal to the interface, while advection carries away the solute laterally. Some analytical solutions and empirical correlations provide the local Nusselt numbers, $Nu(y)$ for plates, and $Nu(r)$[18] for rotating disks. These data can also be used to quantify lateral segregation. For example, Ostrach's local Nusselt number[19] for heat transfer on vertical plates is

$$Nu^{HT}(y) = \left(\frac{Gr_y}{4}\right)^{1/4} \frac{0.75Pr^{1/2}}{(0.609 + 1.221Pr^{1/2} + 1.238Pr)^{1/4}}. \tag{25.64}$$

For mass transfer, substitution of Eqn (25.44) into Eqn (25.64) gives the result,

$$Nu(y) = \frac{hy}{D} = \left(\frac{Gr_y ScLe^{1/3}}{4}\right)^{1/4} \frac{0.75Pr^{1/2}}{(0.609 + 1.221Pr^{1/2} + 1.238Pr)^{1/4}}. \tag{25.65}$$

The average Nusselt number $\overline{Nu_L}$, is defined as the lateral integral average

$$\overline{Nu_L} = \frac{1}{L}\int Nu(y)dy. \tag{25.66}$$

From Eqns (25.65) and (25.66), the average Nusselt number becomes simply

$$\overline{Nu_L} = (4/3)Nu(L) \tag{25.67}$$

25.12 Microsegregation

The length scale of microsegregation and related inhomogeneities range from 1 μm to 1 mm. Generally, microscopic segregation can be classified as either fluctuations in dopant concentration, called striations, or inhomogeneities caused by interface breakdown.

[18] In fluid mechanics and heat transfer, x-direction is parallel to the solid surface, hence $Nu(x)$.
[19] Including LeFevre's interpolation formula for various Pr, see [9].

25.12.1 Doping Striations

The most common microscopic inhomogeneities found in melt-grown semiconductor crystals are fluctuations in the dopant concentration. These fluctuations are revealed by etching techniques and are usually referred to as doping striations. Doping striations result from process fluctuations that are usually caused by one or more of the following factors:

1. unsteady convection causing brief variations in melt temperature;
2. unsteady convection causing fluctuations in dopant concentration in the solute layer;
3. variations in the furnace translation rate or crystal pull rate;
4. temperature fluctuations in the furnace related to the thermal control system;
5. vibrations affecting convection at the interface;
6. crystal rotation in the furnace, which is never perfectly symmetric, causes wobble and rotational striations.

The topics of microsegregation and the formation of microscopic crystalline imperfections are covered in greater detail in chapters by Mueller [65], Rosenberger [19], Glicksman [6], and Rudolph [66].

25.13 Summary

This chapter focuses on solute segregation and component distribution encountered in CZ, DS, and ZM processes.

The influence of melt convection on segregation was first considered in the 1953 BPS theory, where (1) the effective segregation coefficient, k_{eff}, is defined as a function of the solute layer thickness δ, and (2) δ is calculated using the analytical solution by Cochran and Levich, for forced laminar convection near a rotating disk. The complicating, but important, effects of turbulence and buoyancy-induced convection were ignored.[20] Yet, the BPS equation, relating k_{eff} to δ, is possibly the most widely used equation by practical crystal growers.

Considerable attention is given to the recently proposed combined convection (CC) segregation model,[21] where the influence of convection is captured via the Nusselt number, as a "replacement" for δ. In short, (1) the effective segregation coefficient $k_{eff,CC}$ is defined as function of the relevant Nusselt numbers, for forced (Nu_{FC}) and natural (Nu_{NC}) convection, and (2) the Nusselt numbers are calculated using the well-established empirical correlations, developed in laboratory mass transfer experiments, under realistic conditions, including three-dimensional buoyancy-driven flows, turbulence, etc. This phenomenological approach is advantageous, considering the overall complexity and diversity of melt flows during crystal growth.

[20]Unsteady and turbulent ows are not solvable by analytical techniques.
[21]The term combined convection (CC) is used to designate the mixed natural and forced convection.

We emphasize the fact that natural (buoyancy-driven) convection is present in all crystal growth processes. It is unavoidable, unsteady, and difficult to control. In contrast, forced (extrinsically driven) convection is beneficial. Natural convection can be ignored only in CZ experiments, conducted at a sufficiently high rotation rate ω (i.e., for $Re^2 \gg Gr$).

References

[1] Prim RC, Burton JA, Slichter WP. J Chem Phys 1953;21:1987–91.

[2] Prim RC, Burton JA, Slichter WP. J Chem Phys 1953;21:1991–6.

[3] Cochran WG. Proc Camb Phil Soc 1934;30(4):365.

[4] Levich VG. Physicochemical hydrodynamics. Englewood Cliffs (NJ, Berlin): Springer Finance. Prentice-Hall; 1961.

[5] von Karman T. Uber laminare und turbulente reibung. ZAMM 1921;1(4):233–5.

[6] Glicksman ME. Principles of solidification. Springer Verlag; 2011.

[7] Schlichting H. Boundary layer theory. New York: McGraw-Hill; 1968.

[8] Cengel YA, Ghajar AJ. Heat and mass Transfer. McGraw Hill; 2007.

[9] Incropera FP, DeWitt DP. Introduction to heat transfer. New York: Willey; 1990.

[10] Ostrach S. NACA Rep 1953;1111.

[11] Gulliver GH. Metallic alloys: their structure and constitution. London: Charles Griffin and Co.; 1922.

[12] Scheil E. Z Metall 1942;34:70.

[13] Pfann WG. Zone refining. Wiley series on the science and technology of materials. Wiley; 1966.

[14] Tiller WA, Jackson KA, Rutterand JW, Chalmers B. Acta Metall 1953;1:428–37.

[15] Churilov A, Ostrogorsky AG. AIAA J Thermophys Heat Transf 2005;19:542–8.

[16] Smith VG, Tiller WA, Rutter JW. Can J Phys 1955;33:723–45.

[17] Ostrogorsky AG, Marin C, Churilov A, Volz M, Bonner WA, Duffar T. J Cryst Growth 2008;310:364–71.

[18] Ostrogorsky AG, Marin C, Volz M, Duffar T. J Cryst Growth 2009;311:3243–8.

[19] Rosenberger F. Fundamentals of crystal growth, I. Berlin: Springer; 1979.

[20] Ostrogorsky AG, Mueller G. J Cryst Growth 1992;121:587–98.

[21] Yen CT, Tiller WA. J Cryst Growth 1992;118:259–67.

[22] Ostrogorsky AG, Mueller G. J Cryst Growth 1993;128:207–12.

[23] Scheel HJ. J Cryst Growth 1972;13–14:560–5.

[24] Rudolph P. J Cryst Growth 2008;310:1298–306.

[25] Meyer S, Ostrogorsky AG. J Cryst Growth 1997;171:566–76.

[26] Wilson LO. J Cryst Growth 1978;44:247–50.

[27] Brice JC. The growth of crystals from the melt. Amsterdam: North Holland, Publishing Co.; 1965.

[28] Shevchuk IV. Convective heat and mass transfer in rotating disk systems. Springer Verlag; 2009.

[29] Chen YM, Lee WT, Wu SJ. Heat Mass Transf 1998;34:195–201.

[30] Garandet JP, Favier JJ, Camel D. J Cryst Growth 1993;130:113–22.

[31] Ostrogorsky AG. J Cryst Growth 2013;380:43–50.

[32] Camel D, Favier JJ. J Cryst Growth 1984;67:42–56.
[33] Ostrogorsky AG. J Cryst Growth 2012;348:97–105.
[34] Churchill SW, Usagi R. AIChE J 1972;18:1121–8.
[35] Ostrogorsky AG. J Serbian Soc Comput Mech 2012;6:97–107.
[36] Dorfman LA. Hydrodynamic resistance and heat loss of rotating solids. Oliver & Boyd; 1963.
[37] Newman JS. Electrochemical systems. Englewood Cliffs (NJ): Prentice-Hall; 1981.
[38] White F. Viscous fluid flow. McGraw-Hill, Inc.; 1991.
[39] Churchill SW, Chu HS. Int J Heat Mass Transf 1975;18:1323–9.
[40] Lightfoot EN. Chem Eng Sci 1968;23:93.
[41] Masliyah JH, Nguyen T. Int J Heat Mass Transf 1975;18:1443–7.
[42] Shaskov YuM, Gurevich VM. Russ J Phys Chem 1968;24:1082–3.
[43] McDonald JS, Connolly TJ. Nucl Sci Eng 1960;8:369–77.
[44] Ostrogorsky, A.G. J Cryst Growth, submitted.
[45] Globe S, Dropkin D. J Heat Transf 1959;81:24–8.
[46] Nikitin SA, Polezhaev VI, Fedyushkin AI. J Cryst Growth 1981;52:471.
[47] Chang CJ, Brown RA. J Cryst Growth 1983;63:343.
[48] Matthiesen D, Wargo MJ, Motakef S, Carlson DJ, Nakos JS, Witt AF. J Cryst Growth 1987;85:557.
[49] Witt AF, Gatos HC, Lichtensteiger M, Avine MC, Herman CJ. J Electrochem Soc 1975;122:276–83.
[50] Witt AF, Gatos HC, Lichtensteiger M, Herman CJ. J Electrochem Soc 1978;125:1832–40.
[51] Yue JT, Voltmer FW. J Cryst Growth 1975;29:329–41.
[52] Zemskov VS, Shulpina IL, Titkov AN, Belokurova IN, Guseva NB, Safarov VI. Sov Phys Solid State 1979;21:576.
[53] Bourret E, Favier JJ, Bourrel O. J Electrochem Soc 1981;128:2438.
[54] Dutta PS, Ostrogorsky AG. J Cryst Growth 2000;217:360–5.
[55] Fischer B, Friedrich J, Weimann H, Muller G. J Cryst Growth 1999;198/199:170–5.
[56] Kodera H. Jpn J Appl Phys 1963;2:212.
[57] Turkovskii BM. Russ J Phys Chem 1962;36:983–5.
[58] Bridges HE. J Appl Phys 1956;27:746–51.
[59] Carruthers JR. J Cryst Growth 1976;36:212–4.
[60] Ghosh K, Mani VN, Dhar S. J Cryst Growth 2009;312:1521.
[61] Cheung N, Bertazzoli R, Garcia A. J Cryst Growth 2008;310:1274.
[62] Dutta PS, Ostrogorsky AG. J Cryst Growth 1999;197:749–54.
[63] Hartnett JP, Tsai SH, Jantscher HN. J Heat Transf 1965;87:362–8.
[64] Adornato PM, Brown RA. J Cryst Growth 1987;80:155–90.
[65] Mueller G. Convection and inhomogeneities in crystal growth from the melt, vol. 12. Berlin: Springer; 1988.
[66] Rudolph P. Chapter defect formation during the crystal growth from melt. In: Dhanaraj G, Byrappa K, Prasad V, Dudley M, editors. Handbook of crystal growth. Springer Verlag; 2010. p. 153–202.

26 Thermal Stress and Dislocations in Bulk Crystal Growth

Noriyuki Miyazaki[1,2]

[1]KYOTO UNIVERSITY, KYOTO, JAPAN;
[2]KYUSHU UNIVERSITY, FUKUTSU-SHI, FUKUOKA, JAPAN

CHAPTER OUTLINE

26.1 Overview **1050**
26.2 Thermal Stress in Bulk Single Crystals **1050**
26.2.1 Introduction 1050
26.2.2 Methodology for Calculating Thermal Stress 1051
26.2.2.1 Elastic Constant Matrix 1051
26.2.2.2 Thermal Strain Vector 1058
26.2.2.3 Finite Element Formulation 1059
26.2.3 Several Examples of Thermal Stress Analysis 1060
26.2.3.1 Effect of Crystal Anisotropy on Thermal Stress for Cubic Bulk Single Crystals (Si, GaAs, and InP) 1060
26.2.3.2 Thermal Stress Analysis of Lithium Niobate Bulk Single Crystal 1063
26.2.3.3 Thermal Stress Analysis of Lead Molybdate Bulk Single Crystal 1065
26.2.4 Cracking of Bulk Single Crystal Caused by Thermal Stress 1069
26.3 Dislocations in Bulk Single Crystals **1074**
26.3.1 Introduction 1074
26.3.2 Qualitative Estimation of Dislocation Density 1074
26.3.3 Quantitative Estimation of Dislocation Density: Haasen-Alexander-Sumino Model 1075
26.3.3.1 HAS Model for the Uniaxial Stress State 1076
26.3.3.2 HAS Model for a Multiaxial Stress State under Isotropic Assumption 1077
26.3.3.3 HAS Model for a Multiaxial Stress State under Consideration of Crystal Anisotropy 1078
26.3.3.4 Several Applications of the HAS Model to the Quantitative Estimation of Dislocation Density 1079
26.3.4 Modified HAS Models 1083
26.3.4.1 Consideration of Immobilization of Mobile Dislocations and High-Temperature Recovery Mechanisms 1083

Handbook of Crystal Growth. http://dx.doi.org/10.1016/B978-0-444-63303-3.00026-2
Copyright © 2015 Elsevier B.V. All rights reserved.

26.3.4.2 Consideration of Dislocation Annihilation 1084
26.3.4.3 Consideration of Different Types of Dislocations 1085
26.3.4.4 Consideration of the Immobilization of Mobile Dislocations 1086
26.4 Summary **1089**
References **1090**

26.1 Overview

Various single crystals, such as semiconductor single crystals (e.g., Si, GaAs, InP) and oxide single crystals (e.g., $LiNbO_3$, $LiTaO_3$, Al_2O_3) are used as materials for electronic/optical devices. Their bulk single crystals are usually manufactured using melt growth methods, such as the Czochralski (CZ) method, Bridgman (BR) method, and floating zone (FZ) method. Because the melt growth of a bulk single crystal is carried out under severe and complex thermal conditions, large thermal stress is induced in a bulk single crystal during the growth process. Such thermal stress causes the multiplication of dislocations that affect the performance of electronic/optical devices. In the case of oxide single crystals, even cracking may result. Single crystals with cracking cannot be used as materials for devices due to their reduced productivity. Solid mechanics and material strength studies on the melt growth of bulk single crystals are important for understanding and solving problems related to the generation and multiplication of dislocations and the cracking of single crystals.

As for the melt growth of bulk single crystals, attention has been paid to heat transfer problems in a crystal growth furnace, and several review papers have been published to date [1–6] (see also Chapter 20 in Vol. IIB). From the viewpoint of crystal quality, studies of solid mechanics and material strength are important for controlling the dislocation density and cracking of a crystal during the growth process in situ. Only a few review papers [7–9] have been published concerning the solid mechanics and material strength in the manufacturing process of single crystals. In this chapter, we focus on thermally generated stress and associated effects during the melt growth processes of bulk single crystals.

26.2 Thermal Stress in Bulk Single Crystals

26.2.1 Introduction

Dislocations generated during growth process within the growing crystals affect the performance of devices. Sometimes, even macrocracking occurs in single crystals. Dislocations and macrocracking can be caused by thermal stress during crystal growth. Therefore, the first step for the estimation of dislocation density and cracking of a crystal is to calculate the thermal stress in the crystal.

Crystal anisotropy should be considered in the thermal stress analysis of single crystals. Because single crystals have crystal anisotropy in elastic constants and thermal

expansion coefficients, three-dimensional analysis is required in thermal stress analysis, even though a crystal shape is axisymmetric. Single crystals were assumed to be isotropic in all thermal stress analyses performed through the late 1980s [10–13]. Then, Lambropoulos [14,15] and Miyazaki et al. [16–18] performed their pioneering three-dimensional finite element analyses including crystal anisotropy. Without consideration of crystal anisotropy, one cannot obtain the effect of the crystal growth direction on thermal stress within the crystal.

In thermal stress analysis, the elastic constant matrices and thermal strain/thermal expansion coefficient vectors are needed for the respective crystal systems. They are provided in Nye's textbook [19]. These elastic constant matrices and a thermal strain/thermal expansion coefficient vectors for each crystal system are given in the crystallographic coordinate system, a Cartesian coordinate system based on the unit cell of the single crystal. The values for an analysis coordinate system, a Cartesian coordinate system in the analysis space, can be obtained by using tensor transformation.

Only the cubic crystals, such as Si, GaAs, and InP, were dealt with Lambropoulos' works [14,15] and the earlier works by Miyazaki et al. [16–18]. Later, Miyazaki et al. developed three-dimensional finite element codes for trigonal single crystals [20] and monoclinic single crystals [21]. In addition to these three kinds of single crystals, they have also developed three-dimensional finite element codes for tetragonal single crystals [22] and orthorhombic single crystals [23]. Most important single crystals for electronic/optical devices are included in these five kinds.

In this section, the method for three-dimensional finite element thermal stress analysis, including crystal anisotropy, is presented for various kinds of single crystals. Several numerical examples of thermal stress analyses are given to discuss the relationship between crystal quality and thermal stress, depending on the crystal growth directions. Quantitative evaluations of the critical stress for crystal cracking are also shown here based on the thermal stress analysis of experimental data on crystal cracking induced by thermal stress.

26.2.2 Methodology for Calculating Thermal Stress

In the thermal stress analysis of a single crystal, we should consider crystal anisotropy in the elastic constants and thermal expansion coefficients. We can obtain those for arbitrary crystal growth directions using the tensor transformation technique. The details are shown here.

26.2.2.1 Elastic Constant Matrix

The stress–strain relation of single crystals is given as

$$\sigma_{ij} = C_{ijkl}\varepsilon^e_{kl} \tag{26.1}$$

where σ_{ij} and ε^e_{kl} are the stress tensor and elastic strain tensor, respectively, and C_{ijkl} denotes the elastic constant tensor. According to Nye [19], the vector components of

stress σ_i and elastic strain ε_i are related to their correspondent tensor components σ_{ij} and ε_{ij} as follows:

$$\begin{bmatrix} \sigma_{11} & \sigma_{12} & \sigma_{13} \\ \sigma_{21} & \sigma_{22} & \sigma_{23} \\ \sigma_{31} & \sigma_{32} & \sigma_{33} \end{bmatrix} \Rightarrow \begin{bmatrix} \sigma_1 & \sigma_6 & \sigma_5 \\ \sigma_6 & \sigma_2 & \sigma_4 \\ \sigma_5 & \sigma_4 & \sigma_3 \end{bmatrix}, \begin{bmatrix} \varepsilon_{11} & \varepsilon_{12} & \varepsilon_{13} \\ \varepsilon_{21} & \varepsilon_{22} & \varepsilon_{23} \\ \varepsilon_{31} & \varepsilon_{32} & \varepsilon_{33} \end{bmatrix} \Rightarrow \begin{bmatrix} \varepsilon_1 & \varepsilon_6/2 & \varepsilon_5/2 \\ \varepsilon_6/2 & \varepsilon_2 & \varepsilon_4/2 \\ \varepsilon_5/2 & \varepsilon_4/2 & \varepsilon_3 \end{bmatrix} \tag{26.2}$$

Then, the stress–strain relation is given by the matrix notation as follows:

$$\sigma_i = C_{ij}\varepsilon_j^e \tag{26.3}$$

where C_{ij} is the component of the elastic constant matrix. The details of the elastic constant tensor or elastic constant matrix are shown hereafter.

26.2.2.1.1 CUBIC SINGLE CRYSTAL

Let us consider the Cartesian coordinates X_1, X_2, and X_3 that coincide with the crystallographic axes, as shown in Figure 26.1. In case of cubic single crystals such as Si, GaAs, and InP, there exist three elastic constants: C_{11}, C_{12}, and C_{44}. The elastic constant matrix is given by [19]

$$[C_{ij}] = \begin{bmatrix} C_{11} & C_{12} & C_{12} & 0 & 0 & 0 \\ & C_{11} & C_{12} & 0 & 0 & 0 \\ & & C_{11} & 0 & 0 & 0 \\ & & & C_{44} & 0 & 0 \\ & \text{Sym.} & & & C_{44} & 0 \\ & & & & & C_{44} \end{bmatrix} \tag{26.4}$$

Now, let us consider a right-handed Cartesian coordinate system $X_1' - X_2' - X_3'$ (shown in Figure 26.2), where the X_3'-axis coincides with the growth direction of a single crystal, and the X_1'-axis is in the $X_1 - X_2$ plane and normal to the X_3'-axis. Hereafter, we call $X_1' - X_2' - X_3'$ the *analysis coordinate system*. By the standard tensor transformation,

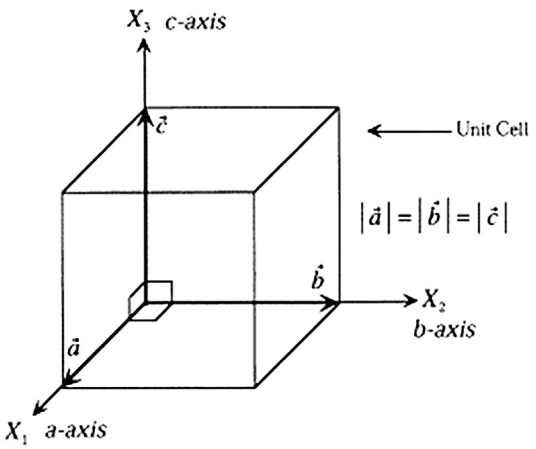

FIGURE 26.1 Coordinate system for cubic crystals. *From Ref. [22] with permission of Elsevier Science.*

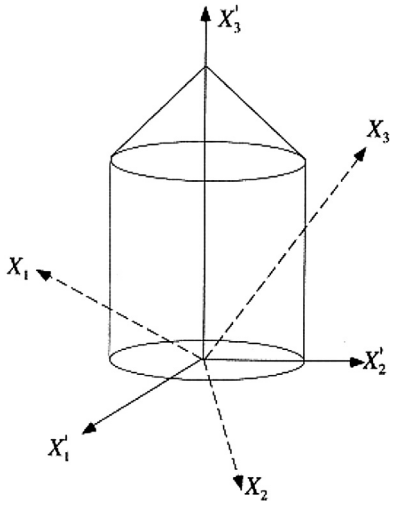

FIGURE 26.2 Analysis coordinate system. *From Ref. [22] with permission of Elsevier Science.*

the elastic constant tensor C'_{ijkl} associated with the $X'_1 - X'_2 - X'_3$ system is related to C_{ijkl} of the $X_1 - X_2 - X_3$ system as follows:

$$\begin{aligned} C'_{ijkl} &= a_{im}a_{jn}a_{ko}a_{lp}C_{mnop} \\ &= C_{11}\left(a_{i1}a_{j1}a_{k1}a_{l1} + a_{i2}a_{j2}a_{k2}a_{l2} + a_{i3}a_{j3}a_{k3}a_{l3}\right) + C_{12}\left\{\left(a_{i1}a_{j1}a_{k2}a_{l2} + a_{i2}a_{j2}a_{k1}a_{l1}\right)\right. \\ &\quad \left. + \left(a_{i1}a_{j1}a_{k3}a_{l3} + a_{i3}a_{j3}a_{k1}a_{l1}\right) + \left(a_{i2}a_{j2}a_{k3}a_{l3} + a_{i3}a_{j3}a_{k2}a_{l2}\right)\right\} \\ &\quad + C_{44}\left\{\left(a_{i2}a_{j3}a_{k2}a_{l3} + a_{i2}a_{j3}a_{k3}a_{l2} + a_{i3}a_{j2}a_{k2}a_{l3} + a_{i3}a_{j2}a_{k3}a_{l2}\right)\right. \\ &\quad + \left(a_{i1}a_{j3}a_{k1}a_{l3} + a_{i1}a_{j3}a_{k3}a_{l1} + a_{i3}a_{j1}a_{k1}a_{l3} + a_{i3}a_{j1}a_{k3}a_{l1}\right) \\ &\quad \left. + \left(a_{i1}a_{j2}a_{k1}a_{l2} + a_{i1}a_{j2}a_{k2}a_{l1} + a_{i2}a_{j1}a_{k1}a_{l2} + a_{i2}a_{j1}a_{k2}a_{l1}\right)\right\} \end{aligned} \tag{26.5}$$

where a_{ij} is the direction cosine of the X'_i-axis and X_j-axis.

We can use the relationship between the indices of tensor and those of matrix shown in Table 26.1 to change the tensor component C_{ijkl} or C'_{ijkl} into the matrix component C_{ij} or C'_{ij}. Finally, the stress–strain relation in the $X'_1 - X'_2 - X'_3$ system can be written as follows:

$$\sigma'_i = C'_{ij}\left(\varepsilon^e_j\right)' \tag{26.6}$$

Table 26.1 Relationship between Tensor Indices and Matrix Indices

Tensor	11	22	33	23, 32	31, 13	12, 21
Matrix	1	2	3	4	5	6

26.2.2.1.2 TRIGONAL SINGLE CRYSTAL

Lithium niobate (LN, $LiNbO_3$) and lithium tantalate (LT, $LiTaO_3$) single crystals with a trigonal class $3m$ lattice have threefold symmetry around the c-axis, as shown in Figure 26.3. When a right-handed Cartesian coordinate system $X_1 - X_2 - X_3$ is taken in such a way that the X_1- and X_3-axes coincide with the crystallographic a- and c-axes, respectively, as shown in Figure 26.3, the elastic constant matrix is written as follows, using six independent constants [19]:

$$[C_{ij}] = \begin{bmatrix} C_{11} & C_{12} & C_{13} & C_{14} & 0 & 0 \\ & C_{11} & C_{13} & -C_{14} & 0 & 0 \\ & & C_{33} & 0 & 0 & 0 \\ & & & C_{44} & 0 & 0 \\ & \text{Sym.} & & & C_{44} & C_{14} \\ & & & & & C_{66} \end{bmatrix} \tag{26.7}$$

$$C_{66} = \frac{1}{2}(C_{11} - C_{12})$$

If we consider the analysis coordinate system $X_1 - X_2 - X_3$ as shown in Figure 26.2, the elastic constant tensor C'_{ijkl} associated with the $X'_1 - X'_2 - X'_3$ system is related to C_{ijkl} of the $X_1 - X_2 - X_3$ system as follows:

$$\begin{aligned} C'_{ijkl} &= a_{im}a_{jn}a_{ko}a_{lp}C_{mnop} \\ &= C_{11}\{a_{i1}a_{j1}a_{k1}a_{l1} + a_{i2}a_{j2}a_{k2}a_{l2} + (a_{i1}a_{j2} + a_{i2}a_{j1})(a_{k1}a_{l2} + a_{k2}a_{l1})/2\} \\ &\quad + C_{12}\{a_{i1}a_{j1}a_{k2}a_{l2} + a_{i2}a_{j2}a_{k1}a_{l1} - (a_{i1}a_{j2} + a_{i2}a_{j1})(a_{k1}a_{l2} + a_{k2}a_{l1})/2\} \\ &\quad + C_{13}\{(a_{i1}a_{j1} + a_{i2}a_{j2})a_{k3}a_{l3} + a_{i3}a_{j3}(a_{k1}a_{l1} + a_{k2}a_{l2})\} \\ &\quad + C_{14}\{(a_{i1}a_{j1} - a_{i2}a_{j2})(a_{k2}a_{l3} + a_{k3}a_{l2}) + (a_{i2}a_{j3} + a_{i3}a_{j2})(a_{k1}a_{l1} - a_{k2}a_{l2}) \\ &\quad + (a_{i1}a_{j3} + a_{i3}a_{j1})(a_{k1}a_{l2} + a_{k2}a_{l1}) + (a_{i1}a_{j2} + a_{i2}a_{j1})(a_{k1}a_{l3} + a_{k3}a_{l1})\} \\ &\quad + C_{33}a_{i3}a_{j3}a_{k3}a_{l3} \\ &\quad + C_{44}\{(a_{i2}a_{j3} + a_{i3}a_{j2})(a_{k2}a_{l3} + a_{k3}a_{l2}) + (a_{i1}a_{j3} + a_{i3}a_{j1})\ (a_{k1}a_{l3} + a_{k3}a_{l1})\} \end{aligned} \tag{26.8}$$

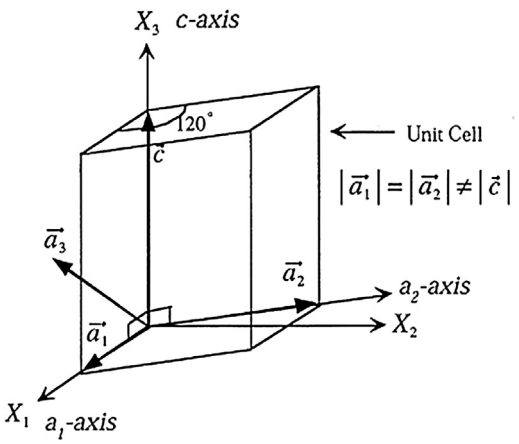

FIGURE 26.3 Coordinate system for a trigonal crystal. *From Ref. [22] with permission of Elsevier Science.*

26.2.2.1.3 MONOCLINIC SINGLE CRYSTAL

A gadolinium orthosilicate (GSO, Gd_2SiO_5) single crystal with a monoclinic lattice has a crystallographic a-axis inclining from the b–c plane ($\alpha = 17.5^\circ$ for the GSO single crystal), as shown in Figure 26.4. When a right-handed Cartesian coordinate system $X_1 - X_2 - X_3$ is taken in such a way that the X_2- and X_3-axes coincide with the crystallographic b- and c-axes, respectively, as shown in Figure 26.4, the elastic constant matrix is written as follows, using 13 independent constants [19]:

$$[C_{ij}] = \begin{bmatrix} C_{11} & C_{12} & C_{13} & 0 & C_{15} & 0 \\ & C_{22} & C_{23} & 0 & C_{25} & 0 \\ & & C_{33} & 0 & C_{35} & 0 \\ & & & C_{44} & 0 & C_{46} \\ & \text{Sym.} & & & C_{55} & 0 \\ & & & & & C_{66} \end{bmatrix} \tag{26.9}$$

If we consider the analysis coordinate system $X_1' - X_2' - X_3'$ as shown in Figure 26.2, the elastic constant tensor C'_{ijkl} associated with the $X_1' - X_2' - X_3'$ system is related to C_{ijkl} of the $X_1 - X_2 - X_3$ system as follows:

$$\begin{aligned} C'_{ijkl} &= a_{im}a_{jn}a_{ko}a_{lp}C_{mnop} \\ &= C_{11}a_{i1}a_{j1}a_{k1}a_{l1} + C_{12}\left(a_{i1}a_{j1}a_{k2}a_{l2} + a_{i2}a_{j2}a_{k1}a_{l1}\right) + C_{13}\left(a_{i1}a_{j1}a_{k3}a_{l3} + a_{i3}a_{j3}a_{k1}a_{l1}\right) \\ &\quad + C_{15}\left\{a_{i1}a_{j1}\left(a_{k1}a_{l3} + a_{k3}a_{l1}\right) + \left(a_{i1}a_{j3} + a_{i3}a_{j1}\right)a_{k1}a_{l1}\right\} + C_{22}a_{i2}a_{j2}a_{k2}a_{l2} \\ &\quad + C_{23}\left(a_{i2}a_{j2}a_{k3}a_{l3} + a_{i3}a_{j3}a_{k2}a_{l2}\right) + C_{25}\left\{a_{i2}a_{j2}\left(a_{k1}a_{l3} + a_{k3}a_{l1}\right) + \left(a_{i1}a_{j3} + a_{i3}a_{j1}\right)a_{k2}a_{l2}\right\} \\ &\quad + C_{33}a_{i3}a_{j3}a_{k3}a_{l3} + C_{35}\left\{a_{i3}a_{j3}\left(a_{k1}a_{l3} + a_{k3}a_{l1}\right) + \left(a_{i1}a_{j3} + a_{i3}a_{j1}\right)a_{k3}a_{l3}\right\} \\ &\quad + C_{44}\left(a_{i2}a_{j3} + a_{i3}a_{j2}\right)\left(a_{k2}a_{l3} + a_{k3}a_{l2}\right) + C_{46}\left\{\left(a_{i1}a_{j2} + a_{i2}a_{j1}\right)\left(a_{k2}a_{l3} + a_{k3}a_{l2}\right)\right. \\ &\quad \left. + \left(a_{i2}a_{j3} + a_{i3}a_{j2}\right)\left(a_{k1}a_{l2} + a_{k2}a_{l1}\right)\right\} + C_{55}\left(a_{i1}a_{j3} + a_{i3}a_{j1}\right)\left(a_{k1}a_{l3} + a_{k3}a_{l1}\right) \\ &\quad + C_{66}\left(a_{i1}a_{j2} + a_{i2}a_{j1}\right)\left(a_{k1}a_{l2} + a_{k2}a_{l1}\right) \end{aligned} \tag{26.10}$$

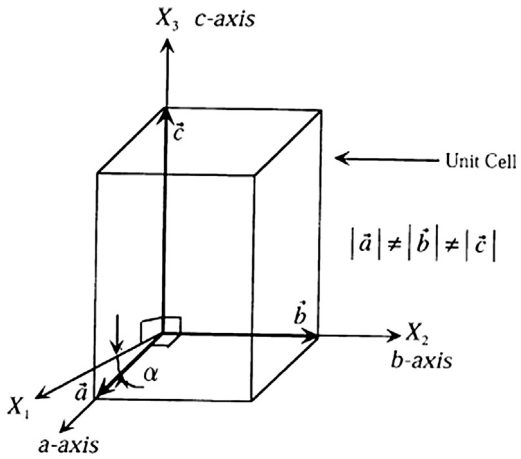

FIGURE 26.4 Coordinate system for a monoclinic crystal. *From Ref. [22] with permission of Elsevier Science.*

26.2.2.1.4 TETRAGONAL SINGLE CRYSTAL

In the case of tetragonal single crystals such as lead molybdate (PMO, $PbMoO_4$), the Cartesian coordinates X_1, X_2, and X_3 are taken in such a way that they coincide with the crystallographic *a*-, *b*-, and *c*-axes, respectively, as shown in Figure 26.5. Then, the elastic constant matrix in the $X_1 - X_2 - X_3$ coordinate system is given as follows, using seven independent elastic constants [19]:

$$[C_{ij}] = \begin{bmatrix} C_{11} & C_{12} & C_{13} & 0 & 0 & C_{16} \\ & C_{11} & C_{13} & 0 & 0 & -C_{16} \\ & & C_{33} & 0 & 0 & 0 \\ & & & C_{44} & 0 & 0 \\ & \text{Sym.} & & & C_{44} & 0 \\ & & & & & C_{66} \end{bmatrix} \tag{26.11}$$

If we consider the analysis coordinate system $X_1' - X_2' - X_3'$ as shown in Figure 26.2, the elastic constant tensor C'_{ijkl} associated with the $X_1' - X_2' - X_3'$ system is related to C_{ijkl} of the $X_1 - X_2 - X_3$ system as follows:

$$\begin{aligned} C'_{ijkl} &= a_{im}a_{jn}a_{ko}a_{lp}C_{mnop} \\ &= C_{11}(a_{i1}a_{j1}a_{k1}a_{l1} + a_{i2}a_{j2}a_{k2}a_{l2}) + C_{12}(a_{i1}a_{j1}a_{k2}a_{l2} + a_{i2}a_{j2}a_{k1}a_{l1}) \\ &\quad + C_{13}\{(a_{i1}a_{j1} + a_{i2}a_{j2})a_{k3}a_{l3} + a_{i3}a_{j3}(a_{k1}a_{l1} + a_{k2}a_{l2})\} \\ &\quad + C_{16}\{(a_{i1}a_{j1} - a_{i2}a_{j2})(a_{k1}a_{l2} + a_{k2}a_{l1}) + (a_{i1}a_{j2} + a_{i2}a_{j1})(a_{k1}a_{l1} - a_{k2}a_{l2})\} \\ &\quad + C_{33}a_{i3}a_{j3}a_{k3}a_{l3} + C_{44}\{(a_{i1}a_{j3} + a_{i3}a_{j1})(a_{k1}a_{l3} + a_{k3}a_{l1}) + (a_{i2}a_{j3} + a_{i3}a_{j2})(a_{k2}a_{l3} + a_{k3}a_{l2})\} \\ &\quad + C_{66}(a_{i1}a_{j2} + a_{i2}a_{j1})(a_{k1}a_{l2} + a_{k2}a_{l1}) \end{aligned} \tag{26.12}$$

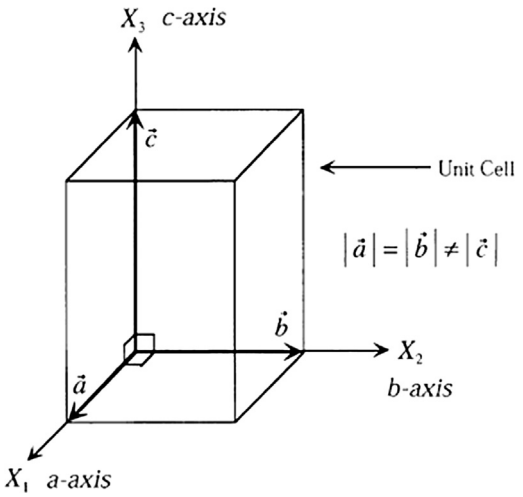

FIGURE 26.5 Coordinate system for a tetragonal crystal. *From Ref. [22] with permission of Elsevier Science.*

26.2.2.1.5 ORTHORHOMBIC SINGLE CRYSTAL

In the case of orthorhombic single crystals, such as alexandrite (Cr-doped BAO, $BeAl_2O_4$: Cr), the Cartesian coordinates X_1, X_2, and X_3 are taken in such a way that they coincide with the crystallographic *a*-, *b*-, and *c*-axis, respectively, as shown in Figure 26.6. Then, the elastic constant matrix in the $X_1 - X_2 - X_3$ coordinate system is given as follows, using nine independent elastic constants [19]:

$$[C_{ij}] = \begin{bmatrix} C_{11} & C_{12} & C_{13} & 0 & 0 & 0 \\ & C_{22} & C_{23} & 0 & 0 & 0 \\ & & C_{33} & 0 & 0 & 0 \\ & & & C_{44} & 0 & 0 \\ & \text{Sym.} & & & C_{55} & 0 \\ & & & & & C_{66} \end{bmatrix} \tag{26.13}$$

If we consider the analysis coordinate system $X_1' - X_2' - X_3'$ as shown in Figure 26.2, the elastic constant tensor C'_{ijkl} associated with the $X_1' - X_2' - X_3'$ system is related to C_{ijkl} of the $X_1 - X_2 - X_3$ system as follows:

$$\begin{aligned} C'_{ijkl} &= a_{im}a_{jn}a_{ko}a_{lp}C_{mnop} \\ &= C_{11}a_{i1}a_{j1}a_{k1}a_{l1} + C_{12}\left(a_{i1}a_{j1}a_{k2}a_{l2} + a_{i2}a_{j2}a_{k1}a_{l1}\right) + C_{13}\left(a_{i1}a_{j1}a_{k3}a_{l3} + a_{i3}a_{j3}a_{k1}a_{l1}\right) \\ &\quad + C_{22}a_{i2}a_{j2}a_{k2}a_{l2} + C_{23}\left(a_{i2}a_{j2}a_{k3}a_{l3} + a_{i3}a_{j3}a_{k2}a_{l2}\right) + C_{33}a_{i3}a_{j3}a_{k3}a_{l3} \\ &\quad + C_{44}\left(a_{i2}a_{j3} + a_{i3}a_{j2}\right)\left(a_{k2}a_{l3} + a_{k3}a_{l2}\right) + C_{55}\left(a_{i1}a_{j3} + a_{i3}a_{j1}\right)\left(a_{k1}a_{l3} + a_{k3}a_{l1}\right) \\ &\quad + C_{66}\left(a_{i1}a_{j2} + a_{i2}a_{j1}\right)\left(a_{k1}a_{l2} + a_{k2}a_{l1}\right) \end{aligned} \tag{26.14}$$

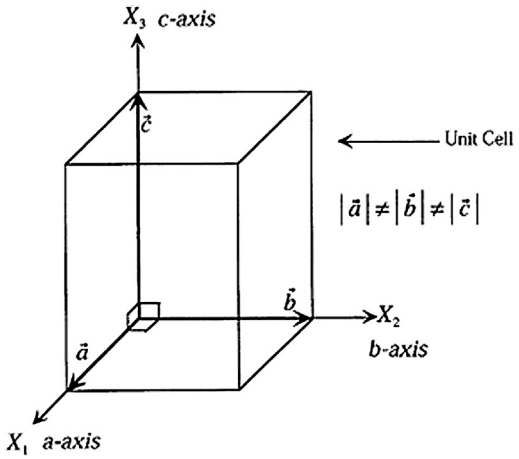

FIGURE 26.6 Coordinate system for an orthorhombic crystal. *From Ref. [22] with permission of Elsevier Science.*

26.2.2.2 Thermal Strain Vector

The thermal strain tensor ε_{ij}^{t} is given as follows:

$$\varepsilon_{ij}^{t} = \int \alpha_{ij} dT \tag{26.15}$$

where α_{ij} is the thermal expansion coefficient tensor and T denotes temperature.

26.2.2.2.1 CUBIC SINGLE CRYSTAL

For a cubic single crystal, Eqn (26.15) in the $X_1 - X_2 - X_3$ system shown in Figure 26.1 can be written by only one thermal expansion coefficient α_1 as follows [19]:

$$\begin{Bmatrix} \varepsilon_1^t \\ \varepsilon_2^t \\ \varepsilon_3^t \\ \varepsilon_4^t \\ \varepsilon_5^t \\ \varepsilon_6^t \end{Bmatrix} = \begin{Bmatrix} \int \alpha_{11}\, \mathrm{d}T \\ \int \alpha_{22}\, \mathrm{d}T \\ \int \alpha_{33}\, \mathrm{d}T \\ 2\int \alpha_{23}\, \mathrm{d}T \\ 2\int \alpha_{31}\, \mathrm{d}T \\ 2\int \alpha_{12}\, \mathrm{d}T \end{Bmatrix} = \begin{Bmatrix} \int \alpha_1\, \mathrm{d}T \\ \int \alpha_1\, \mathrm{d}T \\ \int \alpha_1\, \mathrm{d}T \\ 0 \\ 0 \\ 0 \end{Bmatrix} \tag{26.16}$$

where ε_i^t and α_i are the components of the thermal strain vector and those of the thermal expansion coefficient vector, respectively. Using the standard tensor transformation, we obtain the thermal expansion coefficient tensor α'_{ij} in the analysis coordinate system $X'_1 - X'_2 - X'_3$ shown in Figure 26.2 as follows:

$$\alpha'_{ij} = a_{ik}a_{jl}\alpha_{kl} = \alpha_{11}\left(a_{i1}a_{j1} + a_{i2}a_{j2} + a_{i3}a_{j3}\right) = \alpha_1\left(a_{i1}a_{j1} + a_{i2}a_{j2} + a_{i3}a_{j3}\right) \tag{26.17}$$

We can use the relationship between the indices of tensor and those of matrix shown in Table 26.1 to change the tensor components α_{ij} or α'_{ij} into the vector components α_i or α'_i. Finally, we obtain a matrix form of thermal strain in the $X'_1 - X'_2 - X'_3$ system shown in Figure 26.2 from the following relation:

$$\left(\varepsilon_{ij}^{t}\right)' = \int \alpha'_{ij} dT \tag{26.18}$$

26.2.2.2.2 TRIGONAL SINGLE CRYSTAL

For a trigonal single crystal, Eqns (26.15) or (26.16) in the $X_1 - X_2 - X_3$ system shown in Figure 26.3 can be written with two independent thermal expansion coefficients α_1 and α_3 [19] by substituting α_{ij} with

$$\alpha_{11} = \alpha_{22} = \alpha_1, \quad \alpha_{33} = \alpha_3, \quad \alpha_{23} = \alpha_{32} = 0, \quad \alpha_{31} = \alpha_{13} = 0, \quad \alpha_{12} = \alpha_{21} = 0 \tag{26.19}$$

Then, we obtain the thermal expansion coefficient tensor in the analysis coordinate system $X'_1 - X'_2 - X'_3$ shown in Figure 26.2 as follows:

$$\alpha'_{ij} = a_{ik}a_{jl}\alpha_{kl} = \alpha_{11}\left(a_{i1}a_{j1} + a_{i2}a_{j2}\right) + \alpha_{33}a_{i3}a_{j3} = \alpha_1\left(a_{i1}a_{j1} + a_{i2}a_{j2}\right) + \alpha_3 a_{i3}a_{j3} \tag{26.20}$$

26.2.2.2.3 MONOCLINIC SINGLE CRYSTAL

For a monoclinic single crystal, Eqns (26.15) or (26.16) in the $X_1 - X_2 - X_3$ system shown in Figure 26.4 can be written with four independent thermal expansion coefficients α_1, α_2, α_3 and α_5 [19] by substituting α_{ij} with

$$\alpha_{11} = \alpha_1, \;\; \alpha_{22} = \alpha_2, \;\; \alpha_{33} = \alpha_3, \;\; \alpha_{23} = \alpha_{32} = 0, \;\; \alpha_{31} = \alpha_{13} = \alpha_5, \;\; \alpha_{12} = \alpha_{21} = 0 \tag{26.21}$$

Then, we obtain the thermal expansion coefficient tensor in the analysis coordinate system $X_1' - X_2' - X_3'$ shown in Figure 26.2 as follows:

$$\begin{aligned} \alpha_{ij}' &= a_{ik}a_{jl}\alpha_{kl} = \alpha_{11}a_{i1}a_{j1} + \alpha_{22}a_{i2}a_{j2} + \alpha_{33}a_{i3}a_{j3} + \alpha_{31}a_{i3}a_{j1} + \alpha_{13}a_{i1}a_{j3} \\ &= \alpha_1 a_{i1}a_{j1} + \alpha_2 a_{i2}a_{j2} + \alpha_3 a_{i3}a_{j3} + \alpha_5\left(a_{i3}a_j + a_{i1}a_{j3}\right) \end{aligned} \tag{26.22}$$

26.2.2.2.4 TETRAGONAL SINGLE CRYSTAL

For a tetragonal single crystal, Eqns (26.15) or (26.16) in the $X_1 - X_2 - X_3$ system shown in Figure 26.5 can be written with two independent thermal expansion coefficients α_1 and α_3 [19] by substituting α_{ij} with

$$\alpha_{11} = \alpha_{22} = \alpha_1, \;\; \alpha_{33} = \alpha_3, \;\; \alpha_{23} = \alpha_{32} = 0, \;\; \alpha_{31} = \alpha_{13} = 0, \;\; \alpha_{12} = \alpha_{21} = 0 \tag{26.23}$$

Then, we obtain the thermal expansion coefficient tensor in the analysis coordinate system $X_1' - X_2' - X_3'$ shown in Figure 26.2 as follows:

$$\alpha_{ij}' = a_{ik}a_{jl}\alpha_{kl} = \alpha_{11}\left(a_{i1}a_{j1} + a_{i2}\alpha_{j2}\right) + \alpha_{33}a_{i3}a_{j3} = \alpha_1\left(a_{i1}a_{j1} + a_{i2}a_{j2}\right) + \alpha_3 a_{i3}a_{j3} \tag{26.24}$$

26.2.2.2.5 ORTHORHOMBIC SINGLE CRYSTAL

For a monoclinic single crystal, Eqn (26.15) or (26.16) in the $X_1 - X_2 - X_3$ system shown in Figure 26.6 can be written with three independent thermal expansion coefficients α_1, α_2, and α_3 [19] by substituting α_{ij} with

$$\alpha_{11} = \alpha_1, \;\; \alpha_{22} = \alpha_2, \;\; \alpha_{33} = \alpha_3, \;\; \alpha_{23} = \alpha_{32} = 0, \;\; \alpha_{31} = \alpha_{13} = \alpha_5, \;\; \alpha_{12} = \alpha_{21} = 0 \tag{26.25}$$

Using the standard tensor transformation, we obtain the thermal expansion coefficient tensor in the analysis coordinate system $X_1' - X_2' - X_3'$ shown in Figure 26.2 as follows:

$$\alpha_{ij}' = a_{ik}a_{jl}\alpha_{kl} = \alpha_{11}a_{i1}a_{j1} + \alpha_{22}a_{i2}a_{j2} + \alpha_{33}a_{i3}a_{j3} = \alpha_1 a_{i1}a_{j1} + \alpha_2 a_{i2}a_{j2} + \alpha_3 a_{i3}a_{j3} \tag{26.26}$$

26.2.2.3 Finite Element Formulation

From Eqn (26.6), we can obtain the final form of the stress–strain relation for a thermoelastic problem in the analysis coordinate system $X_1' - X_2' - X_3'$, assuming that the total strain ε_j' is a sum of the elastic strain $(\varepsilon_i^e)'$ and the thermal strain $(\varepsilon_i^t)'$:

$$\sigma_i' = C_{ij}'\left(\varepsilon_j' - \left(\varepsilon_j^t\right)'\right) \tag{26.27}$$

It is very easy to obtain a finite element equilibrium equation using a standard formulation for the finite element method. The components of elastic constant matrix for the respective crystal systems are given in Eqns (26.5), (26.8), (26.10), (26.12), and (26.14). The components of a thermal expansion coefficient vector for the respective crystal systems are given in Eqns (26.17), (26.20), (26.22), (26.24), and (26.26).

26.2.3 Several Examples of Thermal Stress Analysis

26.2.3.1 Effect of Crystal Anisotropy on Thermal Stress for Cubic Bulk Single Crystals (Si, GaAs, and InP)

Thermal stress analyses of Si, GaAs, and InP bulk single crystals during crystal growth are performed for the [001] and [111] growth directions, taking account of the elastic anisotropy [24]. Considering that cubic single crystals have 12 slip systems, Jordan et al. [25] proposed the following parameter σ_{tot}, which can be calculated from the results of thermal stress analysis:

$$\sigma_{tot} = \sum_{n=1}^{12} \left| \sigma_{RS}^{(n)} \right| \tag{26.28}$$

where $\sigma_{RS}^{(n)}$ denotes the resolved shear stress of nth slip system. This parameter can be used as a measure for thermal stress effective for glide strains.

The material properties required for a thermal stress analysis are the elastic constants C_{11}, C_{12}, and C_{44} (dyn/cm^2), and the thermal expansion coefficient $\alpha_1^{(1/\mathrm{K})}$. The following were employed in the present analyses:

Si single crystal [26]:

$$\begin{gathered} C_{11} = 16.564 \times 10^{11} \exp\left(-9.4 \times 10^{-5}(T - 298.15)\right) \\ C_{12} = 6.394 \times 10^{11} \exp\left(-9.8 \times 10^{-5}(T - 298.15)\right) \\ C_{44} = 7.951 \times 10^{11} \exp\left(-8.3 \times 10^{-5}(T - 298.15)\right) \\ \alpha_1 = 3.725 \times 10^{-6}\left(1.0 - \exp\left(-5.88 \times 10^{-3}(T - 124.0)\right)\right) + 5.84 \times 10^{-10} T \end{gathered}$$

GaAs single crystal [27]:

$$\begin{gathered} C_{11} = 12.16 \times 10^{11} - 1.39 \times 10^{8} T \\ C_{12} = 5.43 \times 10^{11} - 5.76 \times 10^{7} T \\ C_{44} = 6.18 \times 10^{11} - 7.01 \times 10^{7} T \\ \alpha_1 = 4.68 \times 10^{-6} + 3.82 \times 10^{-9} T \end{gathered}$$

InP single crystal [28]:

$$\begin{gathered} C_{11} = 10.76 \times 10^{11} - 1.397 \times 10^{8} T \\ C_{12} = 6.080 \times 10^{11} - 8.344 \times 10^{7} T \\ C_{44} = 4.233 \times 10^{11} - 4.035 \times 10^{7} T \\ \alpha_1 = 4.869 \times 10^{-6} - 5.164 \times 10^{-9} T + 6.048 \times 10^{-12} T^2 \end{gathered}$$

The unit of temperature T is K. The melting points of Si, GaAs, and InP are respectively 1685, 1511 and 1335 K.

The isotropic analysis was also carried out for comparison with the anisotropic analysis. In the isotropic analysis, Young's modulus E and Poisson's ratio ν in the {111} plane [29] were used in the same way as in Jordan et al.'s analysis [25].

Thermal stress analyses were performed for bulk single crystals, which have a cylindrical shape of 5 cm in diameter and 5 cm in height. Figure 26.7 shows the temperature distribution used in the thermal stress analysis of a GaAs single crystal. This temperature distribution was obtained from a heat conduction analysis during CZ growth by Jordan et al. [25]. The temperature distributions in Si and InP single crystals are so determined that the temperature difference from the solid–liquid interface, the temperature at which is the melting point of each crystal, is the same as that of a GaAs single crystal shown in Figure 26.7.

Figure 26.8 shows the contour lines of σ_{tot} in the cross-section at 2.474 cm above the solid–liquid interface in case of the [001] growth direction of a Si bulk single crystal. The results of both the isotropic analysis and the anisotropic analysis are given in this figure. The distribution patterns of σ_{tot} obtained from the anisotropic analysis are similar to those obtained from the isotropic analysis, but the isotropic analysis provides larger σ_{tot} values than the anisotropic analysis. Similar results are obtained for GaAs and InP single crystals in case of the [001] growth direction. As can be seen in Figure 26.8, the contour

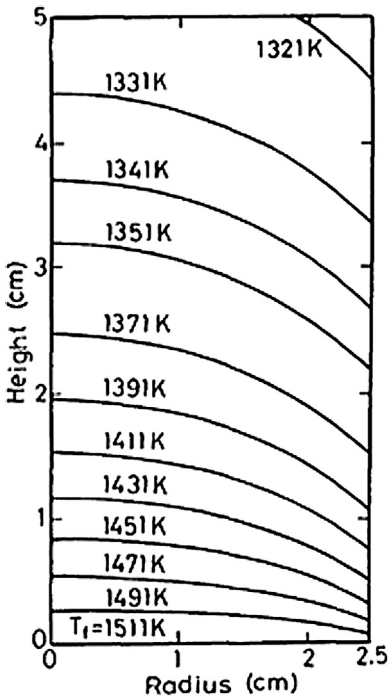

FIGURE 26.7 Temperature distribution used in the thermal stress analysis of a GaAs bulk single crystal. *From Ref. [24] with permission of Japan Society of Mechanical Engineers.*

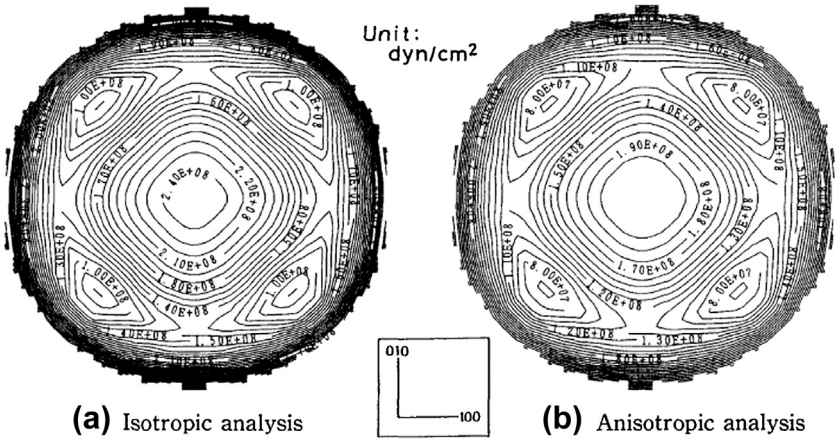

FIGURE 26.8 Contour lines of σ_{tot} in the cross-section at 2.474 cm above the solid–liquid interface in the [001] growth direction of a Si bulk single crystal. (a) Isotropic analysis and (b) Anisotropic analysis. *From Ref. [24] with permission of Japan Society of Mechanical Engineers.*

lines are dense near the side wall. In Table 26.2, the value of σ_{tot} at the side wall is compared between the isotropic analysis and the anisotropic analysis for the respective bulk single crystals in case of the [001] growth direction. In Table 26.2, the parameter A denotes a measure of elastic anisotropy defined as

$$A = 2C_{44}/(C_{11} - C_{12}) \tag{26.29}$$

The parameter A is equal to unity for elastically isotropic materials. It is found from the table that the difference between the isotropic analysis and the anisotropic analysis increases with increase of A.

Figure 26.9 shows the contour lines of σ_{tot} in the case of cross-section at 2.474 cm above the solid–liquid interface in case of the [111] growth direction of an InP bulk single crystal. The results of both the isotropic analysis and the anisotropic analysis are given in the figure. We can see the difference in the distribution patterns of σ_{tot} rather than its value.

Table 26.2 σ_{tot} at the Side Wall

		(dyn/cm²)		
	A	iso.	aniso.	iso./aniso.
Si	1.58	5.4×10^8	4.6×10^8	1.17
GaAs	1.86	8.0×10^8	6.4×10^8	1.25
InP	1.88	4.9×10^8	3.7×10^8	1.32

iso. : Result of isotropic analysis.
aniso. : Result of anisotropic analysis.

From Ref. [24] with permission of Japan Society of Mechanical Engineers.

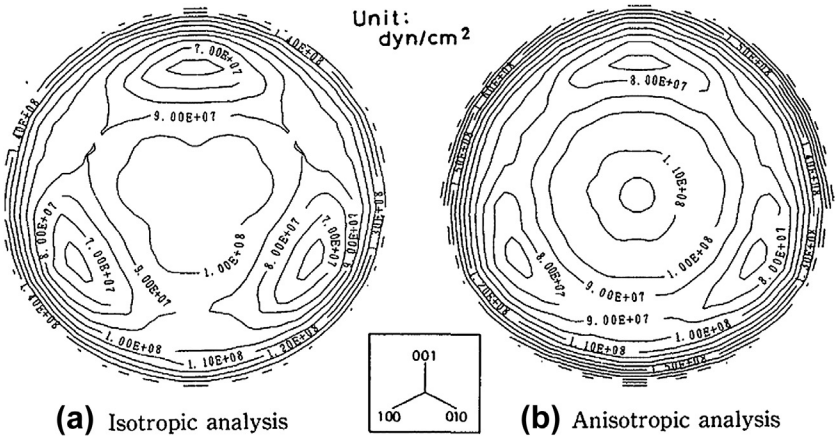

FIGURE 26.9 Contour lines of σ_{tot} in the cross-section at 2.474 cm above the solid–liquid interface in the [111] growth direction of an InP bulk single crystal. (a) Isotropic analysis and (b) Anisotropic analysis. *From Ref. [24] with permission of Japan Society of Mechanical Engineers.*

26.2.3.2 Thermal Stress Analysis of Lithium Niobate Bulk Single Crystal

Trigonal single crystals, such as lithium niobate (LN, $LiNbO_3$) and lithium tantalite (LT, $LiTaO_3$) are important for surface acoustic wave (SAW) and photonic devices. Cracking of the crystals sometimes occurs during the CZ growth, especially during cooling down. Because the cracking can be avoided by adjusting the thermal conditions of the CZ furnace, this defect is supposed to be caused by thermal stress [30,31]. Thus, it is essential to calculate the thermal stress during the growth for the quantitative assessment of cracking. Here, the results of thermal stress analyses for an LN bulk single crystal during the CZ growth are shown for different growth directions by using a three-dimensional finite element computer program [20]. Crystal anisotropy in the elastic constants and thermal expansion coefficients was considered in the analysis.

Thermal stress analyses of LN bulk single crystals of 1-inch diameter were performed using the temperature distribution calculated from a global analysis of heat transfer in an inductively heated CZ furnace [32]. The temperature distribution and crystal shape are shown in Figure 26.10, in which contour lines are so drawn as to divide the difference between the maximum temperature and the minimum one into 20 equal portions. Here, the maximum temperature corresponds to the temperature at the interface between the crystal and the melt (i.e., the melting point of LN: 1526.15 K), and the minimum one corresponds to the temperature at the top of a bulk single crystal (i.e., 1112.08 K). The temperature-dependent elastic constants C_{ij} [33] and thermal expansion coefficients α_i [34] are given as follows:

$$
\begin{aligned}
C_{11} &= 2.030 \times 10^{12}\left(1.0 - 1.74 \times 10^{-4}(T - 298.15)\right)\\
C_{12} &= 0.573 \times 10^{12}\left(1.0 - 2.52 \times 10^{-4}(T - 298.15)\right)\\
C_{13} &= 0.752 \times 10^{12}\left(1.0 - 1.59 \times 10^{-4}(T - 298.15)\right)\\
C_{14} &= 0.085 \times 10^{12}\left(1.0 - 2.14 \times 10^{-4}(T - 298.15)\right)\\
C_{33} &= 2.424 \times 10^{12}\left(1.0 - 1.53 \times 10^{-4}(T - 298.15)\right)
\end{aligned}
$$

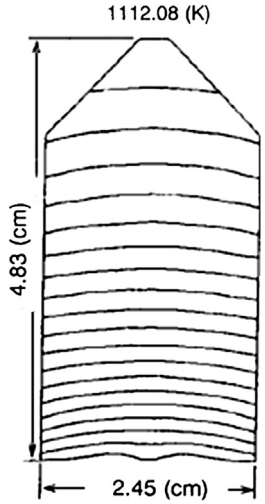

FIGURE 26.10 Temperature distribution and crystal shape of an LN bulk single crystal obtained from a global analysis of heat transfer in an inductively heated CZ furnace [32]. *From Ref. [20] with permission of Elsevier Science.*

$$C_{44} = 0.595 \times 10^{12}\left(1.0 - 2.04 \times 10^{-4}\left(T - 298.15\right)\right)$$
$$\alpha_1 = -2.8540 \times 10^{-6} + 2 \times 2.2573 \times 10^{-8} T - 3 \times 6.3438 \times 10^{-12} T^2$$
$$\alpha_3 = -1.0666 \times 10^{-6} + 2 \times 8.8951 \times 10^{-9} T - 3 \times 5.6895 \times 10^{-12} T^2$$

Three-dimensional finite element thermal stress analyses of LN bulk single crystals were carried out for both *a*-axis growth and *c*-axis growth. The von Mises equivalent stress $\sqrt{3J_2'}$, where J_2' is the second invariant of the deviatoric stress, and the maximum principal stress σ_1 ($\sigma_1 \geq \sigma_2 \geq \sigma_3$) were calculated from the results of thermal stress analyses. The stresses $\sqrt{3J_2'}$ and σ_1 were adopted as a measure for ductile failure or slip and a measure for brittle failure, respectively. The maximum values of $\sqrt{3J_2'}$ and σ_1 are as follows:

$\sqrt{3J_2'}$: 75.1 MPa for the *a*-axis growth and 59.3 MPa for the *c*-axis growth
σ_1: 72.2 MPa for the *a*-axis growth and 40.6 MPa for the *c*-axis growth

It is found from the above results that $\sqrt{3J_2'}$ and σ_1 are much larger for the *a*-axis growth than for the *c*-axis growth. This fact indicates that *a*-axis growth cracks easier than *c*-axis growth, which is consistent with the experience of LT crystal growth [31].

Figures 26.11 and 26.12 show the contour lines of $\sqrt{3J_2'}$ and σ_1 for the case of *a*-axis growth and *c*-axis growth, respectively. In these figures, a quarter of the crystal is eliminated to show the internal part clearly; the numeral 1 indicates the minimum and the numeral 9 indicates the maximum. The differences in stress distribution are shown in Figures 26.11 and 26.12 according to the crystal growth directions. For *a*-axis growth, the maximum values of stresses $\sqrt{3J_2'}$ and σ_1 occur either at the crystal–melt interface or at the outer surface of the crystal, and the lower-stress region spreads widely in the internal part of the bulk single crystal. On the other hand, the bulk single crystal grown in

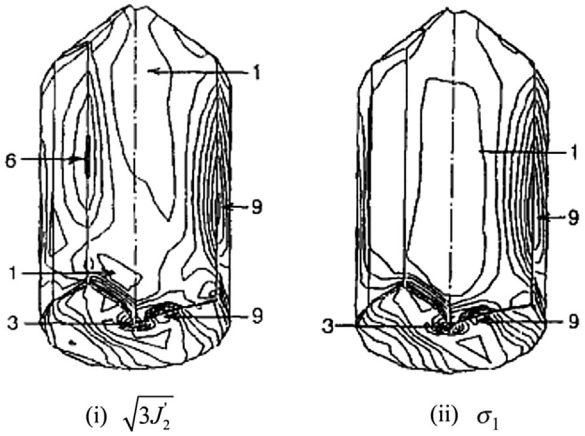

FIGURE 26.11 Stress distributions in an LN bulk single crystal grown in the *a*-axis. *From Ref. [20] with permission of Elsevier Science.*

the *c*-axis has a higher stress region in the internal part of the crystal in addition to the outer surface of the crystal. This fact indicates that one can obtain a bulk single crystal of high quality using *a*-axis growth, which has lower dislocation density than a bulk single crystal grown in the *c*-axis, if one can grow a bulk single crystal without macrocracking.

26.2.3.3 Thermal Stress Analysis of Lead Molybdate Bulk Single Crystal

A lead molybdate ($PbMoO_4$, hereafter abbreviated as PMO) single crystal has a tetragonal crystal structure and is used in acousto-optic light detectors and modulators. Its bulk single crystal is usually manufactured by the CZ growth technique. Several experimental studies have been performed on the relationship between the growth direction of the PMO bulk single crystal and crystal quality [35–42]. Thermal stress analyses of a PMO bulk single crystal were performed to discuss the formation of macrocracking and subgrains.

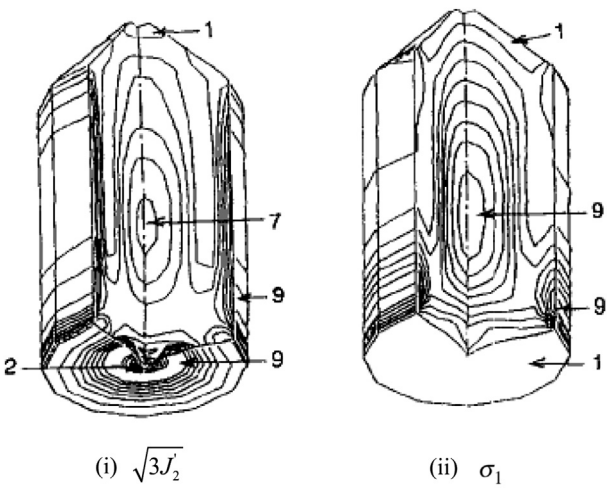

FIGURE 26.12 Stress distributions in an LN bulk single crystal grown in the *c*-axis. *From Ref. [20] with permission of Elsevier Science.*

Table 26.3 Elastic Constants and Thermal Expansion Coefficients of PMO Single Crystals

C_{ij} and α_i	Value	Unit
C_{11}	1.092×10^{12}	[dyn/cm^2]
C_{12}	0.683×10^{12}	[dyn/cm^2]
C_{13}	0.528×10^{12}	[dyn/cm^2]
C_{16}	0.136×10^{12}	[dyn/cm^2]
C_{33}	0.917×10^{12}	[dyn/cm^2]
C_{44}	0.267×10^{12}	[dyn/cm^2]
C_{66}	0.337×10^{12}	[dyn/cm^2]
α_1	10×10^{-6}	[1/K]
α_3	25×10^{-6}	[1/K]

10^7 dyn/cm^2 = 1 MPa

Three-dimensional finite element thermal stress analyses of a PMO bulk single crystal with a cylindrical shape of 5 cm in diameter and 5 cm in height were carried out for various growth directions including the *a*-, *b*-, and *c*-axis directions to discuss the relationship between the thermal stress and the crystal quality obtained from the experiments [22,43]. The temperature distribution used in thermal stress analysis is similar to Figure 26.7 for GaAs single crystals [25]. That is, the temperature difference from the crystal–melt interface is the same as that of a GaAs single crystal shown in Figure 26.7, and the temperature at the crystal–melt interface is the melting point of a PMO single crystal, 1343 K. The elastic constants and thermal expansion coefficients of a PMO single crystal are summarized in Table 26.3 [44].

The maximum principal stress σ_1 and the von Mises equivalent stress $\sqrt{3J_2'}$ were calculated from the results of thermal stress analyses. The maximum values of σ_1 and

Table 26.4 The Maximum Values of σ_1 and $\sqrt{3J_2'}$ in a PMO Bulk Single Crystal for Various Growth Directions

Growth Direction	σ_1(MPa)	$\sqrt{3J_2'}$(MPa)
a (90-0)	36.5	41.7
b (90-90)	36.5	41.7
c (0-0)	19.7	17.3
30-0	27.3	28.3
30-30	26.7	26.3
30-60	27.4	28.4
30-90	27.3	28.4
60-0	35.2	38.3
60-30	36.6	42.2
60-60	34.8	37.8
60-90	35.2	38.3
90-30	41.7	53.9
90-60	35.8	40.2

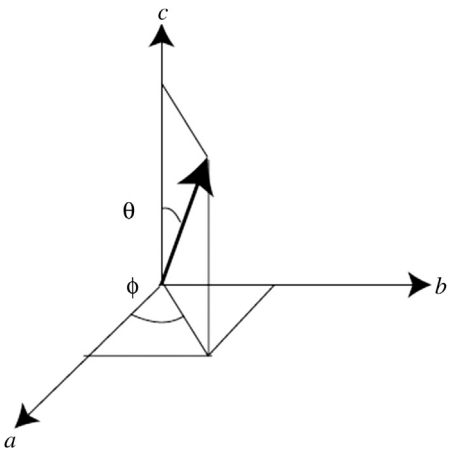

FIGURE 26.13 Notation of angles defining crystal growth direction. *From Ref. [43] with permission of Elsevier.*

$\sqrt{3J_2'}$ for the respective growth directions are summarized in Table 26.4, in which the growth direction is defined as $\theta - \varphi$ by the combination of the angle θ and φ, shown in Figure 26.13. The contour lines of σ_1 and $\sqrt{3J_2'}$ for *a*-, *b*-, and *c*-axis growth directions are shown in Figure 26.14. Due to crystallographic equivalence, the *a*-axis growth provides exactly the same results as the *b*-axis growth, and the stress distributions for *c*-axis growth are perfectly axisymmetric. It is also found from the figure that the stresses are higher in the peripheral region than in the internal region. This fact conforms to the experimental result obtained by Loiacono et al. [36] showing that the subgrain density is maximized at the outer surface of a bulk single crystal. The results of *a*-, *b*-, and *c*-axis growth directions in Table 26.4 show that the *a*- and *b*-axis growth directions provide larger stress values than the *c*-axis growth direction. As Bonner and Zydzik [35] pointed out, large stress is induced in the crystals grown on the *a*- and *b*-axis as a result of an unequal radial coefficient of expansion in the plane normal to the growth direction. Therefore, they are excessively strained after crystal growth and often shatter from the heat of a hand and always with attempted annealing.

Macrocracking and subgrains are the main concerns in the quality of PMO bulk single crystals. As for macrocracking, Bonner and Zydzik [35] concluded from their experimental study that the best orientation for crack-free growth is about 30° off the *c*-axis. Takano et al. mentioned in their paper [37] that the *c*-axis or near *c*-axis growth direction produces large crack-free crystals. Sabharwal et al. [42] found from their experimental study that the growth axis lying between 20° and 30° off the *c*-axis yields crack-free crystals. On the other hand, according to the experiments done by Zeng [41], the most suitable growth orientation for crack-free crystal is [100]. The following are the experimental results concerning the relationship between subgrains and growth direction. A study on the x-ray characterization of PMO single crystals performed by Loiacono et al. [36] showed that crystals grown in the *a*-axis direction had higher quality than those

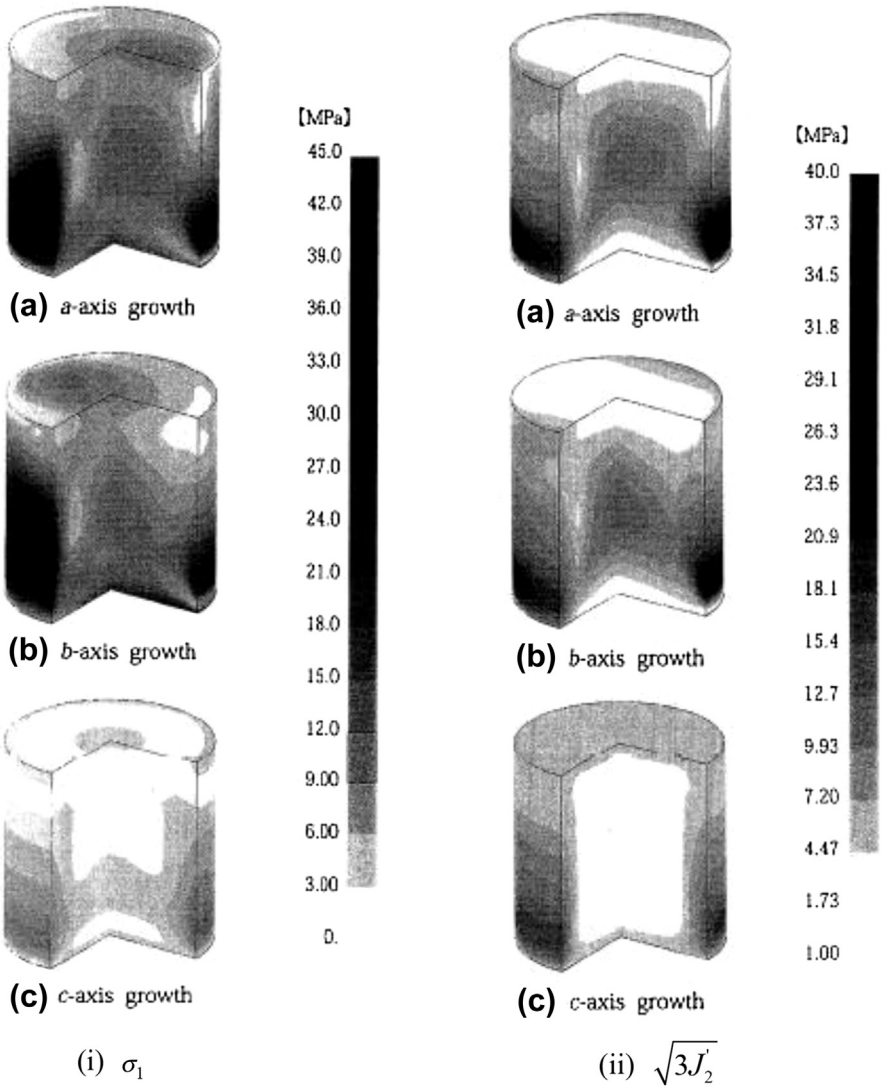

FIGURE 26.14 Stress distributions in a PMO bulk single crystal for various growth directions. *From Ref. [22] with permission of Elsevier Science.*

grown in the *c*-axis direction. Takano et al. [37] carried out PMO crystal growth for the various growth directions, concluding that high-quality single crystals without subgrains are obtained by using orientations inclined more than 30° from the *c*-axis in the intermediate planes between the *a*-*c* plane and the *b*-*c* plane. Based on these results, PMO crystals are usually grown either in the *a*-axis direction [38,39] or in the [110] direction [40], but no definite conclusion has been derived so far on the relationship between subgrains and growth direction.

As shown in Table 26.4, thermal stress is lowest in case of the *c*-axis growth and relatively small in cases of growth directions 30° off the *c*-axis (i.e., the 30-0, 30-30, 30-60, and 30-90 growth directions). This fact validates the experimental results that the *c*-axis or near *c*-axis growth direction produce large crack-free crystals, as pointed out by Bonner and Zydzik [35], Takano et al. [37], and Sabharwal et al. [42], but it does not comply with the experimental results on subgrain distribution in the PMO single crystal obtained by Loiacono et al. [36] and Takano et al. [37]. Loiacono et al. [36] presumed that the thermal conductivity of the *a*-axis direction is much larger than that of the *c*-axis direction by comparing the quality of the *a*-axis grown crystal with that of *c*-axis grown crystal, but no experimental data are available for such anisotropy in the thermal conductivity of the PMO single crystal at elevated temperatures. It may be therefore concluded that subgrains are not related to thermal stress during the growth process [45].

26.2.4 Cracking of Bulk Single Crystal Caused by Thermal Stress

A Ce-doped gadolinium orthosilicate (GSO) single crystal is classified as a monoclinic class $2/m$ single crystal. It is used as a scintillator material [46,47]. GSO bulk single crystals are manufactured by the CZ growth technique. Cracking is one of the biggest problems in GSO single crystal growth [48]. Here, quantitative estimation of the cracking of GSO single crystals is presented based on thermal stress tests and three-point bending tests [49]. The results of failure data obtained from the thermal stress tests are related to those of three-point bending tests.

Figure 26.15 shows the apparatus for thermal stress tests. Figure 26.16 shows a cylindrical test specimen of 50 mm in diameter and 10 mm in thickness used in thermal stress tests. The (100) cleavage plane is depicted in the figure. As shown in Figure 26.15, a test specimen was heated up to approximately 470 K in a silicone oil bath. Then, thermal stress was applied by pouring silicone oil at room temperature into a heated oil bath. Cracking occurred during cooling due to thermal stress. The surface temperatures were

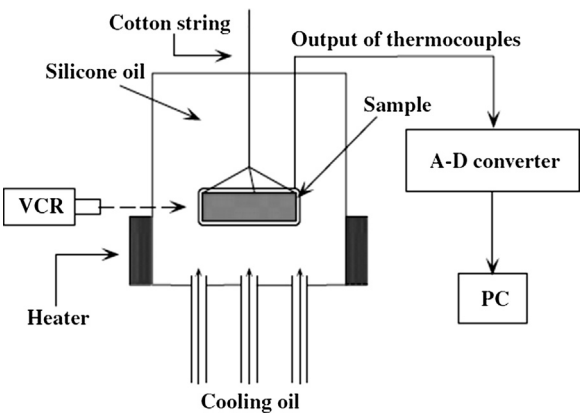

FIGURE 26.15 Apparatus for thermal stress test. *From Ref. [49] with permission of Tech Science Press.*

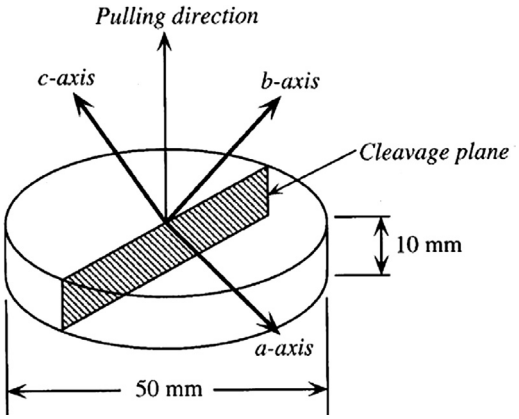

FIGURE 26.16 GSO test specimen for thermal stress tests and cleavage plane. *From Ref. [49] with permission of Tech Science Press.*

measured using thermocouples attached on the surface of the test specimen. The time when the cracking occurred was identified by a video recording. The finite element method was applied both to the heat conduction analysis and to the thermal stress analysis. The density ρ, specific heat C_p, and thermal conductivity λ of a GSO single crystal are required for the heat conduction analysis. The following material properties were used in the heat conduction analysis:

$$\rho = 6.71 \times 10^3 \mathrm{kg/m^3}, C_p = 350\mathrm{J/(kg \cdot K)}, \lambda = 2.98\mathrm{W/(m \cdot K)}$$

The values of C_p and λ were measured by Hitachi Chemical Co. by the laser flash method. The elastic constants C_{ij} and thermal expansion coefficients α_i of the GSO single crystal were reported by Kurashige et al. [50], as summarized in Table 26.5. The detailed method for thermal stress analysis of GSO single crystals is given in Ref. [21].

The thermal stress at the time of cracking obtained from the analysis was converted into the von Mises equivalent stress $\sqrt{3J_2'}$, the maximum principal stress σ_1, the normal stress σ_n acting on the (100) cleavage plane, and the shear stress σ_s acting on the (100) cleavage plane. Figure 26.17 shows an example of the distributions of these stresses at the time of cracking. The cracking shown in Figure 26.18 was observed in all of the test specimens in the thermal stress tests. The crack surface is confirmed to be the (100) cleavage plane by *X*-ray diffraction. Among the four kinds of stress shown in Figure 26.17, the stress σ_n can be used to explain the cracking phenomenon. It is found from Figure 26.17(c) that σ_n is at the maximum at the side surface of the test specimen where the (100) cleavage intersects. Therefore, the crack runs along the (100) cleavage plane. Among the four kinds of stress evaluated for the cracking, it was concluded that the maximum value of σ_n dominates the cracking induced by thermal stress.

Three-point bending tests were also performed to examine the relationship between the critical stress for cracking induced by thermal stress and the three-point bending strength. The details of the three-point bending tests are given in Ref. [51]. Test

Table 26.5 Elastic Constants and Thermal Expansion Coefficients of GSO Single Crystals

C_{ij} and α_i	Value	Unit
C_{11}	2.23×10^{12}	[dyn/cm^2]
C_{12}	1.08×10^{12}	[dyn/cm^2]
C_{13}	0.985×10^{12}	[dyn/cm^2]
C_{15}	0.084×10^{12}	[dyn/cm^2]
C_{22}	1.50×10^{12}	[dyn/cm^2]
C_{23}	1.02×10^{12}	[dyn/cm^2]
C_{25}	0.333×10^{12}	[dyn/cm^2]
C_{33}	2.51×10^{12}	[dyn/cm^2]
C_{35}	-0.06×10^{12}	[dyn/cm^2]
C_{44}	0.788×10^{12}	[dyn/cm^2]
C_{46}	-0.066×10^{12}	[dyn/cm^2]
C_{55}	0.688×10^{12}	[dyn/cm^2]
C_{66}	0.827×10^{12}	[dyn/cm^2]
α_1	4.8×10^{-6}	[1/K]
α_2	14.0×10^{-6}	[1/K]
α_3	6.4×10^{-6}	[1/K]

10^7 dyn/cm^2 = 1 MPa

specimens are 4.5×4.5 mm in cross-section and 50 mm in length. The GSO single crystal has a (100) cleavage plane and a [001] slip direction in the (100) cleavage plane. As shown in Figure 26.19, six cases of three-point bending tests were performed at a temperature of 470 K—the same temperature as silicone oil in the thermal stress test. The average value of the three-point bending strength σ_b for each case is given in Table 26.6. Because Case 2 has the lowest three-point bending strength and complete cleavage fracture was observed both in Case 2 and in the thermal stress test specimens, the three-point bending strength for Case 2 should be compared with the critical stress for the cracking induced by thermal stress.

Weibull plots of the failure data obtained from the thermal stress tests and the three-point bending tests are shown in Figure 26.20 where the cumulative failure probability F is related to the stress σ_n for the thermal stress tests and the stress σ_b for the three-point bending tests. Both sets of failure data show good linearity and obey the Weibull distributions. According to the weakest link model of the Weibull distribution, a larger specimen has lower failure stress. This is why the failure data of the thermal stress tests scatter at lower stress than those of the three-point bending tests. Furthermore, the slopes of both lines are almost the same, which indicates that the Weibull distribution of the thermal stress tests can be estimated from that of the three-point bending test by correcting a size effect. A return period T_r (defined by $T_r = L_1/L_2$, where L_1 and L_2 are respectively the effective lengths for a thermal stress test specimen and a three-point bending test specimen) is used for the correction of a size effect. In thermal stress

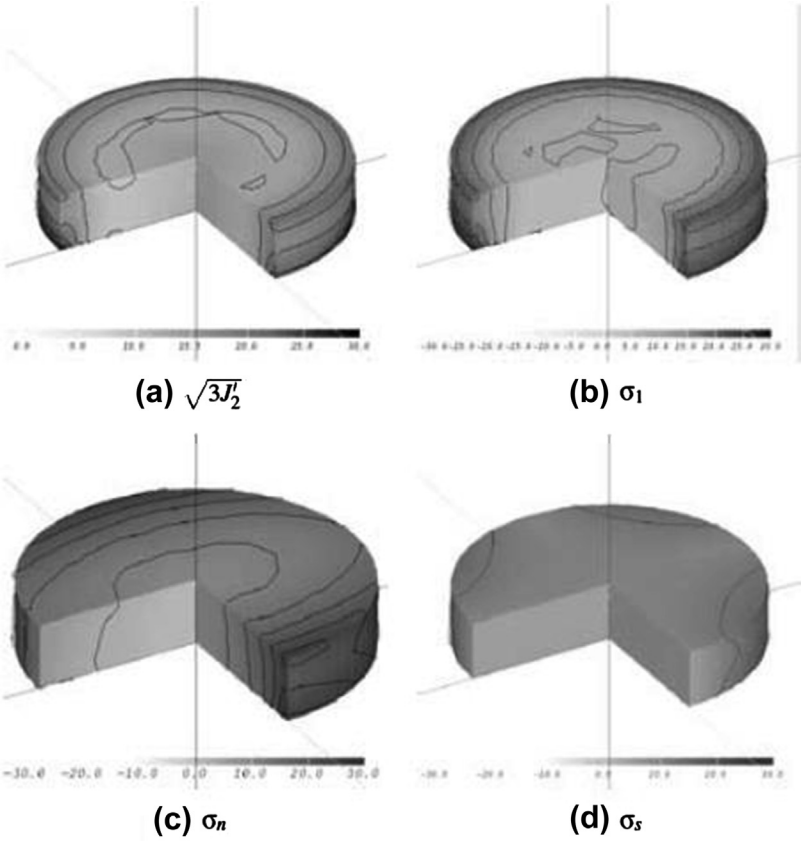

FIGURE 26.17 Distributions of stresses in a GSO test specimen at the time of cracking obtained from thermal stress analysis (unit: MPa, $\Delta\sigma = 5$ MPa). *From Ref. [49] with permission of Tech Science Press.*

FIGURE 26.18 Cracking of a GSO test specimen observed in a thermal stress test. *From Ref. [49] with permission of Tech Science Press.*

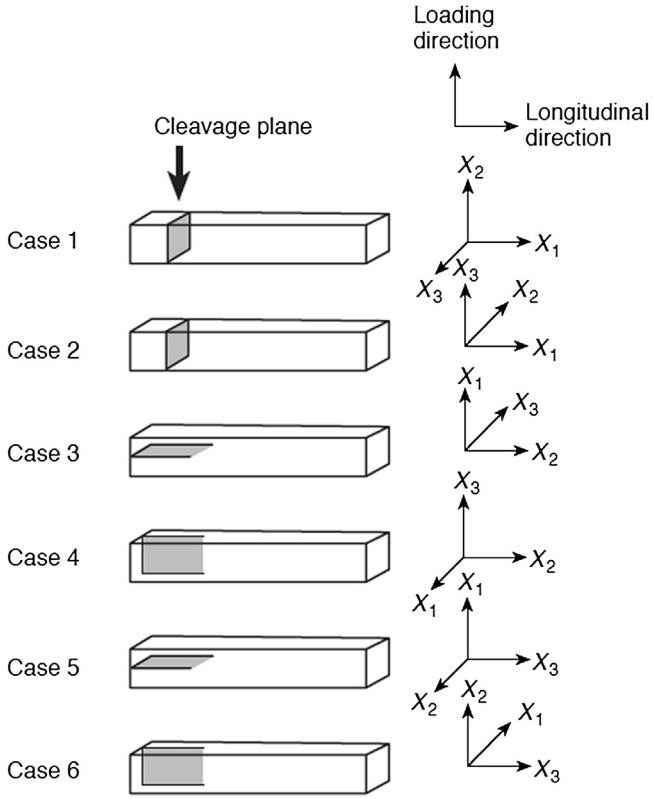

FIGURE 26.19 Schematic diagrams of test conditions for three-point bending tests of a GSO single crystal. *From Ref. [49] with permission of Tech Science Press.*

tests, the origin of cracking is located at the side surface of the cylindrical specimen where σ_n is the maximum, as shown in Figure 26.17(c), so the double thickness of the test specimen, 20 mm, was chosen as L_1. On the other hand, the length of the three-point bending specimen just under the loading location, which is subjected to the maximum tensile stress caused by the bending moment, is chosen as L_2. So, L_2 is equal to 4.5 mm. The broken line in Figure 26.20 is the Weibull distribution estimated from the three-point bending data using the return period. The estimated Weibull distribution agrees very well with that of the thermal stress tests. Miyazaki et al. also performed cracking experiments of the LN single crystal [52] and LT single crystal [53] under thermal loading conditions.

Table 26.6 Average Value of Three Point Bending Strength for a GSO Single Crystal

Case	1	2	3	4	5	6
Average σ_b[MPa]	102.5	44.34	151.2	157.3	—	618.2

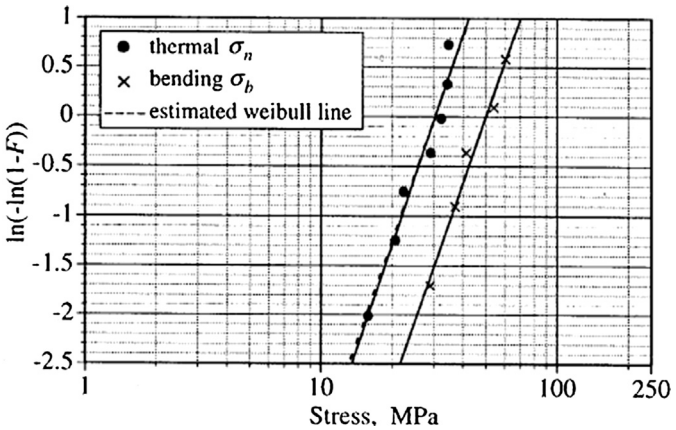

FIGURE 26.20 Weibull plots for failure stresses of a GSO single crystal obtained from thermal stress tests and the three-point bending tests. *From Ref. [49] with permission of Tech Science Press.*

26.3 Dislocations in Bulk Single Crystals

26.3.1 Introduction

Single crystals for electronic and optical devices (e.g., Si, Ge, GaAs, InP, CdTe) are manufactured by the Czochralski (CZ), floating zone (FZ) and vertical gradient freeze (VGF) methods, for example. As crystal growth is carried out under thermal gradients, large thermal stress is induced in a crystal by nonlinear thermal gradients during the growth process. Such thermal stress causes the multiplication of dislocations that affect the performance of devices. In particular, GaAs and InP single crystals have low critical resolved shear stress, and it is easy to multiply dislocations due to thermal stress during the growth process. Therefore, it is important to reduce the dislocations as low as possible. After crystal growth, compound semiconductor single crystals, such as GaAs and InP, are annealed to improve their electrical properties. One of the technical problems of ingot annealing is the increase of the dislocation density caused by thermal stress during ingot annealing. Computer simulations of dislocation density play a major role in determining the process conditions of crystal growth and crystal annealing. Quantitative methods for dislocation density estimation are presented here, as well as a qualitative method.

26.3.2 Qualitative Estimation of Dislocation Density

The main objective of thermal stress analysis of the crystal growth process is to clarify the relationship between defects such as dislocations and thermal stress. For this purpose, Jordan et al. [25] proposed a parameter for the qualitative estimation of dislocation density σ_{ex}. They assumed that dislocation density is proportional to the

amount of slip or glide strain, which is also proportional to the excess shear stress $\sigma_e^{(n)}$ defined by

$$\begin{aligned} \sigma_e^{(n)} &= \left|\sigma_{RS}^{(n)}\right| - \sigma_{CRS}, \quad \text{when} \quad \left|\sigma_{RS}^{(n)}\right| > \sigma_{CRS} \\ &= 0, \quad \text{when} \quad \left|\sigma_{RS}^{(n)}\right| \leq \sigma_{CRS} \end{aligned} \tag{26.30}$$

where the subscript (n) denotes the nth slip system, $\sigma_{RS}^{(n)}$ is the resolved shear stress for the nth slip system calculated from the stress transformation from the analysis coordinate system to the slip system, and σ_{CRS} is the critical resolved shear stress. Considering that cubic single crystals such as Si, GaAs, and InP single crystals have 12 equivalent slip systems {111}<110>, the total excess shear stress is

$$\sigma_{ex} = \sum_{n=1}^{12} \sigma_e^{(n)} \tag{26.31}$$

A positive value of σ_{ex} means that dislocations occur in the crystal. The nondimensional parameter σ_{mex} [18,54] can be also used as a measure for the qualitative estimation of dislocation density:

$$\sigma_{mex} = \frac{\sigma_{tot}}{12\sigma_{CRS}} \tag{26.32}$$

where

$$\sigma_{tot} = \sum_{n=1}^{12} \left|\sigma_{RS}^{(n)}\right| \tag{26.33}$$

When σ_{mex} is larger than the unity, the average resolved shear stress ($\sigma_{tot}/12$) is larger than the critical resolved shear stress. It is concluded that dislocations occur in such a case.

Qualitative estimation of dislocation density was performed by Jordan et al. [25] for the first time. They used the parameter σ_{ex} calculated from the results of the isotropic thermal stress analysis of a GaAs bulk single crystal during crystal growth. After that, they also performed the analyses for InP and Si crystals, in addition to GaAs crystals [55,56]. Quantitative methods for dislocation density estimation described later need creep or viscoplastic constitutive equations as a function of the dislocation density. On the other hand, the qualitative method for dislocation density estimation described here requires only elastic constants, thermal expansion coefficients, the slip system, and critical resolved shear stress. Therefore, this method can be applied to various kinds of single crystals, such as SiC [57] and AlN [58] crystals grown by the sublimitation technique.

26.3.3 Quantitative Estimation of Dislocation Density: Haasen-Alexander-Sumino Model

The quantitative estimation of the dislocation density provides more useful information on the quality of a single crystal than the qualitative estimation. In the quantitative

estimation, the Haasen-Alexander-Sumino (HAS) model [59,60] is used as the constitutive equation relating time-dependent inelastic strain (i.e., creep strain or viscoplastic strain) with dislocation density. Quantitative dislocation density analysis during the crystal growth process using the HAS model was performed by Dillion et al. [61] for the first time, followed by several papers [62,63]. All of these papers dealt with the growth of an Si ribbon. Afterward, several papers were published concerning the dislocation density analyses of compound semiconductor single crystals, such as GaAs and InP grown by the CZ method and the vertical Bridgman method. Some of them [64–66] do not deal with a multiaxial stress state exactly; others [67–70] are quasistatic finite element analyses that assume a constant growth rate and constant radius of a bulk single crystal, and they give only steady-state values of dislocation density. The quasistatic method is only a simple model of the actual growth process, in which the growth rate and radial of a bulk single crystal are dynamically changed. Miyazaki et al. [71–73] developed a computer code for the transient simulation of dislocation density during crystal growth. In this computer code, axisymmetric finite element modeling is used, together with the HAS model for creep constitutive equations. It provides the space and time variations of dislocation density in a bulk single crystal.

Here, we provide methods for the quantitative estimation of dislocation density using the HAS model. In particular, we show a method for expanding the HAS model to a multiaxial stress state that is necessary for finite element analysis. Furthermore, we present another HAS model for a multiaxial stress state that takes into account crystal anisotropy in elastic constants and specific slip directions. Such constitutive equations enable the exact three-dimensional finite element analysis of quantitative dislocation density estimation. Then, the results of finite element analyses are shown for two kinds of quantitative dislocation density problems: dislocation density estimation during the crystal growth process and the ingot annealing process.

26.3.3.1 HAS Model for the Uniaxial Stress State

Time-dependent creep deformation is induced in a bulk single crystal under elevated temperatures during the crystal growth process. The creep constitutive equations for single crystals based on a dislocation kinetics model is known as the HAS model [59,60], in which the creep strain rate is related to the dislocation density. In this model, the creep strain rate $\mathrm{d}\varepsilon^c/\mathrm{d}t$ and the mobile dislocation density rate $\mathrm{d}N_m/\mathrm{d}t$ are given as follows for a uniaxial stress state:

$$\mathrm{d}\varepsilon^c/\mathrm{d}t = \phi N_m v b \tag{26.34}$$

$$\mathrm{d}N_m/\mathrm{d}t = \delta N_m v \tag{26.35}$$

where ε^c is the creep strain, t is the time, N_m is the density of mobile dislocation, and b is the magnitude of the Burgers vector. Hereafter, the superscript or subscript c indicates creep. ϕ is a geometric factor on the order of 1 relating the creep shear strain γ^c and the axial creep strain ε^c as $\varepsilon^c = \phi\gamma^c$. Equation (26.34) is obtained from the Orowan relation

$$\mathrm{d}\gamma^c/\mathrm{d}t = N_m v b \tag{26.36}$$

together with $\varepsilon^c = \phi\gamma^c$. The dislocation velocity v and the parameter δ that characterizes the multiplication rate in the above model are assumed to be

$$v = k_o(\tau_{eff})^p \exp(-Q/kT) \tag{26.37}$$

$$\delta = K(\tau_{eff})^{\lambda} \tag{26.38}$$

Here, τ_{eff} is the effective resolved shear stress and is given by

$$\tau_{eff} = \left\langle \tau_a - D\sqrt{N_m} - \tau_d \right\rangle \tag{26.39}$$

In the above equations, τ_a is externally applied shear stress on the active slip system or resolved shear stress; $D\sqrt{N_m}$ is the back-stress on a given dislocation due to the neighboring ones, which resists its movement through interaction; τ_d is the back-stress caused by the interaction between dislocations and impurity atoms; D is the strain hardening factor; Q is the Peierls potential; k is the Boltzmann constant; k_0, K, and λ are the material constants; and T is the absolute temperature. The value of $\langle x \rangle$ denotes $\langle x \rangle = x$ if $x > 0$ and 0 if $x \leq 0$. The parameters for creep constitutive equations are determined in such a way that the stress–strain curves under constant strain-rate test conditions obtained by solving Eqns (26.34) and (26.35) numerically agree well with experimentally obtained stress–strain curves around the upper and lower yielding points. The parameters are identified for Ge, Si, InSb, InP, GaAs, and so on [64–66,74]. Among them, the values of Si, InP, and GaAs are given later.

26.3.3.2 HAS Model for a Multiaxial Stress State under Isotropic Assumption

When we use the HAS model in a dislocation density analysis, we must expand Eqn (26.34) to a multiaxial stress state. Such an expansion can be done by assuming that a single crystal is isotropic, neglecting crystal anisotropy [75]. According to isotropic creep theory, the multiaxial creep strain rate $d\varepsilon_{ij}^c/dt$ is given by

$$\frac{d\varepsilon_{ij}^c}{dt} = \frac{3d\varepsilon^c/dt}{2\overline{\sigma}} S_{ij} \tag{26.40}$$

where S_{ij} is the deviatoric stress and $\overline{\sigma}$ is the equivalent stress defined by the second invariant of the deviatoric stress J_2' as follows:

$$\overline{\sigma} = \sqrt{3J_2'} \tag{26.41}$$

The following relationships hold for the simple shear characterized by the shear stress τ and the creep shear strain increment $d\gamma^c$:

$$\overline{\sigma} = \sqrt{3}\tau \tag{26.42}$$

$$d\varepsilon^c = d\gamma^c/\sqrt{3} \tag{26.43}$$

Substituting Eqns (26.41) and (26.43) into Eqn (26.40), we obtain

$$\frac{d\varepsilon_{ij}^c}{dt} = \frac{d\gamma^c/dt}{2\sqrt{J_2'}} S_{ij} \tag{26.44}$$

From Eqns (26.36) and (26.37), Eqn (26.44) becomes

$$\frac{\mathrm{d}\varepsilon_{ij}^{c}}{\mathrm{d}t} = fS_{ij} \tag{26.45}$$

$$f = \frac{bk_oN_m\left(\tau'_{eff}\right)^p \exp(-Q/kT)}{2\sqrt{J'_2}} \tag{26.46}$$

where

$$\tau'_{eff} = \left\langle \sqrt{J'_2} - D\sqrt{N_m} - \tau_d \right\rangle \tag{26.47}$$

It is found from Eqns (26.41) and (26.42) that $\sqrt{J'_2}$ represents the equivalent shear stress. The rate of dislocation density is represented by

$$\mathrm{d}N_m/\mathrm{d}t = Kk_oN_m\left(\tau'_{eff}\right)^{p+\lambda} \exp(-Q/kT) \tag{26.48}$$

If we use the creep constitutive equations given by Eqns (26.45) and (26.48), we can perform dislocation density analysis under an isotropic assumption neglecting crystal anisotropy.

26.3.3.3 HAS Model for a Multiaxial Stress State under Consideration of Crystal Anisotropy

Single crystals have crystal anisotropy in elastic constants and specific slip directions. Exact consideration of crystal anisotropy requires a three-dimensional analysis even for an axisymmetric solid. Great amounts of computational time would be necessary for the three-dimensional analysis of dislocation density during crystal growth. Therefore, several attempts have been made to avoid three-dimensional analysis by introducing approximate methods for dealing with the crystal anisotropy. Tsai et al. [68–70] proposed such a method in the framework of a quasistatic analysis. They applied the axisymmetric finite element method to the thermal stress analysis of a cylindrical single crystal, neglecting the crystal anisotropy in the elastic constants, then estimated the dislocation density using the resolved shear stress calculated from the results of the thermal stress analysis. Although their method considers the specific slip directions of a single crystal, it does not deal with the coupled phenomenon of dislocation multiplication and stress relaxation. Miyazaki et al. [76,77] proposed another approximate method for taking account of the crystal anisotropy of cubic single crystals, such as Si, GaAs, and InP. In their method, the effects of elastic constants and slip directions are approximately taken into account by averaging Young's modulus, Poisson's ratio, and the resolved shear stress along the azimuthal direction. Axisymmetric finite element method can be applied to quantitative estimation of the dislocation density by using such an averaging technique together with the HAS model for a creep constitutive equation. This approximate method is able to deal with the coupled phenomenon of dislocation multiplication and stress relaxation.

A full three-dimensional finite element analysis of dislocation density has become possible due to the rapid progress of computer performance [78,79]. Miyazaki and

Sakaguchi [78] expanded the HAS model to a multiaxial stress state based on the theory of crystal plasticity [80], as follows:

$$\frac{\mathrm{d}\varepsilon_{ij}^{c}}{\mathrm{d}t} = \sum_{n=1}^{N} f^{(n)} P_{ij}^{(n)} \tag{26.49}$$

$$f^{(n)} = bk_0 N_m \left(\tau_{eff}^{(n)}\right)^{p} \exp\left(-Q/kT\right) \tag{26.50}$$

$$P_{ij}^{(n)} = \frac{1}{2} \frac{\sigma_{RS}^{(n)}}{\left|\sigma_{RS}^{(n)}\right|} \left(\nu_i^{(n)} b_j^{(n)} + \nu_j^{(n)} b_i^{(n)}\right) \tag{26.51}$$

$$\mathrm{d}N_m^{(n)}/\mathrm{d}t = Kk_0 N_m \left(\tau_{eff}^{(n)}\right)^{p+\lambda} \exp\left(-Q/kT\right) \tag{26.52}$$

$$\tau_{eff}^{(n)} = \left\langle \left|\sigma_{RS}^{(n)}\right| - D\sqrt{N_m} - \tau_d \right\rangle \tag{26.53}$$

where the superscript (n) represents the nth slip system, N is the total number of slip systems, $\sigma_{RS}^{(n)}$ is the resolved shear system for the nth slip system, and ν_i and b_i denote the components of the unit vectors normal to the slip plane and parallel to the slip direction, respectively. Then, the total dislocation density N_m is given as follows:

$$N_m = \sum_{n=1}^{N} N_m^{(n)} \tag{26.54}$$

N should be 12 for a cubic single crystal such as Si, GaAs, or InP.

26.3.3.4 Several Applications of the HAS Model to the Quantitative Estimation of Dislocation Density

26.3.3.4.1 BULK SINGLE CRYSTAL GROWTH PROCESS

Miyazaki et al. [71–73] developed a computer code for a transient simulation of dislocation density during the bulk single crystal growth process, using the creep constitutive equations in Eqns (26.45)–(26.48). In a dislocation density analysis, one needs the parameters of the HAS model shown in Table 26.7. For Si, GaAs, and InP single crystals, the parameters in the HAS model are completely identified for Si, GaAs, and InP [74], as shown in Table 26.8. In this computer code, an axisymmetric finite element analysis is performed by neglecting crystal anisotropy. This computer code can be used as a postprocessor of a global heat transfer code for a bulk single crystal growth system. Such a global heat transfer code provides shape and temperature distributions of a bulk single crystal during the growth process in the time sequence. Figure 26.21 shows the temperature distributions and crystal shapes of a GaAs bulk single crystal with an 8-inch diameter for several times after the CZ growth starts, as are obtained from a global heat transfer code. The results of the global heat transfer analysis are provided at discrete times, and they may be insufficient for a dislocation density analysis. Therefore, we divide a time step between two adjacent times for the global heat transfer analysis into several substeps to deal with the growth process as

Table 26.7 Parameters in the HAS Model

Parameter	Description	Unit
N_m	Density of moving dislocation	$1/cm^2$
b	Magnitude of burgers vector	cm
Q	Peierls potential	eV
k	Boltzmann constant	8.617×10^{-5}ev/K
T	Absolute temperature	K
K	Material constant	cm/dyn
D	Strain hardening factor	dyn/cm
k_0	Material constant	$cm^{2p+1}/dyn^p s$
τ_d	Drag-stress	dyn/cm^2
P	Material constant	–
λ	Material constant	1.0

Table 26.8 Material Properties in the HAS Model for Si, GaAs, and InP Single Crystals

	T_m	b	Q	p	D	K	k_0
Si	1685	3.8×10^{-8}	2.2	1.1	4.3×10^3	3.1×10^{-7}	6.815×10^{-3}
GaAs	1511	4.0×10^{-8}	1.5	1.7	3.1×10^3	7.0×10^{-6}	3.59×10^{-8}
InP	1331	4.0×10^{-8}	1.0	1.4	3.0×10^3	1.2×10^{-5}	5.57×10^{-8}

Tm: melting point (K). Units of other material properties are shown in Table 26.7.

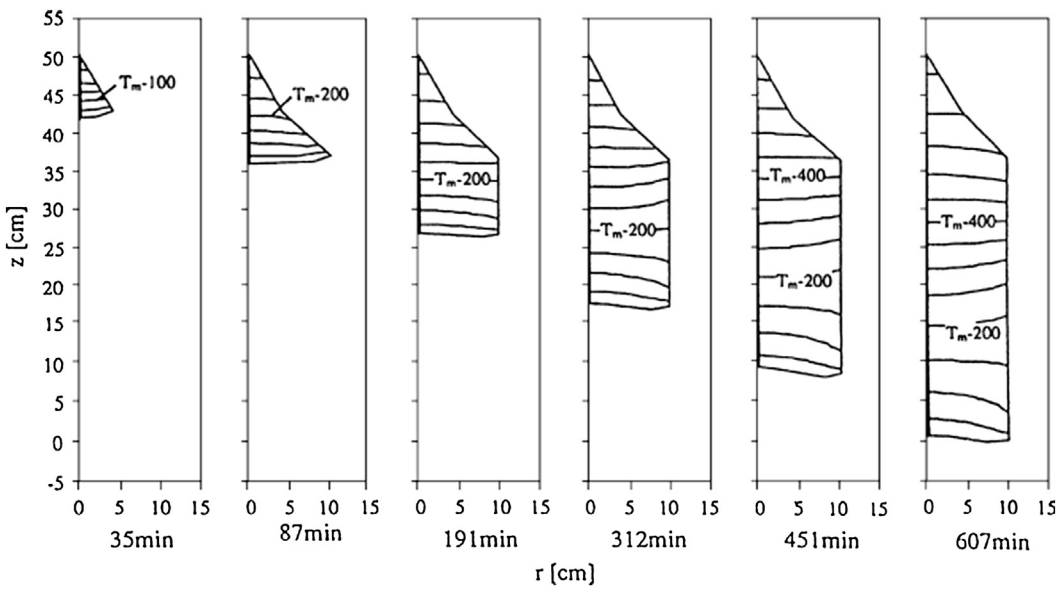

FIGURE 26.21 Temperature distributions and crystal shapes for a GaAs bulk single crystal at several times after the CZ growth starts. *From Ref. [71] with permission of Elsevier Science.*

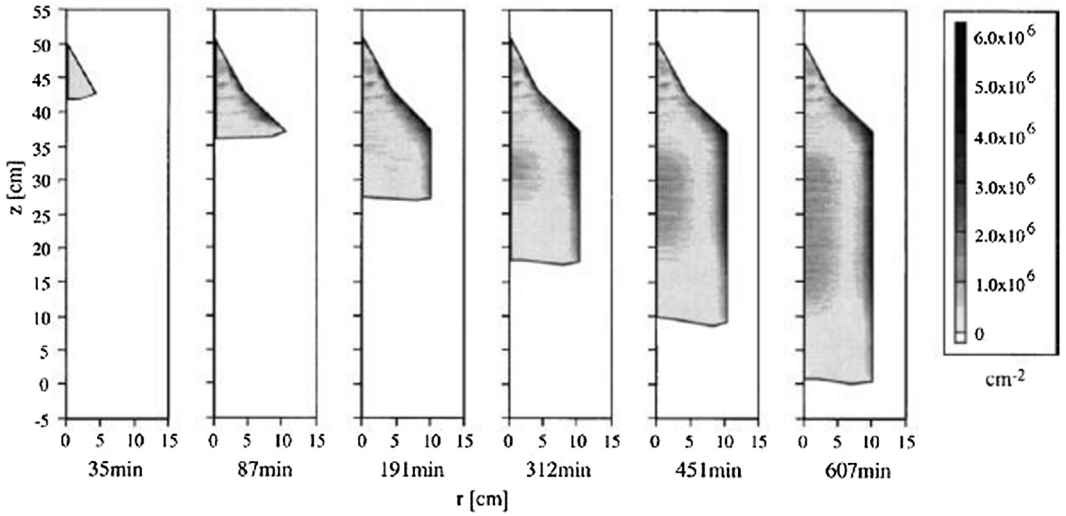

FIGURE 26.22 Dislocation density distributions in a GaAs bulk single crystal at several times after the CZ growth starts. *From Ref. [71] with permission of Elsevier Science.*

continuously as possible. The shape of the crystal–melt interface and the temperature in the crystal at an arbitrary substep are determined by linear interpolation of the results at two adjacent times for the global heat transfer analysis. The incremental form of a finite element equilibrium equation for a creep problem given as follows is solved at the time step in each substep:

$$\mathbf{K}\Delta\mathbf{U} = \Delta\mathbf{F}_t + \Delta\mathbf{F}_C \tag{26.55}$$

where $\mathbf{K}$, $\Delta\mathbf{U}$, $\Delta\mathbf{F}_t$ and $\Delta\mathbf{F}_c$ denote the stiffness matrix, the incremental nodal displacement vector, the incremental load vector due to thermal strain, and the incremental load vector due to creep strain, respectively, and $\Delta\mathbf{F}_c$ is a function of the HAS-type creep strain rate given by Eqn (26.45). Solving Eqn (26.55) at each time step and integrating Eqn (26.48), we can obtain variables such as displacement, strain, stress, and dislocation density.

Figure 26.22 shows the dislocation density distributions for a GaAs bulk single crystal of 8-inch diameter for several times after the CZ growth starts. High dislocation density appears at the central and peripheral regions of the bulk single crystal. The results indicate a W-type dislocation density distribution across the diameter that can be observed from the etch pit density in actual single crystals [81].

26.3.3.4.2 INGOT ANNEALING PROCESS

As an example of the application of a full three-dimensional dislocation density analysis using Eqns (26.49)–(26.53), we show the results of a dislocation density analysis of the GaAs ingot annealing process [82]. Ingot annealing of a GaAs bulk single crystal is an indispensable process to homogenize the electric characteristics of an as-grown single

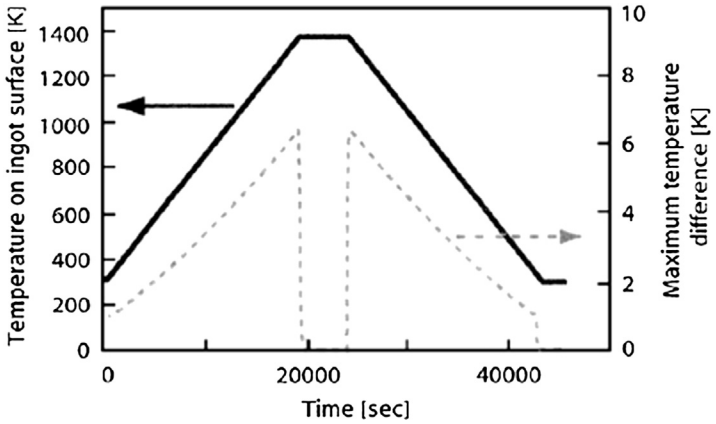

FIGURE 26.23 Time variations of the temperature on a GaAs ingot surface (solid line) and the maximum temperature difference in a GaAs ingot (dashed line) obtained from the transient heat conduction analysis. *From Ref. [82] with permission of Elsevier Science.*

crystal. One of the technical problems of GaAs ingot annealing is the increase of dislocation density due to the thermal stress induced during its annealing. A GaAs cylindrical ingot with a 101.6 mm diameter and 81.0 mm height is considered here. The solid line in Figure 26.23 shows the time variation of temperature on the GaAs ingot surface, and the dashed line in Figure 26.23 shows the time variation of the maximum temperature difference in the ingot obtained from the transient heat conduction analysis. The temperature difference in the ingot induces thermal stress, by which dislocation multiplication is caused during ingot annealing. The dislocation density analyses were performed for the ingot grown in the [001] direction and that grown in the [111] direction. Figure 26.24 shows the distributions of dislocation density at the cross-section of 56.7 mm distant from the bottom of ingot. We can find the difference of the maximum dislocation density between the [001]-grown ingot and the [111]-grown ingot. As for the distribution patterns of dislocation density, the result of the [001]-grown ingot shows fourfold symmetry and that of the [111]-grown ingot shows threefold symmetry. Such differences can be obtained from three-dimensional analyses considering the crystal anisotropy.

In addition to the above research, Miyazaki et al. carried out dislocation density analyses during the annealing of a GaAs ingot using axisymmetric modeling under the isotropic assumption of the GaAs crystal [83]. They also compared the results of dislocation density among three kinds of creep constitutive equations [84]: (1) the HAS model for a multiaxial stress state under isotropic assumption, (2) the HAS model for a multiaxial stress state under approximate consideration of crystal anisotropy, and (3) the HAS model for a multiaxial stress state under exact consideration of crystal anisotropy, the details of which were already described in this section. Kouno et al. [85]. compared the experimental results of dislocation density with analysis results.

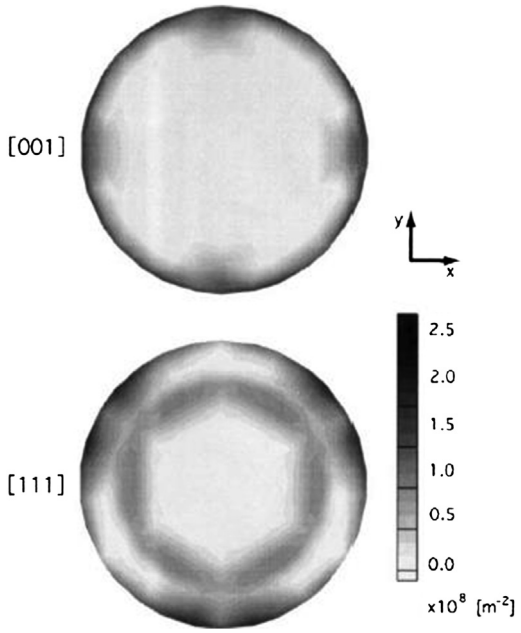

FIGURE 26.24 Distributions of dislocation density at the cross-section of 56.7 mm distant from the bottom of a GaAs ingot after annealing. *From Ref. [82] with permission of Elsevier Science.*

26.3.4 Modified HAS Models

26.3.4.1 Consideration of Immobilization of Mobile Dislocations and High-Temperature Recovery Mechanisms

Moosbrugger [86,87] proposed a modified HAS model to take account of high-temperature recovery mechanisms as well as immobilization of mobile dislocations. In his model, the rate of immobile dislocation density $\mathrm{d}N_i^{(\alpha)}/\mathrm{d}t$ on slip system α is given as

$$\mathrm{d}N_i^{(\alpha)}/\mathrm{d}t = \sum_{\alpha \neq \beta} f_1^{(\alpha\beta)} N^{(\beta)} \left(\mathrm{d}p^{(\alpha)}/\mathrm{d}t\right) - w(T) N_i^{(\alpha)} \tag{26.56}$$

$$\mathrm{d}N_m^{(\alpha)}/\mathrm{d}t = \mathrm{d}N^{(\alpha)}/\mathrm{d}t - \mathrm{d}N_i^{(\alpha)}/\mathrm{d}t \tag{26.57}$$

where N is the total dislocation density, N_m is the mobile dislocation density, and $\mathrm{d}p^{(\alpha)}/\mathrm{d}t = \left|\mathrm{d}\gamma_c^{(\alpha)}/\mathrm{d}t\right|$. In Eqn (26.56), the first term represents the immobilization rate with dislocations on slip system α by interactions with the system β. The matrix $f_1^{(\alpha,\beta)}$ is meant to reflect various relative strengths of types of slip system interactions in immobilizing dislocations, following the suggestion of Basani and Wu [88]. The second term in Eqn (26.56) allows for "remobilization" of dislocations by a recovery mechanism such as dislocation climb, in which $w(T)$ is the temperature-dependent empirical recovery function. Moosbrugger [86,87] determined empirical model constants and temperature-dependent functions in his modified HAS model for CdTe, using trial-and-error fitting of the experimental data.

26.3.4.2 Consideration of Dislocation Annihilation

The original HAS model shown in Section 26.3.3.1 allows only for dislocation multiplication and for no dislocation annihilation by the interaction of dislocations with opposite Burgers vectors. Gondet et al. [79] proposed a model to take account of dislocation annihilation. They give the effective shear stress as follows, taking account of the dislocation density in each glide plane:

$$\tau_{eff}^{i} = \left\langle \left|\sigma_{RS}^{(i)}\right| - \frac{Gb}{\beta}\sqrt{N_i} - \frac{Gb}{\beta^*}\sum_{j\neq i}\sqrt{N_j} \right\rangle \tag{26.58}$$

where the superscript (i) and the subscript i denote the glide system under consideration, and j is the other glide system. G is the shear modulus, and β and β^* are constants reflecting the intensity of the interaction.

Gondet et al. [79] give the dislocation multiplication rate as

$$\mathrm{d}N_i^{+}/\mathrm{d}t = \left(K + K^*\sum_{j\neq i}N_j\right)N_i v_i \tau_{eff}^{(i)} \tag{26.59}$$

The first term proportional to N_i accounts for self-multiplication—that is, multiplication on a pinning point created by double cross-slip of the dislocation, for instance. The second term proportional to N_iN_j accounts for dislocation sources on pinning points resulting from intersections between dislocation systems i and j.

Two dislocations gliding in the same system but with opposite signs are likely to annihilate each other. Considering that the phenomenon depends on the dislocation density and velocity, Gondet et al. [79] proposed the following relationship for the dislocation annihilation rate:

$$\mathrm{d}N_i^{-}/\mathrm{d}t = A_o N_i^2 v_i^2 \tag{26.60}$$

where A_0 is the annihilation parameter, the value of which is adjusted in order to get a satisfactory agreement with experimental results. Annihilation is important near the solid–liquid interface of a growing single crystal, which is subjected to high temperatures. Then, the total dislocation density rate becomes

$$\mathrm{d}N_i/\mathrm{d}t = \mathrm{d}N_i^{+}/\mathrm{d}t - \mathrm{d}N_i^{-}/\mathrm{d}t = \left(K + K^*\sum_{j\neq i}N_j\right)N_i v_i \tau_{eff}^{(i)} - A_0 N_i^2 v_i^2 \tag{26.61}$$

According to Orowan's law, the creep shear strain rate is given as follows, considering that annihilated dislocations participated in plasticity before annihilation:

$$\frac{\mathrm{d}\gamma^c}{\mathrm{d}t} = \left(N_i + \frac{\mathrm{d}N_i^{+}}{\mathrm{d}t}\Delta t\right)b v_i \tag{26.62}$$

For an InP single crystal, Gondet et al. gave the values of β and K based on Ref. [64] and those of β^* and K^* based on Ref. [89]. They also determined the value of the annihilation parameter A_0 from the dislocation density analysis [79]. Table 26.9 summarizes the values of parameters used for the dislocation interaction model.

Table 26.9 Parameters Used in the Dislocation Interaction Model for InP Single Crystal

β	β^*	K	K^*	A_0
3.3	2.2	1.2×10^{-2} m/N	10^{-12} m^3/N	5×10^{-7} s

Gondet et al. [79] performed a three-dimensional dislocation density analysis for the growth process of an InP bulk single crystal using the modified HAS model mentioned above. In the creep constitutive equations proposed by Gondet et al., the annihilation term is given by Eqn (26.60) together with the annihilation parameter A_0. They did not provide a reason why the annihilation term is expressed by Eqn (26.60). In addition, the parameter A_0 has only meaning as an adjustment parameter and no physical meaning.

26.3.4.3 Consideration of Different Types of Dislocations

As shown in Figure 26.25, the dislocations in the diamond structure of single crystals, such as Si, GaAs, InP, and InSb, belong mostly to the closely packed (111) system of glide planes with $<110>$ directions. They are screw dislocations, α dislocations, and β dislocations with different mobilities, respectively denoted by S, α and β (Figure 26.25). Kalan and Marniatty [90], Lohonka et al. [91], and Pendurti et al. [92] considered these three kinds of dislocations. According to Ref. [92], the creep shear strain rate $\mathrm{d}\gamma^c/\mathrm{d}t$ is given as follows by extending the Orowan equation:

$$\mathrm{d}\gamma^c/\mathrm{d}t = (N_\alpha v_\alpha + N_\beta v_\beta + N_S v_S)b \tag{26.63}$$

where N_α, N_β, and N_S are respectively the densities of α, β and S dislocations in the (111) plane with the Burgers vector in the $[\bar{1}10]$ direction; v_α, v_β, and v_S are the corresponding velocities; and b is the magnitude of the Burgers vector. According to Ref. [92], $\mathrm{d}\gamma^c/\mathrm{d}t$ is given as follows:

$$\mathrm{d}\gamma^c/\mathrm{d}t = 2N_S v_S b \tag{26.64}$$

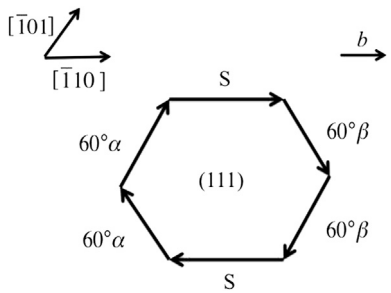

FIGURE 26.25 Geometry of a hexagonal dislocation loop on the (111) plane for a diamond structure of single crystals.

A similar treatment was first proposed by Steinhardt and Haasen [93] and used by Yonenaga et al. [94].

Extension of the multiaxial stress state can be done based on the theory of crystal plasticity [80]:

$$\frac{\mathrm{d}\varepsilon_{ij}^{c}}{\mathrm{d}t} = \sum_{n=1}^{12} 2N_S^{(n)} v_S^{(n)} P_{ij}^{(n)} \tag{26.65}$$

where P_{ij} was given by Eqn (26.51), and the superscript (n) represents the nth slip system.

As for a dislocation multiplication law, Pendurti et al. [92] considered multislip systems and proposed the following equation based on Sumino and Yonenaga's research [89]:

$$\frac{\mathrm{d}N_S^{(i)}}{\mathrm{d}t} = KN_S^{(i)} v_f^{(i)} \tau_{eff}^{(i)} + K^* N_S^{(i)} v_f^{(i)} \tau_{eff}^{(i)} \sum_{f \neq i} f_{ij} N_S^{(i)} \tag{26.66}$$

where the superscript (i) denotes the ith slip system, and $v_f^{(i)}$ is the velocity of the fastest dislocation. Almost the same equation was proposed by Kalan and Maniatty [90]. In the right-hand side of Eqn (26.66), the first term represents an increase in dislocation due to the glide on the slip plane, and the second term represents the formation of jogs on screw dislocation. f_{ij} in Eqn (26.66) is related to the formation of jogs. The value of f_{ij} is 1 when a jog is formed on a screw dislocation of the system i cut by a forest dislocation of system j; otherwise, it is 0. The complete table for the value of f_{ij} is given in Ref. [92]. $\tau_{eff}^{(i)}$ is the effective shear stress necessary for dislocation motion in the ith slip system, as given by

$$\tau_{eff}^{(i)} = \left\langle \left| \sigma_{RS}^{(i)} \right| - \frac{Gb}{\beta} \sqrt{N_S^{(i)}} - \frac{Gb}{\beta^*} \sum_{j \neq i} g_{ij} \sqrt{N_S^{(i)}} \right\rangle \tag{26.67}$$

This equation is essentially the same as Eqn (26.58). The second term on the right-hand side is the self-hardening term, while the third term represents the cross-hardening term together with the parameter g_{ij}, depending on the type of interaction between the dislocations of different slip systems. The values of g_{ij} and other parameters such as K, K^*, β, and β^* for an InP single crystal are calculated from shear stress–shear strain curves experimentally obtained under the constant shear strain rate [92]. Pendurti et al. performed a dislocation density analysis for the high-pressure CZ growth of an InP single crystal, using these parameters; the results are shown in Figure 26.26 [95]. Kalan and Maniatty [90] determined the material parameters for an InP single crystal based on the experimental data. Lohonka et al. [91] obtained the stress–strain curves not only for an InP single crystal but also for GaAs and InSb single crystals by using a modified HAS model that they developed.

26.3.4.4 Consideration of the Immobilization of Mobile Dislocations

In the creep constitutive equations for Si proposed by Gao et al. [96], all material parameters are identified by the experimental data obtained by Cochard et al. [97], and no adjustment parameter, such as A_0 in Eqn (26.60) of Gondet et al.'s research [79], is

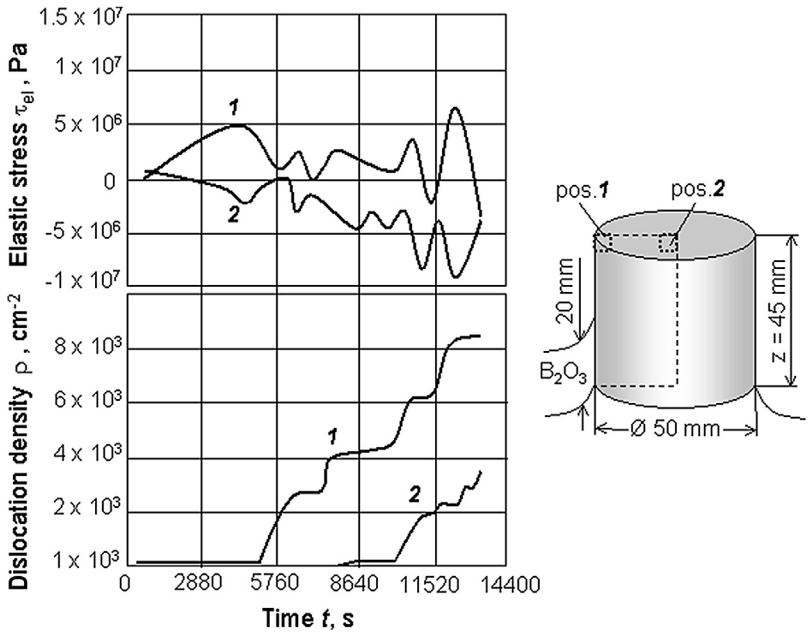

FIGURE 26.26 Sketched stress and dislocation density development with time along a CZ InP crystal considering the boric oxide encapsulation layer. *From Ref. [95] with permission of Springer.*

needed in the creep constitutive equations. In addition, they take account of multislip systems, immobilization of mobile dislocations, the jog formation between different slip systems and its influence on dislocation generation, and the internal stress due to short-range interactions from the total dislocation density.

Here, we summarize the creep constitutive equation for an Si single crystal proposed by Gao et al. The creep strain rate $\mathrm{d}\varepsilon_c^{(\alpha)}/\mathrm{d}t$ is given by the Orowan relationship:

$$\mathrm{d}\varepsilon_c^{(\alpha)}/\mathrm{d}t = N_m^{(\alpha)} v^{(\alpha)} b \tag{26.68}$$

where the subscript m denotes the mobile dislocation, the superscript (α) is the slip system, b is the magnitude of the Burgers vector, N is the dislocation density, and v is the velocity of dislocation. The rate of the mobile dislocation density $\mathrm{d}N_m^{(\alpha)}/\mathrm{d}t$ in the slip direction α is given by

$$\mathrm{d}N_m^{(\alpha)}/\mathrm{d}t = KN_m^{(\alpha)} v^{(\alpha)} \tau_{eff}^{(\alpha)} + K^* N_m^{(\alpha)} v^{(\alpha)} \tau_{eff}^{(\alpha)} \sum_{\beta \neq \alpha} f_{\alpha\beta} N_m^{(\beta)} - 2r_c N_m^{(\alpha)} N_m^{(\alpha)} v^{(\alpha)} \tag{26.69}$$

The above equation is an extension of Eqn (26.66), as proposed by Pendurti et al. [92]. That is, the first and second terms of the right-hand side in Eqn (26.69) are the same as those in Eqn (26.66), and the third term represents the sink for the mobile dislocation (i.e., immobilization). According to Ref. [97], the immobilization rate $\mathrm{d}N_i^{(\alpha)}/\mathrm{d}t$ can be expressed as

$$dN_i^{(\alpha)}/dt = 2r_c N_m^{(\alpha)} N_m^{(\alpha)} v^{(\alpha)} \tag{26.70}$$

The dislocation velocity v is given by

$$v^{(\alpha)} = v_0\left(\tau_{eff}^{(\alpha)}/\tau_0\right)^m \exp\left(-U/kT\right) \tag{26.71}$$

where $v_0 = 500$ m/s, $\tau_0 = 1$ MPa, $m = 1$, and $U = 2.2$ eV for an Si single crystal [97]. The values of K, K^*, and r_c are given as follows [97]:

$$K(T) = 7.6 \times 10^{-1} \exp(-0.72/kT)(\mathrm{m/N}), \quad K^* = 8.0 \times 10^{-15}\mathrm{m^3/N},$$
$$r_c(T) = 7.2 \times 10^{-3} \exp(-1.48/kT)(\mathrm{m}) \tag{26.72}$$

The effective shear stress necessary for dislocation motion is given by

$$\tau_{eff}^{(\alpha)} = \left\langle \left|\sigma_{RS}^{(\alpha)}\right| - \tau_i^{(\alpha)} - \tau_b^{(\alpha)} \right\rangle \tag{26.73}$$

where $\tau_i^{(\alpha)}$ is the stress required to overcome short-range obstacles, and $\tau_b^{(\alpha)}$ is the internal long-range elastic stress generated by mobile dislocation. They are given by [97]

$$\tau_i^{(\alpha)} = Gb\sqrt{\sum_\beta a_{\alpha\beta}\left(N_m^{(\beta)} + N_i^{(\beta)}\right)} \tag{26.74}$$

$$\tau_b^{(\alpha)} = Gb\sum_\beta A_{\alpha\beta}\sqrt{N_m^{(\beta)}} \tag{26.75}$$

where the coefficients $A_{\alpha\beta}$ and $a_{\alpha\beta}$ are summarized in Table 26.10. Then, the total dislocation density and the multiaxial creep strain rate $\mathrm{d}\varepsilon_{ij}^c/\mathrm{d}t$ is expressed by

$$N_m = \sum_{\alpha=1}^{12} N_m^{(\alpha)} \tag{26.76}$$

$$\frac{\mathrm{d}\varepsilon_{ij}^c}{\mathrm{d}t} = \sum_{\alpha=1}^{12} P_{ij}\frac{\mathrm{d}\varepsilon_c^{(\alpha)}}{\mathrm{d}t} \tag{26.77}$$

where P_{ij} is already given by Eqn (26.51).

Using the above-mentioned constitutive equations, Gao et al. [96] performed dislocation density analyses of seed cast-grown Si single crystals in the [001] and [111] growth directions to study the effective reduction of dislocation by controlling the cooling process.

Table 26.10 Long-Range Interaction Coefficients $A_{\alpha\beta}$ and Short-Range Interaction Coefficients $a_{\alpha\beta}$ for Si Single Crystal

Interaction	Self	Coplanar	Collinear	Hirth Locks	Lomer Locks	Glissile Junction
$A_{\alpha\beta}$	0.21	1/16	1/20	1/12	1/12	1/12
$a_{\alpha\beta}$	0.09	0.09	0.41	0.06	0.12	0.12

26.4 Summary

The research activities related to the solid mechanics and mechanical strength of the crystal growth process and crystal annealing process are reviewed in this chapter. Although single crystals are the basic materials supporting the present advanced technologies and such research activities play an important role in manufacturing high-quality single crystals, only a few researchers have been involved in such research activities. It is hoped that more researchers will take part in such research activities.

The finite element method is a powerful tool for the stress analysis of solids. It can be applied not only to elastic thermal stress problems of single crystals, taking account of anisotropy in elastic constants and thermal expansion coefficients, but also to nonlinear analysis such as dislocation density problems, in which the rate of creep strain or viscoplastic strain is related to dislocation density. The finite element method is one of the numerical methods for boundary value problems of partial differential equations, and it provides very accurate solutions if an appropriate finite element modeling is used.

To make progress in research, we need the material properties and deformation behaviors of single crystals at very high temperatures near the melting point. We need material properties near the melting point in cases of thermal stress and dislocation density analyses during crystal growth. Although a large research project called Kimura Metamelt [98] was organized by the Japan Science and Technology Agency to measure the various properties of the Si melt and oxide melts, no research project has been performed to clarify the mechanical behaviors of single crystals under elevated temperatures near the melting point. Even for elastic constants and thermal expansion coefficients of single crystals, we have no experimental data near the melting point. We have to extrapolate the measured data to the melting point to get the material properties near the melting point. It is much more difficult to get stress–strain curves under constant strain rates at elevated temperatures near the melting point, which are required to formulate constitutive equations for creep.

We are expecting both experimental and numerical research concerning the mechanical behaviors of single crystals at elevated temperatures. Atomistic simulation techniques, such as the first-principle calculation and molecular dynamics method, for example, are promising tools for obtaining the mechanical behaviors of single crystals at elevated temperatures. Simulation techniques based on computational mechanics, such as the finite element method, will provide more useful information to establish the manufacturing process of high-quality single crystals, if the mechanical behaviors of single crystals at elevated temperatures are properly represented by material properties, such as elastic constants, thermal expansion coefficients, and creep constitutive equations.

References

[1] Brown RA. AIChE J 1988;34:881.

[2] Kakimoto K. J Appl Phys 1995;77:1827.

[3] Rudolph P, Jurisch M. J Cryst Growth 1999;198–199:325.

[4] Müller G. J Cryst Growth 2002;237–239:1628.

[5] Müller G, Friedlich J. J Cryst Growth 2004;266:1.

[6] Lan CW. Chem Eng Sci 2004;59:1437.

[7] Miyazaki N. J Cryst Growth 2007;300:452.

[8] Miyazaki N. J Cryst Growth 2007;303:302.

[9] Prasad V, Pendurti S. In: Dhanaraj G, Byrappa K, Prasad V, Dudley M, editors. Springer handbook of crystal growth. Springer, Heidelberg; 2010. p. 1335.

[10] Jordan AS, Von Neida AR, Caruso R. J Cryst Growth 1984;70:555.

[11] Kobayashi N, Iwaki T. J Cryst Growth 1985;73:96.

[12] Dupret F, Nicodeme P, Ryckmans Y. J Cryst Growth 1989;97:162.

[13] Tsukada T, Hozawa M, Imaishi N. J Chem Eng Jpn 1990;23:186.

[14] Lambropoulos JC. J Cryst Growth 1987;84:349.

[15] Lambropoulos JC. J Mater Res 1988;3:531.

[16] Miyazaki N, Hagihara S, Munakata T. J Cryst Growth 1990;106:149.

[17] Miyazaki N, Uchida H, Hagihara S, Munakata T, Fukuda T. J Cryst Growth 1991;113:227.

[18] Miyazaki N, Uchida H, Munakata T, Fujioka K, Sugino Y. J Cryst Growth 1992;125:102.

[19] Nye JF. Physical properties of crystals. Oxford: Clarendon Press; 1957.

[20] Miyazaki N, Uchida H, Tsukada T, Fukuda T. J Cryst Growth 1996;162:83.

[21] Miyazaki N, Tamura T, Kurashige K, Ishibashi H, Susa K. J Cryst Growth 1997;182:73.

[22] Miyazaki N. J Cryst Growth 2002;236:455.

[23] Miyazaki N, Imahase D. Simulation 2001;20:274 [in Japanese].

[24] Miyazaki N, Uchida H, Munakata T, Fukuda T. JSME Int J Ser A 1994;37:124.

[25] Jordan AS, Caruso R, Von Neida AR. Bell Syst Tech J 1980;59:593.

[26] INSPEC. Properties of silicon, EMIS datareview series, No.4. The Institute of Electrical Engineers; 1988. 14.

[27] Jordan AS. J Cryst Growth 1980;49:631.

[28] Jordan AS. J Cryst Growth 1985;71:559.

[29] Brantley WA. J Appl Phys 1973;44:534.

[30] Brandle CD, Miller DC. J Cryst Growth 1974;24–25:432.

[31] Brice JC. J Cryst Growth 1977;42:427.

[32] Tsukada T, Hozawa M, Imaishi N. J Chem Eng Jpn 1994;27:25.

[33] Smith RT, Welsh FS. J Appl Phys 1971;42:2219.

[34] Gallagher PK, O'Bryan HM. J Am Ceram Soc 1985;68:147.

[35] Bonner WA, Zydzik GJ. J Cryst Growth 1970;7:65.

[36] Loiacono GM, Balascio JF, Bonner R, Savage A. J Cryst Growth 1974;21:1.

[37] Takano S, Easashi S, Mori K, Namikata T. J Cryst Growth 1974;24–25:437.
[38] Lim LC, Tan LK, Zeng HC. J Cryst Growth 1996;167:686.
[39] Senguttuvan N, Moorthy Babu S, Subramanian C. Mater Sci Eng 1997;B47:269.
[40] Senguttuvan N, Moorthy Babu S, Dhanasekaran R. Mater Chem Phys 1997;49:120.
[41] Zeng HC. J Cryst Growth 1997;171:136.
[42] Sabharwal SC, Sangeeta, Desai DG. Cryst Growth Des 2006;6:58.
[43] Miyazaki N, Matuura Y, Imahase D. J Cryst Growth 2006;289:659.
[44] Coquin GA, Pinnow DA, Warner AW. J Appl Phys 1971;42:2162.
[45] Rudolph P. Cryst Res Technol 2005;40:7.
[46] Takagi K, Fukazawa T. Appl Phys Lett 1983;42:43.
[47] Ishibashi H, Shimizu K, Susa K, Kubota S. IEEE Transactions Nucl Sci 1989;36:170.
[48] Ishibashi H, Kurata Y, Kurashige K, Susa K. Proc Int Workshop Heavy Scintillators Sci Industrial Appl Crystal 2000;1993:389.
[49] Miyazaki N, Tamura T, Yamamoto K. CMES-Computer Model Eng Sci 2000;1:99.
[50] Kurashige K, Kurata Y, Ishibashi H, Susa K. Jpn J Appl Phys 1997;36:2242.
[51] Miyazaki N, Tamura T, Yamamoto K, Kurashige K, Ishibashi H, Susa K. J Mater Sci Lett 1998;17:935.
[52] Miyazaki N, Hattori A, Uchida H. J Mater Sci Mater Electron 1997;8:133.
[53] Miyazaki N, Koizumi K. J Mater Sci 2006;41:6313.
[54] Matakef S, Witt AF. J Cryst Growth 1987;80:37.
[55] Jordan AS, Caruso R, Von Neida AR, Nielsen JW. J Appl Phys 1981;52:3331.
[56] Jordan AS, Von Neida AR, Caruso R. J Cryst Growth 1986;76:243.
[57] Zhmakin IA, Kulik AV, Karpov S Yu, Demina SE, Ramm MS, Makarov Yu N. Diam Relat Mater 2000; 9:446.
[58] Wu B, Ma R, Zhang H, Dudley M, Schlesser R, Sitar Z. J Cryst Growth 2003;253:326.
[59] Alexander H, Haasen P. Solid State Phys 1969;22:27.
[60] Suezawa M, Sumino K, Yonenaga I. Phys Status Solidi (a) 1979;51:217.
[61] Dillon Jr OW, Tsai CT, De Angelis RJ. J Appl Phys 1986;60:1784.
[62] Tsai CT, Dillon Jr OW. Int J Solids Struct 1987;23:387.
[63] Tsai CT, Dillon Jr OW, De Angelis RJ. J Cryst Growth 1987;82:695.
[64] Völkl J, Müller G. J Cryst Growth 1989;97:136.
[65] Maroudas D, Brown RA. J Cryst Growth 1991;108:399.
[66] Motakef S, Kelly KW, Koai K. J Cryst Growth 1991;113:279.
[67] Tsai CT. J Cryst Growth 1991;113:499.
[68] Tsai CT, Gulluoglu AN, Harley CS. J Appl Phys 1993;73:1650.
[69] Tsai CT, Subramanyam N. Model Simul Mater Sci 1995;3:93.
[70] Zhu XA, Tsai CT. J Appl Phys 2000;88:2295.
[71] Miyazaki N, Okuyama S. J Cryst Growth 1998;183:81.
[72] Miyazaki N, Kuroda Y. Metals Mater 1998;4:883.
[73] Miyazaki N, Kuroda Y. J Cryst Growth 1999;196:62.

[74] Lambropoulos JC, Wu CH. J Mater Res 1996;11:2163.

[75] Tsai CT, Dillon Jr OW, De Agelis RJ. J Eng Mater Technol 1990;112:183.

[76] Miyazaki N, Kuroda Y. JSME Int J Ser A 1999;42:485.

[77] Miyazaki N, Kuroda Y, Sakaguchi M. J Cryst Growth 2000;218:221.

[78] Miyazaki N, Sakaguchi M. Transactions JSME, Ser A 2002;68:21 [in Japanese].

[79] Gondet S, Duffar T, Louchet F, Theodore F, Van Den Bogaert N, Santailler JL. J Cryst Growth 2003; 252:92.

[80] Asaro RJ. J Appl Mech 1983;50:921.

[81] Barrett DL, McGuigan S, Hobgood HM, Eldridge GW, Thomas RN. J Cryst Growth 1984;70:174.

[82] Miyazaki N, Kutsukake H, Kumamoto A. J Cryst Growth 2002;243:47.

[83] Miyazaki N, Yamamoto S, Kutsukake H. J Cryst Growth 2000;216:6.

[84] Miyazaki N, Kumamoto A, Harada C. J Cryst Growth 2004;271:358.

[85] Kouno J, Yosida H, Kawase T, Sawada S, Nakai R, Tatsumi M. SEI Tech Rev 2001;158:65 [in Japanese].

[86] Moosbrugger JC. Int J Plasticity 1995;11:799.

[87] Moosbrugger JC, Levy A. Metallurgical Mater Transactions A 1995;26A:2687.

[88] Bassani JL, Wu TY. Proc Royal Soc A 1991;435:21.

[89] Sumino K, Yonenaga I. Phys Status Solidi (a) 1993;138:573.

[90] Kalan RJ, Mainiatty AM. J Cryst Growth 2001;233:645.

[91] Lohonka R, Vanderschaeve G, Kratochvil J. Mater Sci Eng 2002;A337:50.

[92] Pendurti S, Prasad V, Zhang H. Model Simulations Mater Sci Eng 2005;13:249.

[93] Steinhardt H, Haasen P. Phys Status Solidi (a) 1978;49:93.

[94] Yonenaga I, Onose U, Sumino K. J Mater Res 1987;2:252.

[95] Rudolph P. In: Dhanaraj G, Byrappa K, Prasad V, Dudley M, editors. Handbook of Crystal growth. Berlin: Springer; 2010. p. 159.

[96] Gao B, Nakano S, Harada H, Miyaura Y, Kakimoto K. Cryst Growth & Des 2013;13:2661.

[97] Cochad J, Yonenaga I, Gouttebroze S, M'Hamdi M, Zhang ZL. J Appl Phys 2010;107:033512.

[98] http://www.jst.go.jp/erato/en/research_areas/completed/kyd_P.html.

27 Defect Generation and Interaction during Crystal Growth

Helmut Klapper[1], Peter Rudolph[2]

[1]INSTITUTE OF CRYSTALLOGRAPHY, RWTH AACHEN UNIVERSITY, AACHEN, GERMANY;
[2]CRYSTAL TECHNOLOGY CONSULTING, SCHÖNEFELD, GERMANY

CHAPTER OUTLINE

27.1 Introduction **1094**
27.2 Point Defects **1096**
27.2.1 Native Point Defect Thermodynamics 1096
27.2.2 Point Defect Dynamics 1098
27.2.3 Extrinsic Point Defect Incorporation 1100
27.2.4 Native and Extrinsic Point Defect Interaction (Complex Formation) 1101
27.2.5 Point Defect Engineering 1103
27.3 Dislocations **1105**
27.3.1 Growth Dislocations and Postgrowth Dislocations 1105
27.3.2 Sources of Growth Dislocations 1105
27.3.3 Propagation of Growth Dislocations 1106
27.3.3.1 Characteristic Configurations, Theory of Preferred Direction 1106
27.3.3.2 Verification of the Minimum Energy Approach and Examples 1110
27.3.4 Postgrowth Dislocations 1111
27.3.5 Dislocation Dynamics (Patterning, Cell Structures, Clustering) 1111
27.3.6 Dislocation Engineering 1119
27.4 Grain Boundaries **1121**
27.4.1 Dynamic Polygonization-Low-Angle Grain Boundaries 1121
27.4.2 Large-Angle Grain Boundaries-Polycrystallinity 1123
27.5 Foreign Phase Particles **1125**
27.5.1 Precipitates (Retrograde Solidus, Defect Decoration) 1125
27.5.2 Solvent Inclusions 1126
27.5.2.1 Faceting ("Capping") of Rounded Surfaces 1126
27.5.2.2 Fluctuation of Growth Conditions (Growth Accidents) 1128
27.5.3 Melt Growth Inclusions 1129
27.5.4 Structural Consequences of Second-Phase Particles 1129

Handbook of Crystal Growth. http://dx.doi.org/10.1016/B978-0-444-63303-3.00027-4
Copyright © 2015 Elsevier B.V. All rights reserved.

27.6 Faceting and Twinning 1130
27.6.1 Faceting during Growth 1130
27.6.2 Growth Twins and Postgrowth Twins 1131
27.6.4 Measures to Avoid Twinning 1135
27.7 Concluding Remarks 1136
References 1136

27.1 Introduction

The quality of single crystals (and the devices made from them) is very sensitive to atomistic and structural deficiencies generated during the crystal growth process. This is one of the main challenges for crystal growers to determine the conditions for the control, minimization, or even prevention of deficiencies.

Most of the important defect-forming mechanisms are well understood, as summarized by Hurle and Rudolph [1]. Today, an enormous body of knowledge exists about the defect genesis in as-grown crystals, supported by demanding theoretical fundamentals and computational modeling. As a result, the present state of technology makes it possible to produce crystals of remarkably high quality, with tailored parameters that fit the demands of the device industry quite well. However, not all problems have been solved. This chapter includes still-open questions and investigates the optimal measures of defect engineering.

The international standard crystal lattice defects (in short, defects) are usually classified according to their dimensions, as described in the following sections (e.g., Ref. [2]).

Zero-dimensional defects

Zero-dimensional defects are *point defects*, often called by the unpopular name *atomic size defects*, which include the intrinsic defect types *vacancies*, *interstitials*, and, in compounds, *antisites*. If extrinsic atoms are introduced unintentionally (as residual *impurities*) or intentionally (as *dopants*), they occupy interstitial or substitutional (lattice) positions. At growth temperatures, the point defects are isolated and usually electrically charged. The charge state of point defects can lead to their interaction with electrically active dopants, creating *point defect complexes*.

One-dimensional defects

One-dimensional defects include all kinds of *dislocations*, such as perfect screw and edge dislocations, mixed dislocations, partial dislocations (always in connection with a stacking fault), and dislocation loops. In crystals growing under low- or zero-temperature gradients and in their brittle state (e.g., from solutions), dislocations usually originate from inclusions and propagate with the growing face. In crystals growing at

high temperatures and under temperature gradients in their plastic state (e.g., from melts), the propagation and interaction of dislocations over mesoscopic distances are the subjects of *dislocation dynamics*.

Two-dimensional defects

Two-dimensional defects are grain boundaries, stacking faults, phase boundaries, facets, and twins. A *low-angle grain boundary* structure is formed by the mechanism of dynamic polygonization (DP) and belongs conventionally still to a single crystalline state. In contrast, *large-angle grain boundary* structures are formed by polycrystalline growth due to spontaneous or foreign nucleation processes. *Facets* are formed along atomically smooth planes, indicating the tendency of high-quality crystals to form polyhedra. *Growth twins* originate from a false stacking sequence, especially when the two-dimensional nucleus on a growing facet is disoriented.

Three-dimensional defects

Three-dimensional defects include second-phase particles (*precipitates*), intrinsic vacancy conglomerates (*microvoids*), and foreign particles (*inclusions*). It is important to differentiate between precipitates and inclusions, which are often mixed up in the literature. Precipitates and microvoids are formed by supersaturation-driven condensation of intrinsic point defects (i.e., interstitials and vacancies, respectively), whereas inclusions are melt-solution droplets, gas bubbles, and foreign microparticles incorporated at the growing melt–solid interface, especially when the melt composition is deviated from the congruent melting point or contaminations are presented.

Defects have deleterious effects on the performance, reliability, and degradation behavior of devices. Following the early classification of Pick [3], defects influence the following:

- Structural properties (vacancies and interstitials may change the lattice constant; grains affect the single crystallinity)
- Chemical properties (defects participate in chemical reactions; their redistribution causes composition inhomogeneities)
- Electronic properties (defects occupy a specific state in the band structure)
- Scattering properties, or the defect interaction with particles (phonons, photons of any energy, electrons, positrons, etc.)

As can be seen, the interaction processes are many-sided and require broad interdisciplinary research with direct correlation to advanced technical progress. In fact, a large part of the world's technological progress depends on the control and manipulation of defects in crystals, particularly in the semiconductor, optical, and biotechnology industries. An enormous number of monographs and publications deal with this subject. In this chapter, however, only selected examples of defect impacts are discussed.

27.2 Point Defects

27.2.1 Native Point Defect Thermodynamics

In growing crystals at all temperatures above absolute zero, the total concentration of native (intrinsic) point defects (consisting of vacancies, self-interstitials, and, in the case of compounds, antisite defects) strive toward a thermodynamic minimum that does not reach zero. In other words, point defects are always present. This is also due to the increase of configurational entropy, leading to the decrease of total Gibbs free energy. Realistically, at low temperatures, such as 300 K, the equilibrium is rarely obtained. This is primarily due to the decreasing point defect diffusivity in the course of cooling down of the as-grown crystals, freezing the superior equilibrium concentration at much higher temperatures. Thus, it is not possible to grow an absolutely perfect (point defect-free) crystal. In reality, only an "optimal" crystalline state can be obtained, not an "ideal" one.

Neglecting the effects of volume change, defect interaction, and local vibration state around the defect, at constant pressure the change of the Gibbs potential caused by adding, for example, n vacancies (Schottky defects) can be written as

$$\Delta G = H_d - S_d T \tag{27.1}$$

where $H_d = nE_d$ is the internal energy of n defects, having a total defect formation energy E_d, and $S_d = k \ln W = k \ln(N!)/[n!(N-n)!]$ is the accompanying change of configuration entropy. W is the number of ways in which N atoms and n point defects can be arranged, and k is the Boltzmann constant. After substitution and application of Stirling's approximation $[\ln N! \approx N \ln N, \ln n! \approx n \ln n, \ln(N-n)! \approx (N-n)\ln(N-n)]$ for multiparticle systems such as a crystal, Eqn (27.1) becomes

$$\Delta G = nE_d - kT[N \ln N - n \ln n - (N-n)\ln(N-n)]. \tag{27.2}$$

Setting the first derivative of Eqn (27.2) $\partial \Delta G/\partial n = 0$, which equals the energetic minimum defect concentration n_{min}, and considering $N >> n$, the "perfection limit" of the crystal is

$$n_{min} = N \exp(-E_d/kT), \tag{27.3}$$

increasing exponentially with T.

Figure 27.1 shows the realistic (Schottky) point-defect excess against the thermodynamic minimum when a restricted mobility (diffusivity) is considered.

In the case of formation of vacancy-interstitial complexes (Frenkel defects), the value of $n_{min}^{(F)}$ is somewhat modified and yields $\sqrt{N_{is}N}\exp(-E_d^{(F)}/kT)$, with N_{is} being the total number of interstitial positions (depending on the given crystal structure) and $E_d^{(F)}$ being the formation energy of a Frenkel defect. More fundamental details are given in Kröger's compendium [4].

The typical energies of isolated neutral point defects E_d are in the region between 1 and 5 eV. Usually at high temperatures, point defects are electrically charged and therefore show a certain affinity to complex formation with other point defects or

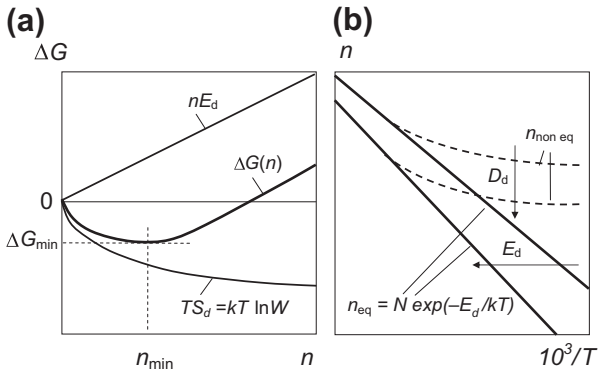

FIGURE 27.1 (a) Sketched equilibrium point defect (Schottky) concentration n_{min} at a given temperature T, obtained by superposition of defect enthalpy $H_d = nE_d$ and configurational entropy $S_d = k \ln W$ using Eqns (27.1)–(27.3). (b) Two equilibrium defect concentrations n_{eq} of various defect energies E_d vs reciprocal temperature $10^3/T$ following Eqn (27.3). The dashed lines show the nonequilibrium ("frozen") curves obtained in reality due to decreasing defect diffusivity D_d with decreasing T.

present impurities. Depending on the crystal structure and temperature, their diffusivities vary near the crystal melting points between 10^{-5} and 10^{-4} cm^2/s. Note that the values given in the literature, mostly obtained by numeric modeling such as quantum Monte Carlo or density functional theory, can differ substantially. The reason for this includes the specification of point defect configuration, such as the number and arrangements of neighboring atoms, and also the careful examination of electron density (as reported for silicon [5]).

The intrinsic point defect situation is best known in high-purity silicon crystals growing from the melt. This has been intensively studied by Voronkov [6]. It was found that there are remarkably low concentrations of both vacancies and interstitials in the order of 5×10^{14} cm^{-3} at melt temperature T_m and very high diffusivities of 3×10^{-4} and 5×10^{-4} cm^2/s, respectively. At the growing interface, vacancy and interstitial fluxes take place, which are both directed into the crystal. Although one flux component is driven by the propagating growth interface (i.e., the crystallization (pulling) velocity v), the second one is driven by a temperature-dependent vacancy-interstitial recombination behind the interface, which creates a concentration gradient with Fickian diffusion flow and is proportional to the temperature gradient G_T. At high crystallization rates, the first component dominates, leading to a higher vacancy flow into the crystal. This is due to their lower formation energy (~4.0 eV) than that of self-interstitials (~4.8 eV). In contrast, at low crystallization velocities, the diffusion is dominant and leads to an excess of interstitials due to their larger diffusivity than vacancies. The type and concentration of "surviving" point defects is controlled by the v/G_T ratio, which is for Czochralski growth larger in the crystal core than in the peripheral regions, thus leading to different vacancy and interstitial excesses in both regions. The critical transition ratio for which vacancy and self-interstitial fluxes are equal and the recombination is optimal is $v/G_T = 1.34 \times 10^{-3}$ cm^2/K/min, as summarized by von Ammon [7]. A given native point defect content belongs to each crystalline phase like a "solute component" in a system of ideal mixing. When the defect solubility is exceeded, the dominant point defects begin to conglomerate, forming defects of higher order, such as microvoids, due to vacancy

condensation and precipitates due to interstitial fusion. Usually, such defects are generated during the cooling-down process because of the retrograde behavior of the existing solubility limits. For instance, in vacancy-rich silicon crystals, characteristic microvoids with dimensions of 100 nm are formed [8].

Compared with elementary materials (metals, Ge, Si), in compound crystals (e.g., alloys, $A_{II}B_{IV}$, $A_{III}B_{V}$, dielectric and organic compounds) additional antisite defects and a characteristic phase region (called the existence or homogeneity region) are present. Depending on the temperature and atomic interaction energies, the solubility of point defects of the given excess component (e.g., A or B interstitials in AB, respectively) deviates more or less from that of the stoichiometric composition (AB). Then, at a given T, the deviation δ of the concentrations of the present native point defects in each sublattice can be estimated as follows [4,9]:

$$\delta = \delta A - \delta B = \{[A_i] - [V_A] + 2[A_B] - 2[B_A]\} - \{[B_i] - [V_B] + 2[B_A] - 2[A_B]\} \tag{27.4}$$

with $[A_i]$, $[B_i]$, $[V_A]$, $[V_B]$, $[A_B]$, and $[B_A]$ being the interstitial, vacancy, and antisite contents, respectively.

As can be seen from Figure 27.2, the shape and maximum width of the phase extent are material-specific features from concentrations of 10^{-5} (e.g., InP [10], Figure 27.2(a)) up to several mole fractions (e.g., $LiNbO_3$ [11], Figure 27.2(d)). Due to the retrograde behavior of the solidus curves, the crystals pass during cooling through a process of excess point defect condensation, which may generate second-phase particles (see Section 27.5.1). Note that there are compounds in which the homogeneity region is located off the stoichiometric composition, making it quasi-impossible to grow second-phase free crystals (e.g., SnTe [12], Figure 27.2(c)). Even for GaAs, thermochemical calculations [13] confirmed the earlier and newer growth observations [14] showing that the phase extent is deviated exclusively toward the arsenic-rich side (Figure 27.2(a)).

Thus, nonstoichiometric point defects play a role because the crystallization path starts always usually at the boundary (solidus) of the existence region but not at exact stoichiometry. This is also the case in solution growth dealing mostly with compounds. However, compared with melt growth, the situation is much more advantageous due to its considerably smaller extent at low temperatures. In this way, for growth from solutions or fluxes, the crystal composition approaches stoichiometry with a much smaller content of native point defects.

27.2.2 Point Defect Dynamics

Principally, the energetic interplay between point defect types, the applied temperature field consisting of gradients and fluctuations, crystallization rate, differing growth kinetics along various crystal planes, and out-diffusion through the crystal surface under real growth conditions cause marked deviations from the thermodynamic equilibrium. As already mentioned, the related point defect dynamics have been well studied in silicon crystals [6]. In semiconductor and oxide compound crystals, however, these

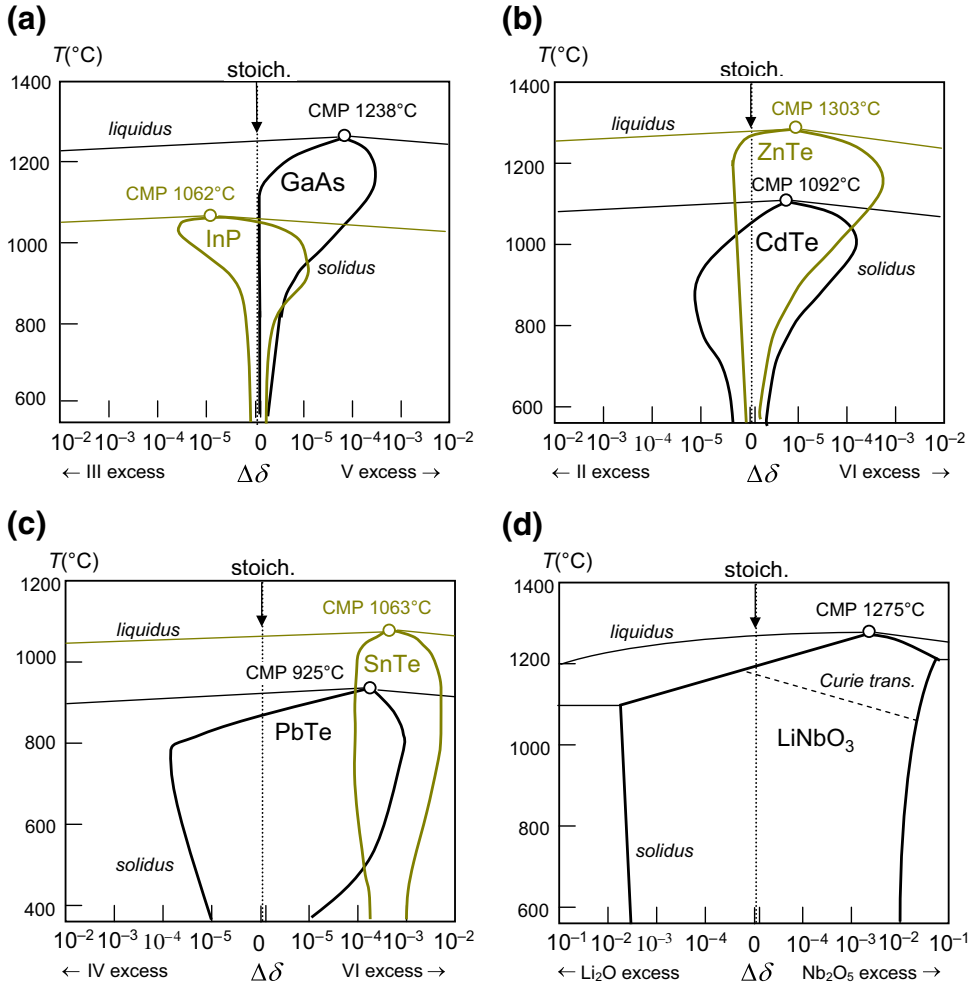

FIGURE 27.2 Selected phase projections of various compounds showing the diverseness of shape and deviation of the existence region $\Delta\delta$ from stoichiometry and temperature. (a) GaAs and InP; ZnTe and CdTe; SnTe and PbTe; CMP, congruent melting point [10–15].

processes are not nearly as well understood. One reason is that the presence of dislocations acting as effective point defect getters hampers point defect analysis in its pure form. Furthermore, as follows from Eqn (27.4), the situation in multicomponent materials is complicated due to the presence of equivalent defect types and antisites in each sublattice. For instance, it has been established that As_{Ga} antisites in GaAs crystals, known as neutral EL2 defects with the charged states $EL2^{+}$ and $EL2^{2+}$, do not appear at the growth temperature but form during the cooling-down process only. In materials grown from a near-congruent composition (i.e., slightly As-rich melt), the As_i content removes the $[V_{Ga}]$ by producing As_{Ga} as soon as the lowering temperature evokes

supersaturation [9]. A nearly identical mechanism takes place in CdTe. In cooling Te-saturated samples, the antisite Te_{Cd} is formed and may become important as singly- and doubly-ionized midgap donors $Te_{Cd}^{1+,2+}$ that are responsible for the compensation of the shallow native acceptor $V_{Cd}^{1-,2-}$ [16].

For estimation of the defect trapping kinetics along a propagating melt-solid interface, one first must clarify whether the front moves by atomically rough or smooth morphology [17]. Although metals show atomically rough interfaces, dielectrics crystallize mostly with atomically smooth interfaces; the semiconductor materials stand in between. Semiconductors with diamond, zinc blende, and wurtzite structures grow from the melt along most directions by the atomically rough mode. However, they tend to form atomically smooth interfaces on their most closely packed {111} planes. On atomically rough interfaces, atoms can be added singly without the need for nucleation—that is, at a very low chemical potential difference between solid and liquid phases. As a result, possible defect sites are added to the crystal under quasi-equilibrium conditions. On the contrary, for atomically smooth planes, much higher supercooling is required in order to initiate two-dimensional nucleation followed by layer-by-layer growth. In such a case, vacancies, interstitials, and foreign atoms can be overgrown very rapidly; hence, they can be incorporated in metastable states in much higher concentrations than equilibrium if their diffusion-back rate into the melt is not high enough [18,19].

One can assume that the fluid phase provides sufficient imperfections due to its "structural" instability and disordered character. According to Motooka's molecular dynamics simulations [20], point defects can be formed directly at the interface due to the density misfit between the liquid and solid phases.

The same situation takes place when extrinsic point defects (foreign atoms, such as impurities) are presented. On atomically smooth planes, they can be made quasi-metastable by enhanced concentrations due to the high-speed lateral layer-by-layer overgrowth that downplays the effect of segregation.

27.2.3 Extrinsic Point Defect Incorporation

As was introduced in Section 27.1, the term *extrinsic point defect* describes unintentionally and intentionally present foreign atoms such as residual impurities and dopants, respectively. They occupy interstitial or substitutional (lattice) positions. When growing crystals with dopant concentrations below the solubility limits, the matrix contributes one component in the phase diagram and the solute contributes another. Thus, the system can be considered as binary. The equilibrium between the chemical potentials of the species involved in the liquid (i.e., solvent) i and solid phases $\mu_{il}(x,T) = \mu_{is}(x,T)$ yields

$$\mu_{is}^{o} + kT \ln x_{is}\gamma_{is} = \mu_{il}^{o} + kT \ln x_{il}\gamma_{il} \tag{27.5}$$

where μ^o is the standard potential and γ is the interaction activity between i and atoms or molecules of the matrix. Setting $\mu_{il}^{o} - \mu_{is}^{o} = \Delta\mu_i^o = \Delta h_i^o - \Delta s_i^o T$ and $s_i^o = h_i^o/T_{mi}$, with

h_i^o, s_B^o as the intensive standards enthalpy and entropy, respectively; T_{mi} as melting point of the dopant; and $\Delta h_{Mis,l}^o = kT \ln \gamma_{is,l}$ as the mixing enthalpy, the transformed Eqn (27.5) becomes [21]

$$\frac{x_{is}}{x_{il}} = k_o = \exp\left[-\frac{\Delta h_i^o}{k}\left(\frac{1}{T} - \frac{1}{T_{mi}}\right) + \frac{\Delta h_{Mil} - \Delta h_{Mis}}{kT}\right] \tag{27.6}$$

with $k_o = x_{is}/x_{il}$ being the (thermodynamic) equilibrium distribution (or segregation) coefficient, which can be assumed as a constant for residual impurity or low dopant concentrations if the solidus and liquidus curves allow their linearization.

The homogeneous redistribution of dopants (and also impurities) along the growing crystal proves to be a great challenge for the crystal grower. The deviation of the equilibrium distribution coefficient k_o (Eqn (27.6)) from unity causes segregation phenomena during melt and solution growth, which can be treated in terms of an effective segregation coefficient $k_{eff} = x_{is}/x_{il}^{(\infty)}$, with $x_{il}^{(\infty)}$ being the mole fraction of the dopant or impurity in the fluid far away from the crystallizing interface. During the solidification process, the solute is rejected ($k_o < 1$) or preferentially absorbed ($k_o > 1$) by the propagating solid–liquid interface, forming an enriched or depleted solute boundary layer in front of it. The width δ_s of this boundary layer is determined by the growth rate R and by the diffusive and convective species transport in the melt, which is very often difficult to predict. A very popular model that is commonly used in melt growth was introduced by Burton, Prim, and Slichter (BPS) [22] for the steady state of segregation:

$$k_{eff} = \frac{k_o}{k_o + (1 - k_o)\exp(-R\delta_s/D)} \tag{27.7}$$

Thus, when characteristic convective fluctuations in the melt cause related R oscillations, the k_{eff} varies accordingly. As a result, mesoscopic transversal impurity or dopant inhomogeneities ("striations") are generated. More details, especially on quantification of the δ_s value depending on the melt convection regime, are given by Müller and Ostrogorsky [23] and also in this volume by Ostrogorsky and Glicksman (see Chapter 25).

27.2.4 Native and Extrinsic Point Defect Interaction (Complex Formation)

Impurities and dopants are incorporated on lattice sites or interstitial positions. In compounds, depending on their position in the periodic table, the foreign atoms may occupy one or both sublattice sites. In general, their incorporation efficiency is affected by the present intrinsic point defects, which at growth temperatures can be isolated and are usually electrically charged [9]. (Note that in undoped silicon, the self-interstitials are assumed to be electrically neutral but negatively charged in n-doped Si and positively charged in p-doped Si [24]—an often-observed phenomenon in many materials.) Generally, the charge state of point defects depends on the Fermi position

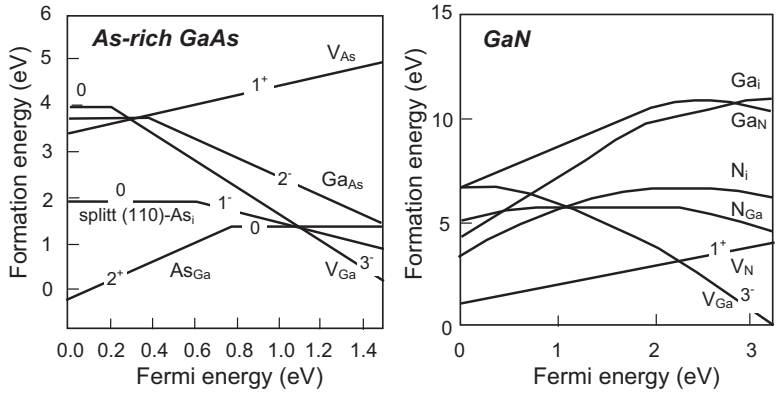

FIGURE 27.3 Dependence of native point defect formation energies and ionization levels of native point defects on the Fermi energy in As-rich GaAs [27] and GaN [28]. Ionization levels are added.

leading to their complex interaction with electrically active dopants. As a result, the dopant solubility can be markedly influenced and, controversially, doping can affect the native point defect solubility and also the formation energy. This phenomenon has been well known for a long time in numerous melt-grown semiconductor compounds, such as GaAs doped with Te and Si [25], CdTe doped with Ag and Cu [26], and GaN. As can be seen from Figure 27.3, in GaN the native V_{Ga} and V_N defects show the lowest formation energies, leading at n-doping to the highest presence of the acceptor-type V_{Ga} [29]. However, p-type GaN is difficult to obtain because of its highest concentration of the shallow donator V_N with the lowest formation energy in such material [28].

The influence of the electron or hole concentration generated by the ionized impurities and dopants X^z on the charge state of the native point defects is called the Fermi level effect [27], whereby the degree of ionization z depends on the position of the Fermi level [30] (Figure 27.3). For instance, the charge state of the Ga vacancy in GaAs changes from neutral V_{Ga}^{o} in p-type material over double-negatively-charged V_{Ga}^{2-} in the midgap to a triple-negatively-charged V_{Ga}^{3-} in n-type material that affects the compensation level and enhances the *complex formation* probability as well. An example of a complex reaction in the common form is

$$\left(V_A^{3-} + 3h\right) + \left(X_B^{+} + e\right) \leftrightarrow \left(V_A X_B\right)^{2-} + 2h \tag{27.8}$$

This can be found in the form of $[Te_{As}V_{Ga}]^{2-}$ or $[Si_{Ga}V_{Ga}]^{-}$ in GaAs crystals or in the form of neutral $[V_{Ga}O_N]$ complex in GaN stabilizing the V_{Ga} presence during the cooling-down process [29].

Thus, nonstoichiometry in compound crystals influences the incorporation efficiency of impurities and dopants as well. Larger deviations from stoichiometric composition during growth lead to higher possibilities of vacancy generation within the compositionally impoverished sublattice. As a result, the incorporation density of atoms at the

growing interface occupying these vacant sites increases with nonstoichiometry. This was demonstrated by Rudolph et al. [26], who grew CdTe crystals by a vapor pressure–controlled Bridgman method from different melt compositions containing silver as the dopant. At near-stoichiometric growth conditions, the concentration of Ag^{o}_{Cd} is drastically reduced down to 2×10^{13} cm^{-3}. Compared to that, a Te excess of 5×10^{17} cm^{-3} leads to an incorporation of Ag atoms on V_{Cd} sites of about one order of magnitude higher concentration.

27.2.5 Point Defect Engineering

To ensure specified electrical and optical qualities of single crystals and devices made from them, the control of native point defects plays an important technological role, especially if harmful secondary reactions are evoked by point imperfections, such as precipitation and microvoid generation. From an experimental point of view, there are two possible ways of defect mastering: (1) in situ control during the crystal growth process and/or (2) postannealing of the as-grown crystal bulk or pieces (wafers) cut from them.

In the case of dislocation-free crystals, a quasi-homogeneous point defect interplay without catalytic effects takes place. As a result, the relatively high supersaturation promotes vacancy and/or interstitial condensations within the cooling crystal volume, escalating to unfavorable micro- and meso-conglomerations. As discussed in Section 27.2.1, in silicon at high pulling rates, vacancies are incorporated in excess and condense during cooling down to form octahedral voids of ~100 nm [8]. At low pulling rates, interstitials are in excess, forming a network of dislocation loops [7]. The balance between the number of vacancies and interstitials is the controlling factor. Based on these experimental observations, three ways to achieve microdefect-free silicon have been investigated [31]:

- Keep the growth conditions within the defect-free regime, which is approximately ±10% of the critical ratio $v/G_T = 1.34 \times 10^{-3}$ cm^2 K^{-1}min^{-1}, where v is the growth velocity and G_T is the temperature gradient at the interface. However, such a small tolerance permits only very low pulling velocities of about 0.5 mm/min and extended cooling times.
- Keep a maximum pulling rate with fast cooling followed by a wafer annealing process to reduce the microvoids.
- Use a "flash wafer" step, where a thin active Si layer of 0.5 μm is deposited onto the wafer surfaces, which combines the maximum pull rate and fast cooling with low-cost treatment.

The in situ control of native point defects in compound crystals is coupled with the feasibility of accurate composition control during the growth process and, therefore, with the exact knowledge of the phase diagrams. When the T-x shape of the homogeneity region is better known, the in situ control can be more accurately

adjusted. The application of a temperature-fixed vapor source of the volatile component during the horizontal Bridgman (HB) method without covering of the melt is well known [32]. In this technique, there is direct contact of the vapor phase with the crystallizing melt-solid phase region, which guarantees near-phase equilibrium conditions during the whole growth run. Also, the vertical Bridgman (VB) and vertical gradient freeze (VGF) techniques were introduced by using an extra source for the vapor phase control [33] (see also Volume IIA, Chapter 9). A certain transport transient of the vapor species has to be considered due to the complete covering of the crystallization front by the melt column. As a result, the equilibrium temperatures for the vapor pressure source can somewhat differ between the techniques. Vapor-pressure-controlled HB, VB, and VGF have been successfully used to grow near-stoichiometric compound semiconductors, such as CdTe [34] and GaAs crystals—the latter even without boric oxide encapsulation of the melt surface [35]. If highly purified material is used, high-resistivity CdTe crystals could be obtained [36], caused by intrinsic defect annihilation and compensation. However, ensuring a stable intrinsic semi-insulating state of high reproducibility over the whole crystal length is very complicated due to native point defect segregation. A well-controlled source temperature program that is well fitted with the growth rate would be required. Compensation doping, such as that realized in CdTe [37], may be more promising. At present, however, the stoichiometry is still tuned in cut wafers by postgrowth annealing when required for a given application [38,39].

Much less practicable is the in situ control of stoichiometry in the Czochralski growth of semiconductor compounds. For this, a modified technique without encapsulant is required to influence the melt composition by partial pressure of the volatile element. For instance, the in situ control of stoichiometry was achieved in GaAs by the vapor-pressure-controlled Czochralski (VCz) technique [40] without boric oxide encapsulation [41] (see Volume IIA, Chapter 3). It was demonstrated that near-stoichiometric growth conditions with a Ga-rich melt reduce both the As_{Ga} antisite and V_{Ga} concentrations [41].

Currently, for dielectric compounds, Czochralski growth experiments with precise in situ vapor pressure control are still rare. This is primarily due to the much higher growth temperatures and chemical aggressiveness of oxygen or fluorine, which make it difficult and expensive to insert a chemically resistant and gastight inner growth chamber with an extra source. However, some activities have been described. For instance, high-quality composition-controlled $Bi_{12}GeO_{20}$ (BGO) crystals were grown in an inner chamber made of platinum [42]. A related patent [43] describes the control of stoichiometry during Czochralski growth of $PbMoO_4$ crystals, with markedly improved optical transmission using an MoO_3 evaporation source within a bell covering around the pulling crystal.

For the control of intentionally introduced extrinsic point defects (dopants), the engineering is directed on their homogeneous or linear-gradient distribution, as described in detail in the Volume IIb, Chapter 25.

27.3 Dislocations

27.3.1 Growth Dislocations and Postgrowth Dislocations

Dislocations are generated during crystal growth via plastic deformation and by the condensation of self-interstitials and vacancies. In the study of crystal growth defects, it is useful to distinguish between two categories of dislocations [44,45]:

1. Dislocations that are connected with the growth front and proceed with it during growth (i.e., growth dislocations, grown-in dislocations).
2. Dislocations that are generated behind the growth front, either during the growth run or during cooling down to room temperature (i.e., postgrowth dislocations), later during processing, or by improper handling.

The final arrangement of dislocations in a crystal at room temperature results from growth dislocations, postgrowth dislocations, and the movement, multiplication, and reactions of both after growth. Crystals grown at low temperatures with low- or zero-temperature gradients (e.g., from aqueous solution) and in their brittle state usually contain dislocations in their original "as-grown" configuration; in crystals grown at high temperatures, the original dislocation configurations may be drastically altered by dislocation movement, dislocation multiplication, and dislocation reactions. These processes, which may occur during the growth run (behind the growth front), are induced by thermal stress due to inhomogeneous temperature fields and—particularly in crystals grown at very high temperatures—by the absorption of interstitials and vacancies ("dislocation climb") during cooling. They usually occur in crystals grown from melt because these are always plastic in a more or less extended temperature range below the melting point; thus, they allow the movement of dislocations even under low critical stress. Dislocation arrangements, which are described in Sections 27.3.5 and 27.3.6, result from these processes. Detailed summaries on dislocation multiplication by thermomechanical stress during the growth of crystals from the melt are given by Völkl [46] and Prasad and Pendurti [47].

27.3.2 Sources of Growth Dislocations

For topological reasons, dislocation lines cannot start or end in the interior of a perfect crystal. They either form closed loops, start from external and internal surfaces (e.g., grain boundaries), or start from defects with a break of the crystal lattice. In crystal growth, such defects may arise from all kinds of inclusions (e.g., foreign particles, liquid inclusions, bubbles, solute precipitates). When inclusions are overgrown and "closed" by growth layers, lattice closure errors may occur. These errors are the origin of growth dislocations that are connected to the growth front and propagate with it during further growth [44,45].

It is a common observation that inclusions are the source of growth dislocations. Examples are shown in Figures 27.4, 27.5 and 27.9(a). The appearance of dislocations

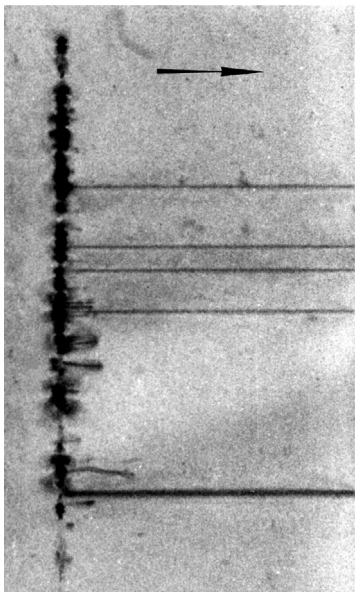

FIGURE 27.4 Liquid (zonal) inclusions in solution-grown potassium alum (water), triggered on a (110) face by an intentionally introduced re-dissolution due to a temporary increase of solution by 1 °C. The original temperature (~40 °C) was restored until a slight rounding of crystal edges had appeared. Arrow *n*: growth direction. A few edge dislocations originate from the inclusions. A section (6×12 mm^2) of an X-ray topograph of a 0.9-mm thick (100) plate is shown. Diffraction vector is $\mathbf{g}(2\bar{2}0)$; MoKα radiation. *With permission from Springer Science + Business Media.*

"behind" an inclusion (viewed in the direction of growth) is correlated with its size: small inclusions emit only few dislocations or are often dislocation free. Large inclusions (>50 μm) usually emit bundles of dislocations.

The generation of growth dislocations by foreign particle inclusions has been experimentally studied on crystals growing in aqueous solution (potassium alum) and in supercooled melt (benzophenone $(C_6H_5)_2CO$, $T_m = 48$ °C; salol $C_{13}H_{10}O_3$, $T_m = 42$ °C) [48]. Similar studies were reported by Forty [49], who presented a rich collection of photographs of growth spirals and other surface patterns on growth faces of various crystals.

27.3.3 Propagation of Growth Dislocations

27.3.3.1 Characteristic Configurations, Theory of Preferred Direction

As summarized in the reviews by Klapper [44,45,50], a dislocation line ending on a growth face will proceed with it. Its direction depends on the shape and the orientation of the growth face and on its Burgers vector. A crystal growing on planar (habit) face consists of growth sectors belonging to different growth faces (different growth directions **n**; see Section 27.6.1). This leads under ideal conditions (i.e., stress-free growth) to a characteristic configuration of growth dislocations, which is illustrated in Figure 27.6. The dislocations start from inclusions and propagate as straight lines with

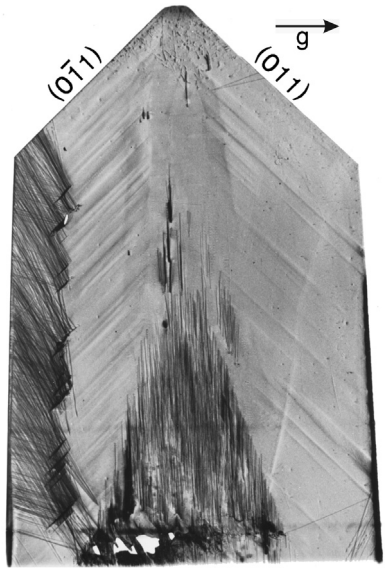

FIGURE 27.5 X-ray diffraction topograph of a (100) plate (approximately 1.5-mm thick, 50-mm long), cut from the rear side of a potassium dihydrogen phosphate crystal rotated through the solution. Due to a closed wake of solution with reduced supersaturation behind the $(0\bar{1}1)$ growth face, liquid inclusions were repeatedly formed. They are the origin of numerous dislocations, which grow out at the side because the prism face is practically not growing. The dislocations in the triangular region above the capping zone belong to one of the growth sectors (101) or (101). At their top ends, they emerge out of the plate *t*. *With permission from Springer Science + Business Media [45].*

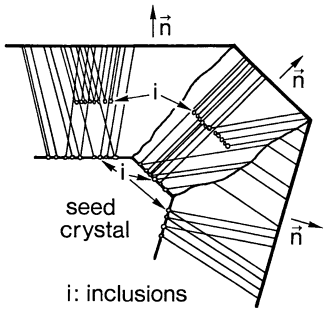

FIGURE 27.6 Typical geometry of growth dislocations in crystals grown on habit faces. The different preferred directions of dislocations lines within one growth sector result from different Burgers vectors. These directions abruptly change their directions when they penetrate a growth-sector boundary, where, during growth, the dislocation outcrops shift over the edge from one face to the other. *After Klapper [44,45], with permission from Springer Science + Business Media [45].*

directions $\mathbf{l}$, which are usually close to, and frequently parallel to, the growth direction of the sector in which they lie. They usually exhibit sharply defined, often noncrystallographic preferred directions $\mathbf{l_o}$, which depend on the growth direction $\mathbf{n}$ and on the Burgers vector $\mathbf{b}$: $\mathbf{l_o} = \mathbf{l_o}(\mathbf{n}, \mathbf{b})$. The dependence of the preferred direction $\mathbf{l_o}$ on the growth

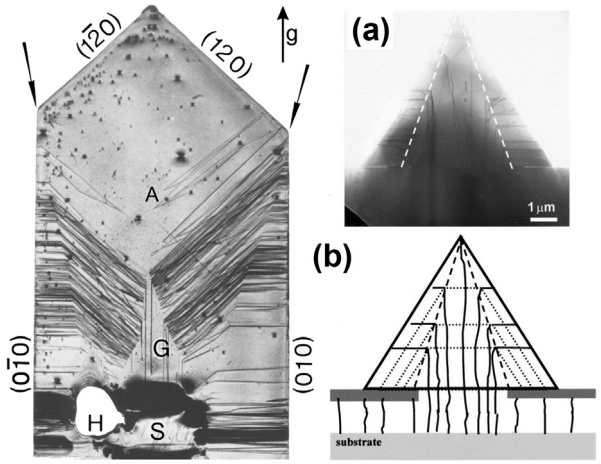

FIGURE 27.7 *Left*: This section of a (001) plate (horizontal width about 15 mm, thickness 1.5 mm) was cut out of a salol crystal (orthorhombic) grown from supercooled melt. The dislocation lines change their preferred directions when they penetrate the boundaries (arrows) from the {120} into the {010} growth sectors. S: seed crystal, H: hole due to a gas bubble, G: grown-out (100) sector, A: dislocation pairs (with opposite Burgers vectors of their components) originating from tiny inclusions, dots: surface damages. *With permission from Springer Science + Business Media [45].*) *Right*: (a) transmission electron micrograph of the dislocation arrangement in GaN grown on a sapphire substrate by MOVPE epitaxial lateral overgrowth (ELO) through the window (width 3 μm) of a mask, viewed along direction [10$\bar{1}$0]. (b) Sketch of growth features and dislocation arrangement. Dotted lines shapes of the GaN crystal with faces {11$\bar{2}$2} and (0001) in successive stages of ELO-growth; dashed lines (white in (a)): boundary between the (0001) and the neighbored {11$\bar{2}$2} growth sectors. The basal (0001) face has the higher growth velocity and, thus, finally vanishes from the crystal shape. The dislocations (full lines), proceeding through the mask window and ending on the basal plane, are bent by 90° into the horizontal direction when penetrating the boundary to the neighbored {11$\bar{2}$2} sectors. *Courtesy of Vennégues et al. [60]; reproduced with permission from [60], copyright (2000), AIP Publishing LLC.*

direction **n** becomes conspicuously apparent when the dislocations penetrate growth-sector boundaries, which implies an abrupt change of the growth direction. As a result, the dislocation lines undergo an abrupt change of their preferred direction $\mathbf{l_o}$. Examples are shown in Figure 27.7.

This preferred direction of growth dislocations is explained by two approaches:

1. The *minimum-energy theorem* (Figure 27.8(a)): The dislocation lines adopt a direction **l** (unit vector), for which its energy within any growth layer is a minimum. For a growth layer of unit thickness $d = 1$, this can be expressed as $E/\cos\alpha = \text{minimum}$, with $E = E(\mathbf{l}, \mathbf{b}, c_{ij})$ being the elastic energy (strain energy) per unit length of the dislocation line (c_{ij} are the elastic constants of the crystal) and α being the angle between **n** and **l**. The factor $1/\cos\alpha$ accounts for the length of the dislocation line in the layer [44,50,52].
2. The *zero-force theorem* (Figure 27.8(b)): A dislocation line emerging at the surface experiences a force dF, which depends on the angle α between the dislocation direction **l** and the surface normal **n**. At the surface, this force is infinitely large. According to Lothe [51], there exists always a direction $\mathbf{l_o}$ for which this force is

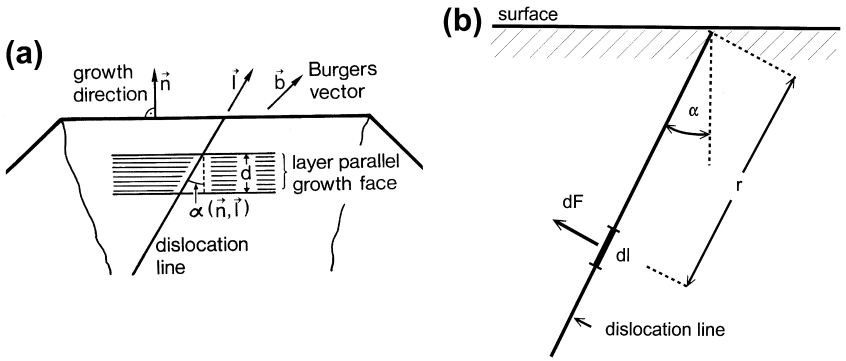

FIGURE 27.8 (a) Derivation of the energy of a straight dislocation line within a layer parallel to the growth face. (b) Illustration of the force d*F* exerted by the crystal surface upon a line segment d*l* of a straight dislocation line emerging at the surface (theorem of Lothe [51]). *With permission from Springer Science + Business Media [45].*

zero for the dislocation line segments at any depth below the surface *r*. It is plausible that a dislocation emerging at the growth face follows this direction of zero force. Using the formula

$$\mathrm{d}F = -\frac{1}{r}\left(\frac{\partial E}{\partial \alpha} + E\tan\alpha\right)\mathrm{d}l, \tag{27.9}$$

(theorem of Lothe), it can be shown that both approaches lead to the same preferred directions.

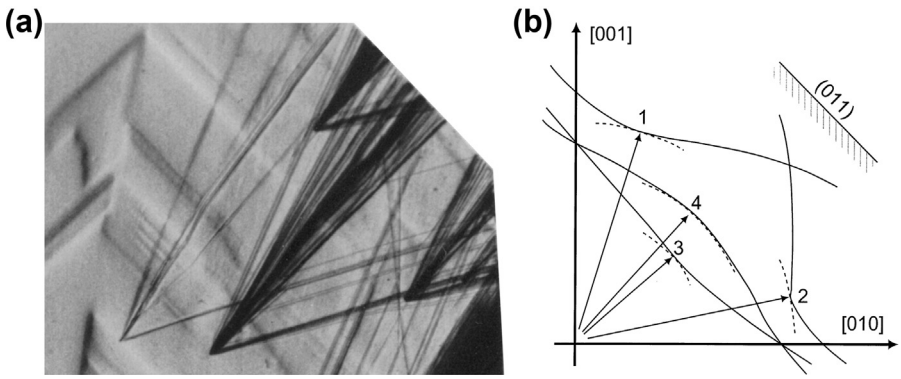

FIGURE 27.9 (a) This section ($\approx 8.5 \times 14\ \mathrm{mm}^2$) of an X-ray topograph (reflection 200, Ag-Kα radiation) of a potassium dihydrogen phosphate (KDP) (100) plate (thickness $\cong$ 1.5 mm) shows bundles of dislocations with non-crystallographic preferred directions emanating from small liquid inclusions. The Burgers vectors of these dislocations can be recognized from their preferred directions. In addition, growth bands and features due to vicinal effects are visible. (b) Plots of calculated energies $E/\cos\alpha$ (arbitrary units) of dislocations with Burgers vectors $\mathbf{b} = [001]$ (1), $\mathbf{b} = [100]$ (2), $\mathbf{b} = [011]$ (3), and $\mathbf{b} = [011]$ (4) in growth sector (011) of KDP (polar coordinates). The preferred directions of minimum $E/\cos\alpha$ are represented by arrows. The dashed lines are circles with radii equal to the minimum values of $E/\cos\alpha$.

27.3.3.2 Verification of the Minimum Energy Approach and Examples

The minimum-energy directions of growth dislocations have been calculated for several Burgers vectors and growth sectors in various crystals grown from solution and supercooled melt [52–54] using the theory of dislocations in elastically anisotropic crystals developed by Eshelby et al. [55]. Although the calculations are only approximate by regarding the crystal as an elastic continuum and neglecting the dislocation core energy, the agreement between observed and calculated directions is satisfactory. Figure 27.9 shows the comparison of observed and calculated preferred directions of dislocations with four different Burgers vectors in the (011) growth sector of potassium dihydrogen phosphate (KDP) [56]. The agreement is excellent with deviations of 3–6°, except for dislocation 4, the observed directions of which scatter by ±5° around a direction deviating by about 20° from the calculated one. This may be due to the very flat minimum of K, which makes the minimum energy directions more subject to other influences, such as surface features and core-energy variations. Similar comparisons have been carried out for various crystals grown on planar faces from solutions and supercooled melts [53,54,57,58]. In general, the agreement of observed and calculated directions is satisfactory and confirms the validity of the above theorems.

On account of the factor $1/\cos\alpha$ in the energy term above, the preferred directions of growth dislocations are mostly normal or nearly normal to the (local) growth face. In some cases of planar interfaces, however, deviations from the growth normal of up to 30° have been observed in agreement with the calculations.

For interfaces with convex curvature, such as in Czochralski growth of oxides, the dislocation lines diverge and grow out of the crystal boule through its side faces, whereas for concave interfaces the dislocation lines are focused into the center of the crystal boule. Trajectories of growth dislocations in Czochralski gadolinium gallium garnet (GGG) have been calculated and compared with observed trajectories by Schmidt and Weiss [59]. The rounding of the interface has been taken into account by performing the calculations stepwise in small increments. Again, the agreement is satisfactory. Moreover, this allowed the assignment of Burgers vectors to the different dislocation trajectories, which were observed optically in polarized light. Preferred dislocation directions and their bending when penetrating a growth sector boundary have been observed by transmission electron microscopy in GaN grown by metal-organic vapor phase epitaxy (MOVPE) using the epitaxial lateral overgrowth (ELO) technique [60,61]. An example is shown in Figure 27.7(b).

Although the agreement of observed and calculated directions of growth dislocations is in general satisfactory, frequently discrepancies are found. The reasons for this may be due to the insufficient approximation by the model on which the calculations are based, the influence of other defects, or particular surface relief. The above calculations are based on linear anisotropic elasticity of the continuum and do not account for the discrete structure of the crystals, the dislocation core energy, or, in piezoelectric crystals, electric energy contributions.

The following four causes have been found to affect preferred directions:

1. Discrete lattice structure of the crystals and the neglect of the core energy
2. Long-range stress
3. Surface relief of the growth face (e.g., growth hillocks, macrosteps)
4. Dislocation movement and reactions after growth

Detailed discussions of these influences are given in Refs [44,45,50,52].

27.3.4 Postgrowth Dislocations

Dislocations formed in the interior of the already-grown crystal without connection to the growth front or other surfaces must be closed loops. It is practically impossible to generate closed loops in a perfect crystal by stress because the stress required for such processes would be extremely high. Inclusions, however, usually represent stress centers and form internal surfaces of the crystal. The stress in the crystal around the inclusions is relieved by the emission of concentric dislocations loops or—more frequently—of dislocation half-loops (see Section 27.5.4, equation 27.17). The half-loops are, strictly speaking, also closed loops (with a virtual closing line element inside the inclusion). Half-loops can also generate growth dislocations: if stress is built up around an inclusion just incorporated and still close to the growth front, half-loops emitted from the inclusion may "break through" to the growth interface, whereby each half-loop forms two separated dislocation lines with opposite Burgers vectors propagating with the growth front. Dislocation half-loops emitted from bubble inclusions in benzil grown from supercooled melt [58] are shown in Figure 27.10. Examples of half-loops in solution-grown crystals, revealed by X-ray topography, are given in Ref. [62] for sodium chlorate and in Ref. [63] for tetraoxane. The latter study shows the successive emission of half-loops from inclusions and their splitting into two separate dislocations when reaching the crystal surface. A very peculiar kind of dislocation loop is observed in octadecanol crystals grown from xylene solution: columns of prismatic loops are punched out from inclusions [64].

More detailed discussions are given in Refs [45,50,54,65].

27.3.5 Dislocation Dynamics (Patterning, Cell Structures, Clustering)

Dislocation dynamics describe the dynamic organization of dislocations into spatially heterogeneous substructures [66]. Bulk crystals are grown in heat fields with temperature differences (gradients) being not of ideally linear but, typically, nonlinear character. As a consequence, thermomechanical stresses are present in the growing crystal ingot [67]. Under such conditions, even at high temperatures, the existing dislocations exhibit both (1) *glide*, with a velocity proportional to the power of acting stress; and (2) *climb* motion, with a rate that is a function of applied stress, temperature, and, especially, density and diffusivity of available point defects. Dislocation motions result from both

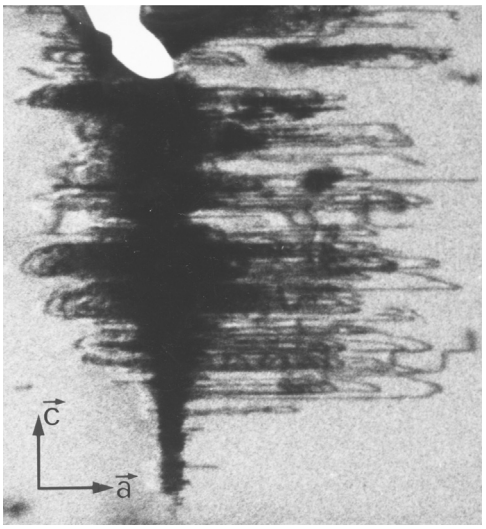

FIGURE 27.10 Postgrowth dislocation half loops in benzil (grown from supercooled melt) emitted from a trail of bubbles. Section 4.5 × 5 mm of a (0110) plate. The dislocations belong to the ⟨100⟩(0110) glide system and are purely screw in their horizontal segments [58]. *With permission from Springer Science + Business Media [45].*

long-range force fields, such as overall thermomechanical stress, and short-range reactions between individual dislocations.

When the generated thermomechanical stress within a growing crystal is of the order of the critical resolved shear stress (CRSS), the stored dislocations are shifted with a *glide velocity* of

$$v_g = v_0 (\tau_{eff})^m \exp\left(\frac{-E_a}{kT}\right) \tag{27.10}$$

where v_0 is the empiric material constant (shear wave velocity), τ_{eff} is the effective shear stress on dislocation $= \tau - A\sqrt{\rho_0}$, A is the strain hardening factor, ρ_0 is the mobile dislocation density, m is the stress experimentally obtained from deformation experiments, E_a is the activation energy (Peierls potential), k is the Boltzmann factor, and T is the absolute temperature. Note that no obstacles, such as sessile dislocations, foreign phase inclusions, or grain boundaries, are considered in Eqn (27.10).

In addition, dislocation climb (jog dragging) is thermally activated but depends additionally on the diffusive properties of the material, particularly the diffusion of native point defects (vacancies, interstitials), being more mobile than glide, known as *climb velocity*:

$$v_c = v_{0cl} (\tau_{eff})^{N_c} \exp\left(\frac{-E_{SD}}{kT}\right) \tag{27.11}$$

Here, $v_{0cl} \sim n_j \; D_i/\lambda$ is the characteristic climb velocity depending on point defect diffusivity, in which D_i is the distance between equilibrium point defect concentration

and dislocation line λ. The concentration of jogs per unit length of dislocation $n_j = n_0 \exp(-E_j/kT)$, where n_0 is the thermodynamic equilibrium number of atom sites per unit length of dislocation and E_j is the characteristic jog energy (n_j/n_0 is of the order of 10^{-3} at $T = 1000$ K [68]). N_c is the climb exponent and E_{SD} is the activation energy for self-diffusion.

Generally, in the course of enthalpy minimization, the long-range character of dislocation interaction produces agglomerates and patterns by mutual attraction, ensuring a *screening effect*. At the same time, a dislocation density thinning via annihilation takes place when the Burgers vectors are of opposite signs. Therefore, the total *interaction energy* between dislocations within a cylindrical crystal with radius R and mean distance between homogeneously distributed starting dislocations $\rho_0^{-1/2}$ consists of the following [69]:

$$E_i = -\int_{\rho_0^{-1/2}}^{R} 2\pi r f_a(r,\rho)\left(Gb^2/2\pi\right)\ln(r/r_0)dr \tag{27.12}$$

where $f_a(r,\rho)$ is the distribution function considering dislocation annihilation, whereupon $2\pi r f_a(r,\rho)dr$ is the difference between the number of dislocations with Burgers vector of opposite sign to that of similar sign between distances r and $r + dr$. G is the shear modulus, **b** is the Burgers vector, r is the radial position, and r_0 ($\approx 2 - 4b$), which is the dislocation core within which the linear-elastic theory breaks down.

As it was found experimentally, there are also nonlinear interactions between dislocations, which are phenomenologically described as rate processes rather than force-displacement relationships. Some of these reactions are immobilization, annihilation, dipole formation, junction formation, and dislocation multiplication. For instance, if the stress on a mobile dislocation falls below the friction stress or the dislocation is pinned at a mesoscopic obstacle (impurity conglomerate, second-phase inclusion, grain boundary), it becomes immobile. In particular, barriers caused by point defect agglomerations and grain boundaries produce often *dislocation clusters* of quite increased energy content, which produces prismatic dislocation loops or even microcracks.

Annihilation is the cancellation of two dislocations of opposite Burgers vectors, which approach each other along a given crystallographic plane within a certain critical distance. For two screw dislocations, this distance is $y_s^* \approx \mu b/2\pi\tau$, with μ being the shear modulus and τ being the shear stress required for dislocation glide. In comparison, two edge dislocations annihilate at much smaller critical distances on the order of 1–2 nm. However, they can achieve a stable configuration at a distance greater than the critical distance for annihilation. Such configuration is known as a *dipole*, being stable when the stress on a dislocation is less than the passing shear stress for a dipole $\tau_{dp} \approx \mu b/8\pi\ (1-\mu)y$, with y being the slip plane spacing.

Another important dynamic event is the energetically favorable junction formation. When many mobile dislocations are approaching each other, they can form jog intersections leading in ensemble to well-patterned dislocation networks. In particular, the energetic interplay between edge dislocations of opposite Burgers vector evoke their gathering in dislocation walls. As a result the energy of each individual dislocation within the wall reduces by a factor of three or four compared to its energy within a statistical initial arrangement. Finally, besides the cross-glide of screw dislocations, multiplication occurs by pinning of the dislocation, bowing out, and wrapping around the pinning points, known as the *Frank-Read mechanism*.

When glide and climb motions are competitive, dislocation cell structures form. This process of self-organization minimizes the internal enthalpy of the growing crystal in the course of plastic relaxation. In addition, the continuously acting flows of heat and stress put the crystal in a state somewhat outside the thermodynamic equilibrium accompanied by dissipative structuring via steady entropy production. Thus, the presence of heterogeneous dislocation substructures in as-grown crystals is not an abnormality but rather a common fact.

Cell patterning is studied best in metals under external load but also in postdeformed elemental semiconductor single crystals, such as silicon, and semiconductor compounds, such as III-BVs and II-VIs [70]. They are observed in melt-grown Czochralski [71], horizontal [72], and vertical Bridgman crystals [73], as well as in samples grown from solution [74] and vapor [75] (see Figure 27.11). However, the growth-related process of dynamical structuring, even in semiconductor compounds, has not yet been studied with such profundity as in postdeformed specimens. Of course, this is mainly due to the current impossibility of in situ stress measurements. Thus, the best possible global modeling of the present acting thermomechanical stress field in each given growth situation is increasingly coming to the fore [76].

There is a growing need for clarification of such features in semiconductors and dielectric crystals because they markedly influence the device quality. For instance, in as-grown semi-insulating GaAs, which is important for the production of low-noise high-frequency devices, a mesoscopic resistivity variation occurs due to the accumulation of As_{Ga} antisite defects (EL2) along the low-angle grain walls, which requires a sophisticated after-annealing step. Further, the wide application of $Cd_{1-x}Zn_xTe$ crystals as the most promising candidates for radiation-detection systems is still hindered by the charge-transport nonuniformities along such cellular substructures [77]. In multicrystalline silicon (mc-Si) for PV, an enhanced recombination occurs due to metal decoration in combination with oxygen at the subgrain boundaries, leading to degradation of the carrier lifetime and, thus, solar cell efficiency. Finally, as it is well known in crystals for optical applications, such as CaF_2 for ultraviolet photolithography, subgrain networks impair the transparency and resolution quality.

In general, dislocation cell structures consist of walls with high dislocation density separated by interiors of markedly dislocation-reduced or even dislocation-free material. The detailed analysis by X-ray synchrotron topography of dislocation cells in as-grown 6″

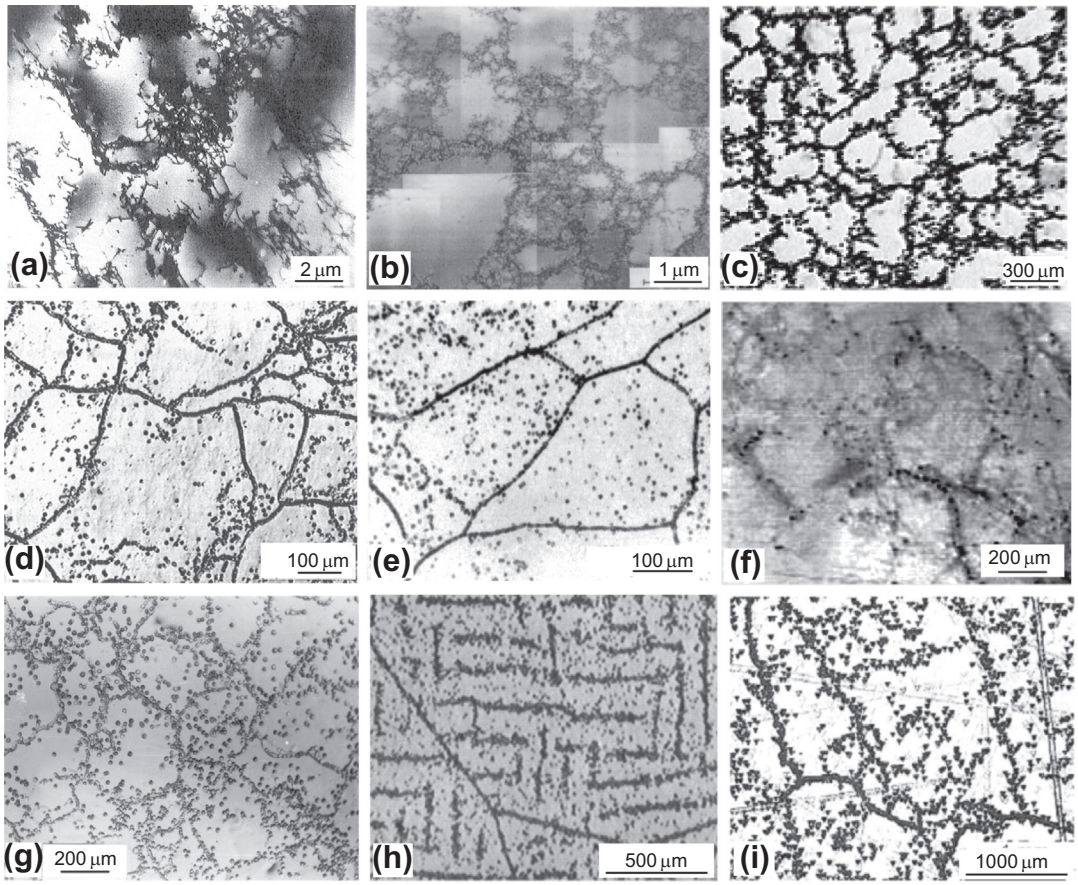

FIGURE 27.11 Dislocation patterns formed in various crystals under differing stress conditions. (a) Mo 12% deformed at 493 K; (b) Cu–Mn crystal deformed at 68.2 MPa; (c) GaAs crystal grown by VCz; (d) CdTe crystal grown by VB; (e) mc-Si crystallized bei VGF; (f) SiC crystal grown by sublimation; (g) $Cd_{0.96}Zn_{0.04}Te$ crystal grown by VB; (h) NaCl crystal with labyrinth structure deformed by 150 MPa at $T/T_m = 0.75$; (i) CaF_2 crystal grown by VB. *Adapted from Ref. [70].*

vapor-pressure-controlled GaAs crystal showed that the dislocations are accumulated in fuzzy walls [78]. Typically, numerous junctions and pins form a sessile dislocation jungle, which is rather stable against postgrowth annealing [79]. Only very small mean tilt angles around 10 arcsec exist between the cells. In comparison, in CdTe, PbTe, mc-Si, and CaF_2, the matrix contains numerous isolated dislocations and the cell walls are much sharper, consisting of only one row of dislocation pits that can be ascertained by transmission electron microscopy [75]. Such behavior is well known from the standard type of polygonized low-angle grain boundaries (primary subgrain formation), containing only the excess dislocations of similar Burgers vector after the annihilation is completed. Tilt angles of 60–120 arcsec were reported for such crystals [34]. Obviously,

compared with GaAs in these materials, the substructure reacts much more sensitively to variations of the stress field acting during crystal growth. Additionally, in II–VI and IV–VI substances, the dislocation mobility is markedly enhanced compared with III–Vs due to the much higher bond ionicity.

By ascertaining the mean cell diameter using the rules of correspondence, which are valid for most materials [80], we are able to estimate the value of once-acting thermomechanical stress. At first, after Holt's relation [69], the cell diameter is approximately given by $d \approx K\rho^{-1/2}$ (K-similitude coefficient); there is a correlation between cell size and dislocation content. Next, according to the rule of Kuhlmann-Wilsdorf [81], $d = K\,G\,\mathbf{b}\,\tau^{-1}$, the cell diameter also correlates with the acting shear stress. For instance, a mean cell diameter of 100 μm in an as-grown crystal correlates with a former τ of about 3–5 MPa. Finally, Taylor's rule [82], $\tau = K\,G\,\mathbf{b}\,\rho^{1/2}$, shows the relationship between stress and expected dislocation density (Figure 27.12). Of course, from these relationships follows that substructures should be damped by adherence of the lowest possible thermomechanical stress during growth—that is, assurance either of even or, as it was postulated by Indenbom [67], polynomial-shaped isotherms.

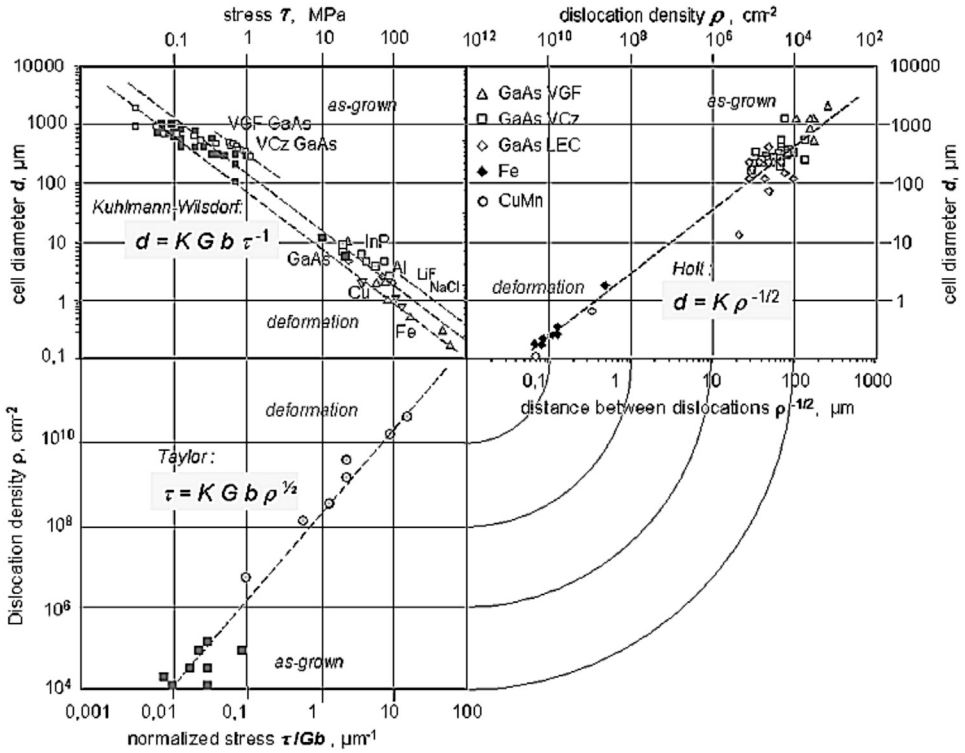

FIGURE 27.12 Kuhlmann-Wilsdorf's $d(\tau)$, Holt's $d(\rho)$, and Taylor's $\rho(\tau)$ dependencies of similarities with inserted experimental points from deformation tests and crystal growth (d-cell diameter, G-shear modulus, **b**-Burgers vector, τ-shear stress, ρ-dislocation density, K-similitude constant ≈7.5) [83].

Dislocation clustering (bunching) is a well-known harmful defect mode in as-grown and loaded crystals that has been a long-term subject of investigation. This phenomenon is not only typical in dislocation containing semiconductor crystals, such as mc-Si or III–Vs, but also in metals, alloys, and dielectrics. They are most intensively studied on metals under load with high dislocation densities. Usually, they are related to acting mechanical and thermomechanical stresses. However, they also correlate with polycrystallinity, such as in the presence of large-angle grain boundaries. Further, dislocation clustering can appear even in crystals with low defect density, especially when foreign-phase inclusions are presented (Figure 27.13). Dislocation bundles are also formed during crystallization if concave–convex and morphologically unstable melt-solid interfaces are obtained. Even in the concave part, the minimum energy theorem, shown in Section 27.3.3.1, is responsible for dislocation bundling. In sum, their appearance and origins are versatile and often of stochastic character.

For instance, in mc-silicon ingots for PV crystallized by directional solidification, dislocation clustering is a hotly debated object due to its continuous presence and harmfulness. About 10% of the surface area of commercially available mc-wafers is covered with such clusters of diameters between 0.1 and 1.0 mm containing dislocation densities of 10^6–10^8 cm^2 [84]. They degrade the minority carrier life and, hence, the solar cell efficiency by more than 3–4 percentage points [85]. Once they are formed, they mostly follow the propagating solidification interface through the whole crystal, remembering veins. Due to their ability as getters for highly diffusive metallic impurities, the shorting of p-n junctions is most likely. Therefore, their avoidance in solar cells is of highest priority. It has been demonstrated that in multicrystalline (mc) Si ingots consisting of multigrains of uniform small size, dislocation clusters can be localized in intragrains and often disappear when those grains are overgrown by others. Accordingly, the defect multiplication is easily terminated. Such so-called high-performance mc-Si has high industrial applicability for photovoltaics, mainly because the solar cell efficiency is 17.8%, which is comparable with more defect-inherent large-grain-size material [86].

Dislocation clusters are formed around presented second-phase particles (inclusions, precipitates; see Section 27.5.3). Mostly during the solidification of nonstoichiometric

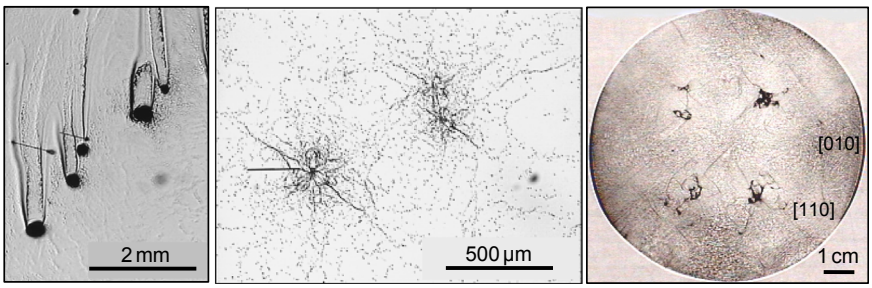

FIGURE 27.13 Dislocation clustering around Ga inclusions in GaAs (left), in directionally solidified mc-Si (middle), and at concave interface regions in an LEC GaAs crystal (right). *Images by U. Juda from IKZ Berlin.*

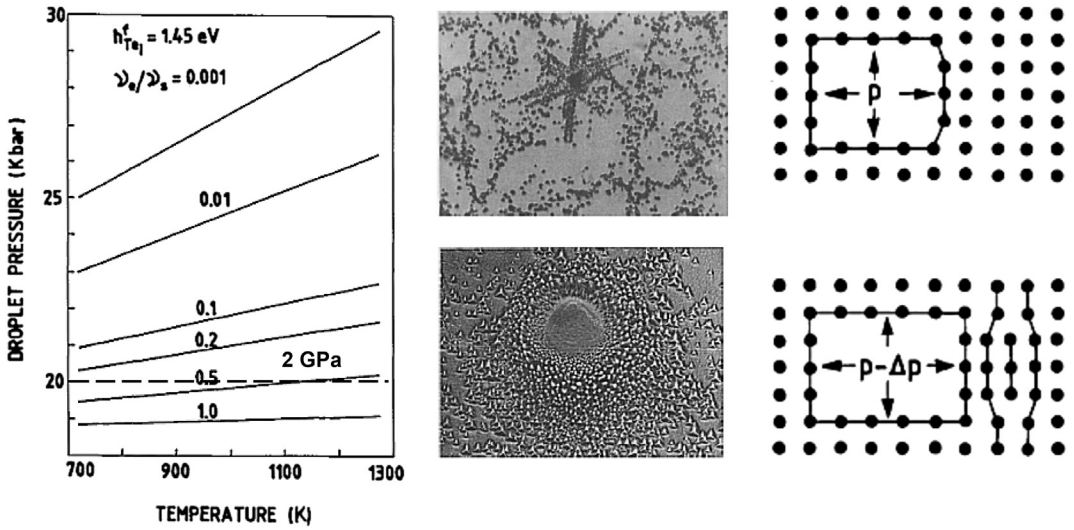

FIGURE 27.14 *Left*: Te droplet pressure p versus T curves in CdTe (h^f_{Te}-Te interstitial formation energy; ν_l/ν_s-liquid to solid vibrational frequency). *Middle*: dislocation bundling around Te precipitates with nearly spherical morphology (below) and with crystallographically regular (triangular) cross-section (above). *Right*: schematic illustration of Greenwood–Foreman–Rimmer mechanism of interstitial dislocation loop punching (above) before and (below) after a loop is punched. *Adapted with permission from Ref. [89].*

compounds, the excess component is incorporated as small liquid inclusions, crystallizing at a much lower temperature than the matrix (Figure 27.14). Different thermal expansion coefficients, volume expansion, and lattice misfits before and after the inclusion are solidified, causing marked stress that generates dislocations at the boundary to the matrix (see e.g., Refs [87,88]), which can be explained by the Greenwood–Foreman–Rimmer mechanism [89] (see Section 27.5.4).

An inhomogeneous dislocation redistribution takes place when unfavorable convex–concave (W-shaped) interfaces are present, mostly in cylindrical crystals growing from the melt. The lowest dislocation density is found at the inflection point with a concave minimum of $d\tau/dx = 0$ [90]. There, a characteristic clustering appears, with assembly symmetry according the Schmid factor. After Shibata et al. [91], effective depression of such dislocation bunching is successful when the ratio between the crystal diameter D and the radius of interface curvature r is >0.5.

Another important clustering effect, observed even in polycrystals with large-angle grain boundaries, is the dislocation pile-up. In fact, the predominant portion of dislocation bunching in mc-Si samples is observed at such boundaries [84]. If a series of dislocations with the same Burgers vector all lying in the same slip plane meet a hard obstacle, such as large-angle grain boundary, the dislocations mostly pile up behind the leading dislocation. Large long-range stress is produced at the head of the pile-up, increasing with the involved dislocation number. It can cause dislocation multiplication by cross-slip of screw dislocations held up at obstacles such as precipitates, thus

forming a dislocation gnarl. For comparison, a near screw aggregation was ascertained at the grain boundary in mechanically loaded titanium [92]. In particular, the pile-up of dislocations at grain boundaries generates a back stress; this tends to suppress further activation of the dislocation source and a stress intensification ahead of the pile-up, thus promoting grain boundary fracture, slip transfer, or twin nucleation into the neighboring grain.

As we can see, the dislocation dynamics within a growing crystal are quite manifold and complex. It is worth noting that the above-mentioned particular events must not be taken out of context. There exists a strong correlation between the dislocation dynamics and other defect types of lower and higher orders.

What about the state-of-the-art of dislocation dynamics and its modeling? Good progress has been made in the field of metal physics, especially metallurgy and cold forming of alloys, as summarized in the book by Kubin [83]. In comparison, the full ascertainment of dislocation dynamics in growing crystals is still uncertain. Consider the explanation of the dynamic processes evoking characteristic dislocation rearrangements in all stressed materials, such as the ones found in as-grown crystals. According to Kubin [83], in either case, the plastic flow is not uniform at a fine scale, such as along a pile-up band as discussed above. The inhomogeneous release of elastic energy gives rise to the emission of acoustic waves (avalanches) interplaying with stored sessile dislocations and micro-obstacles (precipitates, vacancy condensations). In the course of cooling down, sporadic clouded dislocation patterns are frozen up (Figure 27.15), recalling the well-known cluster structures in mc-silicon, for example (Figure 27.11). Thus, it will be hard for the crystal grower to maintain perfect homogeneously distributed stored dislocations.

27.3.6 Dislocation Engineering

Dislocation engineering deals with practical measures of control of dislocation density and patterns or even their in situ prevention during the crystal growth process.

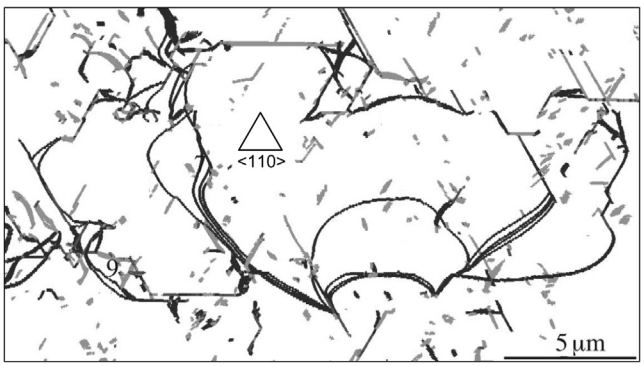

FIGURE 27.15 Modeled avalanches on the [011](111) slip system of a stressed [001] thin copper layer, sporadically pinned at obstacles. The contour of the expanding avalanche is shown in black. The light gray lines are forest dislocations and junctions formed between primary and forest dislocations. *From Devincre et al. [162].*

Generally, for dislocation-reduced growth of compound and mixed crystals with large diameters, the proper combination of the following conditions are required [19]:

1. Use of a *dislocation-free seed* crystal, preventing a thermal shock when it contacts the melt in order to avoid grown-in dislocations, which are the most serious sources for dislocation multiplication
2. Achievement of a strongly *uniaxial heat flow* with very small temperature gradients—that is, nearly flat isotherms at all stages of the growth process
3. If possible, *omission of fluid encapsulants* (boric oxide), the presence of which introduces markedly thermomechanical stresses at the crystal periphery and, possibly, its replacement by a detached growth mode [93],
4. In situ *stoichiometry control* by partial vapor pressure regulation over the melt in order to reduce the intrinsic point defect content, which promotes high-temperature dislocation multiplication by climb and also cell structure formation
5. Prevention of *constitutional supercooling* at the interface by proper selection of a noncritical G_T/v ratio
6. Minimization of atmospheric *pressure fluctuations* around the growing crystal to minimize heterogeneous dislocation rearrangements

The highest temperature nonlinearities and, hence, related thermal stress values (which increase very sensitively with diameter) appear in liquid-encapsulated Czochralski (LEC) crystals [47]. The situation can be improved by using the VCz method, which has been successfully tested not only for growth of semiconductor compounds [40] but also oxide materials [42].

However, the lowest dislocation density in compound materials is obtained by VGF, which has been investigated on industrial scales since the mid-1990s as the most promising growth variant for important semiconductors (InP, GaAs, CdTe), fluorides (CaF_2), and oxides (sapphire, BGO, PMNT, PZNT), as well as quasi-mono PV silicon (see Volume IIA, Chapters 9 and 10). The decisive technological measure is the maintenance of uniaxial heat flow through the growing crystal during the whole growth run by proper control of the cooling rate between a top and bottom heater flanked by a booster heater to avoid radial heat outflow [94]. Using solution hardening by doping, even the lowest dislocation densities ($<10\ cm^{-2}$) can be achieved [95].

Another phenomenon to be controlled in situ is dislocation cell patterning. Independently of the materials used, the cell formation can be reduced very effectively by doping. No cell structuring was observed in GaAs crystals doped with In or Si at concentrations greater than $10^{18}\ cm^{-3}$ [19]. Such an effect is due to the impurity gettering at the dislocation core. In consequence, the yield stress is enhanced by dislocation locking. No low-angle grain structure was found in CdTe and PbTe crystals when solution hardening by mixing components Se ($x > 0.4$) and Sn ($x > 0.15$) was provided, respectively. However, there is the drawback of segregation when dopants are added to the melt and the danger of morphological interface instability by constitutional supercooling. Obviously, the best way to exclude dislocation patterning is the reduction of the

dislocation density by minimization of the thermomechanical stress. In undoped VGF GaAs at ρ values $<5 \times 10^3/\text{cm}^2$, the cell structure began to disappear [41]. Also, the minimization of the native point defect content by in situ control of stoichiometry during growth can depress the dislocation cell patterning. The stoichiometry can be regulated by the partial pressure of the volatile component over the melt, applying an extra heat source within the growth chamber [40], which has been tested by HB growth [96], the hot-wall Czochralski method [97], and VCz [40]. Using a VCz arrangement without a boric oxide encapsulant, the cellular structure could be suppressed in undoped GaAs crystals when the stoichiometry is controlled by growth from a Ga-rich melt composition [14,41]. This result was confirmed by numeric simulations of the cell-structuring phenomenon in face-centered cubic (fcc) metals [98].

The pile-off and dissolute cell structures after annealing is a complicated tool. As was demonstrated by high-temperature real-time X-ray tomography, annealing in a homogeneous temperature field only 100 K below the melting point of GaAs crystals [79] did not change or rearrange the cell pattern. Only heat treatments combined with temperature differences and/or mechanical bending can be used, as described elsewhere (e.g., Ref. [99]).

27.4 Grain Boundaries

A grain boundary is the interface between two near-perfectly-built structural regions in solid materials. Their presence can influence the material properties markedly. Grain boundaries correlate with other defect types, such as dislocations and point defects, collecting them at the boundaries and therefore evoking the unfavorable qualities of inhomogeneities. It is convenient to separate grain boundaries by the misorientation angle between the two grains. *Low-angle grain boundaries* are those with a misorientation that is less than approximately 11° [99]. Generally speaking, they are composed of an array of dislocations, and their properties and structure are functions of the misorientation. In particular, the grain boundary energy γ_{GB} depends on the tilt angle between grains θ_{GB}-that is, $d\gamma_{GB}/d\theta_{GB} > 0$. In contrast, the properties of *large-angle grain boundaries*, whose misorientation is larger than approximately 11° (depending on the material, this angular limit varies from 10° to 15° [99]), are normally found to be independent of the misorientation; mathematically expressed, $d\gamma_{GB}/d\theta_{GB}$ becomes 0. From these observations, material scientists willingly differentiate between monocrystallinity ($\theta_{GB} < 10°$) and polycrystallinity ($\theta_{GB} > 10°$).

27.4.1 Dynamic Polygonization-Low-Angle Grain Boundaries

Low-angle grain boundaries are formed during cooling down of as-grown crystals in course of plastic relaxation tightly coupled with the previously discussed dislocation dynamics. With this in mind, the dislocation cellular structuring proves to be a process of structural matching to the thermal field situation. The larger the thermal inhomogeneities—that is, the thermoelastic stress—the greater is the driving force of

fragmentation of the bended crystal lattice into subregions (cells, domains), with ideal structures differing in orientation from each other by the tilt angle θ_{GB} in the region of some arcsec to arcmin. On the whole, the fragment sizes decrease and their misorientations increase with increasing plastic deformation.

The geometrically necessary dislocations (GNDs) [100] involved in the accommodation are usually concentrated at the boundaries of the crystal fragments. Higher-density GNDs of one sign at the boundaries lead to higher crystallographic misorientation of the corresponding crystal fragments. During crystal bending by thermomechanical stress in the initial stage of plastic relaxation, the mechanism of dynamic polygonization (DP) begins, correlating with dislocation slip mode only (easy-glide stage). During DP, vertical walls of dislocations perpendicular to the dislocation slip plane are formed. Unlike static polygonization (SP), which is the point-defect-assisted formation of misoriented block dislocation structures at elevated temperatures, the DP is observed down to relatively moderate temperatures. Therefore, the DP is also called *slip polygonization* because the formation of walls consisting of dislocations does not involve diffusive dislocation climb, in contrast to the case of SP [101]. As a result, by DP, a dynamic polygon structure arises in the form of a periodic system of tilt walls of dislocations (Figure 27.16). Of course, the dislocation distribution in the form of walls corresponds to a minimum energy of the dislocation array. This can be proven by comparing the dislocation self-energy E_s for initial random distributions, which is equal to the sum of the self-energies of the dislocations and their interaction energy and the total energy of GNDs, E_n, forming a system of $n = L/\lambda_w$ vertical walls (where L is the crystal width and λ_w is the average spacing between walls) [101]:

$$E_s = \frac{Gb^2}{2\pi(1-\mu)}\rho \ln\frac{1}{r_0\rho^{1/2}} \leftrightarrow E_n = \frac{Gb^2}{2\pi(1-\mu)}\rho \ln\frac{h_n}{r_0} \tag{27.13}$$

Using the relationship $\rho = (h_n\lambda_w)^{-1}$, the difference in energy (gain) between single dislocations and GNDs within the wall becomes

$$E_s - E_n = \frac{1}{4}\frac{Gb^2}{\pi(1-\mu)}\rho \ln\frac{\lambda_w}{h_n} > 0 \tag{27.14}$$

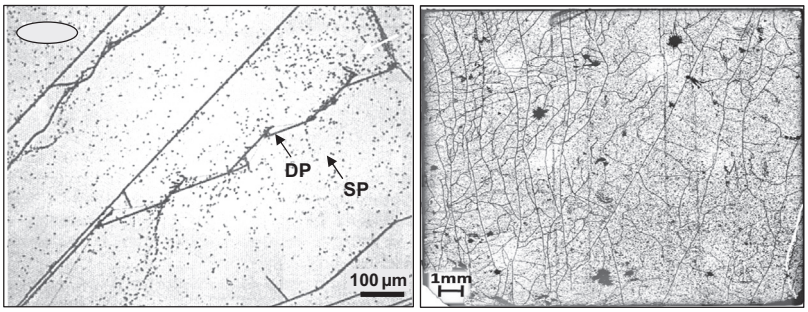

FIGURE 27.16 Dynamically polygonized dislocation walls together with statically polygonized dislocation cells in mc-Si and THM CdTe. *From Refs [163,164], respectively.*

where G is the shear modulus, b is the Burgers vector, μ is the Poisson ratio, ρ is the dislocation density, $\rho^{-1/2}$ is the mean spacing between dislocations of the random distributed configuration, r_0 is the dislocation core radius, and h_n is the distance between dislocation in walls. This result is due to the fact that the dislocation interaction energy decreases with decreasing spacing between dislocations when $\rho^{-1/2} > h_n$. The misorientations of the corresponding crystal fragments increase for the reverse relationship as $\theta_s < \theta_n$, where $\theta_s = b\rho^{1/2}$ and $\theta_n = b/h_n$.

Figure 27.16 shows both typical dislocation walls obtained by DP and dislocation cells formed at a higher T in the course of SP.

In numerous melt-grown compound crystals, such as in as-grown CdTe, PbTe, and CaF_2, for example, the cell arrangement resembles the classic low-angle grain boundary structure, with relatively high tilt angles on the order of arcmin, obviously originated by DP. The grain matrix usually contains some residual dislocations but the walls are formed very abruptly, consisting of only one dislocation row of identical Burgers vector [102]. On the other hand, there are materials with fuzzy cell walls of some thickness consisting of many tangled dislocations, such as Cu and GaAs [78], indicating SP assistance by high point defect diffusivity. They show relatively low tilt angles, around 10–20 arcsec. Additionally, there are crystals consisting of both somewhat elongated one-row dislocation walls and cellular substructures (Figure 27.16).

Finally, low-angle grain boundaries need a certain ripening time, which is not only influenced by the acting stress and cooling rate but also by the material properties, such as dislocation mobility and given content of point defects.

Note that there is also a totally different origin of formation of low-angle grain boundaries, which are not so easy to differentiate from DP in as-grown crystals. In case of morphological instabilities of the propagating melt-solid crystallization fronts caused by constitutional supercooling [103], characteristic cellular-shaped interfaces appear. They produce columnar grain boundary patterns similar to polygonized cell structuring, because the growing-in dislocations are assembled by their line bending toward the concave cusps (i.e., along the column boundaries). This has been very clearly observed by real-time synchrotron X-ray topography on Al-0.73 wt% Cu alloy [104].

27.4.2 Large-Angle Grain Boundaries-Polycrystallinity

As mentioned, large-angle grain boundaries are a characteristic feature of polycrystallinity, with tilt angles between the grains of more than 11°. A markedly disoriented grain ensemble appears when no monocrystalline seed is used to initiate a directional solidification. For instance, in metallurgical casting processes, multicrystalline ingots are intentionally produced by spontaneous nucleation of the solid phase within the melt in order to obtain enhanced mechanical strengths and macroscopic parameter homogeneity. In the field of monocrystal growth, however, it is the cardinal aim to prevent large-angle grain structures that impair the favorable anisotropic, electronic, and optical

qualities. The pioneering works aimed insert a seed into the solution tanks, dip a seed into the melt crucibles, or ensure grain selection by container necking. Many experiments have focused on grain coarsening based on the Gibbs–Thomson effect, whereupon grains of small dimension disappear due to their heightened chemical potential compared to the larger ones. To enhance the coarsening effect, an alternative remelting of the growing interface has been achieved (e.g., Refs [105,106]). In some materials, such as Te or Bi_2Te_3, the grain selection is even intrinsically supported due to the high anisotropy of thermal conductivity, favoring the overgrowth of the grains of highest conductivity along the growth direction. However, there are also materials where the artificial seeding fails. For example, CdTe and ZnSe have stable melt structuring due to their high bond ionicity, which prefers self-orientation around $\langle 110 \rangle \langle 111 \rangle$, even when a spontaneously nucleated first-to-freeze region is present [34].

With the increasing importance of directional solidification of the cheapest mc-Si ingots for PV, the control of large-angle grain growth comes to the fore. Grains formed by spontaneous nucleation at the container bottom (Figure 27.17(a)) may markedly degrade solar cell efficiency, especially when a high density of dislocations and impurities are captured. Such structures can be avoided by grain selection via initiating the crystallization in a bottom nozzle [107] or at the bottom corner of the crucible [108], by supporting grain coarsening via interface oscillation [106], as well as by

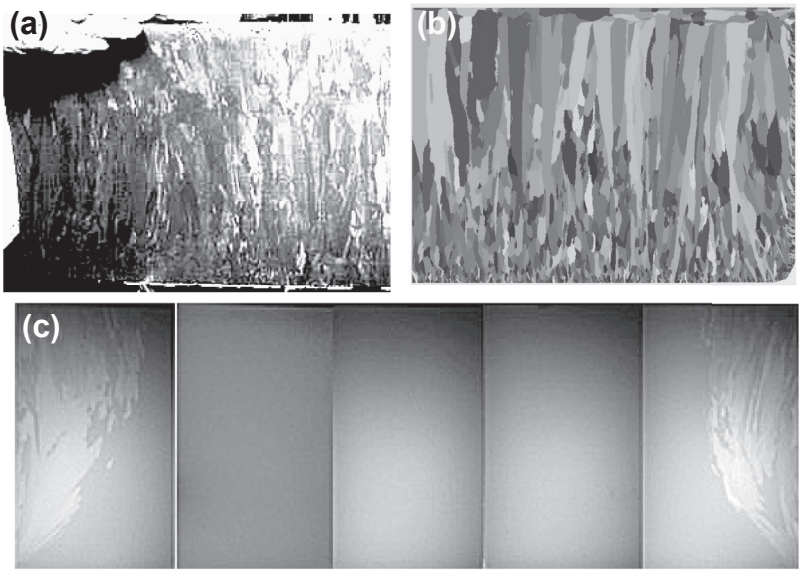

FIGURE 27.17 (a) Characteristic large-angle grain structure in a mc-Si ingot obtained by spontaneous nucleation at the container bottom; (b) simulated grain structure of case *a*; (c) cross-sectional photo from a G5 quasi-mono Si ingot directionally solidified from parquet-arranged dislocation-free Czochralski seed plates on the container bottom. As can be seen from *c*, in the course of solidification from bottom to top the polycrystalline growth is still induced at the container walls and spreading toward the volume. *Figures (a) and (b) are taken from Ref. [165] with permission; (c) is taken from Ref. [144] with Elsevier's permission.*

quasi-monocrystalline growth beginning on inserted seed plates [109]. In a study of the growth conditions for predominant grain orientations, Fujiwara [110] found that ⟨111⟩-oriented grains prevail for low-interface undercooling (low growth rate), whereas ⟨100⟩- and ⟨110⟩-oriented grains dominate at high undercooling (high growth rate).

Large-angle grain boundaries can also appear when the heat balance between melt and solid phases is disturbed, such as when the mechanically or electronically enforced moving rate of the isotherm exceeds the maximum thermal equilibrated growth velocity [111]. Also, prenucleations within the constitutionally supercooled diffusion boundary layer along the propagating interface may be responsible for disoriented growth. To avoid this, the criterion of Tiller [103] has to be obeyed.

27.5 Foreign Phase Particles

The presence of microparticles of foreign phase (second phase) or microvoids (bubbles) within the matrix of single crystals has been the object of research due to its harmful character. Such features are observed in nearly all crystalline materials. Microparticles affect the optical transmission, electrical carrier life, and structural perfection. They are sites of misfit stress and therefore of dislocation bunching; they are also sources of out-diffusing of embedded impurities. Characteristic microvoids in silicon crystals appearing at economically favorable high growth rates affect the wafer quality for epitaxial processes onto them.

There are two main origins of microparticle/microvoid generation:

1. Native *point defect condensation,* which during cooling leads to the nucleation of precipitates and microvoids via interstitial and vacancy agglomeration, respectively
2. *Incorporation* in favorable sites along the propagating crystallization front

Usually, both kinds of foreign phases differ in size. Whereas precipitates show characteristic dimensions in the range of 10–1000 nm, inclusions are typically of diameters >1 μm [34]. This classification, however, is only approximate and cannot serve as an exact criterion of distinction. The size of both kinds of microparticles or voids depends on various parameters, such as the concentration ratio of the components, degree of supersaturation, interface instabilities, and growth and cooling rates, which markedly influence the ripening time and extent. Nevertheless, the two features are treated separately in the following sections because of their usually differing backgrounds.

27.5.1 Precipitates (Retrograde Solidus, Defect Decoration)

One of the most serious consequences of compound crystal growth under conditions of native point defect formation is their condensation in precipitates and microvoids. This phenomenon is due to the retrograde behavior of the boundary of the compound

existence region (solidus) and therefore is related to nonstoichiometry. As the as-grown crystal is cooling down, the solidus is crossed and nucleation of the second phase takes place. Favored sites of precipitate ripening are dislocations, as has been concluded from infrared laser scattering tomography in GaAs crystals grown under As-rich conditions (e.g., Ref. [112]). Average tellurium precipitate densities of about 10^8 cm^{-3} and up to 10^{12} cm^{-3} have been found in CdTe [34]. Typical sizes between 10 and 100 nm have been determined for As precipitates in GaAs [113] and Te precipitates in CdTe [114]. Half-empty precipitates have been found by transmission electron microscopy in GaAs [115] and CdTe [116], probably caused by vacancy condensation in one of the sublattice components accompanied by conglomeration of excess atoms of the opposite sublattice.

Precipitates of both components are observed in most compound crystals, such as Te and Cd in CdTe and (Cd,Zn)Te (e.g., Ref. [117]), depending on the composition of the melt from which the crystal was grown (Te- or Cd-rich, respectively); in melt-grown GaAs crystals, only As precipitates were observed [112]. This is due to the different widths and positions of the compound homogeneity region against the stoichiometry. In CdTe, like in most compounds, they extend to both sides of stoichiometry [118]. On the contrary, in GaAs the phase extent region is completely located on the As-rich side [13], being comparable with the phase diagram of SnTe [12]. Thus, in order to reduce the precipitate content and size, the stoichiometry control during growth is of cardinal importance [34,35].

Many authors propose postgrowth wafer annealing as the most effective controlling step for producing stoichiometric and, hence, precipitate-free materials (e.g., Ref. [38]). Today, it is the industrial standard of GaAs crystal production to anneal the whole as-grown boule a few degrees below the melting point to obtain the dissolution of precipitates and their rediffusion from dislocation cell walls into the interiors during this first step. Then, a second step of a cooling shock of approximately 100 K downstops their ripening and back diffusion toward dislocations, thus keeping their size at an electronically compatible dimension of $<$100 nm [119].

27.5.2 Solvent Inclusions

Solvent inclusions are very common in crystals grown by all variants of solution growth (aqueous and organic solvents, flux). Two main origins are distinguished: faceting ("capping") of rounded surfaces and fluctuation of growth conditions (growth accidents).

27.5.2.1 Faceting ("Capping") of Rounded Surfaces

In general crystals grow from solutions with planar faces (habit faces), whereby faces with low surface energies grow slowly and determine the final morphology of the crystal (Wulff's theorem [120]). If surfaces are rounded (e.g., of the seed crystal or after redissolution), during first growth facets of habit faces and (between them) terraces of these faces are formed. The facets become larger and the terraced regions grow out until

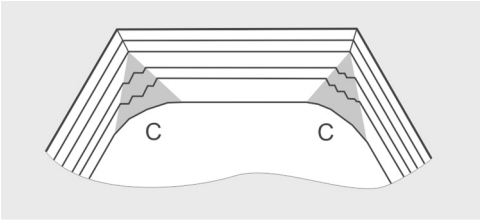

FIGURE 27.18 Faceting and "capping" on rounded crystal surfaces. The shaded regions C of terraced growth favor the entrapment of liquid inclusions. They grow out and finally form the growth-sector boundary between the main habit faces. *With permission from Springer Science + Business Media [45].*

a single edge between the two habit faces engaged is formed (see also "growth on spheres" [121], p. 130), as is shown in Figure 27.18. The "healed-out" regions often have the shape of caps (capping region). The growth on terraced surfaces favors the entrapment of solvent inclusions, which may lead in extreme cases to a spongy structure of the capping region. This usually happens during first growth on seed crystals, which are usually rounded due to final etching (which is necessary in order to remove surface impurities and defects) before seeding-in. Therefore, the zone of first growth around seed crystals is usually more or less disturbed by liquid inclusions. These inclusions, however, can be largely avoided by a very slow (and thus time-consuming) growth under low supersaturation during the seed-faceting period.

A conspicuous example of capping is provided by KDP grown in aqueous solution on (001) seed plates (Figure 27.19). KDP develops habit faces {100} (tetragonal prism) and {101} (tetragonal dipyramid), but {001} is not a habit face. Thus, in the first stage of growth on (001) seed plates, a spongy capping zone in the form of a tetragonal pyramid {101} over the (001) seed plate as basis is formed, followed by clear further growth on {101} pyramid faces (Figure 27.19). Detailed descriptions of this (001) capping process in

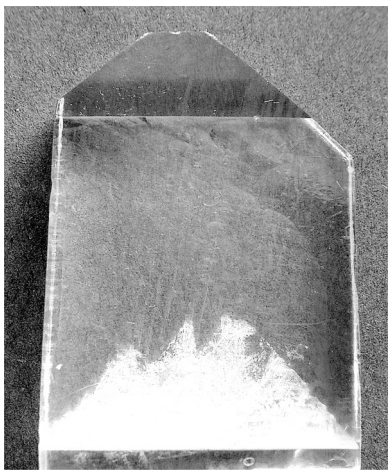

FIGURE 27.19 A potassium dihydrogen phosphate crystal (length 45 mm) with {011} capping pyramid on a (001) seed plate. *With permission from Springer Science + Business Media [45].*

KDP and ammonium dihydrogen phosphate crystal growth are presented by Zerfoss and Slawson [122] and Janssen-Van Rosmalen et al. [123].

27.5.2.2 Fluctuation of Growth Conditions (Growth Accidents)

A sufficiently strong change of growth conditions (e.g., of supersaturation, stirring rate, stirring direction) may introduce—due to local variations of supersaturation—a (temporary) instability of growth faces. Regions of retarded and promoted growth occur, leading to elevations and depressions on the growth face. Finally, overhanging layers spread over the depressions and close them, thus trapping nutrient solution. Usually, a group of inclusions arranged in a plane parallel to the growth face is formed ("zonal inclusions", Figure 27.4). If all growth faces of the crystal are affected by the same growth disturbance, inclusions are formed on all faces. After stabilization of growth conditions and further clear growth, the inclusions are visible by scattered light (if the crystal is transparent) and reveal the shape of the crystal in the instant of the disturbance ("phantom crystal" in mineralogy).

The tendency to form solvent inclusions may strongly depend on the type of growth face {hkl}. In general, the formation of solvent inclusions is favored on faces with high surface (attachment) energy and therefore high growth rate. An instructive example is provided by potassium alum growing from aqueous solution: fluctuations of growth conditions pronouncedly lead to liquid-inclusion entrapment on the smaller and fast-growing cube faces {100}, whereas the slow and morphologically dominant octahedron faces {111} resist the formation of inclusions, even for strong changes of growth parameters. The reason for the preferred inclusion trapping of certain growth faces is their specific surface structure, which favors the incorporation of solvent (and other) molecules. This phenomenon corresponds to the so-called hourglass inclusions, which have been studied in detail for potassium sulfate (e.g., Ref. [121], p. 415–420; Vetter et al. [124]; and Kahr et al. [125,126]).

The hydrodynamics of the solution flow around the growing crystal may also play a significant role in the formation of liquid inclusions (e.g., Chernov et al. [127]). A particularly interesting example of this influence in the growth of KDP crystals was reported by Janssen-Van Rosmalen and Bennema [128], Janssen-Van Rosmalen et al. [123], and van Enckevort et al. [129]. In their experiments, the growing KDP crystals (shape: tetragonal prism {100} terminated on both side by dipyramid {011}) were rotated on a lever in the solution in such a way that the solution flow was toward one (front) pyramid and off the other (rear) pyramid. On the pyramid faces of the rear side, solvent inclusions are often formed in a quasi-periodic sequence (Figure 27.5), whereas at the front side inclusions do not appear. This phenomenon is explained by the hydrodynamic situation at the rear-side pyramid face: in the wake "behind" the crystal, a swirling region with no or strongly reduced liquid exchange with the bulk mother solution is formed. Thus, the saturation locally decreases and growth is retarded compared to neighboring regions, leading to a depression in the growth face. After some amount of further growth, the flow situation changes and supersaturation is restored. This causes an overgrowth of the cavity, forming

a solvent inclusion. As is shown in Figure 27.5, this process is repeated several times in a quasi-periodic manner. A detailed study of this effect, including flow simulation experiments in a model system, was presented by Janssen-Van Rosmalen et al. [128] and van Enckevort et al. [129], who also reported that the formation of these inclusions is avoided by stronger stirring. In any case, strong stirring smoothes out supersaturation differences on the growth face and thus may largely avoid interface instabilities.

27.5.3 Melt Growth Inclusions

Second-phase inclusions may appear when a segregation-driven diffusion boundary layer is formed in front of the growing interface. If the enriched impurity concentration exceeds the solubility limit, microparticles are nucleated and very likely incorporated. Chernov [18] estimated undercritical growth rates at which such particles and gas bubbles should be rejected by the propagating solid front. However, he assumed an ideal flat interface. In reality, when both the diffusion boundary layer and low-temperature gradient are simultaneously present, the front region is constitutionally undercooled and the interface shape becomes morphologically instable. As a result, microgrooves are formed, transforming into cellular or facetted structures with favorable sites of particle capturing [19]. Note that trapping interfacial nooks can also form by coinciding grain boundaries, typically for mc-Si growth [130,131]. Hence, during silicon crystallization, SiC and Si_3N_4 precipitates are nucleated when the solubility limit of carbon (5×10^{18} cm^{-3}) and nitrogen ($\sim 1 \times 10^{19}$ cm^{-3}) is exceeded. It is always preferable to counteract against the diffusion boundary layer by complete melt mixing, such as by using a nonsteady magnetic field, inert gas sparkling, or mechanical vibration [132].

27.5.4 Structural Consequences of Second-Phase Particles

During the cooling-down process, both precipitates and inclusions induce mechanical stress due to their differing crystallographic structure and thermal expansion compared to the matrix configuration. Moreover, the particle components can exhibit a lower melt temperature than the matrix and remain in the molten (or vapor) state down to the eutectic point. In case of volume increase during their solidification, additional stress is generated. These effects were treated in various publications. A representative example is reported in the theoretical paper by Yadava et al. [89], which deals with Te precipitation in CdTe crystals.

Consider the temperature region where the incorporated second-phase particle is still a droplet. The net pressure at the interface with the solid matrix is

$$p' = p - \frac{2\gamma_{IF}}{r_d} \tag{27.15}$$

where p is the internal droplet pressure, γ_{IF} is the surface tension of the liquid Te–solid CdTe interface, and r_d is the droplet radius. In general, $p' \neq 0$; therefore, the interface will be mechanically unstable. To attain mechanical equilibrium, the isotropic droplet

volume will decrease by the amount of $\Delta V_{\text{rel}} = 3/4\ p'(V/G)$, where V is the unstressed droplet volume and G is the shear modulus. This process will generate strain in the surrounding matrix and in the interface.

Using a thermodynamic approach, the included droplet pressure is given by [89]

$$p = kT\rho_l x + 2Z\varepsilon\rho_l\left[\left(1 - \frac{kT}{2Z\varepsilon}\right)x^5 - x^3\right] \tag{27.16}$$

where k is the Boltzmann constant, ρ_l is the liquid density of Te at given T (temperature), $x = \rho/\rho_l$ is the liquid density normalized with respect to the density at 1 atm (for droplets to be in compression, $x > 1$), Z is the average coordination number in liquid Te ≈ 3.1, ε is the pair association energy (≈ 1.2 eV), and k is the Boltzmann constant. The calculated dependence of the Te droplet pressure on the temperature for various interstitial concentrations is shown in Figure 27.14. Taking the precipitated Te interstitial number per droplet as a quantity of size, it follows from the figure that the pressure increases with particle volume.

The Greenwood–Foreman–Rimmer mechanism of interstitial dislocation loop punching is one of the possible processes that can effectively reduce the overall free energy. The mechanism is schematically illustrated in Figure 27.14 (right). The excess internal pressure p' (Eqn (27.16)), acting outwardly on the droplet/matrix interface, produces shear strain in the neighboring solid region; above a threshold level, this punches a part of an atomic layer and places it as a platelet of the interstitials sandwiched between two adjacent regular atomic planes. Of course, the punching occurs on the energetically-most-favorable atomic planes. In the process, the droplet volume increases and, thus, the pressure decreases. Theoretically, it is shown that the loop punching will occur if [89]

$$p' = p - \frac{2\gamma_{IF}}{r_d} \geq \frac{G_m b}{2\pi r_d}\ln\left(\frac{r_d}{b}\right) \tag{27.17}$$

where b is the Burgers vector of the dislocation loop and G_m is the shear modulus of the matrix. All another parameters are specified in Eqns (27.15) and (27.16).

27.6 Faceting and Twinning

27.6.1 Faceting during Growth

In general, crystals grow from solutions, supercooled melts, and vapor phases with planar faces (habit faces), whereby faces with low surface energies grow slowly and determine the final morphology of the crystal (Wulff theorem [120]). A crystal that has fully grown on the habit faces consists of growth sectors—that is, regions grown on different habit faces and separated by growth-sector boundaries (Figure 27.20). These boundaries are formed by the path of the edges between neighboring habit faces during growth. Due to their different growth directions and often also different crystallographic (i.e., symmetrically nonequivalent) nature, growth sectors usually exhibit slightly different, growth-induced

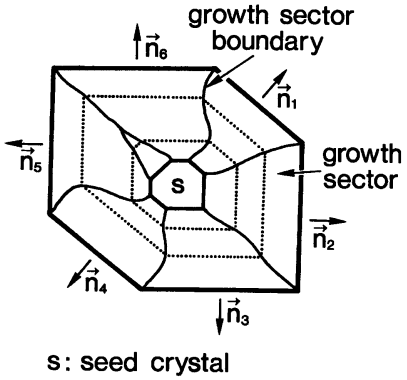

FIGURE 27.20 Fully faceted crystal, divided into growth sectors (i.e., regions grown on different habit faces). They are separated by growth-sector boundaries, which are internal surfaces generated by the movement of the edges joining neighbored faces during growth. The vectors $\mathbf{n}_i$ indicate the growth directions. Dashed lines: contours of the crystal at different stages of growth. One of the growth sectors has "grown-out." *With permission from Springer Science + Business Media [45].*

physical properties, such as different optical birefringence ("optical anomaly" [133]). Due to this phenomenon, growth sectors are sometimes misinterpreted as twins.

Similar features can be observed at crystal growth from melts, especially in materials with atomically smooth (i.e., singular) planes. Most dielectrics show such planes parallel to lattice planes of small Miller's indices. The common semiconductor materials, with their covalent bonding, tend also to form facets during melt growth, although only on their most closely packed (i.e., {111}) planes [1].

27.6.2 Growth Twins and Postgrowth Twins

A twin is a frequently occurring aggregate or intergrowth of two or more crystals of the same species (same chemical composition and crystal structure) with a defined crystallographic orientation relationship (determining the orientation states of the twin components), which in mineralogy is called the "twin law". Besides the twin law, the boundary between twin domains (the contact relation) plays a decisive role: twins occur in those crystals in which boundaries of low energy can be formed. This has quantitatively been proven by Gottschalk et al. [134], who showed that the ease and frequency of the formation of (111) spinel twins (Figure 27.24) in the zinc blende structure of III–V semiconductor compounds is correlated to the (111) stacking fault (twin-boundary) energy: the lower the stacking fault energy, the more frequent the twinning. There is, however, also a theory stating that the boundary energy is of minor importance and that kinetic influences play a decisive role in the formation of twins [135]. This approach, however, has been critically discussed [136,137].

Twins are mainly classified by morphological features (dove-tail, contact, penetration, sector, polysynthetic twins, etc.), their genetic origin (growth, transformation, mechanical or deformation twins), and their lattice coincidence features, such as

merohedral twins (full or partial three-dimensional lattice coincidence, also called CSL lattice in the treatment of grain boundaries). Reviews on twinning are presented in many textbooks of mineralogy and crystallography (e.g., Refs [138,139]). A comprehensive treatment has been provided by Hahn and Klapper [140] (see here especially for growth twinning, p. 412–14). A survey of X-ray topographic characterization of twinned crystals was given by Klapper [141].

In the growth of technologically significant crystals, the spinel twins of cubic crystals with twin law "reflection plane" (111) or "twofold axis" [111] require particular attention. They occur as growth twins in crystals with diamond structures (Si, Ge), zinc blende structures (e.g., ZnS, GaAs, InP, CdTe [134,142]), and sodium chloride structures (photographic materials AgCl and AgBr [143]). They are characterized by a partial lattice coincidence of one-third of the lattice points (so-called Σ3 twins), which form a hexagonal sublattice, with its principal axis along the threefold axis [111] common to both twin components. Preferred twin boundaries are planes {111} and {112}. The typical shapes of spinel twins grown from solutions are shown in Figure 27.21. For semiconductor crystals grown from melts, see, for example, Refs [1,145,146].

In many cases, twins are formed during the first stage of spontaneous nucleation, possibly before the subcritical nucleus reaches the critical size necessary for stable growth. This formation is strongly evidenced for penetration and sector twins, where all domains are of similar size and originate from one common, well-defined point in the center of the twinned crystal, which marks the location of the spontaneous nucleus

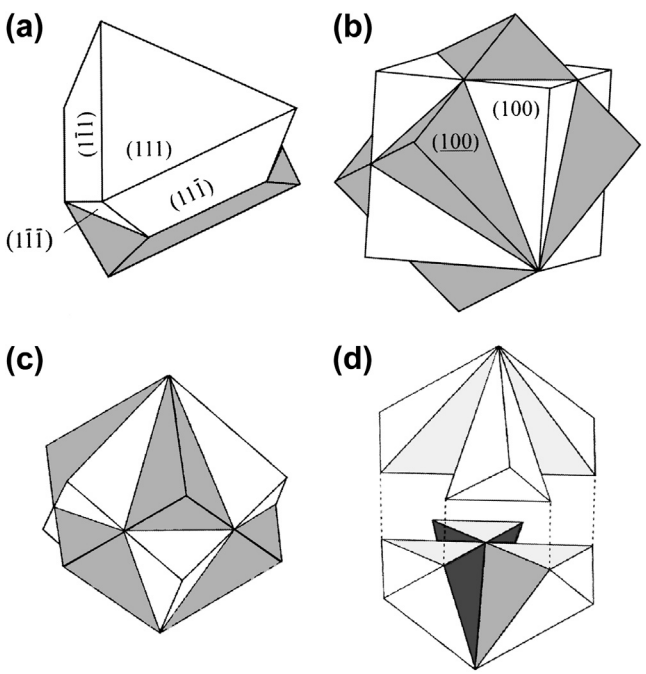

FIGURE 27.21 Spinel twins of cubic crystals with twin reflection plane (111) or twofold twin axis [111] (or alternatively ±60° rotation around [111]). The domains of the two orientation states are white and shaded. (a) Contact twin with (111) contact plane (two twin components). (b, c) Penetration twin (idealized) with one [111] and three $\{11\bar{2}\}$ contact planes (12 twin components, six of each orientation state) in two different views: (b) with one [001] axis vertical, (c) with the axis [111] common to both domains (twin axis) vertical. (d) Skeleton of the six components (exploded along [111]) of the shaded orientation state of (c). *With permission from Springer Science + Business Media [45].*

(Figure 27.22). Other prominent examples are the penetration twins in rhombohedral crystals such as corundum (aluminum oxide, Al_2O_3 [147]) or iron borate ($FeBO_3$, calcite structure [141]), and sector twins of pseudo-hexagonal crystals such as ammonium lithium sulfate (Figure 27.22), potassium sulfate [140], and aragonite $CaCO_3$, which form twins with three orientation states. The origin of twinning by nucleation must also be assumed for contact twins (Figure 27.21(a)) if both partners of the final twin have roughly the same size, or if all spontaneously nucleated crystals in one batch are twinned. For example, all crystals of monoclinic lithium hydrogen succinate precipitated from aqueous solution are without exception dove-tail contact twins.

An approach to the twin formation during crystal nucleation has been advanced by Senechal [148], who proposed that the crystal nucleus first formed has a symmetry that is not compatible with the lattice of the (macroscopic) crystal. This symmetry may even be noncrystallographic. It is assumed that, after the nucleus has reached a critical size beyond which the translation symmetry becomes decisive, the nucleus collapses into a twinned crystal with domains of lower symmetry and continues to grow as a twin. This idea of twin formation from noncrystallographic nuclei has been experimentally substantiated by high-resolution transmission electron microscopy investigations of nanocrystalline diamond-type and fcc cubic crystals, such as Ge, Ag, and Ni [149].

According to Hurle [145], also in zincblende crystals, the twinning starts at two-dimensional nucleation on the {111} facets during CZ and VGF growth when such

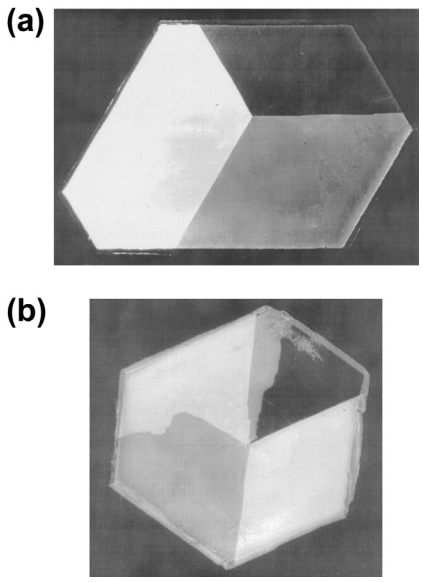

FIGURE 27.22 Photographs of (001) plates (approximately 20-mm diameter, 1-mm thick) of orthorhombic pseudo-hexagonal NH_4LiSO_4 between crossed polarizers, showing sector growth twins. (a) Nearly regular threefold sector growth twin (three orientation states, three twin components). (b) Irregular sector twin (three orientation states, but five twin components). *With permission from the internat. Union of Crystallography (IUCr) [140, p. 413].*

planes are adjacent to the three-phase boundary of melt, crystal, and ambient. This model demonstrates that, because of the orientation dependence of interfacial energies in the presence of facets, there is a configuration of the three-phase boundary for which, for sufficiently large supercooling, the free energy of formation of a critical nucleus is actually lowered by forming that nucleus at the three-phase boundary in twinned orientation (i.e., specified by a rotation of the lattice by 60° about a ⟨111⟩ axis). Such a twinned nucleus is thermodynamically favored if the supercooling exceeds a critical value. Rudolph [34] postulated that even a residual melt association in the form of tetrahedra can promote a false stacked nucleation. This fluid configuration appears demonstrably, especially in melts of high ionicity such as II–VIs (CdTe, ZnSe) [150,151] but also in InP, which shows the highest ionicity (>40%) and lowest stacking fault energy of III–Vs.

As for dislocations (see Section 27.3.2), inclusions are also frequently sources of twins. It is assumed that a nucleus in twinned orientation forms at the inclusion and proceeds in this orientation during further growth. An instructive experimental key study of this process was presented by Sunagawa et al. [152] for Dauphiné and Brazil twins in synthetic quartz. Amethyst quartz contains much more Dauphiné and Brazil twins than normal (colorless) quartz. The higher frequency of twin formation is doubtlessly due to its relatively high content of iron [153]. Sunagawa et al. [152], and references therein, grew amethyst quartz hydrothermally in various solutions containing ferric iron on amethyst seed plates of various orientations. They studied the twinning generated on as-grown faces, on etched growth faces, and on cut surfaces by light-microscopic methods. In all cases, the Dauphiné and Brazil twins originated from solid inclusions containing iron (probably as Goethite, FeOOH). In some cases, the Brazil twins are associated with dislocations originating from the same inclusion.

There are two causes for the formation of postgrown twins during cooling to room temperature after growth: *phase transitions* and ferroelastic switching [154].

Crystals often can only be grown at elevated temperatures where they crystallize in another (high-temperature) phase, of usually higher symmetry than what they adopt at room temperature. On cooling below the transition temperature, the twin domains are formed, whereby the lost symmetry elements of the mother phase act as twin elements (twin laws) relating the twin domains. For instance, lithium niobate $LiNbO_3$ is grown from the melt at $T_m = 1275\,^{\circ}C$ and undergoes a paraelectric–ferroelectric transition at $T_c \approx 1140\,^{\circ}C$, whereby ferroelectric domains are formed. The high-temperature superconductor $YBa_2Cu_3O_{7-\delta}$, usually grown from flux, is subject to a transition at approximately 750 °C from the tetragonal parent phase into an orthorhombic modification, whereby it develops two nearly orthogonal systems of twin lamellae parallel to the two {110} mirror planes of the tetragonal mother phase, lost in the transition [155]. These lamellae are ferroelastic and can be changed or even removed (detwinned) by mechanical stress. A similar case was reported by Rudolph et al. [156]: ZnSe crystals underwent a phase transition from wurtzite to zinc blende structure at ∼100 K below the melting point $T_m = 1520\,^{\circ}C$. Thus, during the cooling down of melt-grown crystals,

numerous twin lamellae were formed. An example related to mineralogy is provided by quartz, which is stable in its trigonal phase below 575 °C (α-quartz, point group 32) and hexagonal (β-quartz, point group 622) above this temperature. The transition from the hexagonal to the trigonal modification invariably leads to the formation of Dauphiné twinning (loss of the twofold axis in the sixfold axis). The shape and arrangement of twin domains generated by crystal growth or by phase transformation (e.g., for Dauphiné twins) is quite different. In mineralogy, these different features of twin textures are very helpful for the determination of the conditions of mineral formation. Brazil twins of quartz and his homeotypes (e.g., gallium phosphate $GaPO_4$) cannot be generated by the phase transition; they are always growth twins.

The twin domains of ferroelastic crystals switch by mechanical stress from one orientation state into the other. This occurs quite easily at elevated temperatures where the coercive stress is strongly reduced. Thus, in a ferroelastic crystal grown without twinning, twin domains may be introduced by stress developed during cooling to room temperature. Here again, inclusions forming stress centers are the main reason. The ferroelastic twin pattern is often correlated to the growth defects of the crystal, such as with growth striations ([157], Figure 100; [141], p. 379). Postgrowth formation of twins by *ferroelastic switching* has been observed, for example, in ammonium sulfate $(NH_4)_2SO_4$ [158] and Rochelle salt ([157], p.184), which are both grown from aqueous solution.

27.6.4 Measures to Avoid Twinning

In most cases, twinning of technologically important crystals seriously impairs their usability for technical devices. This is largely avoided by optimizing the growth conditions. For solution growth, the most important measure is to use twin-free seed crystals and avoid inclusions.

A more serious and recurrent problem is given by facet-induced twins of melt-grown crystals. Many LEC and Bridgman experiments have demonstrated that the twin probability is reduced markedly if the temperature oscillations of the growth system, and therefore undercoolings with related excursions of the angle of the contacting meniscus, are minimized. This is due to the reduced probability of encountering the critical angle when the meniscus angle fluctuations are reduced [1,145]. In fact, Hosokawa et al. [159] succeeded in twin-free InP crystal growth with diameters up to 100 mm by careful maintenance of thermal stability during growth assisted by convection damping of the magnetic field around the melt.

Neubert et al. [146] accentuated the importance of growth rate stability during LEC and VGF. They proposed highly sophisticated and robust model-based feedback control to avoid crystallization velocity fluctuations and, thus, reduce twin frequency in compound semiconductor growth [160]. Rudolph et al. [156,161] obtained a minimized twin density in CdTe and ZnSe melt-grown Bridgman crystals when the fluid phase was markedly overheated before the crystallization started. They attributed this effect to the reduced

degree of melt association, preventing the probability of false stacking sequences when associated species, such as tetrahedra are still present and being incorporated.

27.7 Concluding Remarks

The most important defect types and possible origins during crystal growth from melt and solution have been discussed in this chapter. Today, most of the defect-forming mechanisms are well understood. However, some important questions remain to be solved. For instance, the influence of the melt configuration on the growth kinetics, which probably plays an essential role in II–VI systems, it is not yet fully understood. Furthermore, the dislocation patterning and bunching mechanisms related to the growth conditions have not yet been decoded completely. Also, the main twinning origin has not yet been revealed.

Eminent success has been achieved in technological developments. Computer-controlled VGF has become the leading industrial production method for semiconductor compound crystals. However, that is not to say that all defects can be avoided. For example, the relatively poor thermal conductivity and low yield stress of III–V and II–VI compounds as compared with Ge and Si mean that it is not possible to reduce thermal stress to a sufficiently low level to avoid dislocations.

Scaling up to achieve cost reduction is an ever-present pressure. Increasing crystal diameter also increases the thermal stresses experienced during cooling. Avoiding increased dislocation density requires ever-increasing refinement of furnace design; here, computer modeling plays a key role.

An additional problem posed by scaling-up is the increased turbulence that occurs in the melt. The use of magnetic fields or another external force is being exploited to achieve damping of this turbulence [132]. In many chapters of this book, the correlation between growth parameters and all previously discussed defect types, as well as measures of prevention, are discussed.

References

[1] Hurle DTJ, Rudolph P. J Cryst Growth 2003;264:550.

[2] van Bueren HG. Imperfections in crystals. Amsterdam: North-Holland Publ.; 1960.

[3] Pick H. Naturwissenschaft 1954;41:346. in German.

[4] Kröger FA. The chemistry of imperfect crystals. Amsterdam: North-Holland Publ.; 1964 and 1973.

[5] Mattsson AE, Wixom RR, Armiento R. Phys Rev B 2008;77:155211.

[6] Voronkov VV. J Cryst Growth 2008;310:1307.

[7] von Ammon W. In: Müller G, Metois JJ, Rudolph P, editors. Crystal growth – from fundamentals to technology. Amsterdam: Elsevier; 2004. p. 239.

[8] Itsumi M. J Cryst Growth 2002;237–239:1773.

[9] Hurle DTJ. In: Müller G, Metois JJ, Rudolph P, editors. Crystal growth – from fundamentals to technology. Amsterdam: Elsevier; 2004. p. 323.

[10] Rudolph P. Cryst Res Technol 2003;38:542.

[11] Erdei S, Ainger FW. J Cryst Growth 1997;174:293.

[12] Rogacheva EI. Inorg Mater 1991;27:194.

[13] Dreyer W, Duderstadt F. On the modelling of semi-insulating GaAs including surface tension and bulk stresses, Treatise No. 995. Berlin: Weierstraß-Institut; 2004.

[14] Rudolph P, Kiessling F-M. J Cryst Growth 2006;292:532.

[15] Rosenberger F. Fundamentals of crystal growth I. Berlin: Springer; 1979.

[16] Berding MA. Phys Rev 1999;60:8943.

[17] Jackson KA. Kinetic processes. Weinheim: Wiley-VCH; 2004.

[18] Chernov AA. Modern crystallography III. Berlin: Springer; 1984.

[19] Rudolph P. In: Dhanaraj G, Byrappa K, Prasad V, Dudley M, editors. Handbook of crystal growth. Berlin-Heidelberg: Springer; 2010. p. 153.

[20] Motooka T, Nishihira K, Oshima R, Nishizawa H, Hori F. Phys Rev B 2002;65:813041.

[21] Rudolph P. In: Fornari R, Paorici C, editors. Theoretical and technological aspects of crystal growth. Switzerland: Trans Tech Publications; 1998. p. 1.

[22] Burton JA, Prim RC, Slichter WP. J Chem Phys 1987;21:1991.

[23] Müller G, Ostrogorsky A. Convection in melt growth. In: Hurle DTJ, editor. Bulk crystal growth – growth mechanisms and dynamics, vol. 2b. Amsterdam: Elsevier; 1994. p. 709.

[24] Dornberger E. [thesis]. Universite Catholique de Louvain; 1997.

[25] Hurle DTJ. J Appl Phys 1999;85:6957.

[26] Rudolph P, Rinas U, Jacobs K. J Cryst Growth 1994;138:249.

[27] Northrup E, Zhang SB. Phys Rev B 1993;47:6791.

[28] Neugebauer J, Van de Walle CG. Phys Rev B 1994;50:8067.

[29] Boguslawski P, Briggs EL, Bernholc J. Phys Rev B 1995;51:17255.

[30] Luken KM, Morrow RA. Semicond Sci Technol 1996;11:11556.

[31] Dornberger E, Virbulis J, Hanna B, Hoelzl R, Daub E, von Ammon W. J Cryst Growth 2001;229:11.

[32] Rudolph P, Kiessling FM. Cryst Res Technol 1988;23:1207.

[33] Monberg E. In: Hurle DTJ, editor. Handbook of crystal growth, vol. 2a. Amsterdam: Elsevier; 1994. p. 51.

[34] Rudolph P. Prog Cryst Growth Charact Mater 1995;29:275.

[35] Kiessling F. In: Capper P, Rudolph P, editors. Crystal growth technology. Weinheim: Wiley-VCH; 2010. p. 75.

[36] Rudolph P, Kawasaki S, Yamashita S, Yamamoto S, Usuki Y, Konagaya Y, et al. J Cryst Growth 1996; 161:28.

[37] Biswas K, Du M-H. New J Phys 2012;14:063020.

[38] Franc J, Sedivy L, Belas E, Bugar M, Zazvorka J, Pekarek J, et al. Cryst Res Technol 2013;48:214.

[39] Oda S, Yamamoto M, Seiwa M, Kano G, Inoue T, Mori M, et al. Semicond Sci Technol 1992;7:215.

[40] Neubert M, Rudolph P. Prog Cryst Growth Charact Mater 2001;43:119.

[41] Kiessling F-M, Rudolph P, Neubert M, Juda U, Naumann M, Ulrici W. J Cryst Growth 2004;269:218.

[42] Borovlev UA, Ivannikova NV, Shlegel VN, Vasiliev YaV, Gusev VA. J Cryst Growth 2001;229:305.

[43] Pfeiffer E, Rudolph P. Patent DD 290 226; 1989.

[44] Klapper H. Mater Chem Phys 2000;66:101.

[45] Klapper H. In: Dhanaraj G, Byrappa K, Prasad V, Dudley M, editors. Springer handbook of crystal growth. Berlin-Heidelberg: Springer; 2010. p. 93.

[46] Völkl J. In: Hurle DTJ, editor. Handbook of crystal growth, vol. 2b. Amsterdam: Elsevier; 1994. p. 821.

[47] Prasad V, Pendurti S. In: Dhanaraj G, Byrappa K, Prasad V, Dudley M, editors. Springer handbook of crystal growth. Berlin-Heidelberg: Springer; 2010. p. 1335.

[48] Neuroth G. [Ph.D. thesis]. University of Bonn; 1996.

[49] Forty AJ. Adv Phys 1954;3:1.

[50] Klapper H. In: Tanner BK, Bowen DK, editors. Characterization of crystal growth defects by X-ray methods. New York: Plenum Press; 1980. p. 133.

[51] Lothe J. Phys Nor 1967;2:154.

[52] Klapper H, Küppers H. Acta Crystallogr 1973;A29:495 (correction: read K/cos α instead of K cos α).

[53] Klapper H. Phys Status Solidi A 1972;14:99.

[54] Klapper H. Phys Status Solidi A 1972;14:443.

[55] Eshelby JB, Read WT, Shockley W. Acta Metall 1953;1:251.

[56] Klapper H, Fishman Yu M, Lutsau VG. Phys Status Solidi A 1974;21:115.

[57] Klapper H. In: Karl N, editor. Crystals: growth, properties and characterization, vol. 13. Berlin-Heidelberg: Springer; 1991. p. 109.

[58] Scheffen-Lauenroth T, Klapper H, Becker RA. J Cryst Growth 1981;55:557.

[59] Schmidt W, Weiss R. J Cryst Growth 1978;43:515.

[60] Venégues P, Beaumont B, Bousquet V, Vaille M, Gibart R. J Appl Phys 2000;87:4174.

[61] Gradezcak S, Stadelmann P, Wagner V, Ilegems M. Appl Phys Lett 2004;85:4648.

[62] Klapper H. In: Authier A, Logomarsino S, Tanner BK, editors. X-ray and neutron dynamical diffraction: theory and applications. Proc. NATO ASI, Erice 1996, NATO science series B, vol. 357. Plenum Publ. Corp.; 1997. p. 167.

[63] Watanabe T, Izumi K. J Cryst Growth 1979;46:747.

[64] Izumi K. Jpn J Appl Phys 1977;16:2103.

[65] Klapper H. Mater Sci Forum 1998;276–277:291.

[66] Amoedo RJ, Ghoniem NM. Dislocation dynamics I and II. Phys Rev 1990;41:6958–68.

[67] Indenbom VL. Krist Tech 1979;14:493 [in German].

[68] Hull D, Bacon DJ. Introduction to dislocations. 5th ed. Amsterdam: Elsevier; 2011.

[69] Holt DL. J Appl Phys 1970;41:3197.

[70] Rudolph P. Cryst Res Technol 2005;40:7.

[71] Mullin JB. J Cryst Growth 2004;264:578.

[72] Shimizu A, Nishizawa J, Oyama Y, Suto K. J Cryst Growth 2001;229:119.

[73] Bünger Th, Behr D, Eichler St, Flade T, Fliegel W, Jurisch M, et al. Mater Sci Eng B 2001;80:5.

[74] Genzel C, Gille P, Hähnert I, Kießling FM, Rudolph P. J Cryst Growth 1990;101:232.

[75] Durose K, Russel GJ. J Cryst Growth 1988;86:471.

[76] Frank-Rotsch Ch, Juda U, Kiessling F-M, Rudolph P. Mater Sci Technol 2005;21:1450.

[77] Bolotnikov AE, Camarda GS, Cui Y, Yang G, Hossain A, Kim K, et al. J Cryst Growth 2013;379:46.

[78] Tuomi T, Knuuttila L, Riikonen J, McNally PJ, Chen W-M, Kanatharana J, et al. J Cryst Growth 2002; 237:350.

[79] Gröschel A, Will J, Bergmann Ch, Grillenberger H, Eichler St, Scheffer Czygan M, et al. Solid State Phenom 2011;178–179:360.

[80] Zaiser M. In: Müller G, Metois J, Rudolph P, editors. Crystal growth – from theory to technology. Amsterdam: Elsevier; 2004. p. 215.

[81] Kuhlmann-Wilsdorf D. Metall Trans A 1985;16A:2091.

[82] Taylor GI. J Inst Met 1938;62:307.

[83] Kubin LP. Dislocations, mesoscale simulations and plastic flow. Oxford: Oxford University Press; 2013.

[84] Ryningen B, Stokkan G, Kivambe M, Ervik T, Lohne O. Acta Mater 2011;59:7703.

[85] Sopori B, Li C, Narayanan S, Carlson D. Mater Res Soc Symp Proc 2005;864:233.

[86] Yang YM, Yu A, Hsu B, Hsu WC, Yang A, Lan CW. Prog Photovolt Res Appl 2013. http://dx.doi.org/10.1002/pip.2437.

[87] Rudolph P, Engel A, Schentke I, Grochocki A. J Cryst Growth 1995;147:297.

[88] Yang G, Bolotnikov AE, Fochuk PM, Kopach O, Franc J, Belas E, et al. J Cryst Growth 2013;379:16.

[89] Yadava RDS, Badai RK, Borle WN. J Electron Mater 1992;21:1001.

[90] Rudolph P, Frank-Rotsch Ch, Juda U, Eichler St, Scheffer-Czygan M. Phys Status Solidi C 2007;4: 2934.

[91] Shibata M, Suzuki T, Kuma S, Inada T. J Cryst Growth 128(193):439.

[92] Benjamin Britton T, Wilkinson AJ. Acta Mater 2012;60:5773.

[93] Duffar T, Dusserre P, Picca F, Lacroix S, Giacometti N. J Cryst Growth 2000;211:434.

[94] Althaus M, Sonnenberg K, Küssel E, Naeven R. J Cryst Growth 1996;166:566.

[95] Müller G, Birkmann B. J Cryst Growth 2002;237–239:1745.

[96] Parsey JM, Thiel FA. J Cryst Growth 1985;73:211.

[97] Tomizawa K, Sassa K, Shimanuki Y, Nishizawa J. J Electrochem Soc Solid State Technol 1984;131: 2394.

[98] Bako B, Groma I, Györgyi G, Zimanyi G. Comp Mater Sci 2006;38:22.

[99] Gottstein G. Physikalische Grundlagen der Materialkunde, 3. Auflage. Berlin: Springer; 2007.

[100] Ashby MF. Philos Mag 1970;21:399.

[101] Malygin GA. Phys Solid State 2002;44:1305. Translated from Fiz Tverd Tela 2002;44:1249.

[102] Sabinina IV, Gutakovski AK, Milenov TI, Lykakh NN, Sidorov YG, Gospodinov MM. Cryst Res Technol 1991;26:967.

[103] Tiller WA, Jackson KA, Rutter JW, Chalmers B. Acta Metall 1953;1:428.

[104] Grange G, Billia B. J Phys Fr 1994;4:293.

[105] Scholz H. Solid State Commun 1976;19:429.

[106] Koji Arafune, Eichiro Ohishi, Hitoshi Sai, Yoshio Oshita, Masafumi Yamaguchi. J Cryst Growth 2007;308:5.

[107] Li TF, Yeh KM, Hsu WC, Lan CW. J Cryst Growth 2011;318:219.

[108] Kiessling F-M, Frank-Rotsch Ch, Dropka N, Rudolph P. Patent DE 10 2011 076 860 (2011).

[109] Takahashi I, Usami N, Kutsukake K, Stokkan G, Morishita K, Nakajima K. J Cryst Growth 2010;312: 697.

[110] Fujiwara K, Obinata Y, Ujihara T, Usami N, Sazaki G, Nakajima K. J Cryst Growth 2004;266:467.

[111] Rudolph P. In: Wang M, Tsukamoto K, Wu D, editors. Selected topics on crystal growth – the 14th International Summer School on crystal growth in Dalian, China. Melville (New York): AIP Conf. Proc. No. 1270; 2010. p. 107.

[112] Steinegger T, Naumann M, Jurisch M, Donecker J. Precipitate engineering in GaAs studied by laser scattering tomography. Mater Sci Eng B 2001;80:215.

[113] Fornari R, Frigeri C, Gleichmann R. J Electron Mater 1989;18:185.

[114] Rai RS, Mahajan S, Mc Devitt S, Johnson DJ. J Vac Sci Technol B 1991;9:1892.

[115] Sonnenberg K. IFF Bull Forschungszent 1997;51:14.

[116] Shen J, Aidun DK, Regel L, Wilcox WR. J Cryst Growth 1993;132:250.

[117] Brion HG, Mewes C, Hahn I, Schäufele U. J Cryst Growth 1993;134:281.

[118] Greenberg J. Thermodynamic basis of crystal growth. Berlin: Springer; 2002.

[119] Jurisch M, Flade T, Hoffmann B, Köhler A, Korb J, Kretzer U, et al. Mater Sci Eng B 1997;44:198.

[120] Wulff G. Z Krist 1901;34:449–512.

[121] Buckley HE. Crystal growth. London, New York: Wiley; 1961.

[122] Zerfoss S, Slawson SI. Am Mineral 1956;41:598.

[123] Janssen-Van Rosmalen R, van der Linden WH, Dobinga E, Visser D. Krist Tech 1978;13:17–28.

[124] Vetter WM, Totsuka H, Dudley M, Kahr B. J Cryst Growth 2002;241:498.

[125] Kahr B, Guerney RW. Chem Rev 2001;101:893.

[126] Kahr B, Vasquez L. Cryst Eng Commun 2002;4:514.

[127] Chernov AA, Kuznetsov Yu G, Smolskii IL, Rozhanski VN. Sov Phys Crystallogr 1986;31:705.

[128] Janssen-Van Rosmalen R, Bennema P. J Cryst Growth 1977;42:224.

[129] van Enckevort WJP, Janssen-Van Rosmalen R, Klapper H, van der Linden WH. J Cryst Growth 1982; 60:67.

[130] Fujiwara K. Int J Photoenergy 2012;2012:1.

[131] Nadri A, Duterrail-Couvat Y, Duffar T. J Cryst Growth 2013. http://dx.doi.org/10.1016/j.jcrysgro.2013.04.013.

[132] Rudolph P, Kakimoto K. MRS Bull 2009;34:251.

[133] Kahr B, McBride JM. Optically anomalous crystals. Angew Chem Intern Ed 1992;31:1.

[134] Gottschalk H, Patzer G, Alexander H. Phys Status Solidi A 1978;45:207.

[135] Donnelly TW. Am Mineral 1967;52:1.

[136] Carstens H. Am Mineral 1968;53:342.

[137] Donnelly TW. Am Mineral 1968;53:344.

[138] Bloss FD. Crystallography and crystal chemistry. New York: Rinehart & Winston; 1971. p. 324.

[139] Giacovazzo C. Fundamentals of crystallography. Oxford: University Press; 1992. p. 80 and 133.

[140] Hahn Th, Klapper, H. International Tables for Crystallography, vol. D. 1. Edition: Dordrecht, Kluver Academic Publishers, 2003. pp. 393–448. 2. Edition: John Wiley & Sons, Inc., 2014, pp. 413–483.

[141] Klapper H. In: Krishna P, editor. Progress in crystal growth and characterization, vol. 14. Oxford: Pergamon; 1987. p. 367.

[142] Faust JW, John HF. J Phys Chem Soc 1964;24:1407.

[143] Bögels G, Meekes H, Bennema P, Bollen D. J Cryst Growth 1998;191:446.

[144] Gu X, Yu X, Guo K, Chen L, Wang D, Yang D. Sol Energy Mater Sol Cells 2012;101:95.

[145] Hurle DTJ. J Cryst Growth 1995;147:239.

[146] Neubert M, Kwasniewski A, Fornari R. J Cryst Growth 2008;310:5270.

[147] Wallace CA, White EAD. In: Peiser HS, editor. Crystal growth. Oxford: Pergamon Press; 1967. p. 431.

[148] Senechal M. Sov Phys Crystallogr 1980;25:520.

[149] Hofmeister H. Cryst Res Technol 1998;33:3 [especially sect. 4].

[150] Prigent G, Bellissent R, Ceolin R, Fischer HE, Gaspard JP. J Non Cryst Solids 1999;250–252:297.

[151] Godlevsky VV, Jain M, Derby JJ, Chelikowsky JR. Phys Rev B 1999;60:8640.

[152] Sunagawa I, Taijing L, Balitsky VS. Phys Chem Miner 1990;17:320.

[153] MacLaren AC, Pitkethly DR. Phys Chem Miner 1982;8:128.

[154] Janovec V, Přívratská J. In: Authier A, editor. International tables for crystallography, vol. D. Dordrecht: Kluwer; 2003. p. 449.

[155] Roth G, Ewert D, Heger G, Hervieu M, Michel C, Raveau B, et al. Z Phys B 1987;69:21.

[156] Rudolph P, Schäfer N, Fukuda T. Mater Sci Eng 1995;R15:85.

[157] Zheludev IS. Physics of crystalline dielectrics. Vol. 1: Crystallography and spontaneous polarisation. New York: Plenum Press; 1971.

[158] Docherty R, El-Korashi A, Jennissen H-D, Klapper H, Roberts KJ, Scheffen-Lauenroth T. J Appl Crystallogr 1988;21:406.

[159] Hosokawa Y, Yabuhara Y, Nakai R, Fujita K. In: Indium Phosphide and related materials, 1998, IPRM IEEE international conference on 11–15 May 1998. Tsukuba (Japan), p. 34.

[160] Winkler J, Neubert M, Rudolph J. J Cryst Growth 2010;312:1019.

[161] Rudolph P, Koh HJ, Schäfer N, Fukuda T. J Cryst Growth 1996;166:578.

[162] Devincre B, Hoc T, Kubin L. Science 2008;320:1745.

[163] Ervik T, Kivambe M, Stokkan G, Ryningen B, Lohme O. Acta Mater 2012;60:6762.

[164] Buis C, Cros d'aillon E, Marrakchi G, Lafford TA, Brambilla A, Verger L. IEEE Trans Nucl Sci 2013; 60(Part 2):199.

[165] Wu B, Scott S, Stoddard N, Clark R, Sholapurwalla A. Miner Met Mater Soc.

28 Automation of Crystal Growth from Melt

Jan Winkler[1], Michael Neubert[2]

[1]INSTITUT FÜR REGELUNGS- UND STEUERUNGSTHEORIE, TECHNISCHE UNIVERSITÄT DRESDEN, DRESDEN, GERMANY; [2]LEIBNIZ INSTITUTE FOR CRYSTAL GROWTH (IKZ), BERLIN, GERMANY

CHAPTER OUTLINE

28.1 Introduction 1144
28.2 Basics about Control Systems 1145
28.2.1 Modeling in Crystal Growth Analysis and Control 1146
28.2.2 Reference Trajectory Generator 1147
28.2.3 State Estimator 1147
28.2.4 Feed-Forward Controller 1149
28.2.5 Feedback Controller 1150
28.2.5.1 Proportional-Integral-Derivative Controller 1150
28.2.5.2 Model-Based Control 1151
28.2.5.3 Model Predictive Control 1152
28.3 Cz Process 1153
28.3.1 Process Characteristics and Control Objectives 1153
28.3.1.1 Importance of the Meniscus Region 1154
28.3.1.2 Lumped Parameter Modeling 1155
28.3.1.3 Stability 1156
28.3.2 State Estimation 1156
28.3.2.1 Weighing Technique 1157
28.3.2.2 Detection of the Bright Meniscus Ring 1159
28.3.3 Feed-Forward Control 1160
28.3.4 Conventional PID-Based Control 1161
28.3.4.1 PID-Based Control Using Optical Diameter Estimation 1161
28.3.4.2 PID-Based Control Using Weight Measurement 1161
28.3.4.3 Improvements and Optimizations 1162
28.3.5 Model-Based Control 1163
28.3.5.1 Lumped Parameter Model-Based Control 1163

Handbook of Crystal Growth. http://dx.doi.org/10.1016/B978-0-444-63303-3.00028-6
Copyright © 2015 Elsevier B.V. All rights reserved.

28.3.5.2 Distributed Parameter Model-Based Control ... 1164
28.3.5.3 Model Predictive Control ... 1165
28.4 Vertical Bridgman and Vertical Gradient Freeze Process ... 1165
28.4.1 Process Characteristics and Control Objectives ... 1166
28.4.2 Conventional Control ... 1167
28.4.3 Model-Based Control ... 1167
28.4.3.1 Temperature Control and Interface Shape Detection ... 1168
28.4.3.2 Flow Speed Control ... 1169
28.5 Detached Bridgman Process ... 1169
28.5.1 Process Characteristics and Control Objectives ... 1170
28.5.1.1 Choice of the Manipulated Variable ... 1171
28.5.1.2 Lumped Parameter Model ... 1171
28.5.1.3 Stability and Operational Limits ... 1171
28.5.2 PI-Based Control ... 1172
28.5.3 Model-Based Control ... 1173
28.6 Floating Zone Process ... 1174
28.6.1 Process Characteristics and Control Objectives ... 1174
28.6.2 Measurement Techniques ... 1174
28.6.3 Reference Trajectory Planning and Conventional Control ... 1175
28.6.4 Model-Based Control ... 1176
28.7 Kyropoulos Process ... 1176
28.7.1 Process Characteristics and Control Objectives ... 1176
28.7.2 Control Approaches ... 1177
28.8 Conclusions ... 1178
References ... 1178

28.1 Introduction

The demand for crystals of well-defined structural, chemical, optical, and electrical properties produced with a maximum level of yield and reproducibility is the motivation to develop highly sophisticated automatic control systems. For example, the better a crystal meets its desired diameter and the better the diameter constancy in the cylindrical part of the crystal, the less material has to be cut off after growth. On the other hand, strong diameter changes influence the structural properties of the crystal [1–4]. Hence, ensuring the desired diameter is a main purpose of control systems in processes in which no shaping devices or forming containers are available. Not only the diameter but also other quantities like the crystal growth rate are of special importance. For example, the growth rate directly influences the properties of the growing crystal. It correlates with the amount of imperfections, like the amount of native point defects,

residual impurities and that of intentionally introduced dopants or higher dimensional defects like dislocations, twins, precipitates, or inclusions. Consequently, for process technology there is also a huge interest in growth rate control. A typical example can be found in Czochralski (Cz) silicon crystal growth where the relation between growth rate and thermal gradients at the interface is of great importance in order to ensure an extremely low content of native point defects [5–9]. More recently, the focus of control design has been extended to maintain additional degrees of freedom that affect crystal quality as well as crystal shape, for example, in Cz growth also during the neck, shoulder, and tail sections in addition to the main body [10–16].

When designing a control system the first task is to characterize the dynamic relations between the inputs and the outputs of the process to be controlled, usually by means of a mathematical model. Secondly, the control objectives have to be defined, which are mainly determined by the desired material requirements. They are specified as the particular process phenomena that have to be controlled [17]. Based on these results a control structure is chosen. Here, different levels of mathematical complexity, questions about linear or nonlinear control design, robustness, and real time capability come into play. In any case and no matter which control strategy is chosen to address these issues, crystal growth processes are usually an extremely challenging control object.

This chapter will give a broad overview of the approaches found for different bulk crystal growth processes from melt with respect to topics like model-based analysis, process characteristics, open- and closed-loop control, reference trajectory design, and state estimation. Of course, it is impossible to cover all crystal growth processes from melt in this chapter. As examples, the Cz , the Floating Zone, the Bridgman, the Detached Bridgman, and the Kyropoulos methods are treated. Of all of these, the Cz system is by far the most thoroughly investigated one in the literature. Please note that additionally a state-of-the-art control system approach for the Floating Zone technique is discussed in detail in Vol. IIA, Chapter 7 of this handbook.

28.2 Basics about Control Systems

The purpose of a control system is to keep a set of process quantities, in the following referred to as the *controlled variables*, on a certain set point or to track them along a given *reference trajectory*. This is done by appropriately manipulating the inputs of the process, in the following referred to as the *manipulated variables*. It can be achieved by predetermined knowledge of the process (*open-loop control*) and/or by feedback of certain measured process information (*closed-loop control*). The intention of this section is to introduce some of the basic concepts used in control technology as far as they are required for an understanding of the numerous strategies for control of the discussed crystal growth processes. For this purpose, the essential components of a control system are briefly summarized according to [14,18,19]. A broader introduction can be found in [20,21], and a graphical overview showing all essential components of a control system is given in Figure 28.1. Since modeling and computer simulation play an important role in

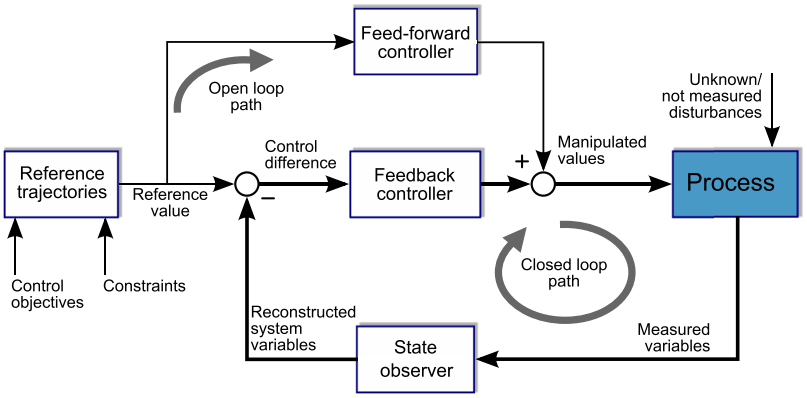

FIGURE 28.1 Sketch of a modern feedback control loop.

crystal growth process design as well as in control applications, a short comparison of how models are used in automatic control in contrast to numerical approaches in crystal process design will be given first. The approaches and requirements differ quite a lot [19] between both fields.

28.2.1 Modeling in Crystal Growth Analysis and Control

A mathematical model that takes the spatial distribution as well as the time dependency of material parameters into account leads to a system of coupled *partial* differential equations with the corresponding initial, boundary, and compatibility conditions. They belong to the so-called *infinite dimensional* or *distributed parameter* systems. Such systems are usually solved numerically using finite element methods (FEMs). Using this approach one can obtain results reflecting the reality rather accurately. FEM is an absolutely essential resource in solving problems in plant design, thermal and stress analysis, etc. However, computational effort increases dramatically depending on the accuracy required, especially for solving *time-dependent* problems.

The approach used in control technology, especially in model-based control (cf. Section 28.2.5), is to keep the models as simple as possible. This is achieved by partitioning the system under consideration into domains that may reasonably well be considered as homogeneous, i.e., the material parameters of which are assumed to be constant. Heat and mass transfer between these domains is calculated from appropriate mass and energy balance equations. Since any spatial dependence of the parameters is neglected, one ends up with a set of *ordinary* differential equations. Such approaches are called *finite dimensional* or *lumped parameter* models. They can be used to calculate the basic system behavior leading to a qualitatively and quantitatively sufficient insight into the process. Powerful methods for controller and observer design (cf. Section 28.2.3), trajectory planning, and dynamic analysis exist for this class of models. The lack of accuracy can be admitted by the introduction of feedback. Another advantage of these

models is the fact that one is able to run them on the limited computer hardware usually available at the growth furnaces.

The big challenge in applying model-based control strategies to problems in crystal growth technology is that the dynamics of these processes are mainly driven by complex nonlinear radiative, conductive, and convective heat transport phenomena. They cannot be fully captured by either a linear or a nonlinear lumped parameter model. Above all, melt growth processes are systems with free boundaries (at least the solid–liquid interface, in case of processes where the crystal grows freely from the melt, e.g., in Cz growth, also the crystal shape) making it even more complicated to solve the underlying dynamic equations. Many unknown physical parameters and the complex structure of the inner assemblies worsen the situation. Here, from a control technological point of view, one has to find a balance between accuracy and real time capability of the models [10,14,22].

28.2.2 Reference Trajectory Generator

The *reference trajectory generator*, cf. Figure 28.1, calculates reference values for the main variables to be controlled, e.g., crystal diameter, crystallization rate, or other useful quantities. Usually the independent parameter of this calculation is the growth time or the crystal length. These reference values are used in the feed-forward and the feedback controllers of the control system. Planning of trajectories has to consider the physical properties of the system in order to avoid not realizable or not favorable values for the manipulated variables. Furthermore, one cannot request physically impossible behavior from the system, such as steps in any of the system quantities or their derivatives. For example, in Floating Zone crystal growth it is reasonable to keep the crystal diameter and the zone length in a certain range in order to maintain a stable melt zone. Also, the crystal growth rate in Bridgman growth must be kept below a critical value to ensure perfect growth of the crystal.

Such constraints must be carefully considered during reference trajectory planning. It may be useful to reschedule the reference trajectories during growth to guarantee smooth behavior of the controller.

28.2.3 State Estimator

It is not always possible to measure the controlled variable directly using a sensor. As will be shown in the next sections, this is the case in a lot of crystal growth processes. For example, in Cz growth usually the force measured by a load cell or the diameter of a bright ring on the meniscus is the only measured quantity available while one is interested in the control of crystal diameter and growth rate. In Bridgman process nothing can be measured directly describing the state of the growing crystal. In such cases one might reconstruct the required variables from measured variables by means of a state estimator, often called an *observer*. This is possible if a suitable model of the system is available and the system is observable (a certain system property, cf. [23,24]).

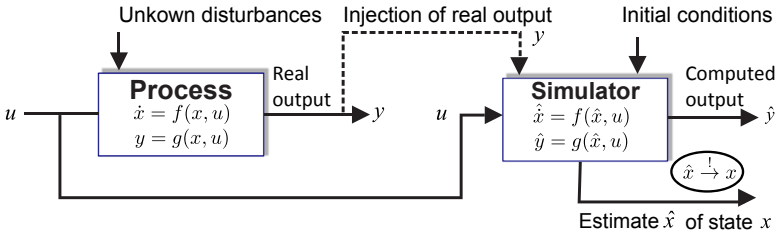

FIGURE 28.2 Working principle of a state estimator.

An observer is based on the following idea, cf. Figure 28.2, also. Assume a lumped parameter mathematical model

$$\dot{x}(t) = f_1(x(t), u(t)), \quad y(t) = f_2(x(t), u(t)), \quad x(0) = x_0$$

of a process with $(x(t),\ u(t)) \in \mathbb{R}^n \times \mathbb{R}^r$ and $y(t) \in \mathbb{R}^m$. If some components of x are not directly measured, one might implement a "copy"

$$\dot{\hat{x}}(t) = f_1\left(\hat{x}(t),\ u(t)\right), \quad \hat{y}(t) = f_2\left(\hat{x}(t),\ u(t)\right), \quad \hat{x}(0) = \hat{x}_0$$

of the system model with the estimated state $\hat{x}$ in a computer program. The trajectories of the manipulated variables u acting on the real system are fed into this computer program, too. Then one has access to all components of $\hat{x}$. However, since the initial values of $\hat{x}$ are not known, i.e., $\hat{x}_0 \neq x_0$, and because of model inaccuracies as well as disturbances acting on the system, generally the values calculated for $\hat{x}(t)$ will not be equal to the real values $x(t)$. However, under certain circumstances it is possible to inject the error $\hat{y} - y$ between the estimated value $\hat{y}$ and the measured value y in such a way that the difference between the estimated value $\hat{x}$ and the real value x will converge to zero as time advances [23]. In this case the system

$$\dot{\hat{x}}(t) = h\left(\hat{x}(t), u(t), \hat{y}(t) - y(t)\right), \quad \hat{x}(0) = \hat{x}_0$$

$$\hat{y}(t) = f_2\left(\hat{x}(t), u(t)\right)$$

is called an *observer*.

Design and dimensioning of the injection of the error related to the measured variable is the key task when developing an observer. However, it is important to know if it is possible to reconstruct a quantity from the measured variable at all. This property is commonly referred to as "observability." If the stochastic properties of the process are incorporated into the design of such an observer, it is usually called Kalman filter or extended Kalman filter [25]. An introduction to practical observer design is given in Ref. [26]. Especially for Cz growth, many approaches deal with this topic (cf. Section 28.3.2 for more details).

28.2.4 Feed-Forward Controller

The *feed-forward controller* calculates the manipulated values (like heater powers or crystal/crucible/feed rod translation rates) from the reference values of the controlled variables (e.g., crystal diameter) generated by the reference trajectory generator. This can be done empirically or by means of a mathematical model describing the system behavior. In crystal growth, a common method in practice is to determine the feed-forward control by careful analysis of repeated growth runs, resulting in a trajectory for the manipulated variables that can then be used as part of the process recipe in the following runs.

While this method is widely accepted, it suffers from the fact that it is extremely time consuming and, thus, expensive. It functions only if the same conditions are repeatedly met and there are no significant variations from run to run. However, any change in plant setup or change in reference values for the controlled variables means repeating this procedure. Finally, not all details of the system dynamics can be determined by this empirical approach.

If a sufficiently exact model of the process is available, this model can be used as a basis for determining proper feed-forward control trajectories that then can be fine-tuned in an empirical manner afterward. A short example is given as follows illustrating this strategy [19]. One may have a system with the manipulated variable $u \in \mathbb{R}$ (for example, a heater power), the output variable $y \in \mathbb{R}$ (which has to be controlled, e.g., a bright meniscus ring diameter in Cz growth), and two internal states $x_1, x_2 \in \mathbb{R}$ (e.g., the crystal diameter and a value describing the cone angle). Its dynamics may be captured by the following very simple, fictive lumped parameter model of order 2:

$$\dot{x}_1 = x_2 \tag{28.1a}$$

$$\dot{x}_2 = x_1^2 + (x_2 + 2)u \tag{28.1b}$$

$$y = x_1. \tag{28.1c}$$

From this model, a model-based feed-forward control can be easily calculated. Solving Eqn (28.1b) for the heater power u one obtains:

$$u = \frac{\dot{x}_2 - x_1^2}{x_2 + 2}. \tag{28.2}$$

Now, one would like to steer the system, namely the diameter y, along a reference trajectory $t \mapsto y_{\mathrm{ref}}(t)$. This reference trajectory is assumed to be two times continuously differentiable, i.e., $\dot{y}_{\mathrm{ref}}(t)$, $\ddot{y}_{\mathrm{ref}}(t)$ exist. Since according to system (28.1) one has $x_1 = y$, $x_2 = \dot{x}_1 = \dot{y}$, and $\dot{x}_2 = \ddot{y}$ the resulting reference trajectory for the manipulated variable u reads (cf. Eqn (28.2)):

$$u_{\mathrm{ref}} = \frac{\ddot{y}_{\mathrm{ref}} - y_{\mathrm{ref}}^2}{\dot{y}_{\mathrm{ref}} + 2}. \tag{28.3}$$

Using the calculated feed-forward control, one might be able to *steer* the system along its reference trajectory if the system is stable, only small perturbations are acting on the system, and the model is accurate enough.

The example given above demonstrates the general design procedure of a lumped parameter model-based feed-forward control. However, the dynamics of crystal growth process will certainly never be captured sufficiently by such simple models. Hence, this example also reveals one of the main problems in control system design for crystal growth—finding the appropriate balance between simple models suitable for control system design and accuracy of the models describing the system dynamics. The sections dealing with the control of the particular growth processes will focus especially on this topic.

28.2.5 Feedback Controller

Obviously, the main component of the control system is the *feedback controller*. Its purpose is to compensate for disturbances acting on the process and to correct inaccuracies in trajectory tracking resulting from imprecise feed-forward control. This is achieved by feedback of the measured variable (or its estimate, cf. Section 28.2.3) and a correction of the manipulated variable.

28.2.5.1 Proportional-Integral-Derivative Controller

It is common practice to realize feedback control by means of a proportional-integral-derivative (PID) controller. The PID controller processes a deviation $e(t)$ between the reference and the real value of the controlled variable in order to calculate a change $\Delta u(t)$ of the manipulated variable:

$$\Delta u(t) = K_P e(t) + K_I \int_{t_0}^{t} e(\tau)\mathrm{d}\tau + K_D \frac{\mathrm{d}e}{\mathrm{d}t}(t). \tag{28.4}$$

The dynamic behavior of the PID controller is determined using the three real-valued constants K_P, K_I, and K_D. It is an implementation of the following natural assumptions: (1) The larger the control deviation, the more one has to counter steer, an implication that is covered by the proportional part $K_P e(t)$. (2) The longer the control deviation is pending, the more the manipulated variable has to be changed in order to reduce it. This behavior is realized by the integral part parameterized using the factor K_I, the second term in Eqn (28.4). (3) The faster the control deviation changes, the stronger one has to counteract—this is covered by the third term in Eqn (28.4)—the differential part with parameter K_D. To avoid the influence of measurement noise, usually this differentiation is combined with a first-order low-pass filter. A detailed introduction and discussion of the application of PID controllers under industrial conditions can be found in [27–29].

The PID controller is suitable for a wide range of technological systems found in practice and has some advantages: its operating principle is simple and it can be easily implemented. If certain conditions hold, it can be adjusted using some simple rules [30,31]. Typical examples for its application are all kinds of temperature control, flow rate control, or position tracking in which only small perturbations occur. However, there are some drawbacks: Its parameterization is adjusted for a certain operating point of the process. If

one does not have a steady state operating point, parameters have to be continuously changed. This is usually the case in crystal growth processes. Furthermore, the performance of PID controllers is limited if the system shows nonlinear behavior. The reason for this is the fact that a change of the manipulated variable results in an "unexpected" nonlinear response of the system. The situation worsens if the system contains time delays (dead times). Then, a reaction y of the system to a change of the manipulated variable u appears delayed by the delay time $\tau > 0$, for example, $y(t) = u(t - \tau)$. Dead times must not be mixed up with a time constant T of a dynamic system, e.g., in a first-order low-pass filter: $T\dot{y}(t) = -y(t) + u(t)$. Time delays may result in an undamped increasing integral of the PID algorithm (cf. Eqn (28.4)). For example, in Cz crystal growth, the liquid-encapsulated Czochralski (LEC) process with its boron–oxide layer covering the melt belongs to the class of delay systems, cf. Section 28.3.1.1.

28.2.5.2 Model-Based Control

Fortunately, theory and application of control systems have been developed very rapidly in the last decades. Increasing capacity of microcontrollers and programmable logic controllers (PLC) combined with powerful mathematical control design methods prepared the ground for the use of sophisticated model-based controllers in practice. A model-based controller uses a mathematical model of the system, i.e., its structure and parameters fit to the system. This means that the controller can be used in a wide range of operating points and reflects the nonlinear system characteristics as well as time delays. In addition, parameterization effort is dramatically reduced. Refer to Ref. [32] for a broad overview of nonlinear model-based strategies. Such controllers show good performance only if the underlying model matches the structure and the parameters of the system appropriately. This is the crucial point when trying to enhance the capability of conventional control systems.

In order to make the strategy of model-based control more clear, the design of a simple nonlinear feedback controller based on the lumped parameter model (28.1) from Section 28.2.4 is sketched. Exactly how this type of model-based controller design is successfully applied, for example, is shown in the Cz method (Section 28.3.5.1) and in the Detached Bridgman method (Section 28.5.3). If one wants to make the output y (e.g., a diameter) follow a reference trajectory $y_{\mathrm{ref}}(t)$, the controller is designed in such a way that the tracking error $y - y_{\mathrm{ref}}$ satisfies the linear second-order differential equation

$$\left(\ddot{y} - \ddot{y}_{\mathrm{ref}}\right) + k_1\left(\dot{y} - \dot{y}_{\mathrm{ref}}\right) + k_0\left(y - y_{\mathrm{ref}}\right) = 0 \tag{28.5}$$

with k_0, $k_1 > 0$.

The values of y_{ref}, $\dot{y}_{\mathrm{ref}}$, and $\ddot{y}_{\mathrm{ref}}$ are defined by the reference trajectory. If one desires the dynamics of the tracking error to satisfy Eqn (28.5), the second time derivative of the output y must behave as

$$\ddot{y} = \ddot{y}_{\mathrm{ref}} - k_1\left(\dot{y} - \dot{y}_{\mathrm{ref}}\right) - k_0\left(y - y_{\mathrm{ref}}\right). \tag{28.6}$$

This can be achieved by a proper choice of the input u because by inserting the right-hand side of Eqn (28.6) in the equation used for calculation of u (cf. Eqn (28.2)) one obtains

$$u = \frac{\dot{x}_2 - x_1^2}{x_2 + 2} = \frac{\ddot{y} - y^2}{\dot{y} + 2} = \frac{\ddot{y}_{\text{ref}} - k_1\left(\dot{y} - \dot{y}_{\text{ref}}\right) - k_0\left(y - y_{\text{ref}}\right) - y^2}{\dot{y} + 2}. \tag{28.7}$$

This equation determines the manipulated variable u (e.g., the heater power) in such a way that the tracking error satisfies the given error dynamics Eqn (28.5). The coefficients k_0, k_1 in Eqn (28.5) are the controller parameters defining the dynamical behavior of the tracking error, i.e., the way the error converges to zero (e.g., fast with an overshooting or slowly creeping). The real value inputs are $y, \dot{y},$, and the desired value inputs are $y_{\text{ref}}, \dot{y}_{\text{ref}}, \ddot{y}_{\text{ref}}$.

28.2.5.3 *Model Predictive Control*

The model-based strategy presented so far relies on an *analytical* expression of the control law, cf. Eqn (28.7) as a possible example. A special model-based approach currently becoming more and more important is the so-called *model predictive control* strategy that is often used in process technology. Roughly speaking, in this approach no analytical control law is derived. Instead, the way of calculating values for the manipulated variable is based on optimization methods, cf. Figure 28.3. For this purpose, in each time step the set of control activities recorded so far is evaluated (i.e., the manipulated variables and the resulting controlled or measured variables) in order to

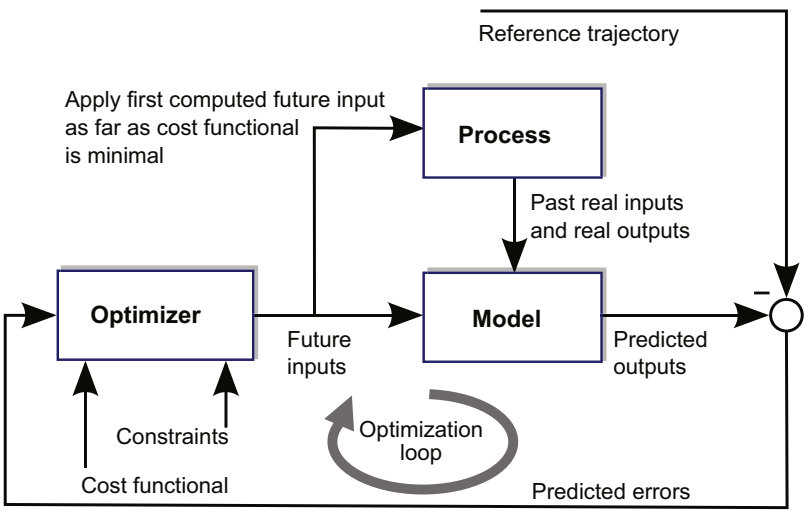

FIGURE 28.3 Model predictive control.

predict the values of the manipulated variable over a finite prediction horizon by means of a dynamic mathematical model of the process. Now, the basic idea is to repeat this calculation until an optimization criterion is minimized. Then, the first predicted manipulated value is applied to the process. In the next time step, this procedure is repeated. The optimization criteria, in some sense the "parameters" of a model predictive controller, reflect, for example, the dynamics of the deviation between desired and real values and the control effort. The solution of such optimization problems is well known and widely used in mathematics.

The advantage compared to the analytical model-based approaches presented above is that the underlying models can be arbitrarily complex as long as they can be *repeatedly numerically solved* in each time step over a finite time horizon. This is, of course, the limiting factor—one has to keep in mind that for computing a new set point value of the manipulated variables, several time-dependent solutions of the model are required. Another advantage of this method is that it is easy to account for constraints on the system states or the manipulated variables. A disadvantage is that it is more difficult to prove the stability of the closed-loop system because of the "trial and error" character of the method. A detailed introduction into this method can be found in Refs [33,34]. Application examples of this control method can be found for Cz growth in Section 28.3.5.3 and for Floating Zone growth in Section 28.6.

28.3 Cz Process

The Cz process is one of the most important crystal growth technologies used in the industrial mass production of single crystals, cf. Vol IIA, Chapters 2–4 of this handbook. Accordingly, a large amount of literature exists that deals with modeling, analysis, and control of this process.

28.3.1 Process Characteristics and Control Objectives

In Cz, as it is mostly practiced nowadays, the crystals are grown freely from the melt, i.e., there are no shaping devices ensuring a constant or well-defined diameter, which is mainly important in matters of technological requirements.[1] Next to the diameter, the crystal growth rate is also an important quantity that should be controlled, cf. Section 28.1. As manipulated variables, the power of one or several heaters and the vertical translation rates of the pulling rod as well as of the crucible are available. The rotation rates of the crucible and the crystal can be used to affect the growth, too. However, these

[1]In the past, especially in III–V semiconductor growth, a so-called coracle—a ceramic silicon nitride ring floating on the melt—was applied. Besides a thermal stabilization of the meniscus region, a self-stabilization effect due to the conical shape of the coracle and nonwetting conditions between melt and coracle was utilized, see e.g., Refs [35–38]. However, this was only an episode because of upcoming automatic diameter control.

are barely used in automatic control systems but under certain circumstances might be helpful for skilled operators to quickly influence the process.

28.3.1.1 Importance of the Meniscus Region

The key task when automating this process is an exact control of the meniscus region, the interconnection between melt and crystal, cf. Figure 28.4. The meniscus and its shape result from gravitational forces and surface tension. Its shape can be determined by numerically solving the Laplace–Young equation [39,40] or by suitable analytical approximations, e.g., by Hurle [41], Boucher and Jones [42,43], or Landau [44]. Furthermore there exist widely used analytical approximations for the meniscus height h_i itself derived by Tsivinskii [45], Boucher and Jones [42,43], or Johansen [46]. At the meniscus upper end, the so-called phase boundary, or interface, is located where crystallization takes place. Thereby the latent heat is released. Because the crystal is pulled upward into colder regions of the furnace, a temperature gradient is established, leading to a heat flow by conduction from the hot interface into the colder crystal [47]. By this mechanism, crystallization is maintained throughout the growth process. The amount of heat transported into the crystal consists of the amount of heat transported from the meniscus region into the interface and the amount of heat released by crystallization. In general, the following relation holds for the vector $\vec{v}_\mathrm{g}$ of the growth rate along the phase boundary described by $z = \mathbf{Z}(r), r \in [0, r_\mathrm{i}]$ (keep in mind that the vector v_g is directed in negative z-direction):

$$\vec{v}_\mathrm{g}(r, \mathbf{Z}(r)) = \frac{1}{\rho_\mathrm{s} \Delta H_\mathrm{f}} \left(\lambda_\mathrm{m} \nabla T_\mathrm{m}(r, \mathbf{Z}(r)) - \lambda_\mathrm{s} \nabla T_\mathrm{s}(r, \mathbf{Z}(r))\right), \quad r \in [0, r_\mathrm{i}]. \tag{28.8}$$

In this equation one has the heat of fusion ΔH_f, the density ρ_s of the solid at melting point temperature, and the crystal radius r_i at the interface. The heat conductivities of the solid and the melt are denoted by λ_s and λ_m, respectively, and $T_\mathrm{s}(r, z)$ and $T_\mathrm{m}(r, z)$ represent the temperatures of the solid and the melt. A necessary condition for growth is that the heat flux is directed from the melt into the crystal.

Changes in the temperature gradients on the melt or solid side of the phase boundary lead to an immediate change of the growth rate, as can be easily seen from Eqn (28.8).

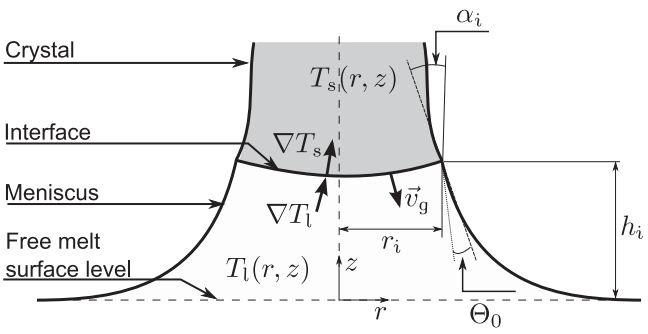

FIGURE 28.4 Sketch of the interface region with important physical quantities.

On the one hand, a local change of the growth rate results in a deformation of the phase boundary and in a change of the crystal diameter if this deformation is located at the rim of the interface. On the other hand, a change in interface geometry again initiates a change in heat transport. Furthermore, the shape of the meniscus depends nonlinearly on the radius r_i of the crystal at the interface as well as on the growth angle $\alpha = \Theta_0 + \alpha_i$ with the equilibrium growth angle Θ_0 and the crystal slope angle α_i [39,42,48], cf. Figure 28.4. Consequently, the demand of growing crystals of well-defined shape requires exact control of the thermal conditions in the interface region. Without any precise measurements characterizing the state of this region, this is an overwhelming task. An approach trying to realize such a direct control by blowing inert gas around this region is presented by Brice et al. [49]. However, usually any measurements available at the process are more or less distant to this region, complicating the control of the process.

A big challenge in achieving a proper control of the thermal situation in the meniscus region arises from the so-called "batch character" of the Cz process. This means that it does not have a steady state operating point, mainly resulting from the fact that the whole system configuration changes during the growth—while one has a crucible filled with melt in the beginning, it is nearly empty at the end of the process and the melt mass is transferred into the crystal. The falling melt level leads to a continuously changing heat entry form the heaters into the system. Thus, the process dynamics changes heavily throughout the process. Understanding the influence of these variations on the process dynamics provides a foundation for developing a robust process control system. Detailed discussions on these subjects can be found in Refs [17,22,50,51].

Besides that, variants of the process are even more difficult to control. In the LEC method [52], the liquid boron–oxide layer upon the melt introduces time delays (cf. end of Section 28.2.5.1) into the process [53–56]. In the so-called vapor pressure–controlled Czochralski (VCz) method [57] with intentionally reduced axial and radial temperature gradients, diameter control is even more difficult [4].

28.3.1.2 Lumped Parameter Modeling

First analyses of the principal system behavior of the Cz process were published by Bardsley, Hurle et al. in the 1970s [58–62] in order to improve diameter feedback control. A *global* lumped parameter model of the overall Cz crystal growth system was first presented by Steel et al. [63]. In order to simplify and improve parameterization of PID controllers, they analyzed a linearized model in terms of a transfer function in several growth stages. The central idea of their approach consists in partitioning the Cz system into the four areas: melt—meniscus—crystal—ambient. This is still the basis of all lumped parameter models of the Cz process used to date. In Ref. [64] Hurle presents a method for experimentally determining a lumped parameter model (in the form of a transfer function) of the Cz process. Other models suitable for system analysis and control system design on a lumped parameter basis have been presented by Hurle

[22,36,65], Satunkin [66,67], Looze [53], Gevelber [10], and Sveshtarov [68–70]. A more in-depth analysis using FEM methods has been presented by Derby, Brown, et al. [47,71–74].

28.3.1.3 Stability

An important matter in control theory is the question whether the system under consideration is stable or not, since unstable systems have a limitation to achievable control performance. When discussing this subject it is very important which type of model is used for stability analysis and which physical effects are included in the model. Surek's initial stability analysis was only of the capillary problem, i.e., for the meniscus region [75]. He came to the conclusion that the capillary system is unstable. However, if the heat fluxes are taken into account, one comes to a different conclusion, depending on the assumptions made during modeling. Tatarchenko [76–78], Surek [48], Hurle [65], as well as Derby [73] show stable behavior of the growth system under certain operating conditions. Nevertheless, Crowley [79] and Johansen [80] show that the system is unstable for the cases they evaluated, even if the thermal effects are included in the analysis. A more recent in-depth analysis and summary of this problem is provided by Tatarchenko in Ref. [81].

28.3.2 State Estimation

The quantities that one would like to control are mainly the crystal diameter and the crystal growth rate. Unfortunately, they cannot be directly measured. However, three different approaches exist to acquire indirect information about at least the crystal diameter:

1. Evaluation of the force acting on a load cell mounted at the top of the pulling rod, originally presented by Levinson and Rummel [82,83], discussed in detail by Bardsley et al. [58,60–62]. Alternatively, weighing of the crucible is possible [84,85].
2. Capturing of the meniscus shape, typically by detecting and evaluating the bright meniscus ring resulting from reflections of the hot glowing heaters [86–90].
3. Image processing of the whole crystal [91–93].

The third method has no technological relevance because on the one hand it is very complicated to be realized and on the other hand because changes in the growth are detected not until they have already influenced the crystal [94]. (This is actually not the case when using the first and second technique where changes in the meniscus precede a change in the crystal diameter).

Consequently, the first two approaches are widely used in industry. Which one is chosen depends on the constraints given by the process and plant setup; since silicon has a large Laplace constant (i.e., high surface tension and low density resulting in large meniscus heights) and because of its metallic reflectivity, this material is an obvious candidate for the second technique. In the LEC process the boron–oxide layer covering

the melt prevents optical detection of the meniscus. Hence, in this process the weighing method is used. The same holds for the growth of oxides with their high melting points. There the inner assemblies required for a good insulation prevent a sufficient view on the meniscus from the top of the growth furnace. Additionally, more light is emitted from the crucible, making it difficult to detect the bright ring on the meniscus. A combination of both approaches is proposed by Bruni in Ref. [95].

28.3.2.1 Weighing Technique

The idea behind the weighing technique is that, at a first glance, the rate of change of the force acting on the load cell—the so-called differential weight gain signal—might be proportional to the crystal cross-section area at the growing interface. This can be evaluated by a controller. The gravitational force F_c of a rotationally symmetric crystal of length l and density ρ_s can be calculated by

$$F_c = \pi g \rho_s \int_0^l r_i^2(\lambda) \mathrm{d}\lambda \tag{28.9}$$

with crystal radius r_i and gravitational acceleration g. However, the force measured by the load cell is not equal to F_c of the crystal in Eqn (28.9) and, hence, the differential weight signal is not equal to the time derivative of Eqn (28.9). In fact, it is also influenced by forces resulting from the surface tension of the meniscus, the hydrostatic pressure of the melt raised over the melt level [58], and in case of LEC by the buoyancy forces resulting from the liquid boron oxide [54]. For this reason, things become considerably more complicated as it might seem from a first glance at Eqn (28.9).

A major problem when using this method occurs if the density of the solid is smaller than the density of the liquid. Then, a well-known anomaly comes into play, which consists of the fact that, e.g., an increase of the crystal diameter is not necessarily accompanied by an increase in the differential weight gain signal. The reason for this effect is that an increasing crystal diameter first results in a decrease of the meniscus height and of its volume (cf., Figure 28.5, middle). Hence, since the density of the melt is larger than the density of the solid, a decreasing meniscus volume makes the differential weight gain signal decrease at first although the crystal diameter is increasing (cf., Figure 28.5, bottom). For materials that do not completely wet their solids, i.e., $\Theta_0 \neq 0$, a similar effect can be observed since an increase in crystal diameter ($\alpha_i > 0$) leads to a reduction of the vertical component of the surface tension acting on the crystal (it is proportional to $\cos(\Theta_0 + \alpha_i)$) [60]. Unfortunately, all commonly grown semiconducting materials show this effect. A detailed discussion on this topic can be found in Ref. [60,96,97] for the standard Cz process and in Ref. [55,56] for the LEC process.

The anomaly also leads to crucial problems during the transfer from the shoulder into cylindrical growth, cf., Figure 28.6 (top)—a sudden increase of the derivative of the force acting on the load cell with respect to time is observed just before the crystal diameter reaches the cylinder. This behavior can be explained by the fact that the height (and

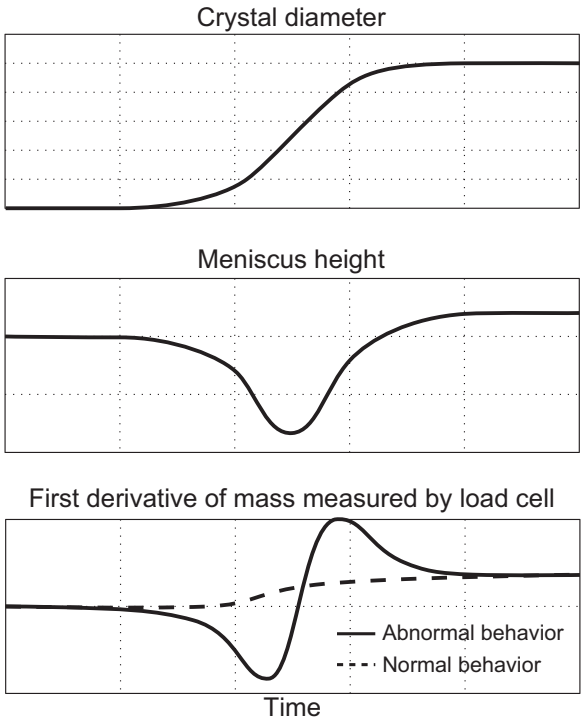

FIGURE 28.5 A slight change of the crystal diameter (top) results in a temporary break of the differential weight gain signal (bottom). The reason for that is the reduction of the meniscus height during the diameter transfer (middle).

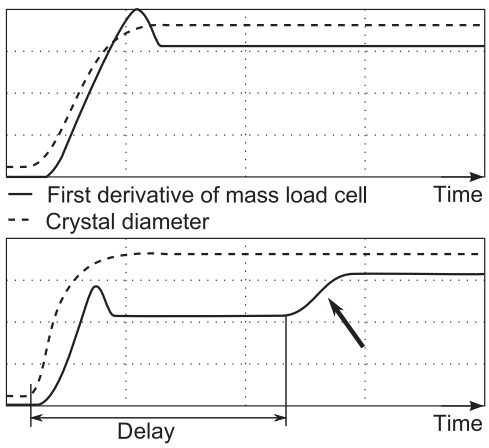

FIGURE 28.6 Top: Increase of the derivative of the differential weight gain signal before the crystal reaches the phase of cylindrical growth. Bottom: The impact of the time delay (or "dead time", cf. Section 28.2.5.2) is illustrated in the case of the LEC process: An "aftershock" occurs in the differential weight gain signal when the crystals emerge from the boron oxide layer. The dashed curves represent the corresponding diameter trends.

thus, volume) of the meniscus changes significantly at this phase of the process. More detailed discussion with respect to this subject can be found in Refs [11,66,97]. The strength of the effect depends on several factors discussed in detail in Ref. [61]. Especially the growth rate is of great importance. Roughly speaking, the lower the pulling speed, the stronger the effect.

In case of LEC growth, additionally the influence of the boron–oxide layer comes into play. One has to take into account the buoyancy as well as the time delay introduced by the emerging crystal, resulting in additional dynamical effects. For example, Figure 28.6 (bottom) shows an "aftershock" occurring in the differential weight gain signal when the crystal begins to emerge from the boron–oxide layer. These effects are discussed in Refs [54–56] and must be carefully considered during control system design.

Yet another factor limiting the weighing technique is the diameter of the crystal body. The larger it is the larger the measured force at the load cell. However, the larger the nominal load cell capacity, the worse the absolute resolution for small loads. This is problematic especially during the initial phase of the process. A discussion of the load cell dynamics and its consideration in the control system can be found in Ref. [66].

The reconstruction of the crystal diameter and other quantities by means of an observer (cf. Section 28.2.3) from the weighing signal is the subject of several publications. Satunkin and Leonov discuss the question of observability in case of Cz and LEC growth in Ref. [66]. A Kalman filter approach can be found in [98]. In both cases, the discussion is based on a linearized model of the overall process, which is bound to the knowledge of some thermodynamic parameters. An elegant approach is presented in Refs [99,100] where, roughly speaking, an iterating algorithm is used that fits the theoretically calculated mass of the load cell to its real value by heuristically changing the crystal diameter in every step. However, this algorithm contains a parameter that must be empirically determined to guarantee convergence. A reduced order nonlinear tracking observer for the Cz and the LEC system including full meniscus dynamics is presented in Ref. [15]. As far as the system is tracked along its reference trajectory, this approach produces very accurate results.

If the influence of the changing meniscus can be more or less neglected, a simple approach is presented in Refs [101,102]. Here the basic idea is to exclude the meniscus dynamics from the model, making it easy to solve the remaining equations for the radius. This method is useful for reconstruction of the radius during cylindrical growth and for crystals with slowly increasing diameter in the cone. If one is obliged to grow crystals with large slope angles in the shoulder, this method fails, especially when fading into the cylinder. Another approach modulates the crystal pulling velocity with a small sinusoidal signal with a period much shorter than the dominant time constant of the process. In such a setup it is possible to reconstruct the diameter by a versatile algorithm [103,104].

28.3.2.2 Detection of the Bright Meniscus Ring

The idea behind this measuring technique is based on the fact that light emitted by the red-hot heaters is reflected in an upward direction from the meniscus surface. These

reflections can be seen and detected by an optical camera as a so-called “bright ring.” Then, image processing software is able to determine the diameter of the ring in real time [105,106]. This can be achieved in a similar way by measuring the radiation intensity using a pyrometer [87,90,107]. The determined diameter of the bright ring, scaled by an empirically determined factor accounting for the difference between measured bright ring radius and expected crystal radius, is used as the measured variable in the control system. Hence, although the crystal radius itself is not measured, this technique is widely and successfully used especially in silicon Cz growth. However, one has to take into account that the measure is the diameter of the meniscus at a certain height, not the crystal diameter at the three-phase boundary. This means that the anomaly discussed above comes into play again—if the crystal radius begins to decrease, first the meniscus height will increase. This means that the diameter of the bright meniscus ring will increase, which might result in incorrect reactions of the controller if it is not adapted to this behavior [17]. A detailed discussion on how to obtain an estimate of the real crystal diameter from the camera system under these constraints is given in Refs [108,109].

28.3.3 Feed-Forward Control

Model-based lumped parameter approaches are presented in Ref. [50] (4″ silicon), Ref. [102] (InP), and Ref. [110]. Since the underlying models neglect the spatial distribution of system properties (cf. Section 28.2.1), most often some empirical corrections (e.g., in Ref. [102]) are introduced to fit the result to reality. An approach trying to circumvent this problem is proposed in Ref. [111], based on a mathematical description regarding the most important qualitative dependencies between the relative changes of manipulated and controlled variables during growth. For a certain thermal setup this approach allows easy calculation of reference trajectories for different crystal shapes, growth, and crucible translation rates.

In order to overcome such limitations one may describe the system behavior without neglecting the spatial dependence of some of the system properties. Then one is confronted with the problem of numerically solving a set of time-dependent 2D/3D partial differential equations with free boundary conditions. Even though powerful FEMs for solving such problems exist, and computational performance has dramatically increased in the last several years, this still is one of the most challenging tasks [112,113]. The situation gets even worse if feed-forward trajectories need to be rescheduled in real time during growth, for instance, in order to react to some perturbations. Extensive studies on this task can be found in Refs [114–117], presented for the examples of growth of large diameter silicon and germanium crystals. To reduce the computational effort, one might restrict the problem to the quasi-stationary case. The feed-forward trajectory is then generated piecewise. This very powerful strategy has been presented in detail by Derby and Brown in Refs [47,72]. An approach using a simplified 2D model especially designed for control purposes can be found in Ref. [118].

A proper reference trajectory planning for the controlled variables is essential to obtain suitable feed-forward control trajectories. A good introduction into this subject w.r.t. Cz growth is given by Satunkin in Ref. [119].

28.3.4 Conventional PID-Based Control

28.3.4.1 PID-Based Control Using Optical Diameter Estimation

When designing a control system that tracks crystal diameter and growth rate, one has to reflect the different time constants that the manipulated variables have on the system: (1) Changes in pulling speed are affecting the system quite quickly; (2) Changes in heater power need some time depending on the thermal conditions occurring in the system [11,17]. Therefore, most often a cascaded control structure is chosen assuming that pulling speed v_p is more or less equal to the growth rate (cf. Figure 28.7) [120]. Deviations Δr_i from the reference value $r_{i,ref}$ of the crystal radius r_i are fed into a PID controller manipulating the reference value $v_{p,ref}$ of the pulling speed by an amount of Δv_p. This value, indicating a deviation of the real pulling speed trajectory from its precalculated reference value, is fed into a second PID controller manipulating the reference value P_{ref} of the heater power by an amount ΔP. By this strategy it is ensured that the system is able to react quite quickly on perturbations occurring in crystal diameter. Accumulated deviations in the pulling speed trajectory lead to a change of the heater power trajectory ensuring that the system is kept in its reference state in a long-term manner. Especially the pulling speed is brought back to its reference. This control approach requires very careful planning of the feed-forward trajectories, especially for the pulling speed needed to obtain a certain growth rate trajectory.

28.3.4.2 PID-Based Control Using Weight Measurement

If one does not have the possibility to capture the diameter of the bright meniscus ring, the usual control strategy is to use the crystal or the crucible "weight" as measured variable. When growing crystals from volatile melts, crystal weighing is preferred

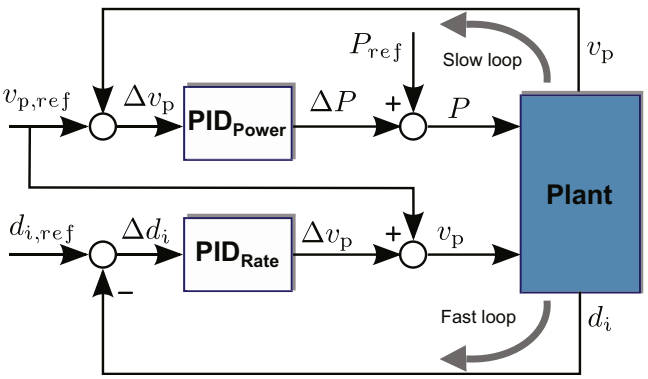

FIGURE 28.7 Cascaded PID-based control scheme utilizing pulling speed $v_{p,ref}$ and heater power (P) for diameter (d_i) control. Reference values are denoted by the subscript ref.

compared to crucible weighing because melt evaporation falsifies the signal in the latter one. The same holds when using rf-heaters where additional vertical forces induced in the crucible susceptor come into play [36]. One has to distinguish between two modes of operation [36,58]:

Weight mode: The weight measured by the load cell is compared to the reference value and the difference is used as an error signal for the PID controller. Hence, in this mode the controller tries to keep the weight on its reference value, meaning that a previous error in crystal radius later results in an error of opposite sign. This, on the one hand, is usually not preferable when trying to grow a crystal of well-defined shape. On the other hand, this mode circumvents noise generation by numerical differentiation of the force raw signal as required in differentiated weight mode.

Differentiated weight mode: The force raw signal is differentiated with respect to time and then compared to the reference value resulting from the predefined shape of the crystal. If one neglects the dynamics of the meniscus, this signal is proportional to the crystal radius, i.e., this mode tries to keep the radius on its reference value without being influenced from the past. The differentiation of the raw signal leads to a phase advance in the control system, which tends to make the system "more stable". On the other hand, sophisticated signal processing and filtering methods as well as high resolution load cells are required.

The most crucial part in this technique is the *anomalous* behavior of the signal, cf. Section 28.3.2. The consequence of this anomaly is that the performance of the control system is fundamentally limited [10]. The controller "is only allowed to respond carefully" to any sort of perturbation since they could be of opposite direction, not indicating what really goes on at the interface.

28.3.4.3 Improvements and Optimizations

In this section some approaches trying to compensate for the problems mentioned above are sketched.

In Refs [61,62] Bardsley, Hurle, et al. present a sophisticated control algorithm containing a method to overcome the problems resulting from the anomalous behavior. They try to estimate the anomalous components in the measured weight gain signal and subtract them from the signal. The estimation is done using a linear model calculating the radius change δr_i induced by changes in heater power. This value can be used for calculating an estimate of the anomalous component of the signal. Experimental results demonstrate the performance of this approach. However, it is restricted to the knowledge of a sufficiently precise model of the process, especially of the thermal conditions in the furnace.

A challenging task in this control approach is the choice of the parameters of the PID controller. Most often this is done by trial and error. However, there are some interesting approaches trying to determine optimal parameters of the PID controller on the basis of the model knowledge available. Satunkin et al. [66,121] propose an approach based on a cost functional for adjusting parameters in a single, as well as, multiloop control system utilizing heater power and pulling speed as manipulated variables. The same authors

present a modeling approach focusing on inaccuracies of the weight sensor and the consideration of these in the control system [66].

As already mentioned, the dynamic characteristic of the process changes during crystal growth. As a consequence, parameters of the PID controller determined for one set point may not produce acceptable results as the process proceeds. The strategy to overcome this problem is to change the parameters on relevant intervals. This strategy is commonly known as *parameter* or *gain scheduling* in the field of adaptive control [122,123]. An approach for Cz growth can be found in Ref. [16].

28.3.5 Model-Based Control

28.3.5.1 Lumped Parameter Model-Based Control

In Refs [10–13] Gevelber et al. propose a model-based multiloop control system. The first two publications of this series are based on a seventh-order model of the process, while the latter ones make use of a more refined model of order 34. In these publications, a multiloop control system is proposed not only to ensure a correct diameter during the process but also to compensate identifiable disturbances before they affect the growth dynamics. Two main disturbances are identified, both related to the melt drop: the thermal state of the melt, which changes the heat flux entering the interface; and the thermal environment that the crystal is exposed to, affecting the heat flux from the interface and thus the growth dynamics. By adding a closed loop around the melt temperature, the impact of this disturbance is significantly reduced, enabling tighter control of diameter and thus minimizing growth rate variations in a robust manner. Additionally, this work analyzes the importance of controlling the interface shape in addition to the crystal diameter. This requires the use of additional actuators, and an important part of the design task is to select an actuator set that can control both degrees of freedom relatively independently. To further obtain design insight, Gevelber et al. derive a model that especially reflects the influence of radiation heat transfer within the furnace as exactly as possible within a lumped parameter model.

Further model-based approaches have been presented by Satunkin [98] (using a linear state space controller), Sabanskis [118] (using a 2D approximation), and Riedling [124] (combining heuristic and deterministic techniques in the 4″ growth of GaAs crystals using the LEC method).

The bottleneck of the lumped parameter model-based approaches is the appropriate modeling of the thermal effects. An elegant solution to circumvent this is the following approach [14]: for the Cz process, a relatively simple second-order lumped parameter model of the meniscus dynamics only can be derived if rotational symmetry and a planar solid–liquid interface is assumed [14]. It reads:

$$\dot{r}_\mathrm{i} = v_\mathrm{g} \tan(\alpha_\mathrm{i}) \tag{28.10a}$$

$$\dot{\alpha}_\mathrm{i} = \frac{v_\mathrm{p} - v_\mathrm{c} - c_{\alpha z}(r_\mathrm{i}, \alpha_\mathrm{i}) v_\mathrm{g}}{c_{\alpha n}(r_\mathrm{i}, \alpha_\mathrm{i})}. \tag{28.10b}$$

In these equations, r_i denotes the crystal diameter at the solid–liquid interface, α_i the cone angle (cf. Figure 28.4), v_p the crystal pulling rate, v_c the crucible translation rate,

and v_g the crystal growth rate. Furthermore, $c_{\alpha z}$ and c_{an} are some nonlinear functions that can be found in Ref. [14]. The growth rate results from the thermal situation in the furnace, cf. Eqn (28.8), but is considered as unknown in this approach.

Although this capillary model does not cover the complete process dynamics, it can be utilized to derive a partial model-based control system [14,15]. Considering the relation $\dot{x}/v_g = (dx/dt)/(dl/dt) = (dx/dl) = x'$ in which l is the crystal length and x an arbitrary quantity, one can divide the differential equations of the model (10) by the growth rate $v_g = dl/dt$. As a result, one obtains a model that is parameterized in crystal length instead of time:

$$r_i' = \tan(\alpha_i) \tag{28.11a}$$

$$\alpha_i' = \frac{v_z - c_{\alpha z}(r_i, \alpha_i)}{c_{\alpha n}(r_i, \alpha_i)} \quad \text{with} \quad v_z := \frac{v_p - v_c}{v_g}. \tag{28.11b}$$

The dimensionless quantity v_z is denoted as the *lift ratio*. Now, a model-based control law can be derived according to the procedure described in Section 28.2.5, Eqns (28.5)–(28.7) with $y = r_i$ and $\dot{y} = r_i' = \arctan(\alpha_i)$. One obtains:

$$\begin{aligned} v_{z,ref} &= \nu \frac{c_{\alpha n}(r_i, \alpha_i)}{1 + (r_i')^2} + c_{\alpha z}(r_i, \alpha_i) \quad \text{with} \\ \nu &= r_{i,ref}'' - k_1\left(r_i' - r_{i,ref}'\right) - k_0\left(r_i - r_{i,ref}\right). \end{aligned} \tag{28.12}$$

This model-based controller calculates desired values $v_{z,ref}$ for the intermediate quantity v_z. Since one lacks a model of the thermal behavior, PID controllers are placed around this model-based controller, transforming this intermediate value into the real inputs pulling speed v_p and heater power P available at the process. This approach is sketched in Figure 28.8. A nonlinear state estimator provides values for r_i, α_i [15]. Parameter scheduling for the PID parameters and the proper assignment of the manipulated variables to the controlled variables are discussed in Ref. [16]. By this strategy, a large amount of lumped parameter model knowledge is introduced into the control system. A similar procedure can be found in model-based control of the Detached Bridgman process, cf. Section 28.5.3.

In all cases discussed in this section, the overall closed-loop performance is considerably enhanced, however, because of the lumped parameter character, some more or less strict constraints exist with respect to process setup, model validation, or trajectory planning.

28.3.5.2 Distributed Parameter Model-Based Control

Some publications try to overcome the limitations resulting from the lumped parameter approach by directly working on the partial differential equations of the distributed parameter models. Such approaches, for example presented by James Ng et al. in Refs [125–127] and Wang in [128], are fundamentally important for understanding the dynamics of the process, especially when focusing on the effects related to heat transport phenomena or variable phase boundary problems. However, for an implementation

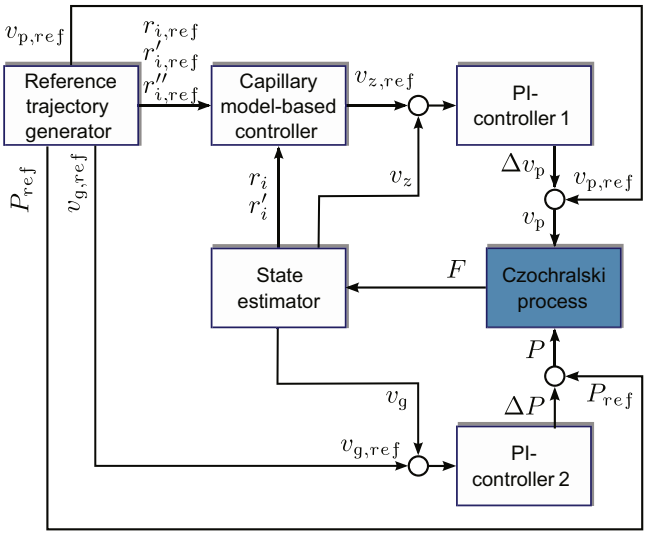

FIGURE 28.8 Combination of model-based and PID control. *Adapted from Refs [14,15].*

under real world conditions and controller parameterization they are not suitable. The reason for this is that in these models the manipulated variables are also spatially distributed, e.g., a temperature distribution on the heater surface. But, what the controller actually manipulates is the current entering the heater, which is a lumped quantity being connected to the temperature distribution on the heater surface in an unknown way.

28.3.5.3 Model Predictive Control

An interesting approach based on this strategy can be found in Refs [129,130]. The model used in this approach is of lumped parameter type. It includes melt convection, which requires very strict assumptions to be fulfilled in order to make the model applicable. Another approach to establish such a model-based control on the basis of a lumped parameter model has been published by Voronkov et al. [9,120]. It is closely related to the v_g/G theory [5,7], which requires very precise tracking of the growth rate v_g.

28.4 Vertical Bridgman and Vertical Gradient Freeze Process

From a control technological point of view, the Vertical Bridgman (VB) and the Vertical Gradient Freeze (VGF) crystal growth processes (cf. Vol. IIA, Chapter 9) are outstanding challenging tasks. On the one hand, one has—compared to other processes—a relatively large number of strongly coupled manipulated variables, and on the other hand, one has exactly zero measurement information about the most important process quantities.

28.4.1 Process Characteristics and Control Objectives

Common to both processes is the continuous movement of a (more or less) fixed temperature gradient in vertical direction of an ampule or crucible containing the molten material. This movement is done in such a way that crystallization inside the ampule takes place in a well-defined manner from the bottom toward the top. In the VB process this is realized by the relative mechanical movement between ampule and the axially arranged heaters, independently, which of both is really moved. In contrast, in the VGF process the movement of the temperature gradient is solely realized by an appropriate tracking of the heater powers.

The key problem when trying to establish a feedback control for the Bridgman process is the fact that no measurement information about the variables that should primarily be controlled is available. The most prominent candidate for the controlled variable would be the growth rate (the crystal shape is already fixed by the ampule). Assuming a flat interface shape, it could be treated in a lumped parameter sense as done in the Cz process above. However, in real systems the interface represents the melting point isotherm inside of the furnace and is never completely flat. The deflection of the interface, its convex or concave shape, directly influences the crystal quality. Usually a slightly convex interface shape is preferred in order to avoid a concentration of grown-in defects (cf. Vol. IIA, Chapter 9). To achieve this goal, the interface shape has to be detected in situ and feedback controlled. However, besides manually detecting the position of the interface [131] (which may lead to contamination issues and mechanical generation of structural defects at the interface) or using a transparent ampule [132] (which is limited to few materials) up to now no feasible method for an in situ measurement under industrial conditions of this process quantity is known. The most promising technique for this task seems to be the application of ultrasound. Here the basic work was done by Parker and Manning [133] followed by Carter et al. [134] (Germanium) and Schmachtl [135] (metal alloys) first presented acceptable resolutions. A modern approach is presented, e.g., by Azizi et al. [136] for multicrystalline PV silicon normal freezing and for FZ in Dold et al. [137]. Achieved growth rate resolutions were roughly in the range of $\pm$ (1…2) mm/h. This is acceptable to have approximate information about the position of the phase boundary. However, for Bridgman growth with its low growth rates just in that range of several mm/h, the resolution has to be better by a factor of 5–10 for using it in a robust feedback control system.

In both processes, the heater powers are important manipulated variables. The correct adjustment of the heater powers in order to maintain the required temperature field is a challenging task. In the VB process, the heaters have to be controlled in such a way that despite the moving ampule and the phase transformation in it, the temperature field remains constant. In the VGF process, the temperatures of the heaters have to be continuously changed in a predefined manner in order to establish the movement of the temperature gradient. In both cases, only very small tolerances are acceptable. The main problem here is that one has a system of several heaters that are responsible for the

temperature and its dynamics at several points of the furnace. However, each heater does influence the *whole* temperature field. Hence, when designing a temperature control system, one deals with a typical multi-input-multi-output (MIMO) system with a strong cross-coupling. Because of this, controller design is much more complicated compared to single-input-single-output (SISO) systems. An additional control task in VB growth is the proper tracking of the relative motion between ampule and heaters.

28.4.2 Conventional Control

As stated above, in the majority of applications the primary system quantities, especially the interface shape, cannot be directly measured. However, because a certain interface shape and interface position is directly connected to a certain temperature field within the ampule [138], which itself is characterized by a certain temperature distribution on the ampule's boundary, it makes sense to content oneself with a proper feedback control of the heater temperatures [139] and/or the movement of the ampule. Such an "indirect" control system uses the temperatures of thermocouples installed on the surface of the ampule as the controlled variables and the heater powers as the manipulated variables. For its function, one has to calculate the required boundary temperature distribution using a suitable model of the process. Because of the complexity of the models and possible ambiguities of the solutions, this calculation has to be done a priori. The result is used as a reference for conventional real time MIMO PID feedback control. Control design for such coupled systems using PID controllers is a well-matured task in control technology. A general introduction of the control of such systems is given, for example, in Refs [140–142] and especially for multizone heating systems in Refs [143,144].

The key problem of this indirect control strategy is the correct and unambiguous calculation of the reference temperature profile and/or translation rate of the ampule. This requires not only appropriate model knowledge, usually by means of high order FEM models, but also time-consuming experimental effort to match the models to the relevant plant setup. Furthermore, under industrial conditions, *all* plants have to be kept in exactly the state that has been used for this matching ("copy exactly", cf [145]). A wide range of modeling approaches for this purpose exists in literature; Kuppurao, Derby, et al. [146,147] may be used as a starting point.

28.4.3 Model-Based Control

Only a few publications exist for the model-based control of the VB/VGF process. Apart from the measurement issues, this is due to the fact that models of the system appropriate for *control purposes* are of distributed parameter type, cf. Section 28.2.1. For example, the controlled variable "interface shape" cannot be described by a single variable but by a functional relation. The same holds for the temperature distribution at the ampule boundary. Only the heater powers are of lumped type. The feedback control of such distributed parameter systems with lumped inputs is currently a highly dynamic

subject of investigation in control theory [148,149]. An approach for a very simple model of the VGF process detailing this strategy can be found in Refs [150,151].

Apart from that, model-based approaches exist focusing on subordinate problems and trying to reduce the problem to the control of some lumped parameter quantities. They are detailed in the next two sections.

28.4.3.1 Temperature Control and Interface Shape Detection

The model-based temperature control of the Bridgman processes has been the subject of several publications by Batur et al. In Refs [132,152] a method for the identification of a linear lumped parameter MIMO model of the heating zone system is proposed. The model is used for the design of a self-tuning linear state space controller for tracking of the zone temperatures. Experimental results from an eight-zone VB system with three thermocouples in each zone are provided showing the importance of the consideration of the cross-coupling between the heaters in the controller design. In the investigated setup, a transparent ampule for the growth of lead bromide has been used. This makes it possible to directly detect the interface shape and to close the feedback path. An appropriate algorithm for the detection of the interface from the camera pictures is provided in the mentioned publications as well as in Ref. [153]. Of course such an approach is not possible when growing crystals of nontransparent materials in nontransparent ampules, which is the case in the majority of VGF-grown elemental and compound semiconductors. The controllers used in this approach are of quite complex structure due to the MIMO character of the system and the strong cross-coupling between the zones. Therefore, in Ref. [154] the same authors present reduced-order controllers based on so-called projective control strategies [155].

A much more refined approach is presented by Batur et al. in Ref. [139] on simulation studies, cf. Figure 28.9. Again it is assumed that a certain desired interface shape requires

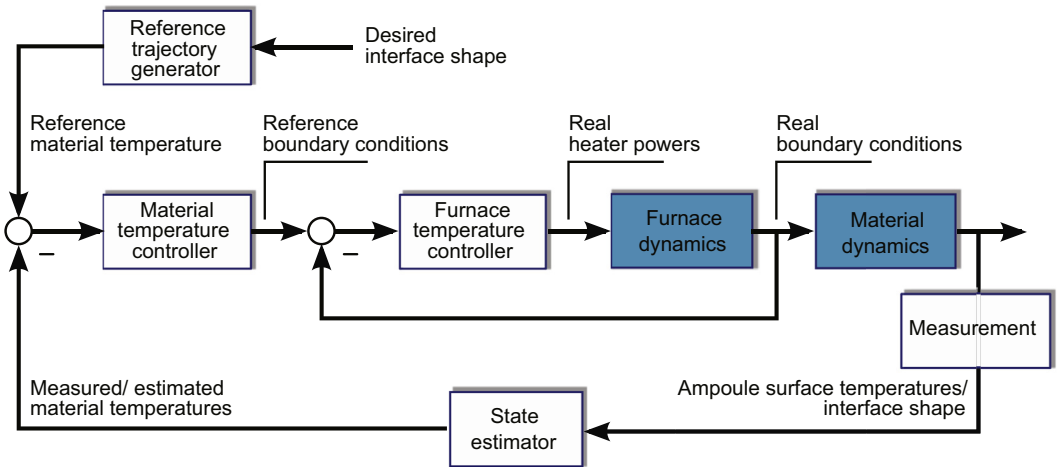

FIGURE 28.9 Bridgman crystal growth control system. *Adapted from Ref. [139].*

a corresponding temperature distribution inside the material. The task of the interface shape control loop is to establish this temperature distribution and can be accomplished by manipulating the boundary conditions around the material. These boundary conditions are established by the furnace temperature controller. If the interface shape or the inside material temperatures can be measured, it is compared with the desired interface shape or the reference material temperatures, and the resulting error signal is sent to the material temperature controller. The required boundary conditions, or equivalently the furnace (or heater) temperatures, are determined by the material temperature controller. The boundary conditions are used as the reference temperatures for the furnace temperature controller. The actual boundary conditions established by the furnace temperature controller determine the temperatures inside the material through the dynamics of the crystal growth mechanism. The approach provides the possibility to estimate the shape of the interface if it cannot be measured directly (cf [156]).

28.4.3.2 Flow Speed Control

In Refs [157,158] Sonda, Yeckel, and Derby present a model-based approach for controlling the melt flow. In their system, the meridional melt speed S is used as the controlled variable. This is the spatial root-mean-square average of the velocity magnitude, defined as

$$S = \sqrt{\frac{1}{V}\int\limits_{(V)} \left(v_r^2 + v_z^2\right) \mathrm{d}V}$$

where v_r and v_z denote the magnitude of the velocities in the radial and axial directions, respectively and V is the total melt volume. The crucible rotation speed is used as the manipulated variable. By this choice, a SISO-controller design procedure is possible. A nonlinear input–output feed-forward controller combined with a state feedback controller [159] is chosen by the authors to address the problem. The model-based controller approach is tested by simulation on models provided by Kim et al. [160,161], Müller et al. [162], and Derby et al. [163,164] assuming two configurations: melt at the top of the ampule ("stable configuration") and melt at the bottom of the ampule ("unstable configuration"). The results are further compared to simple linear P- and PI-controllers. It has been shown that flow oscillations in the melt could be attenuated by a significant amount. Due to the lack of any measurements, especially of S, the approach is of theoretical interest only. However, by such studies one gains deep insight into the process dynamics and the correlation between different process phenomena.

28.5 Detached Bridgman Process

The Detached Bridgman crystal growth process is a promising candidate for the production of bulk, single-crystal semiconductors of extraordinarily quality because it provides zero container contact of the crystal (as in Cz growth) and low thermal stress (as in Bridgman growth) (see Chapter 19 of Volume IIB). Thorough investigations of this

process especially with respect to process control have been provided by Yeckel and Derby [165–167], on which this section is mainly based.

28.5.1 Process Characteristics and Control Objectives

Detached growth occurs when the crystal solidifies into the melt without contacting the ampule wall, cf. Figure 28.10. Hence, a narrow gap that is usually filled with inert gas between the crystal and the ampule remains. In stable detached growth, the melt is in contact with the ampule above the crystal. The gap between the ampule wall and the triple-phase line is bridged by a small liquid meniscus. The primary control task is to achieve a stable growth regime with constant crystal diameter under terrestrial conditions, i.e., the crystal neither contacts the ampule wall nor grows away from it during growth. Compared to zero-gravity conditions, this is more complicated because of the continuously decreasing static weight of the melt on top of the growing crystal. Hence, this effect must be robustly compensated [165]. Another control task would be the regulation of the crystal growth rate or the interface shape as in conventional Bridgman growth. Here, for growth rate control the same issues and limitations exist, cf. Section 28.4, and up to now no publications are available dealing with the feedback control of this important process quantity. Anyway, a proper control of the crystal diameter or equivalently of the gap width is of superior priority since it enables one to maintain the detached state over the full process duration. It has to be noticed that no method for the in situ detection of the gap width has been developed so far. Against this background

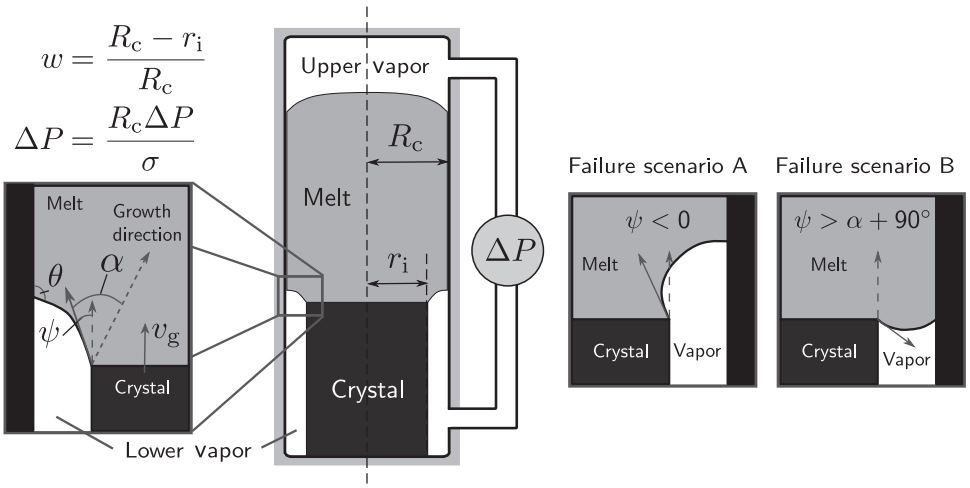

FIGURE 28.10 Sketch of a detached Bridgman growth furnace. One has the growth angle α, the wetting angle Θ, the gap width w, the crystal radius r_i, the inner ampule radius R_c, the melt surface tension σ, and the pressure difference ΔP between the upper and the lower vapor space. The angle between the vertical and the meniscus at the three-phase-line (TPL) is denoted by ψ. The two figures to the right show situations in which stable growth tends to fail because of inadequate values of the manipulated variable ΔP: (a) $\Delta P \ll 0$ (too much suction); (b) $\Delta P \gg 0$ (too much pressure downward). *Adapted from Refs [166,168].*

the following explanations are of more theoretical value, however, they may be helpful in understanding the process and its dynamics in more detail.

28.5.1.1 Choice of the Manipulated Variable

In order to control the crystal diameter and to stabilize the system, an appropriate manipulated variable must be available. Several methods have been developed for this purpose. Duffar et al. [168,169] propose a system in which a second vapor space above the melt is introduced. Then, gas is injected into the upper and lower vapor space in such a way that a stable growth regime is achieved. This configuration is depicted in Figure 28.10. In this case the manipulated variable is the pressure difference ΔP between the two vapor spaces. A similar method is proposed by Palosz [170]. Pätzold [171] alternatively manipulated the pressure on the meniscus by controlling the temperature of the vapor space in the bottom of the ampule.

28.5.1.2 Lumped Parameter Model

Fortunately, it is possible to derive a simple first-order lumped parameter model of the capillary part of the system as appropriate for control purposes if one uses the pressure ΔP as the manipulated variable. It is very similar to that employed in Cz growth. With the denotations from Figure 28.10 one has:

$$\dot{w} = v_g \tan(\alpha - \psi) \tag{28.13a}$$

$$\psi = \arccos\left[\left(\frac{\Delta P}{2} - \cos\Theta\right)(1-w) - \frac{\Delta P}{2(1-w)}\right]. \tag{28.13b}$$

The growth rate v_g depends on the thermal situation at the interface (cf. Eqn (28.8)) and has to be calculated from a model of the thermal system.

28.5.1.3 Stability and Operational Limits

When designing the control system the most important question to be answered is under which conditions stable growth occurs. As in Cz growth, the answer depends on the effects included in the model on which the stability analysis is performed, cf. Section 28.3.1.3. First studies on this topic neglecting any thermal effects and the shape of the crystal–melt interface can be found in Ref. [168] under zero gravity and under terrestrial conditions in Refs [169,171,172]. The influence of the gap width on the interface shape is studied in [173,174]. A linear stability analysis of Epure [175] shows that gravity may have a stabilizing effect on the process, while in Ref. [176] it is shown that mechanical perturbations to the meniscus may lead to dewetting. The most rigorous analysis under zero gravity based on a full thermocapillary model has been provided by Yeckel et al. in Ref. [165]. Their approach interestingly confirmed the basic stability criterion $\Theta + \alpha > \pi$ derived originally by Duffar without regarding thermal effects (refer to Figure 28.10 for an explanation of the symbols). From this stability criterion, it follows that when growing typical semiconductors with growth angles α in the range of $10°\ldots30°$ a strongly non-wetting ampule material with $\Theta > 150°\ldots170°$ is required. Apart from that, this stability criterion combined with the capillary model (13) provides further insight into the system

characteristics important for controller design as carried out in Ref. [166]: Stationary growth with respect to the gap width (i.e., $\dot{w}=0$) occurs if $\alpha=\psi$. The corresponding pressure difference ΔP_e depending on the gap width w follows from Eqn (28.13b):

$$\Delta P_e = -\frac{2(1-w)}{w(2-w)}(\cos(\alpha)+(1-w)\cos(\Theta)). \tag{28.14}$$

The pressure difference ΔP^* below which no equilibrium exists is characterized by the condition $\psi=0$. From Eqn (28.13b) it follows:

$$\Delta P^* = -\frac{2(1-w)}{w(2-w)}(1+(1-w)\cos(\Theta)). \tag{28.15}$$

The difference $\Delta P^*-\Delta P_e$ defines the largest possible perturbation of the manipulated variable and forms a strong restriction on the controller performance. On the other hand, the gap width w_e for stationary growth reads

$$w_e = 1-\frac{\cos(\alpha)\pm\sqrt{\cos^2(\alpha)+\Delta P(\Delta P-2\cos(\Theta))}}{\Delta P-2\cos(\Theta)} \tag{28.16}$$

with shape stable solutions for the positive sign and shape unstable solutions ($\alpha+\Theta<\pi$) for the negative sign. Here, two cases of instability must be distinguished—perturbing the gap width to a smaller value may cause reattachment of the crystal to the ampule; perturbing it to larger values may lead to necking of the crystal.

The gap with w^* at which the dewetting failure occurs is obtained by setting $\psi=0$ in Eqn (28.13b):

$$w^* = 1-\frac{1\pm\sqrt{1+\Delta P(\Delta P-2\cos(\Theta))}}{\Delta P-2\cos(\Theta)} \tag{28.17}$$

with the positive sign for $\Delta P>\cos(\Theta)$ and the negative sign for $\Delta P<\cos(\Theta)$. By a similar procedure, the maximum allowed interval for the wetting angle of the ampule wall can be determined. If the wetting angle increases due to a chemical or physical heterogeneous ampule wall, the meniscus will deform in an upward direction to maintain the pressure balance. This might violate the ΔP^* border. This critical angle Θ^* results from Eqn (28.13b) with $\psi=0$ and using Eqn (28.14) to eliminate ΔP. Hence, the maximum allowed perturbation $\delta\Theta$ of the wetting angle reads

$$\delta\,\Theta = \arccos\left(\frac{\cos(\alpha)+(1-w)\cos(\Theta)-1}{1-w}\right)-\Theta. \tag{28.18}$$

Equations (28.15), (28.17), and (28.18) form the basis to determine the operational limits $\Delta P>\Delta P^*$, $0<w<w^*$, $\delta\Theta$ of a control system.

28.5.2 PI-Based Control

In a first step, it is natural to address the gap width control by means of a P- or PI-controller (cf. Section 28.2.5) with the gap width as the controlled variable and the pressure difference as the manipulated variable. A comprehensive discussion on this

strategy is presented in Ref. [166]. It turns out that due to the strong nonlinearity of the process and the restricted operational limits (cf. previous section) a robust control of this system based on such linear controllers is not favorable. For example, in closed-loop mode a certain *minimum* gap width occurs, making diameter control more complicated. Furthermore, solution multiplicities are introduced. Hence, the applicable controller gain K_P (cf. Eqn (28.4)) is limited. The key problem here is the fact that the P- or PI-controller naturally does not have any model knowledge, which enables it to account for the very restricted limitations of the system. Thus, the possibility is relatively large that the controller drives the system into a state in which immediate detaching failure occurs. This issue can only be addressed by tuning the controller very weakly or by introducing hard limits on its output. This, on the other hand, results in slow actuator performance and, hence, in poor disturbance rejection.

28.5.3 Model-Based Control

The very simple capillary lumped parameter model (13) of the system enables one to derive a nonlinear model-based controller for the system. The procedure in doing so is exactly the same as in the introductory example in Section 28.2.5 and in Cz growth (Section 28.3.5.1). Since the restrictions derived in Section 28.5.1 result from this model, such a controller will account for them. This approach has been published by Yeckel et al. [167] for the case of microgravity and will be sketched in the following:

In order to derive the controller, the control error in the gap width is introduced as $z = (w - w_{\mathrm{Ref}})/w_{\mathrm{Ref}}$ with the reference gap width w_{Ref}. One wants the tracking error to fulfill a stable first-order dynamics, which is defined as

$$k_0 \dot{z}(t) + z(t) = 0 \quad \Leftrightarrow \quad z(t) = z(0)\mathrm{e}^{-\frac{t}{k_0}} \tag{28.19}$$

with the characteristic time $k_0 > 0$, the controller parameter determining how quickly the control error converges to zero (cf. Eqn (28.5) also). Substituting Eqn (28.13a) into Eqn (28.19) and using Eqn (28.13b), one obtains the control law

$$\begin{aligned} \Delta p &= -\frac{2(1-w)}{w(2-w)}\left(\cos(\alpha-\beta) + (1-w)\cos(\Theta)\right) \quad \text{with} \\ \beta &= \arctan\left(\frac{w_{\mathrm{Ref}} - w}{k_0}\right) \end{aligned} \tag{28.20}$$

which provides the pressure difference required for the correction of disturbances in the gap width. Note that ΔP will always exhibit or equal the pressure limit given in Eqn (28.15). Furthermore, this control law naturally reduces to the relation of the equilibrium pressure (Eqn (28.14)) if $w = w_{\mathrm{Ref}}$. A method on how to increase robustness with respect to bias errors by introducing an additional integral part and an in-depth discussion of the proper choice of the parameter k_0 as well as of controller performance can also be found in Ref. [167]. Additionally, it is shown that errors resulting from the static weight of the melt in case of terrestrial growth are accounted for by the controller, too.

28.6 Floating Zone Process

The Floating Zone (FZ) technique is favored if high material purity is required that cannot be ensured by, for example, the Cz method, because of melt contamination by the crucible material. The method itself is explained in detail in Vol. IIA, Chapter 7 of this handbook where a modern model predictive control system is also presented. The next chapter gives a more general overview of FZ control issues.

28.6.1 Process Characteristics and Control Objectives

The primary task of an FZ control system is to ensure a stable molten zone between the feed rod and the growing crystal. Among other parameters it is defined by the diameters of the feed rod and the crystal, respectively, and its height, the so-called zone length. The crystal diameter and the zone length are the controlled variables. A proper control of these quantities is a key issue because inappropriate values may lead at least to a reduced crystal quality and in the worst case to leakage of the melt zone or melt-inductor contact. As manipulated variables, the vertical translation rates of the feed rod (responsible for the melt flux into the molten zone) as well as the heat induced in the molten zone are available. The latter one is usually provided by single coil electromagnetic heaters, i.e., the current entering the inductor is the third manipulated variable. The translation rate of the crystal is usually kept constant in order to support a constant growth rate. This system is of strongly coupled nature—on the one hand, an increase of the heater power will increase the zone height because the amount of melt that is molten is increased. As a result of this, one will observe a temporary diameter deflection until a new steady state is reached. On the other hand, an increase of the feed rod translation rate in the downward direction will decrease the zone height, which results in an increase of the material molten from the feed rod per time unit. Hence, since the volume of the molten zone cannot increase beyond certain limits, the crystal diameter will increase to a new steady state value. These interrelationships are extremely sensitive with respect to the corresponding manipulated variables and require highly skilled operators for manual control or carefully adjusted control systems.

As in Cz growth, a first stability analysis of the Fz process has been provided by Surek in Ref. [75] focusing only on the capillary problem. From this point of view, the system is always inherently stable. A more in-depth analysis has been given by Tatarchenko in Ref. [78] (also briefly summarized in Ref. [81]), including also dynamic effects and the influence of the heat flows in the system. Especially, it has been shown that from a system theoretical stability point of view pulling downward should be preferred compared to pulling upward (pedestal growth). Further investigations on this topic can be also found in Ref. [98].

28.6.2 Measurement Techniques

A big advantage in Fz growth is the fact that the parts of the melt zone that are not hidden by the inductor coil can properly be monitored through a camera system.

The determination of the crystal diameter and the zone length as well as of the phase interfaces from such an imaging system are described in a Siemens patent from 1963 [177]. Additional information can be gathered if one tries to determine the tangent to the melt surface at certain points of the melt zone. This is described in Ref. [178]. Capturing of the *whole* visible molten zone shape enables one to reconstruct information about the state of the process, which is far beyond that gathered from the diameter and zone height, for example, the crystal cone angle or the melt angle. These quantities can be useful in a model-based control system. With respect to this, Lie et al. [179] and Wünscher [180] provided a set of methods for the calculation of the surface shape of the molten zone, including the electromagnetic pressure. One may also consult the contributions of Shyy and Rao [181] and the Kalman-based method by Werner (cf. [182] and Vol. IIA, Chapter 7).

28.6.3 Reference Trajectory Planning and Conventional Control

In the Fz process the planning of the reference trajectories is of special importance. For example, the diameter of the inductor hole limits the size of the melt neck to an upper value since one has to avoid short circuits due to contact of the melt with the heater. On the other hand, the melt neck must not be too thin since this may (in the worst case) result in detaching of the melt from the feed rod [182]. These constraints have to be considered during planning of the reference trajectories for the crystal diameter and the zone length. The size of the latter is also limited to ensure a stable melt zone. This topic is discussed by Heywang [183].

Keeping these constraints in mind, it is possible to implement a control system using standard PI or PID controllers (cf. Section 28.2.5.1). A first control approach was proposed by Rowton in 1965 [184] for a silicon refinement process. There, a relation between the diameter deviation of the feed rod and the inductor frequency is derived. Then, the measured inductor frequency is used as controlled variable. A cascaded control regime ensures proper diameter tracking, in some sense similar to that usually used nowadays in Cz growth (cf. Section 28.3.4). A deviation in the frequency drives a PID controller manipulating the heater power, and the deviation of the heater power is used for a correction of the translation rates in order to keep the disturbances of the ingot diameter away from the refined rod. Such an indirect control regime is also proposed by Otani et al. [185] for the growth of refractory metals. Today, crystal diameter and zone height are directly measured. Hence, a two-loop control system can be established; in this, a first PID controller is responsible for keeping the diameter on its reference value using the heater power as manipulated variable, and a second PID controller uses the feed rod translation rate for keeping the zone length on its reference value. Such an approach is discussed in detail, for example, by Chan et al. [186] for the growth of TiC, and is also claimed by the Shin-Etsu patents [187–189].

28.6.4 Model-Based Control

As in Cz growth, the performance of PID-based control regimes is fundamentally limited due to the nonlinearity and the batch character of the process. Hence, a variety of model-based strategies is proposed in the literature. A model predictive control approach (cf. Section 28.2.5.3) has been presented in a patent by Wacker [190]. There, a reduced order model derived from a high order one is used to perform the required real time optimization calculations. The patent illustrates the basic idea of such an approach rather than providing a realizable model. A linear fourth-order lumped parameter model suitable for controller design (in a certain set point) is derived by Satunkin in Ref. [98]. Werner proposes an eleventh-order nonlinear model in Ref. [182]. Based on this model, a sophisticated nonlinear model predictive control strategy is established, which is also sketched in Vol. IIA, Chapter 7 of this handbook.

28.7 Kyropoulos Process

The Kyropoulos growth method was intentionally designed to grow crystals under extremely low thermal stress. It has tended to be sidelined for decades, but nowadays it is experiencing a kind of renaissance, e.g., for sapphire growth [95,191]. Similarly, new applications occur for the growth of multicrystalline silicon for PV applications [192]. Hence, the demand for a proper control of this process is increasing. Unfortunately, only very few publications exist dealing with this topic. Thus, the following compilation may be useful as a starting point for further research.

28.7.1 Process Characteristics and Control Objectives

The setup of the Kyropoulos technique is sketched in Figure 28.11. In the initial stage of the process, after seeding, the crystal grows into the melt with a sharply convex interface shape, driven by the cooling of the seed crystal. Later, as the diameter increases and the release of latent heat reaches a significant amount, the temperature field inside of the growing crystal and the melt is manipulated by the heater power in such a way that crystallization is maintained. During growth, the crystal is nearly not, only slightly, or moderately pulled in an upward direction [194,195]. The exact translation rate is a question of technological requirements like internal transport of heat, shape control, etc. In modern approaches for sapphire growth – for example – the trend is toward extremely slow movement of the pulling rod [195,196] or to no translation/rotation at all [197]. At least in cases where the crystal is additionally rotated [194], the remaining difference to Cz is that the crystal grows far below the melt surface, i.e., no melt meniscus is present. The submerged growth of the crystal provides very low axial and radial thermal gradients. The finished crystal is irregularly shaped and occupies almost the entire crucible. Usually the crucible is touched by the crystal at the bottom region only. Critical stages of the process are the seeding and initial expanding phase of the shoulder and the end of the process when the crystal reaches the crucible bottom [197]. A process control system

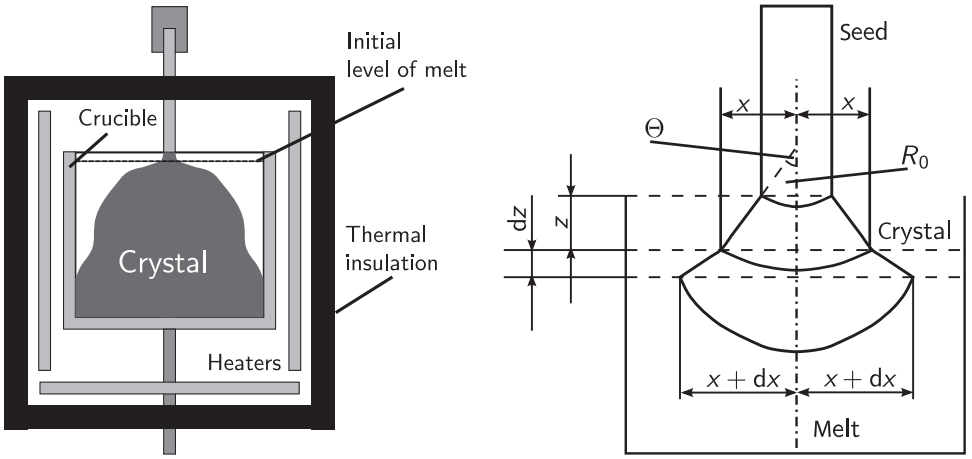

FIGURE 28.11 Sketch of a Kyropoulos plant (left) and geometrical abstraction of the process (right). *Adapted from Ref. [193].*

has to ensure that the crystal diameter does not increase too fast during the initial phase and is kept on a more or less constant value for the rest of the process. Furthermore, a sudden freezing of the melt has to be avoided. Because of the very low thermal gradients in the furnace, this is a challenging task.

28.7.2 Control Approaches

The manipulated variables are the power of one or several heaters, and the preferred controlled variable would be the crystal diameter. Instead, usually the force acting on a load cell connected to the seeding rod is used as the controlled variable [191,198]. For a proper design of the control system using a lumped parameter model, one has to derive a relation between the force acting on the load cell and the evolution of the crystal diameter. Because of the strongly convex interface shape and the irregular growth of the crystal preventing any symmetry assumptions and other simplifications in the models, this is a much more complicated task than in Cz growth where usually a planar interface and rotational symmetry can be assumed for such calculations. The situation still worsens because strong buoyancy effects of the (partially) submerged crystal have to be considered.

First investigations on calculating the crystal shape in Kyropoulos growth were published by Singh [193] using also results from Schönherr [199]. Their technique is based on a pure mass transfer approach assuming that the crystal interface shape can be described as spherical or as an ellipsoid of rotation. Although the influence of the heat transfer and melt convection is not considered in their approach, the results have been verified with acceptable limits of error by numerous experiments. Furthermore, for materials not showing a density anomaly, it is shown that the crystal radius reaches a limit value $r_{\max} = R_c\sqrt{\rho_m/\rho_s}$ with the crucible radius R_c and the densities ρ_m, ρ_s of the

melt and the crystal, respectively. A more refined (also purely geometrical) approach is given by Zhang et al. [196,200].

A common approach for controlling the Kyropoulos process is to numerically calculate the evolution of the temperature field in the furnace, which represents the desired growth of the crystal. The time evolution of the temperature field can be represented by trajectories of the heater powers. Hence, one can apply a feed-forward control regime using these heater power trajectories. A discussion related to this topic can be found, for example, in Refs [201,202]. This approach is similar to that in Bridgman growth, cf. Section 28.4.2. However, because the force on the load cell is available as measurement information about the process state, one is able to add a feedback control loop to the system compensating for the inaccuracies of the feed-forward control. Such an approach is presented by Kokh et al. in Ref. [198].

28.8 Conclusions

In this chapter, different approaches for the control of selected crystal growth processes from melt have been discussed. It has been shown that a deep understanding of the process dynamics makes controller design considerably easier. Here, model-based strategies are a key tool since they reveal the most critical characteristics of the process that have to be considered in the determination of the reference trajectories as well as for open- and closed-loop control design. On the other hand, it has also become apparent that the lumped parameter strategies usually used in control theory hit their limits in these processes. This is mainly because of the complex nonlinear thermal and convective phenomena in these systems that cannot be captured sufficiently by low order lumped parameter models. While they provide insight into subordinate problems, e.g., when dealing with the capillary phenomena, cf. Section 28.3.5.1 (partially model-based control of the Cz process) or Section 28.5.1.3 (operational limits of the Detached Bridgman process), the approach fails where a global treatment of the system quantities is inevitable, for example, in the case of Bridgman growth (cf. Section 28.4.3). With respect to this, the authors are of the opinion that model predictive control strategies (cf. Section 28.2.5.3) are the key for further development of control systems in crystal growth since they are able to rely on more accurate (but much more complex) models of the process. A necessary condition for this is that computational power increases insofar as to solve the underlying full transient high-order models in real time. Model reduction strategies keeping the principal system dynamics are an important discipline that should be involved for this purpose, too. The scientific community is encouraged to follow the path in this sense.

References

[1] Jordan, Caruso R, von Neida A, Nielsen J. J Appl Phys 1981;52:3331.

[2] Jordan, von Neida A, Caruso R. J Cryst Growth 1984;70:555.

[3] Motakef S, Kelly K, Koai K. J Cryst Growth 1991;113:279.

[4] Neubert M, Rudolph P. Prog Cryst Growth Charact Mat 2001;43:119.

[5] Voronkov V.V. J Cryst Growth 1982;59:625.

[6] Hurle D. In: Chambers R, Enderby J, Keller A, Lang A, Steeds J, editors. Sir Charles Frank, OBE, FRS: an 80th birthday tribute. Bristol: Adam Hilger; 1991.

[7] Falster R, Voronkov V. Mater Res Soc Bull 2000;73:28.

[8] Gevelber M, Wilson D, Duanmu N. J Cryst Growth 2001;230:217.

[9] Voronkov V, Mutti P. US Patent Nos US 2002043206 and US 6726764; 2004.

[10] Gevelber M, Stephanopoulos G. J Cryst Growth 1987;84:647.

[11] Gevelber M, Stephanopoulos G, Wargo M. J Cryst Growth 1988;91:199.

[12] Gevelber M. J Cryst Growth 1994;139:271.

[13] Gevelber M. J Cryst Growth 1994;139:286.

[14] Winkler J, Neubert M, Rudolph J. J Cryst Growth 2010;312:1005.

[15] Winkler J, Neubert M, Rudolph J. J Cryst Growth 2010;312:1019.

[16] Neubert M, Winkler J. J Cryst Growth 2012;360:3.

[17] Gevelber M, Wargo M, Stephanopoulos G. J Cryst Growth 1987;85:256.

[18] Winkler J, Neubert M, Rudolph J, Duanmu N, Gevelber M. In: Crystal growth processes based on capillarity. John Wiley & Sons; 2010.

[19] Winkler J, Neubert M, Rudolph J. Acta Phys Pol A 2013;124(2):181.

[20] Marlin T. Process control. McGraw-Hill; 2000.

[21] Kumar AA. Control systems. Prentice-Hall; 2007.

[22] Hurle D, Joyce G, Ghassempoory M, Crowley A, Stern E. J Cryst Growth 1990;100:11.

[23] Luenberger DG. IEEE Trans Mil Electron 1964;8(2):74.

[24] Luenberger D. IEEE Trans Autom Control 1971;16(6):596.

[25] Grewal MS, Andrews AP. Kalman filtering – theory and practice using MATLAB. 3rd ed. Wiley; 2008.

[26] Ellis G, Ellis CD. Observers in control systems: a practical guide. Academic Press; 2002.

[27] Visioli A. Practical PID control, advances in industrial control. London: Springer; 2010.

[28] Astrom KJ, Hagglund T. Advanced PID control. ISA – The Instrumentation, Systems, and Automation Society; 2005.

[29] Johnson MJ, Moradi MB, editors. PID control: new identification and design methods. London: Springer; 2010.

[30] O'Dwyer A. Handbook of PI and PID controller tuning rules. London: Imperial College Press; 2003.

[31] Graf J. PID control: Ziegler–Niccols tuning. CreateSpace Independent Publishing Platform; 2013.

[32] Khalil HK. Nonlinear systems. 3rd ed. Prentice-Hall; 2001.

[33] Allgower F, Zheng A, editors. Nonlinear model predictive control, progress in systems and control theory. Birkhauser Verlag; 2007.

[34] Camacho E, Bordons C. Model predictive control, advanced textbooks in control and signal processing. Springer; 2004.

[35] Kokubun Y, Washizuka S, Ushizawa J, Watanabe M, Fukuda T. Appl Phys Lett 1982;41(9):841.

[36] Hurle D. J Cryst Growth 1977;42:473.

[37] Cole M, Ware R, Whitaker M. In: The 5th international conference on crystal growth, Boston; 1977.

[38] Hadamovsky HF, editor. Werkstoffe der Halbleitertechnik. VEB Deutscher Verlag für Grundstoffindustrie; 1990.

[39] Mika K, Uelhoff W. J Cryst Growth 1975;30(1):9.

[40] Braescu L, Epure S, Duffar T. In: Duffar T, editor. Crystal growth processes based on capillary. Wiley; 2010.

[41] Hurle D. J Cryst Growth 1983;63:13.

[42] Boucher E, Jones T. J Chem Soc Faraday Trans 1 1980;76:1419.

[43] Boucher E, Jones T. Rep Prog Phys 1980;43:497.

[44] Landau LD, Lifschitz EM. Hydrodynamik, Lehrbuch der theoretischen Physik, vol. 6. Berlin: Akademie Verlag; 1991.

[45] Tsivinskii S. Inzheherno Fiz. Zh. Akad. Nauk. Bellorussk SSR 1962;5(9):59. in Russian language.

[46] Johansen T. J Cryst Growth 1994;141:484.

[47] Derby J, Brown R. J Cryst Growth 1986;74(3):605.

[48] Surek T, Coriell S, Chalmers B. J Cryst Growth 1980;50(1):21.

[49] Brice J. J Cryst Growth 1968;2:393.

[50] Kim K, Kran A, Smetana P, Schwuttke G. J Electrochem Soc 1983;130(5):1156.

[51] Duanmu N. [Ph.D. thesis]. College of Engineering, Boston University; 2006.

[52] Mullin J, Straughan B, Brickell W. J Phys Chem Solids 1965;26(4):782.

[53] Looze D, Farzin A, Bernstein B. J Cryst Growth 1995;148(1–2):79.

[54] Jordan A, Caruso R, von Neida A. Bell Syst Tech J 1983;62:477.

[55] Johansen T. J Cryst Growth 1987;84(2):609.

[56] Johansen T. J Cryst Growth 1992;123(1–2):188.

[57] Azuma K. Jap. Patent No. 60-11299; 1983.

[58] Bardsley W, Green G, Holliday C, Hurle D. J Cryst Growth 1972;16:277.

[59] Bardsley W, Frank F, Green G, Hurle D. J Cryst Growth 1974;23:341.

[60] Bardsley W, Cockayne B, Green G, Hurle D, Joyce G, Roslington J, et al. J Cryst Growth 1974;24/25:369.

[61] Bardsley W, Hurle D, Joyce G. J Cryst Growth 1977;40:13.

[62] Bardsley W, Hurle D, Joyce G, Wilson G. J Cryst Growth 1977;40:21.

[63] Steel G, Hill M. J Cryst Growth 1975;30(1):45.

[64] Hurle D, Joyce G, Wilson G, Ghassempoory M, Morgan C. J Cryst Growth 1986;74:480.

[65] Hurle D. J Cryst Growth 1993;128(1–4):15.

[66] Satunkin G, Leonov A. J Cryst Growth 1990;102(3):592.

[67] Satunkin G. J Cryst Growth 1995;154(1–2):172.

[68] Sveshtarov P, Gospodinov M. Cryst Res Technol 1995;30(1):27.

[69] Sveshtarov P, Gospodinov M. Cryst Res Technol 1995;30(2):243.

[70] Sveshtarov P, Gospodinov M. Cryst Res Technol 1995;30(3):405.

[71] Derby J, Brown R. J Electrochem Soc 1985;132(2):470.

[72] Derby J, Brown R. J Cryst Growth 1986;75(2):227.

[73] Derby J, Brown R. J Cryst Growth 1987;83:137.

[74] Thomas P, Derby J, Atherton L, Brown R. J Cryst Growth 1989;96:135.
[75] Surek T. J Appl Phys 1976;47:4384.
[76] Tatarchenko V, Brener E. J Cryst Growth 1980;50:33.
[77] Babkin G, Brener E, Tatarchenko V. J Cryst Growth 1980;50(1):45.
[78] Tatarchenko YA. Shaped crystal growth, fluid mechanics and its applications, vol. 20. Dordrecht, Boston, London: Kluwer Academic Publishers; 1993.
[79] Crowley A. IMA J Appl Math 1983;30(2):173.
[80] Johansen T. J Cryst Growth 1991;114(1–2):27.
[81] Tatarchenko VA. In: Duffar T, editor. Crystal growth processes based on capillary. Wiley; 2010.
[82] Levinson J. US Patent No. 2,908,004; 1959.
[83] Rummel T. US Patent No. 3,259,467; July 5, 1966.
[84] Zinnes A, Nevis B. J Cryst Growth 1973;19:187.
[85] Valentino, Brandle C. J Cryst Growth 1974;26:1.
[86] Digges T, Hopkins R, Seidensticker R. J Cryst Growth 1975;29:326.
[87] Patzner E, Dessauer R, Poponiak M. Solid State Technol 1967;10:25.
[88] Gross U, Kersten R. J Cryst Growth 1972;15:85.
[89] Lorenzini R, Nuff F, Blair D. Solid State Technol 1974;2:33.
[90] Turovskii, Shenderovich I, Shubskii G. Inorg Mater 1977;13:948.
[91] van Dijk H, Jochem C, Scholl G, vander Werf P. J Cryst Growth 1974;21:310.
[92] van Dijk H, Goorissen J, Gross U, Kersten R. Acta Electron 1974;17:45.
[93] Bachmann K, Kirsch H, Vetter K. J Cryst Growth 1970;7:290.
[94] Joyce G, Hurle D, Vaughan Q. J Cryst Growth 1993;132:1.
[95] Bruni FJ. In: Scheel HJ, Capper P, editors. Crystal growth technology. Weinheim: Wiley-VCH; 2008.
[96] Johansen T. J Cryst Growth 1987;80(2):343.
[97] Johansen T. J Cryst Growth 1992;118(3–4):353.
[98] Satunkin G. Prog Cryst Growth Charact Mater 2010;56:1.
[99] Rossolenko S, Pet'kov I, Kurlov V, Red'kin B. J Cryst Growth 1992;116:185.
[100] Abrosimov N, Kurlov V, Rossolenko S. Prog Cryst Growth Charact Mat 2003;46(1–2):1.
[101] Kubota E. Cryst Res Technol 1999;34(4):539.
[102] Masi M, Carra S, Polli M, Ratti M, Guadalupi G. Mater Chem Phys 2000;66:236.
[103] Eidelman L, Goriletsky V, Protsenko V, Radkevich A, Trofimenko V. J Cryst Growth 1993;128(1–4):1059.
[104] Kasimkin P, Moskovskih V, Vasiliev Y, Shlegel V, Yuferev V, Vasiliev M, et al. J Cryst Growth 2014;390:67.
[105] Aufreiter J, Briiss D, Altekrueger B. US Patent 5853479 A; 1998.
[106] Aufreiter J, Brass D, Altekrueger B, Kalkowski K. US Patent 6341173 B2; 1998.
[107] Domey K. Solid State Technol 1971;10:41.
[108] Kimbel S. [Ph.D. thesis]. Washington University; 2000.
[109] Kimbel S, O'Sullivan J. Process imaging for automatic control. Proc SPIE – Int Soc Opt Eng 2001;4188. pp. 45.

[110] Nalbandyan H. J Cryst Growth 1984;67:115.

[111] Neubert M, Winkler J. J Cryst Growth 2014;404:210.

[112] Brown G, Kinney T, Sackinger P, Bornside D. J Cryst Growth 1989;97:99.

[113] Voigt A, Hoffmann KH. Optimal control of complex structures, vol. 139. ISNM International Series of Numerical Mathematics; 2002. 259.

[114] Dornberger E, von Ammon W, van den Bogaert N, Dupret F. J Cryst Growth 1996;166:452.

[115] van den Bogaert N, Dupret F. J Cryst Growth 1997;171:65.

[116] van den Bogaert N, Dupret F. J Cryst Growth 1997;171:77.

[117] Olivari E, Jacmin P, van den Bogaert N, Wertz V, Dupret F. J Cryst Growth 1997;180:627.

[118] Sabanskis A, Bergfelds K, Muiznieks A, Schröck T, Krauze A. J Cryst Growth 2013;337:9.

[119] Satunkin G, Rossolenko S, Kurlov V, Reg'kin B, Tatarchenko V, Avrutik A. Cryst Res Technol 1986; 21(10):1257.

[120] Voronkov V, Mutti P. U.S. Patent No. US 2002/0043208 A1; 2002.

[121] Satunkin G, Rossolenko S. Cryst. Res Technol 1986;21(9):1125.

[122] Åström KJ, Wittenmark B. In: Adaptive control. Prentice Hall; 1994.

[123] Warwick K, Rees D, editors. Industrial digital control systems. IEEE control Engineering solutions, vol. 37. Peter Peregrinus Ltd; 1988.

[124] Riedling K. J Cryst Growth 1988;89(4):435.

[125] Ng J, Dubljevic S. J Process Control 2011;21(10):1361.

[126] Ng J, Dubljevic S. Chem Eng Sci 2012;67(1):111.

[127] Ng J, Aksikas I, Dubljevic S. Int J Control 2013;86(9):1467–78.

[128] Wang P. Optim Control Appl Methods 1995;16:305.

[129] Irizarry-Rivera R, Seider WD. J Cryst Growth 1997;178(4):593.

[130] Irizarry-Rivera R, Seider WD. J Cryst Growth 1997;178(4):612.

[131] Buzniak J, Prunier V. Apparatus and method for monitoring and controlling crystal growth, Tech. Rep., U.S. Patent US 7 959 732 B1; 2011.

[132] Batur, Sharpless RB, Duval WMB, Rosenthal BN. In: Proceedings of the 1991 American Control Conference, Boston, USA; 1991. p. 1722.

[133] Parker R, Manning J. J Cryst Growth 1986;79:341.

[134] Carter JN, Lam A, Schleich DM. Rev Sci Instrum 1992;63:3472.

[135] Schmachtl M, Schievenbusch A, Zimmermann G, Grill W. Ultrasonics 1998;36:291.

[136] Azizi M, Meissner E, Friedrich J. In: Proceedings of the 5th world conference on photovoltaic energy conversion, Valencia, Spain; September 2010. p. 1520.

[137] Dold P, Heidler M, Drevermann A, Zimmermann G. J Cryst Growth 2001;256:352.

[138] Lan W, Ting CC. Chem Eng Comm 1996;145:131.

[139] Batur, Srinivasan A, Duvalt WMB, Singh NB. Prog Cryst Growth Charact 1995;30:217.

[140] Wang QG, Cai EJ, Ye Z, Hang CC. PID control for multivariable processes, lecture notes in control and information sciences. Springer; 2009.

[141] Albertos P, Sala A. Multivariable control systems – an engineering approach, advanced textbooks in control and signal processing. Springer; 2004.

[142] Skogestad S, Postlethwaite I. Multivariable feedback control. 2nd ed. Wiley; 2005.

[143] Abraham R, Lunze J. J Robust Nonlinear Control 1992;2(2):107.

[144] Klein J, Curreri V, DuBois J, Larson D. Advanced thermal control system for a programmable multizone crystal growth furnace. Tech. rep., SAE technical paper 911557; 1991.

[145] Jurisch M, Börner F, Bünger T, Eichler S, Flade T, Kretzer U, et al. J Cryst Growth 2005;275:283.

[146] Kuppurao S, Brandon S, Derby JJ. J Cryst Growth 1995;155:93.

[147] Kuppurao S, Brandon S, Derby JJ. J Cryst Growth 1995;155:103.

[148] Rudolph J. Flatness based control of distributed parameter systems. Aachen: Shaker Verlag; 2003.

[149] Benoussan A, Prato GD, Delfour MC, Mitter SK. Representation and control of infinite dimensional systems, systems and control: foundations & applications. Birkhäuser; 2007.

[150] Rudolph J, Winkler J, Woittennek F. Flatness based control of distributed parameter systems: examples and computer exercises from various technological domains. Berichte aus der Steuerungs- und Regelungstechnik. Aachen: Shaker Verlag; 2003.

[151] Rudolph J, Winkler J, Woittennek F. In: Meurer T, Graichen K, Gilles E, editors. Control and observer design for nonlinear finite and infinite dimensional systems. Lecture notes in control and information sciences, vol. 322. Springer-Verlag; 2005.

[152] Batur R, Sharpless W, Duval B, Rosenthal, Singh N. J Cryst Growth 1992;119:371.

[153] Kasparian V, Batur C, Duval WM, Rosenthal BN, N.S. J Cryst Growth 1994;141(3–4):455.

[154] Batur, Duval MB, Bennett RJ. In: Proceedings of the 1999 American control conference, San Diego, California, USA; 1999. p. 4101.

[155] Medanic J, Uskokovic Z. Int J Control 1983;37:809.

[156] Seidensticker R, Rosch W, Mazelsky R, Hopkins R, Singh N, Coriell S, et al. J Cryst Growth 1999; 198–199(2):988.

[157] Sonda P, Yeckel A, Daoutidis P, Derby J. J Cryst Growth 2004;266(1–3):182.

[158] Sonda P, Yeckel A, Derby J, Daoutidis P. Comput Chem Eng 2005;29(4):887.

[159] Daoutidis P, Kravaris C. AICheE J 1999;35:1602.

[160] Kim K, Witt A, Gatos H. J Electrochem Soc 1972;119(9):1218.

[161] Kim K, Witt A, Lichtensteiger M, Gatos H. J Electrochem Soc 1975;125(3):475.

[162] Müller G, Neumann G, Weber W. J Cryst Growth 1984;70:78.

[163] Sonda P, Yeckel A, Daoutidis P, Derby JJ. Chem Eng Sci 2005;60(5):1323.

[164] Sonda P, Yeckel A, Daoutidis P, Derby JJ. J Cryst Growth 2004;260:263.

[165] Yeckel A, Derby J. J Cryst Growth 2012;314(1):310.

[166] Yeckel, Daoutidis P, Derby J. J Cryst Growth 2012;356:33.

[167] Yeckel, Daoutidis P, Derby J. J Cryst Growth 2012;361:16.

[168] Duffar T, Dusserre P, Picca F, Lacroix S, Giacometti N. J Cryst Growth 2000;211:434.

[169] Duffar T, Dusserre P, Giacometti N. J Cryst Growth 2001;223:69.

[170] Palosz W, Volz M, Cobb S, Motakef S, Szofran F. J Cryst Growth 2005;277:124.

[171] Patzold O, Jenkner K, Scholz S, Croll A. J Cryst Growth 2005;277:37.

[172] Braescu L. J Colloid Interf Sci 2008;319:309.

[173] Sylla L, Duffar T. J Cryst Growth 2007;303:187.

[174] Epure S, Duffar T, Braescu L. J Cryst Growth 2008;310:1559.

[175] Epure S, Duffar T, Braescu L. J Cryst Growth 2010;312(8):1416.

[176] Braescu L. J Cryst Growth 2010;312(8):1421.
[177] Stut H. US Patent 3243509 A (Siemens AG); 1963.
[178] Stut H. US Patent 3757071 A (Siemens AG).
[179] Lie K, Walker J, Riahi D. J Cryst Growth 1990;100(3):450.
[180] Wünscher M, Lüdge A, Riemann H. J Cryst Growth 2011;314:43.
[181] Shyy W, Rao MM. Int J Heat Mass Transf 1995;38(12):2281.
[182] Werner N. [Ph.D. thesis]. Berlin: Technische Universität; 2014.
[183] Heywang W. Z Naturforscher 1956;11a:238.
[184] Rowton E. IEEE Trans Ind Electron Control Instrum 1965;IECI-13(1):66.
[185] Otani S, Tanaka T, Ishizawa Y. J Cryst Growth 1990;106(4):498.
[186] Chan Y, Mailloux PA. Rev Sci Instrum 1993;64(9):2643.
[187] Ikeda Y, Ohara N, Suzuki K, Watanabe M. US Patent 4866230 A (Shin Etsu Ltd); 1987.
[188] Watanabe M, Ohhara N, Taguchi K. US Patent 4876438 A (Shin Etsu Ltd); 1988.
[189] Taguchi K, Watanabe M. US Patent 4931945 A (Shin Etsu Ltd); 1988.
[190] Dornberger, von Ammon W, Ölkrug H, Wasmeier F. US Patent 5868831 (Wacker AG); 1997.
[191] Bliss F. In: Feigelsen RS, editor. 50 years progress in crystal growth. Elsevier; 2004.
[192] Nakajima K, Murai R, Morishita K, Kutsukake K, Usami K. J Cryst Growth 2012;344:6.
[193] Singh, Ghosh B, Deshpande R. Cryst Res Technol 1981;16(11):1239.
[194] Perner, Kvapil J, Stransky V, Kvapil J. Cryst Res Technol 1979;14(6):661.
[195] Xu M, Zhang S, Meng J, Han G, Wang, Zuo H. Cryst Res Technol 2007;42(8):751.
[196] Zhang L, Zuo H, Sun J, Wang X, Han J, Xing D, et al. Cryst Res Technol 2012;47(2):175.
[197] Akselrod MS, Bruni FJ. J Cryst Growth 2012;360:134.
[198] Kokh AE, Vlezko VA, Kokh KA. Instrum Exp Tech 2009;52(5):747.
[199] Schönherr. J Cryst Growth 1968;3–4:265.
[200] Zhang L, Zuo H, Sun J, Wang X, Han J, Xing D. Cryst Res Technol 2011;46(10):1019.
[201] Demina S, Bystrova E, Lukanina M, Mamedov V, Yuferev V, Eskov E, et al. Opt Mater 2007;30:62.
[202] Demina S, Bystrova E, Postolov V, Eskov E, Nikolenko M, Marshanin D, et al. J Cryst Growth 2008; 310:1443.

29 Fundamentals of Crystal Growth from Solutions

Igor Pritula[1], Keshra Sangwal[2]

[1]INSTITUTE OF SINGLE CRYSTALS, NATIONAL ACADEMY OF SCIENCES OF UKRAINE, KHARKOV, UKRAINE; [2]DEPARTMENT OF APPLIED PHYSICS, LUBLIN UNIVERSITY OF TECHNOLOGY, LUBLIN, POLAND

CHAPTER OUTLINE

29.1 Introduction 1186
29.2 Low-Temperature Solution Growth 1187
29.2.1 Basic Concepts of Low-Temperature Crystallization 1187
29.2.1.1 Driving Force for Crystallization 1187
29.2.1.2 Metastable Zone Width 1189
29.2.1.3 Temperature Dependence of Solubility 1191
29.2.2 Selection of Solvents 1192
29.2.3 Crystal Growth Techniques 1193
29.2.3.1 Temperature-Changing Technique 1194
29.2.3.2 Solvent Evaporation Technique 1194
29.2.3.3 Temperature Gradient Techniques 1195
29.2.3.4 Growth from Boiling Solutions 1196
29.2.4 Different Factors Affecting Crystal Growth 1196
29.2.5 Crystal Growth Rates and Dead Supersaturation Zone 1199
29.2.5.1 Basic Concepts of Impurity Effects 1199
29.2.5.2 Effect of Organic Additives on Crystal Growth 1204
29.2.6 Effect of Mechanical Impurities on Crystal Growth 1206
29.2.6.1 Growth of Water-Soluble Crystals with Embedded Organic Molecules 1206
29.2.6.2 Growth of Water-Soluble Crystals with Embedded Nanoparticles 1208
29.3 High-Temperature Solution Growth 1210
29.3.1 Principle of the Method 1211
29.3.2 Composition of Fluxes and Their Selection 1211
29.3.3 Some Properties of High-Temperature Solvents 1215
29.3.4 Crystal Growth Techniques 1219

Handbook of Crystal Growth. http://dx.doi.org/10.1016/B978-0-444-63303-3.00029-8
Copyright © 2015 Elsevier B.V. All rights reserved.

29.3.4.1 Slow-Cooling Method 1219
29.3.4.2 Solvent Evaporation Method 1220
29.3.4.3 Temperature Gradient Methods 1221
29.3.4.4 Other Methods 1222
29.3.5 Growth Instability and Facet Formation 1223
29.4 Summary and Outlook 1223
Acknowledgment 1224
References 1224

29.1 Introduction

Crystallization of substances from supersaturated solutions at normal pressure conditions in suitable nonreactive solvents in which they are fairly soluble is usually referred to as *crystal growth from solutions*. The solvents used for the crystallization of different substances are usually water, various organic liquids and their mixtures, and melts of some chemical compounds and/or their mixtures. Water and organic liquids and their mixtures are in the liquid state under the usual laboratory pressure and temperature conditions, whereas chemical compounds and/or their mixtures are in the liquid state at elevated temperatures. From a consideration of the growth temperature when the solvent used is in the liquid state, one differentiates between crystal growth from low- and high-temperature solutions. In growth from low-temperature solutions, the crystallization temperatures generally do not exceed 70−80 °C; in growth from high-temperature solutions, the crystallization temperatures rarely exceed 1200−1300 °C. In both low- and high-temperature growths, the highest possible growth temperature is the boiling point of the solvent used.

Crystallization from supersaturated solutions devoid of foreign particles with deliberately introduced seeds always occurs in two stages: formation of three-dimensional (3D) microscopic nuclei and development of these 3D nuclei into large entities visible to the naked eye. These two stages are called homogeneous 3D nucleation and crystal growth, respectively. Foreign particles (usually called impurities) in solutions facilitate the formation of 3D nuclei (heterogeneous nucleation) and can change their subsequent growth, whereas seeds introduced in solutions eliminate the nucleation stage and enable crystals to grow without 3D nucleation. Crystallization is usually understood as the nucleation and development of crystalline product, but the term *growth* is used for large-sized crystals with or without the nucleation stage. A necessary condition for the crystallization of a solid mass dissolved in a pure or mixed solvent is the creation of supersaturation in the solution.

In this chapter, the principles and experimental techniques for the growth of crystals from low- and high-temperature solutions are described. The contents of this chapter are an extended and revised version based on a review published previously [1].

29.2 Low-Temperature Solution Growth

Crystal growth from low-temperature solutions is well suited for materials that decompose in the melt or in the solid at high temperatures and that undergo structural transformations while cooling from the melting point. It also allows crystals of the same substance to grow in a variety of morphologies and polymorphic forms by variations of growth conditions or of the solvent. Consequently, materials ranging from micrometer-sized crystalline organic pharmaceutical chemicals to large-sized inorganic nonlinear optical crystals are grown from low-temperature solutions. The method is widely used because: (1) the growth apparatus is relatively simple and cheap; (2) in contrast to other methods involving melts, low growth temperature introduces small thermal stresses (and hence a low concentration of equilibrium defects and dislocations) in the crystals; and (3) the crystals obtained usually have well-developed faces (growth habit) that make it possible to investigate crystal growth processes, including in situ observations of the surfaces and capture of impurities.

Crystal growth from low-temperature solutions has been reviewed in several monographs and reviews [1–9]. The list of compounds grown from low-temperature solutions can be found in the monographs [3,6,7].

29.2.1 Basic Concepts of Low-Temperature Crystallization

29.2.1.1 Driving Force for Crystallization

Crystallization of a compound always occurs from its supersaturated solutions in the metastable zone. The metastable zone is the region between curves representing solubility (solid curve) and supersolubility (dashed curve), shown schematically in Figure 29.1. The supersolubility curve indicates the limiting value of solute concentration when instantaneous 3D nucleation (i.e. precipitation) occurs in the solution.

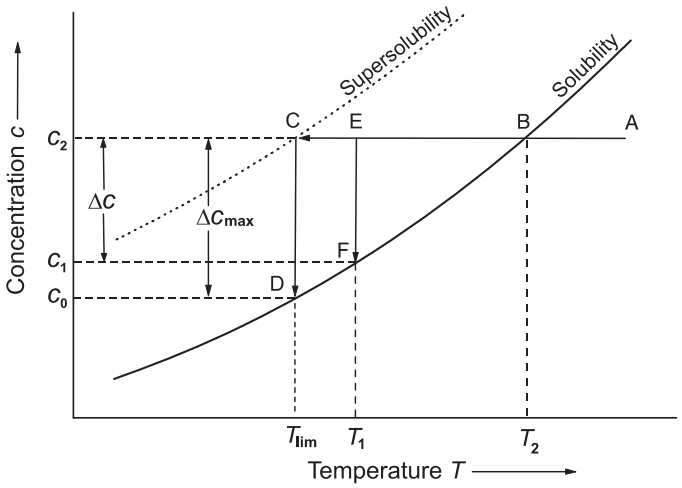

FIGURE 29.1 Schematic illustration of the dependence of solute concentration in a solute–solvent system on solution temperature. Solid and dashed curves represent solubility and supersolubility curves, respectively. See text for details. *Adapted from Ref. [12].*

From Figure 29.1, three areas can be distinguished: (1) stable undersaturated zone, (2) metastable zone, and (3) unstable supersaturated area. In area (1), which lies below the solubility curve, the actual concentration c of a solute in the solution at a given temperature, say T_{lim}, is lower than the corresponding equilibrium concentration c_0 represented by the solubility for the solute–solvent system. In an undersaturated solution, more solute will dissolve. In areas (2) and (3) lying above the solubility curve, the actual solute concentration c at the temperature T_{lim} is higher than its solubility c_0. In these areas, the solution is supersaturated. However, the processes of 3D spontaneous nucleation and crystal growth occur in the region lying between the solubility and supersolubility curves—that is, in the metastable zone. Obviously, the supersolubility curve represents the concentration when 3D spontaneous nucleation ceases to occur.

Deviation in the concentration of a dissolved salt from its equilibrium value at a given temperature or deviation in the temperature of the solute–solvent system of a given equilibrium concentration from a saturation temperature is a measure of the driving force for crystallization. In Figure 29.1, it is the concentration difference $\Delta c = c_2 - c_1$ corresponding to the saturation concentration c_1 at temperature T_1 or the temperature difference $\Delta T = T_2 - T_1$ corresponding to the saturation concentration c_2 at temperature T_2. In terms of solute concentrations in the solution, the driving force for crystallization is the dimensionless supersaturation ratio $S = c_2/c_1$, and the degree of supersaturation or simply supersaturation $\sigma = \ln S \approx \Delta c/c_1$. Obviously, $S < 1$, $S > 1$, and $S = 1$ for undersaturated, supersaturated, and saturated solutions, respectively. In terms of the solubility of a solute, when 3D nucleation of the new phase occurs instantaneously, as shown schematically by the dashed curve in Figure 29.1, the driving force for crystallization is the limiting value of metastable zone.

The metastable zone width can be described by a polythermal or isothermal method. In the polythermal (also called non-isothermal) method, the metastable zone width is measured as the maximum supercooling $\Delta T_{\text{max}} = (T_2 - T_{\text{lim}})$, with reference to a constant concentration c_0 corresponding to the saturation temperature T_{lim} (Point D), by cooling the solution at a constant cooling rate R from a temperature somewhat above T_2 (Point A in Figure 29.1) to a temperature T_{lim} at which first crystals are detected in the solution (Point D). With reference to the temperature T_{lim} corresponding to the maximum solute concentration c_2, this metastable zone width is the maximum concentration difference $\Delta c_{\text{max}} = (c_2 – c_0)$. The isothermal method, on the other hand, consists of attaining solution supersaturation as fast as possible, followed by the measurement of time period for the appearance of first detectable nuclei in the solution. When the appearance of detectable nuclei occurs immediately after attaining the predefined supersaturation corresponding to the limiting temperature T_{lim}, one defines the maximum supersaturation ratio $S_{\text{max}} = (c_2/c_0)$ and the maximum supersaturation $\ln S_{\text{max}} = \ln(c_2/c_0)$ as the width of the metastable zone width with reference to T_{lim}.

When c_{max} is the solute concentration corresponding to the saturation temperature T in Figure 29.1, one obtains the traditional relations for maximum supersaturation ratio $S_{\text{max}} = c_{\text{max}}/c_0$ and maximum supersaturation $\sigma_{\text{max}} = (c_{\text{max}} - c_0)/c_0$. Then, with reference

to the saturation temperature T in Figure 29.1, the temperature difference $\Delta T_{max} = (T - T_{lim})$ is the maximum undercooling. Alternatively, with reference to the limiting temperature T_{lim}, $\Delta T_{max} = (T - T_{lim})$ is the maximum supercooling and defines the metastable zone width.

29.2.1.2 Metastable Zone Width

The polythermal technique is the most widely used method for determining the metastable zone width. In fact, investigation of solubility and metastable zone width of various solute–solvent systems has been a field of intensive research activity for over four decades [10]. However, since 2008 several papers have been devoted to the understanding of the effect of various experimental factors on the metastable zone width. The developments in the understanding of metastable zone width of solute–solvent systems have recently been reviewed [11].

According to the self-consistent Nývlt-like approach [12], the relationship between the maximum supercooling ratio $\Delta T_{max}/T$ and cooling rate R may be given by

$$\ln(\Delta T_{max}/T) = \Phi + \beta \ln R, \tag{29.1}$$

where Φ is the extrapolated value of $\ln(\Delta T_{max}/T)$ when $\ln R \to 0$, and $\beta = 1/m$ (m is the nucleation order). However, according to the approach based on the three-dimensional nucleation theory [13], the relationship between $\Delta T_{max}/T$ and R is of the form

$$\left(\frac{T}{\Delta T_{max}}\right)^2 = F(1 - Z \ln R), \tag{29.2}$$

where F is the extrapolated value of $(T/\Delta T_{max})^2$ when $\ln R \to 0$, and the constant Z is characteristic for a solute–solvent system. Both Eqns (29.1) and (29.2) predict that, at a given saturation temperature T, the quantities $\ln(\Delta T_{max}/T)$ and $(\Delta T_{max}/T)^{-2}$ decrease linearly with an increase in $\ln R$.

The parameters Φ and $\ln(F^{1/2})$ as a function of saturation temperature T may be described by an Arrhenius-type relation, written in the following form [12,13]:

$$\ln y = \ln y_0 - E_{sat}/R_G T, \tag{29.3}$$

where $\ln y$ denotes $-\Phi$ and $\ln(F^{1/2})$; the factor $\ln y_0$, associated with the pre-exponential factor y_0 of the Arrhenius-type relation, denotes the extrapolated values of $-\Phi$ and $[\ln(F^{1/2})]$ when $1/T \to 0$, R_G is the gas constant; and E_{sat} is the activation energy associated with the diffusion of solute molecules in the solution.

Irrespective of the cooling rate R, with an increase in saturation temperature T, the value of maximum supercooling $\Delta T_{max} = T - T_{lim}$ decreases for some solute–solvent systems, it remains practically constant for some others, and it increases for the remaining solute–solvent systems. Typical examples showing such trends are shown in Figure 29.2. This means that the supercooling ratio $\Delta T_{max}/T$ decreases, increases, or remains constant with increasing saturation temperature T. Analysis of the experimental data revealed [11,14,15] that the nature of solute–solvent system is related to the activation energy E_{sat} for diffusion of nucleating species in the solution. When the value of

E_{sat} is comparable with the value of activation energy E_D for diffusion of ideal species, the supersolubility curves are roughly parallel to the solubility curves (i.e., $\Delta T_{max}/T$ is independent of T). When $E_{sat} > E_D$, $\Delta T_{max}/T$ decreases with an increase in T_0. However, when $E_{sat} < E_D$, $\Delta T_{max}/T$ increases with an increase in T.

In the polythermal method, the rate of creation of supersaturation in a solute–solvent system and its metastable zone width are determined by controlling the rate of cooling of the solution at a constant rate. However, this method can be used only for substances whose solubility increases with temperature (i.e., for substances that have a positive temperature coefficient of solubility). Irrespective of the temperature coefficient of solubility, supersaturation in the saturated solution of a solute in a solvent can also be generated by mixing another miscible solvent, usually called antisolvent or nonsolvent, in which the solute is insoluble or poorly soluble. This is associated with the fact that, at a given temperature, the solubility of a solute in different solvents is different. The rate of creation of supersaturation in the solution and its metastable zone width are associated here with the rate of addition of miscible antisolvent. In recent years, there has been a steady interest in understanding the metastable zone width in antisolvent crystallization [16].

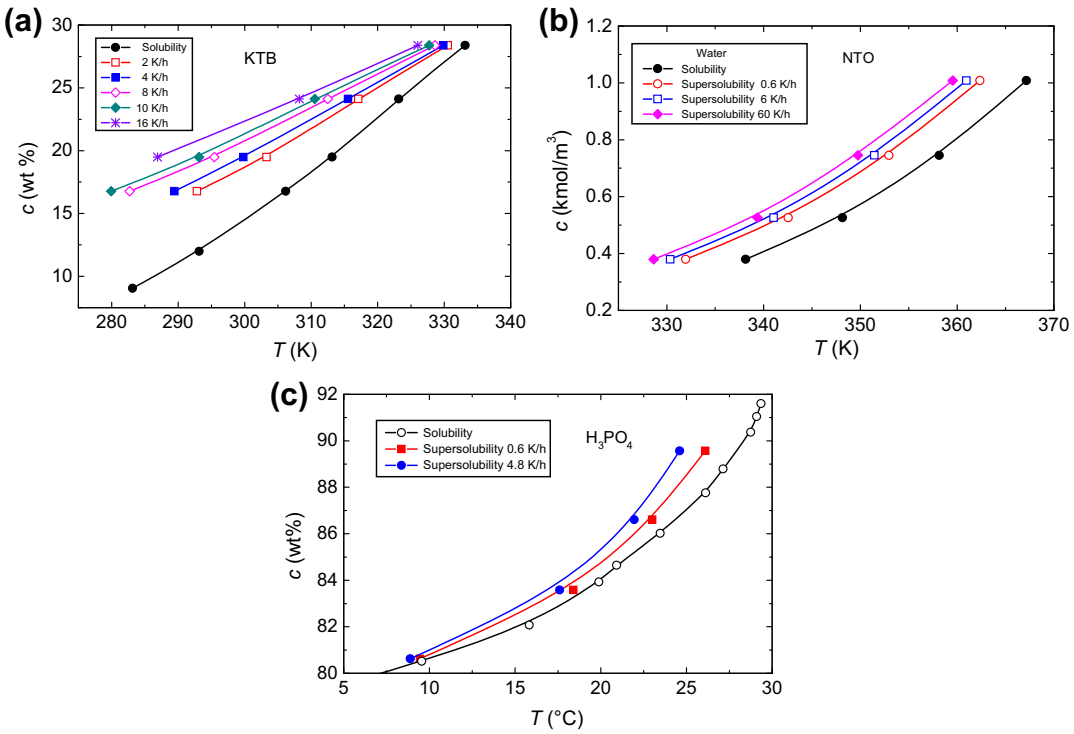

FIGURE 29.2 Typical examples of solubility and supersolubility curves for different systems: (a) KTB (potassium tetraborate tetrahydrate)–water [11], (b) NTO (3-nitro- 1,2,4-triazol-5-one)–water [11], (c) H_3PO_4–water. Supersolubility curves are for various cooling rates [15]. *Reproduced with permission of (a) Royal Chemical Society and (b) Elsevier.*

29.2.1.3 Temperature Dependence of Solubility

The experimental data of the solubility c of a compound in a solvent as a function of temperature T is described satisfactorily according to the empirical relation [16,17]

$$c = C_0 + C_1 T + C_2 T^2, \tag{29.4}$$

where the solubility c is expressed as mass of solute per given mass of solvent or solution; the temperature T is expressed in °C or K; and C_0, C_1, and C_2 are empirical fitting parameters. The data of the temperature dependence of solubility, such as those shown in Figure 29.2, can be represented by Eqn (29.4) in the entire investigated range of temperature. Another relation, based on the theory of regular solutions, that can equally be used to describe the above data is of the form [16,17]

$$\ln c = A - \frac{\Delta H_s}{R_G T}, \tag{29.5}$$

where solubility c is expressed in mole fraction, A is a constant, R_G is the gas constant, and ΔH_s is the enthalpy of dissolution of the solute in the solvent. For ideal solutions, the constant $A = \Delta H_m / R_G T_m$, where T_m is the melting point of the solute and the enthalpy of melting $\Delta H_m = \Delta H_s$. However, for regular solutions, $A \neq \Delta H_m / R_G T_m$ and $\Delta H_m \neq \Delta H_s$.

Although Eqns (29.4) and (29.5) are commonly used to describe the temperature dependence of solubility, they are not satisfied in the entire range of the investigated temperature. Figure 29.3 illustrates typical examples of the temperature dependence of solubility c for some common inorganic compounds in water in the temperature interval 0–100 °C. As seen from the figure, in certain temperature intervals the solubility of different compounds either increases or decreases with an increase in temperature.

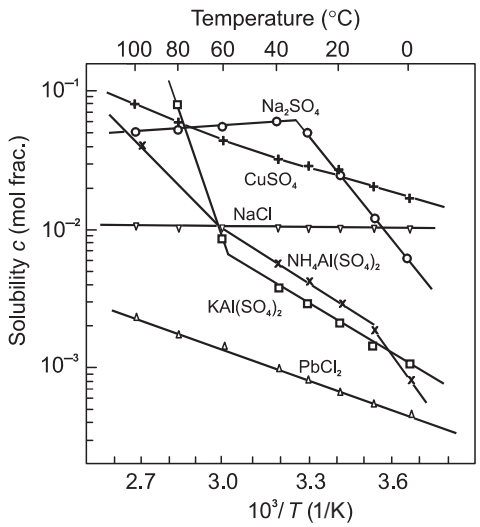

FIGURE 29.3 Examples of the temperature dependence of solubility c for some common inorganic compounds in water. *Adapted from Ref. [9].*

The increasing or decreasing trends of the dependence of solubility c on temperature T are usually discussed in terms of positive or negative temperature coefficient of solubility (i.e., $\partial c/\partial T$) in a particular temperature range. Depending on the nature of solute–solvent system, the solubility coefficient can be high or low and can vary in different temperature intervals.

29.2.2 Selection of Solvents

The first step for crystallization is the choice of solvent. Solution is a homogeneous mixture of a solute in a solvent. Solute is a component that is usually present in a smaller quantity than the solvent in the solution. For a given solution, there may be different solvents. At the growth temperature, an ideal solvent should ensure a sufficient solubility and a good temperature gradient of solubility in it; have low vapor pressure, low toxicity, low flammability, and low viscosity; not corrode the growth apparatus; and be inexpensive.

The most commonly solvent used in low-temperature growth is water because at least 90% of the crystals produced by low-temperature solution methods are soluble in water. It is not toxic and is less volatile than organic solvents, which are generally toxic, volatile, and flammable. Moreover, in comparison with most organic solvents, it is easily available in the pure state and is inexpensive. Because its boiling point is higher than that of most of the organic solvents commonly used for the growth, it provides a reasonably wide range for the selection of the growth temperature. However, water is not a reversible solvent for some materials. It hydrolyzes some materials and introduces water of crystallization to other compounds, which may be desired in the anhydrous form or in the hydrated form of particular composition.

A simple rule of thumb for the proper selection of a solvent is chemical similarity between the solvent and the compound to be grown. For example, crystals of nonpolar organic compounds can be grown easily from nonpolar organic solvents. Chemical similarity also defines solute solubility in the solvent.

The solvent from which a material is crystallized influences the crystal morphology and growth rate. These effects of the solvent on the morphology and growth rates of crystals from solutions are related to the solubility of the crystallizing compound in the solvent and to the nature of crystal–solution interface. High solubility of the solute leads to high viscosity of the solution, which hinders mass transfer at the crystal–solution interface. The crystal–solution interface for a solute–solvent system can be rough at a given temperature as a result of high solubility of the solute in the solvent (thermodynamic roughening) and high supersaturation of the solution (kinetic roughening). Both of these yield high growth rates of crystals and high density of defects. Therefore, to ensure good crystal growth of a substance, it is necessary to use (1) a solvent in which the substance is moderately soluble, (2) medium solution supersaturation, and (3) nonturbulent stirring conditions.

Most crystallized inorganic materials are ionic. This means that dissociation reactions, ionic interactions, and solution acidity (pH) determine the solubility of

inorganic compounds in aqueous solutions. In the case of organic compounds and inorganic compounds in nonaqueous solvents, a wide variety of solvents and solvent mixtures are usually employed. The differences in the solubility of different compounds in various solvents are associated with solute–solvent interactions, which are determined by solute concentration in the solution, solution temperature, composition of the solvent, and impurities present in the solution.

Experiments suggest that a solvent in which the compound has a solubility between 10% and 60% at a given temperature is economically suitable for crystal growth. These growth rates from solutions fall in the range of 0.1–1 mm/day. Very low and very high solute solubilities provide low growth rates due to low solute concentration and increased viscosity, respectively. Therefore, in both cases, it is desirable to use additives to change the solute solubility in a solvent or solution viscosity. Additives not only change the properties of solutions but also lead to changes in crystal growth habits.

29.2.3 Crystal Growth Techniques

Crystal growth methods differ in the way the supersaturation is generated and maintained constant during a growth run, and 3D nucleation is initiated. In general, the selection of a method for the growth of a compound can be made from a consideration of temperature coefficient of its solubility (see Figure 29.3). If a compound has a reasonable temperature coefficient of solubility in a certain temperature interval and does not undergo phase changes, it can be grown by changing the temperature, with simultaneously maintaining the required supersaturation for growth (temperature changing method). In principle, substances with both positive as well as negative temperature coefficients of solubility can be grown by this technique (by decreasing and increasing temperature, respectively), but usually substances having positive temperature coefficients of solubility are grown by it. These substances can also be grown by maintaining a temperature gradient between zones of crystal growth and solute supply (temperature gradient methods). If a compound undergoes phase transition at a particular temperature, the above methods cannot be used. Instead, one can use a method in which both temperature and supersaturation are maintained constant (constant temperature and supersaturation method). However, when the solubility remains practically constant with a change in temperature, the supersaturation can be created by evaporating the solvent (solvent evaporation method).

The importance of selecting an appropriate method lies in the fact that the same crystallization performed under different conditions can yield crystals of different properties (size, morphology, chemical purity, polymorphic form, etc.). However, the design of a cost-effective crystallization process requires many types of data, including mass transfer and equilibrium solubility as a function of the solvent, temperature, and pH. Surface and bulk supersaturation should be made as close as possible to the kinetic regime by suitably stirring solutions so that diffusion processes of supply of solute to the growing crystal do not limit the growth rate (see Section 29.2.4).

29.2.3.1 Temperature-Changing Technique

In this method, the value of supersaturation necessary for the growth of crystals is achieved due to slow temperature reduction, which, as a rule, is controlled by a special program. The mass of the substance Δm depositing during the reduction of temperature by ΔT may be calculated from the relationship

$$\Delta m = \frac{\mathrm{d}c}{\mathrm{d}T} V_0 \Delta T, \tag{29.6}$$

where c is the concentration of the substance in the solution, $\mathrm{d}c/\mathrm{d}T$ is the solubility coefficient, and V_0 is the solution volume. This relationship follows from Eqn (29.4) and holds in a small temperature interval.

Typical vessels for crystal growth by the temperature changing method involve large glass containers with several seeds suspended in the supersaturated solution. For growth, a solution saturated at a temperature T is poured into the crystallizer and heated a few degrees above the saturation temperature to avoid spurious nucleation due to the cooling of its walls during its transfer to the outer water bath. When the solution temperature is slightly above the saturation temperature, the seeds are suspended in the solution and the crystallizer is hermetically sealed. Then, the temperature is lowered to the growth temperature in the metastable zone and solution cooling is commenced at a preassigned rate such that the growing crystals remain the supersaturated solution. After the completion of growth with the temperature steadily decreasing to a terminal temperature, 10–15 °C above the room temperature, the crystals are gently taken out of the crystallizer, wiped, and stored.

The temperature-decreasing method is widely used for commercial crystal growth [3,18]. However, its inherent drawback is variation in the temperature during a growth run, which results in considerable changes in growth rate, adsorption of the impurity on the faces, and capture of the impurities by the growing crystal.

The possibility of obtaining large high-quality single crystals by the temperature reduction method using "point seeds" has been reported [19–21]. In this case, the final size of the crystal does not depend on the size of the seed.

29.2.3.2 Solvent Evaporation Technique

In this technique, the supersaturation required for the growth is produced by evaporating the solvent at a constant temperature [3]. Therefore, the growth rate is regulated by controlling the evaporation rate. Excess mass of the substance for crystallization is created from a consideration of the solubility of the compound in the solvent and the evaporation rate of the solvent. In most cases, the pressure of the solvent vapor over the solutions is higher than that of the solute. This enables one to evaporate solvent vapor into the atmosphere or withdraw it as condensate using water-cooled coils. Therefore, the supersaturation necessary for crystal growth can be maintained by controlled evaporation of the solvent. For nontoxic solvents such as water, solvent evaporation into the atmosphere is permissible; for toxic and flammable

solvents, precautions are taken to avoid the leakage of solvent vapor into the atmosphere.

The mass of the deposited substance Δm is proportional to the volume ΔV of the solvent removed from the solution and to the concentration c of the substance in the solution. Therefore, crystal growth rate is controlled by changing the rate of evaporation of the solvent. During growth by this method, the solution always contains a reserve of the crystallized substance. However, as the amount of the solvent diminishes and the crystal grows, concentration of impurities increases in the solution. Consequently, as growth proceeds, impurity concentration also increases in the crystal. To reduce such an effect, it is necessary to use large volumes of the solvents. However, in this method, it is difficult to maintain constant supersaturation during a long growth run. As the solution volume decreases, the value of supersaturation available in the solution increases when the evaporation is maintained constant. High evaporation rates lead to spurious nucleation followed by mass crystallization in the solution. Spurious nucleation usually occurs on the solution meniscus, where regions of high supersaturation may be formed locally by evaporation of the solvent.

29.2.3.3 Temperature Gradient Techniques

Temperature gradient techniques are based on the creation of two zones of different temperatures. In one of these zones, at a lower temperature T_2 the crystal is grown onto an introduced seed; in the other zone, at higher temperature T_1 the solute is dissolved to obtain saturated solution. The solution supersaturation can be controlled by changing the temperature difference $\Delta T = T_1 - T_2$. Material transport may be ensured by natural, thermal, or forced convection. In growth involving natural convection, the saturation region of temperature T_1 is at the top whereas the growth region at temperature T_2 is at the bottom of the growth setup such as a cylindrical crystallizer. When the growth zone at T_2 is at the top and the nutrient zone of T_1 is at the bottom, material transport occurs by thermal convection. In two-tank crystallizers based on forced convection, solution is pumped between separate tanks for solutions kept at different temperatures. The solution is forced to circulate from one tank to the other through connecting pipes.

The common difficulty with two-tank crystallizers is the occurrence of parasitic nucleation in the connecting pipes; this may result in the cessation of solution circulation. This necessitates running the tubes and pumps at relatively high temperatures. This difficulty is overcome by inserting an additional tank at a temperature $T_3 > T_1$ between the nutrient tank at temperature T_1 and the growth tank at temperature T_2. The additional tank serves as a reservoir of a subsaturated solution, which is pumped to the growth tank and again back to the nutrient tank to be reheated and resaturated. The first well-known three-tank system for crystal growth is due to Walker and Kohman [2]. Nowadays, three-tank crystallizers are widely used for crystal growth from low-temperature solutions [19].

The main advantages of the above method involve economy of solvent and growth of crystals of good quality. However, because the growth rate depends on the temperature

difference between the nutrient and the crystal growth zones, temperature changes have to be kept to a minimum. Moreover, the entire solute in the nutrient tank is not grown as crystals. A method has been introduced [22] to achieve a 100% solute–crystal conversion efficiency. The experimental setup for crystal growth by this method consists of a growth ampoule made of glass with seed mounting pad at its base and a ring heater located at the top of the growth ampoule facilitates solvent evaporation. The main advantages of this method are: (1) the experimental setup is simple, (2) crystal growth occurs essentially at room temperature, (3) it enables the growth of bulk single crystals along specific orientations, and (4) it prevents microbial growth. Because the temperatures in the top and bottom zones essentially remain stable during a growth run and the crystal grows at room temperature, growth occurs at controlled supersaturation and there are minimum thermal stresses in the crystals, resulting in their good quality.

29.2.3.4 Growth from Boiling Solutions

To grow a substance in a given phase and/or composition and at a reasonable rate, the choice of an optimum temperature interval is an important factor in low-temperature solution growth. As in other processes, the growth at elevated temperatures takes place faster. However, at elevated temperatures, smooth growth necessitates better temperature control, while increased vapor pressure creates problems connected with the control of supersaturation and spurious nucleation. These difficulties may be overcome during crystal growth from boiling solutions.

Crystal growth from boiling solutions has features of temperature-changing, evaporation, and temperature gradient methods. Constant supersaturation is developed by withdrawing a known amount of the solvent evaporated from the solution saturated at the boiling point that is constant during growth. Stirring is ensured by bubbles generated in the volume of the solution.

The greatest advantages of the method are constant temperature of boiling and stirring provided by bubbles nucleating at the walls of a reactor without an additional mechanical device. Moreover, the crystals grown from boiling solutions are less defective than those grown at low temperatures. The main drawback of the method stems from the relatively high temperature, which gives rise to problems of leakage of solvent vapor at the joints of the growth assembly. Another difficulty is nonuniform temperature in the growth vessel owing to uncontrolled sources of bubbling, because each bubble origin gives a temperature gradient along the direction of its movement. The principle of the technique, experimental apparatus for growth, and applicability of the method are described in a review [8].

29.2.4 Different Factors Affecting Crystal Growth

Among the important parameters affecting the growth rate and quality of crystals are pH, temperature, and supersaturation of the solution. Change in the composition and, consequently, in the solution pH is one of the parameters that enables control of the

process of crystal growth. In particular, by choosing the acidity of a saturated solution, one can control the growth rate either of one of the crystal faces or of the whole crystal, thereby changing the external shape (also called habit or morphology), and can regulate the incorporation of impurities in the crystal.

There are several explanations of the effect of pH on crystallization. For example, it has been suggested that the presence of free acids or bases modifies the nature and concentration of ions in the solution [2]. The effect of pH on the growth of potassium chloride crystals has been explained in terms of the structure of aqueous solutions involving hydration of ions [23].

Growth rates of different morphologically important faces at temperature T_g usually increase with increasing supersaturation σ at a given pH of the solution of saturation temperature T or supercooling defined in terms of temperature difference $\Delta T = T - T_g$. For instance, it has been observed [24] that the growth rates R of both prismatic and pyramidal faces of potassium dihydrogen phosphate (KDP) crystals increase with increasing supercooling ΔT at different pH of solutions, but for different values of supercooling the highest growth rates for these faces occur at pH of 4.2. The results also indicate that the growth of prismatic faces always occurs above a minimum supercooling for all values of pH, and the lowest value of this critical supercooling for growth for the solution is pH of approximately 4. However, the growth of pyramidal faces occurs practically without the appearance of this minimum supercooling. The region of supersaturation or supercooling where no growth occurs is usually called the dead supersaturation zone; the threshold supersaturation and threshold supercooling are denoted by σ_d and ΔT_d, respectively. The higher value of supersaturation or supercooling for the growth of prismatic face of KDP crystals is associated with the fact that this face is very sensitive to the adsorption of the growth sites by impurities.

Investigation of the effect of temperature on the growth of crystals from solutions has always been of interest. It is well known that the growth temperature has pronounced effects on the quality and morphology of crystals even in the same solvent. In fact, it is a general observation that the crystals grown at relatively high temperatures usually have a better quality than those grown at a low temperature. The effect of temperature is associated with the process of integration of growth species into the surface of a growing crystal. This process becomes favorable at increased temperature.

Crystallization can be regarded as a two-stage process: (1) supply of solute from solution to the crystal surface through a diffusion boundary layer of thickness δ between the growing crystal and the solution by molecular and convective diffusion, and (2) integration of solute ions/molecules into the crystal. The former is rate-limiting if the supersaturation at the crystallization surface is lower compared with the bulk supersaturation. In this case, the growth is said to proceed in the diffusion regime. The second stage is rate-limiting if the bulk supersaturation and crystal surface supersaturation are similar. In this case, the growth regime is said to be kinetic. Crystals are generally considered to grow in a mixed diffusion–kinetic regime. Following Chernov [5], the basic ideas of kinetic and diffusion regimes are given below.

Assuming that a spherical crystal of radius r_x grows in an isotropic environment such that its growth is determined by kinetic coefficient β and the solute concentration in the bulk solution phase and at the crystal surface, separated by distance x, is c and c_0, respectively, the relationship between the resultant growth rate R of the crystal, the concentration difference $(c-c_0)$ across the diffusion layer, and the effective kinetic coefficient β_{eff} for the growth of crystal surface and the rate D/r_x of solution diffusion is given by [5]

$$R = \beta_{\text{eff}}\Omega(c - c_0), \tag{29.7}$$

where the effective kinetic coefficient β_{eff} of growth of crystal surface is defined in terms of the sum of resistances due to the two contributions β and D/r as

$$\frac{1}{\beta_{\text{eff}}} = \frac{1}{\beta} + \frac{r_x}{D} = \frac{1}{\beta}\left(1 + \frac{\beta r_x}{D}\right), \tag{29.8}$$

where D is the solute diffusion coefficient in the solution and Ω is the solute molecular volume ($\Omega = 1/\rho$; ρ is the solute density).

Crystal and environment interact through the medium of the boundary layer, the thickness of which may vary from the minimum (e.g., in stirred solutions) virtually to infinity in unstirred solutions under certain conditions. From Eqn (29.8) the following two extreme cases may be distinguished.

1. *Kinetic regime*. When $\beta r_x/D \ll 1$, the contribution due to diffusion can be neglected. In this case, the rate $R = \Omega\beta(c-c_0)$ does not depend on crystal size, which increases as $r_x = \Omega\beta(c-c_0)t$. Since the kinetic coefficient β depends on supersaturation, it reflects the reaction of the growing surface to the deviations from equilibrium. The specific response, in turn, depends primarily on the interface roughness and defect structure of the surface, which define its growth mechanism: layer (by screw dislocations or two-dimensional nucleation) or continuous (normal).
2. *Diffusion mode*. When $\beta r_x/D \gg 1$, the rate-limiting step is solute diffusion transfer across the boundary layer $\delta \approx r_x$. In this case, the crystal size increases as $r_x = [2\Omega(c-c_0)D]^{1/2}t^{1/2}$ and the rate decelerates as $R = \Omega(c-c_0)D/r_x$. Steady state is never reached in this regime. The main feature here is that, after exceeding a certain critical size that decreases with increasing supersaturation, the crystal loses morphological stability and the starving surface disintegrates into separate sinks for the insufficient nutrient. Morphologically, the event is marked by the onset of hopper and dendritic growth.

In recent years, numerous investigations of surface morphological evolution have been carried out on crystals grown from solutions [25–27]. The results of these studies have been analyzed within the formalism of BCF theory [28] and its subsequent modifications [29], and have led to a broad understanding of the mechanics of dislocation-controlled crystal growth. For example, the growth rate of KDP crystals depends on many parameters, such as growth temperature, supersaturation of growth solution, and impurities. Typically, these KDP crystals grow on vicinal hillocks formed by dislocations.

The normal growth rate R of a crystal face growing by the screw dislocation mechanism is given by the geometrical relation

$$R = pv \tag{29.9}$$

where p is the slope of dislocation hillock and v is the tangential velocity of the elementary steps. According to Eqn (29.9), there are two ways to increase the growth rate: either increase the step velocity v or the slope p of the dislocation hillock.

We consider a composite hillock composed of m equally-spaced dislocations of Burgers vector h, arranged along a line of length L. The slope p of the hillock in this case is given by the relation [28,29]:

$$p = \frac{mh}{y + 2L}, \tag{29.10}$$

where the interstep distance $y = 19r^*_{2D}$, with the radius of the critically-sized two-dimensional given by

$$r^*_{2D} = \frac{\gamma\Omega}{k_B T\sigma} \tag{29.11}$$

where γ is the solute–solvent interfacial energy, which is related to the linear edge free energy γ_l by the relationship $\gamma_l = \gamma a^2$ (the growth unit dimension $a \approx \Omega^{1/3}$); σ is the supersaturation.

As seen from Eqn (29.10), the hillock slope p (and hence R) can be increased by increasing either σ or T or by changing the number m of dislocations in the growth source. In the kinetic regime, the step velocity v is given by the following [27,29]:

$$v = b\beta\sigma \tag{29.12}$$

with the constant b related to the solubility c_0 and the kinetic coefficient

$$\beta = \beta_0 \exp(-E_A/k_B T), \tag{29.13}$$

where β_0 is a constant, E_A is the activation barrier of the slowest stage of growth, and T is the temperature. Thus, the step velocity (and hence R) can equally be increased either by increasing T or σ.

It should be mentioned that direct control of the growth rate by changing the dislocation structure is difficult because of the complicated relationship between the structure of a dislocation source σ and T. However, as was shown by De Yoreo et al. [30], in contradiction to the predictions of simple BCF models, for $\sigma > 5\%$ the activity of a growth hillock is dominated by the presence of strain-induced dislocation cores and is nearly independent of σ.

29.2.5 Crystal Growth Rates and Dead Supersaturation Zone

29.2.5.1 Basic Concepts of Impurity Effects

Growth of crystals occurs by the attachment and detachment of adatoms at kinks in the steps (ledges) present on their flat faces (F faces). Under ideal conditions, growth on a vicinal F face proceeds by step flow, with steady motion of a uniform train of steps.

However, the addition of small concentrations of impurities can greatly change the properties, morphology, and kinetics of the growing crystal, with important consequences in materials applications. Consequently, the effects of impurities on the growth kinetics of crystals have been studied intensively, both theoretically and experimentally. Here, the kinetic effects of impurities are briefly described. For more details, the reader is referred to Ref. [31].

Impurities are usually more effective at low supersaturations due to the favorable competition of impurity species with low concentration of solute particles for the adsorption and occupation of same growth sites available on the growing face. This results in a threshold supersaturation σ_d, below which no growth takes place; this is usually revealed in the dependence of the displacement rate v of steps on the F faces and face growth rate R of crystals growing from solutions containing a certain amount of impurity on supersaturation σ. The value of the threshold supersaturation σ_d increases with increasing impurity concentration c_i in the solution. The occurrence of a dead supersaturation zone induced by impurities has been reported for many crystals growing from solutions. Typical examples are KH_2PO_4, paraffin, $K_2Cr_2O_7$, ammonium oxalate monohydrate [$(NH_4)_2C_2O_4 \cdot H_2O$; AO], and KCl.

Bredikhin et al. [32] reported extensive data on the existence of dead zone in the case of the supersaturation dependence of the linear growth rate R of the (100) face of KDP crystals grown from aqueous solutions containing different concentrations of Al^{3+} and Fe^{3+} ions under the conditions of free convection. These authors observed two different supersaturation barriers σ_d and σ^* for these impurities, such that for $\sigma < \sigma_d$, there is no growth; for $\sigma_d < \sigma < \sigma^*$, the growth rate slowly increases following the classical Burton–Cabrera–Frank (BCF) parabolic law: $R = b(\sigma - \sigma_d)^n$, where b is an empirical constant and the exponent $n = 1$ or 2; while for $\sigma > \sigma^*$, the growth rate rapidly increases following an $R[(\sigma - \sigma^*)^{5/4}]$ dependence.

Rashkovich and Kronsky [33] studied the effect of trivalent cations on the supersaturation dependence of displacement velocity v of steps on the (100) and (101) faces of KDP crystals and made observations similar to those described above. These authors found three regions of $v(\sigma)$ dependence: (1) there is no growth for $\sigma < \sigma_d$; (2) the velocity v increases slowly with σ for $\sigma_d < \sigma < \sigma^*$; and (3) for $\sigma^* < \sigma < \sigma^{**}$, v steeply increases with σ above σ^*. In the region $\sigma > \sigma^{**}$, the $v(\sigma)$ curve becomes a straight line passing through the origin, as expected from the theoretical linear dependence, and the step velocity v in the presence of attains a value equal to the velocity v_0 for the system without impurities occurs at a threshold supersaturation σ^{**}. These authors attributed the behavior of the $v(\sigma)$ curves to the effect of impurities at low values of σ. The appearance of these different threshold supersaturations is illustrated schematically in Figure 29.4.

The origin of the appearance of the above threshold supersaturations σ_d, σ and σ^* may be explained in terms of adsorption of impurity particles at kinks in step ledges (Kubota–Mullin model) and on the surface terrace between successive ledges (Cabrera–Vermilyea model). These two models differ in the way impurity particles arriving from the bulk medium at the terraces between the ledges on an F face are

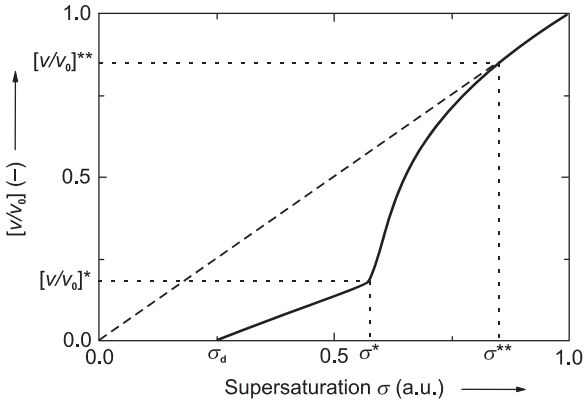

FIGURE 29.4 Schematic presentation of the above $v(\sigma)$ data illustrating the appearance of different threshold supersaturations at a hypothetical concentration c_i of an impurity. *Adapted from Ref. [15].*

adsorbed. Once they are adsorbed, they physically block the motion of advancing step ledges (pinning mechanism), as illustrated in Figure 29.5. This figure shows two steps from an array of steps, moving from left to the right, with an average distance y_0 and an average distance x_0 between the kinks in a step.

There are two extreme cases for the impurity particles to block the motion of steps. When the adsorbed impurities are sufficiently mobile on the surface, they can reach some of the kinks in the step ledges instantaneously (mobile impurities). These adsorbed impurity particles not only block the integration of solute molecules in the advancing step ledges but also physically block their movement by the pinning mechanism. However, the impurity particles can also be firmly adsorbed onto the surface terrace as soon as they reach there (immobile impurities). When the advancing step contacts an impurity particle, it tends to curl around it. The step will stop when the average distance between the adsorbed particles $L < 2r^*_{2D}$, while it will squeeze between a pair of neighboring particles when $L > 2r^*$. The critically sized two-dimensional nucleus radius r^*_{2D} on the surface is given by expression (29.11). The configuration of the advancing steps is thus changed by the adsorbed impurity particles and their average velocity v in the presence of the impurity become smaller than the velocity v_0 in the absence of the impurity. The mechanism of blocking of the movement of a step ledge by two firmly adsorbed particles is shown in Figure 29.5.

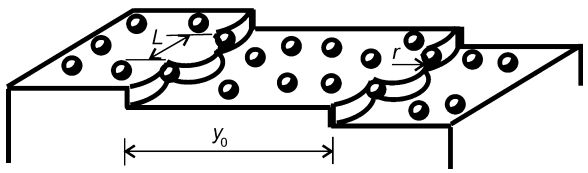

FIGURE 29.5 Illustration of blocking of movement of step ledge by two firmly attached impurity particles. *Adapted from Ref. [31].*

Using the relationship between the advancement velocity v_r of a curved step and the radius r of the curvature of the step, given by [34]

$$v_r/v_0 = 1 - r^*_{2D}/r, \tag{29.14}$$

one obtains the minimum velocity v_{min} corresponding to the curvature $r = L/2$ in the form

$$v_{min}/v_0 = 1 - 2r^*_{2D}/L. \tag{29.15}$$

In the absence of impurity when $L \to \propto$, $v_{max} = v_0$. In Eqn (29.15) when v is taken as the arithmetic mean velocity $v = (v_{min} + v_0)/2$ and the geometric mean velocity $v = (v_{min}v_0)^{1/2}$, one obtains [28,31,35]

$$v/v_0 = 1 - r^*_{2D}/L = 1 - \sigma_{dl}/\sigma, \quad \text{Kubota} - \text{Mullin model;} \tag{29.16}$$

$$v/v_0 = \left(1 - r^*_{2D}/L\right)^{1/2} = (1 - 2\sigma_{ds}/\sigma)^{1/2}, \quad \text{Cabrera} - \text{Vermilyea model.} \tag{29.17}$$

In Eqns (29.16) and (29.17), σ_{dl} and σ_{ds} are the threshold supersaturation barriers by Kubota–Mullin and Cabrera–Vermilyea models, respectively, given by

$$\sigma_{dl} = \frac{\gamma_l a}{k_B T L} = \left(\frac{\gamma_l a}{k_B T x_0}\right)\theta_l, \tag{29.18}$$

$$\sigma_{ds} = \frac{\gamma_l a}{k_B T L} = \left(\frac{\gamma_l a}{k_B T \lambda}\right)\theta_s^{1/2}, \tag{29.19}$$

where x_0 is the average distance between kinks in a step; λ is average distance between possible adsorption sites on the surface terrace, the fractional linear coverage $\theta_l = x_0/L$, and fractional surface coverage $\theta_s = (\lambda/L)^2$; and the terms given in the brackets are measures of impurity effectiveness. Because x_0 is much larger than $\lambda \approx a$, for a solute–impurity system the impurity effectiveness and the threshold supersaturation σ_{dl} according to the Kubota–Mullin mechanism is always much lower than σ_{ds} predicted by the Cabrera–Vermilyea mechanism.

According to the above concept, growth proceeds according to the usual growth mechanism after the occurrence of the threshold supersaturation barrier σ_d, up to a particular value of supersaturation σ^* when impurity adsorption on the growing surface becomes time dependent. However, in the case of time-dependent impurity adsorption at kinks, there is a time constant τ characterizing the upper limit when impurity adsorption ceases to be time-dependent [28,35–37]. This upper limit corresponds to a third threshold supersaturation σ^{**} when the step velocity v approaches the value v_0.

The theoretical interpretation of effect of impurities and threshold supersaturations σ_d and σ^* relates step velocity v with supersaturation σ for crystal growth, but no theoretical relationship between face growth R and supersaturation σ has been reported. However, in comparison with the $v(\sigma)$ data, there is a large amount of published data on face growth R as a function of supersaturation σ, where threshold supersaturations have been observed.

The $\sigma_d(c_i)$, $\sigma^*(c_i)$, and $\sigma^{**}(c_i)$ data for different impurities used during the growth of crystals may be described by the following dependences [28,31,37]:

$$\frac{1}{\sigma_c^{1/\rho}} = Q^{1/\rho}\left(1 + \frac{1}{K_L c_i}\right), \tag{29.20}$$

$$\sigma_c^{1/\rho} = B_0 + B_1 c_i, \tag{29.21}$$

which are derived by using Langmuir and Freundlich adsorption isotherms, respectively. In these equations, K_L is the Langmuir constant, the constants B_0 and B_1 are related to the parameters of Freundlich isotherm, the exponent $1/\rho = 1$ or 2, and Q is a parameter related to the value of step velocity v corresponding to the type of threshold supersaturation. Figure 29.6 presents the plots of σ_d, σ^* and σ^{**} for the (100) face of KDP crystals against the concentration c_i of different trivalent impurities, according to Eqn (29.21).

Analysis of the data according to Eq. (29.21) revealed [36] that the average interkink distance x_0 corresponding to the three threshold supersaturations σ_d, σ^* and σ^{**} follows the trend: $x_0(\sigma_d) > x_0(\sigma^*) > x_0(\sigma^{**})$. These distances correspond to three different values of supersaturation representing three average distances $y_0 = 19r_{2D}^*$ between successive steps (cf. Eqn (29.11)): (1) when the steps are completely stopped, $y_0 \geq l_d$; (2) when the steps squeeze out through the fence of adsorbed impurity particles as a result of decreasing r_{2D}^* until $y_0 = l^*$; and (3) when the steps essentially become straight and impurity adsorption no longer takes place on the steps. Steady-state (or instantaneous) and unsteady-state (or time-dependent) impurity adsorption occur in the supersaturation regions $\sigma < \sigma^*$ and $\sigma > \sigma^*$, respectively. Finally, impurity adsorption becomes time independent at $\sigma > \sigma^{**}$.

The above conclusion of three distances corresponding to the three threshold supersaturations is consistent with the concept advanced by Rashkovich and Kronsky [33]. According to these authors, the barrier σ_d occurs at $2r_{2D}^* = l_d$ when the steps are

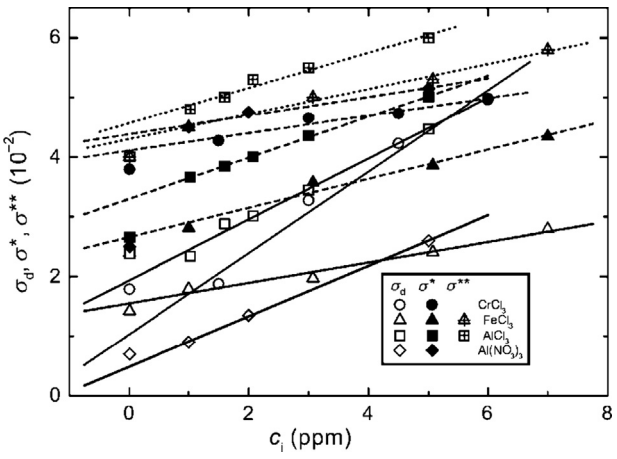

FIGURE 29.6 Example of the plots of σ_d, σ^* and σ^{**} for the (100) face of KDP crystals against the concentration c_i of different trivalent impurities, according to Eqn (21). *From Ref. [37], reproduced with permission of Wiley-VCH.*

completely blocked, while the origin of σ^* is associated with the burial of adsorbed impurity particles as a result of curling of advancing steps around them when the depth of the bent steps reaches a depth δ. The burial of impurity particles occurs when the critical nucleus diameter $2r^*_{2D} \propto \sigma^{-1}$ (see Eqn (29.11)) becomes equal to l^* between the adsorbed impurity particles. The threshold supersaturation σ^{**} corresponds to l^{**}, when the burial of impurity particles is complete and the successive steps are parallel to each other.

In the late 1950s, Frank [38] and Cabrera and Vermilyea [39] used the concept of time-dependent impurity adsorption to explain the origin of kinematic waves and step bunching in terms of relationships between flux of steps passing across a point and the density of steps on the surface. According to this concept, at given concentration of an impurity its adsorption is time-dependent at low density of steps but the impurity adsorption becomes time independent at high density of steps (i.e., low interstep distance y_0). Later, van der Putte et al. [40] suggested that adsorption of an impurity remains time independent at high concentrations of the impurity.

In a study of the effect of Fe(III), Cr(III), and Al(III) ions on the growth of KDP, Land et al. [41] proposed that recovery of crystal growth beyond the dead supersaturation zone in KDP is accompanied with the propagation of macrosteps (bunches of monolayer steps) in contrast to the growth of elementary steps considered in the Cabrera–Vermilyea model. Weaver et al. [42] suggested an improved model for describing impurity effects on crystal growth by synergizing the Langmuir model of adsorption dynamics along with the Cabrera–Vermilyea model.

Extensive studies on the growth kinetics of AO crystals from pure aqueous solutions and from aqueous solutions containing various impurities revealed that the appearance of different threshold supersaturations is associated with the nature of solute–additive–solvent system [36,43–47]. It was found that, for a given impurity concentrations, the face growth rate R approaches a value corresponding to pure solutions for supersaturation $\sigma > \sigma^{**}$, a behavior similar to that for KDP crystals [33]. Analysis of the experimental data on the kinetics of growth of different faces of the crystals in solutions containing Cr(III) impurity suggested that the appearance of threshold supersaturations at $\sigma > \sigma_d$ occurs when there is a transition in the mechanism of adsorption of an impurity from Cabrera–Vermilyea to Kubota–Mullin mechanism.

29.2.5.2 Effect of Organic Additives on Crystal Growth

Foreign substances inherently present in a growth medium or deliberately added to it affect growth rates in different ways. They can change the properties of the growth medium, whereby the equilibrium saturation concentration (i.e., solubility) of the solute and, hence, the supersaturation available for the formation of 3D nuclei and their subsequent growth in the medium, are altered. The affect of foreign substances on the growth of crystals is associated with kinetic and thermodynamic terms involved in the growth models. The kinetic parameters involved in the growth models are connected with the density of kinks and obstructions provided by impurity particles in the

movement of step ledges on the surface, whereas the thermodynamic parameter in these models is the crystal–medium interfacial energy γ. The kinetic effects of impurities were discussed in the preceding section, where no attention was paid to the thermodynamic parameters on growth kinetics. In fact, the above treatment holds when the interfacial energy γ remains unchanged during growth.

It is well known that the solubility c_0 of various substances in aqueous solutions is related to their interfacial energy γ [10]. The higher the solubility c of a substance in a solvent, the lower is its interfacial energy γ, and, consequently, the higher is the step velocity v and the face growth rate R of its crystals. Following this line of argument, it can be concluded that the usual retardation of step velocity v or face growth rate R by an impurity leads to an increase in the solute–solvent interfacial energy γ. However, consideration of the adsorption process in terms of adsorption isotherms and reversible adsorption equilibrium shows that adsorption of foreign substances decreases the value of γ [48,49]. This decrease in γ will, consequently, lead to an increase in v and R. Impurity particles firmly adsorbed at step ledge and onto the surface terrace can also serve as sources of additional kinks for the integration of solute molecules, thereby leading to an increase in v and R [31].

The above considerations show that, at relatively low concentrations of an impurity, one expects opposite effects of kinetic and thermodynamic parameters on growth kinetics. The kinetic parameter tends to decrease v and R, whereas the thermodynamic parameter tends to increase them. Thus, at low supersaturations that ensure a low density of kinks in the step ledges, the rates increase for small impurity concentrations and decrease as the impurity concentration is increased. However, at relatively high supersaturations when a high density of kinks is available in the step ledges, impurity adsorption always decreases v and R for all values of impurity concentrations c_i. With an increase in impurity concentration c_i, an initial increase and then a decrease in R passing through a maximum at a particular impurity concentration c_i were first observed by Bliznakov and Kirkova [50] for the growth rates of the (100) and (111) faces of $Pb(NO_3)_2$ crystals grown from aqueous solutions in the presence of methyl blue.

For many crystals, the ionic surface structure of different faces is fundamentally different. Therefore, organic additives interact differently with different crystal faces [51]. For example, in the case of KDP crystals, the {101} faces are terminated by a layer of K^+ ions whereas the {100} faces by a layer of both K^+ ions and $H_2PO_4^-$ groups. Consequently, because alcohols contain hydroxyl groups, adsorption of alcohols onto the {100} faces through the formation of H-bonds between the alcohols and $H_2PO_4^-$ groups is more favorable than that onto the {101} faces. Similarly, the effect of urea is less pronounced on the growth rate than that of alcohol. Enqvist et al. [52] showed that the negative charge on O atoms of alcohols containing the hydroxyl group is about 1.6 times higher than that of urea containing the carbonyl group. Therefore, the adsorption of alcohols on the {101} faces is more favorable than that of urea. Consequently, alcohols inhibit the growth of the {101} faces more than that of urea.

Small amounts of organic impurities can also cause a growth promoting effect. The positive effects of organic additives on crystal growth and quality have been reported by several authors [53–56]. For example, during ADP and KDP crystal growth, the addition of ethylene glycol, glycerol, and ethylenediamine tetra-acetic acid (EDTA) significantly increases the width of the metastable zone and the crystal growth rate in comparison with those from pure solutions [55,56]. These observations are usually explained by the ability of formation of complexes of additive molecules with multivalent ions inherently present in growth solutions.

29.2.6 Effect of Mechanical Impurities on Crystal Growth

Nonlinear optical (NLO) materials capable of second harmonic generation (SHG) have received a great deal of attention due to their commercial importance in optical communication, signal processing, sensing, and instrumentation. Systematic investigations of NLO materials are devoted to inorganic and semiorganic crystals such as KDP, K_2SO_4, KAP, and LAP with embedded organic molecules and inorganic nanoparticles. These impurities offer mechanical obstruction during growth. The studies were aimed at correlating structural properties to the nonlinear responses with the ultimate goal being the possibility of "tuning" the structure to enhance the nonlinear properties. Therefore, crystallization of some inorganic and semiorganic salts in the presence of organic molecules and inorganic nanoparticles is an important process still under careful examination by several research groups.

29.2.6.1 Growth of Water-Soluble Crystals with Embedded Organic Molecules

Gliko et al. [57] studied the morphology and growth kinetics of the pyramidal face of KDP crystals in the presence of the dye Chicago Sky Blue. The crystals were grown in crystallizers of about 10 L volume at the initial temperature of about 60 °C and impurity concentration $c_i = 1.4$ ppm ($1.4 \cdot 10^{-6}$ mol/mol KDP). It was found that staining of the crystal begins only at temperatures below 35 °C when the crystal already reaches a sufficiently large size. This observation is a consequence of a sharp increase in dye adsorption with decreasing temperature.

Figure 29.7 shows the dependence of normal growth rate R of dislocation hillocks on supersaturation σ of aqueous solutions containing different dye concentration c_i. It may be seen from the figure that the measured values of normal growth rate R in the pure solution and in the presence of the dye are close. The minor difference between them can be attributed to the difference in the activity of dislocation sources and influence of temperature. The experimentally derived dependence of velocity v of movement of steps on supersaturation σ, shown in Figure 29.8, has a character that is unusual for pyramidal faces. The $v(\sigma)$ dependence is sublinear for the shallow sector below $\sigma \approx 0.035$ (top curve), whereas v is nearly proportional to σ for steep sectors in the whole region of supersaturation (bottom curves). From the figure, it may also be seen that the dye concentration does not noticeably affect the velocity of the growth layer's movement.

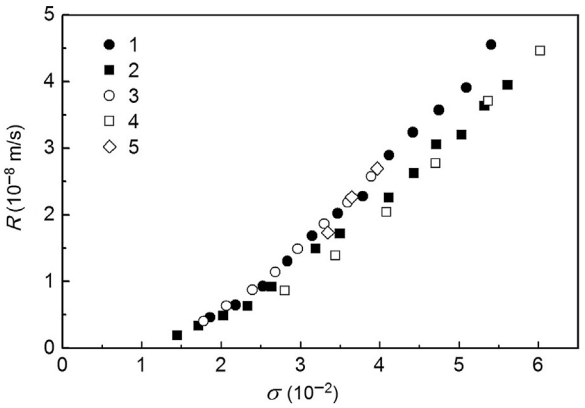

FIGURE 29.7 Dependence of normal growth rate R of dislocation hillocks on supersaturation σ of aqueous solutions containing different dye concentration c_i: (1,2) no additive, (3) 1 ppm, (4) 1.5 ppm, and (5) 2 ppm. Saturation temperature: (1,3) ca. 33 °C, and (2,4,5) ca. 37.5 °C. *Adapted from Ref. [57], with permission of the Materials Research Society.*

The fact that the capturing of a dye starts only at a sufficiently high velocity of the step in the case of the shallow sector composed of array of parallel steps with large interstep distance y_0, but it is not captured by the steepest vicinal sectors comprised of arrays of parallel steps with small y_0, is evidence of a short lifetime of dye molecules on the surface. Another observation in support of this argument is the occurrence of capturing impurity particles only at sufficiently high concentration in the solution. Gliko et al. [57] explained the observation of the capture of dye particles in the framework of a model [58], describing the movement of a step and its morphological stability in the presence of mobile impurity stoppers.

In an *in situ* atomic force microscopy (AFM) study of potassium sulfate (K_2SO_4) crystal growth in the presence of acid fuchsin and pyranine, Moret [59] found that these polysulfonated dyes adsorb onto the {110} and {010} faces, producing strong habit

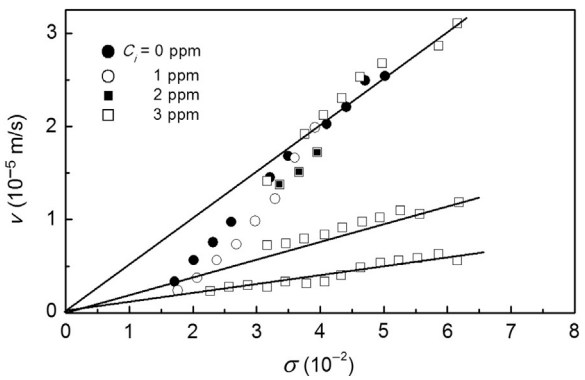

FIGURE 29.8 Dependence of velocity v of moving growth layers in three vicinal sectors on supersaturation σ. Saturation temperature about 37.5 °C. *Adapted from Ref. [57], with permission of the Materials Research Society.*

modification and changes in the surface micromorphology of the crystals. The main observations of this study were the following:

1. The presence of dye molecules at concentrations as low as about $2 \cdot 10^{-6}$ and $4 \cdot 10^{-4}$ M for pyranine and acid fuchsin, respectively, produces significant changes in the step morphology and growth rates.
2. Bunching of steps occurs as a result of absorption of impurities binding to the crystal surface.
3. Additive molecules attach to the terraces pinning the growing front and lead to the roughening of edges of the growing steps.
4. At a given supersaturation, there exists a critical value of dye concentration above which crystal growth is stopped along particular crystallographic directions (i.e., dead supersaturation zone).
5. At low supersaturations, layers grow by step flow at preexisting steps by the addition of growth units at the step edges.

The first four observations may be explained by the Caberera–Vermilyea mechanism, whereas the last observation suggests that growth is controlled by volume diffusion.

The validity of Cabrera–Vermilyea mechanism in the above study is associated with the adsorption behavior of acid fuchsin and sulfonated pyrene molecules on the two faces of K_2SO_4 crystals. Acid fuchsin and sulfonated pyrene are strong polyelectrolytes that can adsorb on terraces because of the high number of simultaneous attaching points on a molecule (three/four sulfonated groups) strongly interacting with the surface via long distance electrostatic forces. This class of molecules should remain practically immobile once adsorbed onto the surface due to the strong interactions with the host surface, provided that sulfonate–sulfonate distances reasonably match the distance between the sulfate ions on the surface host lattice and with sulfonate groups substituting for surface anions. This should particularly hold for pyranine due to its conformational rigidity, and its effects on K_2SO_4 are indeed significantly stronger than those produced by acid fuchsin.

A major goal in crystal growth studies is to ascertain whether the additives adsorb onto the surface terraces between steps or at kink sites on the steps. For example, correlation of distribution of foreign molecules inside the host crystal with surface microtopography can shed light on the relationships between surface structure, growth mechanism, and additive incorporation. For layer growth, specific affinity for dye incorporation into a growing surface is associated with its detailed structural features (i.e., density of kinks and ledges). Because nonequivalent crystallographic directions have different structural properties, they differ in their affinities toward the capture of an additive.

29.2.6.2 Growth of Water-Soluble Crystals with Embedded Nanoparticles

The methods of growth of single crystals with inclusions of the second fine-crystalline phase (of nanometric dimensions) are of great interest for designing new composite

crystalline materials with new valuable properties. Examples of such materials are the so-called combined nonlinear–optical media based on inorganic matrix (single crystal) with incorporated nanoparticles [60,61,62]. In the case of KDP crystals, SiO_2 and CdTe nanoparticles of size up to 250 nm were found to be captured [60,63].

Rudneva et al. [60] carried out an interesting study devoted to the nature of interaction of nanocrystals and crystalline SiO_2 particles with the growing face and the mechanism of their incorporation into KDP crystal. This study showed that in unstirred solutions the capture of nanocrystals and crystalline SiO_2 particles by a growing crystal face takes place at a growth rate exceeding a certain critical value which depends on particle size. The smaller the particles, the higher is the growth rate. Crystal growth from stirred solutions in the presence of solid particles showed that capture of particles by a growing crystal is also possible. As in the case of growth from unstirred solutions, the probability of capture of particles depends mainly on particle size and decreases with decreasing particle size. The specific feature of the experiments on crystal growth under the conditions of solution stirring was the formation of long channels during the capturing of particles. Such channels are not observed from unstirred solutions. It was found that at the growth rates exceeding the critical values the influence of supersaturation and growth rate of a crystal on the probability of the particle capture is insignificant.

Pritula et al. [61] carried out a similar study on the growth of KDP crystals from aqueous solution in the presence of TiO_2 nanoparticles by the temperature reduction method onto a point seed. The authors found that, under the conditions of intense stirring, TiO_2 nanoparticles are captured predominantly by the pyramidal growth sector and, to a considerably lesser extent, by the prismatic sector. Difference in the nature of interaction of the nanoparticles with the {100} and {101} growth faces is obviously caused by differences in the structure of the two faces and the nature of adsorption of impurity particles onto them. These differences are responsible for the threshold value of supersaturation necessary for the growth of the faces.

Capture of mechanical impurities in crystal growth from solutions may be explained from a consideration of two forces [5]: (1) force pressing impurity (e.g. SiO_2 particles) at the crystallization front against the crystal surface, and (2) repulsive force of disjoining pressure arising in a thin (10^{-5}–10^{-7} cm) solution layer between a particle and a crystal. The pressing force, in addition to the hydrodynamic component, also has a component related to the effect of the particle entrainment by a diffusion flow. The disjoining pressure arises mainly because of the molecular (van der Waals) and electrostatic (Debye) forces and the structural component of the disjoining pressure due to partial ordering of the liquid in the vicinity of solid surfaces. According to this concept [5], if the distance between a particle of radius r and a crystal surface becomes less than a certain critical distance ca. $0.1r$, the particle screens the surface of a growing face from the diffusion flow. This decreases solution supersaturation under the particle, which, in turn, leads to the formation of a V-like depressions on the growing face. At certain critical growth rate, the conditions for capture of a foreign particle by the crystal are created and a channel filled with mother solution is formed.

Pritula et al. [62] showed the possibility of creating a composite material on the basis of KDP crystal with incorporated $Al_2O_3 \cdot nH_2O$ (NAO) nanoparticles. These authors investigated the effect of NAO nanoparticles on the growth kinetics of KDP crystal faces and showed predominant interaction of the nanoparticles with the {100} crystal faces. KDP:NAO crystals were grown from aqueous solutions containing 1–100 ppm NAO impurity (with respect to KH_2PO_4) by the temperature reduction method. It was found that the nature of the $R(\sigma, \Delta T)$ curves for the {101} and {100} faces of KDP in the presence of NAO nanoparticles and their incorporation in different sectors is similar to that observed in the case of TiO_2 nanoparticles discussed above and trivalent cationic impurities [32,33].

29.3 High-Temperature Solution Growth

Complex multicomponent compounds usually have high melting points, high vapor pressure, or decompose incongruently before melting. It is difficult to grow such substances from conventional methods such as growth from their melts. Crystallization of these compounds is carried out from high-temperature solution where temperature for their growth is much lower than their melting points.

High-temperature solution growth has features similar to those of growth of substances from low-temperature solutions. The compound to be crystallized, or components reacting to form it, is first dissolved in a solvent at high temperature. Then, a supersaturation in the solution is attained by slow cooling of the solution or evaporation of the solvent such that crystals nucleate and grow in the supersaturated solution. Supersaturation can also be attained by creating a temperature difference between the locations of growing crystal and nutrient. Growth is carried out either in the air or in any other suitable atmosphere. The growth temperature is usually between 300 and 1800 °C, and the concentration of the solute in the high-temperature solution is between 1 and 30 wt%.

The main advantage of the method is that practically any material can be grown in some solvent whose composition may be found from a knowledge of the composition of solvents used for the crystallization of chemically similar compounds. Because the growth temperature in this method is lower than that in melt growth, technically the control of growth temperature is easier and the quality of the crystals is better in terms of dislocation densities and point defects. The main disadvantage of the method is that the solvent provides a variety of impurities, which can be incorporated into the grown crystals either substitutionally as solvent ions or as solvent inclusions.

Crystallization from high-temperature solutions has been described before in excellent books [3,64,65] and reviews [66–69]. The reader is referred to these literature sources for more information on experimental procedures for growth, characterization methods, and the materials crystallized before 1998.

29.3.1 Principle of the Method

High-temperature solution growth method employs the fact that complex compounds with high melting points have high solubilities in appropriate molten salts and oxides used as solvents. Once appropriate solvents are found for substances to be grown, crystal growth is carried out on seeds spontaneously nucleated in the bulk molten solution or on seeds introduced into the solution, using some procedures to achieve supersaturation.

The range of substances grown as single crystals from high-temperature solutions extends from elements, such as diamond and metals; semiconducting compounds, such as GaP, GaN, and AlGaAs; borates; and various oxides. Table 29.1 lists some examples of substances grown from high-temperature solutions. This table contains examples of fluxes published in the literature in recent years.

A usual growth experiment consists of weighing and mixing of required constituent materials, loading them into a crucible, tightly closing the crucible to avoid solvent losses by evaporation, placing the crucible in a furnace initially heated to the maximum temperature, holding the crucible for several hours of soaking time to dissolve and homogenize the solution, slow cooling of the furnace to the desired temperature to create supersaturation for nucleation and growth of crystals, fast cooling down of the furnace to room temperature, and finally leaching out the crystals. The crystals obtained after growth can also be separated from the solution by decanting it. The typical procedure used for crystal growth from high-temperature solutions is summarized in Figure 29.9.

29.3.2 Composition of Fluxes and Their Selection

The selection of a suitable solvent for the material to be grown from high-temperature solutions is also a critical step in this method. In the selection of a solvent, both its physical and chemical properties are important. At the growth temperature, a solvent should ensure a sufficient solubility of the compound and its components, and the solubility should show sufficient change with temperature. The compound to be crystallized should also be stable in the solvent. The solvent should have low melting point, low vapor pressure (low volatility), low viscosity, and low toxicity. It should also not corrode the growth apparatus (crucible and furnace) and should be cheaply available in the pure state.

There is no universal high-temperature solvent that satisfies all of the conditions mentioned above. Most of the solvents used for crystal growth are various individual chemical compounds or their mixtures, and up to about 1990 they were selected by a trial-and-error method. However, in later years the composition of solvents for the growth of different materials have been established from knowledge of solvents proposed before for the crystal growth of similar compounds.

For the growth of oxides from high-temperature solutions, the following fluxes are commonly used: (1) compounds containing lead and bismuth; (2) borates; (3) vanadates,

Table 29.1 Some Examples of Single Crystals Grown by Different High-Temperature Methods[a]

Crystal	Solvent/Solution	Method	Ref.
KTP	$K_8P_6O_{19}$–BaF_2	Top-seeded solution growth; Pt crucible, homogenization at 1100 °C, cooled at 40 °C/h to about 900 °C, seed introduced at about 10 °C above saturation temperature, temperature decreased at 0.2–1 °C/day until end of growth; rotation rate 60–120 rpm with rotation direction reversed every 120 s with interval pause of 5 s; after growth crystal, withdrawn from solution and furnace cooled to room temperature at 20 °C	[70]
KTP:Zr	K_2O–P_2O_5–TiO_2–ZrF_4	Slow cooling method; Pt crucibles, homogenization at 1100 °C for 10 h, cooled to 750 °C at 3 K/h	[71]
NdP_5O_{14}	$H_2P_4O_7$	Slow solvent evaporation; platinum crucible, growth temperature 500 °C	[72]
$KNbO_3$	K_2CO_3–NbO_5	Micropulling down; Pt crucible, cooling rate 30 °C/min, pulling rate 0.5 mm/min	[73]
$LaMn_{1-x}Co_xO_3$	Cs_2MoO_4–MoO_3	Electrochemical growth; Pt crucible, anode current density 5–10 mA/cm^2, 80–100 h	[74]
$LiNbO_3$	$(Li_2O{:}Nb_2O_5)$–K_2O	Czochralski method; pulling rate 2 mm/h, rotation rate 20 rpm	[75]
β-$FeSi_2$	Sn	Temperature gradient solution growth; quartz ampoule, $T_G = 880$ °C, $T_S = 920$–960 °C, temperature gradient 40 K/cm	[76]
PZN–PT (6–10 mol% PT)	1.7–3.0 mol% TiO_2 +($ZnO{:}Nb_2O_5{:}PbO$ = 19:11:68)	Temperature gradient method; Pt crucible, homogenization at 1160 °C for 8 h, self-nucleation, cooling at 0.5–0.75 °C/h to 890 °C, crucible cooling in 70 h	[77]
3C-SiC	Si	Top-seeded dipping method (LPE); graphite crucible, growth on dipping 6H-SiC(0001) seed mounted at the end of graphite rod at 1300 °C for 50 h	[78]
$BaAlBO_3F_2$	$LiF{:}B_2O_3{:}NaF = 5{:}2{:}0.6$	Middle-seeded solution growth; Pt crucible, homogenization at 950 °C for 24 h, slowly cooled to, temperature 10 K above melting, insertion of seed, mounted on Pt rod, temperature decrease at 0.6–2.6 K/day, rotation rate 20–40 rpm with inversion; grown crystal withdrawn from solution surface by 10 mm, cooled down to RT at 10 K/h	[79]
$KBi(WO_4)_2$	80% $K_2W_2O_7$	Top-seeded solution growth; Pt crucible, homogenization at about 800 °C for 24 h; b-oriented seed, crucible rotated slow cooling at 10 rpm; after 10 days of growth at 730 to, 720 °C, crystal cooled to room temperature at rate 10 K/h	[80]
$Y_{1-x}Ca_xBa_2Cu_3O_{7-\delta}$	Y:Ba:Cu	Top-seeded solution growth; mixtures of Y_2O_3, $BaCO_3$, $CaCO_3$ and CuO homogenized in air in alumina crucible at 880 °C for 2 days; growth in ZrO_2 crucible on MgO seed, temperature gradient 15 K/cm above melt in air or oxygen; soaking temperature ca. 1050 °C; seed and crucible rotated at 40 rpm in opposite directions	[81]

Table 29.1 Some Examples of Single Crystals Grown by Different High-Temperature Methods[a]—cont'd

Crystal	Solvent/Solution	Method	Ref.
$La_2CaB_{10}O_{19}$(LCB)	LCB:CaO:Li_2O:B_2O_3	Top-seeded solution growth; solution homogenization at 1000 °C for 48 h, seed introduced into solution 10 °C above T_S, after initiation of growth temperature decreased between 0.24 and 0.5 °C/day, crystal rotation rate 15–45 rpm	[82]
NBT–KBT (5% KBT)	Na_2CO_3–K_2CO_3–Bi_2O_3 (20% excess flux)	Top-seeded solution growth; Pt crucible, homogenization at 1360 °C, growth on seed mounted on a rod, pulling rate 1.0–1.5 mm/day, rotation rate 5–10 rpm, crystal withdrawn, from melt, furnace cooled down to room temperature at 30–50 °C	[83]
$CsLiB_6O_{10}$	Cs_2CO_3:Li_2CO_3:H_3BO_3: NaF (1:1:12:0.5)	Top-seeded solution growth; Pt crucible, homogenization at 850 °C for 24 h, z-oriented seed introduced in melt, for growth cooling rate 0.1–0.6 °C/h, rotation rate 20–40 rpm, crystal withdrawn from melt, furnace cooled to room temperature at 10–15 °C/h	[84]

[a]Abbreviation: T_S, saturation temperature.

molybdates, and tungstates; and (4) various chlorides and fluorides. Fluxes from the first group are very effective for growth. They are volatile, toxic, and relatively active with platinum crucibles. They dissolve in hot aqueous HNO_3 solutions. Fluxes from the group of borates have relatively low melting points but they are very viscous (see Figure 29.10) and have a strong tendency to creep out of the crucible. They also dissolve in hot diluted HNO_3, whereas some of them also dissolve in water. Vanadium, molybdenum, and tungsten oxides are good solvents but they are very volatile at high temperatures. Consequently, their salts (i.e., vanadates, molybdates, and tungstates) are usually used.

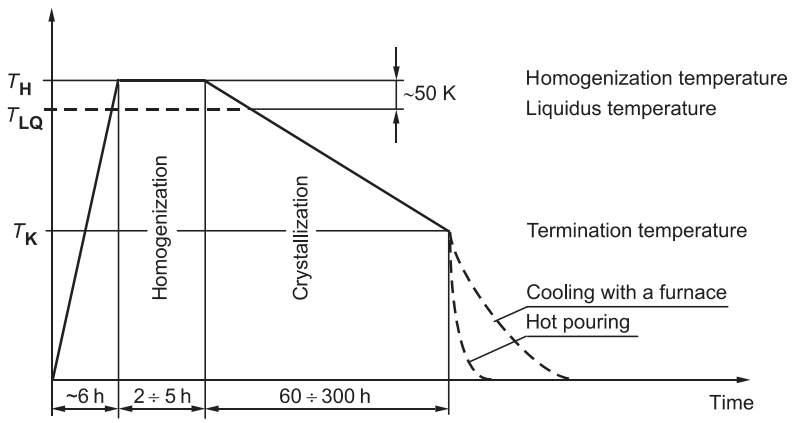

FIGURE 29.9 Typical procedure for crystal growth from high-temperature solutions. *Adapted from Ref. [68].*

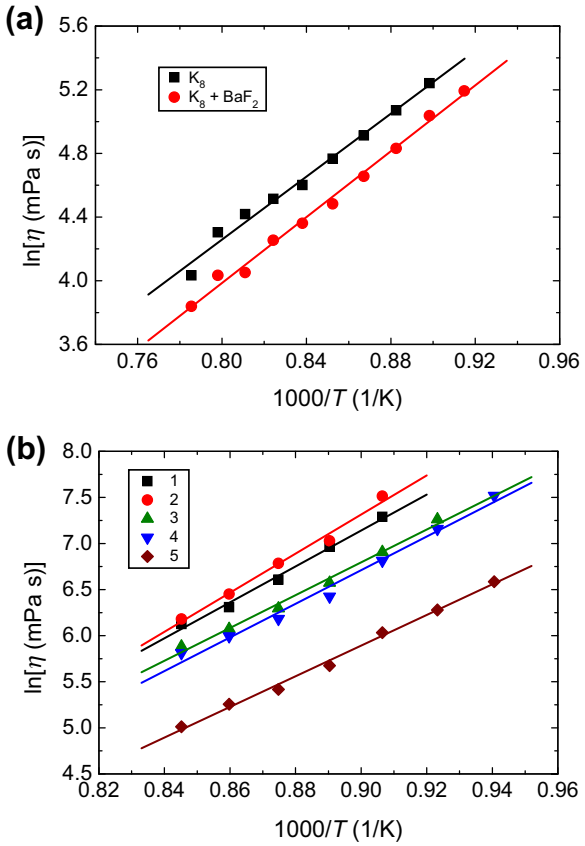

FIGURE 29.10 Plots of ln η on $1/T$ according to Eqn (29.16) for the data of viscosity η of two different solutions of (a) KTP in K_8 and K_8–BaF_2 solvents and (b) $CsLiB_6O_{11}$ (CLBO): (1) Cs_2CO_3:Li_2CO_3:H_3BO_3 = 1:1:12, (2) Cs_2CO_3:Li_2CO_3:H_3BO_3 = 1:1:11, (3) Cs_2CO_3:Li_2CO_3:H_3BO_3:NaF = 1:1:12:0.5, (4) Cs_2CO_3:Li_2CO_3:H_3BO_3:NaF = 1:1:12:0.667, and (5) Cs_2CO_3:Li_2CO_3:H_3BO_3:NaF = 1:1:12:2. *Original data from: (a) Ref. [70] and (b) Ref. [88].*

They all dissolve in aqueous solutions of acids and alkalis. Chlorides and fluorides are good solvents with low viscosity but they are volatile (see Figure 29.11). Fluorides dissolve in acids, whereas chlorides in hot water.

Oxide superconductors usually have complex composition and have two or more oxide components. As the complexity of composition of oxide superconductors increases, they become increasingly less stable. It is known that practically all high-temperature T_c oxide superconductors decompose before melting. Consequently, these materials are usually grown from high-temperature solutions. Three types of fluxes are used for their growth [69]: (1) self-fluxes, (2) partial self-fluxes, and (3) other fluxes. When components of the composition of an oxide superconductor serve as a solvent for growth, they are said to be the self-fluxes. When one of the components of the oxide superconductor is a part of its chemical structure while the other is partially

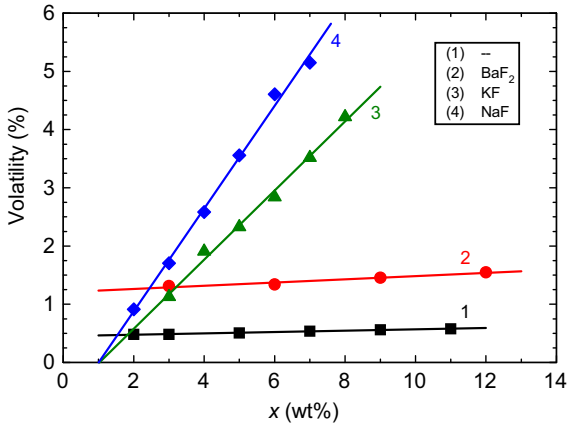

FIGURE 29.11 Volatility of KTP in four fluxes as a function of additive content *x*: (1) K_8 ($K_8P_6O_{19}$), (2) K_8–BaF_2, (3) K_8–KF, and (4) K_8–NaF. Additives to the pure solvent K_8 are given in the inset. *Adapted from Ref. [70].*

or entirely related to its structure, one talks of partial self-flux. However, when the solvent is completely unrelated to the chemical composition of the superconductor, it is categorized as other flux. For the growth of $YBa_2Cu_3O_{7-\delta}$ (YBCO), for example, CuO, CuO–BaO, and In_2O_3 are self-flux, partial self-flux, and other flux, respectively.

For the growth of crystals of complex phosphates, such as potassium titanyl phosphate ($KTiOPO_4$; KTP), potassium polyphosphates ($K_6P_4O_{13}$ and $K_8P_6O_{19}$, popularly abbreviated as K_6 and K_8 solvents, respectively) are known as good fluxes. A common problem with these fluxes is that they have high viscosity (Figure 29.10). Introduction of additives such as alkali and alkaline-earth fluorides are well known to reduce solution viscosity and increase solute solubility. However, these additives lead to an increase of their volatility, which strongly increases with the additive content in the solvent (see Figure 29.11). The increase in the flux volatility is enormously high in the fluorides of alkali metals.

29.3.3 Some Properties of High-Temperature Solvents

The solubility of a substance in a given flux and the width of the metastable zone width are associated with the formation of ions and complexes [67,85,86]. Consequently, composition of the components of the original flux and addition of impurities, usually known as additives, determine the solubility curve and metastable zone width in it for a given compound.

Garnets ($A_3B_5O_{12}$), spinels (AB_2O_4), and perovskites (ABO_3) are usually grown at high temperatures from solvents composed of oxides and fluorides (see Table 29.1). These solvents are characterized by the dissociation of oxide supplying O^{2-} ions to the solution (basic behavior) and association of O^{2-} ions to the second component (acidic behavior) [87]. Successful growth of the compounds takes place in a wide range of composition of the solvents and the ratio of the garnet-forming oxides, and there is a correlation

between oxygen ion concentration (OIC) and the range of crystallization of primary phases of a garnet, spinel, or perovskite.

Volatility of a flux used for growth of a compound has an adverse effect on the quality of crystals grown from solutions and causes problems associated with spurious nucleation on the solution meniscus, decomposition of seed crystals, and unstable growth. Therefore, while selecting the composition of a flux suitable for the growth of a compound, knowledge of the volatility of the flux is very important.

Volatilization of the solution may be determined from the weight loss of the charged crucible during each crystal growth experiment [70]. Figure 29.11 shows an example of the volatility of four fluxes used for the growth of KTP ($KTiOPO_4$) crystals as a function of the content x of K_8 ($K_8P_6O_{19}$), and three fluoride additives (BaF_2, NaF and KF) in the starting high-temperature solution for volatility experiments. The parameter x defines the weight fraction of K_8 (curve 1) or fluoride additive (curves 2–4) in the K_8–KNT–additive solution. As seen from this figure, the volatility of different solutions increases practically linearly with increasing x of K_8 as well as of all fluoride additives. As indicated by the slope of the plots of the volatility of different substances against their initial content x, above approximately 3 wt%, the volatility of NaF and KF additives increases very rapidly with an increase in their content, and the volatility of NaF is much higher than that of KF. However, as in the case of K_8 solvent, the volatility of BaF_2 increases poorly with its content in the solution.

In the above study, the authors [70] used working seeds mounted on a platinum seed-rod for crystal growth. They observed deposition of volatilized mass on seed-rod in the case of NaF and KF additives, but no such deposition was found on the seed-rod in BaF_2 additive. These results suggest that pure K_8 solvent and BaF_2 additive contained in K_8 are favorable for the growth of KTP crystals.

As in the case of different low-temperature solutions and solvents, the viscosity of high-temperature solutions decreases with an increase in temperature. The viscosity of high-temperature solution strongly depends on solution composition. For example, the viscosity of halide-free solutions used for the growth of KTP and CLBO crystals differs by a factor of about 5, and solutions of the CLBO system are more viscous than those of the KTP system. Moreover, fluoride additives, as a rule, decrease the viscosity of different systems and the relative decrease in the viscosity of the solution usually increases with increasing concentration of the fluoride additive.

The viscosity of different liquids usually follows the Arrhenius relationship:

$$\eta = \eta_0 \exp(E_a/R_G T), \tag{29.22}$$

where η_0 is a constant and E_a is the activation energy for viscous flow. Figure 29.10(a) and (b) show the viscosity of solutions of solute KTP in solvent K_8 or K_8–BaF_2 in the weight ratios between 0.4 and 0.5 and of flux composition used for the growth of $CsLiB_6O_{11}$ (CLBO) crystals, respectively, in the form of plots of ln η against $1/T$ according to Eqn (29.22). The calculated values of the pre-exponential factor η_0 and the activation energy for E_a viscous flow are given in Table 29.2. Obviously, the activation energy for

Table 29.2 Calculated Values of Parameters A and E_a for Growth Solutions for KTP and CLBO

Crystal	Solution	ln η_0	η_0 (mPa s)	E_a (kJ/mol)
KTP	K_8	-3.65 ± 0.35	$2.6 \cdot 10^{-2}$	82.2 ± 3.5
	$K_8 + BaF_2$	-4.28 ± 0.25	$1.4 \cdot 10^{-2}$	86.0 ± 2.5
CLBO	Cs_2CO_3:Li_2CO_3:H_3BO_3 (1:1:11)	-11.77 ± 1.11	$7.7 \cdot 10^{-6}$	176.3 ± 10.5
	Cs_2CO_3:Li_2CO_3:H_3BO_3 (1:1:12)	-10.40 ± 0.90	$3.0 \cdot 10^{-5}$	162.0 ± 8.5
	Cs_2CO_3:Li_2CO_3:H_3BO_3:NaF (1:1:12:0.5)	-9.22 ± 0.73	$9.9 \cdot 10^{-5}$	147.9 ± 6.9
	Cs_2CO_3:Li_2CO_3:H_3BO_3:NaF (1:1:12:0.67)	-9.69 ± 0.84	$6.2 \cdot 10^{-5}$	151.5 ± 7.9
	Cs_2CO_3:Li_2CO_3:H_3BO_3:NaF (1:1:12:2)	-9.07 ± 0.47	$1.2 \cdot 10^{-4}$	138.3 ± 4.4
$KLu(WO_4)_2$	$KLu(WO_4)_2$:$K_2W_2O_7$ (12:88)	0.68 ± 0.38	1.96	28.0 ± 4.0

viscous flow for solvents of different composition varies in a wide range. The highest activation energy is encountered for multicomponent solvents and its value is decreased by the alkali fluoride additives and their concentration.

Figure 29.12 shows the dependence of solubility c of KTP in KTP–$K_8P_6O_{19}$ and KTP–$K_8P_6O_{19}$–BaF_2 solutions on temperature. In the study, the solubility of the solute KTP was determined from its known weights dissolved in the solution at different temperatures by using the traditional method of introducing trial seeds and changing the solution temperature. The saturation temperature of the solution was identified when the seed size remained unchanged. In the figure, open and filled squares represent solubility data from two different studies and are somewhat different from each other. They are represented by a single curve drawn for the data shown by open squares. The other two curves are for KTP solubility in solutions prepared from solid-reacted and solution-reacted materials. Solid-reacted solutions were prepared by homogenizing KTP solute with K_8 or K_8–BaF_2 solvents in weight ratio between 0.27 and 0.42 (filled squares

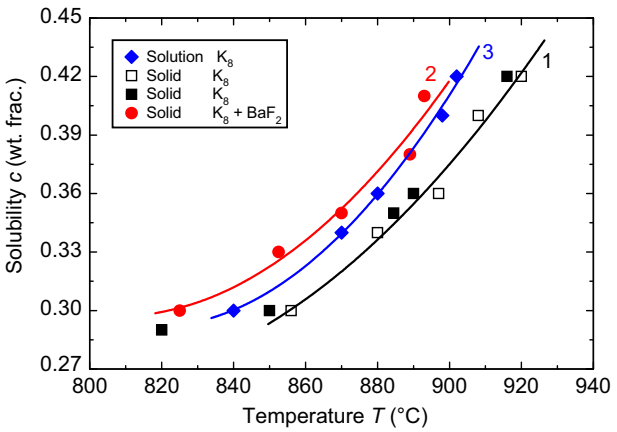

FIGURE 29.12 Temperature dependence of solubility c of KTP in (1,3) KTP–$K_8P_6O_{19}$, and (2) KTP–$K_8P_6O_{19}$–BaF_2 solutions. Curves (1, 2) and (3) are for KTP solubility in solutions prepared from solid-reacted and solution-reacted materials, respectively. *Data represented by filled squares and circles are from Ref. [70], whereas those shown by filled diamonds and open squares are from Ref. [88].*

and circles) and between 0.30 and 0.42 (open squares) at a temperature of about 50 °C above the saturation temperature for 24 h [70,88]. However, solution-reacted materials were prepared by reacting a solution of tetrabutyl titanate dissolved in ethanol with appropriate amounts of KH_2PO_4 and K_2CO_3 dissolved in water, which gave a white precipitate [88]. The excess amount of water was evaporated by heating the precipitate; finally, the material was dried at 50 °C for 24 h and grinded into powder in an agate mortar (filled diamonds).

From Figure 29.12, one notes differences in the solubility c of KTP obtained not only from solid- and solution-reacted materials (compare data of filled diamonds with those of open and filled squares) but also from two different solid-reacted solutions (compare open and filled squares). Moreover, the solubility of KTP is increased by BaF_2 additive (compare data of filled and open squares with those of filled circles). It may be seen that the solubility of KTP in solution-reacted materials is higher than that in the solid-reacted materials, whereas it is somewhat different in the two different solid-reacted materials. The former observation is due to small amounts of TiO_2 insoluble in high-temperature solutions [88], whereas the latter observation is associated with the difference in the initial composition of the solutions. BaF_2 additive increases the solubility of KTP at all temperatures. Using relation (29.5), these solubility differences can be analyzed from the plots of ln c against $1/T$, as shown in Figure 29.13. The values of the pre-exponential factor A and the enthalpy of dissolution ΔH_s obtained from the plots are given in Table 29.3. Obviously, the differences in the solubility for the three systems are reflected by the values of A and ΔH_s. Because for ideal solutions $A = \Delta H_s / R_G T_m$, from the values of A and ΔH_s listed in Table 29.3, one finds $T_m \approx 700$ K. This temperature is much lower than the saturation temperature T_s for the above systems, so one may conclude that high-temperature solutions are regular.

Dependence of the solubility of a solute on the composition of flux is intimately connected with the complexing properties of solute and solvent molecules/atoms. In the

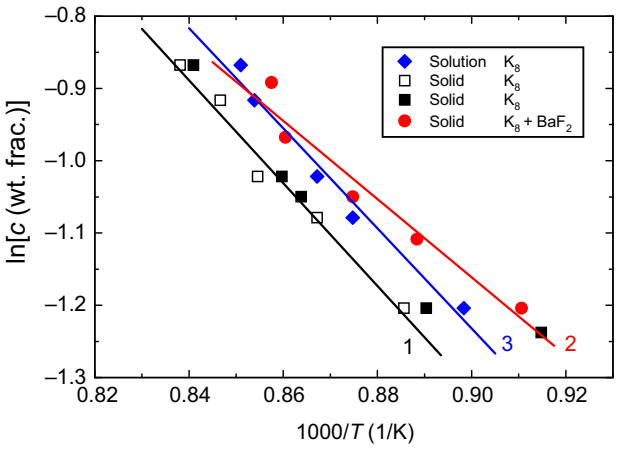

FIGURE 29.13 Plots of ln c against $1/T$ for KTP in different solvents according to Eqn (29.5). *Data from Figure 29.12.*

Table 29.3 Parameters A and ΔH_s for Solubility of KTP Prepared from Solution and Solid in K_8 and $K_8 + BaF_2$ Solvents

Solute Origin	Solvent	A	ΔH_s (kJ/mol)	T_m (K)
Solution	K_8	5.0 ± 0.54	57.6 ± 5.1	722 ± 78
Solid	K_8	5.09 ± 0.49	59.1 ± 4.8	715 ± 68
	$K_8 + BaF_2$	3.71 ± 0.63	45.0 ± 5.9	685 ± 116

case of temperature dependence of solubility of a solute in different solvents, the solubility difference is reflected by the enthalpy of dissolution ΔH_s. For example, the increase in the solubility of KTP due to the addition of BaF_2 to K_8 solvent leads to a decrease in ΔH_s. The relationship between ΔH_s and solvent composition is associated with solute–solvent interactions. The increase in the solubility of a solute with an increase in one of the components of high-temperature solvents is also associated with these solute–solvent interactions.

29.3.4 Crystal Growth Techniques

Depending on the method of achieving supersaturation in the solution, the techniques of growing crystals from high-temperature solutions may be grouped into three types. These are temperature reduction (i.e., slow cooling of the solution), solvent evaporation, and temperature gradient methods. In these methods, the driving force (i.e., supersaturation) for growth is ensured by the values of the cooling rate of the solvent, the solvent evaporation rate, and the temperature difference between saturated and growth zones, respectively. In the slow-cooling method, the cooling rate is typically around 1 K/h.

Crystal growth in high-temperature solutions may be carried out on spontaneously nucleated seeds as well as on seeds grown and prepared independently. Growth involving spontaneously nucleated seeds is usually carried out in slow cooling and solvent evaporation methods, but the crystals obtained by these methods are relatively small. These small crystals developed on self-nucleated seeds are subsequently used as seeds to grow large samples by temperature gradient methods.

29.3.4.1 Slow-Cooling Method

Crystal growth by slow cooling is commonly used for producing small specimens. The method has the advantage that the apparatus is simple (a furnace, a crucible, and a temperature programmer) and a growth run requires poor attention after the beginning of the growth process. Conventional horizontal muffle furnaces and small crucibles are usually sufficient for crystal growth by this method.

The main difficulties of growth by slow cooling are that the flux introduces strain in the crystals due to its different thermal expansion coefficient than that of the crystal, and the high nucleation density results in small size of crystals. The former difficulty is overcome by draining away the flux before starting fast cooling. The latter difficulty may

be solved by using small temperature oscillations at the nucleation stage or by initiating nucleation in a small region by localized cooling by blowing a stream of cold air (cold finger technique).

A silicon carbide heating element furnace, with a recrystallized alumina tube lining, in a vertical configuration ensures the growth of large single crystals of high melting-point materials [89]. The main components of this growth arrangement are silicon carbide heating element, crucible support, and double crucible system. For the growth of crystals of relatively low melting-point materials, a kanthal-wire bound furnace operating up to about 1200 °C can be used instead of a silicon carbide heating element.

The furnace arrangement enables one to grow crystals of different materials and composition by changing the muffle and crucible support. The double crucible system involves an inner, smaller crucible containing a crystal growing mixture and a bigger crucible placed inverted over the smaller one. After the completion of growth when this system is inverted, the solution left over in the inner crucible is drained out into the outer bigger crucible and the cooling program is commenced to cool the crucible to room temperature. This procedure enables one to obtain big crystals free of flux adhering to them.

It should be mentioned that horizontal muffle furnaces have traditionally been used for the growth of different materials by the slow-cooling method. After the completion of a growth run, the grown crystals are extracted from the unused flux by dissolving in water or in some acid or alkali.

29.3.4.2 Solvent Evaporation Method

The solvent evaporation method is usually used to grow single crystals of substances that are stable over a narrow temperature range. A simple horizontal muffle furnace to maintain a constant temperature and a crucible containing the chemicals are sufficient for crystal growth experiments. Unlike in the case of slow-cooling method, even a temperature programmer is not required. Because growth occurs at a constant temperature, the concentration of equilibrium defects and the incorporation of solvent ions as impurities remains constant in a growing crystal. The main problem is of control of the rate of evaporation of the solvent (and hence the growth rate), and the poisonous and/or corrosive nature of the solvent vapor released when an open growth system without provision of collection of solvent vapor is used.

The above problem is overcome in closed systems (Figure 29.14) in which the evaporation rate is controlled by varying the temperature T_2 at which solvent condensation takes place. In these closed systems, a crystal is made to grow in the lower part of the crucible where the temperature $T_1 < T_2$. Consequently, mass transport to the growing crucible is possible mainly by solutal convection. Therefore, growth is solutal diffusion controlled unless stirring is applied. For closed systems, this can be achieved by the accelerated crucible rotation technique (ACRT). In this arrangement, the evaporation rate is determined by the dimensions r_1 and r_2 and by the temperatures T_1 and T_2.

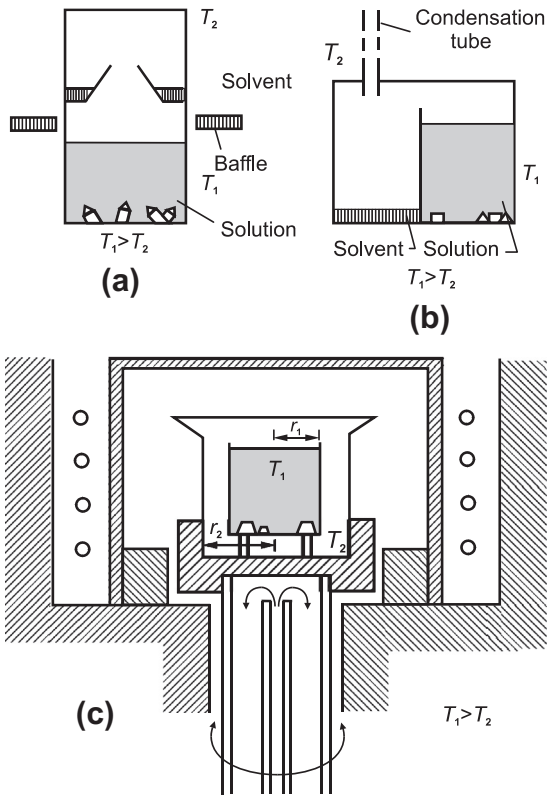

FIGURE 29.14 Arrangement for growth by flux evaporation: (a) system with collection of condensed solvent, (b) condensation of solvent in a tube, and (c) flux evaporation–condensation system with ACRT stirring. *From Ref. [64], with permission of Elsevier.*

29.3.4.3 Temperature Gradient Methods

In the temperature gradient methods, nutrient (solute) is held at a temperature T_1, whereas a growing crystal is held at a temperature T_2 such that $T_1 > T_2$. Due to the temperature difference, the solution is supersaturated and growth takes place on self-nucleated seeds or on an appropriately mounted seed surface in the supersaturated solution. Solute transport to the seed is ensured by natural or forced convection. Depending on the direction of the temperature gradient, crystal growth may be carried out either at the bottom of the crucible/ampoule or in the top part of the solution.

In the temperature gradient methods, introduction of the seed in the top part of the solution is popular. This method is known as the top-seeded solution growth (TSSG) method. An example of the apparatus used for such a growth is presented schematically in Figure 29.15 [90]. It consists of a vertical muffle furnace heated by a resistance heater, a platinum crucible, and a seed rotating system. The platinum crucible is placed on an alumina support and the furnace top is covered by an alumina lid with observation

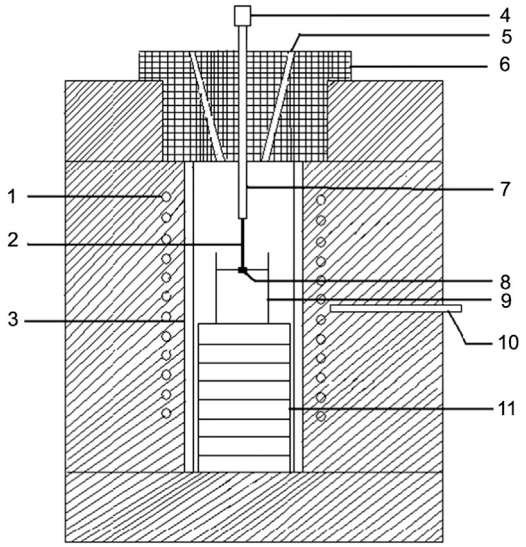

FIGURE 29.15 Schematic diagram of apparatus used for top-seeded solution growth: (1) resistance heater, (2) platinum rod, (3) alumina tube, (4) seed rotator, (5) observation hole, (6) alumina lid, (7) seed holding rod, (8) mounted seed, (9) platinum crucible, and (10) alumina support. *From Ref. [90], with permission of Elsevier.*

holes. Instead of large alumina support (10), crucible support bases on a long rods passing through the furnace bottom have also been proposed [79,84].

In some cases, the mounted seed has also be allowed to grow in the interior of the solution instead of keeping it in the top layer. This type of growth technique has been called the dipping solution technique [91]. The high growth yield in this arrangement of the seed in the solution is due to the high-temperature gradient in the lower part of the solution.

29.3.4.4 Other Methods

Among the other methods of crystal growth from high-temperature solutions are electrocrystallization and micropulling-down method. The principle of electrolytic crystallization from high-temperature solutions is essentially the same as used in conventional electrocrystallization from low-temperature solutions. The most difficult step is the selection of a solvent for growth. However, once a solution composition is known, crystallization can be carried out at constant current, constant potential difference between cathode and anode, or at a constant overpotential. Materials as diverse as bronzes, elemental and compound semiconductors, high T_c oxide superconductors, borides, CeS, ThS, MoS_2, Mo_2C, and lanthanum manganates have been grown by this method. However, the method has been poorly explored. For further details, the reader is referred to the literature [69,92–98].

A micropulling-down method from molten solutions has been proposed for the growth of high-quality fiber crystals [73,99]. The principle of the method is similar to

crystal pulling. Crystalline fiber of the desired material nucleated at the tip of a platinum pipe is pulled down from the central part of the bottom of a crucible containing molten solution of appropriate composition. Growth of $KNbO_3$ fiber crystals has been reported by this method.

29.3.5 Growth Instability and Facet Formation

It is usually observed that crystals grown by top-seeded solution growth show a tendency to develop faceting at the crystal–liquid interface. The faceting planes are usually the slowest growing, low-index planes. Faceting leads to deterioration of the quality of the growing crystal as a result of trapping of inclusions of solution and bubbles and release of internal stresses related to facet formation. Therefore, knowledge of optimum experimental parameters ensuring facet-free growth from high-temperature solution is useful.

An interesting study devoted to origin of facet formation was carried out by Szaller et al. [100], who grew stoichiometric lithium niobate (sLN) along the z-direction from 12.3 mol% K_2O and $Li_2O/Nb_2O_5 = 1$ in the starting liquid. Growth was carried out with a pulling rate of 0.2 mm/h and constant rotation rate in the range of 8–28 rpm, as well as a gradually decreasing rotation rate starting from 30−45 rpm at the shoulder down to 26 rpm at the end. In the experiments, a cone angle of 120 and 75° maintained the crystal-to-crucible diameter ratio at approximately 1:2 at the cylindrical part, whereas height-to-diameter of the crucible was 40/50 mm. Evolution of crystal quality was studied on the (0001) slices cut perpendicular to the growth direction.

This study showed that the degree of structural perfection in the crystals is strongly affected by the necking process and that growth ridges on the shoulder surface and facets on the growth front are the main sources of crystal defects. After the introduction of seed, crystal grows with conically increasing diameter on a strongly convex growth front until the desired diameter is attained. Increases in the crystal diameter and ridge formation depend on the cone angle, whereas stresses associated with large ridges favor both cracking and mechanical twinning of the as-grown crystal during its final cooling down.

It was found [100] that growth of high-quality, facet-free stoichiometric lithium niobate crystals was possible by applying gradually variable rotation rate. Optimal conditions for the growth of good-quality crystals was achieved for $\mathrm{Gr}/\mathrm{Re}^2 > 1$, where the dimensionless Grashof number $\mathrm{Gr} = g\beta\Delta T R^3/\nu^2$ is characteristic for buoyancy and the Reynolds number $\mathrm{Re} = \omega r^2/\nu$ is characteristic for forced convection. In these relationships, R is the crucible radius, r is the crystal radius, β is the volume expansion coefficient of the crystal, g is the acceleration due to gravity, ΔT is the radial temperature difference at the melt surface, ν is the kinematic viscosity of the melt, and ω is the crystal rotation speed.

29.4 Summary and Outlook

Crystallization in a laboratory, in an industrial plant, or in nature always occurs in a fluid medium of known or unknown composition in which a solid crystalline phase is

produced. In all these cases, an understanding of the processes involved in the formation of the solid crystalline phase is important. Intensive studies devoted to the understanding of crystallization processes started in the 1960s, with simultaneous rapid development in the techniques of growing single crystals due the increasing demand of materials for technological applications. These studies resulted not only in improvement in our general understanding of crystallization processes but also provided insight into the processes responsible for the nucleation and growth of crystals and the dependence of nucleation and growth rates on various external and internal factors. However, despite a long history and broad application of solution growth, a complete understanding of the detailed mechanisms that determine how crystal surfaces grow from a surrounding solution still remains elusive.

A strong influence of growth of single crystals from solutions in the present-day technology is evident from recent advances in the fields of the production of materials ranging from micrometer-sized, crystalline organic pharmaceutical chemicals to mass-scale, large inorganic nonlinear optical crystals. The growth of large single crystals from aqueous solutions is of interest for essentially two reasons. First, these large crystals find applications in the area of high-power laser technology. Second, research into this area of crystal growth and the corresponding in-depth examination of several key systems provides fundamental case studies generating theory and technology applicable to all of solution crystal growth, including new aqueous growth systems and high-temperature solution growth. Moreover, rapid-growth techniques developed during recent years have stimulated studies on the processes of single-crystal growth from solution at high supersaturations and have revealed new phenomena that were difficult to see before in crystals growing slowly at low supersaturations.

Acknowledgment

The authors express their gratitude to Dr K. Wójcik for preparing several figures presented in this chapter.

References

[1] Sangwal K. In: Encyclopedia of materials science: science and technology. Amsterdam: Elsevier; 2001. p. 3670.

[2] Buckley HE. Crystal growth. New York: Wiley; 1951.

[3] Brice JC. The crystal growth from liquids. Amsterdam: North-Holland; 1973.

[4] Petrov TG, Treivus EB, Punin Yu O, Kasatkin AP. Vyrashchivanie Kristallov iz Rastvorov [Crystal growth from solutions]. Leningrad (Russia): Nedra; 1983.

[5] Chernov AA. Modem crystallography III, crystal growth. Berlin: Springer-Verlag; 1984.

[6] Wilke K-Th, Bohm J. Kristallzüchtung. Berlin: VEB Deutscher Verlag der Wissenschaften; 1988.

[7] Henisch HK. Crystals in gels and Liesegang rings. Cambridge: Cambridge University Press; 1988.

[8] Rodriguez-Clemente R, Veintemillas-Verdaguer S, Rull-Perez F, Sangwal K. Prog Cryst Growth Charact 1988;17:1–40.

[9] Sangwal K, Sokołowski T, Wiktorowska B. In: Sangwal K, editor. Elementary crystal growth. Lublin: Saan Publishers; 1994. p. 255 [chapter 8].

[10] Nývlt J, Söhnel O, Matuchova M, Broul M. The kinetics of industrial crystallization. Prague: Academia; 1985.

[11] Sangwal K. CrystEngComm 2011;13:489.

[12] Sangwal K. Cryst Res Technol 2009;44:231.

[13] Sangwal K. Cryst Growth Des 2009;9:942.

[14] Sangwal K. J Cryst Growth 2011;318:103.

[15] Sangwal K. J Cryst Growth 2010;312:3316.

[16] Sangwal K, Mielniczek-Brzóska E, Barylska S. Chem Eng Res Des 2014;92:491.

[17] Mullin JW. Crystallization. 4th ed. Oxford: Butterworth-Heinemann; 2001 [chapter 5], p. 181–215.

[18] Yokotani A, Koide H, Yomanuro K, Sasaki T, Yamanaka T, Yamanaka C. Rev Laser Eng 1983; 11:162.

[19] Sasaki T, Yokotani A. J Cryst Growth 1990;99:820.

[20] Zaitseva NP, Rashkovich LN, Bogatyreva SV. J Cryst Growth 1995;148:276.

[21] Zaitseva NP, DeYoreo JJ, Dehaven MR, Vital RL, Montgomery KE, Richardson M, et al. J Cryst Growth 1997;180:255.

[22] Sankaranarayanan K, Ramasamy P. J Cryst Growth 2005;280:467.

[23] Mohameed HA, Ulrich J. Cryst Res Technol 1996;31:27.

[24] Sharma SK, Verma S, Shrivastava BB, Wadhawan VK. J Cryst Growth 2002;244:342.

[25] Rashkovich LN, Mkrtchyan AA, Chernov AA. Sov Phys Crystallogr 1985;30:219.

[26] Maiwa K, Tsukamoto K, Sunagawa I. J Cryst Growth 1990;102:43.

[27] Vekilov PG, Kuznetsov Yu G, Chernov AA. J Cryst Growth 1992;121:643.

[28] Burton WK, Cabrera N, Frank FC. Philos Trans R Soc Lond A 1951;243:299.

[29] Chernov AA. Sov Phys Uspekhi 1961;4:116.

[30] De Yoreo JJ, Land TA, Rashkovich LN, Onischenko TA, Lee JD, Monovskii OV, Zaitseva P. J Cryst Growth 1997;182:442.

[31] Sangwal K. Additives and crystallization processes: from fundamentals to applications. Chichester: Wiley; 2007.

[32] Bredikhin VI, Ershov VI, Korolikhin VV, Lizyakina VN, Potapenko SYu, Khlyunev NV. J Cryst Growth 1987;84:509.

[33] Rashkovich LN, Kronsky NV. J Cryst Growth 1997;182:434.

[34] Sangwal K. J Cryst Growth 2002;242:215.

[35] Kubota N, Yokota M, Mullin JW. J Cryst Growth 2000;212:480.

[36] Sangwal K, Mielniczek-Brzóska E. J Cryst Growth 2002;242:421.

[37] Sangwal K. Cryst Res Technol 2005;40:635.

[38] Frank FC. In: Doremus RH, Roberts BW, Turnbull D, editors. Growth and perfection of crystals. New York: Wiley; 1958. p. 411.

[39] Cabrera N, Vermilyea DA. In: Doremus RH, Roberts BW, Turnbull D, editors. Growth and perfection of crystals. New York: Wiley; 1958. p. 393.

[40] van der Putte P, van Enckevort WJP, Giling LJ, Bloem J. J Cryst Growth 1978;43:659.

[41] Land TA, Martin TL, Potapenko S, Palmore GT, DeYoreo JJ. Nature 1999;399:442.

[42] Weaver ML, Qiu SR, Hoyer JR, Casey WH, Nancollas GH, DeYoreo JJ. Chem Phys Chem 2006;7:2081.

[43] Mielniczek-Brzóska E, Giełzak-Koćwin K, Sangwal K. J Cryst Growth 2000;212:532.

[44] Sangwal K, Mielniczek-Brzóska E. Cryst Res Technol 2001;36:837.

[45] Sangwal K, Mielniczek-Brzóska E. J Cryst Growth 2001;233:43.

[46] Sangwal K, Mielniczek-Brzóska E, Borc J. Cryst Res Technol 2003;38:103.

[47] Mielniczek-Brzóska E, Sangwal K. Cryst Res Technol 2004;11:993.

[48] Kern R. In: Sheftal NN, editor. Rost Kristallov (Growth of crystals), vol. 8. Moscow: Nauka; 1967. p. 5.

[49] Davey RJ. In: de Jong EJ, Jancic SJ, editors. Industrial crystallization. New York: North-Holland; 1979.

[50] Bliznakov GM, Kirkova EK. Z Phys Chem 1957;206:271.

[51] De Vries SA, Goedtkindt P, Bennett SL, Huisman WJ, Zwanenburg MJ, Smilgies D-M, et al. Phys Rev Lett 1998;80:2229.

[52] Enqvist Y, Partanen J, Louhi-Kultanen M, Kallas J. Trans IChemE 2003;81:1354.

[53] Kern R, Dassonville R. J Cryst Growth 1992;116:191.

[54] Kim WJ, Kim SD, Jung HS, Hayhurst DT. Micropor Mesopor Mater 2002;56:89.

[55] Kuznetsov V, Okhrimenko T, Rak M. J Cryst Growth 1998;193:164.

[56] Srinivasan K, Meera K, Ramasamy P. J Cryst Growth 1999;205:457.

[57] Gliko O, Zaitseva N, Rashkovich LN. Res Soc Symp Proc 2001;620. M9.9.1.

[58] Voronkov VV, Rashkovich LN. J Cryst Growth 1994;144:107.

[59] Moret M. Mater Chem Phys 2000;66:177.

[60] Rudneva EB, Manomenova VL, Voloshin AÉ, Kaminskiĭ AA, Vasil'ev AB, Mchedlishvili BV. Crystallogr Rep 2006;51:142.

[61] Pritula I, Gayvoronsky V, Kolybaeva M, Puzikov V, Brodyn M, Tkachenko V, et al. Opt Mater 2011; 33:623.

[62] Pritula IM, Kosinova AV, Vorontsov DA, Kolybaeva MI, Bezkrovnaya ON, Tkachenko VF, et al. J Cryst Growth 2012;355:26.

[63] Bensouici A, Plaza JL, Halimi O, Boudine B, Sebais M, Dieguez E. J Optoelectron Adv Mater 2008; 10:3051.

[64] Elwell D, Scheel HJ. Crystal growth from high-temperature solutions. London: Academic Press; 1975.

[65] Timofeeva VA. Rost Kristallov iz Raztvorov-Razplavov (Crystal growth from the flux). Moscow: Nauka; 1978.

[66] Wanklyn BM. In: Pamplin BR, editor. Crystal growth. Oxford: Pergamon; 1975. p. 217.

[67] Görnert P, Voigt F. In: Kaldis E, editor. Current topics in materials science, vol. 11. Amsterdam: North-Holland; 1984. p. 1.

[68] Dąbkowska HA. In: Sangwal K, editor. Elementary crystal growth. Lublin, Poland: Saan; 1994. p. 303 [chapter 9].

[69] Chen C-K. Prog Cryst Growth Charact Mater 1998;36:1.

[70] Hu J, Hu Z-G. J Cryst Growth 2009;311:4235.

[71] Ivanenko VI, Zatovsky IV, Slobodyanik NS, Nadgornyi PG, Baumer NV. Cryst Res Technol 2008;43:355.

[72] Watanabe K. Cryst Res Technol 1999;34:47.

[73] Chani VI, Shimamura K, Fukuda T. Cryst Res Technol 1999;34:519.

[74] Khalyavin DD, Shiryaev SV, Bychkov GL, Barilo SN, Istinovich SN, Szymczak H, et al. Cryst Res Technol 2003;38:748.

[75] Sun DL, Hang Y, Zhang LH, Luo GZ, Zhu SN, Lim PK, et al. Cryst Res Technol 2004;39:511.

[76] Udono H, Matsumura K, Osugi IJ, Kikuma I. J Cryst Growth 2005;275:e1967.

[77] Dąbkowski A, Dąbkowska HA, Greedan JE, Ren W, Mukherjee BK. J Cryst Growth 2004;265:2004.

[78] Ujihara T, Seki K, Tanaka R, Kozawa S, Alexander, Morimoto K, et al. J Cryst Growth 2011;318:389.

[79] Yue T, Hu Z, Chen C. J Cryst Growth 2008;310:1264.

[80] Xie HD, Shen DZ, Xie CZ, Wang XQ, Shen GQ. Cryst Res Technol 2006;41:961.

[81] Lin CT, Liang B, Chen HC. J Cryst Growth 2002;237:778.

[82] Jing F, Wu Y, Fu P. J Cryst Growth 2006;292:454.

[83] Sun R, Li X, Zhang Q, Fang B, Zhang H, Lin D, et al. J Cryst Growth 2012;341:34.

[84] Yu X, Hu Z-G. J Cryst Growth 2010;312:2415.

[85] Wanklyn B. J Cryst Growth 1983;65:533.

[86] Görnert P, Sinn E. In: Kaldis E, editor. Crystal growth of electronic materials. Amsterdam: Elsevier; 1985. p. 23.

[87] Sinn E, Linzen D, Fischer K. Cryst Res Technol 1985;20:965.

[88] Lu Y, Jie W, Wang T, Zheng X, Xu Y, Luan L. J Cryst Growth 2012;355:33.

[89] Rao SM, Wu MK, Srivastava JK, Monk BH, Yen NY, Lin HY, et al. Cryst Res Technol 2006;41:859.

[90] Yu X, Yue Y, Yao J, Hu Z-G. J Cryst Growth 2010;312:3029.

[91] Ujihara T, Maekawa R, Tanaka R, Sasaki K, Kuroda K, Taeda Y. J Cryst Growth 2008;310:1438.

[92] Elwell D. In: Kaldis E, Scheel HJ, editors. Current topics in materials science, vol. 2. Amsterdam: Elsevier; 1977. p. 605.

[93] Elwell D. J Cryst Growth 1981;52:741.

[94] Feigelson RS. Adv Chem 1980;186:243.

[95] Elwell D, Feigelson RS. Sol Ener Mater 1982;6:123.

[96] Elwell D, Rao GM. J Appl Electrochem 1988;18:15.

[97] McCarroll WH, Ramanujachary KV, Greenblatt M, Cosandey F. J Solid State Chem 1998;136:322.

[98] McCarroll WH, Fewcett ID, Greenblatt M, Ramanujachary KV. J Solid State Chem 1999;146:88.

[99] Yoon DH, Yonenaga I, Fukuda T, Ohnishi N. J Cryst Growth 1994;142:339.

[100] Szaller Zs, Peter A, Polgar K, Szabo Gy. J Cryst Growth 2012;360:181.

30 Crystallization Mechanisms of High Critical Temperature Superconductors

Yuh Shiohara, Teruo Izumi

SUPERCONDUCTIVITY RESEARCH LABORATORY, INTERNATIONAL SUPERCONDUCTIVITY TECHNOLOGY CENTER, KAWASAKI, KANAGAWA, JAPAN

CHAPTER OUTLINE

30.1 Introduction **1230**
30.2 High T_c Oxide Superconductors **1231**
30.2.1 Variety of HTSC Materials 1231
30.2.2 Crystal Structure and Characteristic Properties of YBCO System 1232
30.3 Requirement for Applications of HTSC Materials; Key Factors for Higher J_c **1233**
30.4 Phase Diagram of HTSC Material **1233**
30.4.1 Phase Diagrams of Y-Ba-Cu-O and RE-Ba-Cu-O Systems 1234
30.4.2 Quasi-ternary Phase Diagram 1235
30.4.3 Standard Gibbs Free Energy Change for Formation 1236
30.5 Bulk Crystal Growth Methods from the Melt **1239**
30.5.1 Melt Texture Growth 1239
30.5.2 Quench and Melt Growth and Melt Powder Melt Growth 1240
30.5.3 Seeding Method 1240
30.5.4 Directional Solidification Method 1242
30.6 Single Crystal Growth Methods from the Solution **1243**
30.6.1 Flux Method 1243
30.6.2 Traveling Solvent Floating Zone Method 1244
30.6.3 Top-seeded Solution Growth Method (Solute-rich Liquid Crystal-Pulling Method) 1244
30.6.3.1 SRL-CP Method 1244
30.6.3.2 Enlargement of Single Crystal Size in SRL-CP Method 1246
30.6.3.3 Other RE-123 Single Crystal Growth 1248

Handbook of Crystal Growth. http://dx.doi.org/10.1016/B978-0-444-63303-3.00030-4
Copyright © 2015 Elsevier B.V. All rights reserved.

30.7 Controlling Factors of Crystal Growth from the Melt and Solution 1248
30.7.1 Supersaturation as a Driving Force for Crystal Growth 1248
30.7.2 Faceted Growth 1249
30.7.3 Experimental Measurements of Anisotropic Growth Rate 1249
30.7.4 Trapping Phenomena of High-temperature Stable Phase (Y-211) Particles into Y-123 Crystal 1250
30.8 Crystal Growth Mechanism 1251
30.8.1 Rate-Limiting for Crystal Growth 1251
30.8.2 Solute Diffusion Model for Unidirectional Solidification 1252
30.8.2.1 Basic Growth Mechanism 1252
30.8.2.2 Driving Force of Solute Diffusion 1253
30.8.2.3 Flux Provided by Dissolution of Y-211 Particle 1255
30.8.2.4 Flux Required for Y-123 Growth 1255
30.8.2.5 Steady State Growth Rate 1256
30.8.2.6 Macrosegregation Mechanism of Pushing/Trapping Model 1256
30.8.3 Crystal Growth Mechanism of SRL-CP Method 1257
30.8.3.1 Basic Growth Mechanism of Solute Diffusion Model with Interfacial Kinetics 1257
30.8.3.2 Interface Kinetics Estimated from Spiral Growth 1259
30.8.4 Crystal Growth Mechanism Using Ternary Phase Diagram 1261
30.9 Tetragonal to Orthorhombic Phase Transition (Twin Formation) 1263
30.9.1 Experimental Measurements of Oxygen Diffusion Coefficient in $REBa_2Cu_3O_{7-\delta}$ (RE: Y & Nd) Crystal 1264
30.9.2 Diffusion Mechanism 1265
30.9.3 Twins and Tweed Pattern Due to Strains in Orthorhombic Phase 1268
30.9.4 Detwinning and Twin-free Crystal by Mechanical Stress 1269
30.10 Conclusion 1270
Acknowledgments 1271
References 1271

30.1 Introduction

The discovery of high critical temperature (T_c) superconducting (HTSC) materials with superconductivity characteristics above 30 K in the La-Ba-Cu-O system by Bednorz and Müller [1] in 1986 initiated great excitement in the field of superconductivity research and spurred an unprecedented effort by many research groups to discover and/or explore materials with a higher T_c. Some exhibit superconductivity above the boiling point of liquid nitrogen, which is much less expensive, easier to handle, and has a higher heat capacity than liquid helium, and can be used as a coolant.

The disappointing low critical current density (J_c) for HTSC systems worried many scientists about future potential for application. In particular, the critical current (I_c) and T_c characteristics were regarded as important benchmarking characteristics for HTSC applications, and these initial findings temporarily quelled the superconductor fever. Together with the opinions held by renowned physicists from around the world, *Science*, a world-class science magazine, published a shocking abstract entitled, "Superconductivity: is the party over?" [2]. Since J_c and I_c are strongly microstructure dependent rather than the intrinsic property of T_c, the control of the microstructure is very important. In principle, high J_c applications require a structurally perfect matrix of bulk superconductors. Consequently, understanding and R&D of crystal growth are indispensable especially in the field of HTSC.

Of the many HTSC materials discovered so far, $YBa_2Cu_3O_{7-\delta}$ (Y-123) [3] or RE $Ba_2Cu_3O_{7-\delta}$ (RE-123), in which RE represents a rare earth element, is the most widely studied. In this chapter, we review the progress in HTSC crystal growth research concerning the solidification process, and crystal growth mechanisms of Y-123 and other RE-123 superconducting oxides. Some of the problems related to crystal growth and epitaxy of HTSC compounds were reviewed by H. J. Scheel. [4]

30.2 High T_c Oxide Superconductors

30.2.1 Variety of HTSC Materials

Since Bednorz and Müller discovered high T_c oxide superconductors (La-Ba-Cu-O system) [1], a variety of attempts have been made to find new high T_c superconducting materials. This has led to the rapid discovery of superconducting materials above the boiling point of liquid nitrogen (77 K), first in the Y-Ba-Cu-O (YBCO) system ($T_c \sim 90$ K) [3], later in the Bi-Sr-Ca-Cu-O (BSCCO) ($T_c \sim 110$ K) [5], Tl-Sr-Ca-Cu-O (TSCCO) ($T_c \sim 120$ K) [6], and Hg-Ba-Ca-Cu-O (HBCCO) ($T_c \sim 130$ K) [7] systems. These compounds possess perovskite or oxygen-deficient perovskite structures. Furthermore, numerous new superconductors have been discovered including MgB_2 ($T_c \sim 39$ K) [8] and $LaFeAs(O_{1-x}F_x)$ ($T_c \sim 26$ K) [9] systems, although their T_c values are below 77 K.

The following specific characteristics are common in high T_c superconductors, at least in oxide superconductors:

1. the compounds consist of a number of elements including copper and have layered CuO_2 structures;
2. the two-dimensionality (anisotropy) in characteristics is large;
3. the coherence length (ξ), which is the characteristic length determining the superconducting property, is extremely short (less than 20 Å).

These three factors must be considered to fabricate the superconducting crystalline materials [10].

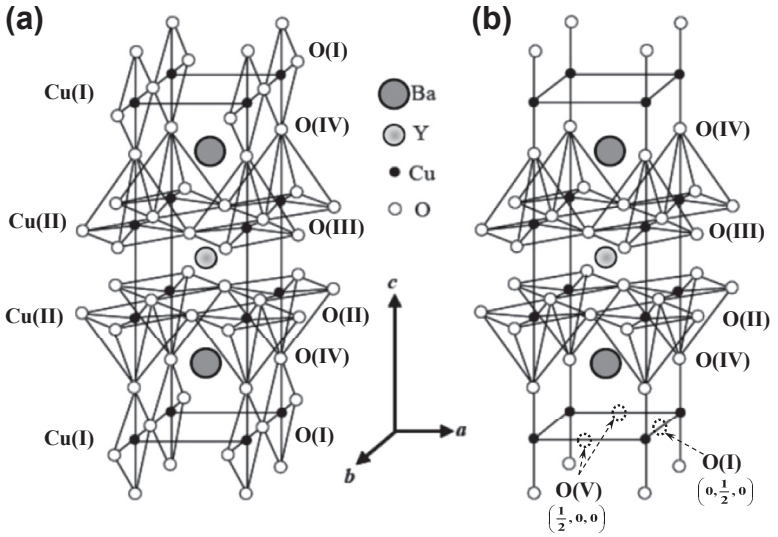

FIGURE 30.1 Crystal structure of $YBa_2Cu_3O_{7-\delta}$: (a) orthorhombic phase ($\delta < 0.5$); (b) tetragonal phase ($0.5 < \delta < 1.0$).

30.2.2 Crystal Structure and Characteristic Properties of YBCO System

YBCO materials have a distorted oxygen-deficient perovskite structure of $YBa_2Cu_3O_{7-\delta}$ (Y-123), where $\delta = 0 \sim 1$. $YBa_2Cu_3O_{7-\delta}$ is orthorhombic (Figure 30.1(a)) when the δ value is smaller than approximately 0.6, but when δ increases more than about 0.6, a transition occurs to form a tetragonal structure (Figure 30.1(b)) [10,11]. The tetragonal phase is not superconducting and shows a temperature dependence of resistivity similar to that of semiconductors and/or insulators; the orthorhombic phase is a superconductor below T_c and exhibits a metallic resistivity trend above T_c, as shown in Figure 30.2. T_c value strongly

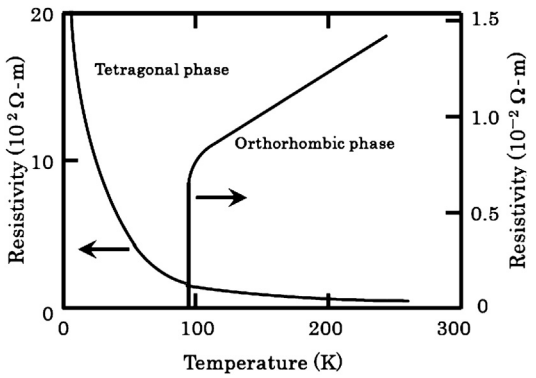

FIGURE 30.2 Temperature dependence of the resistivity for orthorhombic and tetragonal phases in Y-123 [12].
© 1987. The Japan Society of Applied Physics.

depends on oxygen concentration of 7-δ in the orthorhombic Y-123 [13,14]. The phase transition from tetragonal to orthorhombic depends on oxygen partial pressure in the atmosphere (P_{O_2}) and temperature (T) [15,16]. At higher T and/or low P_{O_2}, the tetragonal phase is stable. The Y-123 materials fabricated by high temperature processes, including sintering, melt growth, and vapor deposition with high substrate temperatures, have a tetragonal phase. Accordingly, the materials should be slowly cooled or post-annealed in an oxygen atmosphere for oxygenation to obtain an orthorhombic phase with high T_c, as was mentioned by H. J. Scheel [17].

Most rare earth (RE) elements can be substituted for yttrium (Y) without any destructive effects on the superconducting characteristics of Y-123 crystal. For example, the T_c value of Nd-123 reached about 96 K, which is several degrees higher than that of Y-123. In general, T_c and peritectic temperature (T_p) increase with increasing ionic radius [10]. This is because RE^{3+} ions easily substitute into the Ba^{2+} site [18–20].

30.3 Requirement for Applications of HTSC Materials; Key Factors for Higher J_c

Even in the best prepared high density bulk sintered samples, the J_c values remain very low (of the order of 10^3 A/cm^2 at 77 K) in zero applied magnetic field and decrease drastically when a magnetic field is applied, even though the T_c values are the same [10]. This can be considered to be mainly due to the random orientation of grains, i.e., the existence of high angle grain boundaries. This is supported by the fact that single crystals exhibit one or two orders of magnitude larger J_c values than polycrystalline samples [21]. We call the grain boundaries "weak links," which decrease J_c. Dimos et al. [22] have shown that J_c decreases with increasing misorientation angle between the neighbored grains, and such behavior is independent of the preparation method. This result suggests that a high angle grain boundary is intrinsically weak links, which is due to an extremely short coherence length (ξ) in oxide superconductors.

The following are dominant factors required for fabrication of high J_c materials [10]:

1. fewer weak links (no secondary inclusion at the grain boundary);
2. highly oriented texture (grain alignment);
3. presence of effective magnetic flux pinning;
4. highly and appropriately doped oxygen content (higher T_c).

30.4 Phase Diagram of HTSC Material

Equilibrium phase diagram is a useful tool to optimize a parameter used in the fabrication processes of materials and to understand crystal growth mechanisms. The following difficulties in determination of reliable phase relations were pointed out [23]: (1) the complexity of the ternary or multicomponent systems, (2) the valency change of Cu^{2+} and Cu^{+} and the very slow oxygenation of the investigated sample to the

saturated amount for the equilibrium state even with a high external oxygen partial pressure, (3) the sluggish reactions typical for peritectic systems and for large melting point differences of constituent oxides, and (4) corrosion of all candidates of commercial crucibles [24].

In the field of HTSC materials, much effort has been made to determine the thermodynamically stable and metastable phases as a function of temperature and oxygen partial pressure [25–30]. Most these investigations were concentrated for the solid state. However, for better understanding of crystal growth from the liquid (melt), the detailed information about a higher temperature phase diagram, including liquid phase, is extremely important.

30.4.1 Phase Diagrams of Y-Ba-Cu-O and RE-Ba-Cu-O Systems

The calculated isothermal sections of the Y_2O_3-BaO-CuO ternary system are reported by B. J. Lee and D. N. Lee [31,32] on the basis of the results obtained by Lay and Renlund [29] and Lindemer et al. [16]. The two-phase equilibrium composition region of liquid and $YBa_2Cu_3O_{7-\delta}$ is reduced rapidly by increasing temperature because of evolution of Y_2BaCuO_5. To show this more effectively, a vertical section containing Y_2BaCuO_5 (Y-211), $YBa_2Cu_3O_{7-\delta}$ (Y-123), and a mixture of $3BaCuO_2$ and 2CuO is shown in Figure 30.3. This figure shows that the liquidus line of liquid/Y-123 is very steep over the temperature range from 1237 to 1275 K. Krauns et al. [33] have experimentally measured the liquidus compositions of yttrium in the $Ba_3Cu_5O_8$ solvent (melt), which are superimposed in Figure 30.3 [10].

As for most rare earth elements (RE≡Y, Yb, Dy, Gd, Sm, Nd, etc.), yttrium can be substituted with the 123 structure. Although the RE-123 phase is formed by similar peritectic reactions to the Y-Ba-Cu-O system, the high temperature stable phase in the

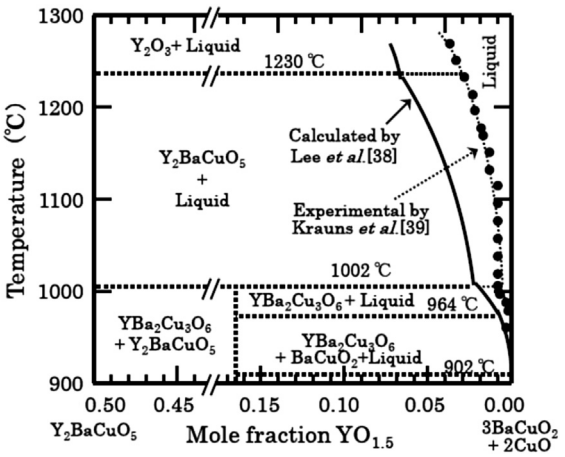

FIGURE 30.3 Calculated vertical section of the Y_2O_3-BaO-CuO_x system at 0.21 atm oxygen pressure and experimental results of liquidus line [10,33].

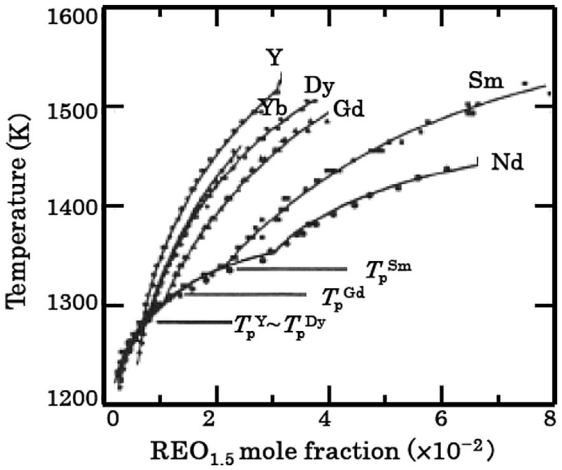

FIGURE 30.4 Liquidus lines (solubility) of RE elements in the $Ba_3Cu_5O_8$ melt under an air atmosphere. RE≡Y, Yb, Dy, Gd, Sm and Nd [10,33–35].

Nd-Ba-Cu-O system is not the same stoichiometric composition ratio as that of Y-211 but $Nd_4Ba_2Cu_2O_{10}$(Nd-422). Figure 30.4 shows the liquidus lines of the rare earth elements in the $Ba_3Cu_5O_8$ solvent (melt) in the air atmosphere [33–35]. The peritectic temperature (T_p) increases with the atomic number of the RE element (i.e., ionic radius). Near the T_p temperatures, the slopes of the liquidus decrease and the RE solubility increases with the atomic number of RE elements.

The effects of oxygen partial pressures on the liquidus lines were also reported [36]. The results indicate that decreasing the oxygen pressure decreases the T_p and increases the steepness of the slope of the liquidus lines near the T_p, which means a similar tendency could be observed when increasing oxygen partial pressure and/or when increasing the atomic number of RE elements.

30.4.2 Quasi-ternary Phase Diagram

The phase relations in the neodymium (Nd) system have been intensively investigated [30,37–40]. For the purpose of fabricating a crystal of Nd-123 crystals through melt processing, quasi-ternary phase diagrams of the $NdO_{1.5}$-BaO-CuO_x system at the temperatures near the T_p of the Nd-123 phase were reported [41,42].

Figure 30.5(A) and (B) show the quasi-ternary phase diagrams of the $NdO_{1.5}$-BaO-CuO_x system near the CuO_x corner near the T_p temperatures (1073 °C and 1030 °C) in the air atmosphere [41]. As the temperature decreases, the two-phase field of the "Nd-123 + liquid" becomes large. The substitution content, i.e., Nd^{3+} ions substitute Ba^{2+} ions, in the Nd-123 crystals decrease as the BaO/CuO ratios of the liquid composition increase, and this tendency is emphasized at lower temperatures. This fact indicates that $Nd_{1+x}Ba_{2-x}Cu_3O_{6+\delta}$ (Nd-123) crystal with $x \approx 0$ could be fabricated in the air atmosphere by using the higher BaO/CuO composition ratios of the liquid.

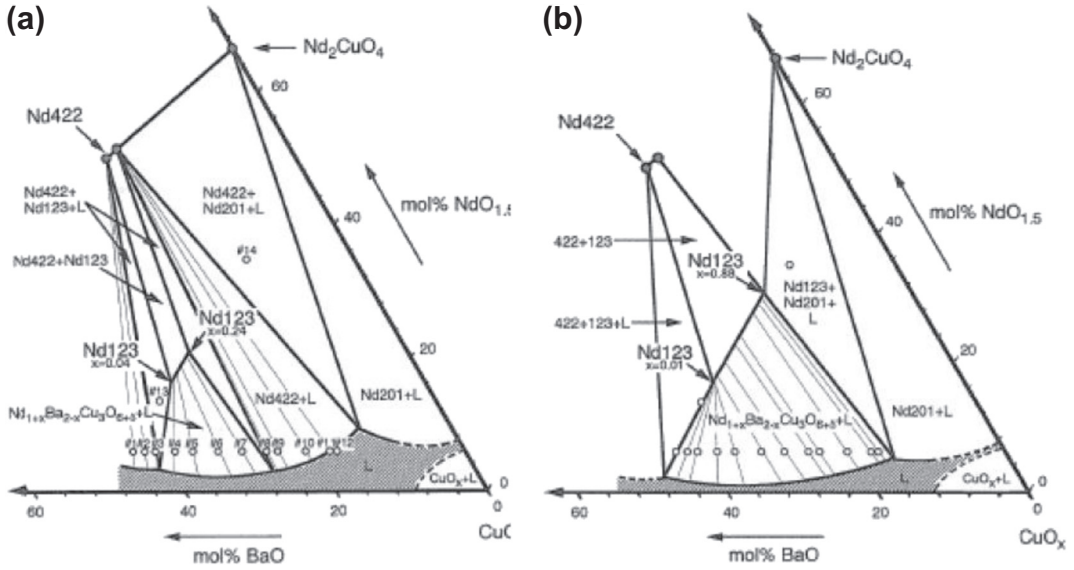

FIGURE 30.5 Quasi-ternary phase diagrams of the $NdO_{1.5}$-BaO-CuOx system near the CuOx corner at/around the peritectic temperatures. (a) 1073 °C, and (b) 1030 °C in air of the $Nd_{1+x}Ba_{2-x}Cu_3O_{6+\delta}$ (Nd-123) solid solution phase [41]. © *1998 Wiley-Blackwell.*

Another significant feature in the RE-Ba-Cu-O systems is the existence of a solid solution in the RE-123 phase of $RE_{1+x}Ba_{2-x}Cu_3O_{6+\delta}$, for light RE elements such as RE ≡ La, Nd, Sm, Eu, Gd, while Y-123 is a stoichiometric compound for cations [18,37,38]. This is considered to be due to the relatively large radii of the RE ions. It was reported that the solid solutions of $Nd_{1+x}Ba_{2-x}Cu_3O_{6+\delta}$ and $Nd_{4+y}Ba_{2-y}Cu_2O_{10+z}$ and that the solubility limits were $x < 0.6$ and $y < 0.2$, respectively, and oxygen contents of $6 + \delta$ and $10 + z$ change accordingly [37].

Effects of the oxygen partial pressure in the atmosphere on the temperature range of the solid solution of the Nd-123 phase are shown in Figure 30.6 [42]. The solubility range of Nd-123 under 0.01 atm of P_{O_2} is quite narrow. On the contrary, in the 1.00 atm of P_{O_2}, the range is wider than that in air.

30.4.3 Standard Gibbs Free Energy Change for Formation

Standard Gibbs free energy changes (ΔG°) for syntheses of $YBa_2Cu_3O_{6.5+x}$, Y_2BaCuO_5, and $Y_2Cu_2O_5$ were reported with experimental results by using chemical thermodynamic methods [43]. For the reaction where $YBa_2Cu_3O_{6.5+x}$ was synthesized by the $Y_2Cu_2O_5$-$BaCO_3$-CuO mixture with the discharge of the CO_2, the equilibrium temperature and the relations of the partial pressure of CO_2 were examined by thermal gravimetric analysis. The equilibrium temperature (1080–1190 K) was determined by observing the change of sample weight at a given temperature in a stream of a CO_2-O_2-N_2 gas mixture. A similar experiment was carried out for the synthesis of Y_2BaCuO_5 from a $Y_2Cu_2O_5$-Y_2O_3-$BaCO_3$

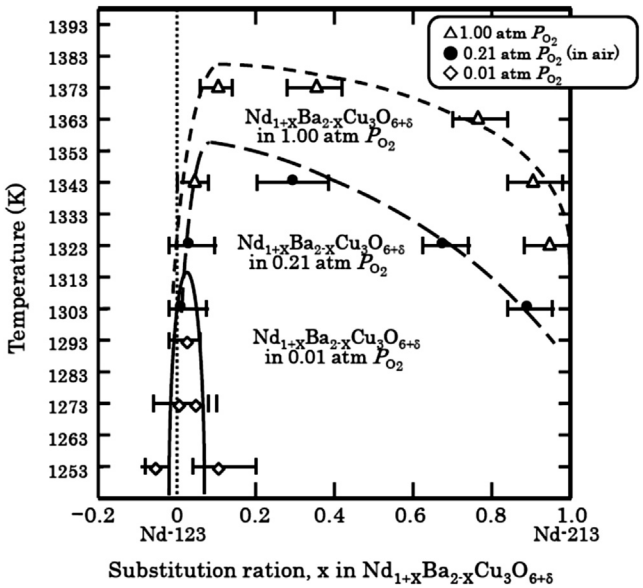

FIGURE 30.6 Solubility limit of the $Nd_{1+x}Ba_{2-x}Cu_3O_{6+\delta}$ in the temperature-composition section for different partial oxygen pressure atmospheres. ($P_{O_2} = 0.01$, 0.21, 1.00 atm) [42].

mixture. Measurements of electromotive force of the galvanic cell with a zirconia solid electrolyte were conducted for the synthesis of Y_2BaCuO_5 from Y_2O_3 and CuO. The standard Gibbs free energy change for formation of Y_2BaCuO_5 was derived from the partial pressure of O_2 in the equilibrium among Y_2BaCuO_5, Y_2O_3, and Cu_2O. By combining these results, the standard Gibbs free energy changes for formation of $YBa_2Cu_3O_{6.5+x}$ and Y_2BaCuO_5 from Y_2O_3, $BaCO_3$, and CuO were obtained.

$YBa_2Cu_3O_{6.5+x}$ decomposes to liquid and Y_2BaCuO_5 at about 1280 K in the air atmosphere. Effects of the oxygen partial pressure (P_{O_2}) on the decomposition were also examined by means of powder X-ray diffraction analysis, thermal gravimetric analysis, and differential thermal analysis [44]. The relation between $YBa_2Cu_3O_{6.5+x}$ and temperature when the decomposition occurred was expressed as:

1.

$$x = 0.00353T - 5.08 \quad (1218 - 1313\ \text{K}) \tag{30.1}$$

Several reactions and standard Gibbs free energy changes related to the formation of $YBa_2Cu_3O_{6.5+x}$ are summarized as follows [43–45]:

2.

$$\frac{1}{2}Y_2Cu_2O_5 + 2BaCO_3 + 2CuO + \frac{x}{2}O_2 = YBa_2Cu_3O_{6.5+x} + 2CO_2 \tag{30.2-a}$$

$$\Delta G_1^\circ = -2RT \ln \frac{P_{CO_2}}{P^\circ} + \frac{x}{2}RT \ln 0.21 = 480000 - 341T \pm 6000\ (\text{J/mole}) \quad (1080 - 11190\ \text{K}) \tag{30.2-b}$$

3.

$$\frac{1}{2}Y_2Cu_2O_5 + \frac{1}{2}Y_2O_3 + BaCO_3 = Y_2BaCuO_5 + CO_2 \tag{30.3-a}$$

$$\Delta G_2^\circ = 273000 - 205T \pm 4000 \text{ (J/mole)} \quad (1090 - 1210 \text{ K}) \tag{30.3-b}$$

4.

$$\frac{1}{2}Y_2BaCuO_5 + \frac{3}{2}BaCO_3 + \frac{5}{2}CuO = YBa_2Cu_3O_{6.5} + \frac{3}{2}CO_2 \tag{30.4-a}$$

$$\Delta G_3^\circ = 34600 - 241T \pm 7000 \text{ (J/mole)} \quad (1090 - 1210 \text{ K}) \tag{30.4-b}$$

5.

$$Y_2O_3 + 2CuO = Y_2Cu_2O_5 \tag{30.5-a}$$

$$\Delta G_4^\circ = 9100 - 14T \pm 1000 \text{ (J/mole)} \quad (1025 - 1220 \text{ K}) \tag{30.5-b}$$

6.

$$\frac{1}{2}Y_2O_3 + 2BaCO_3 + 3CuO = YBa_2Cu_3O_{6.5} + 2CO_2 \tag{30.6-a}$$

$$\Delta G_5^\circ = 482000 - 344T \pm 6500 \text{ (J/mole)} \quad (1080 - 1190 \text{ K}) \tag{30.6-b}$$

7.

$$Y_2O_3 + BaCO_3 + CuO = Y_2BaCuO_5 + CO_2 \tag{30.7-a}$$

$$\Delta G_6^\circ = 278000 - 212T \pm 4500 \text{ (J/mole)} \quad (1090 - 1210 \text{ K}) \tag{30.7-b}$$

8.

$$\frac{1}{2}Y_2O_3 + 2BaCO_3 + 3CuO + \frac{x}{2}O_2 = YBa_2Cu_3O_{6.5+x} + 2CO_2 \tag{30.8-a}$$

$$\Delta G_7^\circ = 485000 - 348T \pm 6500 \text{ (J/mole)} \quad (1080 - 1190 \text{ K}) \tag{30.8-b}$$

9.

$$\begin{gathered} YBa_2Cu_3O_{6.5} = Y_2BaCuO_5 + \text{Liquid} + O_2 \\ \text{Liquid} : YO_{1.5}(2.0 \text{ mol\%}), BaO(37.0 \text{ mol\%}), CuO + CuO_{0.5}(61.0\%) \end{gathered} \tag{30.9-a}$$

$$\begin{gathered} \Delta G_8^\circ = -RT \ln\left(P_{O_2}/P^\circ\right) = 965000 - 736T \text{ (J/O}_2\text{mole)} \quad (1080 - 1190 \text{ K}) \\ P^\circ = 1.013 \times 10^5 \text{ Pa(1atm)} \end{gathered} \tag{30.9-b}$$

10.

$$\frac{1}{2}Y_2BaCuO_5 + \frac{3}{2}BaCuO_2 + CuO = YBa_2Cu_3O_{6.5} \tag{30.10-a}$$

$$\Delta G_9^\circ = -3500 + 6.65T \text{ (J/(123)mole)} \tag{30.10-b}$$

11.

$$2\mathrm{CuO} = \mathrm{Cu_2O} + \frac{1}{2}\mathrm{O_2} \tag{30.11-a}$$

$$\Delta G^{\circ}_{10} = 146300 + 25.5T \log T - 185T \ (\mathrm{J/mole}) \tag{30.11-b}$$

12.

$$\mathrm{Nd_4Ba_2Cu_2O_{10}} + \mathrm{Liquid} + \mathrm{O_2} = \mathrm{NdBa_2Cu_3O_{7-\delta}} \tag{30.12-a}$$

$$\Delta G^{\circ}_{11} = 779T - 1077000 \ (\mathrm{J/(O_2)mole}) \tag{30.12-b}$$

30.5 Bulk Crystal Growth Methods from the Melt

Although sintering was very common and showed a lot of advantages in ceramics processing, it was not able to produce oxide superconductors with the high values of critical current densities (J_c) primarily due to the existence of weak links at the grain boundaries as mentioned before. It was pointed out that a high angle grain boundary was intrinsically the weak link due to a combination of a small coherence length and large anisotropy. The melt solidification process has overcome this weak link problem by grain alignment leading to high J_c superconductors. Solidification methods for synthesis of bulk HTSC crystals could be classified into two groups [10]:

1. solidification from semisolids (i.e., liquid + Y-211 phase) provides high J_c Y-123 bulk crystals;
2. solidification from solution (i.e., liquid) provides high crystallinity bulk single crystals.

We must make the various phenomena, which are caused with the phases (liquid, liquid + solid, solid), clear to control the microstructures of HTSC materials, which have an influence on crystallinity as well. Microscopically, the similar phase transitions take place in nondirectional solidification processing, including melt-texture-growth (MTG) [46], quenched-melt-growth (QMG) [47], and melt-powder-melt-growth (MPMG) [48] methods and the solute rich liquid crystal pulling (SRL-CP) method [49,50]. The SRL-CP method was developed for pulling a Y-123 single crystal, which is in fact a modified top-seeded solution growth (TSSG) technique.

30.5.1 Melt Texture Growth

Melt processing of Y-123 was initiated by Jin et al. [46], and it was named the MTG process. As shown in Figure 30.3, there are two peritectic reactions in the Y-Ba-Cu-O system. At high temperatures above 1200 °C, the Y_2O_3 solid phase and Y-deficient Ba-Cu-O liquid phase are stable. On cooling, these two phases transform peritectically to produce Y_2BaCuO_5 (Y-211). At around 1000 °C, Y-211 reacts with liquid to produce $YBa_2Cu_3O_{7-\delta}$ (Y-123).

In the case of the MTG process, precursor samples with a stoichiometric formula of $YBa_2Cu_3O_{7-\delta}$ are slowly cooled through either of these two peritectic reactions, or at least the latter reaction in the presence of the temperature gradient of 20–50 °C/cm in an oxygen atmosphere. The MTG sample so produced exhibits a dense structure consisting of locally aligned, long, needle-shaped grains and higher transport J_c (above 10^4 A/cm^2) at 77 K in a zero applied magnetic field than that (several hundreds A/cm^2) of typical sintered (bulk) materials [46].

30.5.2 Quench and Melt Growth and Melt Powder Melt Growth

The QMG and MPMG methods were developed to control the size of the dispersed Y-211 particles as effective magnetic flux pinning centers in order to increase J_c in magnetic fields [47,48]. First, the sintered sample is heated to the Y_2O_3 + liquid region and splat quenched using cold copper blocks. The quenched sample consists of Y_2O_3 particles and the solidified liquid phases (a mixture of $BaCu_2O_2$, CuO, and amorphous phases). The quenched plates are then reheated to the Y-211 + L region, where the Y-211 phase is formed by a peritectic reaction between Y_2O_3 and the liquid. Then, the sample is cooled to form a crystal of the Y-123 phase. By the QMG method, Y_2O_3 particles tend to segregate due to sedimentation, which causes nonuniform distribution of the Y-211 phase particles. By the MPMG method, melt quenched plates are crushed into fine powders and mixed well in order to refine the Y_2O_3 particles with uniform distribution. The pellets are then rapidly heated to the Y-211 + L region. After an appropriate holding time, the sample is rapidly cooled to the temperature just above T_p and then slowly cooled. It is remarkable that the size of the Y-211 phase crystals is much finer and their distribution is much more uniform than those in the MTG and QMG sample, resulting in high J_c-B characteristics, i.e. high critical current density in magnetics fields of B.

30.5.3 Seeding Method

The nucleation of the crystal is affected by the frequency of occurrence of nucleation events for the Y-123 phase. Accordingly, multiple nucleation takes place, resulting in the existence of several grains within a small pellet. The control of crystal orientation and number of grains is also required, since HTSC materials are highly anisotropic and possess weak links due to high angle grain boundaries, which reduce the J_c values.

It was shown that certain materials, such as Y_2O_3 powder, Sm_2O_3 powder, Nd_2O_3 powder, ZrO_2 powder, MgO single crystal, and various oxide thin films could be employed as heterogeneous nucleation reagent seeds for Y-123 [51]. However, the single domain of RE-123 can rarely be obtained. Morita et al. [52] and Sawano et al. [53] demonstrated that single crystals or quasi-single crystals of other RE-123 systems, such as Sm-123 and Nd-123, which have higher peritectic temperatures than Y-123, could act as seeds for crystal growth because the seed remains in a solid form when Y-123 is

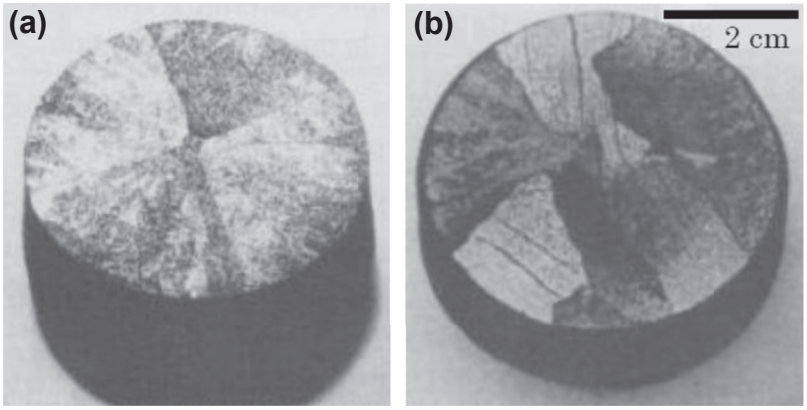

FIGURE 30.7 Appearance of (a) single-grained and (b) poly-grain melt grown bulk crystals. Note that in the single-grained crystal, the growth started at the center of the sample where a seed crystal was placed [53]. © *1991 The Japan Society of Applied Physics.*

heated above T_p. On subsequent cooling, a Y-123 crystal grows epitaxially from the seed. The entire pellet with a seed is composed of only one grain due to the elimination of the multiple nucleations as shown in Figure 30.7. The seeding method has been widely used to produce melt-textured YBCO and NdBCO samples [54–56].

Researchers all over the world have investigated several oxide seed materials that are suitable for Y-123 epitaxial growth. The fundamental criterion for the epitaxial growth is defined by the crystal lattice mismatch, ϕ, which can be given by:

$$\phi = (\lambda_c - \lambda_s)/\lambda_s \tag{30.13}$$

where, λ_c and λ_s are the crystal lattice parameters of the crystal and the substrate (seed), respectively.

For the case of $SrTiO_3$ seed crystal ($\lambda_a = 3.905$ Å), as an example, for the c-axis epitaxial growth, the lattice mismatch with the lattice parameter of the Y-123 crystal (3.8578 Å) is calculated as in the following Eqn (30.14), which is explained before in Eqn (30.13):

$$\frac{3.8578\ \text{Å} - 3.905\ \text{Å}}{3.905\ \text{Å}} \times 100\% \approx -1.21\% \tag{30.14}$$

Consequently, it is possible to select a seed material with less lattice mismatch to the Y-123 crystal lattice. Pseudocubic lattice parameters in Table 30.1 were defined as the following Eqn (30.15):

$$\lambda_{a_{cubic}} = \lambda_{b_{cubic}} = \frac{\sqrt{\left(\frac{\lambda_{a_{cubic}}}{2}\right)^2 + \left(\frac{\lambda_{b_{cubic}}}{2}\right)^2}}{2} = \lambda_{110} \quad or \quad \frac{\lambda_{a_{cubic}}}{n \times \sqrt{2}} \tag{30.15}$$

where n is integer. Pythagoras' theorem from the actual cubic lattice parameters could provide the pseudocubic lattice parameters. For the case of Y_2O_3 seed crystal

Table 30.1 Structure, Lattice Mismatch Data for *c*-axis Epitaxial Growth of YBCO for Various Seed Crystals

	Structure Type		% Lattice Mismatch
Buffers Layer Material	**Cubic Lattice Parameter Å**	**Pseudocubic Å**	**vs YBCO**
$BaCeO_3$	4.377		−11.86
MgO	4.203		−8.21
$BaZrO_3$	4.193		−7.99
La_3TaO_7	11.054	3.908	−1.30
$SrTiO_3$	3.905		−1.28
$YBa_2Cu_3O_{7-\delta}$	3.8578		0
Eu_2O_3	10.868	3.842	0.41
$NdGaO_3$	5.431	3.840	0.46
CeO_2	5.411	3.826	0.83
Gd_2O_3	10.813	3.823	0.91
$La_2Zr_2O_7$	10.786	3.813	1.17
$LaAlO_3$	5.364	3.793	1.71
Ga_3NbO_7	10.659	3.769	2.36
Y_2O_3	10.604	3.749	2.90
$Gd_2Zr_2O_7$	5.264	3.722	3.65
Y_3NbO_7	5.250	3.712	3.93
Yb_2O_3	10.436	3.690	4.55
YSZ($Y_2O_3$13%–$ZrO_2$87%)	5.125	3.624	6.45

($\lambda_a = 10.604$ Å), as an example, the pseudocubic lattice parameter is calculated as in the Eqn (30.16),

$$\frac{10.868\ \text{Å}}{2 \times \sqrt{2}} = 3.749\ \text{Å} \tag{30.16}$$

and the lattice mismatch with the lattice of the c-axis epitaxially grown Y-123 crystal is calculated as in the following equation:

$$\frac{3.8578\ \text{Å} - 3.749\ \text{Å}}{3.749\ \text{Å}} \times 100\% \approx 2.90\% \tag{30.17}$$

30.5.4 Directional Solidification Method

Meng et al. [57] fabricated a bar of the Y-123 compound with grain alignment by moving a sintered sample in a horizontal tube furnace with a temperature distribution almost equivalent to the temperature history at the time of crysta1 growth in the QMG/MPMG process. McGinn et al. [58–60] produced textured polycrystals in extruded Y-123 wires by zone melting in a vertical tube furnace. Izumi and Shiohara [61] applied a horizontal Bridgman method and a floating zone melting method to the YBCO system and obtained $J_c = 2 \times 10^4$ A/cm^2 at 77 K and 1 T of the applied magnetic field. Figuredo et al. [62] used

a laser-heated floating zone technique, which can provide higher temperature gradient (G) above 1000 °C/mm compared with a resistance heater, and J_c values larger than 10^5 A/cm^2 at 77 K and self field were achieved.

The temperature gradient (G) and the growth rate (R) are important process parameters to control microstructures in directional solidification. In general, G/R and $G \times R$ affect the crystal grain alignment and the grain size. In the Y-Ba-Cu-O system, the effect of the G/R ratio on the changes in the morphology of the growth interface was examined by Izumi et al. [63]. Although no nucleation ahead of the interface was recognized in the samples grown at high growth rates, the Y-123 phase crystal grains were discontinuous and possessed equiaxed-like and blocky structures. In contrast, the samples grown at slow rates with higher G (i.e., high G/R) showed continuous growth and a cellular structure composed of very well-aligned grains. Faceted interfaces were recognized in the samples, and the cell spacing increased with decreasing growth rate R. The morphological change from the equiaxed-like to the planar with increase of the G/R ratio accords with the theory of constitutional supercooling [64], at least its tendency. As a result, the increase in the J_c values of zone-melted samples with increasing G/R could be recognized even at the same cooling rates ($G \times R$) [63,65].

30.6 Single Crystal Growth Methods from the Solution

High quality single crystals have been fabricated by the flux method, but their size is limited due to uncontrollable nucleation events, the very low solubility of yttrium in the BaO-CuO flux melt, and the steep slope of the liquidus line in the equilibrium phase diagram for the primary phase crystallization temperature range. Therefore, continuous growth processes, i.e., TSFZ and TSSG methods, have been applied widely to the Y-Ba-Cu-O system, enabling fabrication of large-sized Y-123 crystals.

30.6.1 Flux Method

The flux method is one of the most commonly used processes to produce bulk single crystals in the case of incongruent melting systems such as Y-123 phase crystals [66–73]. The commonly used solvent is composed of CuO and BaO, which is called the "self-flux method." Schneemeyer et al. and others [73–76] grew single crystals. The crystals form with a layer-type morphology, similar to mica, but generally with square corners. Wolf et al. [73] optimized the melt composition and the cooling rate to obtain thick crystals, using a melt composition of Y:Ba:Cu = 1:7.5:16.5 and the cooling rate below 0.5 °C/h.

Other solvents have been tried, e.g., In_2O_3 [77], B_2O_3 [78], and KCl-NaCl [69]. The crystals grown using a KCl-NaCl f1ux were found to be relatively large in size, although they seemed to have poor crystallinity with a large number of defects [69].

In addition to the restriction in selection of suitable solvents, the progress in the growth process has also been hampered by the pronounced reactivity of the melt with

most crucible materials, which tends to contaminate the growing Y-123 crystals. Many kinds of crucible material have been used for the f1ux method, such as platinum, gold, $A1_2O_3$, ThO_2, ZrO_2, MgO, etc. Liang et al. and others [79–81] have systematically investigated the crucible materials. It was concluded that yttria-stabilized zirconia (YSZ) and yttria (Y_2O_3) crucibles are good choices for Y-123 crystal growth, preventing contamination from the crucible materials during growth.

30.6.2 Traveling Solvent Floating Zone Method

The traveling solvent floating zone (TSFZ) method is a valuable growth technique for the fabrication of high quality, large single crystals that melt incongruently. Several kinds of RE-123 crystals have been fabricated using the TSFZ method by Oka and Ito [82]. In the TSFZ method, the RE solute in the solvent required for growth of the RE-123 crystal is steadily supplied into the solvent by dissolving the RE-123 feed rod.

One of the main advantages of the TSFZ method involves containerless crystal growth, which can prevent contamination from the crucible material. At the same time, however, problems of keeping the molten zone stable during the crystal growth of RE-123 arise. Since the viscosity of the solvent composed of BaO-CuO is low, the solvent easily falls onto and penetrates deeply into the feed rod, and the solvent composition varies with time. Oka and Ito [82] have overcome this problem using high density crystallized feed rods prescanned at a high pulling rate of 2–15 mm/h.

30.6.3 Top-seeded Solution Growth Method (Solute-rich Liquid Crystal-Pulling Method)

Crystal pulling has a significant advantage in growing large single crystals. The top-seeded solution growth (TSSG) method, which is one of the crystal-pulling methods for incongruent melting materials, had not been applied to RE-123 compounds, because the promising solvent BaO-CuO flux melt is very reactive with crucible materials and cannot be maintained for a long time. Yamada and Shiohara [49] succeeded in growing Y-123 single crystals by a pulling method using a BaO-CuO solution with Y-211 solid, placed at the bottom of the yttria crucible, which supplies Y solute steadily into the solvent. This modified TSSG method has been named the solute-rich liquid crystal-pulling (SRL-CP) method, since the solute content in the solution is steadily enriched from the Y-211 solid.

30.6.3.1 SRL-CP Method

Figure 30.8 shows a schematic drawing of the configuration of the SRL-CP method. Y-211 powder was placed at the bottom of the crucible and BaO-CuO composite (Ba to Cu cationic ratio is 3:5) was placed on the layer of Y-211 powders. A temperature gradient was provided in the melt to satisfy the conditions that the temperature at the melt surface (about 1000 °C) is lower than the peritectic

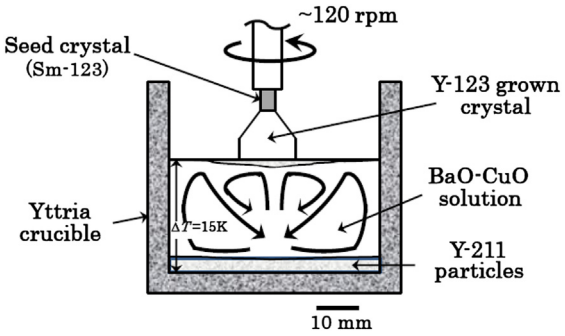

FIGURE 30.8 Configuration in the crucible during Y-123 single crystal growth using the SRL-CP method [49]. © *1993 Elsevier Science B.V.*

temperature ($T_p = 1010\,^{\circ}C$) of Y-123 and the temperature at the bottom of the melt (about 1015 °C) is higher than T_p. Accordingly, Y-211 solid can exist at the bottom of the crucible as a source of the solute. The surface of the melt was supersaturated by yttrium. In this method, the transport of the solute from the bottom of the crucible to the growing crystal is a key factor in obtaining higher crystal growth rates than those in flux methods. The solute was mainly transported by convection in the melt. In terms of the mass balance, the solute supplied from the Y-211 solid and the solvent $Ba_3Cu_5O_8$ react and form only the Y-123 phase crystal without the generation of any other by-products.

$$Y_2BaCuO_5 + Ba_3Cu_5O_8 \rightarrow 2YBa_2Cu_3O_{7-\delta} \tag{30.18}$$

A Y-123 single crystal or thin film prepared separately was used as a seed crystal. The Y-123 crystal was grown at a rotation rate of about 120 rev/min (rpm). This is relatively fast, enhancing forced convection in the melt. Since the high speed rotation makes the surface fluid flow away from the center and toward the crucible wall, it prevents the floating crystals from attaching to the growing crystal.

By optimizing the various growth conditions of the SRL-CP method, large-sized, high quality bulk single crystals of Y-123 were reproducibly fabricated. The shape of the grown Y-123 single crystal pulled along the *c*-axis in the air atmosphere is shown in Figure 30.9(A). The grown crystal is bulky and the typical size is about $14.5 \times 14.5 \times 13$ mm [83]. The square shape observed from the bottom reflects the symmetry of the *c*-axis, showing a strongly faceted nature of the crystal habit. The bottom surface is a (001) plane and the Y-l23 crystals grow epitaxially from the seed crystal. The as-grown surface was examined by atomic force microscopy (AFM), which revealed continuous beautiful spiral growth patterns as shown in Figure 30.9(B). The step height of about a few nanometers is equivalent to one or two unit cell lengths (lattice parameter) of the Y-123 crystal structure along the *c*-axis. Similar macroscopic growth spirals were observed in the films fabricated by liquid phase epitaxy (LPE) [84].

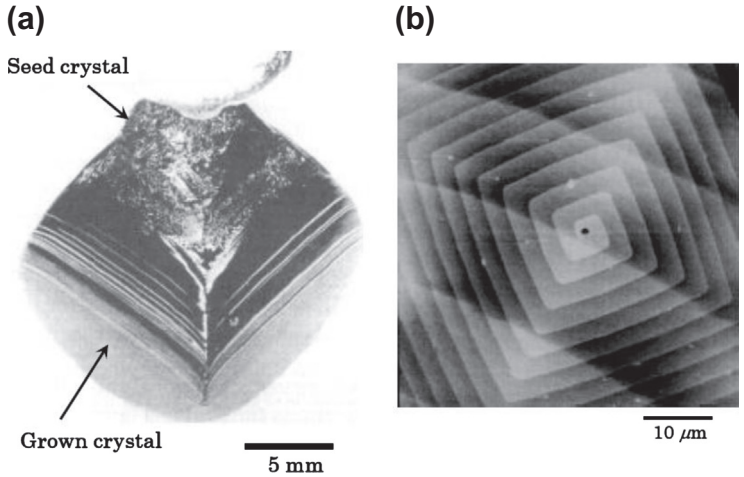

FIGURE 30.9 (a) Photo of grown Y-123 single crystal pulled along the *c*-axis from the Sm-123 seed crystal and (b) AFM image of the surface (growth interface) of the as-grown single crystal showing typical spiral growth [10,83]. © *Springer-Verlag Tokyo 1995.*

30.6.3.2 Enlargement of Single Crystal Size in SRL-CP Method

1. Increase of growth time

In the SRL-CP method, the probability of the nucleation events at the crucible wall can be hardly neg1ected. Floating particles generated on the melt surface may cause po1ycrystalline growth and the surface is finally covered with floating particles, and further growth may become impossible. However, the high speed rotation prevents the floating crystals/particles from attaching to the growing crystal as it makes the surface fluid flow away from the center to the crucible wall.

Similar to other oxide melts, the BaO-CuO flux has high viscosity, a high Schmidt number (Sc), and a high Prandtl number (Pr). Therefore, the Y solute is transferred from Y-211 placed at the bottom of the crucible to the growing Y-123 crystal mainly by melt convection, which may be affected by many factors, such as the crystal rotation rate, size of the grown crystal, temperature gradient, and crucible size.

Figure 30.10 shows the results of numerical simulations using a finite difference method for a two-dimensional axis-symmetric viscous fluid system [85]. The left part and right part of each figure show the streamlines of the melt and isotherms, respectively, within the right halves of the vertical section of the crucible. Forced convection exists below the growing crystal, which is induced by the crystal rotation and natural convection near the crucible wall. As the crystal rotation rate and/or crystal diameter increases, the forced convection becomes stronger and the meeting point of the forced and natural convection near the melt surface moves from the growing crystal to the crucible wall. The isotherms couple strongly to the

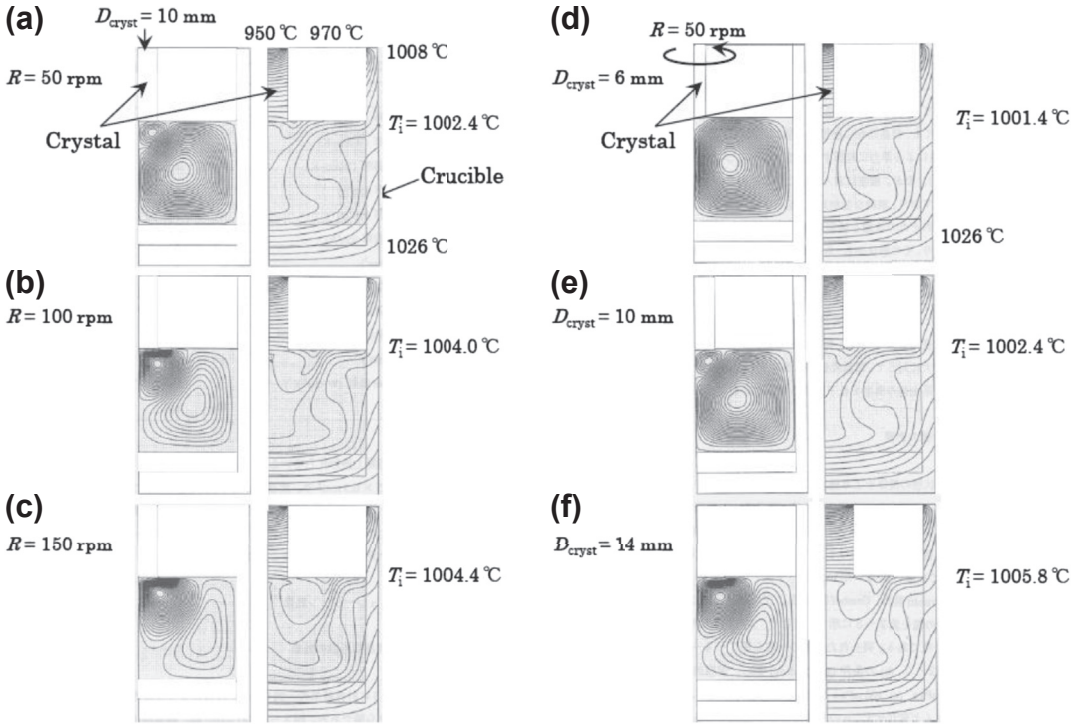

FIGURE 30.10 Numerical calculation results for 10 mm (a–c) and 6, 10, and 14 mm (d–f) diameter crystals; (a), (b), (c) show the results with crystal rotation rates of 50, 100, 150 rev/min and (d), (e), and (f) show 50 rev/min, respectively. The left part of each figure shows the stream-lines of melt convection, and right side shows the isotherms within the right halves of the vertical section of the crucible [85]. © *1996 Materials Research Society.*

convection, and the temperature at the crystal growth interface increases with increasing forced convection, i.e., crystal rotation rate, as well as with increasing the size of the crystal.

During Y-123 crystal growth, the diameter of the crystal increases with increasing the growth time, which causes a change in the crystal growth conditions. In order to maintain constant crystal growth conditions, control of the crystal rotation rate with increasing the crystal diameter is effective. Another way to circumvent this problem is to use a large crucible to make the system insensitive to the change in the crystal diameter.

2. Enhancement of growth rate

Larger single crystals can be obtained within a shorter time if the growth rate is enhanced significantly. To achieve this, supersaturation, which is the driving force for crystal growth, should be increased, e.g., simply by decreasing the surface temperature of the growing Y-123 crystal. In this case, however, the problem of floating particles comes into the picture, resulting in polycrystalline growth. Yao et al. [86]

have grown a large Y-123 crystal of 19.8 × 19.5 × 16.5 mm in size and 20 g in weight by the SRL-CP method under the high oxygen pressure atmosphere ($P_{O_2} = 1$ atm). The growth rate for $P_{O_2} = 1.0$ atm is about twice that for an air atmosphere. This was explained by the fact that, in $P_{O_2} = 1.0$ atm, the solubility of yttrium in the solvent is higher, the slope of the liquidus is lower (see Section 30.4.1), and the crystallization temperature is higher than those at $P_{O_2} = 0.21$ atm.

30.6.3.3 Other RE-123 Single Crystal Growth

The SRL-CP method has also been applied to other $RE_1Ba_2Cu_3O_{7-\delta}$ materials (RE, rare earth ≡ Sm, Nd). It has been found that bulk single crystals of several cubic millimeters in size could be repeatedly produced by the SRL-CP method after optimizing the growth conditions, such as the growth temperature, composition of the solution (melt), crucible materials, etc. [87,88].

In the case of Sm-123, the growth rate is about a factor of five faster than that of Y-123, which could be explained by the fact that the solubility of Sm in the solvent is higher, the slope of the liquidus is lower, and the crystallization temperature is higher than those for Y-123, as shown in Figure 30.4, resulting in higher mass and heat transfer for growth and easy achievement of higher supersaturation for interfacial kinetics.

Contrary to the Sm-123 crystal pulling, Nd-123 single crystals have been fabricated by the ordinary TSSG method. In this case, the high temperature stable phase (Nd-422 phase for NdBCO system) was not placed at the bottom of the crucible, and the Nd solute required for Nd-123 crystal growth was supplied only from the Nd_2O_3 crucible due to the high solubility of Nd in the Ba-Cu-O liquid phase [88].

Solid solutions are known to exist in these systems, which are described as $RE_{1+x}Ba_{2-x}Cu_3O_y$, whereas the Y-123 phase is a stoichiometric compound. In fact, the compositions of these grown crystals were measured by ICP-AES to be $Nd_{1+x}Ba_{2-x}Cu_3O_y$ ($0.01 < x < 0.1$) in which the substitution value (x) depends on the atmosphere during the growth. A low oxygen partial pressure atmosphere during crystal growth was found to be effective for minimizing the substitution of Nd^{3+} into the Ba^{2+} sites as can be seen in Figure 30.6 [88].

30.7 Controlling Factors of Crystal Growth from the Melt and Solution

30.7.1 Supersaturation as a Driving Force for Crystal Growth

In the Y-Ba-Cu-O system, a Y-123 crystal grows from the melt. The crystal melts incongruently and the solubility of yttrium in Ba-Cu-O (solvent) is very small. In the case of crystal growth from dilute solution, the driving force for crystallization is represented by supersaturation (σ) defined as:

$$\sigma = (C - C_e)/C_e \tag{30.19}$$

where C and C_e are the practical and the equilibrium concentrations of the solute in the solution, respectively.

30.7.2 Faceted Growth

The Y-123 phase crystals grown by solidification processing show clearly faceted crystal habits. According to the Jackson model [89], the faceted or nonfaceted habits of the growth interface could be roughly estimated by α (Jackson parameter):

$$\alpha = \zeta(L/k_B T) \tag{30.20}$$

where ζ is a factor (less than unity) depending on the crystallographic anisotropy, L is the latent heat of melting or dissociation, k_B is Boltzmann's constant, and T is the absolute temperature. The values of α with less than two can be taken to imply a tendency to nonfaceted crystal growth, while higher α values imply that faceted growth forms will be produced. The value of α for Y-123 crystals has been estimated to be about 20 [90]. Consequently, the growth interface of the Y-123 and/or RE-123 crystals is considered to be flat in an atomic scale.

30.7.3 Experimental Measurements of Anisotropic Growth Rate

Nakamura et al. [91], Muller and Freyhardt [92], and Imagawa and Shiohara [93] have investigated the anisotropic growth rate of Y-123 crystal, the R_a/R_c ratio, in which R_a and R_c are the growth rates of the {100} faces and the {001} faces, respectively.

In order to obtain the knowledge about the interfacial kinetics of Y-123 crystal growth, Endo et al. [94] used a seeding method using a seed of an Sm-123 crystal, combined with a constant undercooling solidification method, which has the advantages of proper control over the crystal orientation and appropriate estimation of the interfacial temperature. The Y-123 crystals were grown at several different undercoolings (ΔT). Here, ΔT is defined as the temperature difference between the T_p of the Y-123 phase ($T_p = 1010\ ^\circ C$) and the growth temperature (T_g). The dependence of ΔT on R_a is different from that on R_c, as shown in Figure 30.11. The relations between the growth rates and undercooling are described in the following power law equations:

$$R_a = 4.5 \times 10^{-7} \Delta T^{1.9} (\text{mm/s}) \tag{30.21a}$$

$$R_c = 2.8 \times 10^{-6} \Delta T^{1.3} (\text{mm/s}) \tag{30.21b}$$

The growth rate perpendicular to the *ab* plane (R_c) has been reported to be faster than that perpendicular to the *ac* plane (R_a) for Y-123 crystals grown by unidirectional solidification and the interface undercooling at a growth rate of about 1 mm/h was 30–40 K [90]. Equations (30.21a) and (30.21b) indicate that, with undercooling higher than 27 K, R_a becomes larger than R_c. Therefore, the results of the constant undercooling method are not in conflict with those of unidirectional solidification by considering the difference in undercoolings.

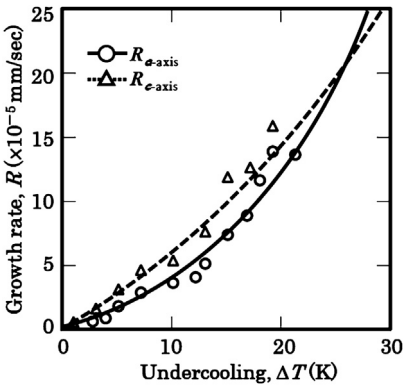

FIGURE 30.11 Relationships between the growth rate and undercooling for the growth direction of *a*-axis and *c*-axis [94]. © *Springer-Verlag Tokyo 1995.*

30.7.4 Trapping Phenomena of High-temperature Stable Phase (Y-211) Particles into Y-123 Crystal

Y_2BaCuO_5, (Y-211) inclusions are considered to act as strong magnetic flux pinning centers. In order to retain the Y-211 phase particles (inclusions) in the crystallized Y-123 grains, an overall composition shifted toward the Y-211 phase from the stoichiometric composition of Y-123 (i.e., Y-123 + x Y-211, $x > 0$) has been used. It has been assumed that the amount of excess Y-211 is completely trapped during the peritectic reaction. Macrosegregation of Y-211 particles in Y-123 crystals, observed by several groups, has stimulated interest in the investigation of the trapping phenomena of Y-211 particles [95–100].

Varanasi et al. [96,99] have observed the inhomogeneous distribution of Y-211 particles, delineating distinguishable patterns in textured Y-123 crystals with platinum additions. Kim et al. [98] also reported that fine particles were pushed out of the advancing Y-123/liquid interface toward the liquid phase in the Y-Ba-Cu-O system with metal oxide (CeO_2, SnO_2, and ZrO_2) addition. In both cases, the observed patterns of Y-211 segregation seem to exist along the boundaries between different growth directions. Investigations on the segregation of Y-211 particles have been systematically carried out by Endo et al. [97,100], which showed that the macrosegregation was dependent on the growth rate (R) as a function of the undercooling (ΔT) as well as on the growth direction.

The effect of R on the macrosegregation of Y-211 particles was reported using the results of two different kinds of heat treatment: constant undercooling and continual cooling by Sm-123 top-seeding melt texture method [94]. As shown in Figure 30.12, the amount of trapped Y-211 with high undercooling (e.g., $\Delta T = 30$ K; i.e., large R) is larger than that with low undercooling (e.g., $\Delta T = 10$ K; i.e., small R), especially in the *c*-direction [97]. The macrosegregation of Y-211 particles and their size in Y-123 crystals depends on the growth rate of the Y-123 crystals and their growth direction. The continual cooling method, such as QMG and MPMG [47,48], is commonly used for melt

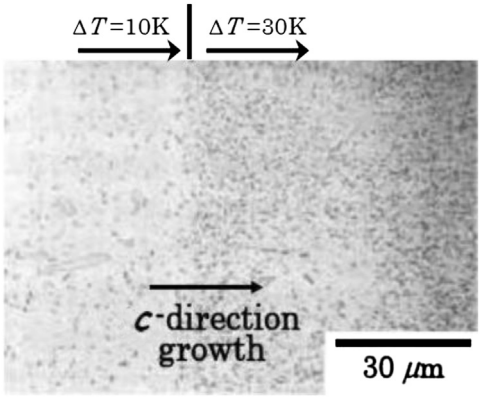

FIGURE 30.12 Cross-sectional microstructures of the grown crystal in the quenched sample. Undercooling of the sample was changed from 10 K to 30 K during the two-step undercooling method, showing drastic change in the amount of trapped Y-211 particles (dark particles in the photograph) from the 10 K undercooled region to the 30 K undercooled region [97]. © *1996 Materials Research Society.*

texture growth in the YBCO system. The distribution of Y-211 particles in the Y-123 bulk samples fabricated by this method might be inhomogeneous.

30.8 Crystal Growth Mechanism

The melt-textured Y-123 materials show a highly aligned structure, which is formed by a peritectic reaction between solid Y-211 phase particles and the liquid phase. Therefore, many studies have been performed to clarify the peritectic solidification mechanism of Y-123 crystals [63,101,102]. The solidification model is generally limited by interfacial kinetics and/or mass transport.

30.8.1 Rate-Limiting for Crystal Growth

Once a nucleus is formed, it will continue to grow. Such growth may be limited by the kinetics of atom attachment to the growth interface including its surface migration, diffusion of the solute from the environmental phase, and diffusion of latent heat for crystallization. Figure 30.13 illustrates the spatial distribution of the concentration of the solute near the growth interface during crystal growth. Initially, the solution has a uniform concentration C_0, then, as a result of cooling, a corresponding change in the equilibrium concentration C_e takes place. If the liquid concentration at the crystal growth interface, C_i, equals to C_0, the growth rate is controlled by an interface reaction process (interface control) as shown in (a) in Figure 30.13. In another extreme case, which is the case, C_i equals to C_e, the growth rate is fully controlled by diffusion in the solution (diffusion control) as shown in (C) in Figure 30.13. When the rate of incorporation of growth units to the crystal is balanced by their diffusion in the solution, C_i is not equal to either C_e or C_0 as shown in (B) in Figure 30.13 [10,103].

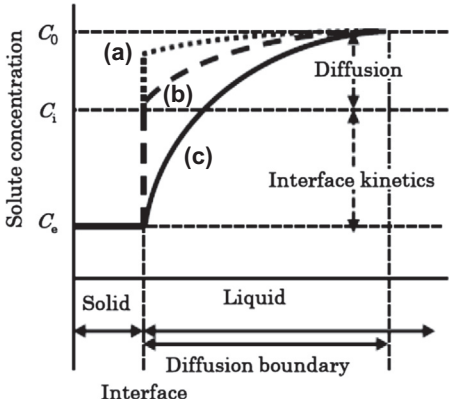

FIGURE 30.13 Solute concentration profile in the liquid in front of the growing crystals, showing the driving forces of diffusion and interfacial kinetics [10]: (a) interfacial control; (b) mixed control; (c) diffusion control.

Although the heat transfer during the crystallization is also an important factor, it could be simplified since the growth rate is sufficiently small compared with the thermal conduction in the case of Y-123 growth, suggesting that heat dissipation is relatively rapid and the assumption of an isothermal or a steady state constant temperature gradient is reasonably acceptable.

30.8.2 Solute Diffusion Model for Unidirectional Solidification

30.8.2.1 Basic Growth Mechanism

At almost the same time, three different groups proposed similar crystal growth models to explain the growth of Y-123 crystals in the directional solidification process controlled by solute diffusion [63,101,102].

Generally, in metallic alloy systems, the required solute from the high temperature stable phase solid for peritectic reaction is transferred through the solid by diffusion as shown in Figure 30.14(A). In some special cases of metallic alloys, such as Al-Mn and Cu-Sn peritectic systems, it was proposed that a part of the solute is diffused through the liquid [104,105]. A sharp faceted growth interface and a drastic change in the Y-211 volume from the semisolid region to the Y-123 crystals are observed in the sample quenched during unidirectional solidification, as shown in Figure 30.15 [63]. This observation supports the fact that the required solute for the peritectic reaction is provided by the liquid diffusion for the crystallization of the Y-123 phase. Assuming the liquid diffusion for Y-123 peritectic crystal growth as shown in Figure 30.14(B), the diffusion zone may exist in front of the planar (faceted) Y-123 interface. The liquid-diffusion-rate-limiting model for the Y-123 peritectic solidification was developed by Izumi, Nakamura, and Shiohara [63]. This so-called INS model is based on the following assumptions:

1. the rate-limiting stage for the growth of the Y-123 crystal is yttrium diffusion in the liquid since the yttrium solubility in the liquid is extremely low;

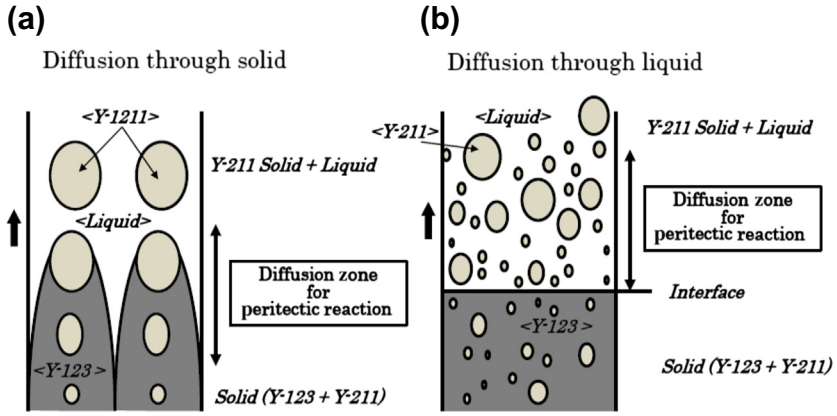

FIGURE 30.14 The expected structure around the interface in two different systems of peritectic reactions [10,61]: (a) required solutes for Y-123 growth are transported through the solid; (b) required solutes for Y-123 growth are provided through the liquid. © *1992 Materials Research Society.*

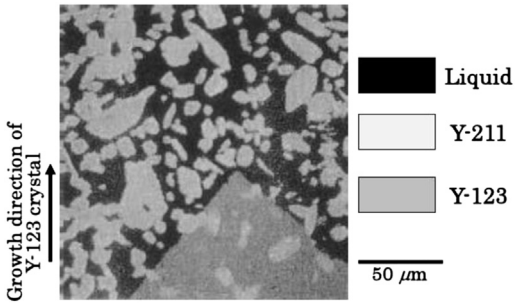

FIGURE 30.15 Y composition mapping image around the Y-123 growth interface of a sample grown at 1 mm/h. The white particles are the Y-211 phase, the gray region is the growing Y-123 phase crystal, and the black matrix is the liquid phase before quenching [63]. © *1993 Elsevier Science Publishers B.V.*

2. the interface of the growing Y-123 crystal is planar, and Y-211 particles are spherical;
3. peritectic reaction takes place isothermally;
4. thermophysical properties are constant;
5. no interaction exists between the Y-211 particles (even among particles of different sizes, e.g., Ostwald ripening).

30.8.2.2 Driving Force of Solute Diffusion

Figure 30.16 shows the principle of the liquid-diffusion-rate-limiting model. The yttrium diffusion flux for Y-123 phase crystal growth from Y-211 particles dispersed in the liquid ahead of the growth interface of the Y-123 crystal was estimated. This diffusion flux was derived from the composition difference in the liquid at the two different interfaces: liquid/Y-211 and liquid/Y-123. This composition difference consists of three origins in

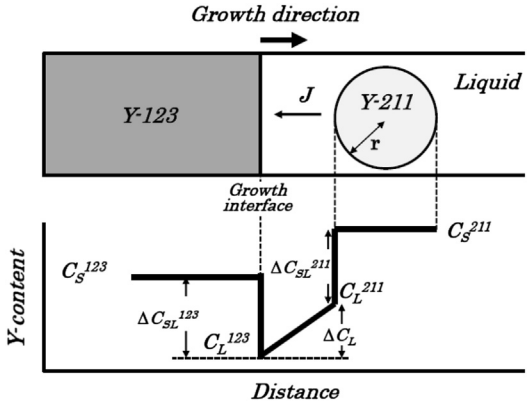

FIGURE 30.16 Sketch of the principle of the INS peritectic solidification model. The composition difference, as a driving force providing the required solute for Y-123 growth, is indicated in the composition profile [63]. © *1993 Elsevier Science Publishers B.V.*

the case of directional solidification: the curvature effect of the dispersed Y-211 particles in the liquid, ΔC_1; undercooling, ΔC_2 [101]; and the temperature gradient, ΔC_3. When the Y-211 particles approach the interface very c1osely, the temperature gradient term, ΔC_3, becomes negligibly small. Accordingly, the total composition difference, ΔC, is the sum of $\Delta C_1 + \Delta C_2$. The concept of these three origins is shown schematically in the phase diagram (Figure 30.17). ΔC can be derived from the following equation:

$$\Delta C = \frac{1}{m_L^{211}}\left(\frac{2\Gamma^{211}}{r} + G_z\right) + \left(\frac{1}{m_L^{123}} - \frac{1}{m_L^{211}}\right)\Delta T \tag{30.22}$$

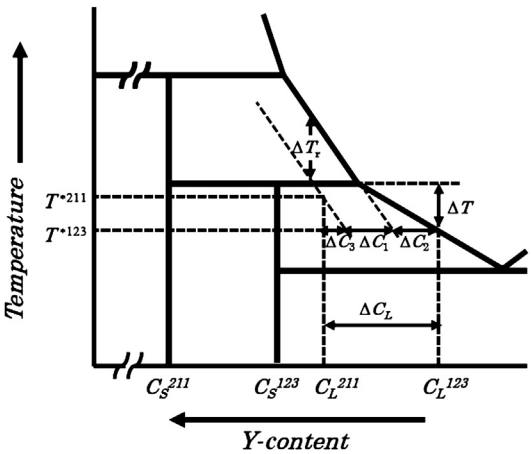

FIGURE 30.17 Origin of the composition difference used in the INS model. In this figure, T*211 and T*123 are the temperatures at the Y-211 interface and the Y-123 interface, and ΔC_1 is the supersaturation (undercooling) due to the change in chemical potential caused by the curvature of the Y-211 particle (Gibbs–Thomson effect) [63].

where m_L^{211} and m_L^{123} are the slopes of liquidus lines of the Y-211 and Y-123 phases, respectively, I^{211} is the Gibbs–Thomson coefficient ($\sigma_{211}/\Delta S_f$), σ_{211} is the Y-211/liquid interfacial energy, ΔS_f is the volumetric entropy of fusion, r is the radius of the Y-211 particle, G_z is the temperature gradient at the distance, z, from the Y-123 interface, and ΔT is the undercooling at the Y-123 growth interface.

30.8.2.3 Flux Provided by Dissolution of Y-211 Particle

The diffusion flux, $J_{r,z}$, from one Y-211 particle with a radius of r at a certain distance, z, from the Y-123 interface was calculated using Fick's first law:

$$J_{r,z} = D_L \frac{\Delta C}{z} = \left(D_L \frac{\Delta C}{\delta_c} \right) \tag{30.23}$$

where D_L is the diffusivity. Here the diffusion zone for peritectic reaction was assumed to be within the region between the maximum effective length δ_c and the Y-123 growth interface. The δ_c could be estimated as the characteristic diffusion length for planar steady state growth, D_L/R.

When the diffusion flux reaches the maximum flux (J_{max}), which is limited by the rate of decomposition of the Y-211 particles, the distance is defined as the critical length δ_c. A constant J_{max} as $4\pi r^2 k_{max}$ was assumed within δ_c using the maximum decomposition rate of the Y-211 particles (k_{max}). If the size distribution of the Y-211 particles in the region, which is out of the diffusion zone, is given initially, the total yttrium diffusion flux (J_{211}) from the Y-211 particles can be estimated by integrating the flux from the individual Y-211 particles (J or J_{max}) with respect to z and r within the diffusion zone:

$$\begin{aligned} J_{211} &= N \int_0^{\infty} \int_0^{\delta_c} J_{r,z} \Psi(r_0(r,z)) dz dr \\ &= N \int_0^{\infty} \pi r^2 \left[4k_{max}^{211} \int_0^{\delta *} \Psi(r_0(r,z)) dz + D_L \int_{\delta *}^{\delta_c} \frac{\Psi(r_0(r,z))}{z} \Delta C_L dz \right] dr \end{aligned} \tag{30.24}$$

N is the number of Y-211 particles per unit volume described as follows:

$$N = \frac{3V_f^{211}}{4 \int_0^{\infty} \pi r_0^3 \Psi(r_0) dr_0} \tag{30.25}$$

where V_f^{211} is the volume fraction of the Y-211 phase out of the diffusion zone, which can be calculated from the initial composition using the equilibrium lever rule, $\Psi(r_o(r,z))$ is the size distribution function of the Y-211 particles in the diffusion zone.

30.8.2.4 Flux Required for Y-123 Growth

According to Figure 30.13, the composition difference ΔC_{SL}^{123} at the growth interface of the Y-123 crystal can be calculated from the yttrium concentration of the Y-123 solid (C_S^{123}) and that of the liquid at the liquid/Y-123 interface (C_L^{123}), and described as follows:

$$\Delta C_{SL}^{123} = C_S^{123} - C_L^{123} = C_S^{123} - C_L^e + \frac{\Delta T}{m_L^{123}} \tag{30.26}$$

where C_L^e is the yttrium concentration of the liquid at the T_p. Then, the diffusion flux per unit area J_{123} required for Y-123 crystal growth is calculated as:

$$J_{123} = (C_S^{123} - C_i)R = \left(C_S^{123} - C_L^e + \frac{\Delta T}{m_L^{123}}\right)R \tag{30.27}$$

where R is the growth rate of the Y-123 crystal.

30.8.2.5 Steady State Growth Rate

In the steady state growth of the Y-123 crystal, the total flux from the Y-211 particles described in Eqn (30.24) should be equated with the flux indicated in Eqn (30.27). Then, the steady state growth rate, R, is given by:

$$R = \frac{3V_f^{211}\int_0^\infty r^2\left[4k_{\max}^{211}\int_0^{\delta^*}\Psi(r_0(r,z))dz + D_L\int_{\delta^*}^{\delta_C}\frac{\Psi(r_0(r,z))}{z}\Delta C_L dz\right]dr}{4\left(C_S^{123} - C_L^e + \frac{\Delta T}{m_L^{123}}\right)\int_0^\infty r_0^3\Psi(r_0)dr_0} \tag{30.28}$$

The order of magnitude of the calculated growth rates is several millimeters per hour, which is in good agreement with the experimentally confirmed growth rate for continuous growth. This model can also be used to estimate the change in size distribution of the Y-211 partic1es from the liquid to Y-123 crystals [63].

30.8.2.6 Macrosegregation Mechanism of Pushing/Trapping Model

The macrosegregation phenomenon of Y-211 particles in Y-123 crystals is similar to the pushing/trapping behavior of foreign particles at an advancing solid–liquid interface during solidification, which has been observed in various materials by many investigators [106–116]. Several theories on pushing/trapping phenomena have been proposed by considering the interaction between an inactive particle and an advancing solid–liquid interface.

Figure 30.18 is schematic drawings showing a particle in front of the solid–liquid interface and the forces acting on the particle. There are two dominant forces: the drag

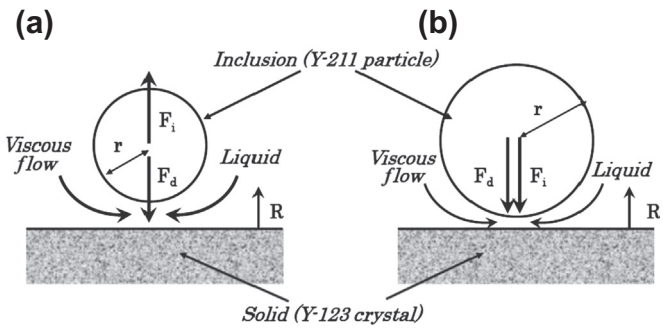

FIGURE 30.18 Schematic drawings showing a particle in front of the solid–liquid interface and the necessary condition of particle pushing [10]. (a) For $\Delta\sigma_0 > 0$. The force (F_i) due to the interfacial energy ($\Delta\sigma_0$) is conductive to pushing. (b) For $\Delta\sigma_0 < 0$. F_i is conductive to trapping. The drag force (F_d) is always conductive to trapping. © *1997 Elsevier Science S.A.*

force (F_d) due to viscous flow around the particle, which moves together with the interface at the growth rate, R, and the force (F_i) due to the interfacial energy ($\Delta\sigma_0$).

The condition for particle pushing can be described as shown in Eqn (30.29) [106]:

$$\Delta\sigma_0 = \sigma_{SP} - \sigma_{LP} - \sigma_{SL} > 0 \tag{30.29}$$

where σ_{SP}, σ_{LP}, and σ_{SL} are the solid–particle, liquid–particle, and solid–liquid interfacial energies, respectively. F_i is conducive to pushing if $\Delta\sigma_0 > 0$, while F_d is always conducive to trapping as shown in Figure 30.18. Since the results of microstructural observations in melt growth processes indicate that Y-123 heterogeneous nucleation rarely takes place on the surface of Y-211 in the supersaturated liquid [117], it is suggested the relation of $\Delta\sigma_0 > 0$ in the Y-123/Y-211 system.

According to the pushing/trapping theory, the critical size (r^*) of a particle, larger than that trapped by the growing solid crystal, is roughly determined by the critical growth rate (R^*) and interfacial energy ($\Delta\sigma_0$):

$$R* \propto \frac{\Delta\sigma_0}{\eta r*} \tag{30.30}$$

where η is the melt viscosity. The relationship between the growth rate and the radius of the inclusion is derived to be $R^* \times r^* = \text{constant}$ using Eqn (30.30).

One should be careful when applying the pushing/trapping theory to the Y-123/Y-211 system, because this theory was proposed to explain the phenomena between inclusions, which are inert for both liquid and solid, and nonfaceted material. Actually, Y-211 partic1es are reactive inclusions as they supp1y Y solute to Y-123 by decomposition for faceted growth of Y-123 materials via peritectic transformation.

30.8.3 Crystal Growth Mechanism of SRL-CP Method

The growth mechanism of the SRL-CP method proposed by Yamada et al. [118] is basically the same as the melt texture process described in Section 30.8.2.1–30.8.2.5. Major differences between these processes include the distance between the Y-211 phase and the growth interface of the Y-123 phase crystal and the solute-transport mechanism.

30.8.3.1 Basic Growth Mechanism of Solute Diffusion Model with Interfacial Kinetics

Figure 30.19 shows the quasi-binary phase diagram illustrating the solute transport path in the melt for the SRL-CP method [119]. T_b and T_i indicate the temperatures at the bottom of the crucible and at the Y-123 growth interface, respectively. The equilibrium compositions are C_L^{123} and C_L^{211}. It was assumed that the Y concentration is uniform in the bulk liquid maintained by the natural and forced convections, except in the diffusion boundary layer near the growth interface of Y-123 phase crystal. The thickness, δ_c, of the solute diffusion boundary layer could be estimated, which is different from the above mentioned D_L/R (see Section 30.8.2.3.). Under the Cochran flow assumption [120], which

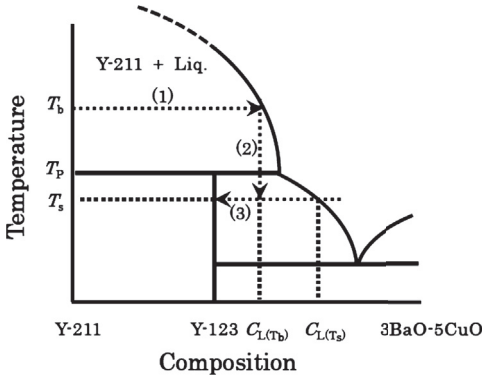

Arrow (1) Y-211 → liquid (solute rich) *at the bottom of the crucible*
Arrow (2) Liquid (solute rich) → liquid (supersaturated) *at the surface of the melt*
Arrow (3) Liquid (supersaturated) → Y-123

FIGURE 30.19 Phase stability and solute transportation processes shown on a schematic quasi-binary phase diagram [119]. © *1996 Elsevier Science B.V.*

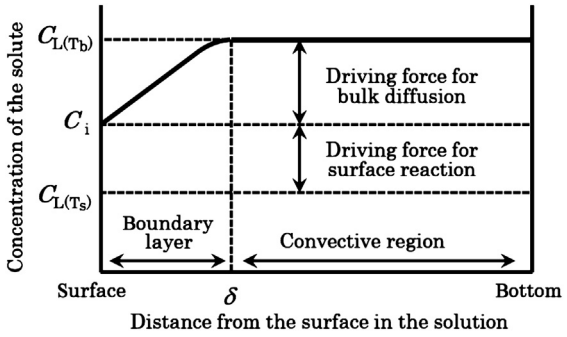

FIGURE 30.20 Schematic illustration of the solute concentration profile in front of the growing interface [118]. © *1995 Materials Research Society.*

is the fluid flow near a rotating disk, Burton et al. [121] introduced the solute boundary layer thickness as:

$$\delta_c = 1.6 D_L^{1/3} \nu^{1/6} \omega^{-1/2} \tag{30.31}$$

where D_L, ν, and ω are the diffusion coefficient of the solute, the kinematic viscosity, and the angular velocity of the rotating crystal, respectively. The Y concentration profile in the solution is schematically shown in Figure 30.20 [118].

The steady state growth rate in the SRL-CP method could be estimated similarly from the mass balance, as described before in Section 30.8.2.1–30.8.2.5. The solute flux from the solution through the boundary layer, δ_c, can be described as the same equation of Eqn (30.23) and the required flux for the Y-123 phase crystal growth is also

the same as Eqn (30.27). The steady state growth rate, R, can be given by equating both diffusion fluxes:

$$R = \frac{D_L}{\delta_c} \frac{\left(C_L^{211} - C_i\right)}{\left(C_s^{123} - C_i\right)} \tag{30.32}$$

Assuming that C_i is equal to C_L^{123}, which means that the effect of the interfacial kinetics for crystal growth are negligibly small, the growth rate reaches the maximum; the value, R_{max}, is estimated to be 5×10^{-4} mm/s by substituting the physical constants/parameters of the typical values of molten oxide and experimental conditions. The value of the R_{max} is larger than the experimental growth rate ($R = 2.8 \times 10^{-4}$ mm/s). If the composition at the interface, C_i, corresponding to supersaturation for interfacial kinetics is estimated using the experimentally measured growth rate, C_i is about 0.64 at%. By converting this value of C_i to the kinetic undercooling (ΔT_k) using the liquidus slope of the Y-123 phase, $\Delta T_k \approx 7$ K. This indicates that Y-123 single crystal growth might be controlled both by the interfacial kinetics and solute diffusion [10,118].

30.8.3.2 Interface Kinetics Estimated from Spiral Growth

1. Growth by screw dislocation (spiral growth)
According to Cabrera and Levine [122] following the BCF theory [123], a better approximation of the step width, λ, of the spiral dislocation is given by:

$$\lambda = 19\rho_c = 19\frac{\gamma a}{k_B T \sigma} \tag{30.33}$$

where ρ_c is the critical radius of the two-dimensional nucleus, γ is the step energy per unit length, and a is the distance between growth units.

The relations between the growth rate and supersaturation can be written as:

$$R \propto \sigma^2, \quad \sigma < \sigma_1 \tag{30.34a}$$

$$R \propto \sigma, \quad \sigma > \sigma_1 \tag{30.34b}$$

where the relation between σ and σ_1 is given by:

$$\frac{\sigma}{\sigma_1} = \frac{2x_s}{\lambda} = \frac{x_s}{9.5\rho_c} = \frac{\sigma}{(9.5\gamma a)/(x_s k_B T)} \tag{30.35}$$

where x_s is a mean diffusive distance of the adsorbed atom.
It should be noted that the equations described in this section are evaluated only for simple growth from vapor. When we discuss the interfacial kinetics of Y-123(RE-123) crystal growth from solution (liquid) precisely, it is necessary to consider complicated structures and multicomponent systems as well as the effect of desolvation on surface diffusion, which has been proposed by Bennema [124,125].

2. Growth by screw dislocation in SRL-CP method
As shown previously, the single crystals grown by the SRL-CP method grow by a spiral growth (Figure 30.9). Kanamori and Shiohara [126] investigated the relation between the composition at the interface and the growth rate, R, from the observed

spiral patterns, including the step width, step height, and shape of Y-123 crystals grown by the SRL-CP method.

According to the approximation by Cabrera and Levine [122], the relation between the terrace width and the supersaturation, σ, is given by Eqn (30.19) and is defined as:

$$\sigma = \frac{C_i - C_L(T_i)}{C_L(T_i)} \tag{30.36}$$

C_i can be obtained from Eqn (30.13) using the experimental results R and $C_L(T_b)$. $C_L(T_i)$ is assumed to be equal to the Y concentration at the temperature, T_s, at the surface of the melt interface, since T_i could not be measured precisely. Consequently, the supersaturation, σ, can be calculated by substituting C_i and $C_L(T_i)$ into Eqn (30.36). The terrace width of spiral growth under each condition from AFM images is plotted as a function of the supersaturation in Figure 30.21 [126]. Also, by choosing the appropriate value (0.13 nm) of $\gamma a/k_B T$ so as to satisfy Eqn (30.33), it is clearly shown that the terrace widths observed on the as grown *ab* plane of the Y-123 single crystals satisfy the BCF theory [123].

In the case of sufficiently small supersaturation, the growth rate taking into account the interfacial kinetics was described in the Eqn (30.34a) and is given by:

$$R = k\sigma^2 \tag{30.37}$$

where k is the kinetic coefficient and expressed by the following equation [10]:

$$k = dfe^{-W/k_B T} \frac{1}{(19/x_s)(\gamma a/k_B T)} \tag{30.38}$$

where d is the lattice constant, f is the frequency of the molecule, W is the dissolution energy of the attached molecule from the surface of the crystal.

Substituting $d \approx 10^{-7}$ (cm) which is the lattice parameter of the c-axis of the Y-123 sing1e crystal, $W \approx 50$ (kcal/mol), which was estimated to be several times larger than

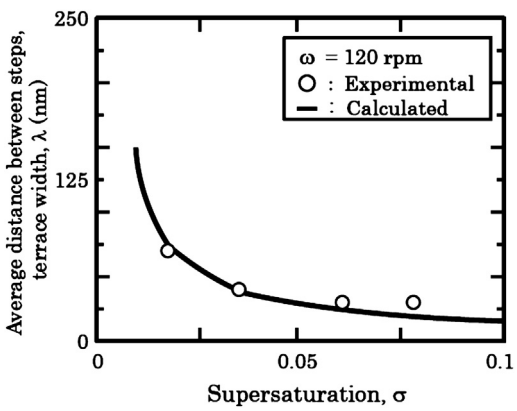

FIGURE 30.21 Supersaturation dependence of the average distance between the steps for YBCO single crystal growth [126]. © *1996 Materials Research Society.*

the value for growth from the vapor, $x_s \approx 100a \approx 4 \times 10^{-6}$ (cm) in which a is the lattice parameter of the a-axis of the Y-123 single crystal, $f \approx k_B T/3h \approx 10^{13}$ (s^{-1}) in which h is Planck's constant and the coefficient 1/3 indicates that the oscillation of the solute molecule is taken into account only in the direction perpendicular to the surface of the crystal and $\gamma a/k_B T = 0.13$ nm into Eqn (30.38), $k = 1 \times 10^{-3}$ (cm/s) was calculated as the interfacial kinetic coefficient. The relation between the growth rate and the supersaturation for the experimental and calculated results is in good agreement with each other [10,126]. Consequently, it is clear that the crystal growth of Y-123 single crystals pulled along the c-axis by the SRL-CP method can be explained by the bulk diffusion model combined with interface kinetics for surface diffusion (BCF theory).

30.8.4 Crystal Growth Mechanism Using Ternary Phase Diagram

In the previous section, the growth mechanism of Y-123 crystals prepared by the SRL-CP method was discussed on the basis of the pseudobinary phase diagram. In the case of the Y-123 system without substitution, this is sufficient because the compositions of the solid and the coexisting liquid are uniquely determined at a certain temperature by assuming that the interfacial kinetics are negligibly small (so-called monovariant system). However, in the case of solid solution systems, a ternary phase diagram should be used due to the increase in freedom (so-called divariant system). A model for the determination of the composition of the solid solution in the SRL-CP method was proposed for the Nd-Ba-Cu-O system as an example, which is modified from the model for the case of the Pr-Ba-Cu-O system [10,127].

The compositions of the solid solution and the coexisting liquid are determined by the tie-line, which links the same chemical potential for the respective solid solution and liquid solution, on the isothermal section of the Nd_2O_3-BaO-CuO ternary phase diagram at the growth temperature such as shown in Figure 30.5. The temperature dependence of the tie-line should be taken into account in the SRL-CP process. Figure 30.22 shows the condition in the crucible and the corresponding ternary phase diagram when the temperature at the bottom of the crucible is higher than the peritectic temperature. T_b, T_p, and T_s are the temperature at the bottom of the crucible, the peritectic temperature of NdBCO, and the temperature at the surface of the liquid, respectively. C_i^0, C_i^{422}, C_i^{ss}, $C_i^L(T_b)$, and $C_i^L(T_s)$ ($i \equiv$ Nd, Ba, and Cu) are the mole fractions of each cation in the initial starting composition, in the Nd-422 phase, in the NdBCO solid solution, in the liquid at T_b, and in the liquid at T_s, respectively. At first, it is considered that the liquid composition in the crucible, except in the solute boundary layer thickness, $\delta_{c,i}$, is uniform due to natural and forced convections. Then, C_i^0 is located on the tie-line connected with C_i^{422} and $C_i^L(T_b)$. The liquid of $C_i^L(T_b)$ is transferred to the solute boundary layer by natural and forced convections. Accordingly, the liquid near the solute boundary layer is supersaturated for NdBCO crystal growth because the temperature around the growing crystal is lower than the peritectic temperature T_p. This supersaturation is the driving

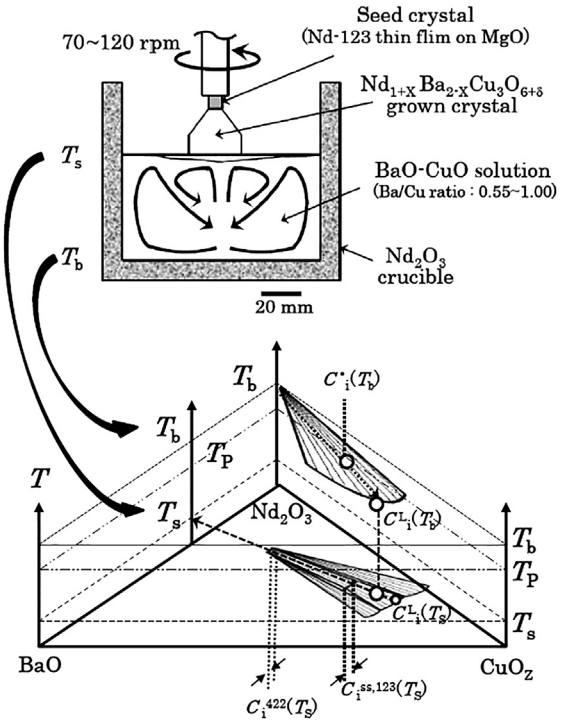

FIGURE 30.22 Condition in the solution (in the crucible) during crystal growth and the corresponding Nd_2O_3-BaO-CuO_Z ternary phase diagram.

force for NdBCO crystal growth. However, it is still uncertain which tie-line on the ternary phase diagram is selected at the growth interface in this system. Then the flux balance for each element is considered to determine the tie-line.

The following assumptions are made to simplify this problem:

1. local equilibrium is assumed at the interface between the crystal and the liquid, i.e., diffusion-controlled growth;
2. steady state solidification occurs only at the surface of the grown single crystal, and no nucleation or growth occurs at other sites (e.g., crucible walls or in the bulk liquid);
3. dilute solution approximation is permitted for the diffusion of Nd;
4. activities of Ba and Cu in the liquid follow Raoult's law;
5. difference between the unit volume of the crystal and that of the Ba-Cu-O solvent is negligibly small, the supersaturation estimated for the mole fraction causes crystallization of the same volume fraction, and the crystal growth rate can be calculated from the supersaturation in the solution given by the mole fraction;
6. crystal growth front is planar;
7. thermophysical properties are constant.

On the basis of these assumptions, the following flux balance equations for each element are derived:

$$R\left\{C_{Nd}^{SS} - C_{Nd}^{L}(T_S)\right\} = D_{Nd}\frac{\left\{C_{Nd}^{L}(T_b) - C_{Nd}^{L}(T_S)\right\}}{\delta_c} \tag{30.39}$$

$$R\left\{C_{Ba}^{SS} - C_{Ba}^{L}(T_S)\right\} = \tilde{D}\frac{\left\{C_{Ba}^{L}(T_b) - C_{Ba}^{L}(T_S)\right\}}{\delta_c} + \frac{C_{Ba}^{L}(T_S)}{1 - C_{Nd}^{L}(T_S)}\left(D_{Nd} - \tilde{D}\right)\frac{\left\{C_{Nd}^{L}(T_b) - C_{Nd}^{L}(T_S)\right\}}{\delta_c} \tag{30.40}$$

$$R\left\{C_{Cu}^{SS} - C_{Cu}^{L}(T_S)\right\} = \tilde{D}\frac{\left\{C_{Ba}^{L}(T_b) - C_{Ba}^{L}(T_S)\right\}}{\delta_c} + \frac{C_{Cu}^{L}(T_S)}{1 - C_{Nd}^{L}(T_S)}\left(D_{Nd} - \tilde{D}\right)\frac{\left\{C_{Nd}^{L}(T_b) - C_{Nd}^{L}(T_S)\right\}}{\delta_c} \tag{30.41}$$

where R is the growth rate, D_{Nd} is the diffusion coefficient of Nd in the liquid, and $\tilde{D}$ is the interdiffusion coefficient between barium and copper in the liquid. C_i^{SS} and $C_i^{L}(T_s)$ satisfying Eqns (30.39)–(30.41) simultaneously and uniquely give us a tie-line at the growing interface.

According to these equations, the selected tie-line is dependent on $\tilde{D}$ and D_{Nd}. In the case of $D_{\mathrm{Nd}} = \tilde{D}$, $C_i^{L}(T_b)$ is located on the tie-line (from C_i^{422} to $C_i^{L}(T_s)$), whereas in the case of $D_{\mathrm{Nd}} \neq \tilde{D}$, the tie-line is shifted by the relationship between D_{Nd} and $\tilde{D}$. Assuming that D_{Nd} is $\tilde{D}$, although these diffusion coefficients are uncertain at present, the composition of the grown single crystal of the NdBCO solid solution can be estimated. The estimated values using this model are in good agreement with the experimental results for various starting compositions. As in the Y-Ba-Cu-O system, the growth model should take into account the interfacial kinetics. Using the SRL-CP method, NdBCO single crystals were grown in the air atmosphere by controlling the liquid composition of the cationic ratio of Ba and Cu (Ba/Cu) to be approximately 0.80. The size of grown NdBCO single crystal was 24 × 24 mm as shown in Figure 30.23. The crystal exhibits high T_c value of about 95 K with a sharp transition width ΔT of less than 0.5 K [128]. This result indicates that the high Ba/Cu ratio in the liquid leads to the low amount of substitution of Nd^{3+} for Ba^{2+}, and consequently results in high superconducting properties.

30.9 Tetragonal to Orthorhombic Phase Transition (Twin Formation)

Y-123 materials have a distorted oxygen-deficient perovskite structure of $YBa_2Cu_3O_{7-\delta}$, as mentioned in Section 30.2.2. The Y-123 crystals grown by high temperature processes have a tetragonal phase, which behaves semiconductive. To attain superconductive characteristics for the crystals, an appropriate heat treatment is required at around 500 °C in an oxygen atmosphere. In this annealing process, the tetragonal-orthorhombic structural phase transition occurs and the obtained crystal composed of the twin structure. In this case, *a*-axes of the tetragonal phase separated into the *a*-axis and the *b*-axis of the orthorhombic phase, and this separation occurs randomly, resulting in formation of a twin structure.

FIGURE 30.23 As grown 1-inch-class size NdBCO single crystal produced by continuous pulling for 67 h from $Ba_3Cu_5O_8$ solvent melt in the Nd_2O_3 crucible in the air atmosphere. Its size is 24×24 mm^2 in the *ab*-plane and 21 mm in the *c*-axis direction [128]. © *1997 The Japan Society of Applied Physics.*

30.9.1 Experimental Measurements of Oxygen Diffusion Coefficient in $REBa_2Cu_3O_{7-\delta}$ (RE: Y & Nd) Crystal

For understanding of the twin formation process, knowledge of kinetics of the oxygen diffusion in both the tetragonal phase and the orthorhombic phase during annealing is important for optimizing superconductive characteristics. A considerable number of studies have been done on the oxygen diffusions in $YBa_2Cu_3O_{7-\delta}$ (Y-123) crystals [129–135] and Nd-123 crystals [136,137], in which diffusion coefficients were estimated by means of the O^{18} isotope tracer and SIMS measurements [129,130,136], the internal friction measurements [126,132], the dynamic and isothermal thermogravimetry [133], the in situ electrical resistivity measurements [134], and in situ observations of twin propagation front [135]. Application of these different evaluation techniques explains the discrepancy of numerical values in literature, which is shown in Figure 30.24.

Diffusion of oxygen in $REBa_2Cu_3O_{7-\delta}$ is anisotropic due to crystallographic anisotropy of their orthorhombic unit cells. Therefore, diffusion in such crystals should be described by (at least) three independent diffusion coefficients along the principal crystallographic directions [129]. The anisotropy is expected to be rather large since the oxygen ion vacancies are concentrated exclusively in CuO basal planes (*ab*-plane), i.e., diffusion in the perpendicular direction (*c*-axis) could be much slower than that in the *ab*-plane. The diffusion is affected by many factors, including $P_{O_2} - T - \delta$ phase-diagram considerations (Rudnyi et al. [138], chemical substitutions in $REBa_2Cu_3O_{7-\delta}$ (RE-ion effect, etc.), grain size, surface quality (Kemnitz et al. [139], Claus et al. [140], Tretyakov and Goodilin [141]), internal stress, availability of oxygen vacancies for diffusion jumps in the almost oxygenated state ($\delta_{lim} \approx 0.003$–$0.08$ according to data of

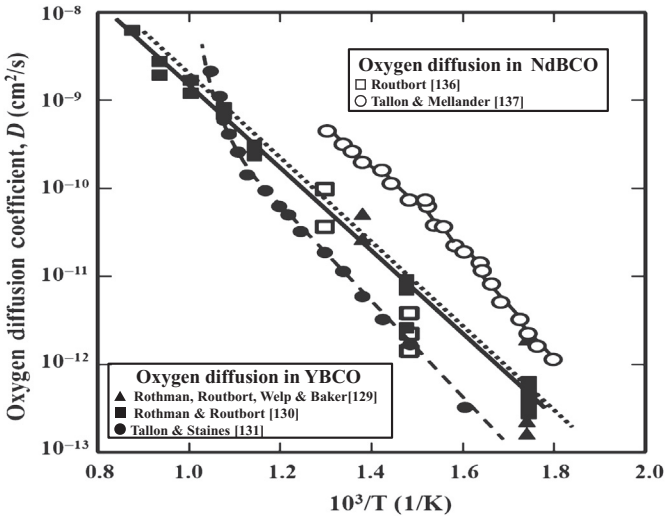

FIGURE 30.24 Summarized Arrhenius plots of the reported oxygen diffusion coefficient in the solid Y-123 and Nd-123 crystals [129–131,136,137].

different authors, Rothman et al. [129], Kruger et al. [142]), etc. Therefore, the overall mechanism of diffusion and, consequently, fitting parameters (pre-exponential factor D_o, activation energy ΔE etc., $D = D_o\ exp(-\Delta E/(kT))$ are usually different depending on experimental conditions (Bokshtein et al. [143]). However, from a practical point of view it is important to note that the chemical (D_{chem}) and self-diffusion (D_{self}) coefficients may differ by several orders of magnitude, $D_{chem} = D_{self}\ \Phi$, where Φ is a thermodynamic factor, which is nearly constant between $1 \leq \delta \leq 0.8$ (Erb et al. [144]). Usually the observable rate of in-diffusion is faster than the rate of out-diffusion because a surface-controlled process of some kind may take place especially for polycrystalline samples (Tu et al. [134], Erb et al. [144]). The intrinsic mechanism of oxygen diffusion was studied, for example, by Xie et al. [145], Rothman et al. [129], and Bredikhin et al. [146].

Reported self-diffusion coefficients and chemical diffusion coefficients of oxygen in solid RE-123 crystals are summarized in Tables 30.2 and 30.3.

30.9.2 Diffusion Mechanism

The diffusion mechanism in the Y-123 crystal should be consistent with the following experimental facts:

1. Arrhenius plot is straight;
2. diffusion coefficient is independent of P_{O_2}
3. $D_b >> D_a$, D_c at least at 300 °C; and
4. defect configuration involved in diffusion is of a type that would also give rise to an internal friction peak [129].

Table 30.2 List of Reported Self Diffusion Coefficients of Oxygen in Solid RE-123 Crystals

Diffusivity	Self Diffusion Coefficient (cm^2/s)	Method and Temperature	References
D_{self} (in *ab* plane)	$\approx 10^{-9} \sim 10^{-13}$,	Ortho- & tetra-Y-123	Rothman et al. [129]
	$D_{self} = 1.4 \times 10^{-4}$ exp (0.97 eV/*kT*)	O^{18} tracer, 350 ~ 850 °C	
	1.7×10^{-13}, 6.7×10^{-13}, 2.9×10^{-12}, 1.3×10^{-11}, 5.3×10^{-11}, 1.7×10^{-10}	Internal friction 400 °C, 450 °C, 500 °C, 550 °C, 600 °C, 650 °C	Xie et al. [145]
	$\approx 3 \times 10^{-12}$, $3.8 \sim 10 \times 10^{-11}$	NdBCO, O^{18} tracer, 400 °C, 500 °C	Routbort [136]
	$8 \times 10^{-13} \sim 10^{-9}$	Y-123, 350 ~ 645 °C	Tallon &
	$2 \times 10^{-11} \sim 2 \times 10^{-9}$	Gd-123, 350 ~ 610 °C	Mellander [137]
	$3 \times 10^{-11} \sim 2 \times 10^{-9}$	Nd-123, 350 ~ 564 °C	
D_{self}	$\approx 10^{-16} \sim 10^{-17}$ (in *c*-direction)	Single crystal, 400 °C	Claus et al. [140]
	$\approx 2 \times 10^{-12}$ (in *b*-direction)	Untwinned, 300 °C	LaGraff & Payne [147]
	$\approx 5 \times 10^{-14} \sim 5 \times 10^{-15}$ (in *a*-direction)	300 °C	Rothman et al. [129]
	$D_{ab} \approx (10^4 \sim 10^6)\, D_c$, $D_b \approx 100\, D_a$, $D_{ab} \approx D_{poly}$, $D_b \approx 10\, D_{ab}$		Shiohara & Goodlin [148]
D_{self} (estimated)	$D_{ab} \approx 10^{-10}$, $D_c \approx 2 \times 10^{-16}$,	450 °C,	Tsukui et al. [149]
	$D_{ab} \approx 7 \times 10^{-10}$, $D_c \approx 2 \times 10^{-15}$	530 °C	
	$D_{ab} \approx 3 \times 10^{-12}$, $D_c \approx 4 \times 10^{-17}$	400 °C,	Bredikhin et al. [146]
	$D_{ab} \approx 7.8 \times 10^{-9}$, $D_c \approx 6.2 \times 10^{-11}$	800 °C	

The first of these criteria suggests that diffusions in both the orthorhombic and tetragonal phases take place by the same type of oxygen atom jump. The second suggests that the diffusion coefficient is independent of the concentrations of oxygen ion vacancies and interstitials. The third of these criteria is related to the structure in the *ab*-plane. The combination of a straight Arrhenius line over the entire temperature range and the finding that $D_b >> D_a$ at 300 °C suggests that $D_b >> D_a$, should hold over the entire temperature range.

The theories of Bakker et al. [153,154] assume that the vacancies on O(I) and the oxygen ions on O(V) occur randomly. Diffusion via randomly arranged single vacancies at high δ values would lead to strong correlation effects and a curved Arrhenius plot. Accordingly, it was believed that diffusion via isolated vacancies is not the mechanism for the diffusion of oxygen in $YBa_2Cu_30_{7-\delta}$. The Monte Carlo calculations of Salomons and deFontaine [155] are based on the ordering of oxygen ions at $\delta < 1$, but still yield a strong P_{O_2} dependence of *D*.

The strong anisotropy of diffusion in the *ab*-plane was suggested by Ronay and Nordlander [156]. The diffusion coefficient may show only a weak dependence on P_{O_2} for the following reason [157]. If only the oxygen ions at the ends of the chains are mobile,

Table 30.3 List of Reported Chemical Diffusion Coefficients of Oxygen in Solid RE-123 Crystals

Diffusivity	Chemical Diffusion Coefficient (cm^2/s)	Method and Temperature	References
$D_{chem,\ poly}$ (in *ab* plane)	$\approx 10^{-10}$	TGA, 500 °C	Tang & Lo [132]
	$10^{-11} \sim 10^{-9}$	In-diffusion, 400 ~ 600 °C	Tu et al. [134]
	5×10^{-8}	94% dense Y-123 solid-state electrochemical cell, 500 °C	O'Sullivan & Chang [150]
	$5 \times 10^{-8} \sim 5 \times 10^{-7}$	Out-diffusion, 350 ~ 600 °C	LaGraff & Payne [147]
	$\approx 5 \times 10^{-5}$	450 ~ 600 °C	Elschner [151]
	7.5×10^{-7}, 1.9×10^{-6}, 3.4×10^{-6}, 6.2×10^{-6}, 1.3×10^{-5}, 1.8×10^{-5}, 2.8×10^{-5}	In- & out-diffusion in air 300 °C, 400 °C, 500 °C, 600 °C, 700 °C, 800 °C, 900 °C	Shi et al. [152]
$D_{chem,}$ single X'tal (in *ab* plane)	$\approx 10^{-7}$	Twin propagation front	Yamada & Shiohara [49]
	$\approx 10^{-5}$	In-diffusion, 725 °C	LaGraff & Payne [147]
	$\approx 10^{-6}$	Out-diffusion, 725 °C	
	$Gd_{0.8}Y_{0.2}Ba_2Cu_3O_z$	In-situ	Erb et al. [144]
	4.94×10^{-5} exp (0.52eV/kT)	resistivity measurement	
	$\approx 3 \times 10^{-8}$	550 °C,	
	$\approx 8 \times 10^{-9}$	420 °C	
	4.5×10^{-8}, 5×10^{-7}, 7×10^{-7}, 10^{-6}, 3×10^{-8}, 2×10^{-7}, 4×10^{-7}, 4.5×10^{-7}	(Nd-123) 300, 400, 500, 600 °C (Y-123) 300, 400, 500, 600 °C	Oka & Shiohara [135]

and the number of chains stays constant with stoichiometry, the number of mobile atoms will be independent of P_{O_2}. In this model, the length of the chains changes with stoichiometry, and the oxygen atom jump distance will also change. The mechanism suggested is that an oxygen ion at the end of a row of O(I) sites jumps into an O(V) site, moves along O(V) sites until it comes to another row end, and attaches itself there. It could be concluded on the basis of the experimental data that diffusion in $YBa_2Cu_3O_{7-\delta}$ probably does not take place by the random movement of vacancies in the CuO plane but rather by the movement of oxygen ion over O(V) sites between the rows of oxygen ions.

From the viewpoints of atomic mechanisms of chemical oxygen diffusion, the diffusion coefficient, D_{chem}, is given by [130]

$$D_{chem} = \frac{1}{2} d^2 \omega f \left(1 + \frac{\partial \ln \gamma}{\partial \ln c}\right) \tag{30.42}$$

where d is the jumping distance of oxygen atoms, ω is the exchange frequency between oxygen atoms and the neighboring vacancies, f is a correlation factor, γ is the oxygen activity coefficient, and c is the oxygen concentration. Assuming the independent chemical oxygen diffusion coefficient with oxygen concentration, D_{chem} is represented

by the first term on the right side of Eqn (30.42). Comparing the factors in Eqn (30.42) for the Nd-123 with those for the Y-123, the jumping distance of oxygen atoms, d, for the Nd-123 single crystals is only about 2% larger than that for the Y-123 single crystals, which was predicted from the lattice parameters of the Nd-123 and Y-123 crystals [148]. The exchange frequency between oxygen atoms and the neighboring vacancies, ω, for the Nd-123 single crystal is about 50 times larger than that for the Y-123 single crystals, which was predicted from the internal friction measurements [137]. Therefore, further assuming that the correlation factor, f, is equal to unity for both the Nd-123 and Y-123 single crystals, the chemical diffusion coefficient, D_{chem}, of the Nd-123 single crystals should also about be 50 times larger than that of the Y-123 single crystals. However, some of the coefficients obtained experimentally are different from that predicted from Eqn (30.42) as described before.

For the reason why the experimental and predicted values of the chemical oxygen diffusion coefficients were different, it should be noted that the Nd-123 crystals are easy to form a nonstoichiometric composition by substitution of a portion of the Nd^{3+} ions for Ba^{2+} ion sites during the fabrication process because of similar radii of Nd^{3+} ion and Ba^{2+} ion to each other as described before in Section 30.4.2 [18,37,88]. It should be noted that this substitution causes different oxygen activities due to different valencies. This nonstoichiometric composition in the Nd-123 crystals should affect the oxygen diffusion during annealing.

30.9.3 Twins and Tweed Pattern Due to Strains in Orthorhombic Phase

The transition of the tetragonal to the orthorhombic RE-123 phase due to oxygen in-diffusion on cooling is normally accompanied by the spontaneous formation of twin domains because the internal strains are relieved [158]. It has been suggested [159] that the spacing of the twins, $\Delta\lambda$, varies as the square root of the size G of the transforming region:

$$\Delta\lambda = \sqrt{\frac{128\pi\gamma G}{ES^2}} \tag{30.43}$$

where γ is the twin boundary energy per unit area, S is the orthorhombicity ratio, and E is the elastic modulus of the material. It is obvious that the twins can be negligibly small and undetectable in tiny particles, however, in large single crystals these twin domains are visible and give contrasted images in polarized optical microscopy.

Lin and coworkers [160] suggested that annealing the orthorhombic phase above the transition temperature at high oxygen partial pressure for a short period of time followed by quenching could result in a tetragonal oxygen-rich phase. Since the oxygen-rich tetragonal phase is a nonequilibrium state, the intrinsic strains can manifest themselves as orthogonally modulated structure distortions with a length of several tens to hundreds of angstroms (tweed structure). They demonstrated the existence of the tweed tetragonal phase in oxygen-rich pure $YBa_2Cu_30_{7-\delta}$ ($\delta < 0.6$) prepared by a similar method. The samples were superconducting with a sharp transition.

Two types of twin structures were observed in the whole range of the $Nd_{1+x}Ba_{2-x}Cu_3O_z$ solid solution: due to the tetragonal-to-orthorhombic phase transition in the region $x < 0.3$, and due to peculiarities of the crystal growth mechanism at $x > 0.6$. Additionally, the tweed structure can be observed near $x = 0.3$ and $x = 0.6$. A strong confirmation of the as-grown nature of the twins in $Nd_{1.85}Ba_{1.15}Cu_3O_z$ can be found by high temperature (hot-stage) in situ optical microscopy [135]. This is a powerful method for visualizing the twin behavior and for a kinetic study of processes in any desired environment and conditions (at certain T, P_{O_2} and applied uniaxial compression). They demonstrated the stability of the twin structure in $Nd_{185}Ba_{1.15}Cu_3O_z$ crystals even at 900 °C in low- P_{O_2} atmosphere. The twins do not disappear after this high-temperature-low-P_{O_2} anneal, contrary to the usual behavior of twins in the $x = 0$ case. To eliminate the twin structure in $Nd_{185}Ba_{1.15}Cu_3O_z$, it is necessary to destroy the crystals or to obtain them without twins under some other growth conditions. At the same time, detwinning in the $x = 0$ single crystals occurs for several minutes depending on the temperature and P_{O_2}.

30.9.4 Detwinning and Twin-free Crystal by Mechanical Stress

In the annealing process, to attain superconductivity, the *a*-axes of a tetragonal phase separate into the *a*- and *b*-axis of the orthorhombic phase, and this separation occurs randomly, leading to the twin structure. Small crystals ($\sim 1\ mm^2$) can be obtained in a twin-free form [161], while larger crystals demand a special detwinning procedure. Since tile stiffness of the materials becomes minimal in the middle of the structural transformation, this phenomenon allows one to obtain a twin-free orthorhombic phase starting with the tetragonal one. This process originates from the idea of ferroelasticity [162] and has been widely investigated [163–168]. Only a few practical examples will be given here. In thin (about 100 μm) flux-grown crystals, the twin structure changes under uniaxial compression of a few MPa, starting from a temperature 200–300 °C. The single-domain crystals obtained in this way show a "memory effect" [164,167], i.e., they retain internal stresses and become retwinned under subsequent annealing without uniaxial compression. The configuration of the twin-domain walls returns to its initial state as predetermined by microstructural defects. Thick crystals (e.g., produced by the SRL-CP method; see in Section 6.3.) cannot be detwinned at such low temperatures. In contrast, when raising the temperature to 500–700 °C, complete detwinning occurs without returning to the initial twin structure. The Ar preheating favors "memory cleaning" because it anneals the defects and cures microcracks of the as-grown crystals as well as homogenizes the oxygen contents and removes it from rare twins if present. Therefore a typical procedure of detwinning is as follows [166,167]. A rectangular piece is cut off from a large single crystal. Uniaxial compressive stress of about 6 MPa is applied. Then, the sample is heated under this uniaxial compression in an argon gas flow up to 600 °C. Then, the gas is changed to oxygen and the sample is cooled at a rate of about 6 °C/h. The resulting microstructure according to polarized optical microscopy observation consists of about 99.9% surface fraction of the twin-free orthorhombic $YBa_2Cu_30_7$ phase [167].

Kutami et al. [166] pressed a single crystal ($1 \times 1 \times 0.3\,mm^3$) with a tetragonal structure at 1000 kgf/cm^2 for 120 h in an oxygen atmosphere. As a result, the crystal annealed with the uniaxial compression was an orthorhombic phase without twins as confirmed by Laue X-ray backscattering, TEM observation, and T_c measurements. Onset of $T_{c,0}$ of the twin-free crystal was about 92 K and the J_c value at 1 T was one-fifth that of the twinned crystal, which indicates a high crystallinity.

30.10 Conclusion

We have reviewed the development of bulk crystal growth of high T_c superconducting (HTSC) oxides especially focusing on $YBa_2Cu_3O_{7-\delta}$ (Y-123) and $REBa_2Cu_3O_{7-\delta}$ (RE-123), the most widely studied HTSC material. By first considering the basic and fundamental solidification processes of the HTSC oxides, we have established physical models of the state of our understandings of the growth process. The Y-123 oxide solidifies (crystallizes) via peritectic reactions from its melt, i.e., incongruent melting. Although some progress has been made in the understanding of peritectic growth, much of the work is rather qualitative, and the rate-limiting stage is considered to be solid diffusion at least in most metallic alloy systems. A unique idea of its reaction with the rate-limiting stages of liquid diffusion as well as interface kinetics was reviewed. Based on a series of experimental results, the model for the peritectic reaction with the particle pushing/trapping mechanism for controlling the microstructures and understanding of the behavior of the high temperature stable solid phase was also reviewed.

With these ideas, we have then reviewed the effects of various process parameters on the bulk oxide crystal growth process, including oxygen partial pressure, growth temperature, liquid compositions, crucible materials, and crystal rotation/pulling rates for controlling the fluid flow, i.e., convections in the liquid solution. Furthermore, a unique crystal pulling process reported for fabrication of the single crystals, and a developed crystal growth model for the ternary component system to control the crystal composition in the solid solution by means of mass and flux balance equations with a local equilibrium assumptions using ternary equilibrium phase diagram together with tie-lines, were reviewed. Although modeling has been successful at least in treating the compositional partitioning of cationic elements at the interface between the solid solution and the liquid solution for the ternary systems, there is no complete theory for quaternary and high-order systems including anionic oxygen. Since oxygenation of grown crystals is necessary to enhance superconductivity, and this is a very delicate procedure in the case of single crystals, oxygen diffusion and twin formation are also reviewed. Obviously, further work is necessary for better understanding of the basic crystal growth processes to achieve a much better control of the fabrication of the superconducting oxides.

Acknowledgments

The authors wish to express their sincere gratitude to all scientists of SRL-ISTEC, and to many collaborative research scientists in the universities, industries, and research institutions all over the world. Parts of the original research reported in this chapter were supported by the New Energy and Industrial Technology Development Organization (NEDO) in Japan.

References

[1] Bednorz JG, Müller KA. Z Phys B Condensed Matter 1986;64:189–93.

[2] Pool R. Science May 26, 1989;244:914–6.

[3] Wu MK, Ashburn JR, Torng CJ, Hor PH, Meng RL, Gao L, et al. Phys Rev Lett 1987;58:908–10.

[4] Elwell D, Scheel HJ. Crystal growth from high-temperature solutions. Chapter 11. London, New York, San Fransisco: Academic Press; 2011. 635.

[5] Maeda H, Tanaka Y, Fukutomi M, Asano T. Jpn J Appl Phys 1988;27:L209–10.

[6] Sheng ZZ, Hermann AM. Nature 1988;332:138–9.

[7] Schilling A, Cantoni M, Guo JD, Ott HR. Nature 1993;363:56–8.

[8] Nagamatsu J, Nakagawa N, Muranaka T, Zenitani Y, Akimitsu J. Nature 2001;410:63–4.

[9] Kamihara Y, Watanabe T, Hirano M, Hosono H. J Am Chem Soc 2008;130:3296–7.

[10] Shiohara Y, Endo A. Mater Sci Eng 1997;R19:1–86.

[11] Izumi F, Asano H, Ishigaki T, Ono A, Okamura FP. Jpn J Appl Phys 1987;26:L611–2.

[12] Hatano T, Matsushita A, Nakamura K, Sakka Y, Matsumoto T, Ogawa K. Jpn J Appl Phys 1987;26:L721–3.

[13] Ito T, Takenaka K, Uchida S. Phys Rev Lett 1993;70:3995–8.

[14] Ando Y, Segawa K, Lavrov AN, Komiya S. J Low Temp Phys 2003;131:793–801.

[15] Cava RJ, Batlogg B, Chen CH, Rietman EA, Zahurak SM, Werder D. Nature 1987;329:423–5.

[16] Lindemer TB, Hunley JF, Gates Jr JE, Sutton AL, Brynestad J, Hubbard CR, et al. J Am Ceram Soc 1989;72:1775–88.

[17] Scheel HJ. MRS Bull September 1994:26.

[18] Wada T, Suzuki N, Maeda T, Maeda A, Uchida S, Uchinokura K, et al. Appl Phys Lett 1988;52:1989–91.

[19] Yoo SI, Sakai N, Takaichi H, Higuchi T, Murakami M. Appl Phys Lett 1994;65:633–5.

[20] Murakami M, Yoo SI, Higuchi T, Sakai N, Weltz J, Koshizuka N, et al. Jpn J Appl Phys 1994;33:L715–7.

[21] Worthington TK, Gallagher WJ, Kaiser DL, Holtzberg FH, Dinger TR. Phys C 1988;153–155:32–7.

[22] Dimos D, Chaudhari P, Mannhardt J. Phys Rev B 1990;41:4038–49.

[23] Scheel HJ, Licci F. Thermochim Acta 1991;174:115.

[24] Scheel HJ, Sadowski W, Schellenberg L. Supercond Sci Technol 1989;2:17.

[25] Aselage T, Keefer K. J Mater Res 1988;3:1279–91.

[26] Oka K, Nakane K, Ito M, Saito M, Unoki H. Jpn Appl Phys 1988;27:L1065–7.

[27] Erb A, Biernath T, Müller-Vogt G. J Cryst Growth 1993;132:389–95.

[28] Ahn B, Lee VY, Beyers R. Phys C 1990;167:529–37.

[29] Lay KW, Relund GM. J Am Ceram Soc 1990;73:1208–13.
[30] Ng WW, Cook LP, Paretzkin B, Hill MD, Stalik JK. J Am Ceram Soc 1994;77:2354–62.
[31] Lee BJ, Lee DN. J Am Ceram Soc 1989;72:314–9.
[32] Lee BJ, Lee DN. J Am Ceram Soc 1991;74:78–84.
[33] Krauns Ch, Sumida M, Tagami M, Yamada Y, Shiohara Y. Z Phys B 1994;96:207–12.
[34] Kambara M, Nakamura M, Shiohara Y, Umeda T. Phys C 1997;275:127–34.
[35] Yao X, Shiohara Y. Supercond Sci Technol 1997;10:249–58.
[36] Nakamura M, Krauns Ch, Yamada Y, Shiohara Y. J Mater Res 1996;11:1076–81.
[37] Yoo SI, McCallum RW. Phys C 1993;210:147–56.
[38] Daeumling M, Seuntjens JM, Larbalestier DC. Nature 1990;346:332–5.
[39] Osamura K, Zhang W. Z Metallkd 1993;84:522–8.
[40] Oka K, Unoki H. J Cryst Growth 1990;99:922–4.
[41] Kambara M, Yao X, Tagami M, Goodlin EA, Shiohara Y, Umeda T. J Am Ceram Soc 1998;81(8): 2116–24.
[42] Yoshizumi M, Kambara M, Shiohara Y, Umeda T. Phys C 2000;334:77–86.
[43] Shimpo R, Nakamura Y. J Jpn Inst Met (in Japanese) 1990;54:549–55.
[44] Kimura S, Shimpo R, Nakamura Y. J Jpn Inst Met (in Japanese) 1992;56:1145–51.
[45] JANAF Thermochemical Table. 3rd ed. J Phys Chem Ref Data 1985;14.
[46] Jin S, Tiefel TH, Sherwood RC, van Dover RB, Davis ME, Kammlott GW, et al. Phys Rev B 1988;37: 7850–3.
[47] Murakami M, Morita M, Doi K, Miyamoto K. Jpn J Appl Phys 1989;28:1189–94.
[48] Fujimoto H, Murakami M, Gotoh S, Shiohara Y, Koshizuka N, Tanaka S. Proc 2nd ISS '89 Adv Supercond 1989;1:285–8.
[49] Yamada Y, Shiohara Y. Phys C 1993;217:182–8.
[50] Nakamura M, Yamada Y, Shiohara Y. J Mater Res 1994;9(8):1946–51.
[51] Kondoh A, Kagiya S, Takaichi H, Sakai N, Murakami M, Fujimoto H, et al. Proc. Int. workshop on superconductivity, ISTEC-MRS, Honolulu, Hawaii; 1992. p. 272.
[52] Morita M, Takebayashi S, Tanaka M, Kimura K. Proc 3rd ISS '90 Adv Supercond 1991;3:733–6.
[53] Sawano K, Morita M, Tanaka M, Sasaki T, Kimura K, Takebayashi S, et al. Jpn J Appl Phys 1991;30: L1157–9.
[54] Gao L, Xue YY, Ramirez D, Huang ZL, Meng RL, Chu CW. Appl Phys Lett 1993;63:260.
[55] Blohowiak KY, Garrigus DF, Luhman TS, McCray KE, Strasik M, Akway IA, et al. IEEE Trans Appl Supercond 1993;3:1049–52.
[56] Lo W, Cardwell DA, Dung SL, Bater RG. J Mater Sci 1995;30:3995–4002.
[57] Meng RL, Kinalidis C, Sun YY, Gao L, Tao YK, Hor PH, et al. Nature 1990;345:326–8.
[58] McGinn PJ, Chen W, Zhu N, Balachandran U, Lanagan MT. Phys C 1990;165:480–4.
[59] McGinn P, Zhu N, Chen W, Sengupta S, Li T. Phys C 1991;176:203–8.
[60] McGinn P, Chen W, Zhu N, Varanasi C, Tan L, Balkin D. Phys C 1991;183:51–6.
[61] Izumi T, Shiohara Y. J Mater Res 1992;7:16–23.
[62] Figueredo AM, Cima MJ, Flemings MC, Haggerty JS, Hara T, Ishii H, et al. Phys C 1995;241:92–102.

[63] Izumi T, Nakamura Y, Shiohara Y. J Cryst Growth 1993;128:757–61.

[64] Rutter JW, Chalmers B. Can J Phys 1953;31:15–39.

[65] Flemings MC. Solidification processing. New York: McGraw-Hill; 1974. p. 290.

[66] Sun BN, Schmid H. J Cryst Growth 1990;100:297–302.

[67] Drake A, Abell JS, Sutton SD. J Less-Common Met 1990;164-165:187–92.

[68] Katsui A, Hidaka Y, Ohtsuka H. Jpn J Appl Phys 1987;26:L1521–3.

[69] Gencer F, Abell JS. J Cryst Growth 1991;112:337–42.

[70] Wang Y, Bennema P, van der Linden P. J Cryst Growth 1990;106:483–6.

[71] Watanabe K. J Cryst Growth 1990;100:293–6.

[72] Watanabe K. J Cryst Growth 1991;114:269–78.

[73] Wolf Th, Goldacker W, Obst B. J Cryst Growth 1989;96:1010–8.

[74] Schneemeyer LF, Waszczak JV, Siegrist T, van Dover RB, Rupp LW, Batlogg B, et al. Nature 1987; 328:601–3.

[75] Asaoka H, Takei H, Iye Y, Tamura M, Kinoshita M, Takeya H. Jpn J Appl Phys 1993;32:L1091–6.

[76] Takei H, Asaoka H, Iye Y, Takeya H. Jpn J Appl Phys 1991;30:L1102–5.

[77] Ono A, Nozoki H, Ishizawa Y. Jpn J Appl Phys 1988;27:L340–3.

[78] Wanklyn BM, Chen C, Watts BE, Haycock P, Platt F, de Goot PAJ, et al. Solid State Commun 1988; 66:441–3.

[79] Liang R, Dosanjh P, Bonn DA, Baar DJ, Carolan JF, Hardy WN. Phys C 1992;195:51–8.

[80] Holtzberg F, Field C. J Cryst Growth 1990;99:915–21.

[81] Dembinski D, Gervais M, Odier P, Coutures JP. J Less-Common Met 1990;164-165:177–86.

[82] Oka K, Ito T. Phys C 1994;227:77–84.

[83] Namikawa Y, Egami M, Shiohara Y. Proc 7th ISS '94 Adv Supercond 1995;7:595–600.

[84] Klemenz C, Scheel HJ. J Cryst Growth 1993;129:421.

[85] Namikawa Y, Egami M, Shiohara Y. J Mater Res 1996;11:288–95.

[86] Yao X, Mizukoshi T, Egami M, Zama H, Nakamura M, Shiohara Y. Jpn J Appl Phys 1996;35:2126–32.

[87] Nakamura M, Krauns Ch, Yamada Y, Shiohara Y. J Cryst Growth 1996;166:859–62.

[88] Nakamura M, Kutami H, Shiohara Y. Phys C 1996;260:297–304.

[89] Jackson KA. Liquid metals and solidification. Cleveland: American Society for Metals; 1958. p. 174.

[90] Nakamura M, Krauns Ch, Shiohara Y. J Mater Res 1996;11:1076–81.

[91] Nakamura Y, Furuya K, Izumi T, Shiohara Y. J Mater Res 1994;9:1350–6.

[92] Muller D, Freyhardt HC. Phys C 1995;242:283–90.

[93] Imagawa Y, Shiohara Y. Phys C 1996;262:243–8.

[94] Endo A, Chauhan HS, Nakamura Y, Furuya K, Shiohara Y. Proc 7th ISS '94 Adv Supercond 1995;7: 689–92.

[95] Kim CJ, Kim KB, Won DY, Moon HC, Suhr DS, Lai SH, et al. J Mater Res 1994;9:1952–60.

[96] Varanasi C, McGinn PJ. Phys C 1993;207:79–84.

[97] Endo A, Chauhan HS, Egi T, Shiohara Y. J Mater Res 1996;11(4):795–802.

[98] Kim CJ, Kim K-B, Hong G-W. J Mater Res 1995;10:1605–10.

[99] Varanasi C, Black MA, McGinn PJ. J Mater Res 1996;11:565–71.

[100] Endo A, Chauhan HS, Egi T, Shiohara Y. J Mater Res 1996;11:795–803.

[101] Cima MJ, Flemings MC, Figueredo AM, Nakade M, Ishii H, Brody HD, et al. J Appl Phys 1992;72:179–90.

[102] Mori N, Hata H, Ogi K. J Jpn Inst Met 1992;6:648–55.

[103] Pamplin B. In: Pamplin B, editor. Crystal growth, science of the solid state. Oxford: Pergamon; 1980. p. 16.

[104] Kerr HW, Cissé J, Bolling GF. Acta Metall 1974;22:677–86.

[105] Fredriksson H, Nylen T. Met Sci 1982;16:283–94.

[106] Uhlmann DR, Chalmers B, Jackson KA. J Appl Phys 1964;35:2986–92.

[107] Bolling GF, Cissé J. J Cryst Growth 1971;10:56–66.

[108] Cissé J, Bolling GF. J Cryst Growth 1971;10:67–76.

[109] Cissé J, Bolling GF. J Cryst Growth 1971;11:25–8.

[110] Chernov AA, Temkin DE. Capture of inclusions in crystal growth. In: Kaldis E, editor. Current topics in material science, vol. 2. Amsterdam: North-Holland; 1977. pp. 3–77.

[111] Chernov AA, Temkin DE, Mel'nikova AM. Sov Phys Crystallogr 1976;21:369–73.

[112] Chernov AA, Temkin DE, Mel'nikova AM. Sov Phys Crystallogr 1977;22:656–8.

[113] Shangguan D, Ahuja S, Stefanescu DM. Metall Trans A 1992;23:669–80.

[114] Grigoryan SG, Oganesyan AS, Sarkisyan AG. Kristallografiya 1983;28:782–5.

[115] ötoschke JP, Rogge V. J Cryst Growth 1989;94:726–38.

[116] Fedorov OP. Interaction of crystals growing in the melt with inclusions and concentration inhomogeneities. In: Growth of crystals. New York: Consultant Bureau; 1992. p. 169.

[117] Rodriguez MA, Chen B-J, Snyder RL. Phys C 1992;195:185–94.

[118] Yamada Y, Krauns Ch, Nakamura M, Tagami M, Shiohara Y. J Mater Res 1995;10:1601–4.

[119] Kanamori Y, Shiohara Y. Phys C 1996;264:305–10.

[120] Cochran WG. Math Proc Cambridge Philos Soc 1934;30:365–75.

[121] Burton JA, Prim RC, Slichter WP. J Chem Phys 1953;21:1987–91.

[122] Cabrera N, Levine MM. Philos Mag 1956;1:450–8.

[123] Burton WK, Cabarera N, Frank FC. Philos Trans R Soc A 1951;243:299–358.

[124] Bennema P. J Cryst Growth 1968;3-4:331–4.

[125] Bennema P. J Cryst Growth 1969;5:29–43.

[126] Kanamori Y, Shiohara Y. J Mater Res 1996;11:2693–7.

[127] Tagami, Shiohara Y. J Cryst Growth 1997;171:409–14.

[128] Yao X, Kambara M, Umeda T, Shiohara Y. Jpn J Appl Phys 1997;36:L400–2.

[129] Rothman SJ, Routbort JL, Welp U, Baker JE. Phys Rev B 1991;44:2326.

[130] Rothman SJ, Routbort JL, Baker JE. Phys Rev B 1989;40:8852.

[131] Tallon JL, Staines MP. J Appl Phys 1990;68:3998.

[132] Tang TB, Lo W. Phys C 1991;174:463.

[133] Shi LT, Tu KN. Appl Phys Lett 1989;55:1351.

[134] Tu KN, Tsuei CC, Park SI, Levi A. Phys Rev B 1988;38:772.

[135] Oka A, Koyama S, Shiohara Y. Phys C 1998;305:213.

[136] Routbort IL. Phys C 1993;214:408.

[137] Tallon JL, Mellander B-E. Science 1992;258:781.

[138] Rudnyi EB, Kuzmenko VV, Voronin GE. J Phys Chem 1998:855.

[139] Kerrmitz E, Galkin AA, Olesch T, Scheurell S. J Therm Anal 1997;48:997.

[140] Claus J, Borchardt G, Weber S, Scherrer S. Phys Chem 1998;206:49.

[141] Tretyakov YD, Goodilin EA. Russ Chem Rev 2000;69:3.

[142] Kruger Ch, Conder K, Schwer H, Kaldis E. J Solid State Chem 1997;134:356.

[143] Bokshtein BS, Bokshtein SZ, Zhukhovitskii AA. Thermodynamics and kinetics of diffusion in solids. Moscow: Metallurgiya Publishers; 1973. translated from Russian, Amerind Publishing (1985) 310.

[144] Erb A, Greb B, Muller-Vogt G. Phys C 1996;259:83.

[145] Xie XM, Chen TG, Wu ZL. Phys Rev B 1989;40:4549.

[146] Bredikhin SI, Emelchenko GA, Shechtman VSh, Zhokhlov AA. Phys C 1991;179:286.

[147] LaGraff JR, Payne DA. Phys C 1993;212:470.

[148] Goodilin EA, Oleynikov NN, Antipov EV, Shpanchenko RV, Popov GY, Balakirev VG, et al. Phys C 1996;272:65.

[149] Tsukui S, Yamamoto T, Adachi M, Shono Y, Kawabata K. Phys C 1991;185:929.

[150] O'Sullivan EJM, Chang BR. Appl Phys Lett 1988;52:1441.

[151] Elschner S, Becket W, Bestgen H, Brand M. Phys C 1992;202:401.

[152] Shi D, Krucpzak J, Tang M, Chen N, Bhadra R. J Appl Phys 1989;66:4325.

[153] Bakker H, Westerveld JPA, Lo Cascio DMR, Welch DO. Phys C 1989;157:25.

[154] Bakker H, Westerveld JPA, Welch DO. Phys C 1988;153:848.

[155] Salomons E, de Fontaine D. Phys Rev B 1990;41(11):159.

[156] Ronay M, Nordlander P. Phys C 1988;153-155:834.

[157] Hong DJL, Mehta A, Peng P, Smyth DM. Ceram Trans 1990;13:129.

[158] Shiohara Y, Goodilin EA. In: Gschneidner Jr KA, Eyring L, Maple MB, editors. Handbook on the physics and chemistry of rare earth, vol. 30. Elsevier; 2000. p. 67 [Chapter 189].

[159] Shaw TM, Shinde SL, Dimos D. J Mater Res 1989;4:248.

[160] Lin CT, Chrosch J, Yan Y, Liang WY, Salje EKH. Phys C 1995;242:105.

[161] Rice JE, Ginsberg DM. J Cryst Growth 1991;109:432.

[162] Aizu K. Phys Rev B 1970;2:754.

[163] Schmid H, Burkhardt E, Sun BN, Rivera JE. Phys C 1989;157:555.

[164] Voronkova VI, Wolf T h. Phys C 1993;218:175.

[165] Asaoka H, Kazumata Y, Takei H, Noda K. Phys C 1996;268:14.

[166] Kutami H, Yamada Y, Koyama S, Nakagawa Z, Shiohara Y. Proc. ISS'96, Sapporo, Japan. In: Nakajima S, Murakami M, editors. Advances in superconductivity, vol. IX. Tokyo: Springer; 1997. p. 689.

[167] Rykov A, Jang A,WJ, Unoki H, Tajima S. Proc. ISS'96, Sapporo, Japan. In: Nakajima S, Murakami M, editors. Advances in superconductivity, vol. IX. Tokyo: Springer; 1997. p. 341.

[168] Oka A, Koyama S, Izumi T, Shiohara Y. Phys C 1999;314:269.

31 Crystallization in Gels

Abel Moreno[1], Ma Eugenia Mendoza[2]

[1]INSTITUTO DE QUÍMICA, UNIVERSIDAD NACIONAL AUTÓNOMA DE MÉXICO, MEXICO;
[2]INSTITUTO DE FÍSICA, BENEMÉRITA UNIVERSIDAD AUTÓNOMA DE PUEBLA, PUEBLA, MEXICO

CHAPTER OUTLINE

31.1 Introduction 1277
31.1.1 Gel Growth History 1280
31.1.2 Gel Properties and Characterization 1282
31.1.3 Diffusion versus Convective Transport 1285
31.1.3.1 Diffusion Coefficient and Size of the Clusters 1288
31.1.3.2 Experimental Methods to Evaluate the Diffusion Coefficient and the Gel–Matrix Interaction 1289
31.1.4 Gel Growth Applications 1294
31.2 Hydrogels, Organic Gels, and Aerogels 1295
31.2.1 Synthesis and Characterization of Hydrogels and Organic Gels 1295
31.2.2 Synthesis and Characterization of Xerogels and Aerogels 1299
31.3 Crystal Growth in Gels of Small Molecules, Minerals, and Biological Macromolecules in Gels 1302
31.4 General Remarks and Future of Crystal Growth in Gels 1302
References 1307

31.1 Introduction

The crystallization of biomacromolecular crystals is of increasing interest in different applications. To date, the growth investigations have been focused mostly on proteins due to their importance for medicine, biochemistry, biology, and biotechnology. However, applications in industrial or technological processes are also possible, such as an alternative to zeolites and in the development of molecular devices, such as solar cells (photovoltaics), using proteins [1]. Many works also have been devoted to the development of new nanodevices using of protein nanocrystals. At present, crystallized protein molecules are mainly investigated for the determination of their atomic structure by X-ray analysis. For that, additional efforts are focused on the further development of X-ray procedures to optimize data collection by using a variety of cryoprotectors. In

Handbook of Crystal Growth. http://dx.doi.org/10.1016/B978-0-444-63303-3.00031-6
Copyright © 2015 Elsevier B.V. All rights reserved.

addition to such improvements in the understanding of the crystallographic three-dimensional (3D) structure, there are certain works focused on increasing the understanding of the crystallization process. Even with precise X-ray diffraction (XRD) analysis, single crystals of high quality are required. Systematic studies on the interaction between chemical or physical growth variables and their influence on the yield of size and high structural quality are still rare. A review was published by Otalora and Garcia-Ruiz [2]; there is also a book chapter about crystal growth and the analysis of this crystal perfection using XRD [3].

High-quality single crystals of a size large enough for X-ray analysis are still difficult to achieve in 3D structure determination. However, novel methods have been recently developed to obtain crystals in small droplets, in a shorter time, using robotic drop-dispenser machines. There is also an additional effort focused on developing procedures to optimize the process of X-ray data using personal computers. Nevertheless, few works are focused on understanding the crystallization process and the kinetics of protein crystallization, or even the physical and chemical parameters that affect protein crystallization behavior. Only a few systematic studies are available to understand how these chemical and physical variables influence the outcome in terms of a crystal's size and high structural quality. It is well known that by reducing the convective transport, high-quality single crystals can be obtained. To achieve this objective, there are currently three main possibilities: (1) to grow crystals in microgravity conditions, (2) to grow crystals in thin capillary tubes, and (3) to grow crystals in gels.

A beneficial influence on the growth properties was expected from the fact that gels reduce convection in the growth medium, prevent sedimentation, suppress foreign nucleation, and reduce twinning [4]. Indeed, the number of nuclei and also the defects of the crystals were reduced. Most growth experiments in gels demonstrated structural and physical crystal qualities comparable with those of samples grown under microgravity conditions. Not yet clarified in detail is the nucleation step. Furthermore, theoretical treatments still have to incorporate the growth-specific gel properties.

Currently, there are two basic methods (at the atomic level) for determining the 3D structure of small molecules, including biological macromolecules: nuclear magnetic resonance (NMR) and XRD/neutron diffraction (ND). For the first method, the experiment needs to be performed in solution or solid state (amorphous powder); for the second method, millimeter-sized single crystals are needed (single crystals) or crystalline powder for proper biocrystallographic work. However, for a protein crystallographic project via single-crystal XRD, from nanometer-sized [1] up to millimeter-sized (for ND) crystals are necessary to know the 3D structure [5,6]. X-ray powder diffraction for proteins is not well-developed yet, although there have been some recent advances [7]. For biological macromolecules (proteins, nucleic acids, and polysaccharides), the larger the size, the higher the amount of mass that is required to obtain a proper crystal for X-ray crystallography.

Recombinant technologies based on gene expression using molecular biology techniques have allowed researchers to obtain recombinant proteins for this type of research,

as mass availability is no longer a limiting step within the crystallographic project [8,9]. Additionally, the use of synchrotron radiation facilities [10,11] has improved not only the time for data collection (exposing the crystals to less radiation damage), but has also reduced the crystal size (in the scale of microns) needed to obtain X-ray data for structural purposes.

In any of these cases, there is still a remaining issue, which is the bottleneck in protein crystallography: obtaining high-quality single crystals with near-to-perfect habits made of molecular arrangements with minimum defects that can produce well-resolved and intense diffraction patterns. There are three basic methods to grow crystals with these near-to-perfect characteristics; in all of them, the basic idea to obtain proper crystals for XRD is to minimize (or to eliminate) solutal convection. The first method is to grow crystals in microgravity conditions, although currently this requires very expensive equipment for the experiment and is a time-consuming procedure [12,13]. It has been demonstrated that crystals grown in gel and under microgravity conditions show higher crystal quality than earth-grown crystals [14]. The second possibility is to grow crystals in thin capillary tubes, with diameters less than 0.3 mm. This capillary method has been demonstrated to yield high-quality single crystals of a variety of biological systems, using either of two basic experimental setups: the gel acupuncture method [15,16] or the counterdiffusion method [17,18]. The third method is to grow crystals in gels. This method is the most practical and effective way to obtain high-quality crystals for X-ray crystallography, with a considerable improvement in the internal order of atoms and molecules that constitute the 3D crystal network. A gel is a semi-solid material rich in liquid, which contains a 3D structure full of pores where atoms or molecules can diffuse and work as multiple crystal growth cells. In gels, the transport control is driven by diffusion processes, as has been demonstrated in a variety of publications [4,19–23].

The improvement in crystal quality is thus independent from the M_r particle. These improvements in the crystal quality are attributed to the gel-growth method for the following reasons: (1) within the hydrogel, mass transport is essentially controlled by diffusion; and (2) the protein concentration gradient (depletion zone) generated by each crystal during its growth is not destroyed by density-driven convective flow or by sedimentation [24–26]. Whereas a very low concentration of agarose (0.04% m/v) in solution is sufficient to overcome buoyancy and crystal sedimentation, a slightly higher one (0.12% m/v) is required to obtain a viscoelastic gel and to avoid mass and heat convective transport [27]. In 0.15–0.5% (w/v) gels prepared at low ionic strength, the pore diameter ranging from 300 to 900 nm [28] is compatible with the diffusion of the greatest known icosahedral viruses. Pore size distribution is broader at lower concentration or at higher ionic strength [29,30]. The randomly distributed polysaccharide fibers revealed by scanning electron microscopy (SEM) might explain why they do not appreciably affect the diffraction quality of crystals [31]. In a gel, the pore network is confined by polymer chains that change their conformation as a function of temperature, solvent, concentration, pH, etc. Therefore, for a specific type of gel, the diffusion of the substance to be

grown and the growth process will depend on these physical and chemical variables. It is possible that anomalous diffusion can be observed when large particles become entrapped in the pores network [27].

31.1.1 Gel Growth History

The usefulness of gels for the crystallization of small inorganic compound crystals is well known. However, the crystal size and quality of many materials could be improved markedly. The first applications of gels to the growth of protein crystals were reported by Robert and Lefaucheux [22], Provost and Robert [32] and Miller et al. [33] in the late 1980s and early 1990s. The crystallization of inorganic molecules in gels dates back to the end of the 19th century, when inorganic compounds were crystallized in either gelatin or gels made of siloxane [4,21,22,34,35]. The pioneering experiment related to crystal growth in gels started in 1896 by Liesegang, who obtained for the first time a group of periodic rings of inorganic compounds grown in gelatin [36]. This early description of repetitive pattern formation by Liesegang focused on the chemical reaction occurring in gels between counterdiffusing electrolytes. Liesegang noticed that stratification of parallel precipitation bands originates from anions (outer electrolyte) diffusing in a capillary containing a gel impregnated with cations (inner electrolyte). The formation of bands resulting from the precipitation of the weakly soluble salt occurs rhythmically and is separated by clear gel instead of forming a continuous precipitation zone, as one would have expected. Wilhelm Ostwald was the first to propose an explanation for the phenomenon observed by Liesegang [37,38]. His hypothesis was based on the propagation of a supersaturation wave; it belonged to the prenucleation theories, in contrast to more recent postnucleation theories [39], in which repetitive patterns are produced in essentially homogeneous and continuous colloids. Both theories use equations derived from Fick's law of diffusion [39,40].

Liesegang patterns obtained in gels are routinely described by four laws: the spacing law [41], the time law [42], the width law, and the Matalon–Packter law [43]. An experimental setup similar to Liesegang's experiments in gel has been used for several decades for protein crystallization by the method of counterdiffusion in capillaries [16,18,44]. Crystals of biological receptors (Toll) as well as Liesegang-like patterns with rings formed of protein crystals using agarose gels have been reported [45]. However, for applications in the crystal growth of proteins, the gel-method started to be used conventionally to grow a variety of single crystals after it was proven to be useful to obtain high-quality crystals for X-ray investigations. The first report on the crystal growth of proteins (albumin) in gelatin was published in the mid-1950s [20]; it took a long time before hydrogels, inorganic-gels (mostly hydrogels), and organic gels (organogels) were reintroduced for protein crystallization [22,46,47]. At that time, the gel method led a nonconventional way to grow crystals, with fewer defects and higher crystal quality. Indeed, protein and virus crystals grown in such gels have enhanced diffraction properties, including sharper Bragg reflections, higher diffraction intensities with regard to

the background noise, and a higher diffraction limit with regard to that of crystals that are grown in solution [14,30,48]. Despite the discovery and plenty of publications related to the gel method and its benefits, protein crystal growers and protein crystallographers poorly exploit the gels [30,49].

Figure 31.1 shows the four basic techniques to grow crystals using the gel-growth method (as described in [4]). The first technique uses a U-tube; on it, two solutions containing two soluble salts A and B diffuse along both sides of the tube. Nearly in the central part, an insoluble salt C is crystallized. The second technique consists of having compound A inside the gel, and a solution of salt B is poured onto the top of the gel. When the diffusion of B throughout the gel is happening, the crystallization process of compound C takes place inside the gel network; this C compound is not soluble in water if the gel is a hydrogel. The third technique is a kind of chemical complexation or chemical decomplexation reaction. At the beginning, a soluble complex AB diffuses throughout the gel network; then molecule B is complexed with molecule D, forming a new compound. The final technique is basically a counterdiffusion process; both substances are included in the gel network, then both counterdiffuse. The place where the synthesis of the new compound will take place will be the area of the compound with the smaller diffusion coefficient.

Another powerful procedure to grow crystals of high quality is the application of magnetic fields to the crystal growth process, which has attracted increasing attention. Metals and semiconductors with relatively high electrical conductivity are subject to a Lorentz force when melt movements takes place. Natural convections and flow oscillations can be damped effectively, leading to structural and chemical homogeneity improvements of the growing crystals [50]. In the case of organic fluids (e.g., proteins)

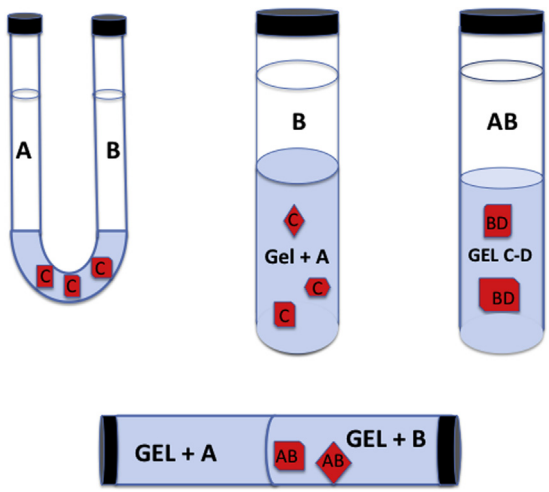

FIGURE 31.1 The four basic procedures to grow crystals in gels. The "U" tube was one of the first devices designed to grow insoluble salts. The other three techniques are use mostly to synthesize new compounds.

with much lower electrical conductivities, the question of the impact efficiency of a magnetic field arises. The existence of anisotropy of the diamagnetic susceptibility has been properly investigated in biological macromolecules, specifically protein molecules; from these, the anisotropy of diamagnetic susceptibility is high due to the existence of alpha-helices and peptide bonds. Here, the orientation/alignment effect comes to be very remarkable in terms of orientation and enhancement of crystal quality. Obviously, the positive effect is due to the alignment of the crystallization units within the magnetic field and the homogeneous transport mode in gel being an exclusively diffusion-controlled process. However, there are also some contradictory reports showing no influence at all, generally when the experiments are performed in solution and using a low-magnetic field. This fact requires further investigation of the decisive effecting parameters.

Pioneering works of the influence of strong stationary magnetic fields on protein crystallization were done by Sazaki et al. [51] and Ataka et al. [52]. A correlation to the crystal alignment within the field was found. Alternating magnetic fields have been also used [53]. An enhancement of the enzymatic reactions was also observed [54]. The first coupling of growth in gels with magnetic fields was carried out by Kinoshita et al. [55], aimed at the improvement of quality and harvest period of protein crystals for structure-based drug design. Using XRD, Lübbert and coworkers [56] analyzed rocking-curve measurements for the differences in mosaicity between lysozyme crystals grown with and without a homogeneous magnetic field of 2.4 T, as well as with and without agarose gel.

31.1.2 Gel Properties and Characterization

In general, a gel is defined as a semi-solid rich in liquid, with a pore-size distribution and structure that depends on the method of its preparation and chemical precursors [4]. Most gels display thixotropy, which is a property that turns them into fluid when agitated but causes them to resolidify when resting. Another property is syneresis, which is a chemical process related to the contraction of a gel accompanied by expulsion of liquid (in small amounts). Hence, the expelled water or organic liquid is called the water/solvent of syneresis. Most of the crystals grown in gels show higher crystal quality than those crystals grown in solution. For many years, direct observation of the gel structure in terms of the pore-size distribution was a difficult task for many researchers. One of the first images of these large pores was obtained at the end of the 1990s by Moreno et al. [26], by means of using SEM (see Figure 31.2).

It is well known that the pore size depends on the preparation conditions of the gels. For example, sodium silicate (SS) prepared by the neutralization method and tetramethyl orthosilicate (TMOS) or tetraethyl orthosilicate (TEOS) gels prepared by hydrolysis showed pores with sizes ranging from 50 to 150 nm for SS gels [26], and from 150 to 250 nm for TEOS gels [57]. The fact that bigger crystals are usually obtained in gels is explained in terms of the size of the pores. Different sizes of crystals are obtained in different types of

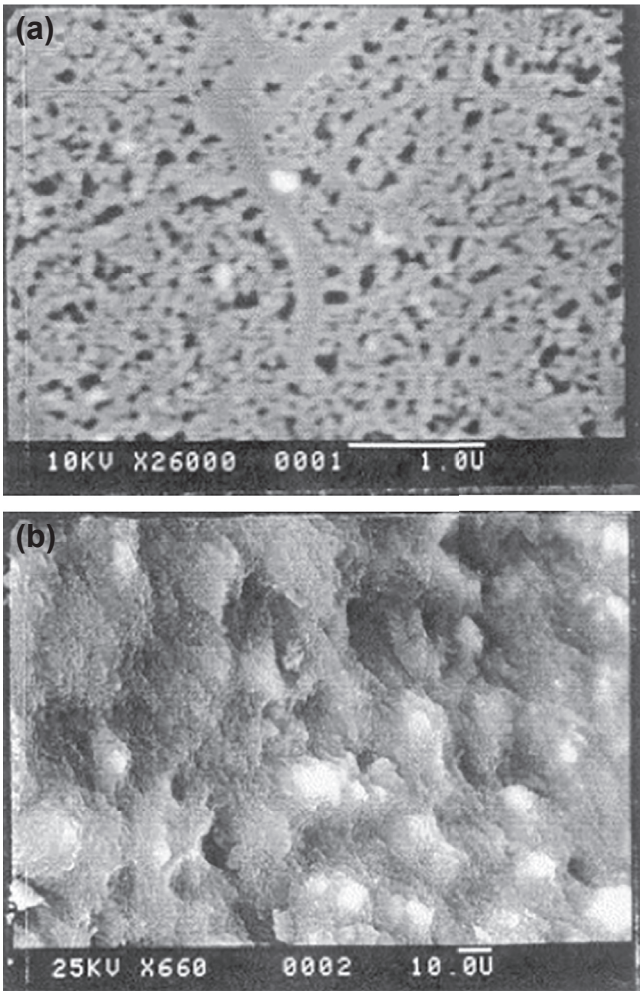

FIGURE 31.2 SEM micrographs of gels from sodium metasilicate solutions. They correspond to silica gel: (a) pH 6.0 and (b) pH 10. *Reprinted from J Cryst Growth 1999;205:375–81, with permission from Elsevier.*

gels, which is explained in terms of the relationship between gel preparation, transport processes, and pore size distribution. This has been demonstrated in previous publications focused on transport processes and protein nucleation control by varying agarose concentration [27]. The control of pore size distribution (randomly or homogeneous pore size distribution) was applied to control the number of protein crystals in the gel acupuncture setup [26]. This control, combining microgravity and gel growth, was also used to obtain large (1 mm from apex-to-apex) and high-quality single crystals of thaumatin grown in agarose gels [14]. These pores, which contain nuclei inside, work as large crystal growth cells. The mechanism of gel structure formation is different in SS or TMOS/TEOS gels. The TEOS gels, for instance, have a conglomerate of multifractal-like structure beads [57], whereas SS gels usually show a lumpy structure [26] (Figure 31.2).

Particularly, gels obtained from TMOS or TEOS hydrolysis are not easily characterized. Their characterization depends on expertise and on the technique used for this purpose. Figure 31.3 shows the peculiar shape of the pores (granular shaped) observed by coupling small angle X-ray scattering (SAXS), atomic force microscopy, and SEM techniques. These polysiloxane gels (TMOS or TEOS) are inert in most inorganics and organics, but sparingly inert for proteins usually prepared in pH buffer solutions. Besides this lack of inertness for biological macromolecules in water, smart mixing strategies allowed their successful use for proteins [21]; more recently, new synthetic strategies, using these TMOS gels compatible with a variety of buffer solutions (usually for proteins), have been published [58].

The first high-resolution micrograph of the structure of agarose gel via SEM of a red algal galactan of different sulfation levels was published in 2008 [59]. The most important characteristic of red algal galactans is their gel-forming ability—that is, the ability to form well-ordered spatial structures during cooling of their hot polymeric solution. The

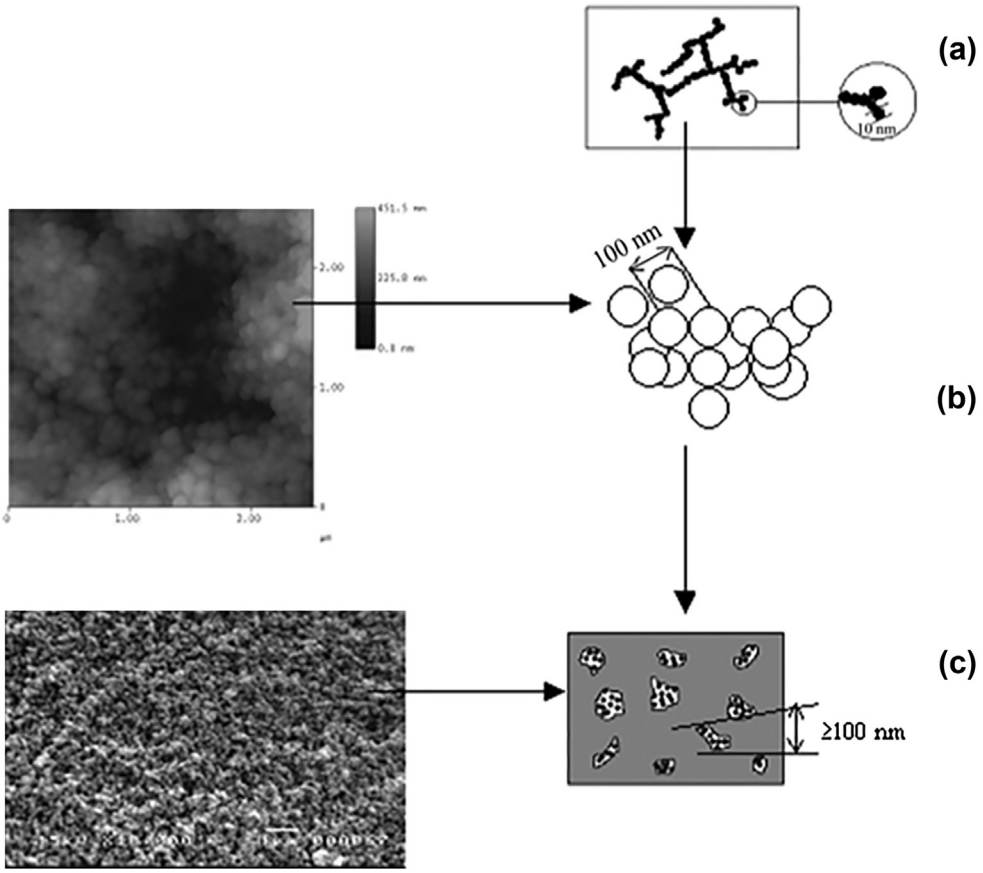

FIGURE 31.3 Multifractal investigation of TEOS silica hydrogels and aerogels. (a) First-generation clusters, as evidenced by SAXS measurements. (b) Second-generation aggregates from atomic force microscopy imaging. (c) Third-generation by SEM observation. *Reprinted from Silicon Chem 2003;2:247–54, with permission from Springer.*

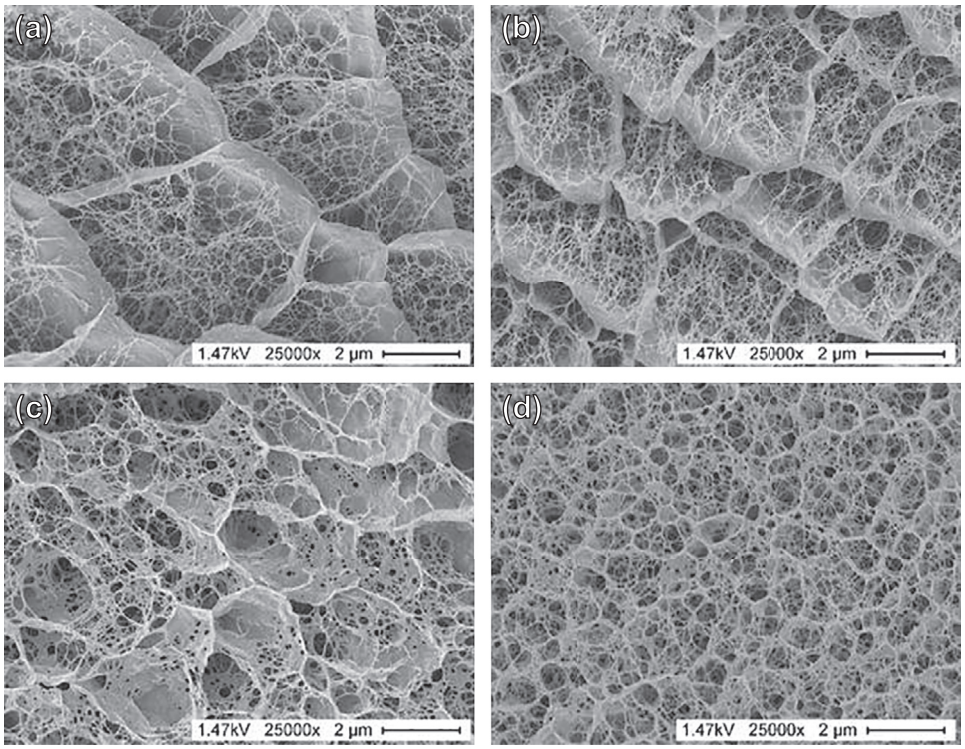

FIGURE 31.4 SEM images of 2% agarose gel network structures at (a) 70 °C, (b) 40 °C, (c) 30 °C, and (d) 20 °C. *Reprinted from J Appl Phycol 2008;20:527–35, with permission from Springer.*

pore-size distribution is in agreement with the models of gel formation described by Anderson et al. [60] for all types of agarose gels obtained from different algae. Figure 31.4 shows these images of low-melting-point agarose at 2% (w/v) concentration, and four different temperatures for gel preparation. It is important to remark that the agar is a mixture of two polysaccharides (agaropectin) and agarose, whereas agarose is a highly pure polysaccharide for hydrogel preparation (see Figure 31.4(d)).

Gels made from purified agarose have a relatively large and homogeneous pore-size distribution, making them useful for size separation of large molecules, such as proteins or protein complexes >200 kDa or DNA fragments >100 base pairs. These hydrogels are suitable for growing protein crystals and also to enhance the crystal quality for X-ray crystallographic research.

31.1.3 Diffusion versus Convective Transport

For growth to occur, the solute species must move from the bulk solution to the crystal surface, be adsorbed on the crystal surface, move to a step, and finally move to a kink on the step. If ionic species are involved, then dehydration and chemical reaction may also be required. The latent heat of crystallization must also move back into the solution because, in solution growth, the crystal is generally surrounded by the solution and there

is no sink within the crystal. The net effect is that the surface of the crystal must be at slightly different temperature from the bulk of the solution. The movement of solute from the bulk solution to the crystal surface by a combination of molecular diffusion and convection (solution movement) occurs under the general title of mass transfer. The processes that occur on the surface may be lumped together under the general title of surface integration [61].

When a crystal is grown in solution, it takes the solute from the solution, thus reducing the concentration of the solution around it. To allow the crystal to keep growing, fresh solute concentrations must be withdrawn from the bulk of the solution, and lead molecules have to move toward the crystal surface of the growing crystal. This motion of the solute is usually referred to as the mass transfer process. In the absence of convection in the bulk of the solution for a gelled system, these molecular motion processes cause mass transference in a controlled manner. These processes are very slow in solids and in gels and sparingly slow in liquids, so any small amount of convection is more than enough to increase the velocity of mass transfer. When the system is in thermodynamic equilibrium, the velocity of mass transfer toward the crystal surface should be exactly like the incorporation of the solute molecules inside the crystal. This velocity is governed by surface processes, the kinetics of mass transport, or both. If the convective transport increases, there is a reduction of the mass transport resistance; then, the influence of the surface kinetics on the crystal growth increases [62].

The crystal growth process depends on transport phenomena such as fluid motion (convection), heat, and mass transfer. All these processes have a strong influence on the crystal growth velocity, crystal morphology, and defect formation, even in gel growth [26,63,64]. Mass transfer, for instance, comes from the concentration gradients, but it can be also caused by thermal gradients (called the Soret effect), electric or magnetic fields, gravity forces, or gravity acceleration. In general, mass transfer in solutions increases due to convective transport; the motion of the solution itself carries out material from the solution. Several driving forces can cause convective transport, such as pressure gradients, mechanical forces, levitation, and electric fields, even by the crystal growth process per se. Convective transport deals with the transport in three directions of any physical property due to fluxes in different directions; we can say then that there is a convective flux [17,21]. On the other hand, the flux growth is the name given to crystal growth from high-temperature solutions, where the flux is typically a molten salt or oxide used as solvent; this method is used to grow single crystals of incongruently melting compounds [65]. The principle of flux growth does not differ significantly from that of growth in solution: temperature is higher and related to the melting temperature of the flux (solvent).

Crystal morphology depends on the kinetics of different faces of a crystal. Surface kinetics and resistance to mass transference are different for each face of the crystal. The crystal habit depends on mass transport and can depend on the amount or on any direction of convective transport inside the solution. The crystal quality will depend also on these transport processes. To increase this crystal quality, from the beginning, the crystal growth process should proceed through diffusion control. Adolf Fick empirically

obtained the basic equations for diffusion transport in 1855; these equations are equivalent to the thermal conductivity proposed by Fourier in 1822, which states that the time rate of heat transfer through a material is proportional to the negative gradient in the temperature and to the area, at right angles to that gradient, through which the heat is traveling [66].

The diffusion of macromolecules through a porous medium is important in many fields of the biological sciences. The phenomenon is relevant to biotechnological separation methods, such as electrophoresis and size exclusion chromatography. Moreover, it has important implications for understanding how macromolecular drugs and naturally occurring macromolecules are transported in living tissue. Diffusive transport is the process by which the matter is transported from one part of the solution to another via random motion at the atomic or molecular scale. In this process, atoms or molecules travel in one direction, eliminating concentration differences and making the concentration homogeneous around crystal growth. These atoms or molecules can be set in motion by applying voltages or external forces to the system [39,40,67].

Table 31.1 shows a comparison of diffusion coefficients in water and in gels for some ions, low-molecular-weight organic compounds, and high-molecular-weight organic compounds such as proteins, ribosomes, and virus particles. In some cases, the diffusion

Table 31.1 Comparison between Diffusion Coefficients of Some Molecules in Water and in Gels

Substance or Biomolecule	M_r (g/mol)	Diffusion Coefficient (cm^2/s) in H_2O	Diffusion Coefficient (cm^2/s) in Gel	References
Cl^-	35.45	2.03×10^{-5}	7.22×10^{-6}	[4]
K^+	39.10	1.98×10^{-5}	2.64×10^{-6}	[4]
KCl	74.50	1.92×10^{-5}	0.493×10^{-5}	[4,68]
Glycerol	92.00	1.3×10^{-5}	2.37×10^{-6}	[69]
Glucose	180.16	7.00×10^{-6}	1.55×10^{-6}	[70]
Sucrose	342.30	5.23×10^{-6}	1.04×10^{-6}	[70]
Ribonuclease	12,640	1.31×10^{-6}	1.20×10^{-6}	[68,71,72]
Lactalbumin	14,178	1.14×10^{-6}	2.37×10^{-7}	[72–74]
Lysozyme	14,500	1.18×10^{-6}	1.04×10^{-6}	[72,75,76]
Thaumatin	22,000	9.40×10^{-7}	N.A.	[72]
Ovalbumin	45,000	4.20×10^{-7}	1.60×10^{-7}	[72–74]
Bovine serum albumin (pH 6.78)	67,000	6.40×10^{-7}	2.45×10^{-7}	[68,72–76]
γ-Globulin	170,000	4.60×10^{-7}	4.4×10^{-7}	[72,77]
Apoferritin	440,000	3.20×10^{-7}	2.50×10^{-7}	[72,78,79]
Ribosome 70S *Escherichia coli*	3,000,000	1.83×10^{-7}	N.A.	[72,80,81]
DNA	6,000,000	1.30×10^{-8}	1.0×10^{-8}	[72]
Satellite tobacco mosaic virus	50,000,000	1.07×10^{-8}	6.00×10^{-10}	[72,82]

N.A. = Not available.

coefficient varies by even one or two orders of magnitude. It is clear that in the particular case of diffusion in gels, the transport and pore size distribution of molecules along the gel network depends on the concentration or method of synthesis of the gel.

31.1.3.1 Diffusion Coefficient and Size of the Clusters

Diffusion of particles in gels is one of the most important issues in transport processes. The molecules are in constant motion; their trajectory from the center of the mass is described in terms of a vector, R(t). If the origin of the coordinates is selected as the location of the particle at $t = 0$, the square displacement is given by $R \times R$. If the trajectory is followed many times for some elapsed time τ, the mean-square displacement is found to be proportional to the elapsed time. The Brownian diffusion law is

$$<R^2> = 6D_s\tau \tag{31.1}$$

where D_s is the self-diffusion coefficient. If the particle is a sphere of radius R_h, the self-diffusion coefficient is inversely proportional to R_h and directly proportional to the temperature of the solution. The explicit formula for the self-diffusion coefficient can be calculated by the method of Brownian dynamics [83].

The solvent is treated as a viscous continuum of dynamic viscosity η and absolute temperature T. A particle in such a solution is subjected to three types of forces: (1) viscous force; (2) external forces, such as gravity, electrical fields, or magnetic fields; and (3) a random movement of ions, atoms, or molecules. On the other hand, the mean-squared displacement of a particle in a solution subjected to no external forces can be expressed as

$$<R_h^2> = 6\left[(k_bT)/\varsigma\right]\tau \tag{31.2}$$

where k_b is the Boltzmann constant and ς is the friction coefficient for a spherical particle given by

$$\varsigma = 6\pi\eta R_h, \tag{31.3}$$

hence, it is a consequence within the limit of the length of elapsed time. This means that the self-diffusion coefficient of a particle in solution is

$$D_s = k_bT/\varsigma \tag{31.4}$$

This last equation is well known as the Stokes–Einstein equation. However, for a particle of arbitrary shape, it is customary to define the hydrodynamic radius in terms of the measured friction coefficient, as follows:

$$\varsigma = 6\pi\eta R_H \tag{31.5}$$

So, finally, the Stokes–Einstein equation becomes in its conventional form:

$$D_s = k_bT/6\pi\eta R_H \tag{31.6}$$

This equation is very useful for investigations related to dynamic or static light scattering methods [84]. By measuring the diffusion coefficient in protein solutions, we could derive the hydrodynamic radius and, as a consequence, the growth of the embryo can be experimentally detected. However, by means of Fick's laws, the diffusivity or diffusion

coefficient can be estimated. Then, Kratochvil's equation [85] can be used to measure the molecular weight of any biological macromolecule, the protein–protein interactions (based on the second virial coefficient) and the radius of the cluster can be investigated [84], all based in the Brownian motion of macromolecules.

In that sense, the determination of the diffusion coefficient of small and large biomolecules by means of different modern techniques is crucial to investigate, not only for transport phenomena research in biological systems, but also to measure useful and important parameters in protein crystal growth research.

31.1.3.2 Experimental Methods to Evaluate the Diffusion Coefficient and the Gel–Matrix Interaction

The purpose in this section is to review some of the experimental methods used in recent years to evaluate the diffusion coefficient and the molecule–gel matrix interactions, as well as the theoretical and the numerical models used to explain these experimental results.

31.1.3.2.1 EXPERIMENTAL METHODS

The experimental methods are generally based on the utilization of at least one appropriate chemical probe. This chemical probe is introduced into the gel to measure one physical property that is related, either directly or indirectly, to the diffusion of the probe. These experimental methods can explore the gel matrix–molecules or the ions, as well as their interactions at a microscopic level. They can therefore show us different parameters in real materials, such as the heterogeneity of porosity and the chemical composition, etc.

I. Single molecule spectroscopy, also called single molecule tracking methods, includes several methods such as beam- and sample-scanning confocal microscopy and wide-field imaging. The molecule probe is usually a dye. The detection of isolated molecules is achieved by using nanomolar (nM) concentrations ranging from approximately 0.01 to 1 nM of the dye probe, and an ultrasmall detection volume of approximately 1 fL. In sample-scanning experiments, the emission features, either time- or spectrally resolved, are registered for each spot. On the other hand, in wide-field imaging experiments, the motion of individual molecules in space and time are registered, taking several images of the same area [86,87]. The effect of confinement in the orientational motion of probe molecules in nanosized pores is performed by single-molecule emission and transmission dichroism. The experiments must be performed simultaneously in two orthogonal polarizations [88] (Figure 31.5).

These techniques have helped researchers to determine that the main interactions between gel matrix components are ionic, hydrogen bonding, and have hydrophobic and steric effects. In silica gels, the ion interaction happens between the deprotonated silanol sites on silica surface and the cationic part of the probe molecules. Data analysis of single molecule trajectory and orientation is performed by orthogonal regression methods [87–89].

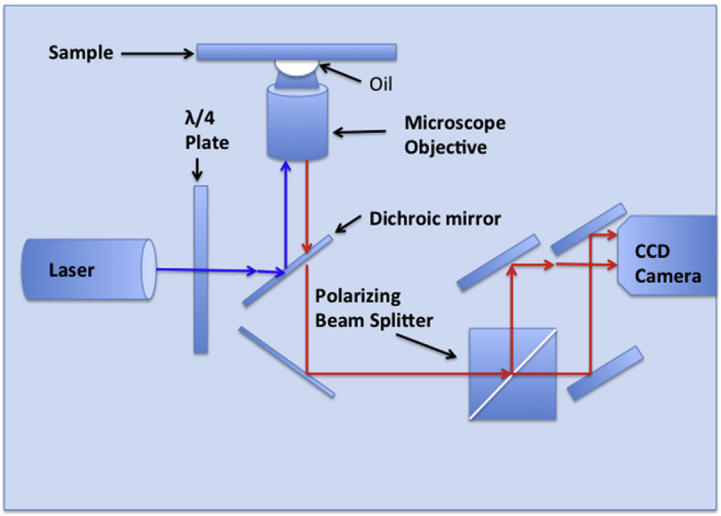

FIGURE 31.5 Schematic setup for the single molecule tracking method. *Reprinted (adapted) with permission from Rajib Pramanik, Takashi Ito and Daniel A. Higgins. J. Phys. Chem C 2013,117, 3668-3673. Copyright 2014, American Chemical Society.*

II. Electron spin resonance (ESR) and electron paramagnetic resonance (EPR): ESR or EPR methods are based on the strong environmental dependency of the electronic properties [89–91]. This makes it suitable for the study of confined species in porous media. In this method, the sample is exposed to a variable magnetic field in order to split the spin states of unpaired electrons. The separation between the lower and the higher energy states is given by $\Delta E = g_e \mu_B B_0$, where g_e is the g-factor $= 2.0023$ for the free electron, μ_B is the Bohr magneton, and B_0 is the strength of magnetic field. By either absorbing or emitting a photon of energy $h\nu$, an unpaired electron can move between the two energy states, obeying the resonance condition $\Delta E = h\nu = g_e \mu_B B_0$. The frequency (9–10 GHz), and the magnetic field (0.35 T) are usually employed in EPR or ESR experiments (Figure 31.6).

One important drawback of this method is the need of at least one unpaired electron in the sample paramagnetic species that is called a *spin probe*. The use of either ESR or EPR to investigate surface interactions in mesoporous materials, employing functionalized spin probes such as molecular nitroxides or 3-carboxy-proxyl, has enabled researchers to estimate the surface interaction enthalpies, the rotation correlation times, the rotation activation, and the position within the pore. These methods are sensitive to changes in polarity and in microviscosity around the paramagnetic group, and have also been used in the study of organogels. Only the amino-TEMPO spin probe was sensitive to the diffusion process in the organogel 12-hydroxystearic acid (12-HSA). However, EPR or ESR spectra were independent of the 12 Human Serum Albumin (12-HSA) concentrations [92].

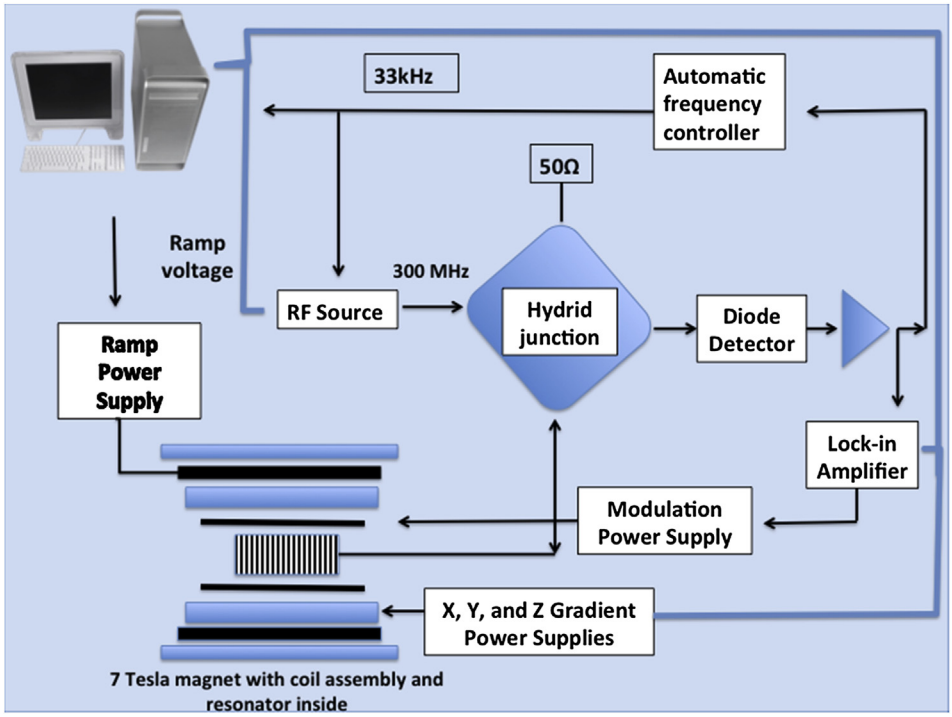

FIGURE 31.6 General setup for Electron Spin Resonance (ESR). *Reprinted (Adapted) with permission from reference A J Fagan, D J Lurie Annual Reports on NMR Spectroscopy 56 (2005) 97-140.*

III. Electron spin resonance imaging (ESRI), a method associated with ESR, has been used to study the distribution of paramagnetic molecules in the sample along the direction of the magnetic field gradient, additionally to the external magnetic field generated in the spectrometer. The spectrum measured under these conditions is a superposition of the spectra of all individual paramagnetic molecules in various positions inside the sample. ESRI allows the study of the diffusion process of a paramagnetic probe from the surface of the sample, by applying the magnetic field gradient in the direction of diffusion. Some of the spin probes used were low-molecular-weight nitroxide and spin-labeled poly(ethylene) oxide (PEO) oligomers, in 2-hydroxyethyl methacrylate (HEMA) hydrogels. It has also been found that the diffusion coefficients depend on the molecular weight of the spin probe, where the systems studied were three different probes in three hydrogels, prepared with different ratios of HEMA and 2-(2-hydroxyethoxy)ethyl methacrylate monomers. Other experiments were performed to determine the diffusion coefficients of low-molecular-weight probes in polystyrene gels cross-linked to various degrees and swollen with the same solvents. Here, the most important result was the dependence of the diffusion coefficients on the degree of crosslinking of polystyrene [93].

IV. Pulsed magnetic gradient spin echo is a method that allows measurement of the displacement of the observed spins by means of the attenuation of the echo signal that arises from the echo pulse sequence containing a magnetic field gradient pulse in each period [67]. Self-diffusion and mutual diffusion coefficients of small analytes in hydrogels have been measured by ^{13}P-NMR. It was found that the coefficients were also reduced by 30%, similarly to those measured in solutions. This could be due to the interaction at the molecular level. Another result shows that, at the mesoscopic level, the open structure of the gel has little influence [94]. The study of rotational and translational motion of the cationic-end of the ionic liquid 1-buthyl-3-methylimidazolyum-bistrifluoromethylsulfonimide, in bulk and confined in mesoporous silica, has recently been reported by pulsed field gradient NMR experiments. These experiments show that the rotational and translational motions of the ionic liquid are reduced at the silica surface, thus allowing the estimation of the mole fractions of fast (bulk) and of the slow populations of the ionic liquid in the partially filled pores of silica [95].

V. NMR imaging is a method in which the spatial resolution is obtained by a magnetic field gradient. A magnetic field gradient G is superimposed to a static field B_0. The frequency ω is shifted, whereas the spatial coordinate corresponds to the resonance frequency of the signal, such that $\omega = \gamma(B_0 + G)$, where γ is the gyromagnetic ratio. Therefore, for ω for a given spin, there is a function of the identity of the spin and of the local field. In NMR-I experiments, the frequency axis is considered as space axis by applying the gradient field in the direction of the desired profile. In the case of a 3D image, however, this has to be done in the *x*, *y*, and *z* directions. The spatial resolution depends on the power of the gradient field and on the width of the resonance line. The magnitude of both parameters in polymer gels is 500 mT/m and $\Delta\omega$ between 0.1 and 2 kHz, given a spatial resolution in gels on the order of 50 μm [96] (Figure 31.7).

31.1.3.2.2 THEORETICAL AND NUMERICAL SIMULATIONS

Hydrodynamic convection is eliminated in gel systems. Several physical obstacles as well as several chemical species can be immobilized in a gel matrix. Charged gels can interact electrostatically with ions prodding changes on their diffusion coefficients [97]. Dynamic surface tension analysis (in agarose gels) showed that the gel network inhibits the nucleation of lysozyme. This was observed by the enhancement of the repulsion and the interfacial structure mismatched between foreign bodies and lysozyme crystals. This produces a reduction of the diffusion process of the protein molecules that cluster towards the crystal–fluid interface, where their rearrangement is inhibited [98]. On this contribution, a detailed study of the kinetics of surface assembly in agarose based on a two-dimensional self-assembly mechanism has been performed.

Another method that we have reviewed is the lattice Boltzmann method (LBM), which is a numerical method used in computational fluid dynamics. Kang et al. extended the LBM method to pore-scale system, including advection, diffusion, homogeneous, and

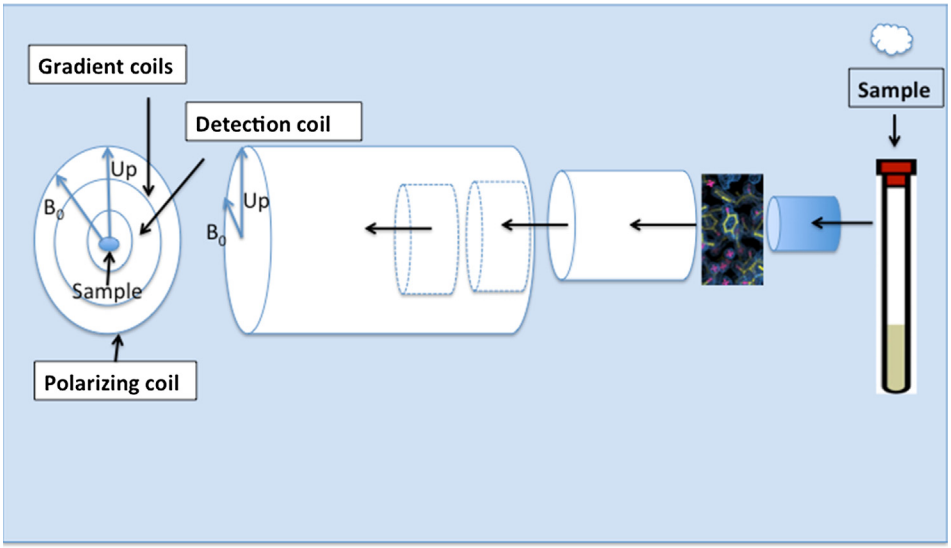

FIGURE 31.7 Schematic arrangement for nuclear magnetic resonance (NMR) imaging. *Reprinted (adapted) with permission from A Mohoric, G Planinsic, M Kos, A Duh, and J Stepisnik Instr. Sci. Technol. 32 (2004) 655.*

heterogeneous reactions, resulting in geometrical changes in pore space (cited in [98,99]). The porous structure of the gel matrix provides the nucleation sites for the heterogeneous nucleation of C, an intermediate colloidal phase. A lower gel concentration (or larger porosity) means fewer nucleation sites [98].

Numerical simulations techniques are very useful tools to support experimental data, even in complex systems such as gels. It is possible to classify them into two groups: those concerning the calculation of atomic-scale interactions that underlie the formation of the gel network and others that are focused on mass transport in the system. In the first group of methods, the gels are considered as a low-density disordered fractal network of interactive molecules with slow relaxation dynamics at low temperatures.

Molecular dynamics (MD) simulations have been used to simulate polymerized silica aerogels with a reactive charge transfer of three-body interaction potential. The calculated fractal dimension depends on the process by which the network is generated [100]. Another example of MD is the study of equilibrium and nonequilibrium routes to gel formation in a wide region of volume fractions of the dispersed phase. This was considered as the anisotropy of interactions, showing that the Arrhenius-type decay for the diffusivity was due to the bonding between colloidal particles [101]. The out-of-equilibrium gels have been explored by MD, constructing a fractal initial configuration by means of a purely kinetic particle diffusion algorithm, considering later an interaction potential between the particles and allowing the relaxation of the initial structure, which is finally followed by the dynamic of the system by means of constant-temperature MD [102]. An alternative approach to equilibrium dynamics was performed by modifying the three-body interactions of the Stillinger–Weber potential for

silicon; the aforementioned interactions can be expressed in terms of angles formed by triplets of particles, which stabilize open network structures in which the particles have very small connectivity [103].

Monte Carlo (MC) simulations of diffusion of nanoparticles in agarose gels have been reported to evaluate the fractal exponent of diffusion, its variation with the reduced hydrodynamic radius R_A/R_C. A systematic offset of the experimental fractal exponent of diffusion as compared to MC simulations could be related to nonspecific van der Walls interactions between diffusing particles and the polymer network [104,105].

Brownian simulation of solute diffusion in a 3D polymer hydrogel structure was reported by using an adaptive time stepping algorithm. The obstruction effect from the gel strands of water and diffusion of dendrimers of different sizes were determined by simulations. The interactions between dendrimers and the gel matrix were done by means of a sticky boundary condition [106].

Mass transport. One interesting contribution to the problem of simulation of mass transport in gels has been published by Zhang et al. [107]. Considering that mass transport is possible due to the elastic properties of the 3D network that enable the gel to retain its shape after deformation, and to the fact that the solvent molecules interact between themselves and with the gel network by physical bonds, a finite method element approach was finally developed. The authors combine some aspects, such as the kinematics of the network, the conservation of the solvent, the conditions of local equilibrium, and the kinetics of migration. The method is implemented in ABACUS/ standard finite element program.

pH-Redox-Equilibrium (PHREEQC) is a program used to simulate mass transport in complex multicomponent systems. The numerical simulation is performed as a function of time-dependent ion concentration gradients and saturation indices. This depends on the initial location of the calcium carbonate precipitate in the additive-free experiment, as well as on the study of the crystallization parameters of calcium carbonate in an agarose viscous sol by using counterdiffusion experiments [108].

31.1.4 Gel Growth Applications

Inorganic gels are widely studied for applications in daily lives [109], catalysis [110], electronics [111–113], thermal insulation [114], sensors [115], ceramics [116], protective and optical films [117], molecular separation [118], and pharmaceuticals [119,120]. Tetraalkoxysilanes particularly have been used as starting materials for preparing glasses and glass ceramics by the sol–gel process and advanced silica-based materials [121,122].

Hydrogels and organic gels that limit the diffusion of solutes and of proteins have numerous applications in different areas, not only for protein X-ray crystallography but also for biotechnological fields ranging from cell encapsulation, through chromatographic separation, to controlled drug delivery in pharmaceuticals. In all of these applications, the hydrogel acts as a means of retarding the diffusion of the molecule

[123]. Other types of gel applications are, for instance, polyacrylamide gels used as dialysis membranes [124–126]. In biochemistry, agarose gels and polyacrylamide gels have been used for direct protein crystallization in the gel electrophoresis setup [26,46]. Agarose gels have been used to control the transport processes in microgravity experiments for protein crystallization [14] and for the orientation of crystals in the presence of strong magnetic fields [50,127], as well as to grow membrane proteins [128,129] to crystallize biomacromolecular complexes, such as the Toll receptor of *Drosophila melanogaster* to obtain Liesegang-like patterns [45]. One application of the gel method has been the reinforcement of protein crystals, incorporating silica fibers (TMOS gel) inside the crystal network, which can be very useful in nanobiotechnological applications and to protect crystals against radiation damage [130].

Novel and practical strategies have been published to apply classic gels to small organic molecules [131], and even to biological macromolecules, using TMOS/TEOS hydrogels [58]. Agarose gels have been used to promote nucleation at different concentrations, ranging from 0.4% to 0.8% (w/v) for protein crystallization [132]. The first suggestion about the use of agarose gels for protein crystallization dates back to the end of the 1990s [47]. The use of agarose gel with different types of additives, compatible with a variety of biological macromolecules for crystallization, was published afterwards [133]. One interesting application for protein crystallization was to screen directly in a gel electrophoresis set up using acrylamide gels [26]. Particularly, for the crystallization of proteins, nucleic acids, and viruses, a full review with plenty of recipes for gel preparation has been published [30]. Novel organic gels based on polyvinyl alcohol (PVA) and PEO have been suggested for the crystallization of soluble proteins and membrane proteins [129]. Organic gels, such as PEO, have been synthetically optimized. The PEO gel was has been suggested for crystal growth in gelled organic solvents of small molecules, either for organic or inorganic compound crystallization [131].

31.2 Hydrogels, Organic Gels, and Aerogels

31.2.1 Synthesis and Characterization of Hydrogels and Organic Gels

Gels are classified as physical or chemical gels when the temperature is the main parameter to be considered for the gelling process or a chemical reaction is carried out for the gelling process, respectively. The synthetic pathways to obtain hydrogels from the neutralization of SS solution are as follows:

$$Na_2SiO_3 + 3H_2O = H_4SiO_4 + 2NaOH \tag{31.7}$$

$$2H_4SiO_4 \rightarrow (HO)_3\text{–}Si\text{–}O\text{–}Si(OH)_3 + nH_2O \tag{31.8}$$

$$\rightarrow \rightarrow \rightarrow ((HO\text{–}Si\text{–}O)_n\text{–}Si))\text{–}(O\text{–}Si\text{–}OH)_n + nH_2O \tag{31.9}$$

or by hydrolysis of TMOS or TEOS (Moreno et al., 1999):

$$Si(–O–CH_2–CH_3)_4 + H_2O \rightarrow H_4SiO_4 + nH_2O + EtOH \quad (31.10)$$

Then;

$$2H_4SiO_4 \rightarrow (HO)_3–Si–O–Si–(OH)_3 + nH_2O \quad (31.11)$$

and finally

$$\rightarrow\rightarrow (HO–Si–O)_n–Si–(O–Si–OH)_n + nH_2O \quad (31.12)$$

This reaction is the same for:

$$Si(–O–CH_3)_4 + H_2O \rightarrow H_4SiO_4 + nH_2O + MeOH \quad (31.13)$$

In both cases (reactions (31.10 and 31.13), the polymerization reaction is a two-step process: hydrolysis (rapid, stirring needed) and polycondensation (slow, solidifies when resting).

Physical gels: Algal polysaccharide agarose forms a thermo-reversible gel; its chains melt above a critical temperature (T_m) and gellation occurs below a characteristic temperature (T_{gel}, gelling point) [134]. Miller et al. [30] used agarose to grow crystals of horse serum albumin in the laboratory, which were of large size and excellent crystallographic quality and almost as good as crystals grown in solution under microgravity, where the driving gradient is limited by the concentration of the solute rather than by the heat gradient (called solutal convection) [30]. Afterwards, crystals of small model proteins grown in agarose gel have been reported to be frequently bigger and always better than reference crystals grown in solution. The former are well-facetted and develop in three dimensions because they are trapped in the network and cannot sediment, have excellent optical properties and have less defects in their lattices, as indicated by their smaller mosaicity, or are not twinned at all [135–139].

The limits for minimization of the impurity effects on the agarose network [140,141], through the formation of a stable impurity depleted zone surrounding the growing crystal [64,142], have been investigated. To characterize the threshold of impurity that can be segregated in a 0.2% m/v gel, an isoform present in trace amounts in thaumatin batches served as a marker. Mass spectrometry analyses have been performed to verify the ratio of two isoforms present in a single batch of thaumatin [143]. In other words, the impurity filtering effect operates only if structural dissimilarities are strong enough. This was the case of hen and turkey lysozymes that have a close M_r (14,313 vs 14,209) but differ by seven amino acids by a net charge of 1, and consequently in solubility [140]. Another example where the effect is amplified is that of ironless apoferritin contaminated by dimers of holoferritin, where each particle contains about 4500 iron atoms [142]. Whether agarose was working as an impurity or an impurity filter was clarified by using laser confocal microscopy combined with differential interference contrast microscopy [144].

Chemical gels: Polysiloxane hydrogels have been used for many years as a crystal growth medium [4] because their porous network permits diffusion of ions and large polymers, such as polyethylene glycols. They have been applied less frequently than

agarose because a chemical reaction is needed. Several macromolecules, including proteins, a virus, and an RNA transfer, have been crystallized in such gels [145,146]. Extensive studies on the model protein, hen lysozymes, have shown that crystal growth in polysiloxane hydrogels minimizes the effects of impurities [140]. Small-angle neutron and quasi-planar X-ray topography investigations have indicated that the gel inhibits nucleation partially [47] and decreases mosaicity [147]. In counterdiffusion or batch conditions, incorporation of the polymer into the crystal lattice at high gel concentrations (2–22%) reinforces the crystals [148]. Furthermore, polysiloxane hydrogel appears to be more effective than agarose [146]. In the peculiar case of hen lysozyme, crystals grown in the former have a lower mosaicity than those grown in agarose [147].

Moreno et al. [26] determined the pore size distribution of the flexible polymer network obtained by neutralization of sodium metasilicate using SEM (Figure 31.2). They found that pore diameter ranges from 50 to 150 nm. Hydrogels formed at pH 10 have a more homogeneous pore-size distribution than those formed at pH 6. The pore in TMOS hydrogels at 10% and 20% v/v measure 150–250 nm and 50–100 nm, respectively [26]. In the gel acupuncture method, this property of the gel matrix has been exploited to control the diffusion of the precipitant and, consequently, the nucleation rate of thaumatin crystals in solution within cylindrical capillaries [26]. SAXS analyses on TEOS hydrogels have shown that their pore-size distribution is random; their polymerization occurs via the interaction of particles whose size and fractal dimension depend on the synthesis pathway and on the final location of the latter between the surface and the heart of the gel [57,149].

A typical classification of gels in general can be summarized as follows:

GELS
- **Physical Gels** (Like agarose, PVA, gelatin, Gel Gro®)
- **Chemical Gels** (Like SS, TMOS/TEOS, acrylamide, etc)

The second classification is related to the nature of the chemical structure (i.e., atoms or molecules chemically bound to form an inorganic or an organic gel network). This depends on the chemical structure of the chain of the polymer.

GELS
- **Inorganic** (SS, TMOS/TEOS, etc)
- **Organic** (Agarose, acrylamide, carboxymethylcellulose, etc).

Novel organic hydrogels: Novel gels (other than agarose and polysiloxanes), such as PVA and PEO, have been suggested for the crystallization of a variety of compounds (including proteins), which can be dispensed into the medium prior to crystallization and easily removed from crystals [129,131]. For each of these gels, the solubility, the concentration required, the corresponding pH, and the effect of pH neutralization

should be determined. Particularly, for applications in the crystallization of biological macromolecules, compatibility with the growth medium is a highly complicated task. Investigations have concentrated on the synthesis and compatibility of PEO gels for the crystallization of small organic molecules [131]. The synthesis pathway to obtain PEO gels, which are promising gels for the crystallization of complex organic or organometallic compounds, follows.

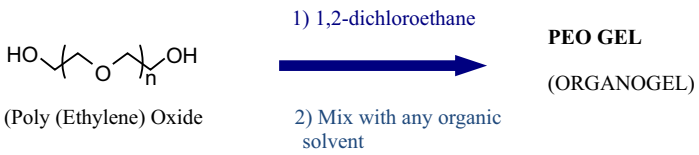

However, in the particular case of proteins, after establishing the proper mixing conditions for any gel precursor, it is mandatory to determine how to remove this gel-cover from the crystals. The gel should allow the cryoprotectant to get into the crystalline structure for high-resolution X-ray crystallography and avoid radiation damage.

A cubic phase (usually called cubic lipid phase) of monoolein [150–152] has been the key to the successful preparation of membrane proteins [153–160]. The peculiar organization of lipids in cubic phases does not restrict their use for solubilization and crystallization of hydrophobic macromolecules. Polar proteins crystallize very well in such media [161,162]. So far, this convectionless crystallization method has not been applied outside the membrane protein crystal grower community [163].

Crystals grown in gels usually demonstrate benefits, such as occurring in fewer numbers or larger sizes. For instance, in 1995, Patel et al. suggested a kind of universal gel based on chromatography theory. They explored the possibility to crystallize various proteins, nucleic acids, and viruses in the presence of soluble polymers, such as carboxymethylcellulose [164]. Currently, there is no universal gel synthesized for the crystallization of all types of biological macromolecules (proteins, nucleic acids, and polysaccharides). In macromolecular crystallization, this universal gel (polymer or high-viscosity fluid) should not interfere with the crystal quality [26].

Several publications demonstrated that crystallization of a biological macromolecule in a hydrogel [6,139] might have at least some advantage over crystallization in pure solution for either proteins (Figures 31.8 and 31.9) or low-molecular-weight compounds [131]. Altogether, the results from the literature and the new ones here presented indicate that crystals grown in gel can be less mosaic and yield more intense diffraction patterns than those prepared in solution. Despite these benefits, a limited number of protein structures at high or atomic resolution have been obtained with crystals grown in agarose gel by vapor diffusion [14,165–167].

Crystallization in gels through the control of mass transport by diffusion mimics in part the microgravity environment and allows one to obtain fewer crystals and larger sizes in some cases. This has been demonstrated for agarose gels, where the critical

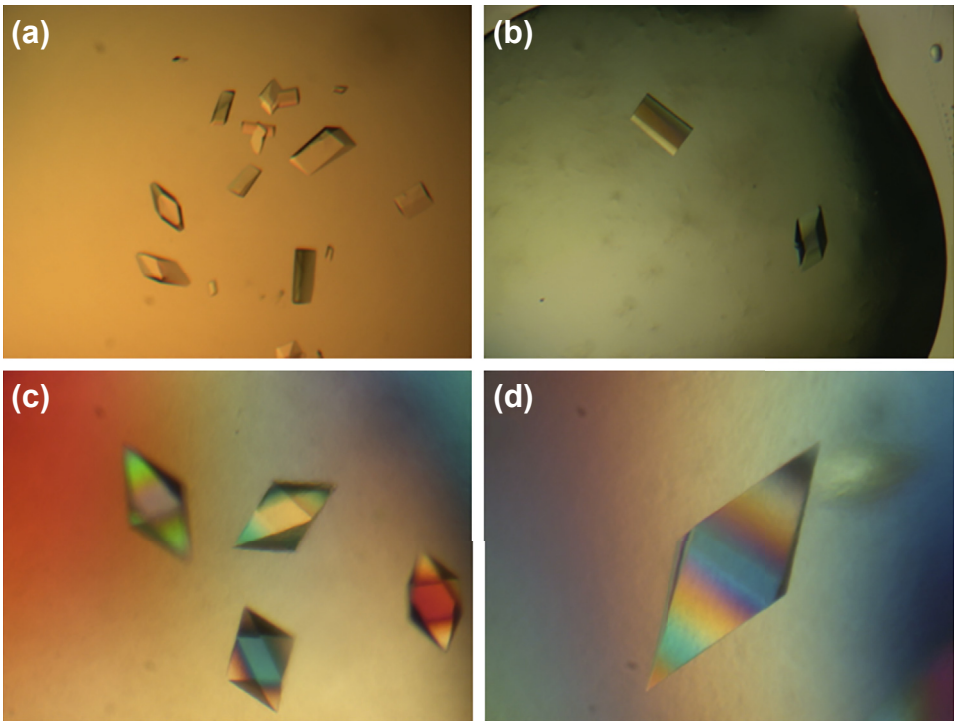

FIGURE 31.8 Pictures of aspartyl-t-RNA synthetase from *Thermus thermophilus*. (a) solution-grown, (b) gel-grown, (c) plant thaumatin crystals grown at 20 °C in solution, and (d) gel-grown single crystal. The size of the largest crystal is 500 μm and is the reference in scale for the other crystals.

concentrations were determined for the crystallization of proteins [132]. Other chemicals that form gels in aqueous solution are being synthesized every day; some of them, such as viscous polymers [164], oriented macroporous polyacrylamide gels [168], hydrogels for tissue engineering [169], supramolecular neutral hydrogels [170], and water gellators [171], may be useful for the crystallization of biological macromolecules. An alternative is the combination of gels and oils [172]. Finally, diffusion-controlled macromolecular interactions are as crucial for optimal crystal growth in gels as for biological reactions occurring in the living cells [173].

31.2.2 Synthesis and Characterization of Xerogels and Aerogels

Depending on the type of solvent (or gas/air) included inside the gel network, gels are classified as organogels (organic solvent, mineral oil, or vegetable oil inside), hydrogels (if water is inside), xerogels (which are dried gels), and aerogels containing different gas or air inside the 3D structure [174]. This third classification includes four main types of gels, which are summarized as follows.

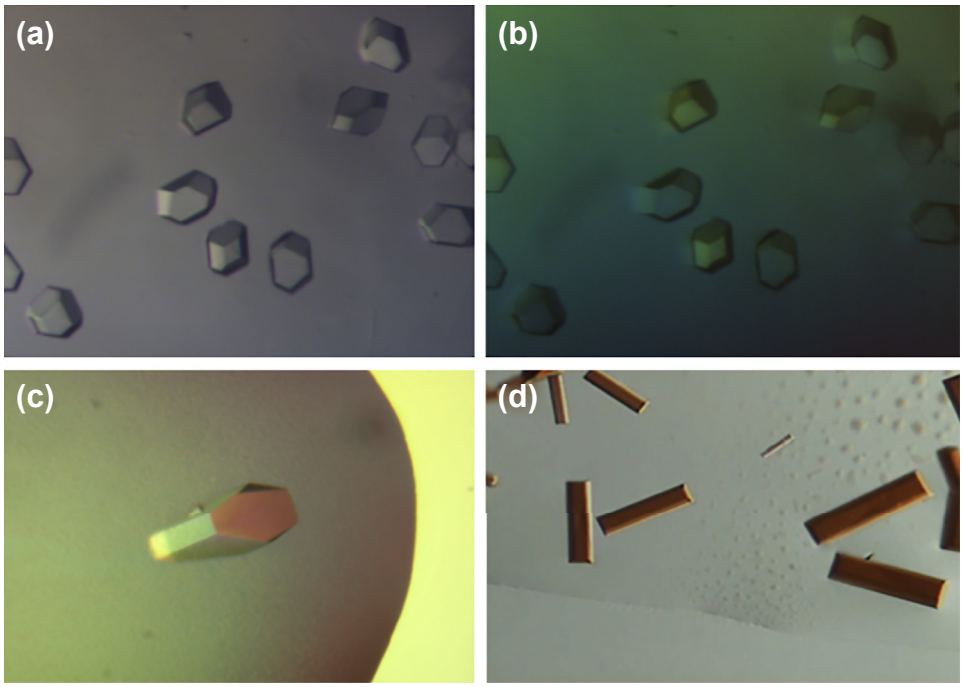

FIGURE 31.9 Pictures of different protein crystals. (a) glucose isomerase, (b) glucose isomerase in polarized light, (c) orthorhombic aspartyl-t-RNA synthetase from *Thermus thermophilus*, and (d) cytochrome C from bovine heart. The size of the largest crystal is 400 μm and is the reference in scale for the other crystals.

GELS

- **Hydrogels** (Like agarose, Gelatin, Gel Gro®, SS, TMOS, TEOS, etc)
- **Organogels** (Carboxymethylcellulose, Acrylamide, etc)
- **Xerogels** (like silica powder commonly use in Chemistry)
- **Aerogels** (using any of the gels from SS, TMOS/TEOS, PVA, PEO, etc., but including air inside the gel network).

A xerogel is a solid formed from a gel by drying with unhindered shrinkage; these gels usually retain high porosity and an enormous surface area, along with very small pore-size distribution [175]. An aerogel is formed when solvent (organic or water) removal occurs under supercritical conditions; the structure does not shrink, is highly porous, and is made of low-density material [57]. During drying of xerogels, the collapse of smaller pores may occur due to the higher capillary tension developed in

the evaporation process. This phenomenon results in a contraction of the solid network, making it denser than that of aerogels. In supercritical fluids, during the drying process, the solvent is removed as a supercritical fluid; this avoids the formation of a meniscus and decreases the effect of surface tension, allowing for the preservation of the porous network [149]. Xerogels have important applications as pharmaceutical drug carriers [176].

The synthesis based on the polymerization of alkoxysilanes, such as TMOS or TEOS, allow one to obtain hydrogels. The process occurs in two steps, hydrolysis and condensation, as shown previously. Therefore, controlling these processes is an important aspect in the development of advanced materials, such as aerogels, with important biotechnological applications using the hydrophilic (for the removal of organic solvents) or hydrophobic properties for the removal of poorly water-soluble pollutants [177]. Because the properties of silicon-containing materials are very dependent on structure, it is of crucial importance to investigate hydrogel, organogel, and aerogel organization and morphology, as shown in Section 31.1.2. This fact allows one to control the pore-size distribution and sol–gel processes for applications to advanced silica-based materials [122].

During the last few years, the bulk structure of silica aerogels has been extensively studied, mainly by scattering techniques (neutrons, X-rays, light). It has been shown that porous silica aerogel has a fractal backbone structure [178]. Its spatial extension and fractal dimension are strongly dependent on the chemical (polymerization) and physical (colloid aggregation) growth process [179]. The typical length of these fractal structures ranges from 1 to 10 nm, and in some cases goes up to 100 nm [180].

The most relevant properties of silica aerogels are the high porosity (75–99.9%), resulting in a low density (3–500 kg/m^3), high specific surface area (800–1000 m^2/g), and pore size in the range of 1–100 nm [181]. The combination of their high porosity with the very small size of their pores leads to unique properties, such as low thermal conductivity (0.01–0.02 W/(m K)) and great accessibility to the internal surface through the porous network [182,183]. In some chemical systems, the porosity of xerogels can reach values close to those of aerogels, as occurs in cases where the liquid inside the pores does not exhibit appreciable interaction with the solid structure of the material. This effect is seen when the synthesized gels, before undergoing drying, have a highly hydrophobic solid network [175]. Additionally, the low density and thermal conductivity values make aerogels attractive for building insulation and for spacecraft components, whereas their very high and controlled porous structure make aerogels excellent candidates for catalysts, sensors, and filters for gaseous pollutants [114,184]. Other aerogel applications include impact absorption, cosmic particles trap, dielectrics, and spacers for vacuum electrodes [185,186]. Recently, carbon aerogels have attracted much attention because of their extraordinary properties and potential uses in a wide variety of technological applications [187].

31.3 Crystal Growth in Gels of Small Molecules, Minerals, and Biological Macromolecules in Gels

Basic research on anisotropic physical properties requires crystalline samples of high quality. Crystal growth in gels is an ideal method to provide this kind of specimen, mostly when the salts to be grown are sparingly soluble in water. The nucleation kinetics and the crystal growth itself depends on gel characteristics such as density, pH, aging time, and salt concentrations. It is important to note that SS is one of the most popular gels used to grow crystals of inorganics (low-molecular-weight compounds). In general, the gel from SS shows some general features: pH ranging from 3 to 5 and density between 1.03 and 1.06 g/cm^3.

Table 31.2 provides a list of inorganic compounds and minerals grown in gels for a variety of applications, which have ferroelectric, ferroelastic, piezoelectric, or nonlinear optical properties, such as second harmonic generation. Table 31.3 shows a few examples as well as the use of other types of gels used to grow these compounds.

Four basic crystallization methods are presently at the disposal of crystal growers to grow such crystals and introduce gel as a growth medium. Crystallization assays can be set up either (1) in batches, (2) by diffusion of vapor between hanging (or sitting) droplets and a reservoir of precipitant, (3) by dialysis across a semipermeable membrane, or (4) with free interface diffusion at the interface of two liquids [242–246]. The most popular gel incorporated into all of these crystallization methods for the crystallization of biomolecules has been agarose (see Table 3 in Ref. [30]). Gels prepared by means of polysiloxanes (alkoxysilanes), such as TMOS or TEOS, have also been suggested since their introduction in the field of protein crystal growth [239]. However, a few biomacromolecular crystals have been crystallized either using these alkoxysilanes [58] or gels prepared from the neutralization of solutions from sodium metasilicate.

Table 31.4 summarizes the protein and biomacromolecular complexes crystals directly grown in these types of gels. Figures 31.9 and 31.10 show the beauty of these protein crystals. Some of them were grown in different types of gels than those mentioned in this chapter.

31.4 General Remarks and Future of Crystal Growth in Gels

The gel method—a practical method to grow large and high-quality protein single crystals—has been poorly explored for many years, despite the large efforts from many groups to prove its effectiveness in obtaining high-quality crystals. Excellent reviews covering the crystallization of small and large molecules in gels have been published by Robert and Lefacheux [22], Garcia-Ruiz [21], Sauter et al. [14], Biertümpel et al. [23], and Lorber et al. [30]. Publications are available on combining gels and capillary tubes in counterdiffusion methods [18], protein crystallization in hydrogel

Table 31.2 Physical Properties of Crystals

Crystal	Dielectric	Optical	Ferroelastic	Piezoelectric	Ferroelectric	Magnetic Behavior	References
Sr-oxalate					X		[187,188]
Cd-oxalate					X	Diamagnetic	[189–191]
$CdMgHPO_4$					X		[192]
Nd-hepthamolybdate					X		[193]
La-hepthamolybdate	X				X		[194]
Cu-succinate	X						[195]
Cu-tartrate						Diamagnetic	[195]
Cu-(IDA)-(bypy)·$6H_2O$							[131]
$[Co(Him)_6]$ Cl_2							[131]
Ba-oxalate					X		[196]
Sr-tartrate•$5H_2O$					X		[197]
Ba + Sr-tartrate					X		[198]
$Ba_xCa_{(1-x)}(IO_3)_4$				X			[199]
Ca-tartrate					X		[200]
Gd-Ba molybdate					X		[201]
Mn + Ba tartrate					X		[202]
KDP					X		[203]
KDP					X		[204]
Gd-Nd oxalate			X		X		[205]
Sm-tartrate					X		[206]
Y-tartrate					X		[206]
Zn phospate[a]							[207]
Cd malonate							[208,209]
Fe tartrate						Diamagnetic	[210,211]
Cu,Fe tartrate						Paramagnetic	[210,211].
KNO_3					X		[212]
(La,Nd,Pr,Sm) heptamolybdate			X	X	X		[213,214]
Pr molybdate			X	X	X		[213,214]
Ce-tartrate	X			X	X		[215]
Nd-tartrate	X			X	X		[216]
Ca-tartrate					X		[217]
K tartrate; Li-doped K tartrate		SHG		X	X		[218]
Ba oxalate							[190]
Ba tartrate	X	SHG		X	X		[219,220]
Ca + Cd tartrate					X		[219,220]
Ca + Sr tartrate					X		[221]
Sr + Ca tartrate		SHG		X	X		[222]

(Continued)

Table 31.2 Physical Properties of Crystals—cont'd

Crystal	Dielectric	Optical	Ferroelastic	Piezoelectric	Ferroelectric	Magnetic Behavior	References
Ba-tartrate					X		[223]
Metal phosphonate							[224]
Ca tartrate doped with Ba, Sr, Co, Ni, Mn, Zn, Cd					X		[225]
Gd tartrate·$3H_2O$		SHG		X	X		[226,227]
Yb tartrate·H_2O		SHG		X	X		[226,227]
Ho tartrate		SHG		X	X		[227]
PbI_2							[228]
K, Mg phosphate							[229]
CuI							[230]
Fe, Mg, Co tartrate					X		[202]
Zn, Cd thiocyanate		SHG					[206]
Cd, Hg thiocyanate		SHG					[231]
$PbCl_2$		AcO					[206]
Ca tartrate					X		[232]
$CaHPO_4 \cdot 2H_2O$							[233]
$Ca_{10}(PO_4)_6(OH)_2$							[234]
$(Ba, Pb)SO_4$							[235]
Na, K bitartrate				X	X		[210,211]
Cu, Fe tartrate							[210,211]
$PbCO_3$							[221]
$Ba,MgHPO_4$							[236]
La,Nd oxalate							[237]
Bi_2IO_3		SHG					[238]

SHG = second harmonic generation, AcO = acousto-optical.
[a]anticorrosive.

Table 31.3 Gels Used to Grow Different Materials (Inorganic and Small Molecules)

Composition	Crystals	References
Sodium metasilicate	Oxalates, tartrates, phosphates, etc.	Listed in Table 31.1
Agar	Yb tartrate	[226]
Poly(ethylene)oxide	Cu-(IDA)-(bypy)·$6H_2O$	[131]
Polyacrylamide	$Ca_{10}(PO_4)(OH)_2$	[234]
Alginate	Metal-phosphonate	[224]

Table 31.4 Proteins or Macromolecular Complexes Directly Grown in Silica Gel or Alkoxysilanes-Made (TMOS or TEOS) Hydrogels

Protein or Macromolecular Complex	Precipitating agent	Type of gel (sodium metasilicate or TMOS/TEOS)	Resolution (Å)	References
HEW lysozyme	NaCl	Sodium metasilicate gel	ND	[239]
HEW lysozyme	NaCl	TMOS	ND	[240]
Thaumatin (*Thaumatococcus daniellii*)	NaK tartrate (pH 6.5)	Sodium metasilicate gel	ND	[146]
HEW lysozyme	NaCl	Sodium metasilicate gel	1.5 Å	[148]
HEW lysozyme, turkey lysozyme,Thaumatin	NaCl (pH 4.5), Na Tartrate (pH 6.5)	Sodium metasilicate gel as growth media and working as a filter for impurities separation	2.1 Å (lysozyme), 2.2 Å turkey lysozyme) and 3.0 Å (thaumatin)	[141]
Thaumatin (*Thaumatococcus daniellii*)	NaK tartrate	TMOS (5%)	ND	[172]
Heme proteins	Potassium Phosphate (pH 6.0–7.0) and PEG-8000	TEOS	ND	[241]
HEW lysozyme Thaumatin (*Thaumatococcus daniellii*) Ferritin	NaCl (pH 4.5) NaK tartrate (pH 6.5) $CdSO_4$ (pH 5.6)	Silica sols (2–22%) TMOS (8–18%)	1.2 Å–1.5 Å (low gel concentrations) Up to 2.6 Å (higher concentrations of silica gel and TMOS)	[130]

ND, Not determined; TMOS, tetramethyl orthosilicate; TEOS, tetraethyl orthosilicate; HEW, hen egg-white.

beads [247], the use of femtosecond laser-induced nucleation in protein crystals grown in agarose gels [248,138], combining electric fields and gels [249], and electric and magnetic fields using the gel-growth technique [127,250]. The use of smart hydrogels either for protein crystallization or for crystal gardens has been suggested [251]. Hydrogels have been used to prevent osmotic shock in protein crystals in drug design technology [252].

The use of agarose for protein crystallization has made this method more popular among the protein crystallography community for the last few years due to the convincing results not only in the crystallization and crystal quality enhancement of large biomolecules or biomacromolecular complexes [132,139,248,253,254], but also due to the easy preparation of these hydrogels and the existence of new types of low-melting-point agarose. There is still a lack in the availability of organic gels for organic molecules where strong organic solvents are used. Additionally, the gel method has been scarcely

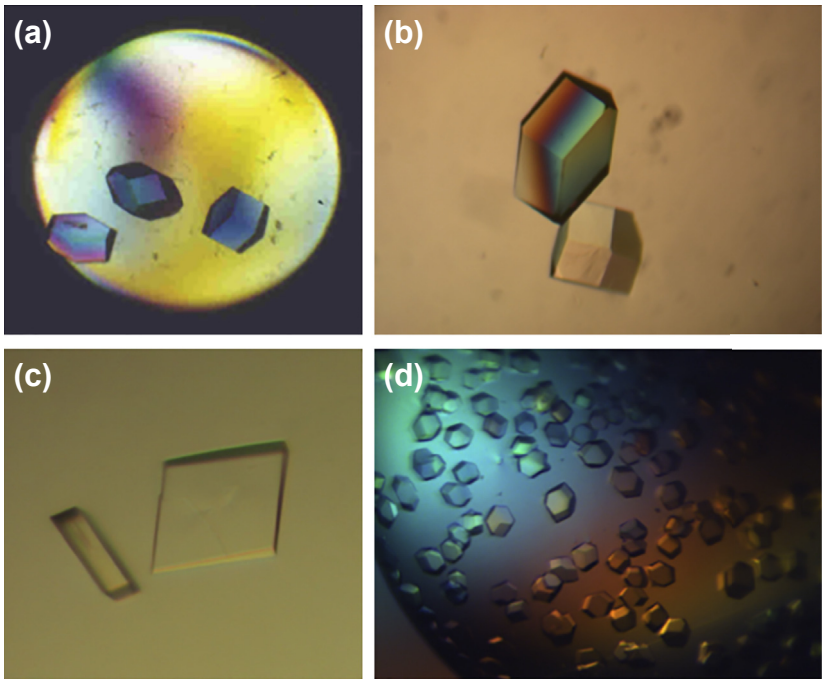

FIGURE 31.10 Pictures of different protein crystals. (a) lysozyme grown in batch method, (b) lysozyme grown in gel, (c) Monoclinic aspartyl-tRNA synthetase from *Thermus thermophilus* and (d) glucose isomerase grown at 4 °C. The size of the largest crystal is 200 μm and is the reference in scale for the other crystals.

used for membrane protein crystallization. There are not many choices for the polymer chemistry; however, the joint effort between crystal growers and synthesis scientists is the next and promising step of crystal growth in gels.

Scientists should understand the great advantages of using the gel method to grow crystals; there is a lot of chemistry and physics, as well as materials science, behind the knowledge of gels (synthesis and structure). The theory, protocols, recipes, and strategies to incorporate gels into the growth solution, where the solute (biological macromolecules) will crystallize, are now available in excellent chapters and published books, which are now classic contributions for crystal growth in gels; for example, see Chapter 6 in Refs [4,243], Chapter 10 in Ref. [244], and p. 226 in Ref. [242]. Chapter 4 in *Crystal Growth: From Fundamentals to Technology* [3] includes a section on macromolecular crystals grown by counterdiffusion (comparing solution and gel growth) and their characterization. A book published by Chayen et al. [246] reviews the different methods of macromolecular crystallization (including the gel method; see Part I, Section 8), and it also provides the theoretical basis and experimental tools to analyze the quality of biomacromolecular crystals for X-ray crystallography. In the previous edition of this handbook, Chapter 46, written by Narayana and Natarajan [255],

discusses crystallization from gels, mostly applied for biomineralization processes and human diseases.

The aim of this short chapter was to update the reader on new discoveries and approaches in the gel method. Nature has taken a long time to grow beautiful gems such as sapphires, rubies, and diamonds, but the gel-growth method allows us to play a game that has been coined as "instantaneous mineralogy" [4]. This gel method has even demonstrated the growth of large crystals of very interesting biological macromolecules that have not been easily crystallized by any other methods.

We hope that this chapter will inspire young scientists to explore gel methodology and obtain large and beautiful single crystals. It is also our goal to reach the chemical synthesis community, who usually deal with difficulties in the structure of complicated molecules (organic or inorganic), to adopt the method—or even join us in the synthesis of new gels. Many laboratories around the world are looking for new and original strategies to crystallize difficult compounds, nonintrinsically ordered proteins, and even large macromolecular complexes of biomolecules, such as ribosomes.

Today, there are still a lot of challenges to obtaining crystals of many membrane proteins, large DNA-protein, or RNA-protein complexes by the gel method, or to obtain crystals for X-ray crystallographic research. The idea of synthesizing a universal gel is still a difficult dream to come true, but there will be wonderful surprises in the coming years. This gel method is one of the areas that inspired our life as scientists, particularly for one of the authors of this chapter, for whom the gel method has been a strong tool to grow high-quality protein crystals—although they were sometimes difficult to achieve in his life as a protein crystal grower and protein crystallographer.

References

[1] Emma P, Akre R, Arthur J, Bionta R, Bostedt C, Bozek J, et al. Nat Photonics 2010;4:641.

[2] Otalora F, Garcia-Ruiz JM. Chem Soc Rev 2014;43:2013.

[3] García-Ruiz JM, Otalora F. Macromolecular crystals-growth and, characterization. In: Müller G, Métois J-J, Rudolph P, editors. Crystal growth from fundamentals to technology. Elsevier; 2004.

[4] Henisch HK. Crystals in gels and Liesegang rings. Cambridge: Cambridge University Press; 1988.

[5] Tomanicek SJ, Standaert RF, Wiess KL, Ostermann A, Schrader TE, Ng JD, et al. J Biol Chem 2013;288:4715.

[6] Matsumura H, Sugiyama S, Hirose M, Kakinouchi K, Maruyama M, Murai R, et al. J Synchrotron Rad 2011;18:16.

[7] Margiolaki I, Wright JP. Acta Crystallogr 2008;A64:169.

[8] García-Caballero A, Gavira J, Pineda-Molina E, Chayen N, Govada L, Khurdish S, et al. Cryst Growth Des 2011;11:2112.

[9] Ruggiero A, Smaldone G, Squeglia F, Berisio R. Proteins Pept Lett 2012;19:732.

[10] Maginn S. Analyst 1998;123:19R.

[11] Stojanoff V, Northrup P, Pietri R, Zhong Z. Protein Pept Lett 2012;19:761.
[12] Bosch R, Lautenschlager P, Potthast L, Stapelmann J. J Cryst Growth 1999;122:310–6.
[13] Lorber B, Ng JD, Lautenschlager O, Giege R. J Cryst Growth 2000;208:665.
[14] Sauter C, Lorber B, Giegé R. Proteins: Struct Funct Genet 2002;48:146.
[15] García-Ruiz JM, Moreno A, Viedma C, Coll M. Mat Res Bull 1993;28:541.
[16] García-Ruiz JM, Moreno A. Acta Crystallogr 1994;D50:484.
[17] García-Ruiz JM. Methods Enzymol 2003;368:130.
[18] Otalora F, Gavira JA, Ng JD, Garcia-Ruiz JM. Prog Biophys Mol Biol 2009;101:26.
[19] Bradford SC. Biochem J 1923;17:230.
[20] Low BW, Richards FM. J Am Chem Soc 1954;76:2511.
[21] Garcia-Ruiz JM. Key Eng Mater 1991;58:87.
[22] Robert M-C, Lefaucheux F. J Cryst Growth 1988;90:358.
[23] Biertümpel C, Basquin J, Suck D, Sauter C. Acta Crystallogr 2002;D58:1657.
[24] Otalora F, Novella ML, Rondon D, Garcia-Ruiz JM. J Cryst Growth 1999;196:649.
[25] Otalora F, Garcia-Ruiz JM, Carotenuto L, Castagnolo D, Novella ML, Chernov AA. Acta Crystallogr 2002;D58:1681.
[26] Moreno A, Juárez-Martínez G, Hernández-Pérez T, Batina N, Mundo M, McPherson A. J Cryst Growth 1999;205:375.
[27] García-Ruiz JM, Novella ML, Moreno R, Gavira JA. J Cryst Growth 2001;232:165.
[28] Pernodet N, Maaloum M, Tinland B. Electrophoresis 1997;18:55.
[29] Maaloum M, Pernodet N, Tinland B. Electrophoresis 1998;19:1606.
[30] Lorber B, Sauter C, Théobald-Dietrich A, Moreno A, Schellenberger P, Robert M-C, et al. Prog Biophys Mol Biol 2009;101:13.
[31] Gavira JA, Garcia-Ruiz JM. Acta Crystallogr 2002;D58:1653.
[32] Provost K, Robert M-C. J Cryst Growth 1991;110:258.
[33] Miller TY, He XM, Carter DC. J Cryst Growth 1992;122:306.
[34] Halberstadt ES, Henisch HK. J Cryst Growth 1968;3–4:363.
[35] Wilke K-Th. Kristallzüchtung. Frankfurt/Main: Verlag Harri Deutsch; 1988. p. 938.
[36] Liesegang RE. Naturwiss Wochenschr 1896;11:353.
[37] Oswald W. Z Phys Chem 1897;22:289.
[38] Oswald W. Kolloid-Z 1925;36:380.
[39] Colfen H. Nat Mater 2010;9:960–1.
[40] Henisch KH, García-Ruiz JM. J Cryst Growth 1986;75:203.
[41] Morse HW, Pierce GW. Phys Rev 1903;17:129.
[42] Jablczinsky K. Bull Soc Chim Fr 1923;4:592.
[43] Matalon R, Packter A. J Colloid Sci 1955;10:46.
[44] Ng JD, Gavira JA, Garcia-Ruiz JM. J Struct Biol 2003;142:218.
[45] Gangloff M, Moreno A, Gay NJ. J Appl Crystallogr 2013;46:337.
[46] Dondi PG. Biochem J 1975;149:475.
[47] Vidal O, Robert M-C, Boué F. J Cryst Growth 1998;192:271.

[48] Maes D, Gonzalez-Ramirez LA, Lopez-Jaramillo J, Yu B, De Bondt H, Zegers I, et al. Acta Crystallogr 2004;D60:463.

[49] Yunzhu G, Huiling C, Jin H, Chao C, Ziging W, Dachuan Y. Cailiao Daobao 2013;27:85.

[50] Moreno A, Quiroz-García B, Yokaichiya F, Stojanoff V, Rudolph P. Cryst Res Technol 2007;42:231.

[51] Sazaki G, Yoshida E, Komatsu H, Nakada T, Miyashita S, Watanabe K. J Cryst Growth 1997;173:231.

[52] Ataka M, Katoh E, Wakayama NI. J Cryst Growth 1997;173:592.

[53] Koizumi H, Fujiwara K, Uda S. Cryst Growth Des 2009;9:2420.

[54] Sakai Y, Oishi A, Takahashi F. Biotechnol Bioeng 1999;62:363.

[55] Kinoshita T, Ataka M, Warizaya M, Neya M, Fujii T. Acta Cryst 2003;D 59:1333.

[56] Lübbert D, Meents A, Weckert E. Acta Cryst 2004;D60:987.

[57] Vinograda EV, Moreno A, Lara VH, Bosch P. Silicon Chem 2003;2:247.

[58] Gonzalez-Ramirez LA, Caballero AG, Garcia-Ruiz JM. Cryst Growth Des 2008;8:4291.

[59] Tuvikene R, Truus K, Kollist A, Volubujeva O, Mellikov E, Pehk T. J Appl Phycol 2008;20:527.

[60] Anderson NS, Campbell JW, Harding MM, Rees DA, Samuel JWB. J Mol Biol 1969;45:85.

[61] Wilcox W. Fundamentals of crystal growth. In: Arend H, Hulliger J, editors. Crystal growth in science and technology; 1987. p. 119. NATO series.

[62] Prieto M, Viedma C, López-Acevedo V, Martín-Vivaldi JL, López-Andrés S. J Cryst Growth 1998; 92:61.

[63] Garcia-Ruiz JM, Novella ML, Otalora F. J Cryst Growth 1999;196:703.

[64] Otalora F, Novella ML, Gavira JA, Thomas BR, García-Ruiz JM. Acta Crystallogr 2001;D57:412.

[65] Elwell D. Fundamentals of flux growth. In: Arend H, Hulliger J, editors. Crystal growth in science and technology; 1987. p. 133. NATO series.

[66] Cheng KC, Fujii T. Heat Transf Eng 2007;19:9.

[67] Price WS. Diffusion Fundamentals 2005;2:112.1.

[68] Kapur V, Charkoudian J, Anderson JL. J Membr Sci 1997;131:143.

[69] D'Errico G, Ortona O, Capuano F, Vitagliano V. J Chem Eng Data 2004;49:1665.

[70] Venancio A, Teixeira JA. Biotechnol Tech 1997;11:183.

[71] McGuinness ET. J Chem Edu 1973;50:826.

[72] Tyn M, Gusek TW. Biotechnol Eng 1990;35:327.

[73] Pluen A, Netti PA, Rakesh KJ, Berk DA. Biophys J 1999;77:542.

[74] Tao L, Nicholson C. Neuroscience 1996;75:839.

[75] Kempe H, Persson P, Axelsson A, Nilsson B, Zachi G. Interscience. Wiley; 2005. http://dx.doi.org/10.1002/bit.20738.

[76] Gutenwik J, Nilsson B, Axelsson A. Biochem Eng J 2004;19:1.

[77] Bosna JC, Wesselingh JA. J Chromatogr B 2000;243:169.

[78] Stefanini S, Chiancone E, Arosio P, Finazzi-Agro A, Antonini E. Biochemistry 1982;21:2293.

[79] Andrews P. Biochem. J 1965;96:595.

[80] Gabler R, Wethead EW, Ford NC. Biophys J 1974;14:528.

[81] Stellwagen N, Gelfi C, Righetti PG. Electrophoresis 2002;23:167.

[82] Lai BE, Geonnotti AR, DeSoto MG, Montefiori DC, Katz DF. Antiviral Res 2010;88:143.

[83] Patterson G. Physical chemistry of macromolecules. CRC Press. Taylor, and Francis Group; 2007. p. 57–59.

[84] Asherie N. Proteins Pept Lett 2012;19:708.

[85] Procházka O, Kratochvíl P. J Polym Sci Polym Phys 1980;18:2369.

[86] Ye F, Collinson MM, Higgins DA. Phys Chem Chem Phys 2009;11:66–82.

[87] Higgins DA, Tran-Ba KH, Ito T. J Phys Chem Lett 2013;4:3095.

[88] Pramanik S, Ito T, Higgings GA. J Phys Chem 2013;C117:3668.

[89] Maeda K, Mizubayashi H. In: Czichos H, Saito T, Smith L, editors. Handbook of metrology and testing. Berlin (Heilderberg): Springer; 2011.

[90] Chiesa M, Giamello E, Che M. Chem Rev 2010;110:1320.

[91] Wessig M, Drescher M, Polarz S. J Phys Chem 2013;C117:2805.

[92] Rogozea A, Savonea F, Ionita G. Rev Roum Chim 2012;57:693.

[93] Pilar J. Dynamic processes in polymer systems studied by electron spin, resonance spin label technique [Ph.D. thesis]. Praha: Akademie ved Ceske Republiky; 2004.

[94] Gagnon MA, Lafleur M. J Phys Chem 2009;B113:9084.

[95] Han KS, Wang X, Dai S, Hagaman EW. J Phys Chem 2013;C117:15754.

[96] Arndt KF, Krahl F, Richter S, Steiner G. In: Gerlach G, Arndt KF, editors. Hydrogel sensors and actuators. Springer series on chemical sensors and biosensors, vol. 6. Berlin (Heidelberg): Springer Verlag; 2009.

[97] Yamaguchi T, Kuhnert L, Nagy-Ungvarai Z, Muller SC, Hess B. J Phys Chem 1991;95:5831.

[98] Chen L, Kang Q, He Y-L, Tao W-Q. Langmuir 2012;28:11745.

[99] Chen L, Kan Q, Robinson BA, He Y-L, Tao W-Q. Phys Rev 2013;E87:043306.

[100] Bhattacharya S, Kiefer J. J Chem Phys 2005;122:094715.

[101] Tartaglia P. In: AIP conference proceedings, 982; 2008. p. 295.

[102] Suarez MA, Kern M, Pitard E, Kob W. J Chem Phys 2009;130:194904.

[103] Saw S, Ellegaard NL, Kob W, Sastry S. J Chem Phys 2011;134:164506.

[104] Fatin-Rouge N, Starchev K, Buffle J. Biophys J 2004;86:2710.

[105] Kang Q, Moran W, Mukherjee PP, Lichtner PC. Adv Mech Eng 2010. http://dx.doi.org/10.1155/2010/142879.

[106] Kvarnstrom M, Vestergard A, Lorén N, Nydén M. Phys Rev 2009;E79:016102.

[107] Zhang J, Zhao X, Suo Z, Jiang H. J Appl Phys 2009;105:093522.

[108] Sancho-Tomás M, Fermani S, Durán-Olivencia MA, Otálora F, Gómez-Morales J, Falini G, et al. Cryst Growth Des 2013;13:3884.

[109] Kajiwara K, Osada Y. Gels handbook. London: Academic Press; 2001.

[110] Schneider M, Baiker A. Catal Rev Sci Eng 1995;37:515.

[111] Baskaran S, Liu J, Domansky K, Kohler N, Li X, Coyle C, et al. Adv Mater 2000;12:291.

[112] Hikmet RAM, Michels I. Adv Mater 2001;13:338.

[113] Hikmet RAM. Gels of liquid crystals and ion-Conducting fluids. In: Weiss RG, Terech P, editors. Molecular gels with self-assembled fibrillar networks. Springer; 2006. p. 773–92.

[114] Yoldas BE, Annen MJ, Bostaph J. Chem Mater 2000;12:2475–84.

[115] [a] Simonian AL, Grimsley JK, Flounders AW, Schoeniger JS, Cheng T-C, DeFrank JJ, et al. Anal Chim Acta 2001;442:15;
[b] Thiessen KJ. Acta Crystallogr 1994;D50:491.

[116] Mackenzie JD. J Non-Cryst Solids 1981;48:1.

[117] Klein LC. Sol–gel technology for thin films, fibers, preforms, electronics, & speciality shapes. Park Ridge (NJ): Noyes; 1998.

[118] Lenza RFS, Vasconcelos WL. J Non-Cryst Solids 2000;273:164–9.

[119] Anand B, Pisal SS, Paradkar AR, Mahadik KR. J Sci Industrial Res 2001;60:311.

[120] Escobar-Chavez JJ, Lopez-Cervantes M, Naik A, Kalia YN, Quintanar-Guerrero D, Ganem-Quintanar A. J Pharm Pharm Sci 2006;9:339.

[121] Brinker CJ, Scherer GW. Sol–gel science: the physics and chemistry of, sol–gel processing. San Diego: Academic Press; 1990.

[122] Ciriminna R, Fidalgo A, Pandarus V, Béland F, Ilharco L, Pagliaro M. Chem Rev 2013;113:6592.

[123] Amsden B. Polym Gels Networks 1998;6:13.

[124] Littke W, John C. Science 1984;225:203.

[125] Zeelen JPh, Wierenga RK. J Cryst Growth 1992;122:194.

[126] Yuefang L, Guo D, Zheng B. RSC Adv 2012;2:4857.

[127] Surade S, Ochi T, Nietlispach D, Chirgadze D, Moreno A. Cryst Growth Des 2010;10:691.

[128] Prudnikova T, Gavira JA, Rezacova P, Pineda-Molina E, Hunalova I, Sviridova E, et al. Cryst Growth Des 2010;10:3391.

[129] Pietras Z, Lin H-T, Surade S, Luisi B, Slattery O, Pos KM, et al. J Appl Cryst 2010;43:58.

[130] Gavira JA, Van Driessche AES, García-Ruiz JM. Cryst Growth Des 2013;13:2522.

[131] Choquesillo-Lazarte D, Garcia-Ruiz JM. J Appl Crystallogr 2011;44:172.

[132] Tanabe K, Hirose M, Murai R, Sugiyama S, Shimizu N, Maruyama M, Takahashi Y, et al. Appl Phys Express 2009;2:125501.

[133] Sauter C, Ng JD, Lorber B, Keith G, Brion P, Hosseini MW, et al. J Cryst Growth 1999;196:365.

[134] Guenet JM. Thermoreversible gelation of polymers and biopolymers. London: Academic Press; 1992.

[135] Sica F, Demasi D, Mazzarella L, Zagari A, Capasso S, Pearl LH, et al. Acta Crystallogr 1994; D50:508.

[136] Lorber B, Sauter C, Ng JD, Zhu DW, Giegé R, Vidal O, et al. J Cryst Growth 1999;204:357.

[137] Lorber B, Sauter C, Robert M-C, Capelle B, Giegé R. Acta Crystallogr 1999;D55:1491.

[138] Murai R, Yoshikawa H, Takahashi Y, Maruyama M, Sugiyama Sh, Sazaki G, et al. Appl Phys Lett 2010;96. 043702/1.

[139] Matsumura H, Sugiyama S, Hiroaki A, Kazufumi T, Satoshi M, Inohue T, et al. Bio Ind 2011;28:30.

[140] Provost K, Robert M-C. J Cryst Growth 1995;156:112.

[141] Robert M-C, Vidal O, Garcia-Ruiz J-M, Otalora F. In: Ducruix A, Giegé R, editors. Crystallization of nucleic acids and proteins: a practical approach. 2nd ed. Oxford, U.K: IRL Press; 1999. p. 149.

[142] Robert M-C, Capelle B, Lorber B, Giege R. J Cryst Growth 2001;232:489.

[143] Lorber B, Giegé R. J Cryst Growth 2001;231:252.

[144] Van Driessche AES, Otalora F, Gavira JA, Sazaki G. Cryst Growth, Des 2008;8:3623.

[145] Robert M-C, Provost K, Lefaucheux F. In: Ducruix A, Giegé R, editors. Crystallization of nucleic, acids and proteins, A practical approach. 1st ed. Oxford: IRL Press; 1992. p. 127–43.

[146] Cudney R, Patel S, McPherson A. Acta Crystallogr 1994;D50:479.

[147] Vidal O, Robert MC, Arnoux B, Capelle B. J Cryst Growth 1999;196:559.

[148] Garcia-Ruiz JM, Gavira JA, Otalora F, Guasch A, Coll M. Mat Res Bull 1998;33:1593.

[149] Vinogradova E, Estrada M, Moreno A. J Colloid Interface Sci 2006;298:209.

[150] Darmanin C, Conn Ch, Newman J, Mulet X, Seabrook Sh, Liang Y-L, et al. ACS Comb Sci 2012;14:247.

[151] Zabara A, Mezzenga R. Soft Matter 2012;8(2012):6535.

[152] Wallace E, Dranow D, Laible PD, Christiansen J, Nollert P. PLoS One 2011;6:e24488/1.

[153] Rummel G, Hardmeyer A, Widmer C, Chiu ML, Nolert P, Locher GP, Pedruzzi I, Landau EM, Rosenbusch JP. J Struct Biol 1998;121:82.

[154] Luecke H. In: Grisshammer R, Buchanan SK, editors. Structural biology membranes; 2006. p. 173–91.

[155] Johansson LC, Woehri AB, Katona G, Engstroem S, Neutze R. Curr Opin Struct Biol 2009;19:372.

[156] Liu W, Hanson MA, Stevens R, Cherezov V. Biophys J 2010;98:1539.

[157] Joseph J, Liu W, Kunken J, Weiss TM, Tsuruta H, Cherezov V. Methods 2011;55:342.

[158] Caffrey M. Biochem Soc Trans 2011;39:725–32.

[159] Cherezov V. Curr Opin Struct Biol 2011;21:559.

[160] Li D, Boland C, Walsh K, Caffrey M. J Vis Exp 2012;66:e4000.

[161] Landau EM, Rummel G, Cowas-Jacob SW, Rosenbusch JP. J Phys Chem 1997;B101:1935.

[162] Laczko-Dobos H, Szalontai B. Biochemistry 2009;48:10120.

[163] Topiol S. Expert Opin Drug Discov 2013;8:607.

[164] Patel S, Cudney R, McPherson A. Biochem Biophys Res Comm 1995;205:819.

[165] Gaboriaud C, Juanhuix J, Gruez A, Lacroix M, Darnault C, Pignol D, Verger D, Fontecilla-Camps JC, Arlaud GJ. J Biol Chem 2003;278:46974.

[166] Sauter C, Lorber B, Théobald-Dietrich A, Giegé R. J Cryst Growth 2001;232:399.

[167] Sauter C, Otalora F, Gavira JA, Vidal O, Giegé R, Garcia-Ruiz JM. Acta Crystallogr 2001;D57:1119.

[168] Charlionet R, Machour-Merlet N, Leclerc S, Malandain J-J. Electrophoresis 1997;18:1133.

[169] Lee KY, Mooney DJ. Chem Rev 2001;101:1869.

[170] Percec V, Bera TK, Butera RJ. Biomacromolecules 2002;3:272.

[171] Estroff LA, Hamilton AD. Chem Rev 2003;104:1201.

[172] Moreno A, Saridakis E, Chayen NE. J Appl Cryst 2002;35:140–2.

[173] Berg OG, von Hipple PH. Ann Rev Biophys Biophys Chem 1985;14:131.

[174] Morosanova EI. Talanta 2012;102:114–22.

[175] Durães L, Ochoa M, Rocha N, Patrício R, Duarte N, Redondo V, et al. J Nanosci Nanotechnol 2012;12:6828.

[176] Alcala-Alcala S, Urban-Morlan Z, Aguilar-Rosas I, Quintanar-Guerrero D. Int J Nanomedicine 2013;8:2141.

[177] Liu H, Sha W, Cooper AT, Fan M. Colloids Surf A 2009;347:38.

[178] Shaefer DW, Keefer KD. Phys Rev Lett 1986;56:2199.

[179] Knoblich B, Th Gerber. J Non-Cryst Solids 2001;296:181.

[180] Marlière C, Despetis FP, Etienne P, Woignier T, Dieudonne P, Phalippou J. J Non-Cryst Solids 2001; 285:148.

[181] Kroschwitz JI, Hawe-Gant M, editors. Kirk-othmer encyclopedia of, chemical technology. 4th ed. New York: John Wiley & Sons; 1998. p. 1.

[182] Štandeker S, Novak Z, Knez Ž. J Hazard Mater 2009;165:1114.

[183] Štandeker S, Veronovski A, Novak Z, Knez Ž. Desalination 2011;269:223.

[184] Yan Zh. Appl Mech Mater 2013;253–255:564.

[185] Gurav JL, Rao AV, Nadargi DY, Park HH. J Mater Sci 2010;45:503.

[186] Biener J, Stadermann M, Suss M, Worsley MA, Biener MM, Rose KA, et al. Energy Environ Sci 2011;4:656.

[187] Shen J, Guan D-Y. In: Aegerter MA, editor. Aerogels handbook, advances in sol–gel, derived materials and technologies. Springer, Science Business; 2011 [Chapter 36].

[188] Dalal PV, Saraf KB. Bull Mater Sci 2011;34:377.

[189] Arora SK, Kothari AJ, Patel RG, Chauhan KM, Chudasama BN. J Phys Conf Ser 2006;28:48.

[190] Raj AME, Jayanthi DD, Jothy VB, Jayachandran M, Sanjeeviraja C. Cryst Res Technol 2008;43:1307.

[191] Chauhan KM, Arora SK. Cryst Res Technol 2009;44:189.

[192] Bamzai KK, Gupta R, Suri S, Singh V. Adv Mater Lett 2014;5:89.

[193] Bhat S, Khosa SK, Kotru PN, Tandon RP. Cryst Res Technol 2006;30:267–73.

[194] Bhat S, Khosa SK, Kotru PN, Tandon RP. Mat Sci Eng 1995;B30:7.

[195] Binitha MP, Pradyumnan PP. Phys Scr 2013;87:065603.

[196] Dalal PV, Saraf KB, Shah S. Cryst Res Technol 2009;44:36.

[197] Firdous A, Quasim I, Ahmad MM, Kotru PN. Cryst Res Technol 2008;43:1015.

[198] Freeda MM, Delphine SM, Priya RK, Freeda TH, Almusallam AW. Rec Res Sci Technol 2010;2:9.

[199] Garud SL, Mahajan NK, Saraf KB. Bull Mater Sci 2009;32:187.

[200] Gon HB. J Cryst Growth 1990;102:501.

[201] Hangloo V, Tickoo R, Bamzai KK, Kotru PN. Mat Chem Phys 2003;81:152.

[202] Joshi SJ, Tank KP, Parekh BB, Joshi MJ. Cryst Res Technol 2010;45:303.

[203] Joshi MS, Antony AV. J Mat Sci 1978;13:939.

[204] Moreno-Cárcamo A, Mendoza-Alvarez ME, Silva-González R, Tabares C. Rev Mex Fís 1992;39:443.

[205] Korah I, Joseph C, Ittyachen MA. J Min Mat Char Eng 2010;9:1081.

[206] [a] Kumari PNS, Kalainathan S, Bhagavannarayana G. Cryst Res Technol 2008;43:276–81; [b] Kumari PNS, Kalainathan S. Cryst Res Technol 2008;43:413–6.

[207] Mangalam G, Das SJ. Arch Phys Res 2010;1:54.

[208] Joseph J, Mathew V, Abraham KE. Optoel Adv Mat 2008;2:707.

[209] Mathew V, Joseph J, Jacob S, Varughese PA, Abraham KE. Ind J Pure Appl Phys 2009;47:691.

[210] Mathivanan V, Haris M. Spectrochim Acta 2013;A102:341.

[211] Mathivanan V, Haris M. Pramana 2013;81:177.

[212] Mukund MR. Int J Adv Sci Res Tech 2012;2:500.

[213] Pandita S, Tickoo R, Bamzai KK, Kotru PN. Mat Sci Eng 2001;B87:122.

[214] Pandita S, Hangloo V, Bamzai KK, Kotru PN, Sahni N. Int J Inorg Mat 2001;3:675.

[215] Patil HM, Sawant DK, Bhavsar DS, Patil JH, Girase KD. Arch Phys Res 2011;2:239–45.

[216] Patil HM, Sawant DK, Bhavsar DS, Patil JH, Girase KD. J Therm Anal Calorim 2012;107:1031.

[217] Prananto YP, Khunur MM, Tjahjanto RT, Sakdi I, Basori MC. J Trp Life Sci 2011;2:1.

[218] Quasim I, Firdous A, Sahni N, Khosa SK, Kotru PN. Phys Stat Solidi 2009;A206:2791.

[219] Sawant DK, Bhavsar DS. Arch Phys Res 2012;3:8.

[220] Sawant DK, Patil HM, Bhavsar DS, Patil JH, Girase KD. J Therm Anal Calorim 2012;107:1047.

[221] Sawant DK. Chim Sin 2013;4:1.

[222] Selvapandiyan M, Sundaramoorthi P. Bulg J Phys 2013;40:78.

[223] Shah A, Patel IB. AIP Conf Proc 2010;1249:192.

[224] Stavgianoudaki N, Papathanasiou KE, Colodrero RMP, Choquesillo-Lazarte D, García-Ruiz JM, Cabeza A, et al. Cryst Eng Commun 2012;14:5385.

[225] Torres ME, López T, Stockel J, Solans X, García-Vallés M, Rodrígez-Castellón E, et al. J Solid State Chem 2002;163:491.

[226] [a] Want B, Ahmad F, Kotru PN. Mat Sci Eng 2006;A431:237;
[b] Want B, Ahmad F, Kotru PN. Cryst Res Technol 2006;41:1167.

[227] Want B, Ahmad F, Kotru PN. Cryst Res Technol 2007;42:822.

[228] Bhavsar DS, Saraf KB, Seth T. Cryst Res Technol 2002;37:225.

[229] Chauhan CK, Vyas PM, Joshi MJ. Cryst Res Technol 2011;46:187.

[230] Gao P, Gu M, Lin-Liu X. Cryst Res Technol 2008;43:496.

[231] Kumari PNS, Margaret MB, Kalainathan S. Cryst Res Technol 2009;44:177.

[232] Parekh BB, Joshi VS, Pawar V, Thaker VS, Joshi MJ. Cryst Res Technol 2009;44:31.

[233] Rajendran K, Keefe CD. Cryst Res Technol 2010;45:939.

[234] Ahymah-Joshy MI, Elayaraja K, Suganthi RV, Narayana KS. Cryst Res Technol 2010;45:551.

[235] Fernandez-González A, Pedreira VB, Prieto M. J Cryst Growth 2008;310:4616.

[236] Sundaramoorthy P, Kanchana G, Kalainathan S. Spectrochim Acta 2008;69:1154.

[237] Want B. J Cryst Growth 2011;335:90.

[238] Patil TK. Int J Sci Res Manag 2013;1:24.

[239] Lefaucheux F, Robert M-C, Bernard Y, Gits S. Cryst Res Technol 1984;19:1541.

[240] Robert M-C, Berthau J. Comptes Rendus de l'Academie des Sciences, Serie II: Mecanique, Physique, Chimie, Sciences de la Terre et de l'Univers 1987;305:847.

[241] Ronda L, Bruno S, Faggiano S, Bettati S, Mozzarelli A. Methods Enzymol 2008;437:311–28.

[242] Bergfors TM. Protein crystallization. Biotechnology series. La Jolla (USA): Int. Univ., Line; 1999.

[243] Ducruix A, Giegé R. Crystallization of nucleic acids and proteins: a, practical approach. 2nd ed. Oxford: IRL Press; 1999.

[244] McPherson A. Crystallization of biological macromolecules. 1st ed. New York: Cold, Spring Harbor Laboratory Press; 1999.

[245] Giegé R, McPherson A. In: Rossmann MG, Arnold E, editors. International table for crystallography, vol. F. Int. Union of Crystallography, KluwerAcad. Pub; 2001. p. 81.

[246] Chayen N, Helliwell JR, Snell EH. Macromolecular crystallization, and crystal perfection. IUCr-Oxford Science Publications, Oxford University, Press; 2010.

[247] Willaert R, Zegers I, Wyns L, Sleutel M. Acta Crystallogr 2005;D61:1280–8.

[248] Sugiyama Sh, Tanabe K, Hirose M, Kitatani T, Hasenaka H, Takahashi Y, et al. J Appl Phys 2009;48:075502/1.

[249] Sazaki G, Moreno A, Nakajima K. J Cryst Growth 2004;262:499.

[250] Moreno A, Sazaki G. J Cryst Growth 2004;264:438.

[251] Whitcombe MJ. Nat Chem 2011;3(211):657–8.

[252] Sugiyama Sh, Maruyama M, Sazaki G, Hirose M, Adachi H, Takano K, et al. J Am Chem Soc 2012;134:5786.

[253] Lei W, Liu X-Y. Biophys J 2008;95:5931.

[254] Ochi T, Bolanos-Garcia VM, Stojanoff V, Moreno A. Prog Biophys Mol Biol 2009;101:56–63.

[255] Narayana K, Natarajan S. Crystallization from gels. In: Springer handbook of crystal growth; 2010. p. 1607.

32 Fundamentals of Industrial Crystallization

Joop H. ter Horst[1,3], Christiane Schmidt[2], Joachim Ulrich[2]

[1]*INTENSIFIED REACTION & SEPARATION SYSTEMS, PROCESS & ENERGY DEPARTMENT, DELFT UNIVERSITY OF TECHNOLOGY, DELFT, THE NETHERLANDS;* [2]*MARTIN-LUTHER-UNIVERSITÄT HALLE-WITTENBERG, ZENTRUM FÜR INGENIEURWISSENSCHAFTEN, HALLE, GERMANY;* [3]*EPSRC CENTRE FOR INNOVATIVE MANUFACTURING IN CONTINUOUS MANUFACTURING AND CRYSTALLISATION, STRATHCLYDE INSTITUTE OF PHARMACY AND BIOMEDICAL SCIENCES, UNIVERSITY OF STRATHCLYDE, GLASGOW, U.K.*

CHAPTER OUTLINE

32.1 Introduction **1317**
32.2 Product Quality **1319**
32.3 Crystallization **1322**
32.3.1 Solubility and Supersaturation 1322
32.3.2 Crystallization Techniques 1324
32.4 Crystal Nucleation **1325**
32.4.1 Primary Nucleation 1327
32.4.2 Secondary Nucleation 1332
32.5 Crystal Growth **1333**
32.6 Crystallization Process Configuration **1337**
32.6.1 Continuous Crystallization 1339
32.6.2 Batch Crystallization 1341
32.7 Ensuring Product Quality in the Future **1343**
References **1346**

32.1 Introduction

Thinking of an industrial crystallization process, the instant association is a large-scale production facility for a particulate product such as table salt (Figure 32.1). Another prominent example for industrial crystallization can be found in the sugar industry, which had an annual production rate in 2011 of 168 million tons of the solid particulate sugar. Also in the pharmaceutical industry, many drug production lines incorporate at least one but usually several crystallization processes.

Handbook of Crystal Growth. http://dx.doi.org/10.1016/B978-0-444-63303-3.00032-8
Copyright © 2015 Elsevier B.V. All rights reserved.

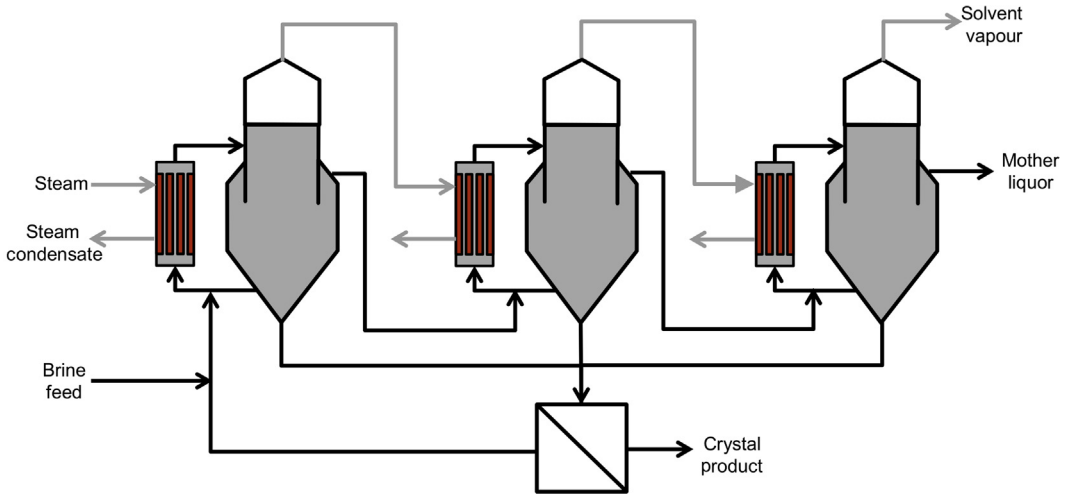

FIGURE 32.1 A cascade of three forced-circulation crystallizers in sequence, each with an external heat exchanger and a circulation pump. A brine is separated into table salt (NaCl-crystal product), water vapor, and a remaining mother liquor. Heat integration is used for the reduction of energy demands: the hot vapor leaving the crystallizer is used for heating in the next crystallizer. In a filtration system, the suspension is separated into a wet crystalline product to be dried and the remaining liquid to be recycled back into the process.

Industrial crystallization is a separation technology that exploits the first-order phase transition between liquid and solid [1,2]. By pushing the system away from equilibrium in a multicomponent liquid, a driving force for crystallization of a specific solid can be created. During crystallization, a suspension of crystals in the solution is formed which after filtration and drying leads to the desired particulate product. The resulting particulate product is usually seen as an advantage. Another advantage that lets crystallization stand out compared to other separation techniques is that the obtained product usually is close to 100% pure, even in a single process step. To achieve high purities in distillation processes, many equilibrium steps are usually needed. Further, auxiliary phases such as the solvent in extraction are often not needed in crystallization processes.

Even on industrial scales with large production rates, crystallization generally remains a molecular-level process [3]. During the growth of each crystal in the supersaturated suspension, molecules or ions incorporate at kinks of steps on the crystal surfaces (see the simplified version in Figure 32.2). These molecular level processes challenge the control over the particulate product from industrial crystallization processes.

Each crystalline product nowadays has to fulfill specific sets of demands of costumers as well as of manufacturers. The demands are not only concerned with the production rate and yield; they further may include specifications on product dissolution behavior, product stability during storage under humid conditions, particulate flow properties, color, and many others while they vary from product to product. The last 25 years showed a focus change in industrial crystallization research from bulk chemicals to fine and pharmaceutical products, showing the increasingly important molecular-level processes even on industrial scales. It is nowadays crucial to control the industrial

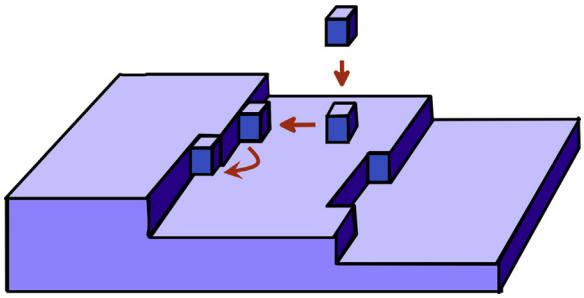

FIGURE 32.2 A simplified schematic of the molecular level process of crystallization. During crystal growth, solute molecules or ions incorporate at kinks of steps on the crystal surface. In solution crystallization next to the solute and solvent, many components can be present. Even though ideally only the solutes are incorporated, also all other components present might have a substantial effect on the crystallization behavior through disruption of the molecular level process.

crystallization process to robustly and reproducibly obtain the crystalline product in a sustainable way. In this chapter, the fundamental basis for industrial crystallization is given, highlighting product quality and the determining crystallization subprocesses. In our view, important achievements in the field of industrial crystallization in the past 20 years or so will be highlighted.

32.2 Product Quality

Figure 32.3 shows *ortho*-amino benzoic acid crystals obtained from a cooling crystallization. These crystals have a specific form, size, shape, and purity. Customer and manufacturer demands for a crystalline product can usually be traced back to these four product quality aspects.

The crystal *form* that is produced is related to the molecular or ionic arrangement in the crystals (crystal structure) and impacts on properties such as solubility, shelf life, drug

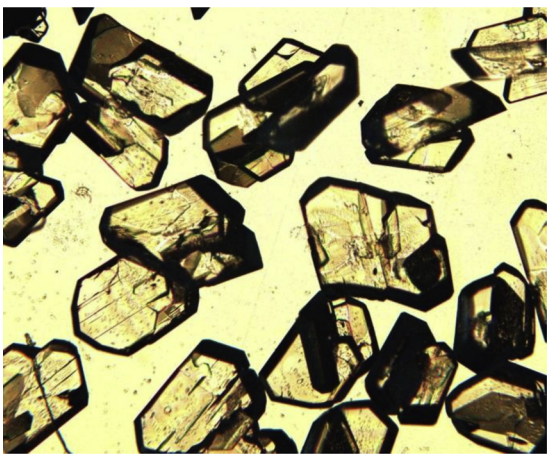

FIGURE 32.3 A crystal product from a small-scale cooling crystallization of ortho-amino benzoic acid.

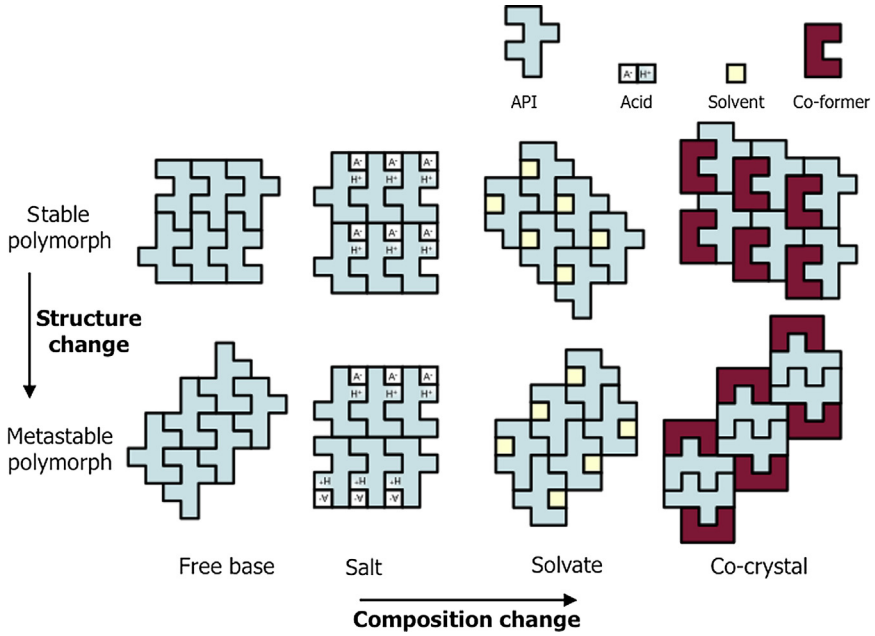

FIGURE 32.4 A chemical compound such as an active pharmaceutical ingredient could form different crystal structures either on its own (polymorphism) or together with other compounds (salt, co-crystal, solvate) which in turn also could form polymorphs or related but stoichiometrically different compounds.

stability, bioavailability, and color. Figure 32.4 shows crystal structures of different forms of a model active pharmaceutical compound. A chemical compound that is able to crystallize in different molecular or ionic arrangements in the crystal structures is named a polymorph [4]. The inability to control polymorphism in industrial crystallization processes and in the crystalline product can cause challenging problems in the pharmaceutical industry [5]. If a solvent molecule is additionally present in the crystal structure, one speaks of solvates. In the case of included water, this is termed a hydrate. Often solvates and hydrates are unwanted due to their instability. In recent years, co-crystals attained substantial attention as a route toward adjustable and improved solid-state properties of pharmaceutical compounds [6]. Co-crystals are multicomponent crystals of components that are, in their pure form, crystalline at room temperature. If the organic components of multicomponent crystals exchange charge or hydrogen, they are characterized as organic salts. These definitions of different forms might overlap: a multicomponent crystal containing a pharmaceutical compound, a singly dissociated dicarboxylic acid and a solvent would be characterized as a co–crystal salt solvate [7].

The crystal *shape* can be vital for the flow and storage properties of a product. Filtration of a suspension after crystallization containing needle-like crystals, furthermore, might become a time consuming step when the needles plug the filter and form an impassable barrier for the liquid. The terms crystal habit and crystal morphology are evident for the description of the crystal shape (Figure 32.5). The crystal habit is linked to

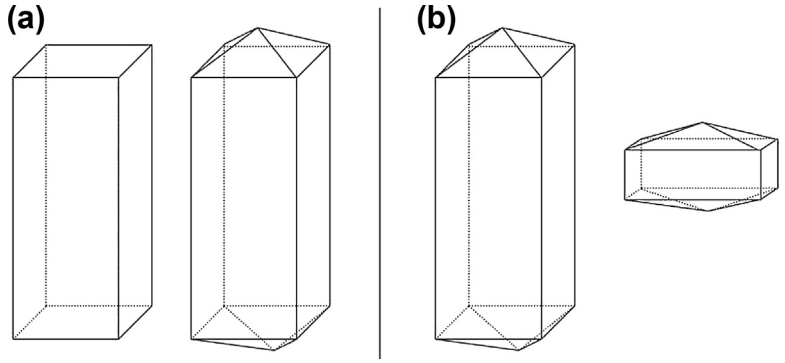

FIGURE 32.5 (a) Two crystals having the same habit but a different morphology; (b) Two crystals having a different habit, but the same morphology. *Adapted from Ref. [8].*

the outer geometrical appearance of a crystal, regardless of the crystal structure. Terms as cubic, acicular, plate-like or tabular are commonly used for the description of the crystal habit. In contrast, the term crystal morphology corresponds to a description related to the crystal structure [8]. The morphology refers to groups of crystal faces having the same relation to the elements of symmetry and can be described in terms of Miller indices. Further details on the relation between morphology and crystal structure is described elsewhere [9,10].

A crystal size distribution (CSD) gives information on the collection of crystal sizes in the product [11,12]. A CSD can be measured with the aid of a number of techniques all capturing a different characteristic length scale of the crystalline product [13]. For the same crystalline product, drastically different CSDs are obtained when using techniques that, for instance, capture a number-based or a volume-based CSD (Figure 32.6). It is, therefore, important to report what kind of CSD is measured or what technique is used to measure the CSD.

Costly downstream processing such as sieving or grinding could be avoided if an optimal CSD is obtained directly from the crystallization process. Often a narrow size

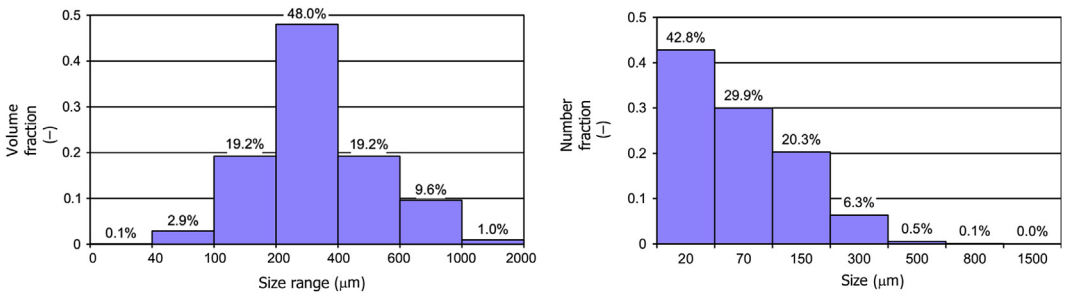

FIGURE 32.6 Volume-based and number-based crystal size distribution of the same crystal product. The majority of the crystals are small and, therefore, are prominently present in the number based CSD (right). The volume of the small crystals, however, is hardly contributing to the total volume and therefore they do not impact the volume-based distribution (left).

distribution has such optimal behavior. The CSD of the product crystals can be responsible for a specific dissolution and flow behavior of the solid crystals. During storage, a classification of the different size fractions may occur where the larger particles will be found towards the bottom and the smaller ones towards the top of the container.

The presence of a very fine, powder-like fraction may lead to caking, due to electrostatic interactions of the particles or humid conditions. During caking, the crystals grow together and form a thick lump of crystals. During caking, impurities and mother liquor are trapped within the caked crystals.

Predominantly in the food, pharmaceutical and fine chemical industries high levels of *purity* are desired. For instance, impurities from side reactions during the synthesis of an active pharmaceutical ingredient could lead to unwanted additional biological activity of the administered drug if they end up in the final product. Impurities can be located on several positions in the final product. First, they could be located on lattice positions. That could occur if the impurity molecule strongly resembles the product molecule. Second, they could be present in small pockets (inclusions) of mother liquor within the interior of the crystals. Third, an agglomerated collection of crystals is often relatively impure since impurities collect within the intergrown regions of the particles. Finally, the impurities can be located on the surface of the crystals if the washing step is not optimal.

32.3 Crystallization

32.3.1 Solubility and Supersaturation

The solubility of a crystalline compound forms the basis for crystallization process design. It describes at which temperature a specific solution composition is in equilibrium with a specific crystalline phase. Now that commercial equipment from several companies is readily available solubility data for a variety of multicomponent systems becomes accessible [14,15]. The solubility is a function of the solvent composition and the temperature, while also other compounds present in significant amounts may affect solubility. For bulk chemicals and proteins, the solvent usually is water; pharmaceutical compounds often are crystallized using organic solvents and solvent mixtures.

The solubility curve of a number of crystalline compounds in water [1] is shown in Figure 32.7. The different compounds show a wide variety of solubilities. While the NaCl solubility is close to constant as a function of temperature, that of KNO_3 shows a strong dependence on temperature. Most organic compounds such as active pharmaceutical ingredients show an increasing solubility with temperature in organic solvents. This solubility often can be described sufficiently accurate using the van't Hoff equation.

$$\ln x = -\frac{\Delta H}{R}\left(\frac{1}{T} - \frac{1}{T_m}\right) \tag{32.1}$$

The van't Hoff equation describes ideal solubility behavior through the heat of fusion ΔH and the melting temperature T_m [16]. Within a sufficiently small temperature region,

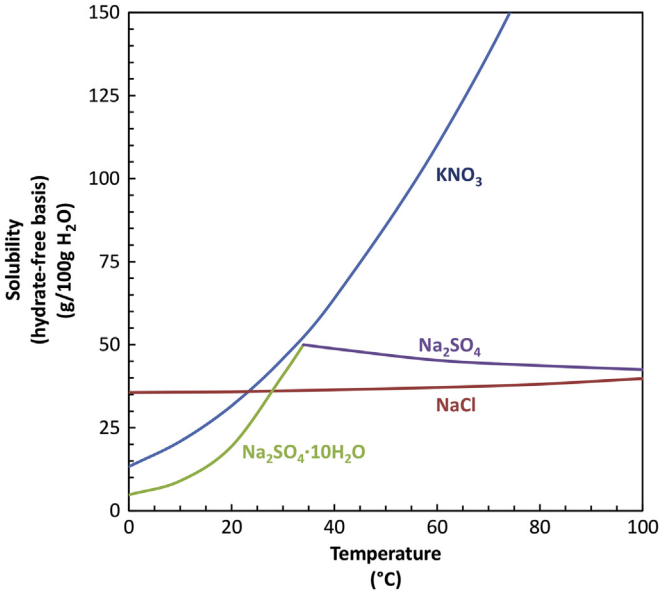

FIGURE 32.7 Solubility as a function of temperature for a number of crystalline compounds in water. While the NaCl solubility is close to constant as a function of temperature, that of KNO_3 shows a strong dependence on temperature. At low temperatures, the hydrated form of Na_2SO_4 has a lower solubility and thus is more stable than the anhydrate. At higher temperatures, this is reversed. *Constructed from data in Ref. [1]*

these could be used as fitting parameters. The nonideality of the system causes the fitted values to deviate from the actual heat of fusion and melting temperature and poor fits in too wide temperature regions.

The driving force for crystallization can be represented by the chemical potential difference between the prevailing out-of-equilibrium state of the system and the corresponding equilibrium state [11,17]. This chemical potential difference thus is a function of both concentration c and solubility c^* at a specific temperature and pressure. Therefore, the driving force for crystallization is usually represented by the supersaturation ratio S:

$$S = \frac{c}{c^*} \tag{32.2}$$

The supersaturation can be increased by, for instance, a concentration increase through solvent evaporation or a solubility decrease by decreasing the temperature. Crystal growth would reduce the solution concentration and thus the supersaturation.

The most stable polymorph has the lowest solubility $c_{\mathrm{I}}^* < c_{\mathrm{II}}^*$. If this is so in the entire temperature region from 0 K to melting temperature one speaks of a monotropic system. In an enantiotropic system, there exists a transition temperature below which one form is stable and above which the other is stable temperature. This means that in an equilibrated suspension of metastable polymorph II ($S_{\mathrm{II}} = 1$) a supersaturation $S_{\mathrm{I}} = c/c_{\mathrm{I}}^* > 1$ exists towards the stable form I. In time, such a system would transform to

a suspension of form I crystals in equilibrium with a solution at concentration c_I^* through nucleation and growth of form I and dissolution of metastable form II. However, this could take a considerable amount of time if nucleation and growth are sufficiently small. A pharmaceutical product consisting of a metastable polymorph then could be stable enough to market as a drug. However, usually the most stable form is preferred as the product.

32.3.2 Crystallization Techniques

Industrial crystallization techniques [11,17,18] are defined by the way supersaturation is created. In case of *evaporative crystallization*, solvent is removed by evaporation from a boiling solution. Upon evaporation of the solvent, the solute concentration increases, which increases the supersaturation. The supersaturation, in turn, is consumed by the growing crystals. Evaporative crystallization thus is operated close to a three-phase equilibrium point where vapor, solution and solid phase are in equilibrium. The solution volume is reduced by transferring solvent to the vapor phase and solute to the solid phase. The operating temperature can be substantially adjusted through changing the pressure-dependent boiling temperature.

Evaporative crystallization can be applied on a large scale in continuous bulk chemical production for products such as table salt [19] and sugar [20]. Evaporative crystallization is chosen if the solubility does not show a strong positive dependence on temperature, for instance in the case of table salt (Figure 32.7). Often the choice for evaporative crystallization is made if the temperature dependence of the solubility is less than 0.005 g/g °C [21]. A recycle stream in a continuous evaporative crystallizer is used to remove crystal product from the remaining solution. A cascade of evaporative continuous crystallizers (Figure 32.1) is used to increase yield while reducing energy consumption: the vapor from a crystallizer is used to evaporate the solvent in a subsequent one.

Cooling crystallization can be chosen if the solubility shows a strong positive dependence on the temperature, larger than 0.005 g/g °C, and if the solubility at the lowest possible temperature is sufficiently low [21]. Upon decreasing the temperature of an equilibrated suspension, the solubility is decreased, and supersaturation is created which is reduced again by the growing crystals in the suspension. Usually cooling crystallization is applied in batch mode. Scaling on cooling surfaces may be an issue in continuous cooling crystallization due to the large temperature differences needed for a substantial production rate.

Another way to create supersaturation is to add an antisolvent. Although an antisolvent dilutes the mixture and reduces the concentration, it also strongly reduces the solubility in the mixture. If the solubility reduction exceeds that of the concentration then a supersaturation can be created which induces crystallization. Precipitation is sometimes named reactive crystallization. Upon mixing two streams, a reaction occurs which results in a sparingly soluble solute. If sufficiently high concentrations are used, the concentration is much higher than the solubility and supersaturation is created.

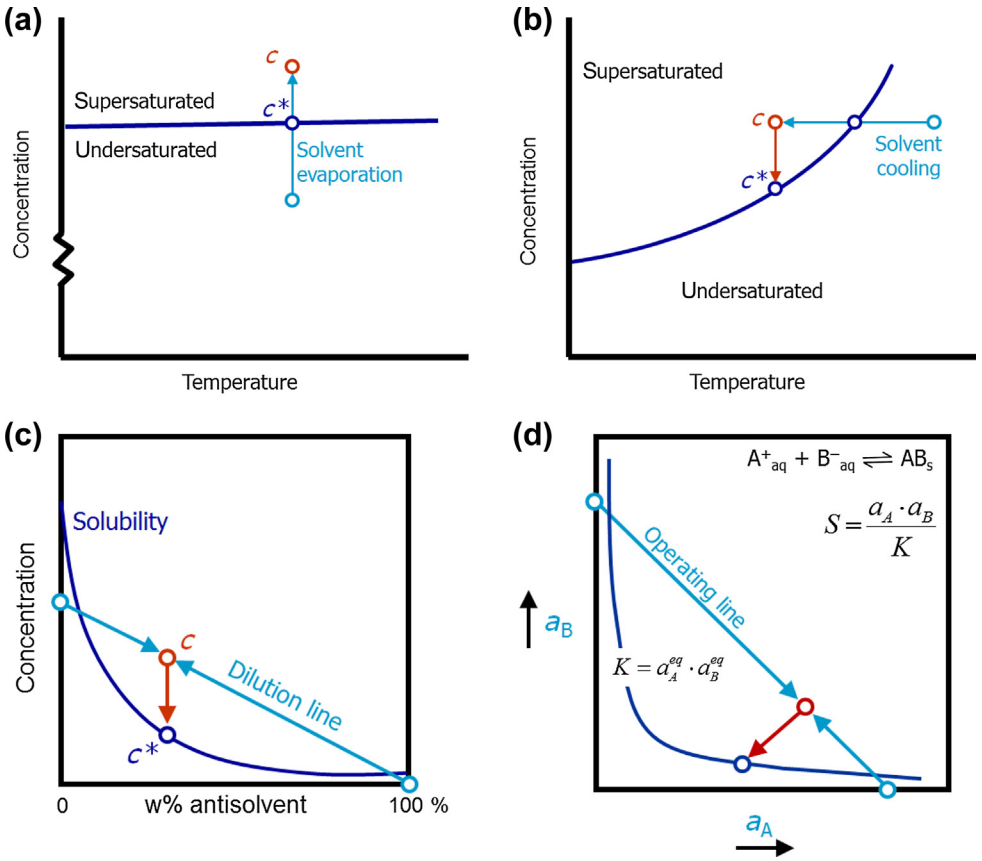

FIGURE 32.8 The phase diagrams, solubility lines, and operating points for the different crystallization techniques: (a) evaporative crystallization; (b) cooling crystallization; (c) antisolvent crystallization; (d) precipitation.

Both antisolvent crystallization and precipitation involve mixing of process streams. This mixing usually coincides with large, local supersaturations close to the inlet points. Therefore, usually locally at the flow inlets nucleation occurs after which the crystals grow out upon suspension in the bulk solution. Due to these mixing effects and local variations in process variables, it is difficult to control such processes.

Figure 32.8 shows the phase diagrams from the different crystallization techniques. It also shows how supersaturation is created and the relation between concentration, solubility and supersaturation ratio $S = c/c^*$.

32.4 Crystal Nucleation

Crystal nucleation is the start of a phase transition towards the crystalline solid phase [22]. It is thus the subprocess of crystallization with which crystals come to existence, and it takes place in a supersaturated mother phase (solution, melt, and vapor, solid).

Since this subprocess determines the number of crystals between which the crystalline material is divided during the crystallization, it plays a key role in determining the CSD: for the same mass crystallized, a higher number of crystals formed during the nucleation stage results in a smaller average product size. It is also thought that crystal nucleation is responsible for the kind of crystalline material formed: if the nucleation rate of a metastable phase is larger than the stable phase the metastable polymorph would dominantly form if the growth rate is not substantially smaller.

Within an industrial crystallization process, crystals can be formed from an initially clear solution (primary nucleation) or due to the presence of parent crystals (secondary nucleation). In turn, primary nucleation generally is divided into homogeneous and heterogeneous nucleation. During heterogeneous primary nucleation, the crystals form at surfaces such as dust particles, crystallizer wall, air-solution interface or deliberately added template particles. Homogeneous primary nucleation takes place in the absence of heterogeneous particles in a clear solution. It is important to note that in the laboratory and more so in large-scale processes on an industrial scale, the presence of many different heterogeneous particles or surfaces is impossible to avoid. Despite their importance, usually no information is available on the amount and kind of heterogeneous particles that are finally responsible for the occurrence of heterogeneous nucleation.

Thus, while an unseeded batch cooling crystallization process usually relies on primary nucleation to provide the crystals, during a continuous crystallization process the omnipresent crystals continuously generate more crystals through secondary nucleation. Only in extreme cases are there indications that homogeneous nucleation is the dominant nucleation mechanism. This is summarized in Figure 32.9. Since primary and secondary nucleation are strikingly different processes, controlling and predicting crystal size from these processes thus need completely different approaches.

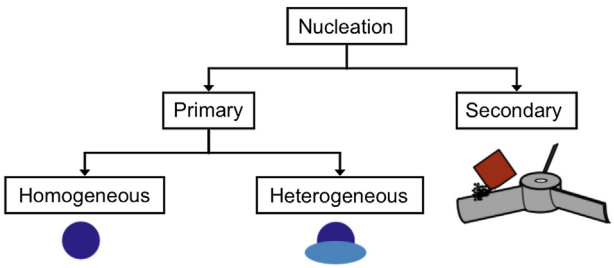

FIGURE 32.9 Crystal nucleation is divided into primary and secondary nucleation. Primary nucleation occurs in a clear liquid either in the absence (homogeneous primary nucleation, HON) or in the presence (heterogeneous primary nucleation, HEN) of heterogeneous particles. Secondary nucleation occurs in the presence of crystals. New crystals can be, for instance, created due to collisions of parent crystals with the stirrer (attrition), but other secondary nucleation mechanisms are also possible.

32.4.1 Primary Nucleation

When cooling down a solution to below its saturation temperature it becomes supersaturated and growth can commence if crystals are present. However, crystals are only detected when already a substantial supersaturation is generated (Figure 32.10). Since this cannot be only attributed to the delayed detection of macroscopically large crystals due to the detectable crystalline amount and the growth rate, it shows that a substantial free energy is needed for nucleation to occur. Thus, there is an energy barrier for nucleation, which is named nucleation work.

Starting with the work of Gibbs, classical nucleation theory (CNT) has served already for almost 150 years to describe the nucleation work and the resulting kinetics of the barrier crossing. This shows CNT is a powerful theory that needs strong, convincing evidence to be put aside. There are, however, some serious issues with the theory, an important one inevitably being the inability to accurately predict crystal nucleation rates [23]. Primary nucleation, its issues and recent advances, will be discussed in the current section from the viewpoint of industrial crystallization.

Although heterogeneous nucleation (Figure 32.9) is the dominant mechanism in industrial crystallization, the nucleation rate equation following from CNT can be best explained through homogeneous nucleation. This equation then can also be used to describe the mechanism that is assumed to be dominant: heterogeneous nucleation. Homogeneous nucleation is a balance between a free energy gain and loss. The gained results from the thermodynamics that drive the system towards the more stable crystalline state through the supersaturation, determined by the chemical potential difference between the two bulk states (bulk solution and bulk crystalline solid) and the

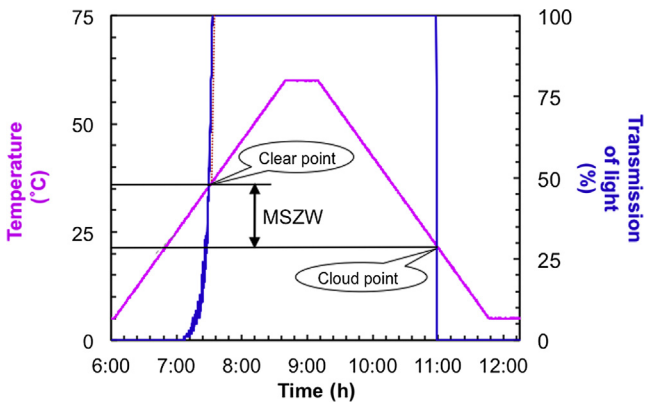

FIGURE 32.10 A measurement of the metastable zone width (MSZW). A sample is heated and cooled with a specific rate while the transmission of light through the sample is recorded. If the transmission is smaller than 100%, crystals are present; if it is 100%, a clear solution is present. The clear point is the temperature at which a suspension turns into a clear solution upon increasing the temperature. For this sample, the clear point is measured to be around 36 °C. The cloud point is the temperature at which a clear solution turns into a suspension upon decreasing the temperature. For this sample, the cloud point is measured to be around 22 °C. The difference between clear and cloud point is the metastable zone width (MSZW).

cluster volume. The loss is due to the surface that has to be created between the formed crystal and the supersaturated solution, and this loss is thus related to the interfacial energy of the solid–solution interface and the interfacial area.

At small cluster sizes, a substantial fraction of the molecules in the cluster are positioned at the surface, and the interfacial term is dominant over the volume term: there is a free energy loss upon creating the cluster. At large cluster sizes, there are many molecules within the bulk of the cluster and the volume term dominates: there is a free energy gain upon creating the cluster. Thus, there is an intermediate cluster size at which the free energy loss is maximum, and this is the nucleus size (sometimes named the critical nucleus size). This is shown in Figure 32.11.

Equations for the nucleus size n^* and nucleation work W^* can be derived from the expressions for the interfacial and volume terms [22]:

$$n^* = \frac{32\pi v^2 \gamma^3}{3k^3 T^3 \ln^3 S}; \quad W^* = \frac{16\pi v^2 \gamma^3}{3k^3 T^3 \ln^3 S} \tag{32.3}$$

With the interfacial energy γ between crystal and solution, the shape factor c relating surface area and volume, molecular volume v of the solid, and supersaturation ratio S. At increased supersaturations and decreased interfacial energies the nucleation work W^* is lower: it becomes energetically easier to nucleate. It should be noted that here the crystal is considered isotropic: the interfacial energy is constant in all directions. As is known for macroscopic crystals this usually is not the case, especially for crystalline material with a high melting temperature and low or moderate solubility: interfacial energies are

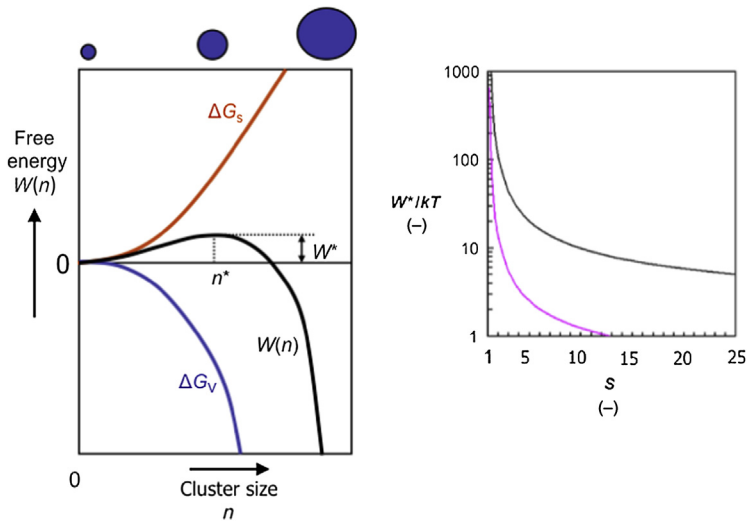

FIGURE 32.11 Left: The free energy associated with the formation of a cluster as a function of the cluster size n at a constant supersaturation S. At the nucleus size n^* the free energy of formation is maximum, which is the nucleation work W^*. Right: The decrease of the nucleation work W^*/kT as a function of the supersaturation ratio S for both HON (upper solid line) and HEN (lower solid line) for typical nucleation parameters.

relatively low for specific crystal surfaces due to the lower number and size of broken bonds at these crystal surfaces. These low interfacial energy surfaces will be dominantly present in the crystal morphology, striving to a low overall interfacial energy.

Thus, crystal nucleation is an activated process with the nucleation work W^* as the free energy barrier. The nucleation rate J, defined as the number of crystals generated per unit of time and volume, then can be described with an Arrhenius-type of equation [22]:

$$J = A\exp\left(-W^*/kT\right) = A\exp\left(-B/\ln^2 S\right) \tag{32.4}$$

While the exponential term describes the thermodynamics of the activated process of nucleation, the pre-exponential term deals with the kinetics of the barrier crossing. In order to describe the pre-exponential factor A, the model behind it has to be physically understood. A supersaturated solution consists of building units that can associate into larger clusters through a stochastic process involving a large amount of random single building unit attachments and detachments. The nucleus is a cluster consisting of n^* building units for which the attachment frequency is equal to the detachment frequency of building units. Clusters smaller than the nucleus size tend to dissolve while clusters larger than the nucleus size tend to grow to become macroscopically large crystals. The nucleus, thus in metastable equilibrium with the supersaturated solution, has about 50% chance to grow out rather than to decay.

The stationary nucleation rate then can be defined as the flux of particles through the nucleus size n^* towards larger size. This flux is defined by the concentration of nuclei $X^*(n^*)$, the attachment frequency f^* of building units to the nucleus making clusters of a size (n^*+1) and the probability $p(n^*+1)$ that a cluster of size (n^*+1) grows out rather than dissolves.

$$J = p(n^*+1)\cdot f^* \cdot X^*\left(n^*\right) \tag{32.5}$$

The *attachment frequency* f^* of building units to nucleus is reported to be an important factor in controlling nucleation and also growth. Molecules can self-associate and form different types of building blocks for different types of crystal structures (polymorphs), as can be seen in Figure 32.12. Several techniques are available to

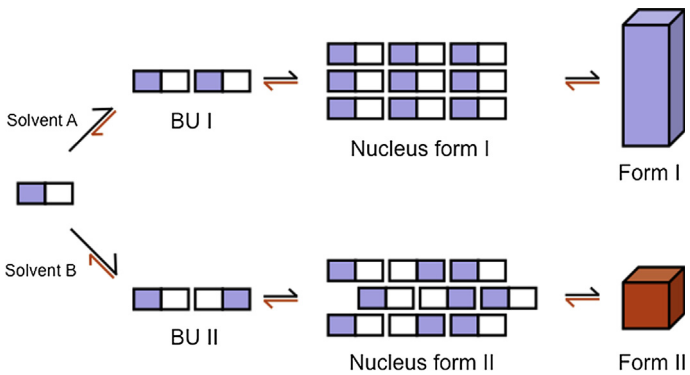

FIGURE 32.12 Effect of self-association on crystal nucleation processes.

determine the kind of association that occurs in solutions [23]. More and more literature reports show that solvents determine the association process and cause solutes to be dominantly present in specific associates that lead to the crystallization of specific polymorphic compounds [24,25].

Unfortunately, the concentration of nuclei $X^*(n^*)$ in a supersaturated solution is not known. Since in case of equilibrium the flux of particles through the nucleus size would be zero, the concentration $C^*(n^*)$ of nuclei is known that develops if equilibrium would be achieved between the supersaturated solution and the nucleus size. This is just a function of the nucleation work and the concentration C_0 of nucleation sites in the system.

$$C^*(n^*) = C_0 \exp(-W^*/kT) \tag{32.6}$$

A relation between the actual concentration $X^*(n^*)$ and the hypothetical equilibrium concentration $C^*(n^*)$ of nuclei can also be derived and the nucleation rate can be written as:

$$J = z \cdot f^* \cdot C_0 \exp(-W^*/kT) \tag{32.7}$$

The Zeldovich factor z accounts for the fraction of clusters of size $(n^* + 1)$ that dissolve rather than grow out as well as for the difference between $X^*(n^*)$ and $C^*(n^*)$. The *Zeldovich factor* z can be expressed as a function of the supersaturation ratio and the exponential term B:

$$z = \frac{\ln^2 S}{\sqrt{12\pi kTB}} \tag{32.8}$$

For a value of $z = 1$, an attachment of a building unit to the nucleus would reduce the possibility to zero for the cluster to dissolve. Furthermore, the concentration $X^*(n^*) = C^*(n^*)$. This would only occur at very high supersaturation ratios for which it is unlikely that nucleation occurs but rather spinodal decomposition. Therefore, reported values for z should lie below one and are usually in the range of 0.001–1.

Equation (32.7) is valid for homogeneous stationary nucleation where nuclei form in a clear solution in the absence of heterogeneous particles. However, in industrial settings such heterogeneous particles cannot be avoided, and it is usually assumed that heterogeneous nucleation (HEN) occurs under these conditions due to the much lower nucleation work $W^*_{\mathrm{HEN}} << W^*$ associated with heterogeneous nucleation, although the concentration $C_a << C_0$ of nucleation sites in heterogeneous nucleation is lower as well.

$$J_{\mathrm{HEN}} = zf^* C_a \exp(-W^*_{\mathrm{HEN}}/kT) \tag{32.9}$$

Since in case of heterogeneous nucleation, the nucleus forms on a heterogeneous particle there are now three interfacial energies involved: next to the interfacial energy between crystal and solution the interfacial energy between heterogeneous particle and crystal and between the particle and the solution have to be considered. Usually not much is known about these interfacial energies due to the ill-defined character of the

heterogeneous particles, and the interfacial effects are captured in an activity factor $0 < \xi < 1$.

$$\gamma_{\mathrm{HEN}} = \xi\gamma \tag{32.10}$$

The activity factor reflects the apparent reduction of the interfacial energy between solution and crystal due to the formation of the crystal on the heterogeneous particle.

The *concentration C_0 of nucleation sites* is another variable determined by the heterogeneous particles present. Since the nucleus cannot form everywhere in the solution but only on the heterogeneous particles the concentration of nucleation sites decreases for heterogeneous nucleation $C_{\mathrm{a}} << C_0$ to a value related to the concentration of heterogeneous particles present:

$$C_{\mathrm{a}} = C_{\mathrm{HEN}} a_{\mathrm{HEN}} \tag{32.11}$$

where C_{HEN} is the concentration of heterogeneous particles and a_{HEN} is the number of nucleation sites per heterogeneous particles.

For the heterogeneous nucleation rate J_{HEN} following the CNT, it follows that [22]:

$$J_{\mathrm{HEN}} = zf^* C_{\mathrm{a}} \exp\left(-\frac{16\pi v^2 \xi^3 \gamma^3}{3k^2 T^2 \ln^2 S}\right) = A_{\mathrm{HEN}} \exp\left(-\frac{B_{\mathrm{HEN}}}{\ln^2 S}\right) \tag{32.12}$$

This then can be used to put next to experimental data on crystal nucleation rates from solution. Recently, a number of different crystal nucleation rate measurement methods were developed based on the double pulse method [26] and microfluidic devices [27] usually in unstirred solutions and turbidity measurements [28,29] in stirred solutions. Once nucleation rates are obtained as a function of supersaturation, they can be analyzed using the nucleation rate equation from Eqn (32.12) giving values for the preexponential factor A_{HEN} and the exponential factor B through a fitting procedure. While the low values reported for B_{HEN} indicate heterogeneous nucleation, the low values for A_{HEN} show that either the attachment frequency f^* of building units or the concentration C_{a} of heterogeneous particles is lower than expected [30,31].

Unfortunately, since usually nothing is known about the kind of heterogeneous particles the obtained values for A_{HEN} and B_{HEN} cannot be analyzed further to obtain molecular information on the crystal nucleation process which then would lead to fundamental understanding of crystal nucleation processes and better nucleation theories and nucleation rate predictions. Currently, more and more research becomes available studying the effect of well-defined heterogeneous particles on nucleation rates under well-defined conditions, which would enable a molecular interpretation. Also, simulation processes of nucleation of larger and more realistic systems become possible.

Next to association processes and heterogeneous particles, a third possibility is to use external energy sources for influencing and possibly controlling nucleation processes. For instance, lasers were used to align molecules in solutions to facilitate the nucleation of specific polymorphs [32]. Lasers were also used to induce cavitation that enabled crystal nucleation [33]. Other external energy sources include electric [34] and magnetic fields [35] and ultrasound [36,37].

There are many discrepancies between classical nucleation theory and observations from experiment and simulations. One of the main assumptions in CNT is that clusters have the same crystal structure and interfacial energy as the macroscopically large crystal. Only the reports of nucleus sizes between one and 1000 molecules already indicate that this may deviate considerably from that of a macroscopically large crystal. In fact, losing the assumption of structured nuclei is the main driver of recently introduced nonclassical nucleation mechanisms such as the two-step nucleation mechanism [38,39].

Molecular simulations [40] gave a first indication that on the transition from solution to crystalline phase it is energetically more favorable to form a liquid-like cluster in which only at larger sizes a structure is introduced. Protein nucleation experiments lead to the observation of a two-step nucleation mechanism where liquid-like clusters with a high protein density form followed by the formation of crystalline nuclei in these liquid-like clusters [38]. This would be a two-step mechanism because a barrier for nucleation exists for both the liquid-like and crystalline phase. Especially for inorganic compounds, it is argued based upon experimental evidence that larger crystalline metastable clusters form that then coagulate to form larger crystals [41,42].

Recent advances in analytical tools, molecular simulations, and measuring techniques continue to boost nucleation research. In the coming years, it is, therefore, expected to see a substantial increase in crystal nucleation knowledge. This will positively influence the industrial crystallization process control and the control over product quality from these processes.

32.4.2 Secondary Nucleation

In stirred solutions in small volumes of around 1 mL, it appeared that often only a single nucleus formed which grows out before other crystals form [43]. When the single crystal is large enough, it initiates secondary nucleation where new crystals originate from this parent crystal. This single crystal was visually observed [44] but earlier also was reported to cause chiral symmetry breaking during the crystallization of sodium chlorate, an achiral compound that crystallizes in a chiral space group [45,46]. This single nucleus mechanism indicates that possibly secondary nucleation mechanisms play an important role in determining the crystal size distribution and polymorphic form, not only in continuous crystallization processes, but even in unseeded batch cooling crystallization processes.

Secondary nucleation, exemplified by attrition in Figure 32.9, takes place in the presence of larger crystals in the suspension. Next to attrition, which seems to be the dominant secondary nucleation mechanism in industrial crystallizers [18], several other mechanisms for secondary nucleation have been identified: initial breeding, needle breeding, fracture, fluid shear, and contact [47].

Attrition causes secondary nucleation fragments due to collisions of the parent crystals with each other, the walls, and the stirrer. The stirrer tip is playing a dominant

role in this process because of its high velocity in respect to the suspension, leading to high-energy collisions of the parent crystals with the stirrer tip. A high tip speed of the stirrer thus is associated with a high attrition rate due to the large parent crystal collision frequency. However, high tip speeds are needed in order to have the crystals suspend through the solution sufficiently well. The balance between the attrition rate and suspension is a major challenge in crystallization scale-up while keeping control over the crystal size distribution.

Another way to influence parent crystal collision frequency is through the crystal mass fraction in the suspension. A higher fraction is often related to a higher number of crystals in the suspension, which in turn then would be related to a higher collision frequency.

Also, the parent crystal size is of influence: above a certain size the large parent crystals do not follow the fluid streamlines such as smaller crystals would do, and the stirrer collision probability increases. Sometimes the attrition size can be estimated from microscopic pictures of the interior of the attritted parent crystals submerged in a liquid with the same refractive index such that the crystal surface does not cloud the view on the crystal interior [48]. This attrition size may be influenced by the density difference between crystalline phase and solution.

The collisions cause fragments that may be strained and stressed and thus contain an increased chemical potential compared to an unaffected crystal. This indicates that some fragments after formation may experience an undersaturation, even though the solution is supersaturated towards the crystalline compound. This means that the supersaturation ratio is another factor influencing secondary nucleation rate: a higher supersaturation increases the probability that attrition fragments survive [49].

Next to the crystallization process conditions, many other parameters may be of influence on the secondary nucleation rate due to attrition of parent crystals with the stirrer. The material properties of crystals such as hardness and Young's modulus may play a role in the attrition propensity in a crystallizing system [50,51]. The geometry of the crystallizer and the type of stirrer, as well as the draft tube and baffle position in relation to the stirrer, can be important factors in determining the attrition rate [52]. Depending on the material, process conditions and process equipment, attrition seems to generate fragments in the range of 1–10 μm [48,53–56].

32.5 Crystal Growth

Crystal growth rates are of key importance to the engineer since they determine the crystal residence time in the crystallizer to achieve a specific crystal size and, therefore, the size of the crystallizer and the investment costs.

The linear growth rate of a specific hkl face is often denoted as R_{hkl}. For faceted crystals, the linear growth rate between hkl faces can be drastically different. The growth rate is different between faces because the surface construction differs from face to face and thus also the integration process into the kink sites is different. The growth rates of

the top faces of a needle-like crystal are usually much larger than the side faces. There is thus a relation between the crystal shape and the linear growth rate: the slowest growing hkl faces determine the shape. Linear growth rates in solution crystallization are in the order of 10^{-7} to 10^{-9} m/s. For melt layer growth, the processes can feature growth rates in the range of 10^{-5} to 10^{-7} m/s while in precipitation processes even smaller growth rates than 10^{-9} m/s could prevail.

Different definitions of growth rates are in use. In case a CSD is recorded during a crystallization process, the increase per unit of time of the characteristic crystal size L is often referred to as an overall growth rate G_L. Growth rates are sometimes also measured in terms of mass increase per surface area per unit of time resulting in a deposition rate G_m. These growth rates can be interconverted provided the crystal shape remains constant during crystal growth (Figure 32.13).

Figure 32.2 shows the route a solute molecule travels from the bulk solution to the integrated state in a kink site of a step on the crystal surface. This involves several steps. Usually the growth process is controlled by either volume diffusion or solute integration. Then the growth process is referred to as respectively volume diffusion controlled growth and integration-controlled growth. In both cases, the crystal growth rate is greater the higher the supersaturation. Only in the case of volume diffusion, the growth rate would be influenced by fluid dynamics since the volume diffusion boundary layer between crystal and bulk solution becomes thinner at higher fluid dynamics.

During growth and also nucleation, the release of the heat of crystallization causes an increased temperature at the surface [57,58]. Usually in solution crystallization this heat can be dissociated quite rapidly from the surface due to the large amount of solvent present that can act as a heat sink. In melt crystallization, this heat can be considerable and strongly affect growth rates [59,60]. Other steps that may play a decisive role in growth rate are the solvent shell removal around the solute and the volume diffusion of solvent and impurities away from the growing surface.

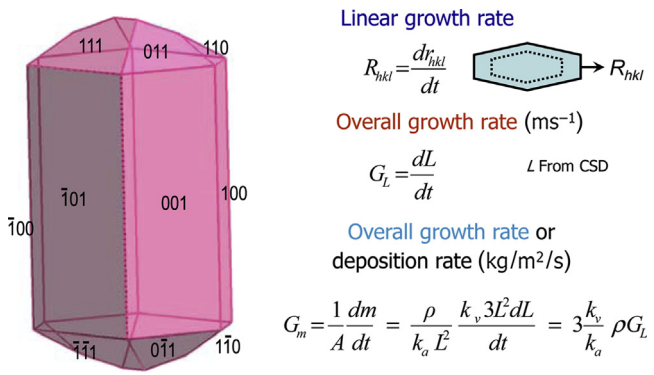

FIGURE 32.13 The relation between the linear growth rate R_{hkl} of a specific hkl face, the overall growth rate G_L, and the deposition rate G_m for a faceted crystal.

Growth rates thus depend not only on the prevailing supersaturation in the solution but may also be a function of temperature, pressure, and composition of the mother liquor, but also of fluid flow conditions, crystal growth history, and the presence of additives or impurities.

Steps and kinks (Figure 32.2) on crystal surfaces are energetically favorable sites to adsorb molecules. One way to introduce a step on a flat surface is to create a two-dimensional nucleus on the flat surface. At the periphery of the nucleus then molecules can be incorporated. This combination of two-dimensional nucleation and lateral growth of the two-dimensional islands on the surface is termed the birth and spread mechanism [61]. Since nucleation is involved, the birth and spread mechanism is a strong nonlinear function of supersaturation. For this mechanism, this leads to zero growth rates at low supersaturations and an exponential rise in the growth rate above that.

At small supersaturation, no growth would occur via the birth and spread mechanism because the energy barrier for two-dimensional nucleation is too large. Experimentally it is, however, observed that crystals grow at small supersaturations. This is explained by the spiral growth mechanism [62]. The presence of lattice imperfections such as screw dislocations in the crystal cause steps on the surface. These steps provide energetically favorable access points for incorporating molecules. Since the step originates from a fixed position of the dislocation at the surface, the incorporating molecules make the step spiral around this dislocation.

For the birth and spread mechanism at higher supersaturations the energy barrier for nucleation decreases. At some upper limit of the supersaturation, the energy barrier for nucleation becomes so low that the thermal energy within the system can overcome the barrier and molecules can freely, without energy penalty, incorporate at any position at the surface without the need of two-dimensional nucleation. The face then becomes rough, and the crystal growth mechanism is referred to as rough growth. The transition from birth and spread to a rough growth mechanism due to supersaturation is termed kinetic roughening. Its counterpart is thermal roughening where the crystal face in equilibrium shows a transition from flat to rough when increasing only temperature. More fundamental details on growth kinetics are given in Volume I of this Handbook.

A simple empirical relation for the linear growth rate R_{hkl} can be given as:

$$R_{hkl} = K(S-1)^n \tag{32.13}$$

where K is an empirical kinetic constant and the power n is the growth order. In case of surface integration-controlled growth, the value of K and n depend on the growth mechanism that occurs. Complex expressions derived from more accurate descriptions exist for the three growth mechanisms, but they all can be simplified to Eqn (32.13) by lumping the complexity in both K or n. The spiral growth, birth and spread, and linear growth mechanism have growth orders n of respectively two, larger than two and one.

In case of volume diffusion controlled growth, often it is more convenient to use the deposition rate G_M in an expression equivalent to Eqn (32.13). The kinetic constant then

is determined by the diffusion coefficient, the boundary layer thickness and the solubility, which makes it a function of for instance temperature and fluid dynamics. Usually a growth order $n = 1$ is taken for volume diffusion controlled growth.

If surface integration and volume diffusion result in competitive rates, neither can be neglected and an appropriate expression accounting for both should be used.

Since the construction of the crystal surface plays an important role in the growth rate the crystal growth history of the crystals is an important factor. The perfection or lack thereof of the surface can influence the growth rate, either accelerating or suppressing crystal growth. Often the growth history of crystals in a suspension is not equal leading to equally sized crystals having a different growth rate. These individual rates fluctuate around an average growth rate but could even lead to dissolution of specific crystals under supersaturated conditions. When crystals display individual growth rates despite identical supersaturation conditions is termed growth rate dispersion (GRD) [63]. Sometimes this is modelled using Size Dependent Growth where the growth rate varies as a function of size.

Foreign compounds such as solvents, impurities, and additives can have a drastic effect on the growth rate [64]. Figure 32.14 shows the effect of an impurity on the growth and dissolution rate of a crystalline compound [65]. Both the dissolution and the growth rate are reduced by the presence of an impurity. The more of the impurity is present, the more the growth rate is reduced. Interestingly, in this case the effect on dissolution and growth rate of the impurity is the same. There are reports that additives lead to increased growth rates [66].

The crystal shape is determined by the faces with the smallest growth rates (Figure 32.15). Growth rates are a function of the supersaturation and, therefore, an

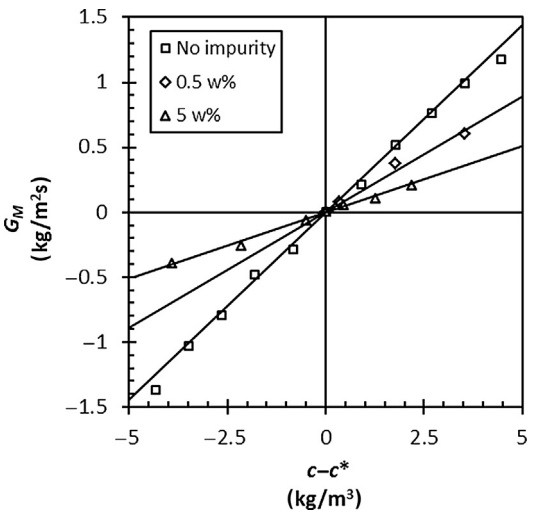

FIGURE 32.14 Growth and dissolution rates of $MgSO_4 \cdot 7H_2O$ in the absence and presence of the impurity borax. Lines are drawn as a guide to the eye. *Figure adapted from Ref. [65].*

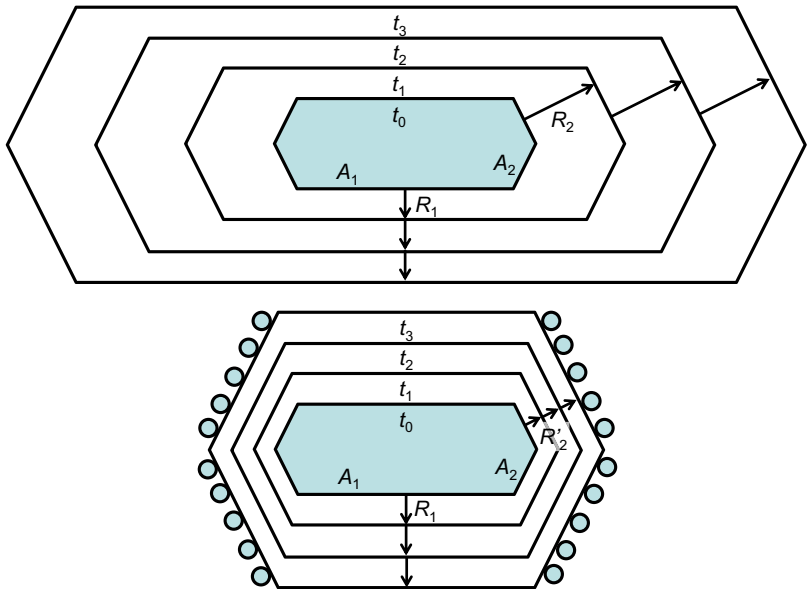

FIGURE 32.15 Impurity induced habit changes due to inhibited growth. Top: In the absence of the impurity the crystal shape does not change and the linear growth rate $R_2 > R_1$. Bottom: In the presence of the impurity on surface two from time t_0 the growth rate of face two is reduced $(R'_2 < R_2)$ while that of face one remains unchanged resulting in a shape change. *Adapted from Ref. [67].*

effect of the supersaturation on the shape can be anticipated. Usually, more needle-like shapes are obtained at higher supersaturations.

Since growth rates are also influenced by foreign compounds such as solvents [64], impurities, and additives, the crystal shape is also influenced by their presence. Specific crystal faces may experience growth inhibition and as a consequence, the crystal shape changes (Figure 32.15). Tailor-made additives then can be used to induce a preferred crystal shape [67]. Top faces of a needle-like crystal could specifically be inhibited with such an additive in order to considerably reduce the needle aspect ratio and in such a way prevent filtration issues or other problems.

32.6 Crystallization Process Configuration

More than 90% of active pharmaceutical ingredients (API) are crystals of small organic molecules [68]. Industrial suspension crystallization is intended to result in the preferred product quality having a good operational efficiency [69]. This means that from a product point of view (1) a sufficiently pure product should be produced of (2) the specified crystal form, having (3) the right particle size distribution and particle shape. Operational efficiency nowadays demands that the process results in (4) a high yield at (5) a high volume productivity using (6) reasonable cycle times.

Conventionally this is achieved by optimizing a limited number of different commercially available crystallizers. There are some excellent books dealing with conventional industrial crystallizer types, choice, and optimization [11,17] and, therefore, this chapter will not deal with that topic. Choosing an existing piece of equipment for a new crystallization process (usually some type of stirred vessel) would mean that the range of product quality and operational efficiency is limited and only incremental changes can be achieved through optimization once the type of equipment is chosen. This is mainly due to the many tasks that have to be performed within the stirred vessel during crystallization. Important tasks are supersaturation generation, crystal nucleation, crystal growth, secondary nucleation, and classification, all subprocesses that are optimally executed in a specific conditional and compositional operating window. These operational windows often do not overlap for optimal operational efficiency and product quality resulting in an optimized industrial crystallizer but not in an optimized crystallization process.

Therefore, nowadays one approach within industrial crystallizer design research is based on the optimization of the different subprocesses (task-based design [70]). The optimization research of the different tasks will in future lead to a toolbox of functional process building blocks for a specific crystallization task. Furthermore, these functional building blocks for different crystallization tasks can be designed into a single crystallization process or even an innovative crystallizer design especially optimized for a specific compound.

Using this task based design approach, it is investigated how to come to large crystal sizes from a crystallization process. A solution lies in having dedicated a growth compartment in the crystallizer of the future in which crystal primary and secondary nucleation are prevented. A promising candidate for a growth compartment is an airlift crystallizer [71], which uses air bubbles rather than a stirrer to cause fluid dynamics. The mild fluid dynamics cause secondary nucleation to be almost absent in the dedicated growth compartment, even for large crystal sizes.

The task supersaturation generation can, for instance, be isolated by using a membrane unit to remove solvent in a recycle loop [72]. In a state of the art evaporative crystallizer, the surface area available for evaporation is limited which also limits the rate of supersaturation generation. Evaporative crystallization processes consume a lot of energy since the heat of evaporation should be provided. To prevent scaling through crystallization, the solvent removal can take place at a higher temperature at which the solubility exceeds the concentration and thus the solution is undersaturated. Cooling down the concentrated solution creates supersaturation with which the crystal growth task can be performed.

Crystal nucleation is possibly the key process to control for good control of industrial crystallization processes. Over the years, many investigators studied possibilities to control crystal nucleation among others by providing structure (solvent [24,25], template surfaces [73]) and energy (laser light [74,75], electric fields [34], ultrasound [37]). Often, a good optimization starts with having a sound and rigorous fundamental understanding of the subprocess investigated.

Another approach to come to well-controlled product quality is by using continuous rather than batch crystallization. Continuous industrial crystallization processes (Figure 32.1) for bulk chemicals such as salt and sugar have already existed for a long time [11,17,76]. Currently, batch crystallization processes are still the preferred process configuration in the pharmaceutical industry. Batch crystallization processes are easily implemented and maintained while they produce relatively large crystals if performed well. Although batch crystallization processes seem simple, the underlying process control is highly complex. This can lead to inconsistent product specifications and batch-to-batch variations [77] as well as to problems in downstream processing and formulation. Milling of a crystalline product is, therefore, a common unit operation in the pharmaceutical industry.

Continuous crystallization would lead to improved manufacture in the chemical and pharmaceutical industry through more efficient use of reagents, solvents, energy, and space while minimizing waste production and crystallizer downtime and maximizing yield. Other advantages mentioned for continuous processes are shorter downtimes, fewer scale-up issues, better control potential for optimal process conditions, improved process safety, and economy, good reproducibility of results and smaller equipment size, which reduce capital and operating costs [78,79]. Severe scale-up problems may be prevented since pharmaceutical quantities can be achieved on benchtop scale. However, sometimes encrustation, slow achievement of steady state, and operational instability are issues to be solved for continuous crystallization processes.

32.6.1 Continuous Crystallization

Current continuous crystallization research focuses on three different process configurations. Historically, the mixed suspension mixed product removal (MSMPR) crystallizer [47] already is well known, especially for precipitation and antisolvent crystallization processes. In an MSMPR crystallizer, a feed stream is continuously fed to the crystallizer vessel and mixed with the already present suspension. An action is required to generate supersaturation, which can be done by solvent evaporation, solution cooling, antisolvent addition or by the addition of reagents that result in a low soluble reaction product. The generated supersaturation causes crystal nucleation, growth, and other subprocesses to occur in the suspension. Also, continuously a suspension stream is leaving the MSMPR crystallizer in which a variety of crystal sizes will be present if no action is taken to selectively remove crystals with the suspension stream. After a start-up period (usually taken as a substantial number of residence times), the suspension composition reaches the stationary state and, in principle, the obtained product quality should be stable.

Even slow growing crystals that need long residence times in the crystallizer to achieve the preferred size can be produced in such MSMPR crystallizers using a single process step. It appears to be relatively easy to switch from batch to continuous operation by applying MSMPR crystallizers.

A way to increase yield is to introduce a recycle stream. After filtering the suspension stream one is left with a solution, which still contains a substantial amount of the

dissolved product if the solubility of the product is relatively high. This solution can be combined with the feed stream in order to remove the remaining product. When using antisolvent crystallization or cooling crystallization, however, an action is required to respectively remove the antisolvent or concentrate the solution so that still a supersaturation can be achieved upon feeding the combined feed and recycle to the MSMPR crystallizer.

Another way to boost yield while increasing the product size is to connect several MSMPR crystallizers in a cascade [80]. In the subsequent crystallizers, the product then is grown to larger sizes. As an example, Figure 32.16 show a cascade of three continuous MSMPR cooling crystallizers with a recycle. Apart from cooling crystallization, also evaporative crystallization, antisolvent crystallization, and precipitation can be performed using MSMPR cascades.

Connecting a large number of continuously operating MSMPR crystallizers approaches a plug flow to some extent [77]. In principle, a plug flow (PF) crystallizer is a long tube to grow out the crystals that nucleate inside the tube. In a PF crystallizer, narrow residence time distributions and narrow crystal size distributions can be achieved if it is operated in true plug flow. For true plug flow conditions, turbulence is required, and that can only be achieved at high flow rates. This means that in order to achieve long residence times for large crystals, long plug flow tubes are needed. Therefore, a PF crystallizer is less suited for slow-growing crystals. Also due to the large amount of crystallizer surface present in the small diameter tube, scaling and clogging of the tube can be a severe issue [78].

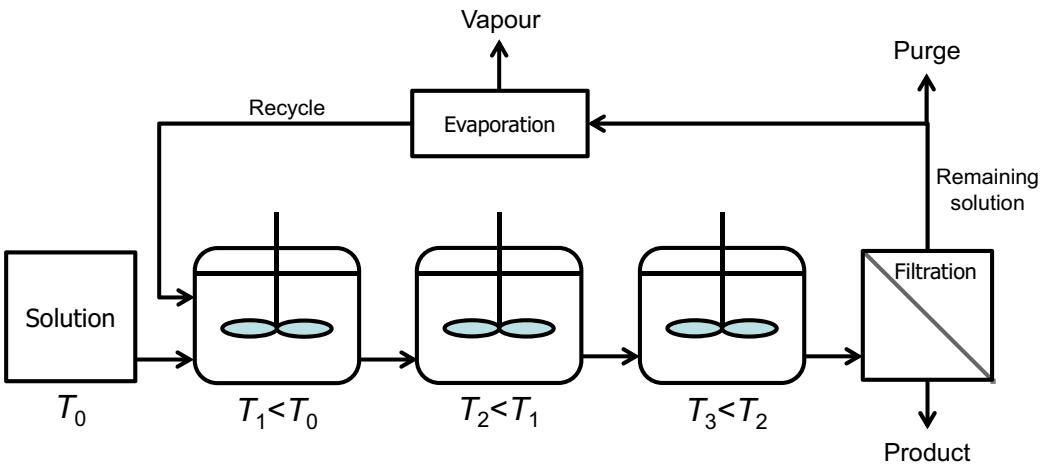

FIGURE 32.16 A cascade of three continuous MSMPR cooling crystallizers in series. Each subsequent crystallizer operates at a lower temperature to enforce a driving force for crystallization in order to increase the suspension density through nucleation and growth. The filtration step continuously separates the crystal product from the remaining solution. To increase the yield, the remaining solution is recycled back into the process after a concentration step through evaporation. A purge stream enables impurities to leave the system. *Adapted from Ref. [80].*

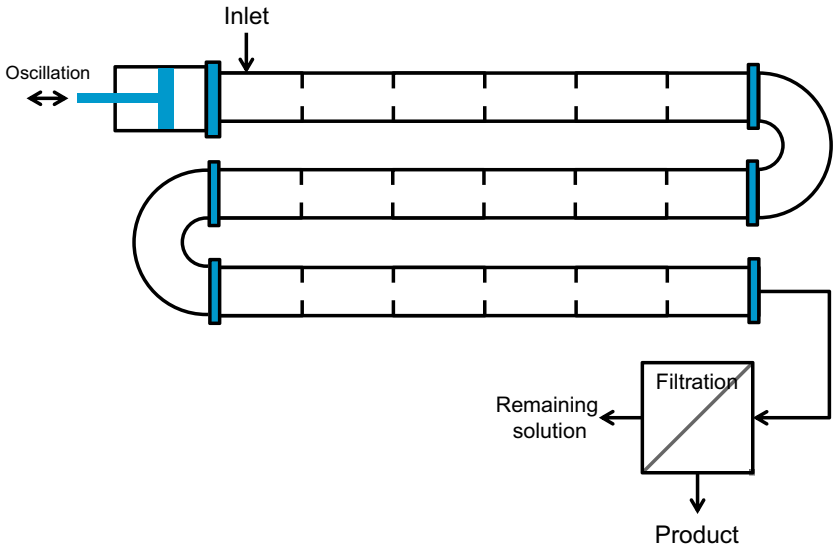

FIGURE 32.17 An oscillatory baffled crystallizer is a tubular crystallizer with periodically spaced orifice baffles. An oscillation is superimposed on the net flow for improved mixing and mass transfer. A driving force for crystallization can be imposed by, for instance, a temperature profile along the length of the tube. The filtration step continuously separates the crystal product from the remaining solution. The remaining solution can be recycled back into the process. *Adapted from Ref. [77].*

In an oscillatory baffled (OB) crystallizer [77], a tubular crystallizer is equipped with periodically spaced orifice baffles (Figure 32.17). An oscillatory flow motion is superimposed on the net flow through the tube. This gives improved mixing and mass transfer compared to the PF crystallizer at lower flow rates. In both a PF and OB crystallizer, the driving force can be controlled through the cooling profile imposed along the length of the tube. Also, solvent or other components can be added at inlets along the length of the tube in order to create the driving force.

32.6.2 Batch Crystallization

During a batch crystallization process, the process conditions change so that the supersaturation needed to grow the crystals is maintained. For instance, during a batch cooling crystallization process the temperature is decreased gradually in order to constantly increase the supersaturation which in turn is constantly reduced by crystal growth. Also, the other crystallization techniques can be performed batch-wise.

Seeding is a way to prevent primary nucleation at the start of a batch crystallization process. In a slightly supersaturated solution within the metastable zone where no nucleation occurs, seeds are added in order to grow them out. The generated supersaturation during the batch is only used for growth and because of the known amount and size of the seeds, the final product size can be controlled if agglomeration and secondary nucleation of the growing seed crystals can be prevented. The crystal size

distribution of the final product depends on the nature of the seeds introduced into the process [11,81–83].

If it is assumed that nucleation and agglomeration do not occur after seeding, the number of crystals remains constant during the batch crystallization. Then it is possible, through the number of crystals, to relate the seed mass M_s to the mass M_p produced during the batch crystallization [11]:

$$M_s = M_p \frac{L_s^3}{L_p^3 - L_s^3} \tag{32.14}$$

where L_s and L_p are seed and product size, respectively. This then can be used to determine the seed mass M_s needed to obtain a certain product size L_p during seeded batch crystallization. Due to the power of three in Eqn (32.14) the seed mass can be very small while still a substantial product size L_s can be achieved. If the seed size $L_s = 10$ μm and the required product size is $L_p = 100$ μm, the seed mass to be used is around 0.1% of the produced mass.

The seed quality depends to some extent on the origin of the seed crystals and how the seeds are added. Fines in the seeds and seed surface irregularities and imperfections can be removed by suspending the seeds in a slightly undersaturated solution and adding them as a suspension rather than a dry powder. This increases the control over the final product quality.

If the metastable zone width is small in batch cooling crystallization, primary nucleation already occurs only a few degrees below the saturation temperature. The temperature region for seeding is relatively small, and seeds could be added too early causing dissolution of the seeds or too late, after primary nucleation already occurred. In both cases, control over product quality is lost. Usually seeding is done at moderate supersaturation entering not more than 30–40% into the metastable zone.

The crystal growth rate determines the batch time since the seeds have to grow out from the seed size L_s to the product size L_p. For instance with a growth rate $R_{hkl} = 10^{-8}$ m/s, the time to grow the seeds from $L_s = 10$ to $L_p = 300$ μm is then estimated to be 4 h. Of course, the supersaturation available for growth can be adjusted through the cooling rate in order to speed up the process.

Three types of temperature profiles for cooling are commonly used in seeded batch cooling crystallization: natural cooling, linear cooling, and parabolic cooling [84–90]. The type of temperature profile has a significant impact upon the resulting crystal quality. During the batch, the crystal size increases and more crystal surface becomes available to consume the supersaturation. Therefore, the crystallizing system can handle larger cooling rates toward the end of the batch. As the crystal surface area is quadratically related to the crystal size, the temperature should, ideally, follow a parabolic function using a slow cooling rate at the start and higher cooling rates toward the end of the batch [11]. When properly controlled, a parabolic temperature profile results in a constant supersaturation and a constant crystal growth rate throughout the duration of the batch process (Figure 32.18), which usually is related to a good crystal quality.

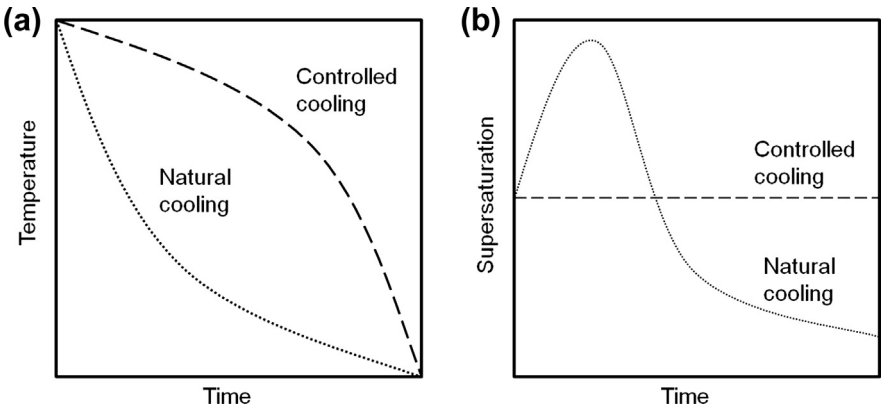

FIGURE 32.18 Temperature profiles (a) and resulting supersaturation profiles (b) for natural and controlled cooling in batch crystallization. *Adapted from Ref. [92].*

The linear and natural cooling profile both have a relatively fast cooling rate in the initial stages of the batch crystallization process. When the cooling rate is too fast during the initial stages of a seeded batch cooling crystallization, the seed crystals cannot consume the generated supersaturation sufficiently fast. Consequently, the supersaturation builds up to a point indicated in Figure 32.18 that extensive secondary nucleation can proceed. At that point, control is lost over the number of crystals and thus over the resulting product quality. If the attrition propensity of a compound is high then secondary nucleation might occur already at relatively low cooling rates, especially if the growth rate is relatively slow [91].

Agglomeration is the aggregation and intergrowth of crystals during crystallization. When agglomeration occurs during the batch, the number of particles in the suspension will decrease. The agglomeration rate depends on the number of crystal–crystal collisions, the growth rate and the agglomeration tendency. If the agglomeration tendency of a compound is high gently mixing and low supersaturations during crystallization might prevent severe agglomeration.

32.7 Ensuring Product Quality in the Future

Industrial crystallization (Figure 32.19) is a subset of processes of primary nucleation, crystal growth, secondary nucleation, and agglomeration. These processes are steered by the solution properties, fluid dynamics, and the prevailing supersaturation. The interplay between the different subprocesses and the process conditions determines the product quality defined from the kind of material produced (form), crystal size distribution, crystal shape, and purity.

Nowadays there are a number of inline process analytical tools [13] available to monitor crystallization characteristics. Raman spectroscopy [93] is a tool that can make a distinction between different forms in the suspension. Sometimes, in parallel the

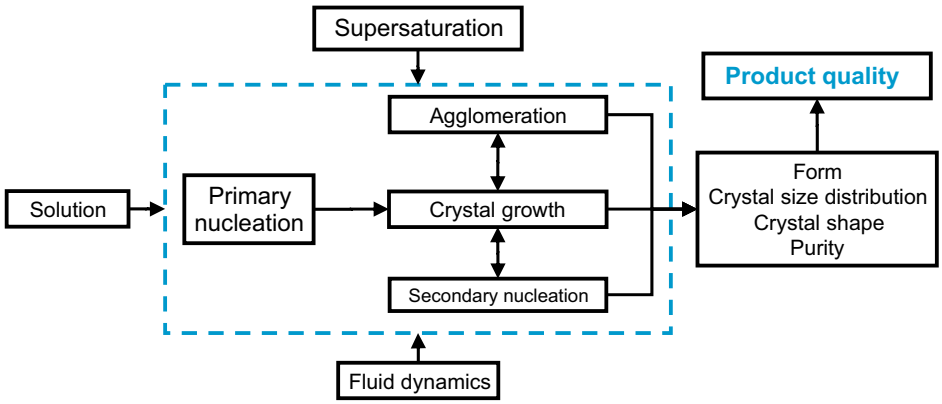

FIGURE 32.19 The crystal product quality is determined by the form, CSD, shape, and purity of the crystalline phase. This in turn is determined by the subprocesses of crystallization: primary nucleation, crystal growth, agglomeration, and secondary nucleation. The subprocesses in turn are determined by the solution, prevailing supersaturation, and fluid dynamic conditions.

solution concentration can be determined as well [94]. Other tools are infrared spectroscopy, particles size, and cord length measurement techniques, conductivity, sound velocity turbidity, and online particle tracking by laser light [13].

These process analytical tools enable process control [95]. For instance, dynamic control over the CSD in batch cooling crystallization processes can be obtained by using an in situ cord length measurement technique [96]. Unintended secondary nucleation outbursts can be detected and with controlled heating combined with an accurate process model these secondary nuclei can be dissolved again. In order to come to true process control, the signal of the process analytical tools should be translated into a process action that has a very specific effect. This means that fundamental understanding of the subprocesses is needed to feed into rigorous process models that enable the accurate prediction of how the system responds to process actions such as temperature profiles.

New active pharmaceutical ingredients show an increasingly larger molecular weight indicating that product molecules become larger while containing more functional groups. This trend toward more complex molecules, but also to more complex and multicomponent product materials, will surely proceed into the future.

A crystalline product has to fulfil certain specifications (e.g., color, stability) that are related to the product quality aspects defined in this chapter: form, size, shape, and purity. Relations between product quality aspects, process conditions, and the molecular components in the product continue to be discovered and understood. However, the resulting product quality is still difficult if not impossible to predict a priori.

One important reason for this is that the relation between the crystallizing molecules and the crystal structure is still not well understood. It is, therefore, still not possible to

reliably know whether specific stable and metastable multicomponent crystal exists. Pushed by demands from the pharmaceutical industry and the world of crystal engineering, crystal structure prediction methods did make a giant leap forward in the last few years [97,98]. At the same time, preparation methods and thermodynamic insight in multicomponent crystals lifted off by discoveries in, for instance, the co–crystal research field [15]. However, an accurate prediction of phase diagrams including multicomponent effects is still not possible. In coming years, the current knowledge should be enlarged and combined into an on-demand joint simulation and experimental approach for the discovery and use of such kind of multicomponent crystals.

Another reason is the inability to predict size, shape, and purity of a crystalline product from an industrial crystallization without experimental information. This predictability is, for instance, limited by the level of understanding of the key process of industrial crystallization, and crystal nucleation [23]. Predictions of nucleation rates with current theories are still orders of magnitude off from those measured in experiments. However, several new measurement methods became available the last few years. Also, newly developed analytical tools can be used to capture the initial stages of crystal nucleation. Molecular simulations, furthermore, become more and more powerful and can handle realistic nucleating systems. This means that the coming years interesting developments in this field can be expected.

Design, operation, and control of large industrial crystallization processes are extremely complex and challenging due to the determining molecular processes that make that all crystalline compounds show different crystallization behavior. The increasing complexity and size of the product components in the future implies that the complexity of the underlying processes will increase as well. At the same time, process technology nowadays strives to sustainable processing which puts limits to waste production, energy, and raw materials. All this brings new separation and particulate challenges also for industrial crystallization processes. The design challenges will be tackled in the future, for instance, by the task-based design approaches mentioned in the section on crystallization process configurations. Another way to overcome many of the problems is to develop continuous crystallization processes.

Increased complexity can also lead to opportunities. For instance, the combination of a racemization reaction and grinding of a conglomerate system in Viedma ripening leads to an enantiopure crystalline product [99]. In other instances, co-crystallization was proposed as a separation technology, for instance, to remove a small concentration of the product from a complex fermentation broth [100]. The use of co-crystals rather than pure component crystals enabled the in situ product removal at much lower concentrations.

The authors hope this chapter is convincing in showing that the solution to future challenges has to be found in a fundamental understanding of the crystallization subprocesses such as crystal nucleation and growth. This fundamental understanding in turn results in the identification of innovative, integrated, and intensified crystallization processes and equipment.

References

[1] Henley EJ, Seader JD, Roper DK. Separation process principles, international student version. 3rd ed. New Jersey: John Wiley; 2011.

[2] de Haan A, Bosch H. Industrial separation processes: Fundamentals. Berlin: De Gruyter; 2013.

[3] Davey RJ, Garside J. From molecules to crystallizers. New York (USA): Oxford University Press Inc.; 2000.

[4] Bernstein J. Polymorphism in molecular crystals, IUCr monographs on crystallography, 14. Oxford (GB): Oxford Science Publishers; 2002.

[5] Lee AY, Erdemir D, Myerson AS. Annu Rev Chem Biomol Eng 2011;2:259.

[6] Fleischman SG, Kuduva SS, McMahon JA, Moulton B, Bailey Walsh RD, Rodrıguez-Hornedo N, et al. Cryst Growth Des 2003;3:909.

[7] Aitipamula S, Banerjee R, Bansal AK, Biradha K, Cheney ML, Choudhury AR, et al. Cryst Growth Des 2012;12:2147.

[8] Hartman P. In: Hartman P, editor. Crystal growth – an introduction. Amsterdam: North-Holland Publ.; 1973. p. 367.

[9] Bennema P. Growth and morphology of crystals: integration of theories of roughening and Hartman-Perdok theory. In: Hurle DTJ, editor. Handbook of crystal growth, 1a. Amsterdam: Elsevier; 1993 [chapter 7].

[10] Sunagawa I. Crystals — growth, morphology and perfection. Cambridge (UK): Cambridge University Press; 2005.

[11] Mullin JW. Crystallization. 4th ed. Oxford (UK): Butterworth-Heinemann; 2001.

[12] Rhodes M. Introduction to particle technology. 2nd ed. UK: Wiley; 2008.

[13] Chianese A, Kramer HJM. Industrial crystallization process monitoring and control. Weinheim: Wiley-VCH Verlag GmbH & Co. KGaA; 2012.

[14] Alsenz J, Kansy M. Adv Drug Delivery Rev 2007;59:546.

[15] ter Horst JH, Deij MA, Cains PW. Cryst Growth Des 2009;9(3):1531.

[16] Nordström FL, Rasmuson ÅC. Eur J Pharm Sci 2009;36:330.

[17] Myerson AS. Handbook of industrial crystallization. Oxford (UK): Butterworth-Heinemann; 2002.

[18] Mersmann S. Crystallization technology handbook. New York (USA): Marcel Dekker, Inc.; 2001.

[19] Westphal G, Kristen G, Wegener W, Ambatiello P, Geyer H, Epron B, et al. Sodium chloride, Ulmann's encyclopedia of industrial chemistry, vol. 33. Weinheim: Wiley-VCH Verlag GmbH; 2012. 319–365.

[20] Schiweck H, Clarke M, Pollach G. Sugar, Ulmann's encyclopedia of industrial chemistry, vol. 34. Weinheim: Wiley-VCH Verlag GmbH; 2012. 557–628.

[21] Kramer HJM, Bermingham SK, van Rosmalen GM. J Cryst Growth 1999;198:729.

[22] Kashchiev D. Nucleation: basic theory with applications. Oxford: Butterworth-Heinemann; 2000.

[23] Davey RJ, Schroeder SLM, ter Horst JH. Angew Chem 2013;52:2166.

[24] Davey RJ, Allen K, Blagden N, Cross WI, Lieberman HF, Quayle MJ, et al. CrystEngComm 2002; 4:257.

[25] Kulkarni SA, McGarrity ES, Meekes H, ter Horst JH. ChemCommun 2012;48:4983.

[26] Galkin O, Vekilov PG. J Phys Chem B 1999;103:10965.

[27] Ildefonso M, Candoni N, Veesler S. Cryst Growth Des 2011;11:1527.

[28] Jiang S, ter Horst JH. Cryst Growth Des 2011;11:256.

[29] Nordström FL, Svärd M, Rasmuson ÅC. CrystEngComm 2013;15:7285.

[30] Kashchiev D, van Rosmalen GM. Cryst Res Technol 2003;38:555.

[31] Kulkarni SA, Kadam SS, Meekes H, Stankiewicz AI, ter Horst JH. Cryst Growth Des 2013;13(6):2435.

[32] Zaccaro J, Matic J, Myerson AS, Garetz BA. Cryst Growth Des 2001;1(1):5.

[33] Soare A, Dijkink R, Rodriguez Pascual M, Sun C, Cains PW, Lohse D, et al. Cryst Growth Des 2011; 11(6):2311.

[34] Hammadi Z, Astier JP, Morin R, Veesler S. Cryst Growth Des 2009;9(8):3346.

[35] Sazaki G, Yoshida E, Komatsu H, Nakada T, Miyashita S, Watanabe K. J Cryst Growth 1997; 173(1–2):231.

[36] Kallies B, Ulrich J, König A. Chem Eng Res Des 1997;75(2):142.

[37] Virone C, Kramer HJM, van Rosmalen GM, Stoop AH, Bakker TW. J Cryst Growth 2006;294(1):9.

[38] Vekilov PG. Cryst Growth Des 2004;4(4):671.

[39] Erdemir D, Lee AY, Myerson AS. Acc Chem Res 2009;42(5):621.

[40] ten Wolde PR, Frenkel D. Science 1997;277:1975.

[41] Gebauer D, Coelfen H. Nano Today 2011;6:564.

[42] Baumgartner J, Dey A, Bomans PHH, Le Coadou C, Fratzl P, Sommerdijk NAJM, et al. Nat Mater 2013;12(4):310.

[43] Kadam SS, Kulkarni SA, Coloma Ribera R, Stankiewicz AI, ter Horst JH, Kramer HJM. Chem Eng Sci 2012;72:10.

[44] Kadam SS, Kramer HJM, ter Horst JH. Cryst Growth Des 2011;11:1271.

[45] Kondepudi DK, Kaufman RJ, Singh N. Science 1990;250:975.

[46] McBride JM, Carter RL. Angew Chem Int Ed Engl 1991;30:293.

[47] Randolph AD, Larson MA. Theory of particulate processes. New York: Academic Press; 1971.

[48] O'Meadhra R, Kramer HJM, Van Rosmalen GM. AIChE J 1996;42:973.

[49] Virone C, ter Horst JH, Kramer HJM, Jansens PJ. J Cryst Growth 2005;275:1–2. e1397.

[50] Gahn C, Mersmann A. Chem Eng Sci 1999;54(9):1273.

[51] Gahn C, Mersmann A. Chem Eng Sci 1999;54(9):1283.

[52] Mueansichai T, Flood AE, Stelzer T, Ulrich J. Cryst Res Technol 2013;48:38.

[53] van der Heijden AEDM, van der Eerden JP, van Rosmalen GM. Chem Eng Sci 1994;49(18):3103.

[54] Nienow AW, Conti R. Chem Eng Sci 1978;33:1077.

[55] Youngquist GR, Randolph AD. AIChE J 1972;18(2):421.

[56] Garside J, Rusli IT, Larson MA. AIChE J 1979;25(1):57.

[57] Matsuoka M, Garside J. Chem Eng Sci 1991;46(1):183–92.

[58] ter Horst JH, Bedeaux D, Kjelstrup S. J Chem Phys 2011;134:054703.

[59] Arkenbout GF. Melt crystallization technology. Western Hemisphere: Technomic Publishing Company; 1995.

[60] Ulrich J, Glade H. Melt crystallization: fundamentals, equipment and applications. Aachen: Shaker Verlag, GmbH; 2003.

[61] Söhnel O, Garside J. Precipitation: basic principles and industrial applications. Oxford: Butterworth-Heinemann Ltd.; 1992.

[62] Burton WK, Cabrera N, Frank FC. Philos Trans R Soc Lond 1951;A243:299.

[63] Ulrich J. Cryst Res Technol 1989;24:249.

[64] ter Horst JH, van Rosmalen GM, Geertman RM. Additives: molecular design. In: Encyclopedia of separation science. Academic Press; 2000. p. 931.

[65] Al Jibbouri S, Ulrich J. Cryst Res Technol 2004;39:540.

[66] Dowling R, Davey RJ, Curtis RA, Han G, Poornachary SK, Shan Chow P, et al. Chem Commun 2010; 46:5924.

[67] Addadi L, Berkovitch-Yellin Z, Domb N, Gati E, Lahav M, Leiserowitz L. Nature 1982;296:21.

[68] Alvarez AJ, Myerson AS. Cryst Growth Des 2010;5:2219.

[69] Variankaval N, Cote AS, Doherty MF. AIChE J 2008;54(7):1683.

[70] Menon AR, Pande AA, Kramer HJM, Jansens PJ, Grievink J. Ind Eng Chem Res 2007;46(12):3979.

[71] Soare A, Lakerveld R, van Royen J, Zocchi G, Stankiewicz AI, Kramer HJM. Ind Eng Chem Res 2012; 51(33):10895.

[72] Kuhn J, Lakerveld R, Kramer HJM, Grievink J, Jansens PJ. Ind Eng Chem Res 2009;48(11):5360.

[73] Aizenberg J, Black AJ, Garetz BA, Whitesides GM. Nature 1999;398(6727):495.

[74] Matic J, Sun X, Garetz BA, Myerson AS. Cryst Growth Des 2005;5(4):1565.

[75] Okutsu T, Furuta K, Terao M, Hiratsuka H, Yamano A, Ferté N, et al. Cryst Growth Des 2005; 5(4):1393.

[76] Hofmann G, Melches C. Continuous crystallization [chapter 11]. In: Beckmann W, editor. Crystallization: basic concepts and industrial applications. Weinheim: Wiley-VCH Verlag GmbH & Co. KGaA; 2013.

[77] Lawton S, Steele G, Shering P, Zhao L, Laird I, Ni Xiong-Wei. Org Proc Res Dev 2009;13(6):1357.

[78] Eder RJP, Schmitt EK, Grill J, Radl S, Gruber-Woelfler H, Khinast JG. Cryst Res Technol 2011;46:227.

[79] Chen J, Sarma B, Evans JMB, Myerson AS. Cryst Growth Des 2011;11(4):887.

[80] Alvarez Alejandro J, Singh Aniruddh, Myerson Allan S. Cryst Growth Des 2011;11(10):4392.

[81] Kubota N. Powder Technol 2001;121(1):31.

[82] Kubota N, Doki N, Ito M, Sasaki S, Yokota M. J Chem Eng Jpn 2002;35(11):1078.

[83] Zhang GGZ, Grant DJW. Cryst Growth Des 2005;5(1):319.

[84] Hu Q, Rohani S, Wang DX, Jutan A. Powder Technol 2005;156(2–3):170.

[85] Costa CBB, Maciel Filho R. Chem Eng Process 2005;44:727.

[86] Mohamed HA, Abu-Jdayil B, Al Khateeb M. Chem Eng Process 2002;41:297.

[87] Miller SM, Rawlings JB. AIChE J 1994;40(8):1312.

[88] Nyvlt J. Chem Eng Process 1988;24:217.

[89] Mullin JW, Nyvlt J. Chem Eng Sci 1971;26:369.

[90] Jones AG. Chem Eng Sci 1974;29:1075.

[91] Ulrich J, Jones MJ. Seeding technique in batch crystallization. In: Chianese A, Kramer HJM, editors. Industrial crystallization process monitoring and control. Weinheim: Wiley-VCH Verlag & Co. KGaA; 2012. p. 127.

[92] Omar W, Zur Bestimmung von kristallisationskinetiken auch unter der einwirkung von additiven mittels Ultraschallmeßtechnik, Dissertation, Universität Bremen, 1999.

[93] Ono T, ter Horst JH, Jansens PJ. Cryst Growth Des 2004;4(3):465.

[94] Cornel J, Lindenberg C, Mazzotti M. Ind Eng Chem Res 2008;47(14):4870.

[95] Barrett P, Smith B, Worlitschek J, Bracken V, O'Sullivan B, O'Grady D. Org Proc Res Dev 2005; 9(3):348.

[96] Nagy ZK, Aamir E, Rielly CD. Cryst Growth Des 2011;11(6):2205.

[97] Day GM, Cooper TG, Cruz-Cabeza AJ, Hejczyk KE, Ammon HL, Boerrigter SXM, et al. Acta Crystallogr B 2009;65:107.

[98] Bardwell DA, Adjiman CS, Arnautova YA, Bartashevich E, Boerrigter SXM, Braun DE, et al. Acta Crystallogr B 2011;67:535.

[99] Noorduin WL, van der Asdonk P, Bode AAC, Meekes H, van Enckevort WJP, Vlieg E, et al. Org Proc Res Dev 2010;14:508.

[100] Urbanus J, Roelands CPM, Mazurek J, Verdoes D, ter Horst JH. CrystEngComm 2011;13:2817.

Index

Note: Page numbers followed by “b”, “f” and “t” indicate boxes, figures and tables respectively

A
A-center, 83
A-form nitrogen, 679
A-swirl defect, 88
A+ wafers, 398–399
A++ wafers, 398–399
A3+ wafers, 399–400
A4+ wafers, 399–400
Accelerated crucible rotation technique (ACRT), 188, 344–345, 469, 497–498, 821, 952–953, 955, 1011, 1028, 1220
  on acceleration/deceleration, 955–956
  Bridgman/ACRT growth, 961f
  in $CdTe/Cd_{1-x}Zn_xTe$ growth, 964–967
  CMT growth, 959–960
  in group-IV growth, 967–968
  high-x CMT material, 960–964
  in material system, 968
  parameters, 959t
  rotation sequence, 957f
Acidic mineralizers, 595–596
ACRT. *See* Accelerated crucible rotation technique
Active pharmaceutical ingredients (API), 1337
Additives, 1215
Advanced Photon Source (APS), 702
Advection, 803
AE model. *See* Atomic emission model
Aerogels, 1296–1301
AFM. *See* Atomic force microscopy
Agarose gels, 1295
Agglomeration, 1343
AHP method. *See* Axial heat processing method
Alcothermal process, 536–537
AlN. *See* Aluminum nitride
$3Al_2O_3$ $2SiO_2$. *See* Mullite
Alternating magnetic field (AMF), 68, 389, 928, 932–934
Aluminosilicates, 427–428
Aluminum berlinites, 556–558
Aluminum nitride (AlN), 595, 622–623. *See also* Crystal growth
  bulk crystal, 623
    growth setups, 624f
    single crystals, 635f
  growth on SiC seeds, 634–635
  powder, 624–625
  spiral growth, 631
  structural defects, 638–640
AMF. *See* Alternating magnetic field; Automatic mirror furnace
Ammonium chloride (NH_4Cl), 648
Ammono-acidic mineralizer. *See* Acidic mineralizers
Ammono-basic mineralizer. *See* Basic mineralizer
Ammonothermal
  process, 536–537
  solution chemistry, 602–604
Ammonothermal growth techniques. *See also* High nitrogen pressure solution growth method (HNPS method)
  historical development, 595–600
  method, 600–602
  properties, 610–612
  prospects and future developments, 613
  solubility in, 604–607
Angular vibration technique (AVT), 344–345
Anisotropic growth rate, 1249
Annealing process, 1269
Annihilation, 1113
Antimonides, 121, 347
API. *See* Active pharmaceutical ingredients

APS. *See* Advanced Photon Source
Aquamarine, 562–563
Arcing, 252–253
Arrhenius-type relation, 1189
Arsenides, 119
Artificially grown crystals, 716
Astrocrystallization, 37
Atomic emission model (AE model), 185–187
Atomic force microscopy (AFM), 1207–1208, 1245
ATR. *See* Attenuated total reflection
Attenuated total reflection (ATR), 703
Autoclaves, 549t
Automatic mirror furnace (AMF), 493
AVC. *See* Axial vibrational control
AVC-assisted
  floating zone method, 979
  zone melting method, 979–980
AVC-assisted Bridgman technique (AVC-Br technique), 973, 977–978, 978f
AVC-assisted Czochralski technique (AVC-Cz technique), 973
  Cz-I method, 974, 976f
  Cz-II method, 977
Avogadro constant, 259–260
Avogadro crystal, 259–260
Avrami formulation, 17
AVT. *See* Angular vibration technique
Axial heat processing method (AHP method), 343
Axial magnetic fields, 68, 914–919
Axial vibrational control (AVC), 344–345, 952–953, 968–969
  on crystal growth, 971–980
  crystal materials, 980
  physical nature, 969–971
Axisymmetric formulations, 769–770

B

Ba-Cu-O system, 1234–1235
$Ba_2Cu_3O_{7-\delta}$ material (RE-123 material), 1231
Band approximation, 814
Barium metaborate (BBO), 188–192
Baroclinic instability, 862
BARS equipment, 677, 677f
Basic mineralizer, 595–596
Batch crystallization process, 1339, 1341–1343
Batch reactors, 539, 551
Bayer's process, 538–539
BBO. *See* Barium metaborate
BC. *See* Boundary condition
Bell-curve furnace profile, 829–832
Belt-type apparatus, 675, 676f. *See also* Multi-anvil apparatus; Toroid-type apparatus
BEM. *See* Boundary element method
BEN. *See* Bias-enhanced nucleation
Bénard cells, 119–120
β angle, 445
β-BaB_2O_4. *See* Barium metaborate (BBO)
β-Ga_2O_3, 212–218
BGO. *See* Bismuth germinate
Bi-Sr-Ca-Cu-O system (BSCCO system), 1231
$Bi_4Ge_3O_{12}$. *See* Bismuth germinate (BGO)
Bias-enhanced nucleation (BEN), 694
BiB_3O_6. *See* Bismuth triborate (BiBO)
BiBO. *See* Bismuth triborate
Binder, 429
Biologically induced crystallization, 11
Biomineralization, 11
Biominerals, 11
Bismuth germinate (BGO), 152, 154–157
Bismuth triborate (BiBO), 201–202
Boiling solutions, 1196
Boron, 70, 684
  Boron-doped type IIb diamond, 684–685
  influence of boron impurities, 685
  oxide, 347
Boule growth approach, 654
Boundary condition (BC), 264, 803–805
Boundary element method (BEM), 263
Boundary layer, 864–865
BPS theory. *See* Burton–Prime–Slichter theory
BR method. *See* Bridgman method
Bridgman method (BR method), 416–417, 796, 1050, 1074, 1147–1148
Bridgman-Stockbarger methods (BS methods), 137–138
Bright meniscus ring detection, 1159–1160
"Bright ring", 1159–1160

Brownian simulation, 1294
BS methods. *See* Bridgman-Stockbarger methods
BSCCO system. *See* Bi-Sr-Ca-Cu-O system
Bubbles. *See* Microvoids
Bulk borate NLO crystal growth
  BiBO, 201–202
  KBBF, 199–201
  LiB_3O_5 family of crystals, 192
  low-temperature phase of barium metaborate, 188–192
Bulk growth, 654
  activities, 952
  crystal growth methods, 1239–1243
  crystalline material, 794
Bulk single crystals, 1050
  dislocations in, 1074–1088
  growth process, 1079–1081
  thermal stress in, 1050
    calculating methodology, 1051–1060
    cracking by, 1069–1073
    thermal stress analysis examples, 1060–1069
Bulk spiral formation mechanism, 180–187
Bunching. *See* Dislocation clustering
Buoyancy convection, 62, 119, 881–882
Burgers vector analysis, 358
Burton–Prime–Slichter theory (BPS theory), 916, 997, 1012–1014

C

Cabrera–Vermilyea model, 1200–1201, 1208
Cadmium mercury telluride (CMT), 955, 959–960
  high-x CMT material, 960–964
Cadmium telluride (CdTe), 820
Cadmium tungstate (CWO), 152, 157–158
Cadmium zinc telluride (CZT), 820
  bell-curve furnace profile, 829–832
  Bridgman growth, 820
  crystals, 964–967
  experimental validation, 828–829
  heat transfer analysis, 822–828
  motivation, 820–822
CaF_2 crystal. *See* Calcium fluoride crystal
CAFÉ numerical method. *See* Cellular automaton finite element numerical method
Calcite, 560–561
Calcium carbonate ($CaCO_3$), 139–140
Calcium fluoride crystal (CaF_2 crystal), 137–138. *See also* Large fluoride crystals
  annealing process, 146
  double-crucible system, 142–146
  growth
    apparatus, 140
    technique, 138–139
  starting materials, 139–140
  technical challenges, 140–142
Caloric fluid, 799
Capillarity for crystal grower
  catching and horizontal conditions, 768
  growth angle, 764–766
  Marangoni convection, 762–764
  surface and cohesion energies, 761–762
  wetting angle, 766–767
  Young–Laplace equation, 764
Capillarity-driven processes, 760–761
Capillary convection, 63
Carbon, 81, 866–867
  conversion methods, 673–674
  doping mechanism, 515–519
  P-T phase diagram, 673f
  particles, 640
  precipitates, 381–382
Carbon-bonded carbon fiber (CBCF), 633
Carbonate rocks, 11
Carbonate-silicate systems, 688–689
Carbonothermal process, 536–537
Carousel magnetic fields (CMF), 389
Catching conditions, 768
Cathodoluminescence (CL), 651
CBCF. *See* Carbon-bonded carbon fiber
CBO. *See* Cesium triborate
CC model. *See* Combined convection model
CCD. *See* Charge-coupled devices
CCz technique. *See* Continuous Czochralski technique
$Cd_{1-x}Zn_xTe$. *See* Cadmium zinc telluride (CZT)
CdTe. *See* Cadmium telluride

$CdWO_4$. *See* Cadmium tungstate (CWO)
Ce^{3+}-doped fluorides, 150–152
Cell patterning, 1114
Cellular automaton finite element numerical method (CAFÉ numerical method), 452–453
Centrifugal effects, 852–854
Centrifuge, 496
Ceramic rod preparation, 290–291
CERN. *See* European Organization for Nuclear Research
Cesium lithium borate (CLBO), 197–199, 1216–1217
Cesium triborate (CBO), 195–197
Charge-coupled devices (CCD), 857
Chechevitsa (lentil), 676
Chemical complexation reaction, 1281
Chemical decomplexation reaction, 1281
Chemical gels, 1297–1298
Chemical vapor deposition (CVD), 348, 673
  DC Arc-Jet, 695–696
  DC Plasma, 695
  diamond CVD process, 692f
  diamond specialties, 703–704
  hot filament, 695
  MPCVD, 696–698
  principles, 692–694
Chemical vapor transport (CVT), 213
Chemomechanical polishing process (CMP process), 749
Chirped-pulse amplification, 152
Chondrules, 37–38
CHPA. *See* Cubic high pressure apparatus
Chuck-less process, 748
CL. *See* Cathodoluminescence
Classical nucleation theory (CNT), 1327
CLBO. *See* Cesium lithium borate
Closed-loop control, 1145–1146
Clusters, 383–385
CMF. *See* Carousel magnetic fields; Cusp-shaped magnetic field
CMP process. *See* Chemomechanical polishing process
CMT. *See* Cadmium mercury telluride
CNT. *See* Classical nucleation theory
Co-crystals, 1319–1320
Coalescence growth technique, 527–531
Cochran–Levich solution, 997
C–O–H system, 690
Cohesion energies, 761–762
Coincidence site lattice (CSL), 379–380
Cold finger, 822–825
Cold pressing, 290–291
Cold traveling heater method (CTHM), 473–474
Colloidal silica, 429
Colored quartz crystals, 555–556
Columnar defective region, 651
Columnar grains, 419–420
Combined convection model (CC model), 998, 1016
Combined mass transfer coefficient, 1016–1018
Complex coordinated crystals, 565–566
Composition
  diagrams, 543–544
  zonation, 9–10
  zoning, 25–28
Conduction, 801
Conductive HNPS-MFS-GaN crystals, 589–593
Conical growth channel, 636
Constitutional supercooling, 300–301
Continuous crystallization, 1339–1341
Continuous Czochralski technique (CCz technique), 62–63, 73–74
Continuous-wave (cw), 703–704
Control system, 1145–1146
  control loop, 1146f
  crystal growth analysis and control, 1146–1147
  feed-forward controller, 1149–1150
  feedback controller, 1150–1153
  model-based control, 1163–1165
  reference trajectory generator, 1147
  state estimator, 1147–1148, 1148f
Controlled variables, 1145–1146
Convection, 388–389, 803, 1040–1042
  convection–diffusion equation, 1001
  convective flow, 58–69
  mass flux, 1006–1009

Convective heat and mass transfer, 1005
correlations for Nusselt numbers, 1009–1010
flow patterns in crystal growth, 1005–1006
melt convection classification, 1010–1012
phenomenological approach, 1009–1010
Convective transport
convective–diffusive transport, 854–855
diffusion transport *vs*., 1285–1295
Conventional control, 1167, 1175
Cooling crystallization, 1324
Cooling-down process, 1129
COP. *See* Crystal originated particles
Corundum (Al_2O_3), 428–429, 561–563
Counting method, 436–437
Coupled vibrational stirring (CVS), 344–345, 982–983
Crack-free thick HVPE-GaN layers, 652–653
Cracks, 302, 1069–1073
Critical Marangoni number, 882–884
Critical resolved shear stress (CRSS), 109–111
Critical Reynolds number (Re_c), 958t
Critical temperature (*Tc*), 1230
CRSS. *See* Critical resolved shear stress
Crucible(s), 348–349
configuration, 825–828
crystal growth drawbacks, 758–760
rotation, 64
rate, 64–65
Crucibleless techniques, 760–761
Crystal
anisotropy, 1050–1051, 1060–1062
defects, 356–365
enlargement, 634–636
morphology, 12, 1286–1287
nucleation, 1325–1326, 1326f, 1338
primary nucleation, 1327–1332
secondary nucleation, 1332–1333
self-association on, 1329f
perfection determination, 444–447
product quality, 1343–1345, 1344f
pulling, 1244
rotation, 64
shape, 1320–1321, 1336–1337
shoulder, 55–56
Crystal growth, 1333–1337. *See also* Aluminum nitride (AlN); Czochralski growth (Cz growth); Defect generation during crystal growth; Diamond crystal growth; Silicon carbide (SiC)
analysis and control, 1146–1147
case of giant crystals, 21–24
controlling factors, 1248–1251
deciphering geological information, 12–16
decoding
disequilibrium mineral patterns, 24–32
polycrystalline textures, 16–21
from deep earth to outer space, 36–39
early earth mineral growth, 32–35
flow patterns in, 1005–1006
geological scenarios for, 4–11
growth rate and surface growth mechanism, 13f
by high temperature dissociative sublimation
anisotropic growth, 630–631
considerations from growth theory, 627–628
crystal habit, 630–631
dissociative sublimation, 628–630
growth conditions, 625–627
rate-limiting species, 628–630
high temperature sublimation growth technology
crystal enlargement, 634–636
doping, 636–638
growth setup and process, 631–633
hot-zone materials, 633–634
seeded growth, 633–634
high-temperature solution growth, 1219–1223
low-temperature solution growth
mechanical impurities effect, 1206–1210
rates, 1199–1206
techniques, 1193–1196
Marangoni convection in, 886–904
mechanism, 1251–1263
origin of life, 32–35
primitive life detection, 32–35
process, 1145, 1286

Crystal growth (*Continued*)
control system, 1145–1153
Cz process, 1153–1165
detached Bridgman process, 1169–1173
FZ technique, 1174–1176
Kyropoulos process, 1176–1178, 1177f
VB process, 1165–1169
VGF process, 1165–1169
from solutions, 1186
high-temperature solution growth, 1210–1223
low-temperature solution growth, 1187–1210
Crystal originated particles (COP), 89
Crystal size distribution (CSD), 1321
Crystalline solid, 795
Crystallization, 24, 1186, 1197
building blocks, 846
Crystallographic orientation, 444–447
CSB_3O_5. *See* Cesium triborate (CBO)
CSD. *See* Crystal size distribution
CSL. *See* Coincidence site lattice
$CSLIB_6O_{10}$. *See* Cesium lithium borate (CLBO)
CTHM. *See* Cold traveling heater method
Cubic high pressure apparatus (CHPA), 678, 678f
Cubic single crystal
elastic constant matrix, 1052–1053, 1052f
thermal strain vector, 1058
Curie's symmetry principle, 954
Cusp-shaped magnetic field (CMF), 914, 923–927
CVD. *See* Chemical vapor deposition
CVS. *See* Coupled vibrational stirring
CVT. *See* Chemical vapor transport
cw. *See* Continuous-wave
CWO. *See* Cadmium tungstate
Cylindrical growth channel, 636
Czochralski growth (Cz growth), 46, 215–216, 849–850, 872–873, 910, 972–973, 998, 1029, 1050, 1074, 1144–1145, 1153
axial magnetic field, 914–917
CMF, 924–927
control objectives, 1153–1156
convective flow in Si melt, 61–66
conventional PID-based control, 1161–1163
crystal growth system, 886–892
economic aspects, 94–95
impact cycle time and costs, 96–97
special issues, 97–98
yield of dislocation-free Cz-grown crystals, 95–96
feed-forward control, 1160–1161
growth kinetics and interface shape, 59
heat and species transfer modeling, 66
heat transfer and growth rate, 59–60
industrial-like silicon Czochralski puller, 47f
intrinsic point defects and aggregates
calculation, 92–93
importance, 88–90
impact of impurities, 93–94
incorporation, 90–91
influence of crystal growth parameters, 91–92
magnetic fields, 67–69
with mixed convection, 1031–1034
principle, 47–48
procedure, 51–58
process characteristics, 1153–1156
RMF in, 929–930
segregation under steady forced convection, 1029–1030
of silicon crystals, 46
silicon Czochralski pulling apparatus setup, 48–51
state estimation, 1156–1160
TMF in, 936–937
transport and incorporation considerations, 69
constitutional supercooling, 75–76
segregation coefficient, 69–72
species distribution in crystal, 72–75
striations, 76–77
unintentional impurity incorporation, 79–81
transverse magnetic field, 920–922
Czochralski method (CZ method). *See* Czochralski growth (Cz growth)
CZT. *See* Cadmium zinc telluride

D
DAC devices. *See* Diamond anvil cell devices
Dai-ichi Kiden Corporation (KDN), 396–397
DAP. *See* Donor acceptor pair
DC Arc-Jet CVD, 695–696
DC Plasma CVD, 695
DDG. *See* Double-disk grinding
Dead supersaturation zone, 1199–1206
Decoding disequilibrium mineral patterns, 24–32
Decoding polycrystalline textures, 16–21
Decoration precipitates (DP), 363
Deep ultraviolet (DUV), 209–210
Defect generation during crystal growth, 1094
  defect-forming mechanism, 1094
  dislocations, 1105–1121
  faceting, 1130–1136
  foreign phase particles, 1125–1130
  grain boundaries, 1121–1125
  point defects, 1096–1104
  twinning, 1130–1136
Defect selective etching method (DSE method), 585
Defect-free silicon, 46–47, 67
DEG. *See* Diethylenglycole
Dendritic casting method, 392–397
"Denuded zone" technique, 82
Detached Bridgman process, 1169–1170, 1170f. *See also* Vertical Bridgman growth (VB growth)
  control objectives, 1170–1172
  model-based control, 1173
  PI-based control, 1172–1173
  process characteristics, 1170–1172
Detwinning, 1269–1270
DFT. *See* Direct film transfer
Diamond, 672. *See also* High pressure high temperature (HPHT)
  boron-doped type IIb, 684–685
  classification, 678–679
  nitrogen-containing type I, 679–682
  nitrogen-free type IIa, 683–684, 683f
Diamond anvil cell devices (DAC devices), 702
Diamond crystal growth. *See also* High pressure high temperature (HPHT)
  conversion methods, 673–674
  high pressure diamond synthesis and growth methods
    synthesis with metallic catalysts, 674
    TGG method, 675
  high pressure equipment, 675
    belt-type apparatus, 675, 676f
    high pressure cell, 678, 679f
    multi-anvil apparatus, 676–678
    toroid-type apparatus, 676, 677f
  high pressure growth
    boron-doped type IIb diamond, 684–685
    diamond classification, 678–679
    nitrogen-containing type I diamond, 679–682
    nitrogen-free type IIa diamond, 683–684, 683f
Diamond growth from gas phase, 691–692
  CVD principles, 692–694
  epitaxial growth and treatment
    doping, 701
    high speed growth, 698–699
    lift-off process, 699
    mosaic structures, 700
    postgrowth treatment, 700–701
  gas activation methods, 694–698
Dichroism, 234–235
Diethylenglycole (DEG), 719–720
Differential thermal analysis (DTA), 284
Differentiated weightmode, 1162
Diffusion, 846–848
  layer, 300–301
  mechanism, 1265–1268
  mode, 1198
  transport, 1285–1295
Diffusion-limited aggregation (DLA), 30
Dipole, 1113
Dipropylenglycole (DPG), 719–720
Direct film transfer (DFT), 745–746
Direct numerical simulation (DNS), 886–888
Directional crystallization, 585
Directional heat dissipation, 421
Directional solidification method (DS method), 374, 938–941, 998, 1242–1243

Directionally solidified castings (DS castings), 414. *See also* Single crystal castings (SC castings)
  ceramic shell molds for, 425–429, 431–434
  elements and wax model assemblies, 430–431
  investigation methods
    crystal perfection determination, 444–447
    crystallographic orientation, 444–447
    macro and microstructure, 436–442
    mechanical properties testing, 435–436
    porosity investigation, 442–444
  manufacturing methods, 415–418
  numerical modeling, 447
    analytical thermal analysis, 448–451
    nucleation and grain growth, 452–454
    temperature field, 451–452
  parameters for, 421–423
Disk-driven forced convection, 1018–1021
Dislocation(s), 173, 356–359, 383–385, 686–687, 1105
  annihilation, 1084–1085
  in bulk single crystals, 1074–1088
  clustering, 1117
  density, 357
    qualitative estimation, 1074–1075
    quantitative estimation, 1075–1082
  dynamics, 1111–1119
  engineering, 1119–1121
  free, 53–55
  growth dislocations, 1105–1111
  multiplication, 109–111
  postgrowth dislocations, 1111
  reduction process, 522–523
Dissociative sublimation, 628–630
Distributed parameter
  model-based control, 1164–1165
  system, 1146
Divariant system, 1261
DLA. *See* Diffusion-limited aggregation
DNS. *See* Direct numerical simulation
Donor acceptor pair (DAP), 610
Dopants, 302
  distribution, 916, 920–922, 926
Doping, 352–356, 636–638, 657–659, 701
  elements, 70
  striations, 1045
Double donors, 84
Double-crucible system, 142–146
Double-disk grinding (DDG), 748
DP. *See* Decoration precipitates; Dynamic polygonization
DPG. *See* Dipropylenglycole
Droplet oscillation method, 876
DS castings. *See* Directionally solidified castings
DS method. *See* Directional solidification method
DSE method. *See* Defect selective etching method
DTA. *See* Differential thermal analysis
DUV. *See* Deep ultraviolet
Dynamic Bond number, 881–882
Dynamic magnetic fields, 858
Dynamic polygonization (DP), 358–359, 1095, 1121–1123, 1122f
Dynamic stability, 782–785

E

EBSD. *See* Electron back-scatter diffraction
EDAX. *See* Energy dispersive X-ray analysis
EDG. *See* Electrodynamic gradient freeze
Edge-defined film-fed growth (EFG), 760–761, 872–873, 897
  crystal growth system, 902–904
  technique, 745
EDTA. *See* Ethylenediamine tetra-acetic acid
EEM method. *See* Elastic emission machining method
Effective segregation coefficient, 379–380, 1000–1001, 1018
  in zone purification, 1038
EFG. *See* Edge-defined film-fed growth
Ekman flow, 956
Elastic constant matrix, 1051–1057
Elastic emission machining method (EEM method), 750
Electrical power, 631–632
Electrical resistance heating, 462–463
Electro-magnetic-field-Czochralski method (EMCZ), 68, 858–859

Electrodynamic gradient freeze (EDG), 798–799, 821
Electrolytic crystallization, 1222
Electromagnetic CZ method-transverse magnetic fields (EMCZ-TMF), 858–859
Electromagnetic field (EM field), 263–264, 268, 858–859
Electron back-scatter diffraction (EBSD), 324
Electron paramagnetic resonance (EPR), 681–682, 1290
Electron probe microanalysis (EPMA), 305
Electron spin resonance (ESR), 1290, 1291f
Electron spin resonance imaging (ESRI), 1290–1291
Electronic-grade polysilicon, 69
Elliptical mirror furnaces, 466
ELOG. *See* Epitaxial lateral overgrowth
EM field. *See* Electromagnetic field
EMCZ. *See* Electro-magnetic-field-Czochralski method
EMCZ-TMF. *See* Electromagnetic CZ method-transverse magnetic fields
Emerald, 561–563
Enclosure analysis, 808–810
Energy dispersive X-ray analysis (EDAX), 305
Energy equation, 800–803
EPD. *See* Etch pits density
Epitaxial lateral overgrowth (ELOG), 520, 652–653, 659, 1110
EPMA. *See* Electron probe microanalysis
EPR. *See* Electron paramagnetic resonance
Equilibrium phase diagram, 1233–1234
  Ba-Cu-O system, 1234–1235
  of HTSC materials, 1234
  quasi-ternary phase diagram, 1235–1236
  RE-Ba-Cu-O system, 1234–1235
  standard gibbs free energy change, 1236–1239
Equilibrium temperature, 1236–1237
ESR. *See* Electron spin resonance
ESRF. *See* European Synchrotron Radiation Facility
ESRI. *See* Electron spin resonance imaging
Etch pits density (EPD), 215, 383–384
Ethyl silicate, 429
Ethylenediamine tetra-acetic acid (EDTA), 1206
ETP. *See* Exterior triple point
EURECA-1 mission, 493
European Organization for Nuclear Research (CERN), 158–159
European Synchrotron Radiation Facility (ESRF), 702
Eutectic solidification, 303
Evaporative crystallization, 1324
Existence region, 1098
Experimental methods, 1289–1292
Experimental validation, 828–829
Exterior triple point (ETP), 260
External fields
  dynamic magnetic fields, 858
  electromagnetic fields, 858–859
  static magnetic fields, 855–858
  vibrational effects, 859–860
Extrinsic point defect incorporation, 1100–1101

F

Face-centered cubic metals (fcc metals), 1120–1121
Faceted dendrites, 392–393
Faceted growth, 1249
Faceting, 1130–1136
Facets, 58, 121–124, 349–352
  formation, 1223
FB. *See* Flat belt
fcc metals. *See* Face-centered cubic metals
FE. *See* Free exciton
Fe-Ni-C system, 675
Feed rod, 251–252
Feed-forward controller, 1149–1150
Feedback controller, 1150–1153
FEM. *See* Finite element method
Fermi-level effect, 356, 1102
FET. *See* Field-effect transistor
FG. *See* Film growth
FIB technique. *See* Focused ion beam technique
Fick's law, 628, 1007
Fickian diffusion, 90

Field-effect transistor (FET), 703
Film growth (FG), 674
Film thickness formulation, 1008–1009
Finite dimensional model, 1146–1147
Finite element formulation, 1059–1060
Finite element method (FEM), 264, 452–453, 1146
First law of thermodynamics, 799
Fixed abrasive sawing, 721–722, 728–729, 735–737. *See also* Slurry-based sawing
Flame fusion method. *See* Verneuil method
Flat belt (FB), 675
Floating zone silicon crystal growth (FZ silicon crystal growth), 243, 246–249. *See also* Multicrystalline silicon (mc-Si)
  crucial FZ details
    feed rod, 251–252
    induction coil and arcing, 252–253
    molten zone and growth angle stability, 251
    origin and analysis of failures, 249
    rotation and pull rates, 250
  crystal morphology, 253
  development, 254–255
  doping techniques, 253–254
  exemplary results, 267–276
  floating zone process automation, 255–260
  historical overview, 262–263
  impurity distribution, 253–254
  mathematical models, 263–267
  numerical simulation, 260
  setup, 245–246
  zone melting purification, 243–245
Floating zone technique (FZ technique), 82, 914, 967–968, 1016, 1050, 1074, 1174
  application, 773
  automation
    Avogadro crystal, 259–260
    choice of reference and manipulated variables, 258–259
    measurement system description, 256–257
    modeling, 257–258
    motivation, 255–256
  axial magnetic field, 918–919
  CMF, 927
  control objectives, 1174
  conventional control, 1175
  measurement techniques, 1174–1175
  model-based control, 1176
  process characteristics, 1174
  reference trajectory planning, 1175
  RMF in, 931–932
  transverse magnetic field, 923
Floating-zone growth (FZ growth), 872–873
  crystal growth system, 892–897
  single crystal growth of intermetallic compounds, 313
    manganese silicides, 321–323
    RuAl, 318–319
    TiAl, 319–320
    TiNb, 323–326
    two-phase inductor and characteristics, 315–316
Flow control
  electromagnetic fields, 341–343
  vibrations, 344–345
Flow instability
  Baroclinic instability, 862
  Rayleigh–Bénard instability, 860–862
  turbulence, 862–863
Flow speed control, 1169
Fluid dynamics
  diffusion, 846–848
  external fields, 855–860
  flow instability, 860–863
  impurity transfer, 864–868
  natural and forced convections, 848–855
Fluid motion, 979
Fluids, 8
Fluorination process, 146–147
Flux. *See* Solvent
Flux growth, 1286
Flux method, 213, 224, 1243–1244
Flux tubes, 301
Focused ion beam technique (FIB technique), 321, 520–521
Forced convection, 61, 64, 496–498, 848–855, 1011
  correlations for disk-driven, 1018–1021
  Cz growth segregation under steady, 1029–1030

disk-driven, 1018–1021
empirical correlations for natural convection, 1021–1023
regimes, 496–498
segregation without, 1023–1028
Foreign phase particles, 1125
melt growth inclusions, 1129
precipitates, 1125–1126
second-phase particles, 1129–1130
solvent inclusions, 1126–1129
Fourier number, 999
Fourier transformed infrared spectroscopy (FTIR spectroscopy), 381, 610
Fourier's first law, 801
Fractal dendrites, 30–32
Frank-Read mechanism, 1114
Frank–van der Merwe growth, 405–406
Freckles formation, 441
Free exciton (FE), 610
FTIR spectroscopy. *See* Fourier transformed infrared spectroscopy
Full width at half maximum (FWHM), 176, 214, 524, 585
Furnace heat transfer, 814–816
FZ growth. *See* Floating-zone growth
FZ silicon crystal growth. *See* Floating zone silicon crystal growth
FZ technique. *See* Floating zone technique

G

Gadolinium gallium garnet (GGG), 812
Gadolinium orthosilicate. *See* Gadolinium silicate (GSO)
Gadolinium silicate (GSO), 152, 160–163, 1055, 1069
Gain scheduling, 1163
Gallium arsenide, 730
Gallium berlinites, 556–558
Gallium nitride (GaN), 133–134, 578, 622
ammonothermal growth techniques
historical development, 595–600
method, 600–602
properties, 610–612
prospects and future developments, 613
solubility in, 604–607
ammonothermal solution chemistry, 602–604
crystal growth, 506–507
condition, 507–509
Na effects, 509–513
doping under ammonothermal conditions, 608–610
growth rates and morphology, 607–608
LPE growth
characterization, 524–525
dislocation behavior, 520–523
GaN. *See* Gallium nitride
$[Ga(NH_3)_5Cl]Cl_2$. *See* Pentaaminechlorogallium (III) dichloride
Garnets ($A_3B_5O_{12}$), 1215–1216
Gas activation methods, 694
DC Arc-Jet CVD, 695–696
DC Plasma CVD, 695
hot filament CVD, 695
MPCVD, 696–698
Gas bubbles, 303
Gas cooling casting (GCC), 415, 418
Gas porosity, 442
Gas-to-solid condensation, 38–39
Gaseous species, 644
GCC. *See* Gas cooling casting
Gd_2SiO_5. *See* Gadolinium silicate (GSO)
Gebhart's analysis, 811–812
Gel, 1279
Gel–matrix interaction, 1289
Gels, crystallization in
aerogels, 1296–1301
biological macromolecules in, 1301–1304, 1305t
crystal
growth, 1301–1307
physical properties, 1302t–1303t
quality, 1279–1280
diffusion *vs.* convective transport, 1285–1295
gel growth
applications, 1295–1296
history, 1280–1282
properties, 1278
gel properties and characterization, 1282–1285

Gels, crystallization in (*Continued*)
hydrogels, 1296–1301
organic gels, 1296–1301
recombinant technologies, 1278–1279
Geometric model materials, 452
Geometrically necessary dislocation (GND), 1122
Geomicrobiology, 563–564
Germanium, 78
gFZ method. *See* granulate FZ method
GGG. *See* Gadolinium gallium garnet
Giant crystals, 21–24
Gibbs–Thomson effect, 58
Global heat transfer, 58–69
Glycothermal process, 536–537
GND. *See* Geometrically necessary dislocation
Golden beryl, 562–563
Grain boundaries, 1121
large-angle, 1123–1125
low-angle, 1121–1123
Grain control, 391–406
Grains selector, 418–420
Granoblastic rocks, 8–9
granulate FZ method (gFZ method), 254–255
Grashof number, 62, 142
Gravitational effects, 850–852
Greenwood–Foreman–Rimmer mechanism, 1130
Grey-Loc sealing, 540
Grid system, 848
Grinding, 748–750
Grown crystal, 1245
Growth
condition fluctuation, 1128–1129
dislocations, 1105
propagation of, 1106–1111
sources of, 1105–1106
kinetics, 645–647
parameters, 654–655
region, 512
speed, 291–292
twins, 1131–1135
Growth accidents. *See* Growth conditions fluctuation
Growth angle, 764–766
stability, 251
GSO. *See* Gadolinium silicate
GT Advanced Technologies (GTAT), 374
Gulliver–Scheil equation, 1002

H

4H-SiC growth, 626–627, 639–640
6H-SiC boules, 626–627
HAADF-STEM. *See* High angle annular dark field–scanning transmission electron microscopy
HAB. *See* High angle boundaries
HAS model. *See* Hassen–Alexander–Sumino model
Hassen–Alexander–Sumino model (HAS model), 388, 1075–1076
modified, 1083–1088
for multiaxial stress state, 1077–1079
for uniaxial stress state, 1076–1077
Hastelloy, 549
HB method. *See* Horizontal Bridgman method
HBCCO system. *See* Hg-Ba-Ca-Cu-O system
Heat exchanger method (HEM), 338
Heat field rotation method (HFRM), 188
Heat transfer, 954
modeling, 66
Heat transfer analysis, 822–828
boundary conditions, 803–805
energy equation, 800–803
experimental practice, 796–799
fundamentals, 799
in melt crystal growth, 805–816
research vignette, 820–833
theoretical developments, 817–820
Heat transport, 846
Heat treatment process, 423–425
Heater powers, 1166–1167
Heater-magnet module (HMM), 389
HEM. *See* Heat exchanger method
2-HEMA. *See* 2-hydroxyethyl methacrylate
HEMT. *See* High electron mobility transistor
HEN. *See* Heterogeneous nucleation
HEpiGANS. *See* Hydride Epitaxial GaN Simulator

Hertz–Knudsen equation, 627–628
Heterogeneous nucleation (HEN), 1330
Heterogeneous nucleation, 1327–1328
Heterosolvents, 470
HF. *See* Hydrogen fluoride
HFRM. *See* Heat field rotation method
Hg-Ba-Ca-Cu-O system (HBCCO system), 1231
High angle annular dark field–scanning transmission electron microscopy (HAADF-STEM), 304
High angle boundaries (HAB), 441
High critical temperature superconductors (HTSC), 1230
  applications of, 1233
  bulk crystal growth methods, 1239–1243
  crystal growth
    controlling factors, 1248–1251
    mechanism, 1251–1263
  high *Tc* oxide superconductors, 1231–1233
  phase diagram, 1233–1239
  single crystal growth methods, 1243–1248
  twin formation, 1263–1270
High electron mobility transistor (HEMT), 578
High energy physics, 164–165
High frequency heater, 135–136
High nitrogen pressure solution growth method (HNPS method), 579
  method and experimental setup, 579–581
  perspective for, 594–595
  seeded growth, 585–594
  spontaneous crystallization, 584–585
  thermodynamic and kinetic aspects, 581–583
High pressure cell, 678, 679f
High pressure high temperature (HPHT), 673
  diamond crystallization in non-metallic systems, 688
    carbonate-silicate systems, 688–689
    C–O–H system, 690
    diamond formation through redox reactions, 690–691
    phosphorus-carbon system, 691
    sulfide-carbon system, 689–690
    sulfur-carbon system, 689–690
  diamond crystals
    extended defects, 686–688
    morphology, 685–686
  diamond CVD process, 692f
  diamond specialties, 701–703
  NPD rods, 693f
  ultra-high pressure synthesis of bulk diamond, 691
High pressure solution growth method (HPSG method), 506, 509
High rate solidification method (HRS method), 414
High speed growth, 698–699
High *Tc* oxide superconductors
  HTSC materials, 1231
  YBCO system, 1232–1233
High-performance mc-Si, 397–403
High-pressure method, 347
High-temperature recovery mechanism, 1083
High-temperature region, 646
High-temperature solution growth, 1210. *See also* Low-temperature solution growth
  crystal growth techniques, 1219–1223
  facet formation, 1223
  fluxes composition and selection, 1211–1215
  growth instability, 1223
  high-temperature solvents properties, 1215–1219
  principle of, 1211
  single crystals, 1212t–1213t
HMF. *See* Horizontal magnetic field
HMM. *See* Heater-magnet module
HNPS method. *See* High nitrogen pressure solution growth method
Homoepitaxial seeded growth (HPSG), 654–656
Homogeneity region, 1098
Homosolvents, 470
Horizontal Bridgman method (HB method), 335, 872–873, 898–899, 914, 1006, 1103–1104
  crystal growth system, 898–902, 900f
Horizontal conditions, 768
Horizontal disks, 1022–1023
Horizontal magnetic field (HMF), 914

Hot filament CVD, 695
Hot zone, 50–51, 337, 632–633
  design, 385
    control of growth front, 386–387
    control of impurities, 389–391
    convection, 388–389
    growth rate, 387–388
    segregation, 388–389
    thermal stress, 388
  materials, 633–634
Hot-wall chemical vapor deposition (HT-CVD), 623
HPHT. *See* High pressure high temperature
HPSG. *See* Homoepitaxial seeded growth
HPSG method. *See* High pressure solution growth method
HRS method. *See* High rate solidification method
12-HSA. *See* 12 human serum albumin; 12-hydroxystearic acid
HT-CVD. *See* Hot-wall chemical vapor deposition
HTSC. *See* High critical temperature superconductors
HTW. *See* Hydrothermal wave
12 human serum albumin (12-HSA), 1290
Hurle's model, 362
HVPE. *See* Hydride vapor phase epitaxy
HVPE-GaN seeds, 588–589
HVPE-grown bulk GaN technique doping, 659
HVPE-grown nitrides, 656–657
Hydride Epitaxial GaN Simulator (HEpiGANS), 649
Hydride vapor phase epitaxy (HVPE), 578, 622. *See also* Aluminum nitride (AlN); Silicon carbide (SiC)
  growth kinetics, 645–647
  growth on foreign substrates
    bulk growth, 654
    characteristics, 649t
    HPSG, 654–656
    quasi-bulk single-wafer growth, 651–653
    substrates and buffers, 649–650
    template growth, 650–651
  growth related properties
    doping, 657–659
    native defects, 656–657
    residual impurities, 656–657
    structural defects, 659–661
  growth thermodynamic analysis, 641–644
  laboratory and industrial setups, 647–649
  nitride semiconductors, 641
  ternary nitride growth, 641–644
Hydrogels, 1295–1301
Hydrogen, 78
Hydrogen fluoride (HF), 139–140
Hydrothermal environments, 9–10
Hydrothermal growth process, 536–537
  advantages, 537–538
  apparatus, 548
    general purpose autoclaves, 551–553
    Morey autoclave, 549–551
    Tuttle–Roy cold-cone seal autoclaves, 551
  crystals, 553–566
  current trends in hydrothermal research, 538–541
  experimental investigations, 544–547
  fine to nanocrystals, 566–571
  history, 538–541
  intelligent engineering, 542
    phase formation principles, 543–544
    physicochemical and hydrodynamic principles, 542–543
    thermodynamic calculations, 547
  kinetics of crystallization, 544–547
  solubility, 544–547
  solution, 544–547
Hydrothermal method, 220–221
Hydrothermal wave (HTW), 884–886
2-hydroxyethyl methacrylate (2-HEMA), 1290–1291
12-hydroxystearic acid (12-HSA), 1290

I

Iceland spar, 560
ICP. *See* Inductively coupled plasma
ID. *See* Inner diameter
IDP. *See* Interplanetary dust particle
IGT. *See* Industrial gas turbines
III-nitride HVPE growth, 648

IISB. *See* Institute of Integrated Systems and Device Technology
Image furnace, 283
Immersion-seeded solution growth (ISSG), 188
Impurities, 302, 1101–1102
  distribution, 265–266, 270–271
  effects, 1199–1204
    mechanical impurities, 1206–1210
  transfer
    boundary layer, 864–865
    gas and melt mass transfer, 866–868
    mass transfer in gases, 865–866
IMS. *See* Institute for Molecular Science
In_2O_3. *See* Indium oxide
Inclusions, 362–365, 482–485
  melt growth, 1129
  solvent, 1126–1129
Indium oxide (In_2O_3), 223–227
Induction coil, 252–253
Inductively coupled plasma (ICP), 162–163
Industrial crystallization, 1317
  crystal growth, 1333–1337
  crystal nucleation, 1325–1333
  crystalline product, 1318–1319
  crystallization techniques, 1324–1325
  ensuring product quality, 1343–1345, 1344f
  molecular level process, 1319f
  process configuration, 1337–1343
  product quality, 1319–1322
  separation technology, 1318
  solubility, 1322–1324
  supersaturation, 1322–1324
  three forced-circulation crystallizers, 1318f
Industrial gas turbines (IGT), 414
Infinite dimensional system, 1146
Infrared (IR), 955
Infrared transmission (IRT), 961–962
Ingot annealing process, 1081–1082
Ingot growth methods
  casting and directional solidification, 374–377
  crucible and coating, 377–379
  impurities and defects, 379–385
Injection method, 347
InN formation, 643–644
Inner diameter (ID), 716, 899–900
Inner liner. *See* Protective inner layer
Inoculation, 796
Inorganic gels, 1295
Institute for Molecular Science (IMS), 148–150
Institute of Integrated Systems and Device Technology (IISB), 825
Integration-controlled growth, 1334
Intentional doping. *See also* Czochralski growth (Cz growth); Unintentional impurity incorporation
  co-doping of solar-grade Si, 78–79
  donors and acceptors, 77–78
  elements, 78
Interface
  effect, 818
  flipping, 807–808
  roughening, 806–807
  shape, 266, 272–274
    detection, 1168–1169
Interfacial kinetics
  solute diffusion model, 1257–1259
  from spiral growth, 1259–1261
Intermediate phase, 608
Intermetallics, 313–314
Internal radiation, 808–809, 812–814
Internal triple point (ITP), 260
International Hydrothermal Symposium, 540–541
International Space Station (ISS), 1004
International standard crystal lattice defects, 1094
Interplanetary dust particle (IDP), 38–39
Interstitials, 88
Intrasectorial zoning, 25
Investment casting process, 430
Ion implantation technologies, 745–746
IR. *See* Infrared
Iron borate ($FeBO_3$), 1132–1133
IRT. *See* Infrared transmission
Isolated substitutional nitrogen (C-centers), 679

Isothermal method, 1188
Isotherms, 487, 801
  condition, 807
Isotropic analysis, 1061
ISS. *See* International Space Station
ISSG. *See* Immersion-seeded solution growth
Itinerant antiferromagnet compound, 321
ITP. *See* Internal triple point

J
Jackson factor, 349–350, 350t
Jackson parameter, 1249
Johnson-Mehl-Avrami-Kolmogorov model, 16
Joulean heat sources, 265

K
Kanthal heater, 339
KBBF. *See* Potassium beryllium borate fluoride
$KBe_2BO_3F_2$. *See* Potassium beryllium borate fluoride (KBBF)
KDN. *See* Dai-ichi Kiden Corporation
KDP. *See* Potassium dihydrogen phosphate
Kerfless technologies, 745
KGT model. *See* Kurz–Giovanola–Trivedi model
Kinetic Monte Carlo simulation, 693–694
Kinetic regimen, 1198
Kinetic roughening, 807
Kratochvil equation, 1288–1289
KTA. *See* Potassium titanyl arsenate
$KTiOPO_4$. *See* Potassium titanyl phosphate (KTP)
KTP. *See* Potassium titanyl phosphate
Kubota–Mullin model, 1200–1202
Kurz–Giovanola–Trivedi model (KGT model), 453–454
Kyropoulos process, 1176–1178, 1177f

L
L-pit defect. *See* A-swirl defect
La-Ba-Cu-O system, 1231
LAB. *See* Low angle boundaries
LAGBs. *See* Low-angle grain boundaries
Lang topogram, 350, 350f
Lapping, 748–750
Large fluoride crystals, 146–147. *See also* Scintillator crystals
  As-grown crystals, 148
  chirped-pulse amplification, 152
  growth technique, 147–148
  solid-state lasers, 150–152
  transmission properties, 148–150
Large Hadron Collider (LHC), 158–159
Large-angle grain boundaries, 1095, 1123–1125
Large-eddy simulation (LES), 886–888
Laser chemical processing, 747–748
Laser crystals, 170
  Tm-and Ho-Doped GGG, 171
    crystal growth, 171–174
    laser properties selection, 176–178
  vanadate crystals, 178
    bulk spiral formation mechanism, 180–187
    crystal growth and quality, 179–180
    properties, 187
Laser-induced damage threshold (LIDT), 199
LASSCGM. *See* Levitation-assisted self-seeding crystal growth method
Latent heat, 808
Lateral convection, 1006
Lateral photovoltage scanning method (LPS method), 249
Lateral segregation, 1039
  convection, 1040–1042
  curved solid–liquid interface, 1039–1040
  local Nusselt numbers, 1044
  nonequilibrium segregation, 1043–1044
Lattice Boltzmann method (LBM), 1293
Laue diffraction indexing, 445
Laue method, 304, 444–445
Layer transfer process from porous silicon, 746–747
LBM. *See* Lattice Boltzmann method
LBO. *See* Lithium triborate
Leach bauxite, 538–539
Lead fluoride (PbF_2), 138, 144–146
Lead magnesium niobate–lead titanate (PMNT), 983
Lead molybdate (PMO), 1056
  thermal stress analysis, 1065–1069

Lead tungstate (PWO), 152, 158–160
LEC technique. *See* Liquid-encapsulated Czochralski technique
LED. *See* Light-emitting diodes
LES. *See* Large-eddy simulation
LEVB method. *See* Liquid encapsulation vertical Bridgman method
LEVGF method. *See* Liquid encapsulation vertical gradient freezing method
Levitation-assisted self-seeding crystal growth method (LASSCGM), 225
LHC. *See* Large Hadron Collider
LiB_3O_5. *See* Lithium triborate (LBO)
LID. *See* Light-induced degradation
LIDT. *See* Laser-induced damage threshold
Liesegang structures, 28–29
Lift-off process, 699
Light scattering tomography (LST), 89
Light-emitting diodes (LED), 133–134, 505–506, 578, 624
Light-induced degradation (LID), 381
Limit theories, 1001–1005
$LiNbO_3$. *See* Lithium niobate (LN)
Liquid Al. *See* Aluminum nitride (AlN)—powder
Liquid encapsulation, 347–348
Liquid encapsulation vertical Bridgman method (LEVB method), 338
Liquid encapsulation vertical gradient freezing method (LEVGF method), 338
Liquid metal cooling method (LMC method), 414, 418
Liquid phase epitaxy (LPE), 962, 1245
  growth
    multifeed seed configuration, 587–594
    single seed configuration, 585–587
Liquid-encapsulated Czochralski technique (LEC technique), 106, 1120, 1150–1151, 1155
  CdTe, ZnTe, and ZnSe, 118
  GaAs, 113–114
  GaP, 114–118
  growth constraints to crystal quality
    B_2O_3 role, 126–127
    evaporative group V loss, 119–120
    facets, 121–124
    nonstoichiometric and alloy melts growth, 124–126
    point defects, 120–121
    twinning, 121–124
  historical background, 106–107
  InAs, 113–114
  InP, 114–118
  semiconductor properties, 107–108
$LiTaO_3$. *See* Lithium tantalate (LT)
Lithium niobate (LN), 1054
  thermal stress analysis, 1063–1065
Lithium tantalate (LT), 1054
  thermal stress analysis, 1063–1065
Lithium triborate (LBO), 192–195
LMC method. *See* Liquid metal cooling method
LN. *See* Lithium niobate
Local equilibrium, 998–999
Local interface shape, 349–352
Local Nusselt numbers, 1044
Local vibration modes (LVM), 83
Longitudinal concentration profiles, 72–73
Loose abrasive sawing technique, 718, 733–735
Low angle boundaries (LAB), 441
Low pressure/high temperature annealing (LPHT annealing), 700–701
Low-angle grain boundaries (LAGBs), 636, 1095, 1121–1123
Low-temperature
  crystallization, 1187–1192
  region, 645–646
Low-temperature solution growth, 1187. *See also* High-temperature solution growth
  crystal growth
    mechanical impurities effect, 1206–1210
    rates, 1199–1206
    techniques, 1193–1196
  dead supersaturation zone, 1199–1206
  factors affecting crystal growth, 1196–1199
  solvents selection, 1192–1193
Low-thermal-gradient CZ technique (LTG CZ technique), 156–157
LPE. *See* Liquid phase epitaxy

LPHT annealing. *See* Low pressure/high temperature annealing
LPS method. *See* Lateral photovoltage scanning method
LST. *See* Light scattering tomography
LT. *See* Lithium tantalate
LTG CZ technique. *See* Low-thermal-gradient CZ technique
Lumped parameter model, 1146–1147, 1155–1156, 1171
  model-based control, 1163–1164
Lutetium, 163
LVM. *See* Local vibration modes
Lyapunov method, 782
Lyothermal process, 536–537

M

Macrosegregation mechanism, 1256–1257
Magmatic environments, 5–8
Magnetic fields (MF), 67–69, 910, 1028
  in crystal growth process, 944t
  electric currents *vs*., 941–943
  magnetohydrodynamics, 911–913
  nonsteady magnetic fields, 928–941
  steady magnetic fields, 914–927
Magnetic liquid–encapsulated Kyropoulos (MLEK), 119
Magnetic resonance imaging (MRI), 164
Magnetohydrodynamics, 911–913
Manganese silicides, 321–323
Manipulated variables, 1145–1146
Marangoni convection, 762–764, 873, 884, 1012
  in crystal growth
    Bridgman method, 897–904
    CZ crystal growth system, 886–892
    EFG crystal growth system, 902–904
    FZ crystal growth system, 892–897
  HTW, 884–886
  Marangoni–Benard instability, 882–883, 882f
  thermo-solutocapillary convection, 878–882
Marangoni effect, 63, 872, 872f
Marangoni flow. *See* Thermocapillary convection
Marangoni number, 764
Marangoni–Benard instability, 882–883, 882f
Mass transfer, 954
  convection coefficient, 1009
  gas and melt, 866–868
  in gases, 865–866
  process, 1286
Mass transport, 846, 1294–1295
Material transport coefficient, 485
Mathematical model, 1146
Matrix precipitates (MP), 363
MBE. *See* Molecular beam epitaxy
mc. *See* Multicrystalline
MC simulations. *See* Monte Carlo simulations
mc-Si. *See* Multicrystalline silicon
MD. *See* Molecular dynamics
Mechanical
  ball milling, 290–291
  machining, 748–749
  stirring, 954
MEG. *See* Monoethylenglycole
Melt
  convection, 388–389, 910
    classification, 1010–1012
    lateral melt convection model, 1015–1016
  equilibrium, 999–1000
  flow, 265, 270–271, 997
  growth inclusions, 1129
  melt-grown compound crystals, 1123
  melt-textured Y-123 materials, 1251
  melting rate, 257
  mixing, 910
Melt crystal growth, heat transfer in, 805–816
Melt-powder-melt-growth (MPMG), 1239–1240
Melt-texture-growth (MTG), 1239–1240
Meniscus region, 1154–1155
Mercury cadmium telluride (HgCdTe), 825
MESFET. *See* Metal-semiconductor field-effect transistor
Metal organic chemical vapor deposition method (MOCVD method), 515, 612
  growth, 652–653
Metal-organic vapor phase epitaxy (MOVPE), 1110

Metal-semiconductor field-effect transistor (MESFET), 703
Metallic alloy system, 1252–1253
Metamorphic
  environments, 8–9
  grade, 8–9
  rocks, 8–9
Metastable phase. *See* Intermediate phase
Metastable zone width (MSZW), 1188–1190, 1327f
MF. *See* Magnetic fields
MFS. *See* Multifeed seed
Micro-pulling-down method (μ-PD method), 773–776, 1222–1223
Microgravity
  environment, 873, 877
  growth, 493
Microparticle generation, 1125
Micropipes, 639
Microsegregation, 1044–1045. *See also* Lateral segregation
Microvoids, 1125
  generation, 1125
Microwave plasma chemical vapor deposition (MPCVD), 696–698
Milne–Eddington approximation, 814
MIMO. *See* Multi-input-multi-output
Mineral morphology, 12
Mineral pattern formation, 24–25
Minimum-energy theorem, 1108, 1110–1111
Mixed convection, 1012, 1017
  CZ process with, 1031–1034
  segregation model with, 1016–1018
Mixed suspension mixed product removal crystallizer (MSMPR crystallizer), 1339, 1340f
MLEK. *See* Magnetic liquid–encapsulated Kyropoulos
Mobile dislocation immobilization, 1083, 1086–1088
MOCVD method. *See* Metal organic chemical vapor deposition method
Model predictive control, 1152–1153, 1152f, 1165
Model-based control, 1151–1152
  control system, 1163–1165
  detached Bridgman process, 1173
  FZ technique, 1176
  lumped parameter approach, 1160
Molding system, 431
Molecular beam epitaxy (MBE), 612
Molecular dynamics (MD), 1293–1294
Molten
  material surface tension, 873–878
  oxide surface tension, 878
  salt electrolysis, 225
  semiconductor surface tension, 877–878
  silicon surface tension, 873–877, 876f
  zone stability, 251
Molybdenum (Mo), 133
Mono-ellipsoid furnaces, 466
Mono-like casting, 403–406
Monoclinic single crystal
  elastic constant matrix, 1055, 1055f
  thermal strain vector, 1059
Monoethylenglycole (MEG), 719–720
Monovariant system, 1261
Monte Carlo simulations (MC simulations), 1294
Morey autoclave, 549–551
Morganite, 562–563
Morphology, 1320–1321
Mosaic structures, 700
MOVPE. *See* Metal-organic vapor phase epitaxy
MP. *See* Matrix precipitates
MPCVD. *See* Microwave plasma chemical vapor deposition
MPMG. *See* Melt-powder-melt-growth
MPS-GaN sub. *See* Multipoint-seed-GaN substrate
MRI. *See* Magnetic resonance imaging
MS focus. *See* Multistable focus
MSMPR crystallizer. *See* Mixed suspension mixed product removal crystallizer
MSZW. *See* Metastable zone width
MTG. *See* Melt-texture-growth
MTHM. *See* Multipass traveling heater method
Mullite, 427–428

Multi-anvil apparatus, 676–678. *See also* Belt-type apparatus; Toroid-type apparatus
Multi-input-multi-output (MIMO), 1166–1167
Multi-wire sawing process, 717
  mono-and multicrystalline silicon process investigations, 722–723
    fixed abrasive sawing, 728–729
    slurry-based sawing, 723–728
  technologies, 718–722
    crystal structures, Vickers and Mohs hardness, 719t
    fixed abrasive sawing, 721–722
    slurry-based sawing, 718–720
Multiaxial stress state, 1077–1079
Multicrystalline (mc), 1117
Multicrystalline silicon (mc-Si), 374, 866–867, 1114. *See also* Vertical Bridgman growth (VB growth)
  crystal growth, 374
  grain control, 391–406
  hot-zone design, 385–391
  ingot growth methods, 374–385
  nucleation, 391–406
  PV industry, 374
Multifeed seed (MFS), 585
Multipass traveling heater method (MTHM), 475
Multipass zone melting, 1039. *See also* Single-pass zone melting
Multipoint-seed-GaN substrate (MPS-GaN sub), 527–528
Multipulling, 48
Multistable focus (MS focus), 27

N

n-type wide band gap semiconductor, 564
Na flux method
  GaN crystal growth, 506–507
    condition, 507–509
    Na effects, 509–513
  GaN LPE growth
    characterization, 524–525
    dislocation behavior, 520–523
    nitrogen dissolution mechanism investigation, 513–515
    nucleation control, 515–519
    point seed and coalescence growth technique, 525–531
Na-flux point seed technique (SPST), 525–527
Nanomolar (nM), 1289
Nanopolycrystalline diamond rods (NPD rods), 693f
Native elements, 563–565
Native point defect thermodynamics, 1096–1098
Natural convection, 61, 628, 1011, 1015–1016, 1023
  centrifugal effects, 852–854
  computation, 848
  convective–diffusive transport, 854–855
  crucible rotations, 849–850
  crystal rotations, 849–850
  empirical correlations for, 1021–1023
  gravitational effects, 850–852
  vanishing, 1024–1028
Navier–Stokes equations (N–S equations), 265, 997, 1001, 1009
  momentum equation, 851
Nd. *See* Neodymium
ND. *See* Neutron diffraction
Near infrared (NIR), 234, 293–294
Necking, 53–55
Needle-eye FZ growth process, 262
Negative coefficient, 606
Neodymium (Nd), 1235
Neodymium-Doped Single Vanadate Crystals, 186t
Neumann principle, 187
Neutron diffraction (ND), 1278
New donors, 84
Newton's iteration scheme, 487
Newton's law of cooling, 804–805
Nickel-based superalloys, 423–425
NIR. *See* Near infrared
Nitrogen, 78
  dissolution mechanism, 513–515
  doping, 637
  nitrogen-containing

synthetic diamond crystals, 687–688
type I diamond, 679–682
nitrogen-free type IIa diamond, 683–684, 683f
precipitates, 381
NLO crystals. *See* Nonlinear optical crystals
nM. *See* Nanomolar
NMPC. *See* Nonlinear model predictive control
NMR imaging. *See* Nuclear magnetic resonance imaging
"No-mixing" diffusion-controlled segregation, 1003–1005
Nobel Symposium, 540–541
Non-isothermal method. *See* Polythermal method
Noncontact crucible method, 405–406
Nonequilibrium, 999
in melt, 999–1000
segregation, 1043–1044
Nonlinear model predictive control (NMPC), 256
Nonlinear optical borate crystals, 187–202. *See also* Laser crystals
Nonlinear optical crystals (NLO crystals), 187–188, 1206
Nonmetallic inclusions, 439
Nonsteady magnetic fields, 928. *See also* Steady magnetic fields
AMF, 932–934
RMF, 928–932
TMF, 934–941
Nonstoichiometric point defects, 1098
Novel organic hydrogels, 1298
NPD rods. *See* Nanopolycrystalline diamond rods
N–S equations. *See* Navier–Stokes equations
Nuclear magnetic resonance imaging (NMR imaging), 1278, 1292, 1292f
Nucleation, 391–406
Nucleation control, carbon doping for, 515–519
Nucleus, 1329
Numerical simulations, 1005, 1292–1295
Nusselt number, 1009–1010, 1018
correlations
for disk-driven forced convection, 1018–1021
for natural convection, 1021–1023
segregation model with, 1016–1018
Nutrient composition concentration diagrams (NC diagrams). *See* Composition—diagrams

O

OB crystallizer. *See* Oscillatory baffled crystallizer
Observability, 1148
Observer, 1147–1148
OD. *See* Outer diameter
OFZ technique. *See* Optical floating zone technique
Ohm's law, 912
OIC. *See* Oxygen ion concentration
One-dimensional defects, 1094–1095
One-dimensional perpendicular convection, 1005
Open-loop control, 1145–1146
Optical diameter estimation, 1161
Optical floating zone technique (OFZ technique), 213, 283, 285t–288t
advantages and disadvantages, 284
ceramic rod preparation, 290–291
congruently and incongruently melting oxides, 298–299
constitutional supercooling, 300–301
crystal
characterization, 301–305
growth termination and cooling, 298
crystallization, 300–301
experimental setup, 288–290
growth
atmosphere, 296–298
conditions, 291–292
overpressure, 296–298
rotation, 294–295
temperature distribution, 292–294
Optical heating, 465–466
Organic additives, 1204–1206
Organic gels, 1295–1301
Orowan's law, 1084

Orthorhombic phase transition, 1263–1270
Orthorhombic single crystal
  elastic constant matrix, 1057
  thermal strain vector, 1059
Oscillatory baffled crystallizer (OB crystallizer), 1341
Oscillatory techniques, 953
  ACRT, 955–968
  AVC, 968–980
  constant-speed rotation in melts, 953–954
  CVS, 982–983
  USV, 981–982
Oscillatory zoning, 25–26
OSF. *See* Oxidation-induced stacking fault
Out-of-specification losses, 96
Outer diameter (OD), 899–900
Oxidation-induced stacking fault (OSF), 76, 86–88
Oxide crystal growth, 888–892
Oxide superconductors, 1214–1215
Oxygen
  diffusion coefficient, 1264–1265
  precipitates, 381
    density, 85–86
    formation, 84–85
  in silicon, 79–88
    atomistic configurations, 82–83
    diffusivity, 83–84
    formation, 84
    OSF, 86–88
    reaction and aggregation, 84–86
    solubility, 83
    technical relevance of oxygen effects, 82
  source, 916–917
Oxygen ion concentration (OIC), 1215–1216

P

P-T conditions. *See* Pressure-temperature conditions
Pacific Northwest National Laboratory (PNNL), 825–826
Parameter scheduling, 1163
Parasitic nucleation, 578
Passivated emitter and rear cell (PERC), 399–400
PB. *See* Pressure balancing
$PbMoO_4$. *See* Lead molybdate (PMO)
PBN. *See* Pyrolytic boron nitride
$PbWO_4$. *See* Lead tungstate (PWO)
PCVM. *See* Plasma chemical vaporization machining
PDAS. *See* Primary dendrite arm spacing
PDG method. *See* Pendant drop growth method
Péclet number, 802–803, 1011–1012
PEG. *See* Polyethylenglycol
Pegmatites, 7–8
Pendant drop growth method (PDG method), 774
Pentaaminechlorogallium (III) dichloride, 603–604
PEO. *See* Poly(ethylene) oxide
PERC. *See* Passivated emitter and rear cell
“Perfect mixing” diffusion-controlled segregation, 1001–1003
Perfect silicon. *See* Defect-free silicon
Peritectic solidification, 1251
Perovskites (ABO_3), 1215–1216
Perpendicular convection, 1006
PET. *See* Positron emission tomography
PF crystallizer. *See* Plug flow crystallizer
Pfann’s segregation function, 479
pH-Redox-Equilibrium (PHREEQC), 1295
Phase, 543
  formation principles, 543–544
  phase-change interface, 805–808
Phenomenological approach, 1009–1010
Phosphides, 119
Phosphorus-carbon system, 691
Photomultiplier tube (PMT), 153
Photovoltaic industry (PV industry), 374
PHREEQC. *See* pH-Redox-Equilibrium
Physical gels, 1296–1298
Physical vapor transport (PVT), 218, 623, 625–631, 865–866
PID controller. *See* Proportional-integral-derivative controller
“Pint-point” inclusions, 687
Plasma chemical vaporization machining (PCVM), 749–750

PLC. *See* Programmable logic controllers
Plug flow crystallizer (PF crystallizer), 1340
PMNT. *See* Lead magnesium niobate–lead titanate
PMO. *See* Lead molybdate
PMT. *See* Photomultiplier tube
PNNL. *See* Pacific Northwest National Laboratory
Point defects, 120–121, 356
  complex formation, 1101–1103
  dynamics, 1098–1100
  engineering, 1103–1104
  extrinsic point defect incorporation, 1100–1101
  native point defect thermodynamics, 1096–1098
Polarity, 603
Polishing, 748–750
Poly(ethylene) oxide (PEO), 1290–1291
Polyacrylamide gels, 1295
Polycrystallinity, 1123–1125
Polyethylenglycol (PEG), 719–720
Polyscale crystal form, 536–537
Polythermal method, 1188–1190
Polyvinyl alcohol (PVA), 1295–1296
Poor man's gemstones. *See* Colored quartz crystals
Population density, 17–19
Porosity investigation, 442–444
Positron emission tomography (PET), 152, 164
Postgrowth
  dislocations, 1111
  processes, 484
  treatment, 700–701
  twins, 1131–1135
Potassium beryllium borate fluoride (KBBF), 199–201
Potassium dihydrogen phosphate (KDP), 1110
Potassium sulfate (K_2SO_4), 1207–1208
Potassium titanyl arsenate (KTA), 559–560
Potassium titanyl phosphate (KTP), 558–560
Power down method, 415–416
Power law equation, 1249
Prandtl number (Pr), 802–803, 971, 1246–1247
Precipitates, 362–365, 482–485, 1125–1126
Preferred direction theory, 1106–1109
Pressure balancing (PB), 106
  Czochralski growth, 108
    LEC technique, 113–118
    MLEK, 119
    VCz techniques, 109–111
Pressure-temperature conditions (P-T conditions), 673–674
Pressurized cold crucible method, 221
Preston equation, 723
Primary dendrite arm spacing (PDAS), 423
Primary nucleation, 480. *See also* Secondary nucleation
Process control, 267
Process' Theory, 479
Programmable logic controllers (PLC), 1151
Proportional-integral-derivative controller (PID controller), 1150–1151
  conventional PID-based control, 1161–1163
Protective inner layer, 602
Protein crystallization, 1305, 1306f–1307f
Pseudocubic lattice parameters, 1241–1242
Pull rates, 96, 250
Pulling systems, 466–467
Pulsed magnetic gradient spin echo, 1291–1292
Purification, 480–482
Pushing/trapping model, 1256–1257
PV industry. *See* Photovoltaic industry
PVA. *See* Polyvinyl alcohol
PVT. *See* Physical vapor transport
PWO. *See* Lead tungstate
Pyrolusite dendrites, 30
Pyrolytic boron nitride (PBN), 338, 348, 822, 825–826
Pythagoras' theorem, 1241–1242

Q

Quartz, 553–556
  sand, 48
Quasi-bulk single-wafer growth, 651–653
Quasi-mono casting. *See* Mono-like casting
Quasi-ternary phase diagram, 1235–1236
Quenched-melt-growth (QMG), 1239–1240

R
Radiation heat transfer, 808–814
Radio frequency (RF), 221, 294
  heating, 463–465
Rafting, 438
Rapid prototyping methods, 430–431
Rapid tooling method (RT method), 430–431
Rare earth (RE), 1233
  ions, 609
  vanadates, 563
Raw powder materials, 139–140
Rayleigh convection. *See* Buoyancy convection
Rayleigh–Bénard
  convection, 1023
  instability, 860–862
RE. *See* Rare earth
RE-123 single crystal growth, 1248
RE-Ba-Cu-O system, 1234–1235
Ready-to-use crucibles, 378–379
Recombinant technologies, 1278–1279
Reconstitution technique, 675
Red sapphire, 132, 561–563
Red zone, 377
Reference trajectory
  generator, 1147
  planning, 1175
Refined approach, 1168–1169
Relative supersaturation, 627
Repetition effect, 482
Resistance heating (RH), 136, 463
Retarded doping, 353
Retrograde solubility. *See* Negative coefficient
Reynolds number, 802–803
RF. *See* Radio frequency
RGS method. *See* Ribbon growth on substrate method
RH. *See* Resistance heating
Ribbon growth on substrate method (RGS method), 745
Ridges, 57–58
RMF. *See* Rotating magnetic field
Rock-forming minerals, 1–2
Rossby number, 862
Rotating magnetic field (RMF), 68, 342, 389, 494–496, 856–857, 928–932
Rotation rates, 250
Rough growth, 1335
Rough interface, 59
Rounded crystal surfaces
  capping, 1126–1128
  faceting, 1126–1128
RT method. *See* Rapid tooling method
Ruby. *See* Red sapphire
Runge-Kutta algorithm, 772–773
Ruthenium aluminides (RuAl), 318–319

S
S-C system. *See* Sulfur-carbon system
S-L. *See* Solid–liquid
Sagging of crucible wall, 49
Sapphire single crystals, 132
  growth
    apparatus, 134–135
    technique, 135–136
  properties, 133t
SAW. *See* Surface acoustic wave
Sawing mechanisms, 738. *See also* Wafer processing
  slurry-based sawing, 738–745
    elastohydrodynamic behavior of slurry and wire, 742–744
    material removal rate, 740–742
    roughness and subsurface damage, 744–745
SAXS. *See* Small angle X-ray scattering
SC. *See* Scattering center
SC castings. *See* Single crystal castings
Scalable compact rapid ammonothermal technique (SCoRA technique), 596–600, 602
Scanning electron microscopy (SEM), 173, 520–521, 1279–1280
Scattering center (SC), 142
SCF technology. *See* Supercritical fluid technology
Scheil's equation, 72–73, 355
Schmidt number (Sc), 1246–1247
Scintillator crystals, 152
  applications, 163–165
  BGO, 154–157

CWO, 152, 157–158
GSO, 152, 160–163
lutetium and silicates, 163
PWO, 152, 158–160
SCoRA technique. *See* Scalable compact rapid ammonothermal technique
Screening effect, 1113
Second harmonic generation (SHG), 558–559, 1206
Second phase particles. *See* Foreign phase particles
Second-phase particles, 1129–1130
Secondary ion mass spectrometry (SIMS), 320
Secondary nucleation, 1332–1333
Sectorial structure, 12
Sectorial zonation, 25
Sedimentary environments, 10–11
Seed
fixation, 635
orientation, 189–190
Seeded growth, 634–636, 654
Seeding, 492–493, 1240–1242, 1341–1342
Segregation, 352–356, 388–389, 475–479, 997. *See also* Lateral segregation; Microsegregation
coefficients, 69–72, 997–1001
convective heat and mass transfer, 1005–1012
CZ process, 1029–1034
without forced convection, 1023–1028
limit theories, 1001–1005
model with mixed convection, 1016–1018
Nusselt number
correlations for, 1018–1023
model with, 1016–1018
theories on solute layer thickness, 1012–1016
ZM, 1034–1039
Selenides, 347
Self-flux approach, 299, 1243
SEM. *See* Scanning electron microscopy
Semi-insulating GaN bulk substrates, 659
Semi-insulating HNPS-MFS-GaN crystals, 593–594
Semiconductor materials, 622
Semitransparent media, 812
Sessile drop method, 766
Seya-Namioka monochromator, 148–150
SF. *See* Stable focus
Shape stability analysis, 776
capillary stability and applications to dewetting, 779–782, 785–788
dynamic stability, 782–785
heat transfer and growth rate importance, 777–779
practical stability, 785–788
static stability, 776–777
Shaping processes, 773–774
Sherwood number (Sh), 1010
SHG. *See* Second harmonic generation
Shrinkage porosity, 442–443
SiC. *See* Silicon carbide
Siemens process, 251–252
Σ3 twins, 1132
Silicon, 716–717
crystal growth, 886–888
Silicon carbide (SiC), 622, 719–720, 865–867. *See also* Crystal growth
bulk crystal, 623
for blue LED production, 624
cross-section drawings of hot zone setups, 623f
industrial synthesis, 623–624
bulk single crystals, 635f
chemical attachment, 636
precipitates, 381–382
spiral growth, 631
structural defects, 638–640, 639f
Silicon on sapphire (SOS), 133
Simple oxides, 563–565
SIMS. *See* Secondary ion mass spectrometry
Simulation tool for atom technology (STATE), 513, 518
Single crystal castings (SC castings), 414. *See also* Directionally solidified castings (DS castings)
grains selector, 418–420
solidification from seed, 420–421
Single crystal growth methods, 1243–1248. *See also* Bulk crystal growth methods
Single indentation tests
fixed abrasive sawing, 735–737

Single indentation tests (*Continued*)
loose abrasive sawing, 733–735
Single molecule spectroscopy, 1289
Single molecule tracking method. *See* Single molecule spectroscopy
Single scratch tests, 735f, 736
Single-component material, 794
Single-crystal dendrites, 30
Single-input-single-output (SISO), 1166–1167
Single-pass zone melting
"partial" mixing, 1038
"perfect" mixing, 1037–1038
Single-phase inductor, 313–314, 314f
SISO. *See* Single-input-single-output
Slicing technologies, 745. *See also* Wafer processing
ion implantation technologies, 745–746
wafering technologies
laser chemical processing, 747–748
layer transfer process from porous silicon, 746–747
Slip polygonization. *See* Dynamic polygonization (DP)
Slivers, 441–442
sLN. *See* Stoichiometric lithium niobate
Slow-cooling method, 1219–1220
Slurry-based sawing, 718–720, 738–745. *See also* Fixed abrasive sawing
dependence on slurry properties, 724–726
elastohydrodynamic behavior of slurry and wire, 742–744
force in ingot feed direction, 723
friction forces, 723–724
material removal rate, 740–742
roughness and subsurface damage, 744–745
saw marks, 727–728
wafer thickness, wire diameter, and particle size distribution, 727
wire tension, 726
Small angle X-ray scattering (SAXS), 1284
SnO_2. *See* Stannic oxide
Sodium flux method, 579
Sodium silicate (SS), 1282–1283
Solar system formation, 37
Solar-grade polysilicon (SoG polysilicon), 375
Solid state recrystallization (SSR), 475, 498
Solid-state lasers, 150–152
Solidification kinetics, 794–795
Solidification path, 5–6
Solid–liquid (S-L), 911
interface, 1039–1040
Solubility, 1322–1324
temperature dependency, 1191–1192
Solute, 1192
Solute diffusion model, 1252–1257
with interfacial kinetics, 1257–1259
Solute layer thickness, segregation theories on, 1012
BPS theory, 1012–1014
lateral melt convection model, 1015–1016
natural convection model, 1015–1016
Wilson–Garandet's model, 1014–1015
Solute-rich liquid crystal-pulling (SRL-CP), 1239, 1244
crystal growth mechanism, 1257–1261
enlargement of single crystal size, 1246–1248
method, 1244–1245
RE-123 single crystal growth, 1248
Solution crystallization, 1333–1334
Solution growth, 794
Solution-stirring technique (SS technique), 199
Solutioned castings, 423
Solutocapillary
convection, 880
flow, 873, 901–902
Solvent, 299
inclusions, 1126–1129
selection, 1192–1193
Solvent evaporation technique, 1194–1195, 1220
Solvothermal process, 536–537
Soret effect, 1286
SOS. *See* Silicon on sapphire
SP. *See* Static polygonization
Sparry calcite, 11
Species distribution, 72
CCz technique, 73–74
lateral nonuniformity, 74–75
longitudinal concentration profiles, 72–73

species transfer modeling, 66
species transport, 69
numerical modeling, 72
Spin probe, 1290
Spinels (AB_2O_4), 1215–1216
Spiral grain selectors, 420
Spiral growth, 631, 631f, 1259–1261
Spiral shearing flow, 956
Spontaneous crystallization, 584–585
Spontaneous nucleation, 491–492
Spontaneously nucleated single crystals, 630f
SPST. *See* Na-flux point seed technique
SRL-CP. *See* Solute-rich liquid crystal-pulling
SS. *See* Sodium silicate
SS technique. *See* Solution-stirring technique
SSR. *See* Solid state recrystallization
Stability, 1156
phase diagram, 27f
Stable focus (SF), 27
Standard gibbs free energy change, 1236–1239
Stannic oxide (SnO_2), 228–230
STATE. *See* Simulation tool for atom technology
State estimation, 1156–1160
State estimator, 1147–1148, 1148f
Static
magnetic fields, 493–494, 855–858
stability, 776–777
Static polygonization (SP), 1122
Steady magnetic fields, 67, 914
axial magnetic field, 914–919
CMF, 923–927
transverse magnetic field, 919–923
Steady state
growth rate, 1256
segregation, 1004
STHM. *See* Sublimation traveling heater method
Stirring effect, 344
Stoichiometric lithium niobate (sLN), 1223
Stokes–Einstein equation, 1288
Strain grains, 441
Stress, 274–275
Striations, 76–77, 303
“String ribbon” method, 745
“Stucco” method, 431–433
Sublimation traveling heater method (STHM), 470
Submerged heater, 343–344
Sulfide-carbon system, 689–690
Sulfides, 563–565
Sulfur-carbon system (S-C system), 689–690
Supercritical ammonia, 595
Supercritical fluid technology (SCF technology), 552
Supersaturation, 1247–1249, 1322–1324, 1339
Surface, 871
energies, 761–762
energy, 761
radiation, 809–812
reaction control, 511
tension, 871–872
of molten materials, 873–878
Surface acoustic wave (SAW), 1063
Surface-active impurities, 685–686
effect, 685–686
Syneresis, 1282
Synthetic diamonds, 677–679
mixed type Ib þ IaA, 682
morphology, 685
nickel and cobalt impurities, 682
sources of nitrogen, 679–680

T

Tammann-Ströber method. *See* Vertical gradient freezing (VGF)
Tantalum carbide (TaC), 633
Taylor number, 862
TC diagrams. *See* Temperature *vs.* concentration diagrams
TCO. *See* Transparent conducting oxide
TCP phases. *See* Topologically close-packed phases
TEDDI. *See* Tomographic energy dispersive diffraction imaging
Tellurides, 347
TEM. *See* Transmission electron microscopy
Temperature
control, 1168–1169
field, 264–265, 269

Temperature (*Continued*)
fluctuations, 96
gradients, 190
techniques, 1195–1196, 1221–1222
Temperature gradient growth method (TGG method), 675
Temperature gradient zone melting (TGZM), 460–462
Temperature *vs*. concentration diagrams (TC diagrams), 543–544
Temperature-changing technique, 1194
Template growth, 650–651
Ternary phase diagram, 1261–1263
Tetraethyl orthosilicate (TEOS), 1282–1284
Tetragonal single crystal
elastic constant matrix, 1056
thermal strain vector, 1059
Tetramethyl orthosilicate (TMOS), 1282–1284
Texture of rock, 16
TGG method. *See* Temperature gradient growth method
TGZM. *See* Temperature gradient zone melting
Theoretical simulation, 1292–1295
Thermal
budget, 96–97
donors, 84
field rotation, 954
strain vector, 1058–1059
stress analysis in bulk single crystals, 1050–1073
Thermo-solutocapillary convection, 878–882
Thermocapillary convection. *See* Marangoni convection
Thermocapillary flow, 63
Thermocapillary Reynolds number, 880–881
Thermodynamic approach, 1130
Thermomechanical stress, 266–267
Thermovibrational convection. *See* Fluid motion
Thin-film technologies, 210
Thixotropy, 1282
THM. *See* Traveling heater method
Three-dimensional defects, 1095
Three-dimensional flow patterns, 1006
Three-phase boundary (TPB), 359–360
Three-phase junction line (TPL), 349
Three-point bending tests, 1070–1071
THZR. *See* Traveling heater zone refining
Time of flight (TOF), 163
Time-dependent
creep deformation, 1076–1077
magnetic fields, 68
Titanium Aluminides (TiAl), 319–320
Titanium Niobium (TiNb), 323–326
Tl-Sr-Ca-Cu-O system (TSCCO system), 1231
TMAl. *See* Trimethylaluminum
TMF. *See* Traveling magnetic field
TMOS. *See* Tetramethyl orthosilicate
TOF. *See* Time of flight
Tomographic energy dispersive diffraction imaging (TEDDI), 545–546
Top-seeded solution growth (TSSG), 188, 1244–1248. *See also* Solute-rich liquid crystal-pulling (SRL-CP)
Topologically close-packed phases (TCP phases), 437
Toroid-type apparatus, 676, 677f. *See also* Belt-type apparatus; Multi-anvil apparatus
Total thickness variation (TTV), 731–733, 744
TPB. *See* Three-phase boundary
TPL. *See* Three-phase junction line
Transient Couette flow, 955–956
Transient modeling, 267, 275–276
Transition metals, 382–383
Transmission edge, 148–150
Transmission electron microscopy (TEM), 89, 218, 520–521
Transparent conducting oxide (TCO), 209–210
Transparent semiconducting oxide (TSO), 209–210
basics, 210–212
electrical and optical properties, 230–235, 232t–233t
growth techniques, 212–230
Transverse magnetic field, 914, 919–923
Trapping phenomena, 1250–1251
Traveling heater method (THM), 931–932, 964, 460
advantages and issues, 461–462

inclusions, 482–485
mass and heat transport, 485–491
materials, 478
precipitates, 482–485
principle, 460–461
purification, 480–482
segregation, 475–479
single crystal growth, 491
forced convection regimes, 496–498
under magnetic fields, 493–496
microgravity growth, 493
seeding, 492–493
SSR, 498
technology, 462
feed material, 468
pulling systems, 466–467
zone heating mode, 462–466
versatile, 468–475
Traveling heater zone refining (THZR), 480
Traveling magnetic field (TMF), 68, 342, 389, 913, 928, 934–941, 934f
Traveling solvent floating zone technique (TSFZ technique), 284, 299, 1244
Traveling solvent method (TSM), 460
Trigonal single crystal
elastic constant matrix, 1054, 1054f
thermal strain vector, 1058
Trimethylaluminum (TMAl), 637–638
TSCCO system. *See* Tl-Sr-Ca-Cu-O system
TSFZ technique. *See* Traveling solvent floating zone technique
TSM. *See* Traveling solvent method
TSO. *See* Transparent semiconducting oxide
TSSG. *See* Top-seeded solution growth
TTV. *See* Total thickness variation
Tungsten (W), 133, 634
Turbulence, 862–863
Turbulent flows, 1020–1021
Tuttle–Roy cold-cone seal autoclaves, 551
Tweed pattern, 1268–1269
Twin formation, 1263–1270
“Twin law”, 1131
Twin-free Crystal, 1269–1270
Twinning, 121–124, 1130–1136
Twins, 359–362, 1131–1132, 1132f
Two-dimensional defects, 1095
Two-dimensional flow patterns, 1006
Two-dimensional formulations, 769–770
Two-phase inductor, 315–316
Two-step epitaxial lateral overgrowth (2S-ELOG), 652–653

U

Ultra-high pressure synthesis of bulk diamond, 691
Ultrasonic sound velocity measurement technique, 324
Ultrasonic vibration (USV), 981–982
Ultraviolet light sources (UV light sources), 146–147
Ultraviolet Synchrotron Orbital Radiation (UVSOR), 148–150
Uniaxial stress state, 1076–1077. *See also* Multiaxial stress state
Unidirectional solidification method, 866–867, 1252–1257
Uniform suction flow, 1003–1004
Unintentional impurity incorporation, 79
carbon, 81
oxygen, 79–81
Unstable focus (UF), 27
Upgraded metallurgical silicon (UMG), 381

V

Vacancies, 302
Vacuum ultraviolet applications (VUV applications), 139–140
van’t Hoff equation, 1322–1323
Vapor phase reaction, 223–224
Vapor pressure–controlled Czochralski techniques (VCz techniques), 106, 109–111, 1104, 1155
Vapor transport growth, 622
VB growth. *See* Vertical Bridgman growth
VCz techniques. *See* Vapor pressure–controlled Czochralski techniques
Velocity magnitude, 1169
Verneuil method, 213, 783

Vertical Bridgman growth (VB growth), 335, 902, 914, 917–918, 1006, 1103–1104
  axial magnetic field, 917–918
  binary compound semiconductors
    crucibles, 348–349
    crystal defects, 356–365
    doping, 352–356
    facets and local interface shape, 349–352
    inorganic compound semiconductors, 332, 333t
    liquid encapsulation, 347–348
    segregation, 352–356
    synthesis, 346–347
  bottom-seeded, 1028
  equipment
    basics, 336–338
    specifics, 338–345
  hardware of, 336
  III-V and II-VI compounds, 335
  optimization and control, 345–346
  optoelectronic devices, 332–334
  problem in, 335
  process, 1165, 1168f
    characteristics, 1166–1167
    control objectives, 1166–1167
    conventional control, 1167
    model-based control, 1167–1169
  RMF in, 930–931
  TMF in, 937–938
  transverse magnetic field, 922–923
Vertical Gradient Freeze process (VGF process), 137–138, 336–337, 914, 1016, 1103–1104, 1165
  axial magnetic field, 917–918
  control objectives, 1166–1167
  conventional control, 1167
  model-based control, 1167–1169
  process characteristics, 1166–1167
  RMF in, 930–931
  TMF in, 937–938
  transverse magnetic field, 922–923
Vertical magnetic field (VMF), 914
Vertical walls, 1021–1022
Very hard materials, 730
VGF process. *See* Vertical Gradient Freeze process
Vibrational effects, 859–860
Viscous fingering, 31–32
VMF. *See* Vertical magnetic field
Void defect, 89
Volume diffusion
  control, 511
  controlled growth, 1334
von Mises stress, 267
Vorobyevite. *See* Morganite
VUV applications. *See* Vacuum ultraviolet applications

W

Wafer processing, 716
  compound and dielectric materials, 729–730
  economic issues and future development, 717
  electronic grade silicon, 729
  grinding, lapping, and polishing, 748
    EEM method, 750
    mechanical machining, 748–749
    PCVM, 749–750
  multi-wire sawing process, 717–730
  wafer properties, 730
    fracture behavior, 737–738
    single indentation tests, 733–737
    surface properties, 731–738
Washington State University (WSU), 825–826
Water-soluble crystals growth
  with embedded nanoparticles, 1208–1210
  with embedded organic molecules, 1206–1208
Water/solvent of syneresis, 1282
Wax model assemblies, 430–431
Weakest link, 737
Weighing technique, 1157–1159
Weight measurement, 1161–1162
Weight mode, 1162
Wetting angle, 766–767
White sapphire, 132
Wide bandgap materials, 622
  high temperature sublimation growth
    bulk SiC and AlN growth, 623–625
    crystal growth, 625–631

high temperature sublimation growth technology, 631–638
structural defects in PVT-grown SiC and AlN bulk crystals, 638–640
Wilson–Garandet's model, 1014–1015
Wire breakage, 728
Wrinkles, 442
WSU. *See* Washington State University

X
X-ray analysis, 1278
X-ray computed tomography (X-ray CT), 152, 163–164
X-ray diffraction (XRD), 585, 1277–1278
X-ray free-electron laser oscillator (XFELO), 702
X-ray rocking curve (XRC), 585
Xerogels, 1300–1301

Y
Y-123 phase crystals growth, 1249–1251
flux requirement, 1255–1256
steady state growth rate, 1256
Y-211 phase crystals growth, 1250–1251
dissolution of, 1255
Y-Ba-Cu-O system (YBCO system), 1214–1215, 1231–1233, 1248–1249
YAG. *See* Yttrium aluminumgarnet
$YBa_2Cu_3O_{7-\delta}$ material (Y-123 material), 1231
YBCO system. *See* Y-Ba-Cu-O system
Young's moduli, 324
Young–Laplace equation, 764
approximations, 770–772
axisymmetric formulations, 769–770
floating zone process application, 773
meniscus shape in Czochralski configuration, 770–772
micro-pulling-down methods, 773–776
nonlinearity, 769
ribbon thickness in pendant drop growth, 773–776
Runge-Kutta algorithm, 772–773
two-dimensional formulations, 769–770
Yttria-stabilized zirconia (YSZ), 1243–1244
Yttrium (Y), 1233
Yttrium aluminumgarnet (YAG), 812

Z
Zebra grains, 442
Zero-dimensional defects, 1094
Zero-force theorem, 1108–1109
Zinc fluoride (ZnF_2), 144–146
Zinc oxide (ZnO), 218–223
Zirconium dioxide, 429
Zirconium silicate ($ZrSiO_4$), 425–426
Zonal structure, 12
Zone melting (ZM), 243, 998, 1034–1039
mode, 462–466
Zone purification, 1038